

# Biomimetic Routes To Hierarchical- Functional Nanomaterials

A thesis submitted for the degree of Doctor of Philosophy

by

Uchechukwu Kingsley Onwukwe

Supervised by

Professor Paul. A. Sermon



Wolfson Centre

College of Engineering, Design and Physical Sciences

Department of Mechanical Engineering

To my beloved parents, Kingsley & Christine Onwukwe.

Find what motivates you,  
and if it happens to be ego and vanity,  
so be it.

© 2019

Uchechukwu Kingsley Onwukwe

All rights reserved

# Acknowledgments

I would like to extend my deepest gratitude to my supervisor, Professor Paul A. Sermon, for helping me craft and realise this vision that is my doctorate project. I am honestly thankful that I had the opportunity to work with someone with such patience and a brilliant mind, who was always found when needed. In the same breath, I would like to acknowledge the enormous contributions from Mrs Mandy Sermon, for making sense of the rambling thoughts of an over-caffeinated brain.

Much appreciation goes to the technical staff: Mr Abdul Ghani for thermal analysis, Dr Ashley Howkins for electron microscopy, Dr Lorna Anguilano for X-ray diffraction, Ms Nita Verma of infrared spectroscopy and Dr Nicholas Nickleby Nelson for Raman spectroscopy. A special mention goes to Dr Lesley Hanna, the maker of ways where bureaucracy thinks otherwise.

Not to be forgotten, I would like to take the opportunity to acknowledge my Wolfson colleagues. They truly were the stars that brought laughter in times of difficulties. In no particular order, Dr. Virginia Torrejon, Dr. Myles Worsley, Dr. Arjang Amini, Dr Alex Metcalfe, Dr. Samuel Rust, Dr. Iman Al-Timimi, Dr. Inma Andreas, Dr. Andrea Mazzocut, Dr. Fatullah Ghazali, Dr. Henry Song, and Dr. J.C. Eloi.

Before I finish, I would like to thank Dr. Pelin Yilmaz and Dr. Shehzad Dorairaj for their constant support and encouragement.

# List of symbols and Abbreviations

°C	Celsius	PVAc (or AC)	Poly vinyl acetate
$\lambda$	Wavelength	TA	Tannic acid
$h$	Planck's constant	AL	Alginate
$\nu$	Velocity of light	J/g	Joule per gram
Å	Angstrom	ppm	Parts per million
$d$	Distance between crystallographic planes	mg	milligram
$\theta$	Bragg angle	ml	Millilitre
$k_1$	First order rate constant	nm	Nano-metre
$k_2$	Second order rate constant	$\mu\text{m}$	micrometre
A	UV-vis absorbance	mm	millimetre
$R^2$	Square of correlation coefficient		
S, min, d	Seconds, minutes, day.	PY	pyridine
$t_{1/2}$	Half life	Ace	acetone
EC	<i>Eucalyptus camaldulensis</i>	at%	Atomic percentage
RR	<i>Rotala rotundifolia</i>	$\beta$	Broadening
CV	<i>Chlorella vulgaris</i>	$\epsilon$	Lattice strain
HA	Hydroxyapatite		
SBF	Simulated body fluid		
PBS	Phosphate buffer solution		
$\beta$	Gentamicin sulphate		
AA	Ascorbic acid		
MO	Methyl orange		
MB	Methylene blue		
PVA (or VA)	Poly vinyl alcohol		
PLA	Poly lactic acid		
PC	Poly caprolactone		

# Abstract

It is undeniable that nanosystems are interesting materials, displaying properties that are fascinating and different from their bulk material counterparts. These exciting properties are perhaps one of the main motivations fuelling the quest for nanoscale as the next frontier in material science. Certainly, as science moves forward, it is becoming more apparent that nature that has been designing materials on a nanoscale for eons and that we have a lot that we can learn from its capabilities in more bottom-up preparations. Learning and borrowing from nature has led to the growth of the biomimetic materials fields.

Here, the author has attempted to produce novel functional nano materials as photocatalysts and bone graft substitutes by combining biomimicry and nano-scaling. It is hoped that the final hierarchical functional nanomaterials will benefit the society in general.

In this thesis, the photocatalytic properties of titania replicas that have been obtained using *Eucalyptus camaldulensis* and *Rotala rotundifolia* biotemplates were synthesised and characterised. It was discovered that the biotemplated replicas ended up forming mixed oxide systems, which could degrade MO and TX-100 in water. They were also successfully incorporated in a novel asymmetric floating film, which retained its photocatalytic properties in an immobilised format.

Bone graft substitutes utilising hydrogel blends were also synthesised to resemble vesicle like membranes, seen during ossification, for the mineralisation of amorphous calcium phosphates (ACP) and crystalline hydroxyapatite (CDHA). The resulting mineralised hydrogel scaffolds showed improved mechanical properties for use in low load bearing areas, as well as being bioactive when tested in SBF. The scaffolds as a whole, showed an ability to take up and release MO, MB and AA, thus highlighting their secondary use as drug delivery devices.

Finally, biodegradable PLA microspheres were synthesised and successfully coated with CaP and a titanium phase. They were shown to be able to uptake and release the drug gentamicin afterwards.

Taken as a whole, this thesis sheds lights on the use of biomimicry to create templates capable of forming functional materials like TiO<sub>2</sub> and CDHA, as well as the factors that need to be considered to ensure that the necessary properties are achieved and preserved.

## Table of Contents

<b>Chapter I</b>	<b>Introduction</b>	<b>17</b>
I.1	Nanotechnology and nanomaterials	17
I.1.1	Properties of nanomaterials	17
I.1.1.1	Toxicity/challenge of using nanomaterials	19
I.1.1.2	The nucleation and growth of nanoparticles/structure	20
I.1.2	Synthesis and fabrication of nanomaterials	24
I.1.3	Biomimicry	29
I.1.4	Case for biotemplating using hierarchical templates to achieve nanostructures	32
I.1.5	TiO <sub>2</sub> model catalytic nanomaterials	33
I.1.6	Functions: Photo assisted adsorption and decomposition	44
I.1.7	Role of nanosizing, biomimicry in catalysis and photocatalysis	46
I.1.8	Nano-sized mineralised tissue, cellular deposition and nucleation of hydroxyapatite	48
I.1.9	Potential functional material role in bone repair	53
I.1.10	Role of nanosizing in mineralised tissue engineering	55
I.2	Aims of the project	57
I.2.1	Sources of sources of templates	59
I.3	Thesis overview	60
I.4	Precision, accuracy, errors and limitations	61
<b>Chapter II</b>	<b>Experimental Methodology</b>	<b>62</b>
II.1	Sol gel synthesis of TiO <sub>2</sub> replicas of biotemplates	62
II.1.1	Materials	62
II.1.2	Pre-treatment procedure for EC and RR	62
II.1.3	Preparation procedure of EC and RR titania replicas	63
II.1.4	Preparation procedure of CV titania replica	63
II.2	Photocatalytic template film preparation	63
II.2.1	Preparation of PVAc based films	63
II.2.2	Preparation of PVA based films	63



II.2.3	Preparation of dual/asymmetric film .....	64
II.2.4	Incorporation of titania, CV and other molecules into the asymmetric films .....	65
II.3	Hydrogel scaffold preparation.....	66
II.3.1	Preparation of pure PVA hydrogel discs .....	66
II.3.2	Preparation of PVA hydrogel blends .....	66
II.4	Calcium <sub>(x)</sub> phosphate <sub>(y)</sub> mineralization of PVA hydrogels and its blends .....	67
II.4.1	Materials.....	67
II.4.2	Mineralisation procedure.....	67
II.5	PLA/PVA Microsphere synthesis using PVA as a surfactant.....	68
II.5.1	Materials.....	68
II.5.2	Modification of the surfactants composition for PLA-PVA microspheres .....	68
II.6	Modification of PLA-PVA Microsphere interior.....	68
II.7	Modification of PLA-PVA Microsphere exteriors.....	69
II.7.1	To produce titanium (TiO <sub>x</sub> ) exteriors .....	69
II.7.2	To produce Calcium <sub>(x)</sub> Phosphate <sub>(y)</sub> (Ca <sub>x</sub> P <sub>y</sub> ) exteriors .....	69
II.8	Principles of characterisation techniques and instruments.....	70
II.8.1	Compression Testing.....	70
II.8.2	Dynamic light scattering (DLS).....	70
II.8.3	Differential Scanning Calorimetry (DSC).....	70
II.8.4	Electron Microscopy.....	71
II.8.5	Energy Dispersive spectroscopy (EDS).....	71
II.8.6	FT-IR Spectroscopy.....	72
II.8.7	Micro-Raman .....	72
II.8.8	UV-vis spectroscopy .....	73
II.8.9	Thermo gravimetric analysis (TGA) .....	73
II.8.10	Powder X-Ray Diffractometry (XRD) .....	73
II.9	Experimental setup and methods.....	74
II.9.1	Colourimetric test for Ca <sup>2+</sup> .....	74
II.9.2	Colourimetric test for phosphate.....	75

II.9.3	UV-vis testing for gentamicin .....	76
II.9.4	Raman spectroscopy testing for gentamicin .....	76
<b>Chapter III</b>	<b>Leaf Biomimicry via Sol Gel Synthesis .....</b>	<b>77</b>
III.1	Introduction .....	77
III.2	Background.....	78
III.2.1	Plants and their leaves .....	78
III.3	Aim .....	81
III.4	Methodology.....	82
III.4.1	Sample preparation .....	82
III.4.2	Characterization Techniques.....	85
III.4.3	Sample nomenclature .....	85
III.5	Results and Discussion.....	86
III.5.1	TGA -Thermal analysis .....	86
III.5.2	Morphological characterisation: .....	89
III.5.3	Compositional analysis .....	95
III.5.4	Infrared characterization:.....	97
III.5.5	Crystallographic characterisation of the calcined samples.....	101
III.6	Summary.....	110
III.6.1	TGA.....	110
III.6.2	Electron Microscopy and elemental analysis.....	110
III.6.3	Infrared characterisation .....	111
III.6.4	Crystallographic characterisation .....	111
III.7	Conclusion.....	112
<b>Chapter IV</b>	<b>Photocatalytic properties of the replica biotemplates .....</b>	<b>114</b>
IV.1	Introduction .....	114
IV.2	Aim .....	115
IV.3	Background.....	115
IV.3.1	Surface reactions and adsorption .....	115
IV.3.2	Model Pollution Candidate (dyes) .....	118

IV.3.3	Transformation kinetics estimation .....	118
IV.4	Methodology.....	119
IV.4.1	Photo-degradation .....	119
IV.4.2	Active site characterisation using FTIR.....	121
IV.4.3	TiO <sub>2</sub> phase characterisation using Raman spectroscopy .....	121
IV.5	Results & Discussion.....	121
IV.5.1	Photocatalysis: UV-vis results .....	121
IV.5.2	<i>Composition: size and crystallographic phases</i> .....	124
IV.5.3	<i>Band gap consideration</i> .....	126
IV.5.4	<i>Acid site analysis</i> .....	127
IV.6	Summary.....	131
IV.6.1	Photocatalysis.....	131
IV.6.2	TOF assessment.....	133
IV.6.3	Composition size and crystallographic phases .....	133
IV.6.4	Band gap consideration .....	133
IV.6.5	Active site analysis.....	134
IV.7	Conclusion/future work.....	135
<b>Chapter V</b>	<b>Assembly of immobilised floating photocatalyst.....</b>	<b>136</b>
V.1	Introduction .....	136
V.2	Aim .....	136
V.3	Background.....	137
V.4	Photocatalyst immobiliser for consideration .....	138
V.5	Model Pollution Candidate (surfactant) .....	139
V.6	Experimental technique and methodology .....	140
V.6.1	Sample preparation .....	140
V.6.2	Experimental setup for photocatalysis.....	140
V.6.3	Analytical instruments and conditions.....	141
V.6.4	Sample nomenclature .....	141
V.7	Results.....	142

V.7.1	Photocatalytic degradation of MO degradation.....	142
V.7.2	Results of the Photocatalytic degradation of Triton (TX-100) .....	154
V.7.3	Electron microscopy of dual-film samples.....	159
V.7.4	Infrared analysis of the dual-film systems.....	163
V.8	Summary.....	165
V.8.1	Photocatalytic performance.....	165
V.8.2	Infrared spectroscopy.....	168
V.8.3	Scanning electron microscopy .....	168
V.9	Conclusion.....	169
<b>Chapter VI</b>	<b>Synthesis of hydroxyapatite hydrogel scaffold .....</b>	<b>171</b>
VI.1	Introduction .....	171
VI.2	Aim .....	172
VI.3	Background Information.....	172
VI.4	Methodology.....	176
VI.4.1	Experimental setup for swelling properties.....	176
VI.4.2	Analytical instruments and conditions.....	176
VI.4.3	Sample nomenclature .....	177
VI.5	Results.....	178
VI.5.1	Non-carbonated method.....	178
VI.5.2	Carbonate-modified template hydrogels.....	181
VI.5.3	Effect of changes in the crosslink density on the carbonate modified sample system.....	184
VI.5.4	Infrared characterisation of the carbonate modified samples with varying crosslinks density .....	185
VI.5.5	Raman of carbonate modified samples with varying crosslinks and increasing deposition cycles.....	188
VI.5.6	Effect of hydrogel composition .....	190
VI.5.7	Swelling properties.....	196
VI.6	Summary.....	197

VI.6.1	Non-carbonated samples.....	197
VI.6.2	Carbonated samples .....	197
VI.6.3	Changes in crosslink density of PVA hydrogels and PVA HA .....	198
VI.6.4	Infrared analysis of PVA hydrogels and PVA HA.....	198
VI.6.5	Raman of carbonate modified samples with varying crosslinks and increasing deposition cycles of PVA hydrogels and PVA HA.....	199
VI.6.6	Effect of composition changes on Raman and FTIR spectra.....	199
VI.6.7	Swelling properties.....	200
VI.7	Conclusion/Future works.....	200
<b>Chapter VII Crystallographic properties of the mineralised hydrogel scaffolds.....</b>		<b>204</b>
VII.1	Introduction.....	204
VII.2	Aim .....	205
VII.3	Background.....	205
VII.4	Methodology.....	208
VII.4.1	Analytical instruments and conditions.....	208
VII.5	Results.....	208
VII.5.1	XRD.....	208
VII.5.2	TEM .....	224
VII.6	Summary.....	232
VII.6.1	XRD & WH -PLOTS .....	233
VII.6.2	TEM .....	235
VII.7	Conclusion.....	235
<b>Chapter VIII Mechanical and thermal properties of the mineralised hydrogel scaffolds.....</b>		<b>237</b>
VIII.1	Introduction.....	237
VIII.2	Aim .....	237
VIII.3	Background.....	237
VIII.4	Methodology.....	238
VIII.4.1	Analytical instruments and conditions.....	238

VIII.5	Results.....	239
VIII.5.1	Compression testing of the scaffolds.....	239
VIII.5.2	TGA of the hydrogels (and mineralised scaffolds).....	245
VIII.5.3	DSC.....	250
VIII.6	Summary.....	258
VIII.6.1	Compression testing of the hydrogels (and mineralised scaffolds) .....	258
VIII.6.2	TGA of the hydrogels (and mineralised scaffolds).....	259
VIII.6.3	DSC of the hydrogels (and mineralised scaffolds) .....	261
VIII.7	Conclusion.....	262
<b>Chapter IX</b>	<b>Bioactivity and degradation of the mineralised hydrogel scaffold .....</b>	<b>264</b>
IX.1	Introduction .....	264
IX.2	Aim.....	264
IX.3	Background.....	264
IX.4	Experimental technique and methodology .....	267
IX.4.1	Analysis conditions.....	267
IX.5	Results.....	269
IX.5.1	Calcium ion and phosphate ion uptake .....	269
IX.5.2	Bioactivity studies using colourimetric analysis.....	271
IX.5.3	pH of the sample during the bioactivity studies.....	275
IX.5.4	Gravimetric analysis of the samples before and after bioactivity studies .....	276
IX.5.5	Infrared spectroscopy of the samples before and after bioactivity test.....	277
IX.5.6	X-Ray diffraction of the samples before and after bioactivity studies.....	279
IX.5.7	Electron microscopy of the samples before and after bioactivity studies .....	281
IX.6	Degradation studies .....	284
IX.7	Summary.....	285
IX.8	Conclusion & future works.....	288
<b>Chapter X</b>	<b>Sorption kinetics of the mineralised hydrogel scaffolds. ....</b>	<b>290</b>
X.1	Introduction .....	290
X.2	Aim.....	290

X.3	Background.....	290
X.4	Methodology.....	292
X.4.1	Analytical instruments and conditions.....	292
X.4.2	Samples nomenclature .....	293
X.5	Results.....	294
X.5.1	Uptake behaviour of MB .....	294
X.5.2	Release behaviour of MB from mineralised and unmineralized hydrogels .....	306
X.5.3	Uptake behaviour of other probe molecules.....	307
X.5.4	Comparison of sorption across all samples .....	310
X.6	Summary.....	313
X.6.1	General uptake behaviour and selectivity of the different probe molecules.....	313
X.6.2	Equilibrium studies of MB on the samples .....	315
X.6.3	Kinetics of MB on the samples .....	315
X.6.4	Adsorbate area.....	315
X.7	Conclusion.....	315
<b>Chapter XI</b>	<b>Microspheres .....</b>	<b>317</b>
XI.1	Introduction .....	317
XI.2	Background.....	317
XI.3	Aim .....	319
XI.4	Methodology.....	320
XI.4.1	Analytical instruments and conditions.....	320
XI.4.2	Sample nomenclature .....	321
XI.5	Results.....	321
XI.5.1	SEM.....	321
XI.5.2	DLS.....	331
XI.5.3	TEM .....	331
XI.5.4	XRD of the microspheres.....	339
XI.5.5	FTIR.....	342
XI.5.6	DSC.....	353

XI.6	Summary.....	357
XI.6.1	Electron Microscopy.....	357
XI.6.2	XRD.....	358
XI.6.3	FTIR.....	359
XI.6.4	DSC.....	360
XI.7	Conclusion.....	361
<b>Chapter XII</b>	<b>Drug (GC) release of the prepared microsphere systems .....</b>	<b>362</b>
XII.1	Introduction .....	362
XII.2	Background.....	362
XII.3	Aim .....	363
XII.4	Methodology.....	364
XII.4.1	Experimental setup.....	364
XII.4.2	Analytical instruments and conditions.....	364
XII.5	Results.....	365
XII.5.1	Drug surface loading and release studies.....	365
XII.5.2	Electron microscopy characterisation.....	368
XII.5.3	DSC analysis .....	374
XII.6	Summary.....	378
XII.6.1	GC release in the microspheres .....	378
XII.6.2	GC release the GC-cored systems.....	380
XII.7	Conclusion.....	381
<b>Chapter XIII</b>	<b>Conclusion .....</b>	<b>383</b>
XIII.1	Introduction.....	383
XIII.2	Aim .....	383
XIII.3	Extent of achieving the initial aims.....	383
XIII.4	Future work.....	385
<b>Bibliography.....</b>		<b>387</b>



## Chapter I Introduction

### I.1 Nanotechnology and nanomaterials

The British Standards Institution proposed definition shall be relied upon to define the meaning of nanotechnology and nanomaterials. Nanotechnology is defined as the “manipulation and control of matter on the nanoscale dimension by using scientific knowledge of various industrial and biomedical application” (Jeevanandam *et al.*, 2018). Nanomaterials are those with “ internal or external structures on the nanoscale dimensions” (Jeevanandam *et al.*, 2018). As one can see, these definitions are deliberately made to be as broad as possible to include most nanosystems. The general aim (especially in terms of nanotechnology) is the establishment of a relationship between the physical properties and phenomena in relation to the nanometre scale (Cao, 2004).

Nanotechnology, and indeed nanomaterials are by no means new, colloidal gold was prepared by Michael Faraday in the 18<sup>th</sup> century. Before that, the Chinese were known to utilise gold nanoparticles for the purposes of dyeing fabrics red (Cao, 2004). The ancient Egyptians also used PbS nanoparticles for the purpose of hair dyeing 4000 years ago; they also created “Egyptian blue”, a synthetic mixture consisting of  $\text{CaCuSi}_4\text{O}_{10}$  and  $\text{SiO}_2$  in the 3<sup>rd</sup> century (Jeevanandam *et al.*, 2018). The only differences between these and present approaches is in our ability to analyse these nanoscale materials, and then manipulate them (Cao, 2004). In the close past, we have seen the shrinking of devices within the semiconductor sector (e.g. seen transistors moving from the cm range to the nm range). Quite recently  $\text{SiO}_2$  nanoparticles were used to replace carbon black in rubber reinforcement, and in 2012 Logitech created the iPad keyboard powered by dye-sensitized  $\text{TiO}_2$  nanoparticles for capturing and converting solar energy (Jeevanandam *et al.*, 2018). Again, this progress was helped along by the advancing technologies of characterisation by electron microscopy and manipulation by scanning tunnelling microscopy. At the same time one has to remember that there are concerns about free nanomaterials (The Royal Society *et al.*, 2004), but the author returns to this in 1.1.2.

#### I.1.1 Properties of nanomaterials

The increased utilisation of nanomaterials (as opposed to bulk materials) is attributed mainly to their novel properties arising from their nanoscale dimensions. For example, nanoparticles (NPs) have:

- I. lower melting point and phase transition. The lower melting point can be attributed to the increased surface energies of the smaller sized nanomaterials, with larger occurrence of surface atoms un-passivated and in a disordered state (Aliofkhazraei, 2016). Gold NPs have lower melting points than 1337K as their size approaches 5nm (Aliofkhazraei, 2016.); this has a long lineage because in 1870-1909 ((Skinner and

Sambles, 1972)) Lord Kelvin, Ostwald and Pawlow developed equations (Equation 8 and Equation 9) showing that as the average material particle size ( $r$ ) (at constant density ( $\rho$ ), temperature  $T$  and surface tension ( $\gamma$ )) *decreased* so its vapour pressure ( $p_{(c)}$ ) *increased* and its solubility ( $S_{(NP)}$ ) *increased* relative to bulk values ( $p_{(\infty)}$  and  $S_{(\infty)}$ ) and at the same time its melting point ( $T_m$ ) decreased.

- II. improved mechanical properties. It is known that mechanical strength increases in a perfect crystal. The main reasoning for this is said to be down to the perfection of the crystal: a crystal/particle with nanoscale dimension supposedly carries very little defects in its grain; some of these act as stress concentration sites in a crystal, magnifying applied stress (Cao, 2004; Callister and Rethwisch, 2009). Eliminating them means a higher theoretical strength is achieved. Sodium whiskers have also been demonstrated to show a size dependent effect on the mechanical strength (Cao, 2004).
- III. increased conductivity and resistivity. Conduction in materials is usually affected by collision with phonons and defects in a lattice etc (Cao, 2004). While a reduction in a material's dimension will increase the likelihood of obtaining a perfect crystal, increased scattering off these surfaces, especially if the dimension is smaller than the electrons free mean path, leads to increased resistivity in the material-especially if the scattering is inelastic.
- IV. designer band gaps due to quantum confinements. The reduced sizing, common in semiconductor particles that are  $1 < r < 25$ nm (Takagahara and Takeda, 1992), creates a quantum size effect where electrons and holes are spatially confined, losing the quasiparticle behaviour in preference for more particle like characteristic. The normally continuous energy levels become quantized, with the band gap increasing quite significantly e.g. 4.8nm PbSe NPs have a band gap of 0.82eV, while bulk PbSe has a band gap of 0.28eV (Wise, 2000; Cao, 2004; Abrams and Wilcoxon, 2005). Another property that undergoes changes is the lifetime of the excitons. In nanosized systems, the lifetimes of excitons are increased due to the shorter distances and the presence of trap states for electrons and holes (Abrams and Wilcoxon, 2005; Stroyuk *et al.*, 2005).
- V. increased surface energies of the smaller sized nanomaterials, with larger occurrence of surface atoms in a disordered state as well as higher surface reactivities due to the high surface energies of the nanoparticles, promotes further reactions on the surfaces (Cao, 2004). It is assumed that when the bulk is reduced to between 1.5-2nm, then the surface is supposed to be made up of about 70-80% of the atoms of the solid. This would mean that surface reaction would dominate almost completely (Abrams and Wilcoxon, 2005).
- VI. lower Reynolds numbers (Equation 1) and higher diffusivity (Einstein-stokes Equation 2), are properties of nanoparticles thus when released into the atmosphere, they

displayed longer lifetimes with very slow gravitational settling at low Reynolds number (Lide and Haynes, 2010; Liyanage *et al.*, 2016). In the equations,  $r$  is given as the particle size,  $v$  is the velocity of the particle,  $\rho$  is the density of the particle and  $\mu$  is the viscosity of the medium,  $D_s$  is the diffusion coefficient,  $k_b$  is Boltzmann's constant, and  $T$  is absolute temperature.

$$Re = \frac{rv\rho}{\mu} \quad \text{Equation 1}$$

$$D_s = \frac{k_b T}{6\pi\mu r} \quad \text{Equation 2}$$

Nanomaterials are therefore attractive for use in the hydrogen economy, environmental remediation, antibacterial properties, cancer therapy and solar cells (Abrams and Wilcoxon, 2005; Altavilla and Ciliberto, 2011) because of their unique properties. However, one has to be able to synthesise, characterise and immobilise them in reactor systems -remembering the concerns of the Royal Society about the hazard posed by free nanoparticles (The Royal Society *et al.*, 2004).

### 1.1.1 Toxicity/challenge of using nanomaterials

An important aspect of nanomaterials that is just as relevant as their positive properties are their potential link to health worries. This is seen in

- Site translocation: As a result of the small sizes of nanomaterials, translocation from the site of implantation is very likely which is related to  $D_s$  from the Einstein Stokes relation (see Equation 2). This is enhanced by their ability to cross barriers at the tissue and cellular level. If the nanomaterials were to remain inert, then their translocation would not necessarily be problematic, but on the contrary they do and are recognised to trigger oxidative stress or cause physical damage to the organelle membrane upon penetration. Another factor is the low Reynolds number of nanoparticles, where low settling tendencies keeps these particles persistent in the body. This is evident in the case of ultrathin fibres of asbestos which were able to travel a longer distance, thus facilitating their translocation to the different body organs (kidney, lungs, brain etc) after inhalation of the particulates (Miserocchi *et al.*, 2008)
- Oxidative stress: The generation of oxidative stress is usually dependent on the composition of the nanoparticle. Reactive oxygen species (ROS) created can lead to lipid oxidation, DNA alteration, protein denaturation, signal interference etc., all of which can affect the normal function of a cell, leading to a cascading effect of cell disfunction (Jeevanandam *et al.*, 2018).
- Purity: the purity of nanomaterials is problematic. The high surface area to volume ratio

increases their interaction with impurities, including certain synthesis precursory materials which can cause an immunogenic response once introduced into the body. (Jeevanandam *et al.*, 2018).

These are just some of the possible safety concerns that can plague the use of nanomaterials in the body. It is important to note that the long term consequences of exposure to nanomaterials are still not well understood, and as such not all nanoparticles will necessarily cause a toxic end result (Aliofkhazraei, 2016). For example, nanomaterials with different shapes have different toxic properties (e.g. exposure to asbestos fibres that are 10µm in length causes lung cancer, while those that are 2 µm in length cause asbestosis, and the intermediate particles have been known to cause mesothelioma (Jeevanandam *et al.*, 2018)). The same can be said for nanoparticles of different polymorphs: rutile(200nm) was seen to cause DNA damage in the dark, while anatase of the same size did not (Jeevanandam *et al.*, 2018). Then there is the effect of aggregation, which can increase nanoparticle size via Ostwald ripening (see coming subsection), until they become harmless. (Jeevanandam *et al.*, 2018). Thus not all nanoparticles behave in the same manner, and more research is still needed to accurately predict their effects on all people coming into contact with them (from workers to end users) (Aliofkhazraei, 2016).

### 1.1.2 The nucleation and growth of nanoparticles/structure.

The nucleation and growth of nanomaterials occurs due to a difference between the chemical potential of a solid phase, in comparison to the liquid phase. This in itself can be divided into two major stages, the nucleation and the growth stage.

- Nucleation: this is characterised by the appearance of smaller clusters, nuclei or droplets of the material (basically atoms clustering together). But this is dependent on supersaturation occurring, where the concentration of the component of interest has exceeded a certain concentration. It is usually triggered by cooling, evaporation, chemical reaction and so on (Myers, 1999), or any process that can cause supersaturation. If the system has not attained a minimum level of saturation pressure, concentration or crystallization temperature, then no coalescence of the atoms occur (Adamson and Gast, 1997). The sustenance of these clusters/nuclei are dependent on the total free energies ( $\Delta G$ ), which is given by the following equation

$$\Delta G = \frac{4}{3}\pi r^3 \Delta G_v + 4\pi r^2 \gamma \quad \text{Equation 3}$$

The first half of the equation gives the minimum volume of an ideal spherical nucleus ( $\frac{4}{3}\pi r^3$ ) and the free energy ( $\Delta G_v$ ) required for the transformation of the nucleus from one phase to

another: the driving force. It is negative if the reaction temperature is below equilibrium solidification temperature (Callister and Rethwisch, 2009). The second half of the equation is a product of the surface area of the nucleus ( $4\pi r^2$ ) and the interfacial surface energy ( $\gamma$ ) it experiences (Adamson and Gast, 1997). The sum of these contributions, surface energies and the volume free energy of the nucleus gives the curves below:

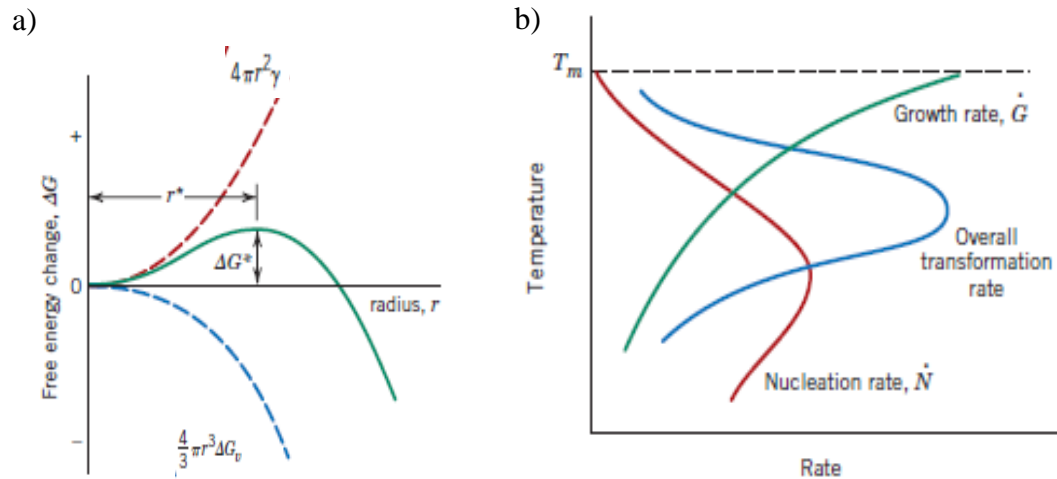


Figure I-1: Schematic curves showing the volume free energy, the interfacial energy and the total free energy ( $\Delta G$ ) a); the nucleation rate ( $N$ ), growth rate ( $G$ ) and the overall transformation rate against temperature b) (Callister and Rethwisch, 2012).

What this (and the curves in Figure I-1) means is that nuclei will grow when  $\Delta G$  is positive, but growth of the nuclei only becomes stable at a certain critical radius ( $r^*$ ), at which point the activation free energy  $\Delta G^*$  has been attained. Below this critical radius and activation energy, the nuclei would be too unstable, and would be prone to dissolving rather than growing (Callister and Rethwisch, 2012). Supercooling is usually enough to decrease the activation energy, encouraging more nucleation events, so far as the atoms are still mobile enough to cluster together at temperatures lower than the melt temperature.

- Growth: As previously explained, once the critical radius  $r^*$  of the nuclei has been attained, dissolution of the nuclei is less likely. Growth is affected by long range atomic diffusion, usually from the mother liquor, boundaries and then to the nucleus (Callister and Rethwisch, 2012). Figure I-1 shows that phase transformation is a balance between the formation of nuclei and their growth, which is an indication that both of these stages occur simultaneously. This is why supercooling to temperatures drastically below the melting results in high nucleation rates  $N$ , while the low growth results in finer and smaller grains; coarser grains are the case if supercooling is closer to the melting temperature.

An important and sometimes unintentional consequence of the smaller sized nuclei is

Ostwald ripening. As a result of the high surface energies (chemical potential) of these nuclei with  $r < r^*$ , Ostwald ripening - an energy minimalization particularly in thermodynamic nonequilibrium - can cause the growth of nuclei at the expense of much smaller nuclei (Cao, 2004; Aliofkhazraei, 2016) in an effort to reduce the interfacial energies of the system. These unstable nuclei ( $r < r^*$ ) dissolve and deposit on the surfaces of the more stable nuclei ( $r^*$ ), as seen in Figure I-2

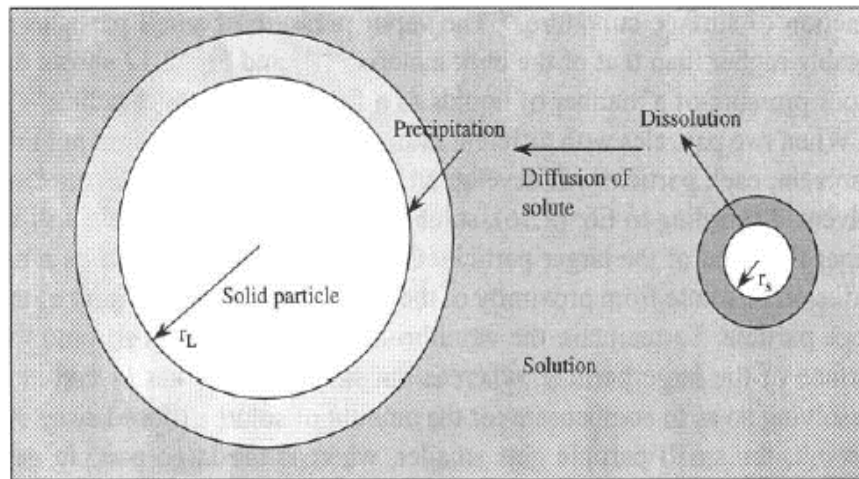


Figure I-2: Illustration of Ostwald ripening process (Cao, 2004).

Curved surfaces are known to have chemical potentials defined by Equation 4. Convex surfaces/spheres tend to have a positive chemical potential. This is to do with the differences in the surface atoms compared to the interior and why the atoms on a flat surface would have a lower surface potential compared to those found on a curved surface (Cao, 2004). Thus, the chemical potential of the surface atoms on a curved spherical surface is given by the following relation, Young-Laplace equation:

$$\Delta\mu = 2\gamma \frac{\Omega}{R} \quad \text{Equation 4}$$

In the above,  $\Delta\mu$  is the chemical potential change,  $\gamma$  is the surface energy,  $\Omega$  the atomic volume and  $R$  is the radius. Thus, one can assume that depending on the radius of the curved surface, the chemical potential will be affected, with smaller particles mathematically inclined to have a higher chemical potential following the Young-Laplace equation. This partly explains the difference in potential of smaller particles compared to bigger ones. Also, assuming the vapour of solid phases obeys the ideal gas laws, then the chemical potential of a curved solid surface can be rewritten as:

$$\mu_v - \mu_c = -kT \ln P_c \quad \text{Equation 5}$$

where  $\mu_v$  is the chemical potential of the vapour of a solid phase and  $\mu_c$  is the chemical potential at the particle surface,  $k$  is the Boltzmann constant and  $P_c$  is the equilibrium vapour pressure of the curved surfaces,  $T$  is the temperature (Cao, 2004). And if two surfaces are close enough to each other to be suitably influenced, then the below is the case

$$\mu_c - \mu_{c_2} = -kT \ln \frac{P_c}{P_\infty} \quad \text{Equation 6}$$

where  $\mu_c$  is the chemical potential at the surface,  $P_\infty$  is the equilibrium vapour pressure of the flat surface (Cao, 2004). Combining Equation 4 and Equation 6 can then give the Kelvin equation (Cao, 2004) below:

$$\ln \frac{P_c}{P_\infty} = \gamma \Omega \frac{R_1^{-1} + R_2^{-1}}{kT} \quad \text{Equation 7}$$

It may be simplified as below:

$$\ln \frac{P_c}{P_\infty} = \frac{2\gamma\Omega}{kRT} \quad \text{Equation 8}$$

$R_1$  and  $R_2$  are the radii of two different nuclei. These expressions can be further expanded to include terms for solubility, as seen with the equation below.

$$\ln \frac{S_c}{S_\infty} = \gamma \Omega \frac{R_1^{-1} + R_2^{-1}}{kT} \quad \text{Equation 9}$$

Just like Equation 7 it relates the difference in radii of the surfaces, their vapour pressures and equilibration that has to occur to balance both nuclei as they are in contact with one another. This applies to Equation 9 which shows the equilibration of two nuclei of different radii within a common solvent, as one dissolves and the other grows to compensate for each other's presence (Cao, 2004). This particular tendency for one nucleus to dissolve in preference for the other has been discussed -Ostwald ripening

This nucleation and growth of nanoparticles are linked processes that are dependent on the establishment of equilibrium due to the difference in the chemical potential between the solid phase and liquid phase. The attainment of a critical radius and eventual growth is dependent on the temperature and long-range diffusion. In the synthesis of bulk materials, there is little concern with arresting growth, thus destabilisation processes might not be too problematic. But in the synthesis of nanomaterials, a suitable synthesis route needs to be chosen to allow for rapid nucleation and controlled growth, or the properties attributed to nanomaterials could be easily lost as coarsening occurs.

### I.1.2 Synthesis and fabrication of nanomaterials

Synthesis of nanomaterials can generally be categorised into two major synthesis pathways: Top down approach and bottom up.

- Top-down approach

The top-down approach tends to use a more physical approach in the achievement of nanoparticles. Utilising processes like attrition, milling, ablation to produce particles that fall within the nanosized range (Cao, 2004; Altavilla and Ciliberto, 2011). It is a method that depends on deconstructing large scale materials (Aliofkhazraei, 2016). Some lithography is also thought to partly fall within this route. This is because the actual deposition of material is considered a bottom-up approach, and then etching away the excess material is more top down. While it is possible to achieve resolutions as small as  $\leq 50\text{nm}$  depending on the sub category of lithography used (scanning probe lithography being the mores precise at  $< 5\text{nm}$ ), it is still not easily done especially at a high enough throughput to offset its high cost (Sotiropoulou *et al.*, 2008; Aliofkhazraei, 2016).

- Bottom-up approach

A bottom up approach usually follows a chemical route or uses chemical precursors. Here, a structure is assembled “atom by atom, molecule by molecule or cluster by cluster” (Cao, 2004). This is typically the preferred route over a top down approach as the “size, shape, and composition” are easy to control over those obtained with a top down approach (Altavilla and Ciliberto, 2011). In the preparation of metal nanoparticles, most of the chemical process involves a step for reduction/decomposition of the metal complex and the eventual aggregation of the metal ion; also, electrochemical deposition is another popular method for metallic nanoparticle formation. Semiconductors may be prepared in various manners including: solvothermal technique which utilises the reaction of chemical in a solvent (water or otherwise within a pressurized vessel), where the crystals nucleate and then grow from the solution sometimes in the presence of a mineraliser like  $\text{HNO}_3$  such as is seen for titania production (Aliofkhazraei, 2016). Chemical vapour deposition (CVD) is another example of a bottom up route where the volatile chemical is reacted with gases to produce solids; in this method gas and surface reaction occurs simultaneously e.g. Pt nanowires have been formed on silica template using a Pt organometallic precursor (Cao, 2004). CVD is similar to physical vapour deposition (PVD) but rather than a precursor chemical, a source or target is utilised which undergoes atomisation (evaporation, sputtering) and then deposited on a substrate (Cao, 2004); it is possible to produce  $< 5\text{nm}$  resolution with PVD and CVD (Aliofkhazraei, 2016). The aforementioned methods are considered quite energetically demanding, with the added problem of utilising toxic solvents and



producing toxic waste as well, so greener methods have been developed. They include sonochemistry technique and microwave techniques. Sonochemistry involves the generation, growth and collapse of bubbles which rapidly generate an intensive amount of heat in conjunction with pressure to drive a reaction e.g. mesoporous TiO<sub>2</sub> has been synthesised under ultrasonic energy (Yu, Zhang and Yu, 2002; Aliofkhazraei, 2016). In the synthesis of nanoparticles with microwave, a solution containing the precursor is irradiated with microwave for a given period to produce nanoparticles e.g. Ag nanoparticles were produced after irradiating a solution of silver nitrate for 5s (Aliofkhazraei, 2016).

Sol gel synthesis method, a very important synthesis route, utilises colloidal suspension of the material destined for deposition in the presence of the colloidal solution which is usually an alkoxide. It is used in the synthesis of silica (see Figure I-3).

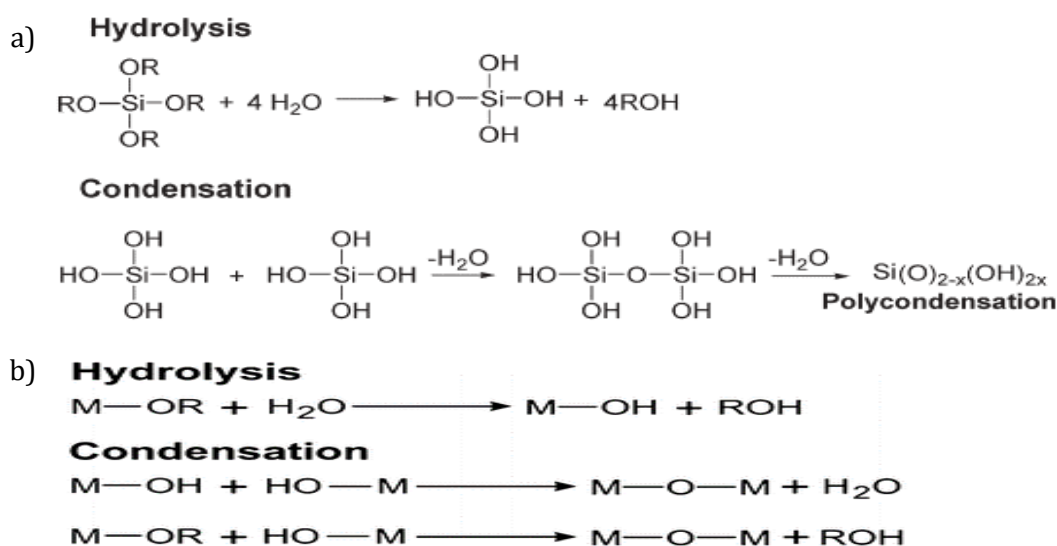


Figure I-3: Sol-gel reaction using alkoxide for the formation of amorphous silica a); schematic showing the sol-gel reaction of a metal alkoxide b) (Zayat, Garcia-Parejo and Levy, 2007; Rechberger and Niederberger, 2017)

Usually the process itself involves the formation of a network through a series of hydrolysis and condensation reactions often occurring simultaneously (Cao, 2004). The starting solution (sol) evolves into a gel before it undergoes some thermal treatment to form the final material of a given morphology (Yang *et al.*, 2017). It is quite useful in low temperature synthesis of metal oxides that are thermodynamically unstable (Cao, 2004) and other multicomponent systems. In terms of inorganic-organic hybrids, a sol-gel approach is the most suitable as it allows the interpenetration of the sol into the organic structure on a nanoscale (Cao, 2004), casting onto the surface and the intricacies that make up the organic material. As such, the organic material is used as a template to generate a final mesoporous material capable of having any geometry that is dependent almost entirely on the starting template material. Even before the use of a template,

the sol gel method is capable of forming a hierarchical material containing pores. Resolutions as low as 50nm are easily achieved (Aliofkhazraei, 2016).

Talk of bottom-up approach cannot be complete without additive manufacturing. This is a group of technologies where objects are assembled from the bottom up, usually rapidly done by the addition of materials layer by layer with control and blueprint generated by a computer aided design software (Ivanova, Williams and Campbell, 2013; Aliofkhazraei, 2016). Additive manufacturing are able to achieve resolutions of 0.1 $\mu$ m and above (Aliofkhazraei, 2016). Several techniques under additive manufacturing methodology include:

- Fused deposition modelling (FDM), it follows the melting and extrusion of metal or polymer in layers, where each preceding layer is allowed to harden before the next advancing layer is added on, until a final 3D object is built (Melchels *et al.*, 2012)
- Stereolithography (SL), another technique, relies on the selective curing of a polymer by a focused source of light; inject printing follows the addition of a colloidal suspension of particles and binder to achieve a 3D object (Melchels *et al.*, 2012)
- Selective laser sintering (SLS) is a technique where a laser is used to heat the layers of powder (usually ceramics) – supplied by a roller -above their  $T_m$ , tracing the shape of the 3D object in the process (Melchels *et al.*, 2012)
- Other methods include robotic assembly, bio-laser printing (Melchels *et al.*, 2012). These processes have been used in the manufacture of scaffolds that are made up of polymers like poly(lactide), 3D printing of calcium phosphate hollow structures (Eliaz *et al.*, 2017), printing of hydrogels ranging from alginates to collagen (Hinton *et al.*, 2015) etc.

Additive manufacturing is still relatively new compared to the other forms of nanoparticle synthesis, with challenges including the initial cost of equipment purchase, agglomeration of particles destined for extrusion and subsequent clogging of extrusion nozzles, functional and chemical changes of materials (metals or alloys) exposed to extreme high temperatures in air, depth of laser curing etc (Ivanova, Williams and Campbell, 2013). Should these challenges be addressed, the additive manufacturing has been projected to be worth more than \$10.8billion in 2021 (Aliofkhazraei, 2016).

### ***1.1.2.1 Templating and replication***

This is an interesting synthesis pathway, utilised to take advantage of hierarchically template material to produce complex geometries, facilitated by the interaction between the precursory solution and the template materials. The final material bears some structural relation to the template material. Different structures with varying length scale from the nano to larger are possible through this templating method. The pore distribution in these template materials is of

interest, with these features seemingly useful in applications ranging from adsorption, separation, sensors, energy and catalysis (Yang et al., 2017). In terms of catalysis for example, the hierarchical porous system can be useful in separating the reactant fragments from intermediate, thus keeping the equilibrium of the chemical reaction in a specific direction. One can also use this to construct multiple step reactors (Yang et al., 2017). In addition to that, the improvement in the surface area provided by the hierarchical features enhances the adsorption of the samples, not to mention the improved diffusion length scale, both of which increases the inherent adsorption potential of the material, thus affecting catalysis, drug delivery and storage (Yang et al., 2017). Energy-wise, specifically photocatalysis, adsorption of the reactant molecule is improved due to the increased surface area and active site distribution that the hierarchical material entails. There is also the improvement in the light path. This is characteristic of microchannels present which allow easier travel of the incident light, as well as scattering off the increased surface, permitting multiple photon adsorption due to the enhanced light path (Yang et al., 2017). The templates used in this method can be derived from various areas:

- Synthetic polymers: Macro porous polymers, sometimes used in conjunction with a crosslinker agent. These polymers are infiltrated with the precursor solution, which might be a sol or nanoparticles. The polymer used can come in any variety of morphology. As a foam, it was used in the synthesis of 'micro-macro-porous zeolite monoliths' (Su, Sanchez and Yang, 2012) from PU polymer foams, after calcination. Also titania nanoparticles were formed inside PAM foam, using titanium isopropoxide (Su, Sanchez and Yang, 2012). Polymeric spheres were also used as a template; with PS-DVB used to form crystallised  $\text{TiO}_2$  beads,  $\text{In}_2\text{O}_3$ ,  $\text{Fe}_2\text{O}_3$  (Su, Sanchez and Yang, 2012). Other polymeric forms used were films and mats e.g.  $\text{LiCoO}_2$  was formed from cellulose acetate thin films, using a precursor solution containing acetates of lithium and cobalt in ethylene cobalt.
- Bio-inspired sources: The template material here is provided by biological sources with porous structures. Much in the same way as with synthetic polymers, the biologically sourced materials are used as a template/scaffold where infiltration and coating are necessary in the templating process. Collagen matrix obtained from egg shells treated with acid treated was utilised for the templating of  $\text{TiO}_2$  (Su, Sanchez and Yang, 2012), which was subsequently calcined; woven  $\text{TiO}_2$  replica was obtained using a template of cotton textile that had been infiltrated with  $\text{TiF}_4$  and then calcined at  $500^\circ\text{C}$ .  $\text{ZnO}$  was templated from softwood fir, managing to preserve the tracheid cell structures; other examples included wood cellulose, plant leaves that have been utilised as templates for the synthesis of nanostructures (Yang et al., 2017). Bacteria and cells have also been utilised as templates; this is seen with the use of aligned *Bacillus subtilis* to create

microporous fibres of silica. In addition, *Saccharomyces cerevisiae* cells were used to form a TiO<sub>2</sub> spherical microporous structures (Su, Sanchez and Yang, 2012).

Templating is certainly an important aspect in producing nanostructures with different morphologies, sizes and potential applications. Its advantages lay in the ability to form or obtain a biotemplate that can then be replicated, using mainly sol-gel methods; however, sol gel methods are not exclusive chemistry (i.e. CVD and ALD are also used). The use of synthetic polymers provides the researcher with the option of designing nanostructures with any number of morphologies, with varying porosity. However, the different structures, as previously mentioned require an additional step to form them (i.e. foams can be made via an oil in water or water in oil polymerisation process) and spheres may be made in a similar manner, mats may be electro-spun, and polymer gels may need preparation with a surfactant, water and the block polymer of choice to form a porous gel structures. All of these methods of template preparation come with their own challenge. Surface defects are an issue, and furthermore there may be a requirement for external fields to correct such problems (Sotiropoulou *et al.*, 2008). The cost of making these specialised components may be problematic (Sotiropoulou *et al.*, 2008). Hence bioinspired template sources may be preferable. This effectively eliminates the need for a template preparation process (as nature would have already provided a structure with different size scale including different architectures such as that seen in Figure I-4).

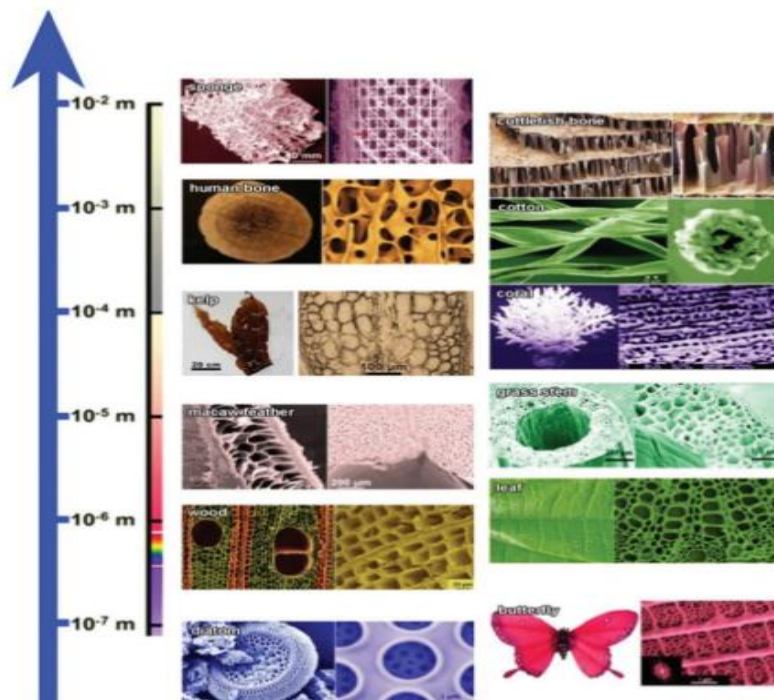


Figure I-4: Overview of hierarchical structured natural materials, alongside their corresponding length scale (Yang et al., 2017).

This saves on time and cost of preparing specialised template substrates. There is also the added advantage of different chemical groups present that may be easily exploited for the nanostructure synthesis under milder conditions, in some cases eliminating the need for additional surface treatment ( compared to when synthetic polymers are used), or making further modification easier (Sotiropoulou *et al.*, 2008). There are still challenges and limitations: the main being the variability of these bio-inspired templates and thus reproduction of the nanostructures and the difficulty in scaling up the process (Sotiropoulou *et al.*, 2008; Su, Sanchez and Yang, 2012; Yang *et al.*, 2017). These are just some of the drawbacks. Notwithstanding that, the opportunity to produce nanostructures in parallel with low cost, obtaining the eco-friendly templates cannot be ignored.

### **I.1.3 Biomimicry**

Having touched upon the importance of templating and the role bio-inspired templates can play in the bottom up synthesis of nanostructures, it would be impossible to not comment on the role nature has in both providing these templates and more importantly in utilising low effort building mechanisms that is inherent in nature to achieve maximum functionality. The latter concept brings one to the field of biomimicry/biomimetics. It has been defined as an “abstraction of good design from nature”(Bharat, 2010) or “biologically inspired design or adaptation or derivation from nature”(Bhushan, 2009). It was a term coined by Otto Schmitt which takes “the practical use of mechanisms and functions of biological science in engineering, design, chemistry, electronics, and so on” (Vincent *et al.*, 2006). One can see that biomimicry is a broad area, which transcends the mere utilisation of biological template source or the copying of structures (like the name ‘mimicry’ implies) and so on. It is a mind-set/an approach to problem solving that takes its cue from nature. Humans have been able to use biomimicry to solve various problems, ranging from the creation and use of antireflective surfaces on solar panels to improve light capture, which have been modelled from antireflective surface of insect eyes, their wings and the underside of leaves (Vincent *et al.*, 2006), the creation of anti-adhesion paint (e.g. Lotusan) for self-cleaning surfaces which are modelled after the varied textured surfaces of lotus leaves that are capable of keeping themselves clean from mud (Vincent *et al.*, 2006), to the creation of motion camouflage capable of giving a false sense of motion seen in dragon flies as they prey on their targets (Vincent *et al.*, 2006). Also, fishing and insect nets have been most likely modelled after a spider web, utilising the trapping and separating function of the web; the use of composite materials to improve the mechanical properties of various vehicles which are derived from natural matrix, filler composite are employed largely in nature as see in the cuticle from insects, nacre in abalone (Bar-Cohen, 2006; Bhushan, 2009). Still touching on the concept of composites and their applicability in human endeavours, the human tooth (composed of inorganic crystals, water and protein), and sea urchin’s tooth (composed of calcite plate with organic matter) are examples

showing the interplay of toughness and stiffness which are used in the development of wear resistant tool and dental implants (Bhushan, 2009).

Many of these properties/functionalities that have been mentioned and many more that are displayed in biology, and then subsequently co-opted and used for human engineering are achieved through hierarchical means:

- Hierarchy and multifunctionality: hierarchical assembly, or hierarchical organisation are common occurrence in nature. The functionalities that are displayed by the systems/structures discussed thus far are a result of the “self-organisation of molecular units or their aggregates that are assembled with other phases, which are in turn are self-organised at increasing size levels” (Su, Sanchez and Yang, 2012). Nature uses these multilevel approaches, where each level regardless of its size scale, provides some input that will affect the final function, structure and ability to adapt to the possible changes that the whole organism would encounter in its environment (Bhushan, 2009), which in a manner are all constructs to resolve technical problems (Vincent *et al.*, 2006). This self-assembly is governed by a genetic imprint, providing the building imprint and the intelligence for the adaptations true to the organism’s habitat, in addition to the available building materials and conditions within said habitat. This is seen in mineralised tissue and plant leaf below:
  - Hierarchy and mineralised tissue: With regards to teeth and by extension bone, at the ultrastructural level (nanometres), its organic portions consist of proteins and collagen, while its inorganics are made up of hydroxyapatite mineral, assembling together to give us a higher organisational level; the next level – the microstructure - tubule within the dentine becomes apparent, for bone the structural units are osteons, thin lamellae and trabeculae dominate (Boskey, 2007). Upwards from there, at the tissue level, the final structure of bone and teeth becomes apparent. Osteocytes are responsible for producing the extracellular matrix (collagen) template, to guide the deposition of the relevant ions in an organised manner. Proteins are also necessary in guiding the biomineralization process. (Boskey, 2007). The hierarchical structure of bone and teeth are in part responsible for the toughness of bone, and its ability to resist cracks which are seen through the complicated architectures of its composite system. Then these un-propagated cracks can be repaired by osteocytes along with ion made available by the blood vessels that run through the osteons of the mineralised tissue (Fratzl, 2008). The ability to constantly repair and remodel, is yet another advantage a hierarchical structure can confer.
  - Hierarchy and plant leaf structure: the hydrophobic property of the leaf, is another example of a hierarchical system. One only has to look at the cuticles of the plant leaf. On

the cellular level, there is the presence of the epidermis cells, which contribute to the texture of the cuticle above it. This is because the central pre-clinical area of the cell can cause an outward growth on the leaf surface which can manifest as a papilla or hair like structure; this is so if the epidermal cell is convex in shape (Koch, Bhushan and Barthlott, 2008). On top of the epidermal cells, separated by a pectin layer, exists the cuticle proper, which is a biopolymer of cutins integrated with phenolics, flavonoids and intra-cuticular and epi-cuticular waxes (Bharat, 2010). The hierarchical assembly of the cells comes to play in aiding the multifunctionality of the leaf. The folds of the cuticle, as a result of the epidermal cells underneath, and the presence of the waxes, provides textural and chemical input increasing the hydrophobicity of the leaf surface. The waxes are additionally thought to prevent water and ion loss from the leaf interiors, keeping pathogens and microorganisms from adhering to its surface, as well as providing UV protection (Koch, Bhushan and Barthlott, 2008; Bharat, 2010). Also the convex shape of the epithelia cell can concentrate light, increasing the intensities that get to the interiors by 20x (Zhou *et al.*, 2010). Away from the cuticle and cell epidermis, the leaf has an arrangement of spongy and palisade mesophyll cells, along with the vascular bundle system (phloem and xylem). The mesophyll cells contain chloroplasts where photosynthesis occurs; for this process to proceed gaseous exchange is paramount and this happens through gaps between these cells; and there is the incident radiation which has been concentrated by the epidermal cell, the parallel arrangement of the palisade mesophyll and the less organised arrangement of the spongy mesophyll increasing the photon scattering surfaces, improving the likelihood of interaction with the chloroplast of the cells (Zhou *et al.*, 2010). Also, the vascular bundle covering more than 50% of the plant structure contribute to the light scattering into the deeper layers while performing as a mass transporter of sugars, nutrients, and minerals (Zhou *et al.*, 2010). From this hierarchical build of a leaf, a multitude of uses ranging from anti- adhesion, mass transport, spectral augmentation, pest control/resistance etc, are seen.

These are just some of the examples of how hierarchy has an interconnection with the function, and multifunctionality in most cases. It is for this reason that the author has decided to utilise biomimicry in an attempt to take advantage of the multifunctionality that could come to play. One has to keep in mind that the dynamicity of these systems might be lacking or simply impossible to copy, seeing as these natural systems are autonomous (using blueprints stored in DNA & RNA) with checks and balances to respond to stimuli dependent on the complexity of the organisms (Vincent *et al.*, 2006), it would be difficult to correctly replicate such autonomy.

### ***1.1.3.1 Chemical route to biomimicry***

This is an important area of biomimicry. While we have already discussed using and relying on

the physical facets provided by biologically derived materials for the synthesis of nanostructures, one has yet to discuss the use of certain biological macromolecules as architectural guides. Here, one considers things like peptides, lipids, DNA, as some examples of these biomolecules that can act as templating agents. For example, certain octapeptides have the ability to self-assemble into a number of different nanostructures, e.g. tubules, which can be used to cast materials into these shapes, followed by the eventual breakdown of these peptides (Sotiropoulou *et al.*, 2008). The same can be said for lipids, where assembled charged lipid tubes can be used for the adsorption of silica particles, resulting in a 3D structure (Sotiropoulou *et al.*, 2008); the lipids were critical in the synthesis of liposomes used for drug delivery vehicles to translocate drugs like doxorubicin, paclitaxel etc (Aliofkhazraei, 2016). Au nanoparticles assembly can be guided by DNA molecules (Sotiropoulou *et al.*, 2008). Other examples outside self-assembly are seen in the synthesis of silica nanostructures, using peptides (silaffins) and proteins (silacidins) to precipitate the structures from silica precursors (Pamirsky and Golokhvast, 2013; Yang *et al.*, 2017). It was also shown that TiO<sub>2</sub> could be precipitated from TiBALD from R5 peptides, R5 derived peptides, HEWL, poly-l-lysine to name a few (Dickerson, Sandhage and Naik, 2008); conversely, certain macromolecules like l-lysine was shown to inhibit the production of hydroxyapatite (Chen *et al.*, 2012; Tavafoghi and Cerruti, 2016). Also, polydopamine has been used to form self-assembled monolayers (Klosterman, Riley and Bettinger, 2015), as well as for the nucleation and control of the morphology of Au structures (Son *et al.*, 2018).

#### **I.1.4 Case for biotemplating using hierarchical templates to achieve nanostructures**

The potential properties/advantages of nano-scaling in section I.1.1 has been investigated, where thermal, electronic, optical and surface properties were just some of the attributes of nanomaterials that underwent drastic improvement. It thus makes sense that if the author wanted to research the synthesis of TiO<sub>2</sub> and hydroxyapatite on biotemplates, then these materials would benefit more if they were made to fall within a nanoscale range. In the case of TiO<sub>2</sub>, a very prominent photocatalyst, its optical and surface properties may be enhanced to improve its overall efficiency. One way to achieve this might be through nanoscaling of the bulk TiO<sub>2</sub> to take advantage of this positive nano-structuring attribute. A photocatalyst is only as good as its band gap, its redox potential and its surface area; all of these are capable of undergoing modification with nano structuring. The same goes for hydroxyapatite. As a very important component of mineralised tissues in humans, the surface properties of the mineral nuclei are just as important as the overall scaffold. In a living system like the human body which continually engages in remodelling, sizing becomes quite important. Nanosized materials which have a significant amount of their atoms located on the surface are more active, and easily resorbable compared to bulk samples. Thus, having hydroxyapatite fall within the nano-scale range could have a positive effect on its biocompatibility.



These nanostructures can be synthesised in any number of ways, with a top down approach or bottom up approach. The top down approach, which relies extensively on lithography has been discounted for use in this project because it is expensive, time consuming; and in the synthesis of TiO<sub>2</sub> and hydroxyapatite which will be used for large scale application, costings and time saving become increasingly important; no top-down approach could satisfy these needs. With a bottom-up approach on the other hand, the sol-gel approach displayed most potential as it was a low temperature approach that could be used to create complicated faceting with multiple components, especially when coupled with the use of a template. This opens the door for the synthesis of nanostructures with a hierarchical component having multifunctionality, just as discussed in many biological systems mentioned in sections I.1.2.1 and I.1.3. Since nature already has systems supporting these hierarchical components, it was decided that attempts would be made here to reproduce certain aspects of these systems

- Directly: This would be done through the use of biotemplate. These will include leaves: *Rotala rotundifolia* and *Eucalyptus camaldulensis* and whole organisms (*Chlorella vulgaris*) that will be used as templates for the synthesis of nanostructures.
- Indirectly: This will be done using templated polymers for the synthesis of nanostructures. Rather than relying on nature as the source of the template materials, polymers including sodium alginate, polyvinyl alcohol, and poly-l-lactic acid will be used as templates for the development on hierarchical nanostructures.

### **I.1.5 TiO<sub>2</sub>, a model catalytic nanomaterials**

Titania exhibits polymorphism, with only one of its numerous phases (anatase, rutile and brookite) being very suitable for photocatalytic activities: anatase. It shows a favourable inclination to undergo photocatalysis in the presence of a suitable source of illumination. It, along with rutile, are the most thermodynamically stable of the different polymorphs, and are considered the most popular, or rather the most studied polymorphs of TiO<sub>2</sub>, with a much better comprehensive understanding of their surface and structural properties. Another polymorph of TiO<sub>2</sub> includes brookite (Tang *et al.*, 1994; Thamaphat, Limsuwan and Ngotawornchai, 2008).

With respect to the popular phases, rutile and anatase, they have the same chemical formula, with titanium occupying a position or configuration where it is surrounded by six oxygen atoms (Diebold, 2003). This ends up forming an octahedral structure. The similarity however ends here with differences in this octahedron leading to the formation of the polymorphs we know. In the case of anatase, the octahedron according to Linsebigler, Lu and Yates (1995) is thought to be extensively distorted. The Ti-Ti bond lengths are 3.79Å (379pm) and 3.04Å (304pm), while the

Ti-O have been recorded as being 1.934 Å (193.4pm) and 1.980 Å (198.0pm); these are all in contrast to the bond lengths that have been recorded for rutile, which have been recorded as being 3.57 Å (357pm) and 2.96 Å (296pm) for the Ti-Ti bond, and 1.949 Å (194.9pm) and 1.980 Å (198.0pm) for Ti-O (Linsebigler, Lu and Yates, 1995). This can be interpreted as the overall structure undergoing deviation with anatase acquiring a sizable deviation from a 90° bond angle (Diebold, 2003). These differences account for the dissimilar densities and electronic band structures that are intrinsic to these polymorphs. In terms of crystallographic arrangements, Figure I-5 depicts a simplistic arrangement of the rutile and anatase molecules.

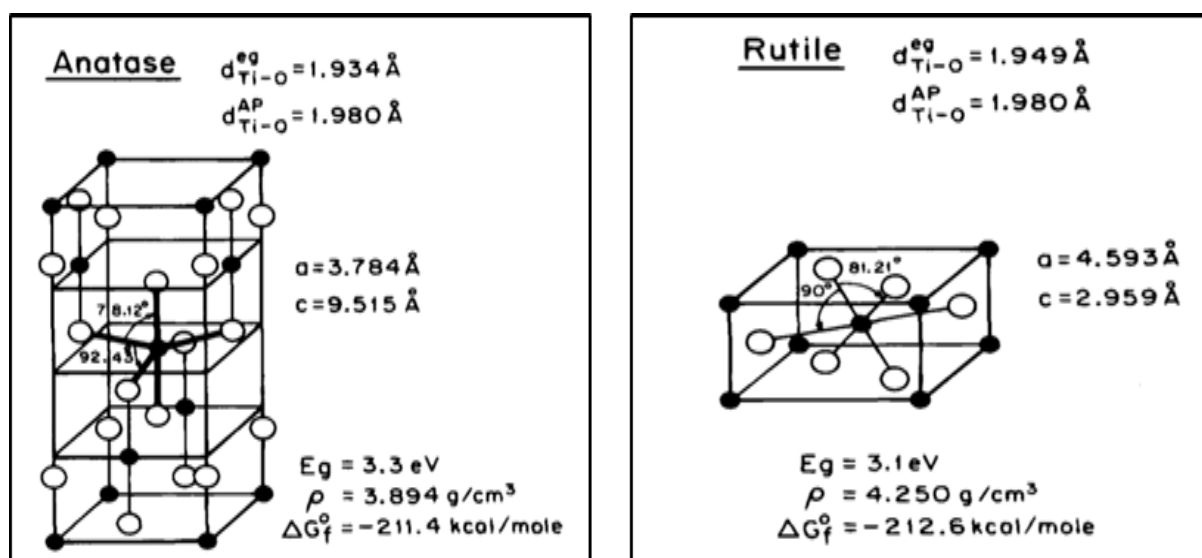


Figure I-5: Bulk structures of anatase and rutile phases of TiO<sub>2</sub> (Linsebigler, Lu and Yates, 1995)

Many of the technologies, which were mentioned earlier, rely on the surface properties of these polymorphs. For example, in the case of rutile, the surface with the lowest energy can be found along the (110) surface, while (001) has the highest surface energy (Diebold, 2003). (100) and other faces were found to undergo transformation to the more thermodynamically-stable phase (110) (Linsebigler, Lu and Yates, 1995). In anatase, surfaces (101), (100/010), (001) have been found in prepared powders. (101) was found to have the lowest energy, with experimental evidence concluding that it was even lower than that found in rutile.

It is obvious that TiO<sub>2</sub> is an interesting semiconductor, with properties that can be utilised for different applications. In the context of its ability to photo-catalyse a reaction on its surface, it shows that there is some harmony with this property and with the primary function fulfilled by a plants leaf-utilising incident radiation for the purpose of catalysing vital reactions that form the basis of photosynthesis. Unfortunately, with regards to its photocatalytic properties, it is quite limited in the respect that its band gap is quite large (3.2eV). This means that its photocatalytic abilities are only at their most efficient under UV conditions, i.e below 382nm (Mathur and Singh,

2007). This severely restricts the portion of the solar spectrum that may be utilised, as it has been estimated that only 4% of the overall solar spectrum is made up of UV radiation (Grätzel, 2001; Mathur and Singh, 2007).

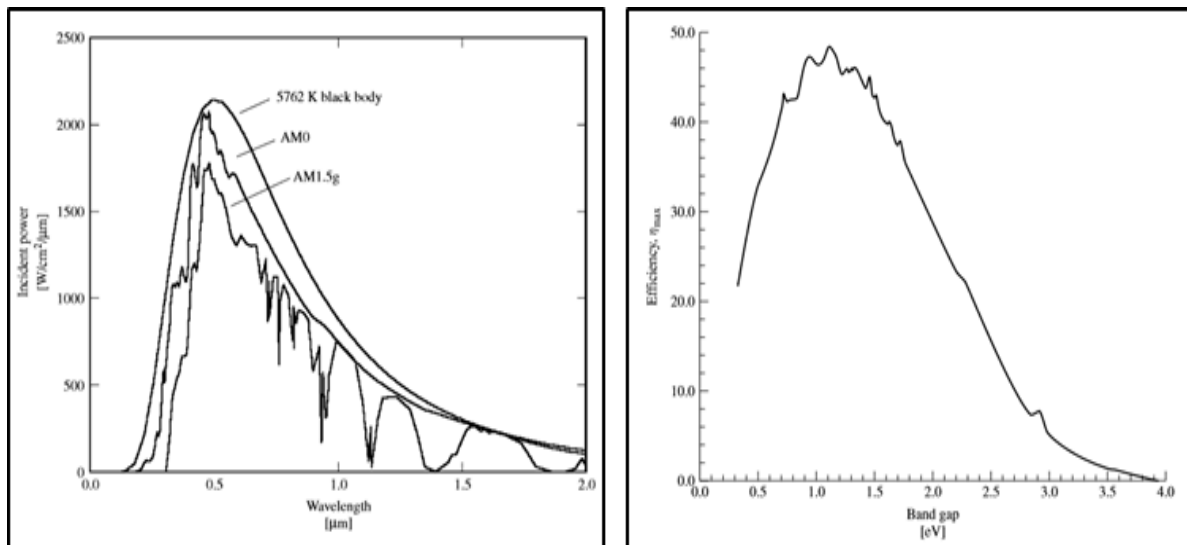


Figure I-6:(On the right) a radiation spectrum of a black body, an AM 0 spectrum and an AM 1.5 spectrum (Luque and Hegedus, 2003); (on the left) a theoretical maximum efficiency as a function of semi-conductors band gap (Luque and Hegedus, 2003).

Hence, there is an interplay of the intrinsic chemical potential of TiO<sub>2</sub> and the sun spectrum in terms of its photocatalytic abilities. The equation below demonstrates this interplay, linking band gap energy to wavelength.

$$E(\lambda) = \frac{hc}{\lambda} \tag{Equation 10}$$

where  $\lambda$  is the wavelength,  $c$  is the speed of light and  $h$  is Planck's constant. Since light is viewed as packets of energy called photons ( $E_\lambda$ ), only the photons with sufficient energy out of the possible  $4.4 \times 10^{17}$  photons which allegedly strike each cm<sup>2</sup> of the earth's surface every second can elicit the semi-conductors to create electron hole pairs. It is perhaps why the theoretical efficiency that has been calculated for semi-conductors, with respect to their band gaps, has been given as about 50%, occurring at band gaps between 1.0 and 1.6eV (Luque and Hegedus, 2003). This does not represent the gap found in TiO<sub>2</sub>.

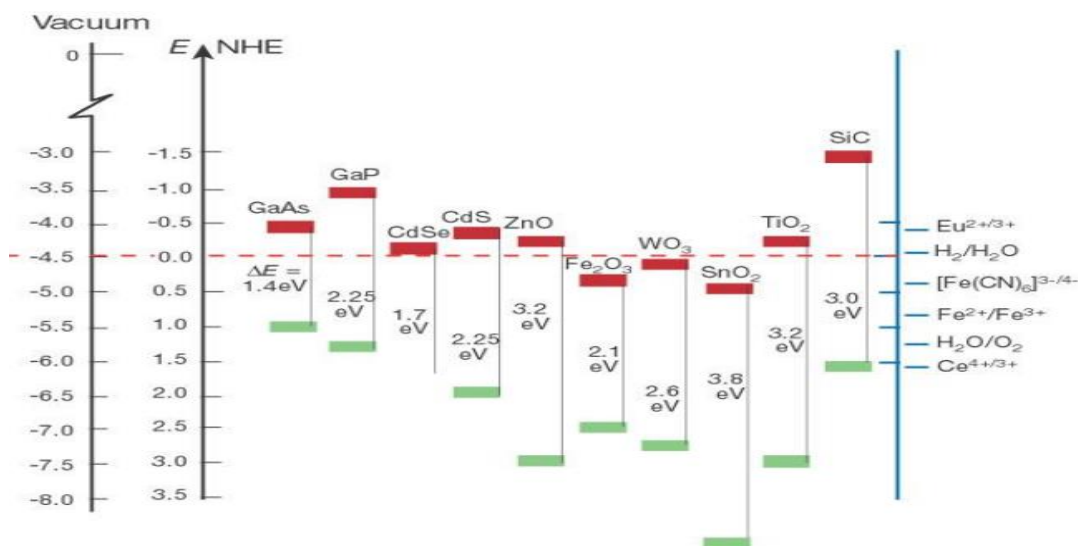


Figure I-7: Band position of some semi-conductors (Grätzel, 2001)

In Figure I-7 for example, one can see the band gaps of a few semiconductors, as well as  $\text{TiO}_2$ . It is true that a few of the semiconductors have band gaps that just approach this efficient region of between 1-1.6eV; unfortunately, all of them seem to have potential wells that are still too wide. Also, the difficulties associated with accessing the rarer elements that make up these metal oxides should not be ignored.

The most likely ways to narrow the band gaps that have been investigated are: doping of the semiconductors to introduce more accessible states close to the valence band edge but not as charger carrier within these wide band gaps (Mathur and Singh, 2007) e.g. in  $\text{TiO}_2$  this usually involves doping with C, S etc, or through nano-structuring, where the particle size of the semiconductor material is decreased, leading to alteration of the width of the band gap.

### 1.1.5.1 Function: Catalysis

$\text{TiO}_2$  cannot be mentioned without discussing the concept of photocatalysis and before this, we need to understand the concept of catalysis. According to Somorjai (1995), one of the main functions of a catalyst is to aid a reaction in the achievement of chemical equilibrium. For example, in the synthesis of ammonia from  $\text{N}_2$  and  $\text{H}_2$ , intermolecular bonds dissociation activation energies of 1120kJ/mol and 412kJ/mol are required; this would be otherwise improbable but on a catalyst, the activation energies drops to about 12kJ/mol, allowing the  $\text{NH}_3$  formation reaction to proceed easily and rapidly (Somorjai, 1995). This is achieved through the creation of alternative reaction pathways, with a lower activation energy, thus increasing the probability of a reaction going on to completion. A heterogenous catalyst like  $\text{TiO}_2$  makes an ideal catalyst as the surface states offer alternative reaction pathways in the form of "large concentration of low energy electronic states and electron vacancy states" (Somorjai, 1995). On the surface, these

areas will be deemed as surface active sites, and are most likely to donate and accept electrons thus being responsible for the formation and breaking of bonds that support the alternative reaction pathways mechanism of (photo)catalysis.

TiO<sub>2</sub> is one of the most popular photocatalysts that is commonly used and investigated. Its popularity reflects its low cost, strong oxidizing properties under UV, and its chemically and biologically inertness and low toxicity (Bezrodna *et al.*, 2002; Schneider *et al.*, 2014). As result of these and many other advantages, TiO<sub>2</sub> has been extensively studied and used in different areas (Nakata and Fujishima, 2012): removal of air and water pollutants, self-cleaning glasses, etc. Most of its uses are down to its semi-conducting properties.

As a semiconductor, TiO<sub>2</sub> has a discontinuity in its electronic state. A gap known as the band gap exists/separates the conduction band and the valance band. The conduction band occupies a higher energy level than that of the valance band gap. Conductors exhibit minimal to no gap; thus, their electrons require little energy to transverse the band gap. Insulators and semiconductors tend to lack “empty states adjacent to the top of the filled valance bands” (Callister and Rethwisch, 2012). These electrons thus need to be supplied with energy  $\geq E_g$  which is equivalent to the difference in the energy between the two states (in the valance band and in the conducting band). Although similar, insulators are strongly covalent or ionic, with electrons that are highly localised, making any sort of movement nearly impossible. This is not the case with semiconductor materials that are mostly covalent, but weakly so. The electrons thus have a better chance of being displaced once energy in the form of light or heat is introduced.

At equilibrium, the electrochemical energy level of the bulk oxides is usually centred between that of the conduction band energy and the valance band energy (Kung, 1989). The conduction band at equilibrium is only occupied by a few electrons that had been excited from the valance band, leaving holes behind. The densities of holes and electrons present in a system is given by the relationships below

$$n = N_C \exp[-(E_C - E_f)/kT] \quad \text{Equation 11}$$

$$p = N_v \exp[-(E_f - E_v)/kT] \quad \text{Equation 12}$$

$n$  and  $p$  denote the densities of electrons and holes respectively;  $N_C$  and  $N_v$  are constants relating to the mass and mobility of the charge carriers in the conduction and valance band;  $E_C$ ,  $E_f$ ,  $E_v$  are the lowest energy level of the conduction band, the Fermi energy and the highest valance energy level. This shows that the Fermi energy may be affected by doping the metal oxides, introducing adsorbates or reducing/oxidising a surface, not to mention the temperature too.

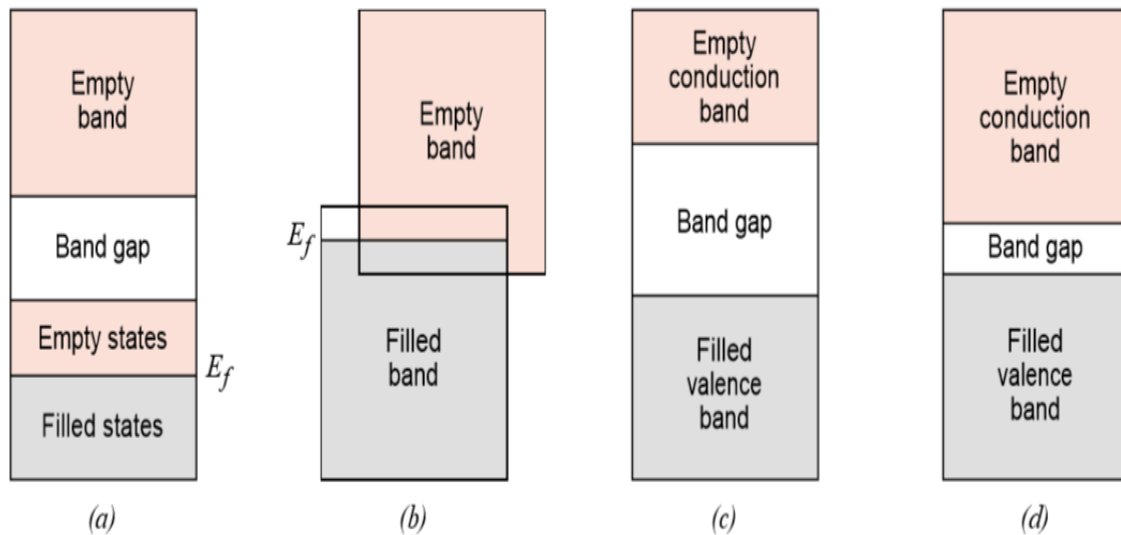


**Figure I-8: Energy band structures in solids. a) in a metal with empty states next and above filled states; b) in metals where there is an overlap of filled and empty states; c) in an Insulator and d) in a semiconductor (Callister and Rethwisch, 2012).**

In many an instance, the semiconductors are often extrinsic semiconductors; that is their electronic behaviour is determined and enhanced by the presence of impurities in their systems. Thus, the holes and electrons that have been mentioned are supplied by donor impurities, especially if the impurities are intentionally included. If the impurity is most likely to donate an electron, then it is termed an *n*-type semiconductor; if excessive holes are the results of these donor species then the semiconductors are referred to as *p*-type semiconductors (Callister and Rethwisch, 2012).  $\text{TiO}_2$  is considered an *n*-type semiconductor as the “intrinsic defects result in *n*-type doping”(Tang *et al.*, 1994; Linsebigler, Lu and Yates, 1995; Diebold, 2003). This property is linked in part to the transitional ability of titanium to exist with multiple oxidation states ( $\text{Ti}^{3+}$  and  $\text{Ti}^{4+}$ ), thus offering electron states that are partially occupied or unoccupied (Ganduglia-Pirovano, Hofmann and Sauer, 2007); as well as the presence of oxygen vacancies (Diebold, 2003).

The manifestation of an *n*-type semiconductor undergoing photo excitation is as follows. When an excitation event is initiated, possibly in the form of a photon of energy, excitation of ground state species occurs as a result of this. Usually, there is an elevation in energy levels to “a higher non-dissociative excited state” (Linsebigler, Lu and Yates, 1995). In the premise of this event, an electron- hole pair is created with sufficient energy to transverse the band gap, undergoing “charge transfer to adsorbed species”. This excitation event is concurrently followed by another de-excitation event in an effort to return the system back to equilibrium i.e. back to the ground state. De-excitation might happen by the emission of radiation, or a non-radiation step (Linsebigler, Lu and Yates, 1995). This non-radiative step as explained by Linsebigler *et al.* (1995)

usually occurs when we have energy levels that are close together, with overlapping vibrational energy levels to boot. This mechanism is roughly divided into conversion events that occur internally or externally. The main difference is that in the external mechanism, energy is transferred to solvents and solutes, but only from the lowest excited state. While internally, the energy transfer can occur from higher excited states to a lower or even ground states, “Heterogeneous photocatalysis” depends on the external mechanism. When excitation occurs, an electron-hole pair is created for a finite period of time. In a heterogeneous photocatalyst, there is a charge transfer to the adsorbed specie. Also, adsorption of species onto the photocatalyst is an important step and a surface process which is aided by the surface reaction of so-called active centres and represents another necessary property that catalysts display.

#### *1.1.5.2 Active sites creation in transition metals and their oxides*

Heterogeneous catalysis is dependent on the dispersion and surface properties of the material in question. This is especially true when one thinks about transition metals and their oxides—especially TiO<sub>2</sub> (which is one focus of this research). Clearly, the term surface chemistry does not just refer to a singular property of a material, but a series of properties that define its surface. For example, Kung (1989) listed the following: presences of charged adsorbed species, surface acidity/basicity, vacancies (anionic and cationic), interaction of the surface with incident photons leading to photo-assisted processes etc.

The aforementioned properties may be linked to the ionic nature of the transition metal oxide lattices; they consists of “metallic cations and oxygen anions”(Kung, 1989). Also, the exposure of surface anions, and cations, as a result of the adsorbent or simply the intrinsic nature of the transition metal oxide surface, is linked to the formation of the surface-active sites. The presence of these surface ionic species, especially in relation to the cations seeing as these had multiple oxidation states, means that the semiconductor has the ability to undergo redox reaction contributing to the presence of anionic and cationic vacancies. It is an important factor in the process of photocatalysis and will be discussed further in upcoming subsections. The formation of these active sites are usually dependent on the preparation methods:

- i. Precipitation, usually involving the “condensation and polymerization of hydroxylated metal ion”. This process typically leads to the formation of a three-dimensional network, consisting of the hydrated metals networked together. A drying step is required to complete the condensation process. Aprotic surfaces, i.e unable to donate H<sup>+</sup>, and with surface coordinative unsaturation ions become apparent during dehydroxylation of metal oxides (see Figure I-9). These coordinatively unsaturated (cus) cations M<sup>n+</sup> and oxides O<sup>2-</sup> according to Zaki et al (2001) are usually terminated by OH groups except when kinetics prevents their formation. The OH groups are as a result of the heterolytic dissociation of

water molecules, thanks to the coordinatively unsaturated pair of anion and cation; this is done in an attempt to reduce the surface charge, as shown in the figure below (and represented in Equation 16 and Equation 17).

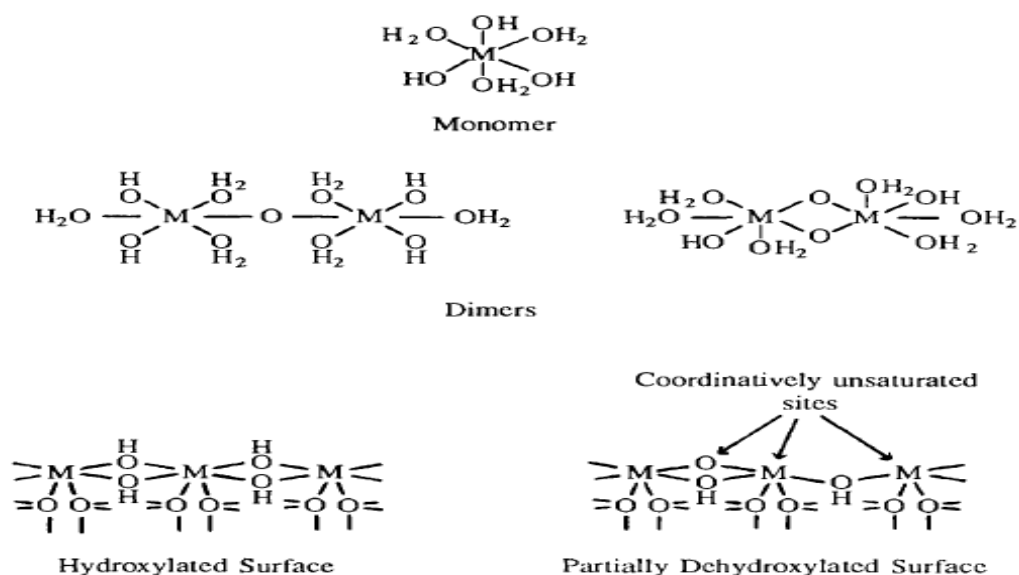
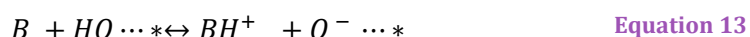


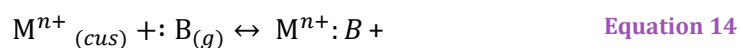
Figure I-9: Condensation and polymerization of a hypothetical hydroxylated metal ion monomer unit (Kung, 1989).

- ii. Other methods (leading to the formation of coordinative unsaturation) such as cleavage of single crystals. This is less applicable to the present research since the condensation and precipitation route is used in the synthesis of the TiO<sub>2</sub> replicas. Briefly, this method involves the cleaving of an “electrically neutral single crystal” (Kung, 1989). Upon cleavage, coordinative unsaturation occurs, created by any number of defects on the surface which could range from macroscopic defects including cracks, dislocations, steps etc, or point defects such as vacancies, interstitial atoms etc. The concentration of these defects is thought to increase as the crystal size decreases, which would explain why nano-scaling of catalyst crystal sizes has such an impact on their catalytic ability.

To describe these active sites, their acidities are considered in acid-base reactions on the catalyst surface (Kung, 1989). Thus, (cus) metal centres, M<sup>n+</sup>, are sometimes deemed to be Lewis acids (centres), while the [cus] O<sup>2-</sup> which are considered to be more basic than the bulk are known as Lewis bases (centres), in addition to OH<sup>-</sup>. Lewis acids are defined as “chemical species capable of accepting an electron pair” usually from adsorbates (see Equation 14), while Lewis bases act as electron donors (Lide and Haynes, 2010).







Brønsted acid sites are defined by the presence of protons (Wang *et al.*, 2006) and their subsequent transfer  $H^+$  to an adsorbate (as illustrated in Equation 13) (Kung, 1989). The Brønsted site is usually in the form of hydroxyl groups and they are able to go on to dissociate in order to protonate adsorbed bases (B) (Kung, 1989). The resulting conjugate acid (which is in the form of the now protonated base) and base (the coordinatively unsaturated  $O^-$ ) that now exist are stabilised as a result of interaction with either each other or with the oxide itself.

According to Schneider *et al.* (2014), in terms of an *n*-type semiconductor (where electrons are the majority carrier and holes the minority) - with numerous oxygen vacancies specifically, these defects (vacancies) are thought to behave as unpaired electrons, “creating an accumulation layer in the near-surface region” that ultimately results in band bending. Furthermore, the accumulated charge at the surface of the material determines the surface chemistry of  $TiO_2$ , especially at these active/acid sites. It is thus this drive to achieve equilibrium between the Fermi level ( $E_f$ ) of the  $TiO_2$  semiconductor and that of the adsorbate (Schneider *et al.*, 2014) that facilitates surface reactions. The reaction between an adsorbate and the surface of  $TiO_2$  is only possible if the electronegativity of the adsorbate exceeds that of  $TiO_2$ , i.e.  $>4.5\text{eV}$ . Should the adsorbate possess lower values then very little electron charge transfer is likely to happen. This is largely down to the energies that are thought to be associated with the binding energy of the adsorbate, in comparison to the surface (Equation 15):

$$\Delta E_{ads} = E_{ads-Ov} - E_{ads-clean} \quad \text{Equation 15}$$

Furthermore, many have found that besides the electronegativity of these adsorbates, their affinity for the  $TiO_2$  surface was also dependent on whether the  $TiO_2$  surface was “stoichiometric, reduced or oxidized”. These are properties which are ultimately summarised by what is known as the active sites.

Now for a surface to be considered active, it “must have surface coordinatively unsaturated ions to adsorb alkene molecules, dissociatively adsorb hydrogen molecules, and bind surface alkyl relatively strongly” (Kung, 1989). Although this description was used to describe the interaction of metal oxides with hydrocarbon, it is easy to see how this is applicable to a vast array of potential adsorbates.

### 1.1.5.3 Active sites, adsorption and deactivation

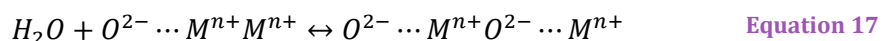
The term adsorption has so far been referenced indirectly to describe what occurs on the surfaces of a material. Formally, adsorption is an artefact of materials with surface interfaces. While it would be nice to consider surfaces as complete and total discontinuities that mark the boundaries

of a material, in reality this is not the case. Surfaces, at least on earth, are always surrounded by gas, liquid or even another solid “from the ambient” (Somorjai, 1995).

Adsorption produces the adsorbed layer. The drive to cover a surface is adsorption. It is brought about by the attractive potential that atoms exhibit over a certain distance from their “core”; molecules are thus attracted onto the adsorbing substrate.

An important feature of surface coordinatively unsaturated sites is the adsorption capacity. Most oxides tend to have a high affinity for water, which is essentially an attempt to reduce coordinative unsaturation. But without heat treatment, the surfaces of oxides tend to be completely covered with water and hydroxyl groups as soon as they are exposed to ambient conditions.

Below are relationships detailing this sorption process (mentioned by Kung (1989)) :



Though some oxides may appear unable to adsorb certain molecules, it may simply be due to their surfaces being completely saturated to some degree with water molecules. It is assumed that the degree of hydroxylation has an effect on the “chemisorptive capacity and the catalytic activity”, with a trend towards increased dehydroxylation being better in terms of activity for the oxides at least in the case of Cr<sub>2</sub>O<sub>3</sub> (Kung, 1989). Unless subjected to some dehydroxylation process, water especially on TiO<sub>2</sub> is almost always present. It adsorbs dissociatively and molecularly. Dissociatively, it adsorbs on the fivefold coordinated Ti site with its hydrogen atoms pointing away from the surface. Multiple hydrogen bonds are formed between the adsorbed species and oxygen atom of the surface substrate, facilitating proton transfer. Adsorption is also dependent on the crystal faces water is exposed to. On the (110) surface, the distance between the O atom adsorbed and the O<sup>2-</sup> of the substrate has been estimated as being larger than 0.3nm (Diebold, 2003) thus precluding the possibility of O-H interaction; the same cannot be said for the situation on TiO<sub>2</sub> (100) which appears to have a much smaller distance between the adsorbed O atom and “the two-fold coordinated substrate O<sup>2-</sup>” thus allowing O-H interaction to occur. It is for this reason TiO<sub>2</sub> is thought to be more likely to cause some form of water molecule dissociation on adsorption. While it appears that a surface of only (110) is wholly responsible for causing dissociation of water molecules on the surface of TiO<sub>2</sub>, the mechanisms mentioned were mainly investigated on rutile surfaces.

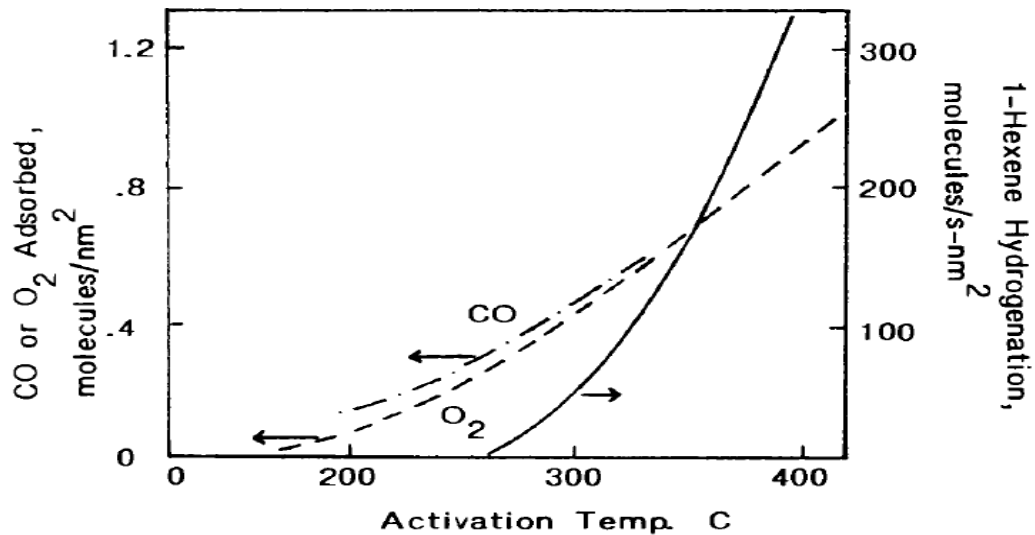


Figure I-10: Chart showing the CO<sub>2</sub> and O<sub>2</sub> adsorption behaviour and hexane catalytic behaviour on Cr<sub>2</sub>O<sub>3</sub> as a function of activation temperature (Kung, 1989).

Kung (1989) mentions several ways molecules interact with an oxide surface:

- dissociative adsorption involving the heterolytic dissociation of H<sub>2</sub>O ions: H<sup>+</sup> and OH<sup>-</sup>, a deprotonation process. This could also occur homolytically via the formation of neutral species less frequently. This form of adsorption may be reclassified as an acid-base reaction.
- molecular adsorption, involving the adsorbate and adsorbent interacting via  $\pi$  and  $\sigma$  non-dissociative bonding.
- abstractive adsorption is common on acidic oxides and involves the adsorbate abstracting species from the surface. In this process, if the adsorbate were to abstract a proton, making itself cationic, it could form an electrostatic bond with the surface, thus forming a viable surface bond. An example of this adsorption mechanism is seen in the protonation of an adsorbate. Again, as in dissociative adsorption, this form of adsorption may be reclassified as acid-base adsorption. This is usually seen in pyridine with the formation of pyridinium ions, showing Brønsted acid centres.
- reductive adsorption involving the oxidation of the adsorbate, and reduction of the surface. This tends to occur when the oxides have cations with multiple oxidation states, such as in transition metal oxides.

It is clear that the way oxide surfaces interact with adsorbates is complex and dependent on a number of factors. This is not just down to the intrinsic nature of the surface, but also to pre-treatment processes, which have the ability to change the oxide such as by dehydroxylation of and alteration of the oxidation state of their surfaces etc. This is without mentioning the array of

molecules and species that are available to participate in the adsorption process.

Deactivation of a catalyst goes hand-in-hand with adsorption. It usually occurs when the active site has been poisoned, reducing the catalytic efficiency. Kung (1989) suggests that these poisons form bonds on the surface capable of changing the atomic layer. Sometimes this occurs over a long period of time or quite rapidly. In petroleum refining, cracking catalysts tend to be deactivated either from coating with coke, or metallic residue. This deactivation is not all bad, as some catalysts are intentionally 'poisoned' with impurities in order to control their selectivity to the reactants (Somorjai, 1995).

Regeneration of some of these catalysts tend to involve the use of heat, especially in oil refining. Of course, this also comes with its own challenges, as certain morphological features e.g. porosity, might be affected on exposure to heat, affecting the catalyst efficacy.

### I.1.6 Functions: Photo assisted adsorption and decomposition

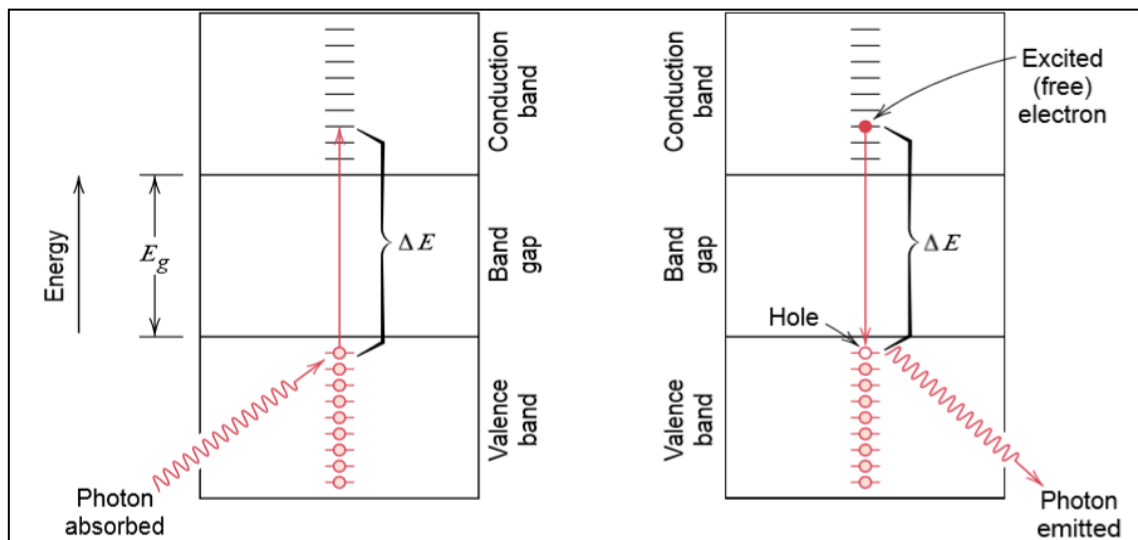


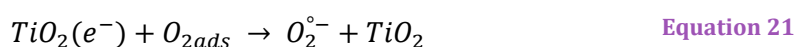
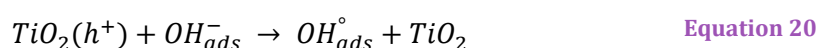
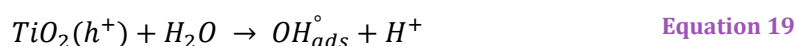
Figure I-11: Photon interaction with energy band in a semiconductor (Callister and Rethwisch, 2012)

This is a similar mechanism that occurs with  $\text{TiO}_2$  in its role as a photocatalyst. In photocatalysis, a photonic event increases the density of the charge carriers. This usually involves the excitement of electrons from the valance band to the conduction band thanks to the excess energy that has been obtained from the photon. The process is dependent on not just  $\lambda$ , but also the solid in question; ultimately, the surface chemistry of the solid is changed thanks to the migration of the electrons and the creation of the holes. Due to the excess space charge that has been generated, an upward band bending occurs near the surface and if there is no mechanism to remove electrons, a situation is set up where there is accumulation of holes and electrons, flattening the

band. The electrons that had been photo generated can go along to participate in various surface based reactions (Kung, 1989).

The photonic effect is only really significant and useful if the lifetime of the electrons and the photo generated holes are long enough to be effective. This is true in TiO<sub>2</sub> and ZnO. But in most cases, the lifetime of these charge carriers is impeded by the presence of impurities, defects and reduction of the oxides, which have the ability to hasten recombination events (Kung, 1989). Another potential problem is the fact that the photons adsorbed can also cause heating of the material, further increasing the rate of recombination events.

Should the lifetime of these charge carriers be meaningful enough, they can go on to interact with the TiO<sub>2</sub> surface. For example in interacting with water, charge carriers (holes and electrons) are produced on exposure of TiO<sub>2</sub> to light with a band gap that corresponds to UV light (3.2eV) (Z. Wang *et al.*, 2013). Holes diffuse from the valance band to the surface, reacting with adsorbed water, resulting in hydroxyl radicals which then go on to oxidise nearby molecules. Meanwhile, the electrons formed initially are said to participate in reduction, reducing oxygen available in air to superoxide radicals. Other chemical reactions that can occur as a result of this include photo-reduction of molecular nitrogen, photoreduction of CO<sub>2</sub>, photo-oxidation of halides etc (Linsebigler, Lu and Yates, 1995). Some of these surface reactions are listed in the equations below (Kung, 1989; Diebold, 2003):



Along with OH• radicals, Yu et al (2012) mentions oxygen superoxide and hydrogen peroxide that can also result from the absorption of electrons from the conduction band. The holes that have been generated can oxidise the organic molecule directly or can oxidize water into OH• which can go on to degrade organic dye. This is one of the ways in which TiO<sub>2</sub> can break down the various contaminants (including dye) via heterogeneous photocatalysis. These radicals are the main species that are thought to be responsible for the decomposition of some organic substances that come into contact with TiO<sub>2</sub>.

TiO<sub>2</sub> photocatalysis is a product of the unique chemistry of titania, arising from its surface structure via the mixed ionic and covalent nature of bonds present in its metal oxide lattice.

### I.1.7 Role of nanosizing, biomimicry in catalysis and photocatalysis

As it has already been established, there are many important advantages that can be obtained through the use of nanoscale systems. Some of the properties that undergo improvement have been mentioned in section I.1.1. In terms of a photocatalyst, the most important of these properties would be that pertaining to the band gap and the surface properties. Briefly, nanostructuring means that they have altered band gaps, different redox potential, improved ability of excitons to reach the adsorbate without undergoing wasteful recombination in bulk, and increased presence of trap states. In terms of surface properties, the fact that the surface accounts for a higher proportion of the entirety of the material means that the surface is considered more as opposed to a surface found in bulk materials.

In practical terms, improved properties have been demonstrated by Zhibo Zhang *et al* (1998) who synthesised TiO<sub>2</sub> nanoparticles of different sizes from titanium isopropoxide. They found that while the photocatalytic efficiency improved, when the particles size was decreased from 21nm to 11nm, further reduction to 6nm actually caused a detrimental effect on the photodegradation of chloroform. It is thought that surface recombination was to blame for the loss in efficiency.

Synthesis of TiO<sub>2</sub> carried out using biotemplates also appear to show positive results. The synthesis of biotemplated TiO<sub>2</sub> using different rice straw powder achieved particles with crystallite size of about 10nm, having improved BET surface areas of 97m<sup>2</sup>/g, improving from a sample made without rice straw powder to 45m<sup>2</sup>/g (Ramimoghadam, Bagheri and Abd Hamid, 2014). Of course, there is no mention of the actual photocatalytic ability, which could very easily be dominated by whatever other phase the carbon-based rice straw powder might add to the calcined biotemplate.

Microcrystalline cellulose was also used as a biotemplate. It was reacted with 0.004M titanium fluoride, using different acids, in a Teflon lined autoclave at 140-180°C for 24h before being calcined at 550°C to produce hierarchically nanostructured TiO<sub>2</sub> (Chen *et al.*, 2015). The resulting product's size and surface area were not mentioned, nor the actual proportion of anatase to other phases. P25 apparently performed better than the biotemplated samples.

Using a bigger biotemplate source (in the form of 50mm x 20mm x20mm pieces of wood) reacted with tetrabutyl titanate, gave TiO<sub>2</sub> crystallites of sizes 10-11nm with corresponding BET surface areas of 45m<sup>2</sup>/g for samples calcined at 500°C and 270 m<sup>2</sup>/g for sample calcined at 400°C (Luo *et al.*, 2015). The photocatalytic degradation of Bisphenol A by the calcined wood/titanate samples revealed a synergetic balance between adsorption and actual photocatalysis, which proved to be more effective compared to pure P25. The bulk of the biotemplated wood/titanate performance

were seen to be as a result of adsorption, rather than photo-assisted breakdown. With the extensive preparation steps, involving multiple periods in heated nitric acid for ion leaching, multiple drying steps before calcination, the performance of the biotemplates is positive. No actual rate constant or turnover number (or frequency or rate) were given to offer any comparison. This would need to be remedied here.

Going to smaller biotemplates e.g. plant extracts from *Moringa oleifera* were reacted with 0.5M of titanium isopropoxide at 50°C for 4h, before calcination at 500°C for a further 4h (Patidar and Jain, 2017). The nanopowder obtained had an average size of 12nm with an estimated band gap of 3.9eV. Photocatalytic performance was not probed there. Also, *Aloe vera* extract was used in the synthesis of TiO<sub>2</sub> after reaction with 0.4M of titanium isopropoxide and subsequent calcination at 500°C. The average crystallite size obtained was found to be 18nm, with a band gap of 3.6eV. Unfortunately, no photocatalytic studies were carried out (Gowri *et al.*, 2016). Extracts were also used by Dobrucka (2017) and Goutam *et al.* (2018) in the synthesis of TiO<sub>2</sub> nanoparticles of sizes 75nm and 120nm respectively.

Yet smaller, macromolecules have been demonstrated as suitable means for TiO<sub>2</sub> synthesis. TiO<sub>2</sub> was synthesised using a protein cage, formed from P22s empty capsid with an internal diameter of 46nm, in the presence of a T1 and T2 peptide sequence to nucleate TiO<sub>2</sub> from 10mM TiBALD for 96h (Bedwell *et al.*, 2015). Product particles were estimated to be less than 10nm in diameter and were shown to have photocatalytic properties in the breakdown of methylene blue. No comparison between P25 or any other standard titania sample was detailed. Still on the nanoscale, precipitation of TiO<sub>2</sub> from TiBALD using silacatein, a protein implicated in silica formation in sea sponge was shown to be successful (Dickerson, Sandhage and Naik, 2008).

The examples in literature show that there are many biomimetically-directed routes in TiO<sub>2</sub> from the use of biotemplates by way of wood pieces and grains, to including the functional macromolecules to direct nucleation and growth. However, there appears to be little done using plant leaves, outside the use of their extract. Hence very little has been done in examining the actual interaction of TiO<sub>2</sub> and the residual matter formed after calcination. Indeed, most literary examples touched on the polymorphic composition of titania, but surprisingly little was done on the presence of the carbon-based residual matter. Perhaps the Ti precursor solution might have been high enough to overshadow the other contribution, with some using concentrations as high as 0.4-0.5M (or the extended harsh treatment process might have been enough) to remove any intrinsic contribution of the biotemplate. With these in mind, the author thinks there is still quite a lot that can be achieved from the biomimicry of TiO<sub>2</sub>, particularly in the light of the premise of lack of leaf biotemplates (that are sourced from terrestrial or aquatic plant species). The researcher therefore wishes to address these significant gaps in present knowledge.

### **I.1.8 Nano-sized mineralised tissue, cellular deposition and nucleation of hydroxyapatite**

Hydroxyapatite, a calcium phosphate, is a major part of the skeletal system in the human body. It is an integral part in the development of mineralised/calcified tissue in humans, where it is incorporated into cells during ossification of specialised tissue (Hollinger, 2005). These cells are osteoblasts, which first lay down osteoid (the organic portion of the bone), which is then followed by the deposition of amorphous calcium phosphate crystals into these osteoids. This is referred to as a mineralisation process and ends in the formation of bones. When these osteoblasts become trapped during the mineralisation process, they differentiate into osteocytes. These cells play an important role in mechano-sensing and activating/suppression that is necessary for bone remodelling processes in response to mechanical (as well as metabolic demands) (Hollinger, 2005). In conjunction with osteoclast, a cell responsible for the resorption of bone, osteoblast and osteocytes are linked through gap junction and paracrine secretion (Hollinger, 2005; Schaffler *et al.*, 2014) forming a network of bone modellers. Studies have pointed to the role of mitochondria in the accumulation of  $\text{Ca}^{2+}$  and phosphate ions and in the delivery of them in vesicles (formed from polarized budding present on osteoblasts) (Abou Neel *et al.*, 2016). Within the vesicles, phosphate occurs as a polyphosphate that forms strong complexes with divalent ions (including  $\text{Ca}^{2+}$ ) responsible for preventing the precipitation into crystalline hydroxyapatite even with supersaturation (Mahamid *et al.*, 2011). The presence of other organic phosphate complexes, the complexation of  $\text{Ca}^{2+}$  by phospholipids also ensures that the calcium phosphate complex remains amorphous. They are aggregated into globules (80nm in diameter) that are translocated to the organic matrix via exocytosis at the growth interface (Mahamid *et al.*, 2011) where crystallization on/in/within the organic matrix occurs (Abou Neel *et al.*, 2016). This amorphous mineral is thought to make up about 1-30% of bone (Combes and Rey, 2010). Studies on Zebra fish, blue shark and mouse have shown that the amorphous phase is the main precursor present before the formation of the final crystalline apatite product (Zhao *et al.*, 2011) stabilised by  $\text{Mg}^{2+}$ , F<sup>-</sup>, phosphates, phosphorylated nucleotides etc, increasing their persistence before they transform into a final phase.

#### **I.1.8.1 Calcium phosphate in mineralised tissue**

The presence of hydroxyapatite within the various calcified tissues like bone and teeth is essential in fulfilling the function of these tissues, such as:

- providing load bearing/protection function in order to facilitate mobility, withstand the effects of gravity, chewing, organ protection and so on. It needs to be able to bear and dissipate the effects of load bearing effectively. This is achieved by its composite nature



i.e. a combination of a mineral (hydroxyapatite) within an organic matrix (water, collagen protein etc). These allows bone to be light weight, tough with an ability to withstand high compressive strength (200MPa for cortical bone) (Hollinger, 2005; Dorozhkin, 2011). The alignment of hydroxyapatite, particularly along the c-axis can be responsible for the excellent wear properties in certain instances (Fu *et al.*, 2016).

- homeostatic maintenance of electrolytes through sequestering of ions like  $\text{Ca}^{2+}$ , phosphate means that bone acts as a storage site for mineral ions (Hollinger, 2005; Amini, Laurencin and Nukavarapu, 2012). Hydroxyapatite is considered as one of these storage sites that can maintain the balance of electrolytes in the body.
- trapping of dangerous metals like Pb can also be sequestered by hydroxyapatite, reducing the occurrence of their free form in blood serum (Amini, Laurencin and Nukavarapu, 2012).

In instances where damage to these mineralised tissue has been brought on by age, pathological diseases (caries, osteoporosis, osteopetrosis, osteonecrosis (Boskey, 2007)), physical damage (fractures) might necessitate treatment with materials that share similar characteristics and biocompatibility to fix these injuries. Here one begins to consider the role of biomimetics in the synthesis of nanostructures and scaffolds in the possible treatment of these conditions. Before we go any further, it is important to consider what exactly is hydroxyapatite.

### ***1.1.8.2 What is exactly hydroxyapatite?***

Hydroxyapatite belongs to a family of materials that consist mainly of  $\text{Ca}^{2+}$  and phosphates anions usually in the forms of orthophosphates ( $\text{PO}_4^{3-}$ ), metaphosphates ( $\text{PO}_3^-$ ) or pyrophosphates ( $\text{P}_2\text{O}_7^{4-}$ ), with minor inclusions of hydroxyl ( $\text{OH}^-$ ) and hydrogen ions ( $\text{H}^+$ ) (Eliaz *et al.*, 2017). The first mention of calcium phosphate was around 1769 (Dorozhkin, 2012b), where it was discovered to be a component of bone by Gahn. As of the 18<sup>th</sup> century, Nicolad Vanquelin discovered the existence of acidic calcium phosphate: MCPM (Monocalcium phosphate monohydrate), MCPA (Monocalcium phosphate anhydrous), DCPA (Dicalcium phosphate anhydrous) and DCPD (Dicalcium phosphate dihydrate) (Dorozhkin, 2012b). CDHA (Calcium deficient hydroxyapatite) was prepared around 1813, and this (along with the differences in the composition between the mineral content of the teeth and the bone) was reported around 1808 (Eliaz *et al.*, 2017). The first mentions of the term “tribasic phosphate of lime” occurred around 1832, the term covers modern day  $\alpha$  and  $\beta$  tricalcium phosphate (TCP). Octacalcium phosphate was prepared soon after in 1843 (Eliaz *et al.*, 2017). Amorphous calcium phosphate (ACP) was mentioned in 1955, effectively the latest addition to the calcium orthophosphate family (Dorozhkin, 2011, 2012b).

**Table I-1: A list of Calcium orthophosphates, their Ca/P ratios, solubilities and formulae (Dorozhkin, 2012a)**

Ca/P molar ratio	Compound	Formula	Solubility at 25°C, -log(K <sub>s</sub> )	Solubility at 25°C, g/L	pH stability range in aqueous solutions at 25°C
0.5	Monocalcium phosphate monohydrate (MCPM)	Ca(H <sub>2</sub> PO <sub>4</sub> ) <sub>2</sub> ·H <sub>2</sub> O	1.14	~ 18	0.0 – 2.0
0.5	Monocalcium phosphate anhydrous (MCPA or MCP)	Ca(H <sub>2</sub> PO <sub>4</sub> ) <sub>2</sub>	1.14	~ 17	[c]
1.0	Dicalcium phosphate dihydrate (DCPD), mineral brushite	CaHPO <sub>4</sub> ·2H <sub>2</sub> O	6.59	~ 0.088	2.0 – 6.0
1.0	Dicalcium phosphate anhydrous (DCPA or DCP), mineral monetite	CaHPO <sub>4</sub>	6.90	~ 0.048	[c]
1.33	Octacalcium phosphate (OCP)	Ca <sub>8</sub> (HPO <sub>4</sub> ) <sub>2</sub> (PO <sub>4</sub> ) <sub>4</sub> ·5H <sub>2</sub> O	96.6	~ 0.0081	5.5 – 7.0
1.5	α-Tricalcium phosphate (α-TCP)	α-Ca <sub>3</sub> (PO <sub>4</sub> ) <sub>2</sub>	25.5	~ 0.0025	[b]
1.5	β-Tricalcium phosphate (β-TCP)	β-Ca <sub>3</sub> (PO <sub>4</sub> ) <sub>2</sub>	28.9	~ 0.0005	[b]
1.2 – 2.2	Amorphous calcium phosphates (ACP)	Ca <sub>n</sub> H <sub>n</sub> (PO <sub>4</sub> ) <sub>2</sub> ·nH <sub>2</sub> O, n = 3 – 4.5; 15 – 20% H <sub>2</sub> O	[b]	[b]	~ 5 – 12 [d]
1.5 – 1.67	Calcium-deficient hydroxyapatite (CDHA or Ca-def HA) <sup>[e]</sup>	Ca <sub>10-x</sub> (HPO <sub>4</sub> ) <sub>x</sub> (PO <sub>4</sub> ) <sub>6-x</sub> (OH) <sub>2-x</sub> (0 < x < 1)	~ 85	~ 0.0094	6.5 – 9.5
1.67	Hydroxyapatite (HA, HAp or OHAp)	Ca <sub>10</sub> (PO <sub>4</sub> ) <sub>6</sub> (OH) <sub>2</sub>	116.8	~ 0.0003	9.5 – 12
1.67	Fluorapatite (FA or FAp)	Ca <sub>10</sub> (PO <sub>4</sub> ) <sub>6</sub> F <sub>2</sub>	120.0	~ 0.0002	7 – 12
1.67	Oxyapatite (OA, OAp or OXA) <sup>[f]</sup>	Ca <sub>10</sub> (PO <sub>4</sub> ) <sub>6</sub> O	~ 69	~ 0.087	[b]
2.0	Tetracalcium phosphate (TTCP or TetCP), mineral hilgenstockite	Ca <sub>4</sub> (PO <sub>4</sub> ) <sub>2</sub> O	38 – 44	~ 0.0007	[b]

From the table above, it is clear that the different members have different properties that make them unique amongst themselves:

- MCPM and MCPA: MCPM is considered the most acidic of the members of calcium orthophosphates, as well as being the most water soluble (~18 mg/ml). It does not occur in nature as a result of the aforementioned properties, as well as being non-biocompatible (Dorozhkin, 2011). MCPA can be formed from heating MCPM to a 100°C. It is therefore considered the anhydrous form of MCPM. It has poor biocompatible properties mainly because of its acidity (Dorozhkin, 2011).
- DCPD and DCPA: DCPD has a low solubility in water (~0.088 mg/ml) that has been linked to its lattice configuration. It consists of CaPO<sub>4</sub> parallel chains, with bi-layers of water trapped between these chains. It is thought that the difference in the ordering of either of the water layers is responsible for its low solubility in water (Wang and Nancollas, 2008). It is most prominent at pH = 6.5; above 6.5 OCP and ACP readily occur. DCPD occurs in nature usually as an intermediate in mineralisation and dissolution of bone (Dorozhkin, 2011). DCPA is an anhydrous form of DCPD formed by heating DCPD to around 80°C. It has a low solubility (~0.048 mg/ml) and does not occur in normal calcification in vivo (Dorozhkin, 2011).
- TCP: can be differentiated into β-TCP and α-TCP. Pure β-TCP does not occur in nature, only as a magnesium substituted form. β-TCP is not precipitated from aqueous solution

but would precipitate from organic solution. Otherwise, it is obtained via high temperature (800°C) decomposition of CDHA or solid state reaction between DCPA and a base (Dorozhkin, 2011). Conversion to  $\alpha$ -TCP occurs at above 1125°C; it may be stabilised at lower temperatures through the addition of silicates.  $\alpha$ -TCP is the less stable TCP, tending to transform into CDHA in aqueous solution. It is not commonly used in physiological settings because of its fast resorption (Dorozhkin, 2011).

- OCP: It is considered an intermediate during the precipitation of hydroxyapatite and is thought to display a structural similarity to hydroxyapatite, as a result of the apatitic layers interspaced with hydrated layers, parallel to the (100) face (Wang and Nancollas, 2008). The similarities between the OCP continues with the ability to prepare OCP with non-stoichiometry i.e. formation of OCP with  $\text{Ca}^{2+}$  excess or deficiency. OCP apparently participates in the initial phases of enamel and bone formation, through precipitation and hydrolysis (Dorozhkin, 2011). This is evidenced by the “ribbon like consistency of the initial enamel crystallites” resembling OCP in comparison with hydroxyapatite (Wang and Nancollas, 2008).
- HA and CDHA: In the apatite category exist hydroxyapatite (HA), calcium deficient hydroxyapatite (CDHA), fluorapatite (FA) and oxyapatite (OA). The former two are the most relevant biomedically and will be the only members of this category considered. HA can either occur having monoclinic unit cells or hexagonal unit cells. In the hexagonal arrangement, (which is the form that is mostly encountered in a natural settings) an array of phosphate ions tetrahedra are held together by calcium ions dispersed in the lattice (Ma and Liu, 2009). The  $\text{Ca}^{2+}$  occurs in two possible sites, either within triangles or columns. These ions form the channels within the lattice. The hydroxyl ions also occur in columns, on the screw axis, which depending on the direction of the adjacent hydroxyl ions, the overall hydroxyl apatite might either end up with a monoclinic or hexagonal unit cell. For the hexagonal unit cell, the adjacent hydroxyl ions are pointed in opposite directions, leading to steric interference between adjacent hydroxyl groups (Elliott, Mackie and Young, 1973; Ma and Liu, 2009). To compensate for this, ionic substitution (fluoride ion, chlorine ion) or vacancy creation (Wang and Nancollas, 2008; Dorozhkin, 2011). For this reason hexagonal hydroxyapatite tends to require some form of substitution to stabilise the lattice at ambient temperature and it is therefore never truly stoichiometric (Wang and Nancollas, 2008).

In a monoclinic HA, the hydroxide ions present in their columns are pointed in a single direction and reversed in the adjacent column. The hydroxyl ions conformation effectively removes the problem of steric hindrance in the structure. For this reason, the monoclinic unit cell is considered more ordered/stable at even ambient temperature (Ma and Liu,

2009), resulting in a stoichiometric material.

Both the hexagonal and monoclinic HA have the molecular formula  $\text{Ca}_5(\text{PO}_4)_3(\text{OH})$ , with unit cells of  $a=9.84 \text{ \AA}$ ,  $b=2a$ ,  $c=6.88 \text{ \AA}$  for a monoclinic cell, and  $a=b=9.84 \text{ \AA}$ ,  $c=6.88 \text{ \AA}$  for a hexagonal cell (Eliaz *et al.*, 2017). Their lattice structure can be seen in Figure I-12. They are actively used in the “coating of orthopaedic and dental implants”, for drug delivery purposes and within toothpastes (Dorozhkin, 2011). This is mainly down to its stability in solution (0.0003 mg/ml). HAs are readily prepared by solid state or with wet state methods involving a  $\text{Ca}^{2+}$  and phosphate containing solutions in the absence of  $\text{CO}_2$ . An ageing step is usually needed to increase the Ca/P ratios, as the first precipitated are ACPs and CDHA (Dorozhkin, 2011).

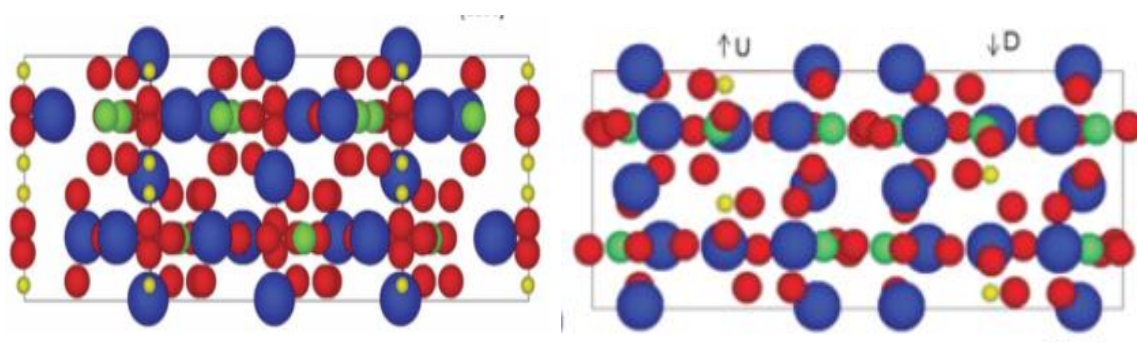


Figure I-12: Schematic projection of hexagonal hydroxyapatite and monoclinic hydroxyapatite, where calcium element is represent by blue spheres, phosphate by green spheres, oxygen by red spheres and hydrogen by yellow sphere (Reyes-Gasga, Martínez-Piñeiro and Brès, 2012)

- CDHA: This is usually the first precipitate formed, along with ACP, from an aqueous reaction of sols of  $\text{Ca}^{2+}$  and phosphate ions, it is usually referred to as precipitated-HA. It is often non-stoichiometric, having variable Ca/P ratios, which have been explained by “surface adsorption, lattice substitution and inter-crystalline mixtures of HA and OCP “ (Dorozhkin, 2011; Eliaz *et al.*, 2017). Its formula is given as  $\text{Ca}_{10-x}(\text{HPO}_4)_x(\text{PO}_4)_{6-x}(\text{OH})_{2-x}$  ( $0 < x < 1$ ). The calcium deficiency that forms the basis of this compound causes a net negative charge, that needs to be compensated through some form of charge balance. This is done by creating phosphate vacancies, but as this is not normally seen, protonation of  $\text{PO}_4^{3-}$  occurs or substitution of  $\text{CO}_3^{2-}$ . It is also possible that a hydroxyl group is also protonated (Dorozhkin, 2011; Eliaz *et al.*, 2017). Other  $\text{Ca}^{2+}$  ion substitution such as  $\text{K}^+$ ,  $\text{Na}^+$ ,  $\text{Sr}^{2+}$  and  $\text{Mg}^{2+}$ ; are possible; carbonates for phosphates; fluorides, chlorides and carbonates for hydroxyls (Dorozhkin, 2011; Eliaz *et al.*, 2017).

The apatites formed in animals and humans occurs as CDHA, which makes it one of the more relevant members of the calcium orthophosphate family. It is thus actively used for

drug delivery, bone substitute and in other non-medical applications (catalysis of bio gasoline) (Dorozhkin, 2011; Eliaz *et al.*, 2017).

- ACP: Amorphous calcium phosphate (ACP) is the first phase to form in the precipitation of CDHA and most likely the other calcium orthophosphates as well. It represents a non-crystalline class of calcium phosphate, as it lacks long range order. Its Ca/P ratio is difficult to pin down (1.18-2.50), as depending on conditions like pH, concentration of mixing solution, the ratio could change (Wang and Nancollas, 2008; Eliaz *et al.*, 2017). The same could be said for its lifetime, as hydrated (low temperatures) ACP is considered a transient phase (changes to the reacting sols pH, ionic strength and temperature can all have effects on how quickly it transforms). Physiologically-speaking, non-pure ACP is found in soft tissue that have undergone pathological calcification. It is used as a filling in dentistry, taking advantage of its solubility and ability to release Ca<sup>2+</sup>, phosphate and other relevant ions in an aqueous environment (aiding osteoinduction). It is also known for better osteo-conduction than HA, and greater biodegradability than TCP (Zhao *et al.*, 2011). Unfortunately this rapid dissolution can quite quickly cause localised physiological harm to cells in particular, thanks to the rapid change in pH (Eliaz *et al.*, 2017); this along with its reported low mechanical properties when prepared as a powder (Dorozhkin, 2012a) makes it problematic to use on its own.

### **I.1.9 Potential functional material role in bone repair**

Some calcium phosphate phases showed reasonable biocompatible properties, only a few of the compounds were deemed reasonable. Hydroxyapatite and its calcium deficient counterpart are the most likely to be used due to their biocompatibility in addition to stability in an aqueous setting. It is for this reason that they are the materials of choice in biomedical applications, specifically bone repair/regeneration. Biocompatibility is relevant for materials used in the body for use in bone repair applications.

To aid in bone repair, the use of bone grafts is crucial, especially in situations where repair cannot occur without some intervention e.g. significant fractures, reconstruction of arthroplasties and treatment of tumours (Goldberg and Stevenson, 1987). Autografts will always be considered the most suitable material for bone repair, mainly because they do not elicit immunogenic response and are biocompatible with the host body system, not to mention them being osteo-inductive and osteo-conductive (Amini, Laurencin and Nukavarapu, 2012). The use of autografts however comes with challenges like infection, morbidity of donor site, pain and bleeding etc. There is always the problem that the site of injury might be too extensive to be ethically fixed by using a graft from the same host. Here is where the need for grafts from other alternatives might need to be considered. The use of allografts, which are sourced from the same species, however

genetically not similar, offers the next means of plugging the issues with supply and demand. Unfortunately, allografts are plagued by immunogenic problems within the host, causing failures of close to 25% (seen for freeze dried grafts (Goldberg and Stevenson, 1987)). There is the added problem of increased infection, which can be addressed by irradiating the specimens. Unfortunately this then causes a loss of osteoinductive properties (Amini, Laurencin and Nukavarapu, 2012). These challenges with allografts and autografts have necessitated the need for alternative therapies, which lay in the use of substitute materials in the form of scaffolds. In order for these substitutes to suitably fulfil their functions as alternatives to bone grafts, they need to be biocompatible, bioactive, with good stability and mechanical properties etc.

- **Biocompatibility:** is quite an important property as it is based around the implant material being able to perform appropriately-meaning non/little negative host response, thus reducing the possibility of rejection. HA and CDHA bearing great similarity to the apatites found in the body are easily incorporated by the body (Eliaz *et al.*, 2017).
- **Bioactivity:** a material is considered bioactive if it can “participate in specific biological reactions or have an effect on living tissue” (Eliaz *et al.*, 2017). This is important, and is linked to
  - **Osteo-integration:** formation of bone tissue through/around a material without the presence of a fibrous layer
  - **Osteo-conduction:** providing a suitable surface/interface for bone deposition
  - **Osteo-induction:** linked to osteogenesis and the stimulation of bone forming cells

These are all essential markers for biomaterials that are aiming to be used as bone grafts. HA and CDHA show bioactivity to various degrees. HA combined with PMMA was shown to improve the composite’s osteo-conductivity (Abou Neel *et al.*, 2016).

- **Stability:** in terms of resorption of the material, the time scale of the implant’s use needs to fall within the range of a few months to years as per the time rate for new bone formation (Eliaz *et al.*, 2017). HA and CDHA are quite stable, thus to tune their dissolution properties, it might be necessary to enhance their porosity, change the degree of substitution or consider the effects of nano-scaling (Eliaz *et al.*, 2017).
- **Mechanical properties:** it is important for materials to be used in areas where its intrinsic load bearing properties will match that of the designated site. Calcium phosphate tends to be quite brittle, especially if used alone. Although they have a higher compressive strength than bone (Eliaz *et al.*, 2017), they need to be confined to low load bearing areas or they might fail. This is especially so with apatites (Abou Neel *et al.*, 2016).
- **Surface properties:** such as wettability and a reactive surface. Wettability affects the ingress of water. Hydrophilic surfaces (high surface energies) tend to experience higher

cell adhesion and differentiation; this was seen with HA coating on an implant in response to mouse osteogenic cell (Eliaz *et al.*, 2017). The surface reactivity can affect the integration of the biomaterial to bone tissue. Higher reactivities allowed the formation of chemical bonds, decreasing the formation of fibrous capsule (Eliaz *et al.*, 2017). HA which is known to have very reactive layers, in part due to different composition of the surface against the interior (further exaggerated in an aqueous setting) would possibly make an ideal candidate (Wang and Nancollas, 2008).

Clearly HA and CDHA appear to possess the necessary properties that will allow them to be used as bone grafts, especially with the nanoengineering of their morphology and chemical composition to further augment these properties. Of course, their poor mechanical properties (low impact resistance and toughness) is an issue, but when restricted to low load bearing areas, the possibilities offered by HA and CDHA cannot be ignored. One aspect that has not been touched on is the role of nano-scaling in HA engineering.

#### **I.1.10 Role of nanosizing in mineralised tissue engineering**

Previously this thesis has explored the role of nano-scaling for catalytic materials like TiO<sub>2</sub> and how it may be used to improve its performance (section I.1.7), so here the role of nano-scaling for apatites will be touched upon.

Nano-scaling mainly affects the surface reactivities and its surface area-volume ratios. The smaller surface area to volume ratio is an important aspect. It has been mentioned (section I.1.1), that nanomaterials have a significant number of their atoms present on the surfaces; this property would further enhance the surface reactivities that are intrinsic to HA. This smaller size also means better interaction on the cellular level. It has been demonstrated that nano-scale HA evoked improved osteoblast adhesion “differentiation and proliferation, osteointegration” compared to micro-sized HA (Kuśnieruk *et al.*, 2016; Eliaz *et al.*, 2017). The smaller size also affects the solubility properties compared to larger sized particles as seen in the adapted Kelvin equation (Equation 9), improving the bone ingrowth possibility. Another advantage attached to the surface area is its drug loading potential, extending to other molecules like DNA, protein, and antibiotics (Eliaz *et al.*, 2017). The size of the particles allows their entry into the circulatory system to deliver the drugs. Nano sized HA have also been shown to exhibit inhibitory actions on certain cancers (Kuśnieruk *et al.*, 2016), while exhibiting little negative effects on normal cells (Eliaz *et al.*, 2017).

It thus makes sense that nano-scaling of an important mineral like hydroxyapatite could be the future. There have already been several attempts by other researchers to utilise biomimetic style to synthesise hydroxyapatite and other calcium phosphate minerals for uses as bone grafts, drug

delivery vehicles and so on.

Sometimes this was achieved through direct blending of pre-prepared hydroxyapatite into the polymer sol, which was then cast. Such preparation steps were used by Xu and co (2008). They prepared a nano HAP/PVA hydrogel by dissolving PVA in DMSO, which was then mixed in with nano HAP. The mixed sol was cast and underwent 7 freeze-thaw cycles to enhance crosslinkage. The scaffold showed biocompatibility towards corneal fibroblast, allowing ingrowth and proliferation. Poly hydroxyethyl methacrylate and HA polymer were prepared as an alternative graft material to allograft and autografts. It was shown here that the interaction between the hydrogel and the mineral HA contributed to the reversible elastomeric properties of the samples under modest loading (Song *et al.*, 2009).

Another take on the blending of HA with the polymer was achieved by Sheikh *et al* (2010). They obtained ground high purity HA from a bovine source. A mixed colloidal solution of PVA, containing different wt% of HA, was used to electro spin fibres. The fibres were consolidated to form mats which were shown to permit apatite-like growth on their surface when incubated in SBF for 6d. It was shown that the HA nanoparticles present were able to act as seeds to foster the growth of biological HA with the SBF.

Alginate was also used as a porous hydrogel matrix in the preparation of alginate/HA nanocomposite scaffold. Here, a solution of alginate was blended with hydroxyapatite powder. Gluconic acid delta lactone was added to aid the release of calcium ion from HA and the resulting colloid was allowed to gel at room temperature. The sample was then freeze dried to form a porous scaffold. The scaffold did well in allowing the growth of dental stem cells, which went on to develop a mineral matrix that consisted of HA and collagen (Sancilio *et al.*, 2018). Similarly, hydroxyapatite powder was added to a sol of alginate, before crosslinking with  $\text{CaCl}_2$  and then lyophilised. In the composites, rat osteoblastic cells showed better attachment than if only alginate was used (Lin and Yeh, 2004).

Another alginate/HA composite was made, but this time, the alginate sol was mixed first with ammonium phosphate, before calcium nitrate was introduced drop wise (Zhang, Wang and Wang, 2010); beads of the composites were formed immediately and then crosslinked for 16h. The release of the drug diclofenac sodium was shown to occur over a longer period using the composite than just sodium alginate.

Combining alginate and PVA, the only 3D printable system had HA present in their formulation. 2.5% of alginate with dissolved sodium phosphate present, and a PVA/HA suspension was mixed, before a final addition of calcium sulphate. They were then printed by a 3D printer. As well as having better printability, the samples containing HA showed better cell viability (Bendtsen,



Quinnell and Wei, 2017). Also, PVA-SA hydrogels loaded with sodium ampicillin were made and crosslinked using freeze -thaw method (18h at -20°C and 6h at 25°C: 3X) (Kamoun *et al.*, 2015). The resulting wound healing membrane was shown to have minimal haemolytic abilities, and enhanced heterolytic properties, with antimicrobial properties courtesy of the loaded drug. Overall all of these makes the membrane compatible for use in wound care.

Microspheres have also been used in the synthesis of HA. Porous PLA microspheres synthesised through a solvent evaporation where ammonium carbonate present in a methylene chloride solution of PLA was emulsified using PVA sol. Evaporation of the organic solvent forms the microspheres, while the decomposition of carbonate forms the pores in the microspheres (Shi *et al.*, 2011). The spheres were rested in 1.5x SBF at 37°C for several days which then saw the growth of hydroxyapatite and adhesion of cells in specific cases. Zhe *et al* (2011) meanwhile coated the nonporous PLA spheres by immersing in CaCl<sub>2</sub> for 2h, followed by the drop wise addition of potassium phosphate.

In comparison to the above, the method developed by Taguchi, Kishida and Akashi (1998) utilised PVA hydrogel with alternating immersion cycles of calcium chloride followed by sodium phosphate which led to the nucleation and formation of HA on the hydrogel template, rather than in tandem with the hydrogel formation or direct seeding of HA. Their work has been utilised by Suzuki *et al* (2001) and Harding, Osmond and Krebs (2017) to synthesise scaffolds of silica-HA, and collagen/HA respectively. Little has been reported on modifying and strengthening the hydrogel matrix, which is a shame as this methodology developed by Taguchi, Kishida and Akashi (1998) is simplistic enough to utilise, alongside the tuning of the amount of apatite in a scaffold (dependent on the number of cycle used). Thus, this researcher has decided to expand on this method.

## **I.2 Aims of the project**

In light of the recent improvements in the properties of materials evidenced in Chapter I through nano-structuring, this researcher aimed to take advantage of biomimicry, using both biological and non-biological sourced templates, as a way to achieve certain goals involving the fabrication of novel nanostructures with enhanced

- i) photocatalytic properties (TiO<sub>2</sub>)
- ii) nanohydroxyapatite composite properties
- iii) bioactive properties
- iv) drug delivery properties

It was a further goal (v) to compare the biotemplate with alternative synthesis template

Goal i) starting with our model photocatalyst, while previous studies melding biomimicry with

nano-structuring appeared to concentrate on the use of extracts obtained from leaves, or the use of biomolecules to facilitate TiO<sub>2</sub> formation, almost no studies have exclusively looked at TiO<sub>2</sub> synthesis and the mixed oxide nature of the resulting nano-structures formed. Thus, this researcher will attempt to remedy this by producing biomimetically enhanced TiO<sub>2</sub> with a hope to attain unique nano-structuring and functionality. Functionality will be tested using model pollutants like methyl orange (MO) which has known mutagenic properties (IV.3.2.1); and triton (TX-100), which is known to have endocrine disrupting abilities (V.5.1.1). Thus, the objectives to achieve this goal are as follows:

- a) Synthesising a leaf based photocatalyst using a terrestrial (*Eucalyptus camaldulensis*), and an aquatic leaf source (*Rotala rotundifolia*)
- b) Characterising their resultant morphology and elemental composition using SEM-EDX; the chemistry using FTIR; the phase changes and thermal properties using TGA; and its phase composition and crystallite size with XRD
- c) Investigating its photocatalytic properties through the decolourisation of MO and the breakdown of TX-100 through the observation of rate constant (k) and turnover frequency (TOF)
- d) Unravelling the nature of its active sites by probing it with pyridine and acetone adsorption, and how the mixed oxide nature of the biomimetically-derived catalyst affects its observed photo-assisted catalytic properties
- e) fabricating and characterising a self-supported floating photocatalyst system

Goal ii) in the improvement of hydroxyapatite, knowing that other researchers have examined the role of nano-scaling and its use to improve apatite and also knowing that hydrogel scaffolds are still the most popular, this researcher aims to borrow the matrix style (vesicles) synthesis normally used in osteogenesis, using the irregularities of a hydrogel system as a matrix in the synthesis and growth of optimised nano hydroxyapatite, while attempting to improve the stability of the hydrogel through blending with alginates and the inclusion of tannic acid. It is hoped that the a novel nanohydroxyapatite-hydrogel composite system will be the result. The objectives to achieve this goal will be as follows

- a) synthesising bioactive mineralised hydrogel scaffold using PVA hydrogel and other hydrogel blends
- b) characterising their morphology and elemental composition using SEM-EDX; chemistry using Raman and FTIR; thermal properties using TGA and DSC; mechanical properties using tensile testing; its mineral phase component and preferred crystallographic orientation using XRD

Goal iii) through the design of an optimised nanohydroxyapatite-hydrogel composite system, it is

anticipated that the bioactive properties would be enhanced as well. The following objectives will help ascertain if the goal has been accomplished:

- a) investigating the uptake of calcium ion and phosphate ion by the different hydrogel systems using pH monitoring and UV-vis spectroscopy
- b) investigating the composite systems bioactivity in situ through the interaction of the scaffold with simulated body fluid (SBF), and its degradation in phosphate buffer saline (PBS)

Goal iv) here, the expected improved drug delivery potential of the nanohydroxyapatite-hydrogel composite system will be assessed by evaluating the rate and extent of adsorption of methylene blue (MB), methyl orange (MO) and Ascorbic acid (AA)

Goal v) was to be achieved by using a designer microsphere system to overcoat hydroxyapatite and TiO<sub>2</sub>. The objectives are as follows:

- a) synthesising of a mineralised and a titania coated microsphere system using poly (lactic acid) that has been emulsified with the surfactant PVA
- b) characterising the morphology and elemental composition using SEM-EDX; the chemistry using FTIR; the thermal properties using TGA; and its phase composition and structure with XRD
- c) investigating its drug loading and release properties with antibiotic gentamicin

### **I.2.1 Sources of templates**

In this project, we are planning the improvement of the photocatalytic characteristic of TiO<sub>2</sub> and nanohydroxyapatite by utilising the framework that has been laid down by nature in engineering selected plant leaf structure in its multifunctional role (as an energy converter, respirator etc). This would mean drawing heavily on the concept of biomimicry for the synthesis of novel multifunctional materials. To start with, this would be achieved on the internal structures of a plant leaf, copying the leaf surface and internal structure, in a hope that using it as a biotemplate could not only help in the creation of structures with unique morphology, but also with interesting optical and chemical properties.

As an alternative to using biologically-derived template material, the author also intends to use synthetically derived polymer templates to build hierarchical materials.

#### ***I.2.1.1 Biologically derived templates***

Leaves were to be used as the biologically sourced templates, as they are quite plentiful and available. A leaf is a vital organ with an incredible assembly of features that direct and permit the conversion of solar energy into chemical energy, which can then be made available in a more accessible manner to be used to release energy and synthesise sugars of various complexities.

Anatomically speaking, plants from different environments possess leaves with different structures, sizes, colours (all of which can be categorised). Nevertheless, most leaves tend to contain certain features common in most eukaryotic plants.

The plant species that will be employed in these experiments include *Rotala Rotundifolia* RR and *Eucalyptus camaldulensis* EC.

### **I.2.1.2 Non-biological derived templates**

The non-biologically sourced templates are polymers. They include:

- sodium alginate
- poly vinyl alcohol PVA
- poly lactide

## **I.3 Thesis overview**

This thesis consists of chapters in the following order:

Chapter III contains some background of photocatalyst materials and TiO<sub>2</sub> active centres. An in-depth background on the biological templates that will be utilised for the synthesis of TiO<sub>2</sub> will include interfacial sol gel process behind the formation of the bio-templated TiO<sub>2</sub> replicas. Further morphological, chemical and crystallographic characterisation will be included in the chapter.

Chapter IV is based around the photocatalytic decolourisation of model pollutants, MO. Rate kinetics and the turnover frequencies will be calculated. The nature of the active sites and how these would have had an effect on the performance of the replicas against a standard material (P25) will be discussed.

Chapter V is centred on the fabrication of a floating photocatalyst structure. It assesses the performance of the floating photocatalytic structure with MO and TX-100. The degradation kinetics and difference arising from the different film assembly and composition will be observed.

Chapter VI deals with the synthesis condition of hydroxyapatite-hydrogel composite. The chemical variation between all of the samples will be studied by Raman and FTIR.

Chapter VII concentrates on the nature of the hydroxyapatite minerals formed on the hydrogel. Information on the preferred orientation, average crystallite size and strain within the crystallites will be estimated using Williamson–Hall (WH) plots.

Chapter VIII deals with the mechanical characterisation of the mineralised hydrogel scaffold to ascertain their elastic modulus and compressive strength.

Chapter IX and Chapter X deals with the drug uptake and bioactivity of the mineralised hydrogels

in the presence of SBF and PBS.

Chapter XI is concerned with the synthesis and characterisation of PLA scaffolds where the surfactants will be varied as a way to change the morphology of the resulting microspheres. The deposition of the microspheres with hydroxyapatite and a titanium-based coating will be carried out.

Chapter XII deals with the uptake and release of gentamicin of the microsphere system using Raman spectroscopy.

Chapter XIII provides the conclusion with an appreciation of the future potential of the novel synthesised nanomaterial systems.

#### **I.4 Precision, accuracy, errors and limitations**

Experiments and methods used in observations undertaken for the fulfilment of this project have to be curated to reduce human error, through the use of duplicates/triplicates, thus errors and standard deviation have been included where possible to highlight the reliability of observations and results.

Errors associated with instrumentation have also been considered: thus soliciting the need for calibration of the instruments like UV-vis, performed with a standard solution of a known concentration; Raman spectroscopy was performed using single crystal silicon wafer to ensure lateral resolution; TGA was performed using the weight loss and known decomposition step of calcium oxalate monohydrate; DSC was performed using the melting and heat of fusion of indium; XRD was calibrated using corundum. Other instruments like SEM, TEM and EDX were calibrated by technical staff to UKAS specification.

Limitations in data collection/characterisation by the instruments has been considered, and where possible, multiple characterisation techniques have been included to improve the quality and thus reliability of the data.

## Chapter II Experimental Methodology

This chapter may be divided into three main sections: the sample synthesis and preparations (II.1-II.7), a section providing background information about the characterisation instruments (II.8), and some experimental setup (II.9).

### II.1 Sol gel synthesis of TiO<sub>2</sub> replicas of biotemplates

This was based on the interaction of the precursor agents and the surface of the chosen biological material.

#### II.1.1 Materials

The following materials were utilised in the replica synthesis process, and unless stated were purchased from Sigma Aldrich, UK. *Rotala rotundifolia* RR (Aquarium gardens); *Eucalyptus camaldulensis* EC (grown on Brunel's grounds); *Chlorella vulgaris* CV (Culture collection of algae and protozoa CCAP); titanium tetra isopropoxide TiPA (98%); titanium bis (ammonium lactate) dihydroxide (TiBALD); 2-propanol (95% anhydrous); ethyl acetate (99.8%anhydrous); hexane (95% anhydrous); sodium hydroxide pellets (NaOH); nitric acid (HNO<sub>3</sub>); hydrochloric acid (HCl); tannic acid and H<sub>2</sub>O (18MΩ).

#### II.1.2 Pre-treatment procedure for EC and RR

- Dewaxing step is as follows:

Eucalyptus leaves were washed, then lyophilised for 5h and subsequently refrigerated for future use. Afterwards, they were cut into a desired dimension and then placed in hexane overnight. A 12h immersion in ethyl acetate followed, and then another 12 in 2-propanol. The dewaxed product was designated DW. EC was the only sample that underwent the full dewaxing treatment. RR was left only in 2-propanol overnight before use.

- Following the dewaxing step, some samples were delignified as follows:

1wt% solution of NaOH in 2-propanol was made up with vigorous stirring and heated to 100 °C. The previously dewaxed leaves were introduced (maintaining a 1:10 solid to liquid ratio) for 1h. They were then rinsed several times with 2-propanol until the pH stabilised at around 7. These samples were denoted DL. Again, only EC underwent this treatment.

- Acid leaching was carried out as follows:

As a final step, some samples here were immersed in a pH1 solution of acid (HCl/HNO<sub>3</sub>) at different duration (5h, 12h). After treatment, the samples were rinsed in deionised H<sub>2</sub>O (3 times), and then left immersed in H<sub>2</sub>O for 2h. Following this, the samples was soaked in 2-propanol for

12h before being used.

### **II.1.3 Preparation procedure of EC and RR titania replicas**

#### **II.1.3.1 Biomimetic synthesis of TiO<sub>2</sub> using EC and RR as biotemplates**

The leaves were treated with a 2-propanol solution of TiPA (1mM; 5mM; 10mM) for 12h. Subsequently, they were rinsed with 2-propanol and then oven dried (100 °C for 30min). Calcination followed in air at 600 °C for 2h (10 °C/min). Further information on the interfacial sol gel chemistry reaction is contained in section III.4.1.1. The leaves were also treated with 5mM TiBALD and calcined using the same conditions for comparison purposes (see Figure III-3).

### **II.1.4 Preparation procedure of CV titania replica**

The treatment of algae samples used TiBALD rather than TiPA. They were first treated with tannic acid at a concentration of 40mg/ml. This lasted for 8 min. Next, the cells were rinsed in deionised water, and then immersed in a solution of 50mM TiBALD for 8min. After, the samples were centrifuged down to collect the titanium coated algal samples which were then dried at 100°C (for 30min) before being calcined at 600°C (for 2h) (10°C/min) in air.

## **II.2 Photocatalytic template film preparation**

### **II.2.1 Preparation of PVAc based films**

The preparation of thin photocatalytic films are as follows

#### **II.2.1.1 Materials**

The following materials were used in the preparation of the samples. Unless stated, all materials would have been purchased from Sigma Aldrich, UK. Poly vinyl acetate (PVAc) and dichloromethane (DCM) 99.8% anhydrous.

#### **II.2.1.2 Preparation procedure**

Preparation began by the dissolution of PVAc granules in DCM to obtain a 1wt% solution of PVAc in DCM. A glass cover slip of dimensions 2.2cm x 2.2cm was dipped in the polymer solution and then allowed to air dry. Afterwards, 0.25mg of P25 dispersed in DCM was pipetted onto the dried PVAc film to produce a film incorporated with P25. The dried films were harvested by floating them off on some water.

### **II.2.2 Preparation of PVA based films**

#### **II.2.2.1 Materials**

The following materials were used for the preparation of the samples in this section. All materials would have been purchased from Sigma Aldrich, UK. Poly vinyl alcohol (PVA) 115,000 ≥88%

hydrolysed purchased from VWR; H<sub>2</sub>O (18MΩ), glutaraldehyde, and HCl.

### ***II.2.2.2 Preparation procedure***

Preparation began by the dissolution of PVA granules in 70°C heated water. A final solution with a concentration of 8wt% of PVA was made. The crosslinker (glutaraldehyde) and then HCl was added, followed by agitation of the mixture to promote optimum dispersion. 1ml of the solution was then cast on the top of a cover slip (2.2cm by 2.2cm). The cast sample was left to dry in a ventilated fume cupboard. To produce films incorporated with the photocatalyst, 0.25mg of P25 was dispersed directly in the PVA solution before casting. The dried film could again be floated off by simply dropping the cover slip along with the cast film in excess water.

### ***II.2.3 Preparation of dual/asymmetric film***

The preparation process is more complicated, featuring more polymers and a mix of solvents. Deconstructed, it was composed of a top and bottom layer. The top consisted of primarily hydrophobic polymers, and the bottom layer consisted of mainly hydrophilic polymers.

#### ***II.2.3.1 Materials***

The following materials were required for the preparation of the samples in this section. Unless otherwise stated, all materials would have been purchased from Sigma Aldrich, UK. PVAc; DCM; sodium alginate (AL); polycaprolactone (PC); calcium chloride dihydrate (CaCl<sub>2</sub>·2H<sub>2</sub>O); N-(2-aminoethyl)-3-amino propyl-tri-methoxy-silane; tetra-ethoxy-silane (TEOS); tannic acid (TA); acetic acid and H<sub>2</sub>O(18MΩ).

#### ***II.2.3.2 Preparation procedure for the production of the top layer***

Several formulations to attain a film capable of self-supporting itself without sinking were attempted. As such, they required slightly different preparation methods

- i. PVAc: PVA: AL formulation

In this layer, 4wt% PVA and 4wt% PVAc also were dissolved in a 50-50 mix of acetic acid and deionised water are used here. In addition, 2wt% alginate was also included. They were mixed in the required ratio for their stability. In this formulation, PVAc is always in excess. The ratios are as follows: 7.5ml of PVAc: 2ml of PVA: 0.5ml of Al; 7ml of PVAc: 2ml of PVA: 0.5ml of Al: 0.2ml of H<sub>2</sub>O.

- ii. PC: PVAc formulation

Here, a 4wt% solution of PVAc dissolved in deionised/acetic acid was made and a PC solution with a concentration of 4wt% were used here. They were mixed in the required ratio to produce a film that could be cast down onto the hydrophilic layer (bottom). These formulations had PC in excess and include: 8ml of PC:2ml of PVAc



### ***II.2.3.3 Preparation procedure for the production of the base layer***

This layer consisted of 4wt% PVA and 2wt% alginate, both of which were dissolved in water. The two ratios used were: 9ml of Al:1ml of PVA and 7ml of Al: 3ml of PVA.

### ***II.2.3.4 Assembly of top and base layers***

The assembly process involved casting the bottom layer down first. This was done on a cover slip and then allowed to dry for approximately 1h. After, the top layer was then cast directly onto the bottom layer.

### ***II.2.3.5 Crosslinking and harvesting of films***

Once the top layer was relatively dry, the cover slide and the cast films were immersed in a solution of the crosslinking media. Three different crosslinking media were tested for the best results; a solution of 1wt % CaCl<sub>2</sub> dissolved in water, amino-functionalized silica sol (made by mixing a ratio of 1ml TEOS-2 diaminosilane-18ml deionised water-6ml 1NHCl (Pannier *et al.*, 2014)); and finally a combination of both of these solution mixed in different ratios (50 CaCl<sub>2</sub>:50amino silica sol or 70CaCl<sub>2</sub>:30 amino silica sol). Crosslinking was allowed to proceed overnight (12h), after which the films were then rinsed repeatedly to halt crosslinking and to rinse any excess unreacted material off.

Harvesting was done during the rinsing process and involved floating the films off in excess water.

## **II.2.4 Incorporation of titania, CV and other molecules into the asymmetric films**

This section details the steps involved in the incorporation of titania and CV into the asymmetric films.

### ***II.2.4.1 Materials***

The materials utilised in this section would have been purchased from Sigma Aldrich, UK unless otherwise mentioned: Evonik P25; RR titania template; CV titania template; algae nutrient BBM+V (CCAP) and H<sub>2</sub>O (18MΩ)

### ***II.2.4.2 Incorporation of materials in the top layer***

For titania incorporation, 0.25mg was measured out and then dispersed in DCM. It was introduced while mixing in the main components of the film before being cast as explained; this was so for the films where PVAc made up the majority component. In the case of films that had PC as the majority polymer, titania was first dispersed with PVAc before PC was introduced.

CV was not present in this layer.

### ***II.2.4.3 Incorporation of materials in the bottom layer***

- Incorporation of TiO<sub>2</sub> here was a lot easier. It was dispersed in deionised water and then sonicated together with PVA and Al before being cast.

- Introducing algae followed exactly the same principle. The main difference here was the fact that the algae was suspended in a BBM+V.

## **II.3 Hydrogel scaffold preparation**

This section details the methodology that was followed in the preparation of pure PVA hydrogel discs and composite hydrogel discs.

### **II.3.1 Preparation of pure PVA hydrogel discs**

#### **II.3.1.1 Materials**

All the chemicals used here would have been purchased from Sigma Aldrich, UK. PVA; 25% glutaraldehyde solution; HCl and H<sub>2</sub>O (18MΩ).

#### **II.3.1.2 Preparation procedure**

7.5ml of 8%PVA sol, 1.2ml of deionised water, 0.26ml of 25% glutaraldehyde and finally 0.1ml of (1M) HCL were mixed together with a glass stirrer. The mixed solution was cast in a petri dish, which was then covered. The crosslinking process was allowed to proceed for 1h until the cast solution could no longer flow, resulting in the formation of a crosslinked disc of hydrogel. The resultant disc was retrieved and then transferred to a dish filled with H<sub>2</sub>O to neutralise the pH, as well as in removing the excess unreacted glutaraldehyde.

After exchanging the water three times, within 15min, the hydrogel was rested for 5h in deionised water. Following this, it was returned to a damp petri dish for temporary storage.

The total amount of glutaraldehyde was varied by 15% and 30% to alter the degree of crosslinking of the hydrogel.

### **II.3.2 Preparation of PVA hydrogel blends**

The preparation of PVA blend sample followed a similar manner as in section II.3.1 with changes in the blended polymers.

#### **II.3.2.1 Materials**

The following materials were used: sodium alginate; TA; TiBALD and other materials are as listed in II.3.1.1

#### **II.3.2.2 PVA-Alginate blended disc**

With the exception of using 1.2ml of Sodium alginate (2wt% of sodium alginate dissolved in deionised water) in place of 1.2ml of deionised water, the preparation process followed the same route as in II.3.1.2. Alginate made up 20vol% of the overall blend.

### ***II.3.2.3 PVA-Alginate-tannic acid blended disc***

Following the procedure detailed in II.3.1.2, tannic acid was introduced by adding 0.174g of tannic acid (0.174g) to the 2wt% alginate solution (200ml) and stirred for 12h in a foil covered reagent bottle. The solution's colour changed from a pale yellow, to a light maroon colour in this time. It was then dialysed twice with 2-propanol for purification before the residue was lyophilised and then stored in an airtight container for future use. Before use, a 2wt% alginate-tannic acid solution was made. To form the final blend, 1/4<sup>th</sup> of the alginate-tannic acid solution made up the 20vol% of alginate that went into the hydrogel blend. This was cast, rinsed and stored as explained in II.3.1.2.

### ***II.3.2.4 PVA-Alginate-tannic acid Titanium blended disc***

This is almost a continuation of the previous procedure. The final composite consisted of an 80vol% fraction of PVA and 20vol% fraction of alginate (of which 20-25vol% consists of the tannic acid infused alginate). Due to the increased crosslinking potential of tannic acid (see Figure VI-4), the amount of glutaraldehyde (and by extension acid) was reduced, as the hydrogel gel was setting too quickly to allow proper mixing. The sample was cast, rinsed and then stored as explained in II.3.1.2.

## **II.4 Calcium<sub>(x)</sub> phosphate<sub>(y)</sub> mineralization of PVA hydrogels and its blends**

The process behind infusing the hydrogel samples with the necessary precursors to elicit the formation of the appropriate calcium phosphate phase is as follows.

### **II.4.1 Materials**

The materials involved include CaCl<sub>2</sub>·2H<sub>2</sub>O; disodium hydrogen orthophosphate (Na<sub>2</sub>HPO<sub>4</sub>); sodium carbonate (Na<sub>2</sub>CO<sub>3</sub>) and H<sub>2</sub>O (18MΩ). They were purchased from Sigma Aldrich, UK.

### **II.4.2 Mineralisation procedure**

The precursor solution was prepared by individually dissolving the salts of the essential components to attain the following concentrations: 50mM CaCl<sub>2</sub>, 50mM Na<sub>2</sub>CO<sub>3</sub> and 13mM Na<sub>2</sub>HPO<sub>4</sub>. The pre-prepared hydrogel discs (preparation detailed in section II.3) were immersed first into a solution of Na<sub>2</sub>CO<sub>3</sub>, followed by CaCl<sub>2</sub> and finally Na<sub>2</sub>HPO<sub>4</sub>. Each of the immersion steps lasted for 1h and was then followed by a quick rinse. The completion of the immersion step sequence (Na<sub>2</sub>CO<sub>3</sub> ⇒ CaCl<sub>2</sub> ⇒ Na<sub>2</sub>HPO<sub>4</sub>) ends in a single cycle and depending on the amount of mineralisation which was required, the number of cycles could be increased. 4 and 8 cycles were used.

In the case of the non-carbonated samples, the Na<sub>2</sub>CO<sub>3</sub> step was eliminated.

## **II.5 PLA/PVA Microsphere synthesis using PVA as a surfactant**

To prepare PLA PVA microspheres, the following methodology was utilised.

### **II.5.1 Materials**

These chemicals were utilised in the preparation of a PLA-PVA microsphere system: Poly -L- lactide (PLA) number average molecular mass ( $M_n$ ) of 40,000; chloroform 99.8% anhydrous; PVA; sodium alginate and H<sub>2</sub>O (18M $\Omega$ ). They were all purchased from Sigma Aldrich, UK.

#### **II.5.1.1 Preparation procedure**

10ml solution of 2.5wt% PVA in water was added to 1ml of 0.5wt% chloroform solution of PLA and immediately mixed at 7000rpm with a mechanical flea for 1h in a sealed 150ml reagent bottle. After 1h, the reagent bottle was opened while the mixing proceeded unhindered. Stirring continued until the emulsion's colour changed from milky to more translucent. At this point, the majority or all of the chloroform present in the system is thought to have evaporated, leaving behind the microspheres dispersed in a PVA-rich solution. The PLA-microsphere's were obtained by first centrifuging at 4000rpm for 10 min and then the supernatant was siphoned off leaving the microsphere to precipitate. The microspheres were then resuspended in deionised water, and the rinsing process was repeated (x2). Afterwards, the precipitate was dispersed onto a clean microscopic slide and left to dry at 40°C for 48h, at which point they were ready for further use.

### **II.5.2 Modification of the surfactants composition for PLA-PVA microspheres**

Modification of the surfactant simply followed the replacement of 20% of the PVA surfactant solution with either sodium alginate (2 wt% concentration), tannic acid-infused sodium alginate (80% of 2wt% concentration sodium alginate + 20% of tannic acid infused sodium alginate of 2wt% concentration), or titanium crosslinked sodium alginate infused with tannic acid (80% of 2wt% concentration sodium alginate + 20% of tannic acid infused sodium alginate of 2wt% concentration+50 $\mu$ l of 10mM TiBALD).

The preparation was similar as above.

## **II.6 Modification of PLA-PVA Microsphere interior**

Modification of the inside of the PLA-PVA system was carried out to encapsulate GC and AA in the microspheres interior.

### **II.6.1.1 Materials**

The following reagents were used: GC Gentamicin sulphate solution (50mg/ml); AA Ascorbic acid; PVA, chloroform; phosphate buffer saline (PBS) tablets and H<sub>2</sub>O (18M $\Omega$ ). They were purchased from Sigma Aldrich, UK.

### **II.6.1.2 Preparation procedure**

A gentamicin stock solution was diluted with 100mM PBS to a concentration of 5mM. To 4ml of a 0.5wt% of PLA solution in chloroform, 1ml of gentamicin sulphate was added with mixing for 15-30min with a mechanical flea at 7000rpm in a closed 150ml reagent bottle. After 30min, 40ml of 2.5wt%PVA was added and mixing continued for 1 h, for complete homogenisation. The reagent bottle then opened up to allow the evaporation of chloroform (1-3h). Once the cloudy solution became transparent, the microspheres were harvested following the same procedure as that detailed in II.5.1.1.

## **II.7 Modification of PLA-PVA Microsphere exteriors**

Further modification of the samples were carried out after the microsphere systems have been synthesised as above.

### **II.7.1 To produce titanium (TiO<sub>x</sub>) exteriors**

The production of samples with a titanium exterior are given below.

#### **II.7.1.1 Materials**

The chemicals used here included: TA; TiBALD; Trizma base (Tris); HCl and H<sub>2</sub>O (18MΩ).

#### **II.7.1.2 Preparation procedure**

The dried microspheres were measured out into a 50ml centrifuge tube which was then topped with a 20ml tris buffered solution of tannic acid (0.10mg/ml) at pH of 7.4 (adjusted with HCl) and mixed in an ultrasonic bath. The centrifuge tube was then transferred to a mechanical roller for 3h of mixing, after which the homogenised sample was centrifuged down. The precipitate was collected, and the supernatant was discarded. The centrifugation process was repeated again after the tube was topped with deionised water to remove any excess tannic acid. Following this, 15ml of the as pre-prepared solution of 25mM TiBALD was added to the centrifuge tube containing the rinsed tannic acid-coated PLA-PVA microspheres. They were dispersed using an ultrasonic bath and then transferred to the mechanical roller for further mixing (48h). The dispersion was then centrifuged down, and the precipitate collected. It was rinsed twice with deionised water twice and then dried at 40°C on a glass slide. The sample could now be used as it was.

### **II.7.2 To produce Calcium<sub>(x)</sub> Phosphate<sub>(y)</sub> (Ca<sub>x</sub>P<sub>y</sub>) exteriors**

Coating of the microsphere with calcium and phosphate precursors followed a similar procedure as that for titanium coating. The only difference was the reagents used.

### **II.7.2.1 Materials**

The materials utilised here include  $\text{CaCl}_2 \cdot 2\text{H}_2\text{O}$ ;  $\text{Na}_2\text{CO}_3$ ;  $\text{Na}_2\text{HPO}_4$ , TA and  $\text{H}_2\text{O}$ .

### **II.7.2.2 Preparation Procedure**

The same preparation procedure is followed as in section II.7.1.2, 14mM of  $\text{CaCl}_2$ , 8.4mM of  $\text{Na}_2\text{HPO}_4$ , and 4mM  $\text{Na}_2\text{CO}_3$  were used in place of TiBALD.

### **II.7.2.3 Separation and harvesting of samples**

The final samples were separated and harvested in the same manner as stated in II.7.1.2.

## **II.8 Principles of characterisation techniques and instruments**

### **II.8.1 Compression Testing**

This is the only mechanical characterisation technique used in this thesis. Compression testing is an important technique that aims to observe the behaviour of a material as it is subject to a load of a known magnitude in compression. This is an essential test for materials that will be used for structural applications. Stress and strain were to be used to ascertain the compression modulus and compression strength of the untreated and mineralised hydrogel. A Hounsfield Instron universal testing machine was used.

It was appreciated that maintaining the same test shape from sample to sample was difficult and could have a drastic effect on the mechanical properties observed.

### **II.8.2 Dynamic light scattering (DLS)**

This technique as the name implies is based on the scattering of light as a result of the interference by a body's size and shape. It relies on the Brownian motion of particles in solution, and models their motion over a specific period of time in order to return results of the hydrodynamic size or rather the diffusion coefficient of the particles being measured (Stetefeld, Mckenna and Patel, 2016). This diffusion coefficient is affected by temperature, the viscosity of the dispersant, in addition to the actual size of the particles. It is for this reason that measurements need to be carried out in a static temperature condition. It returns an estimate of a sample's size and their distribution. A Malvern Zatesizer Nano range was utilised.

DLS is an excellent technique assuming the particles present in a solvent are monodisperse. In polydisperse systems, the differences in particles can sometimes lead to masking of the intensity signal from smaller particulates.

### **II.8.3 Differential Scanning Calorimetry (DSC)**

DSC follows the endothermic and exothermic changes in the sample as a function of temperature (Leng, 2013). A typical DSC instrument measures the heat flow difference between the sample

and a given reference against temperature or time in a controlled atmosphere (Auroux, 2013; Leng, 2013). Calorimetric readings are capable of showing exothermic or endothermic readings depending on the thermal event that is taking place. Endothermic transition which could be any one of the following: melting, sublimation, dehydration, evaporation, desorption etc, exothermic transition include, crystallization, adsorption, oxidation, combustion, decomposition (Auroux, 2013). Calorimetric studies were performed using TA DSC.

## **II.8.4 Electron Microscopy**

### **II.8.4.1 Scanning Electron Microscopy**

Scanning electron microscopy is a form of microscopy which works by scanning the surface of a material with a focused beam of electrons over the surface area of a sample (Leng, 2013). An SEM produces an image by way of electron sample interaction. SEM uses high energy electron with a wavelength which is proportional to the velocity of the accelerated electron (Callister and Rethwisch, 2009). Upon striking the surface of a sample, a number of signals e.g. secondary, backscattered, transmitted, auger electrons, X-rays and photons (Bell and Erdman, 2012) are generated. Secondary electrons are utilised for imaging as they emerge closer to the surface with lower energy levels. SEM was carried out on the Zeiss Supra 35VP and the LEO 1455VP.

### **II.8.4.2 Transmission Electron Microscopy**

Electron microscopes just like the scanning electron microscopes are able to generate images of extremely high resolution with the ability to produce selected area electron diffraction (SAED) patterns of samples. They share some similarity with optical microscope, due to common components such as “light source, condenser lens, specimen stage, objective lens, projector lens” (Leng, 2013). The difference is down to the electron excitation source and the use of electromagnetic lenses. TEM here was done with Joel 2100 field emission gun TEM.

Along with aberrations due to the lenses (spherical, chromatic, and astigmatism), the preparation of specimen slices can introduce image artefacts from staining agents, imbedding resin and microtoming implements.

## **II.8.5 Energy Dispersive spectroscopy (EDS)**

Energy dispersive spectroscopy is done in complement with SEM and TEM. It relies on the use of X-rays to generate chemical signatures. These X-rays are emitted as a result of the bombardment of a sample with high energy particles (electrons, neutrons or X-ray photon) (Leng, 2013). When an energetic beam strikes the inner shell of an atom, it causes one of the electrons present in the shell to be liberated, resulting in an excited atom. In order to return back to equilibrium, the vacant spot needs to be refilled by an electron originating from one of the atom’s outer orbitals. As a result, the energy difference can either cause the emission of a characteristic X-ray or the

ejection of another electron.

The EDS detector (which is capable of detecting and separating the X-rays to produce an energy dispersive spectrum) was installed on both the SEM and TEM had their individual detectors.

### **II.8.6 FT-IR Spectroscopy**

This is a non-invasive investigation technique which utilises infrared radiation (from  $\lambda \sim 780\text{nm}$  to  $1000\mu\text{m}$ ) to access structural and chemical information of a variety of samples. The mid infrared region (from  $2.5\ \mu\text{m}$  to  $25\ \mu\text{m}$ ) with photon energies from  $0.05\text{eV}$  to  $0.5\text{eV}$  coincides with the allowed “quantized vibrational transition of intra and inter molecular bonds of bonded atoms in molecules” (Bellisola and Sorio, 2012). Thus, when a selected molecule or substance is sampled using an FTIR, the sample molecules interact with the IR portion of the radiation, which incidentally overlaps with its own vibrating molecules, allowing it to achieve resonance. The frequency of vibration is related to the atomic mass and to the bond strength (also referred to as the force constant). The frequency of vibration of the bond can thus be related to Hooke’s law and to the mass (Bellisola and Sorio, 2012). In the attenuated total reflectance (ATR) mode, the FTIR principle is still followed although the setup is modified to allow for the total internal reflectance phenomenon. In this instance, the IR beam generated by the light source is directed through an internal reflection element (Bellisola and Sorio, 2012) in a manner to allow reflection off the interior of the element. When IR radiation passes through the element, total internal reflection occurs and, in the process, establishes an evanescent wave of radiation that penetrates a few microns (at an angle above the critical incident angle) into the sample surface, thus interacting with the IR sensitive groups, and producing information of the sample’s composition.

The FT-IR spectroscopy was carried out on a Shimadzu IRAffinity 1 with an ATR-accessory.

### **II.8.7 Micro-Raman**

Micro Raman microscopy is part of a group of techniques that analyses molecules through the use of electromagnetic radiation (near visible portion). The energies of molecular vibration match with the radiation that falls within the near visible portion of the electromagnetic spectrum (Leng, 2013), in the range  $10^{-2}$  -  $10^{-1}\text{eV}$  (Leng, 2013) - similarly for FTIR (Bellisola and Sorio, 2012).

Raman originates from inelastic scattering i.e. light that has a different frequency and thus a different energy from the irradiating source (Lewis and Edwards, 2001). The energy of the scattered (emitted) photon is equivalent to the difference between the initial ground state and the final state of the molecule (Leng, 2013) and depending on whether it is higher or lower, it is called Stokes (Raman) or anti-Stokes scattering respectively. Raman spectroscopy involves two photon events, compared to infrared spectroscopy which achieves its elevated vibrational energy state by a single photon event.



Raman spectroscopy was carried out on a Horiba Micro-Raman, using a 534nm green laser.

Although Raman is extremely simplistic, there are certain disadvantages that affects it as a preferred choice e.g. sample fluorescence, sample heating, cosmic rays, dark noise, specimen surface and placement etc are just some things that can generate inconsistencies (Bowie *et al.*, 2003).

### **II.8.8 UV-vis spectroscopy**

This is an important analytical technique that uses radiation across a broad range of wavelength (from the ultraviolet - visible) to probe the response of the analyte to these perturbations. Upon absorbance of photons, there is a transition of electrons from one energy level to another, usually a lower energy level to an empty orbital in a higher energy level. Transitions with electrons that are non-bonded are easier to observe than electrons involved in bonds hence  $\pi \rightarrow \pi^*$ ,  $n \rightarrow \pi^*$  are the most likely to be observed form of transition in UV-vis spectroscopy (Faust, 1997). Using this along with Beer-Lambert law makes it possible technique to follow changes in the concentration analytes. Here, UV-vis was carried out on the Perkin Elmer Lambda 650.

The concentration of the analyte is crucial, too high or low and no change in signal will be recorded. Thus, experiments can only be run within a meaningful concentration range, and this is not necessarily a real-life concentration range. This can often lead to negative readings, especially if a calibration curve is used for concentration interpolation-extrapolation.

### **II.8.9 Thermo gravimetric analysis (TGA)**

This is a technique which is used to measure mass change in a sample as a function of its temperature in an inert, oxidising or reducing atmosphere. It is defined as “a technique in which the mass of the sample is recorded versus time or temperature while the temperature of the sample is programmed” (Auroux, 2013). Several transformations like: dehydration, evaporation, composition, adsorption, pyrolysis etc may be ascertained for a sample (Leng, 2013). Here, TGA was performed on a Discovery TGA instrument.

Just like DSC the absolute sensitivity of the instrument makes it very easy to end up with artefacts over real thermal events.

### **II.8.10 Powder X-Ray Diffractometry (XRD)**

It utilises the diffraction effect which is produced when “electromagnetic radiation impinges on a periodic structures with geometrical variation on the length scale of the wavelength of radiation” (Birkholz, 2005) to help determine the crystal structure of materials.

In an ideal condition, a sample containing single grains or multiple grains would produce diffraction patterns. This pattern is a composition of the varying diffraction intensity with respect

to  $2\theta$ . In this pattern, each intensity maxima should theoretically correspond to a specific crystallographic plane that is responsible for interacting with the incident X-Ray beam- resulting in a wave interference pattern. Bragg's law describes this condition necessary for the production of these peaks by constructive interference in the equation below.

$$n\lambda = 2d\sin\theta \quad \text{Equation 22}$$

where  $\lambda$  is the wavelength (nm),  $d$  is the distance between the adjacent crystallographic planes,  $\theta$  is the Bragg angle "at which one observes a diffraction peak" and finally  $n$  is an integer that represents the order of reflection (Messerschmidt, 2007). Bragg's condition will be satisfied if the diffracted beams produced have a phase difference of  $n\lambda$  resulting in constructive interference according to Leng (2013). XRD was carried out on a Bruker X-Ray diffractometer using a  $\text{Cu}(K\alpha)$  radiation ( $1.54\text{\AA}$ ).

This method is limited when processing results in composite samples, especially when the sample of interest is below the detection limit (1-5wt%) (Zhao *et al.*, 2004).

## II.9 Experimental setup and methods

Several tests were performed to evaluate the mechanical integrity (swelling ratio, compression testing), the simulated biological activity (biomineralization and degradation); and the drug delivery potential of the scaffold (using ascorbic acid, caffeine, gentamicin sulphate, methyl orange and methylene blue). This section will detail the more complex pre-experimental set-up associated with biomineralization and degradation.

### II.9.1 Colourimetric test for $\text{Ca}^{2+}$

The test for  $\text{Ca}^{2+}$  uses the intensity of a coloured compound to gauge the amount of  $\text{Ca}^{2+}$  based on a standard calibration curve. This test was integral to bioactivity, degradation and calcium ion uptake studies (see Chapter IX).

#### II.9.1.1 Materials

The following materials were used in this test: O-Cresolphthalein complexone (Sigma Aldrich, UK); 2-amino-2-methyl-1-propanol AMP; HCl; 8-hydroxy quinoline; calcium carbonate  $\text{CaCO}_3$  and  $\text{H}_2\text{O}$  (18M $\Omega$ ).

#### II.9.1.2 Calcium O-Cresolphthalein complexone method

The main reasoning for using this test was to address the interference of magnesium in the colourimetric reading using the calmagite method. The use of o-cresolphthalein complexone was thought to be more sensitive, in addition, the use of 8-hydroxy-quinoline as well as buffering the

pH closer to alkaline masks the interference of magnesium and thus preserved the UV-vis spectrum (Chauhan and Ray Sarkar, 1969; Morin, 1974). The protocol for this method was adopted from Kanagasabapathy and Kumari (2000). The only change was the exclusion of benzoic acid in the final preparation. In this method, a purple coloured complex is formed to indicate the presence of  $\text{Ca}^{2+}$ , which could then be studied with a UV-vis. Carrying out a test required the use of an AMP buffer at pH10.7 and the colour reagent. Regents were prepared as follows:

- 15ml of HCl was added to a volumetric flask of 250ml, containing some water
- 25mg of the o-cresolphthalein solid was washed into the volumetric flask
- Following this, 250mg of 8-hydroxy-quinoline was added and then the entire content was then made up with deionised water to the 250ml mark, forming a yellow coloured reagent
- Separately, the buffered solution was made by adding 37.8ml of AMP into some deionised water, using 6M HCl to adjust the pH. The buffered solution was then made up to 250ml.
- A 500ml standard stock solution of  $\text{CaCO}_3$  was also made with 625mg of  $\text{CaCO}_3$  and 3.5ml of conc. HCl for use as a quality control system as well as to make the calibration curve.

### **II.9.1.3 Calcium ion test procedure**

The testing procedure was as follows:

- 0.1ml of the test solution was added to 1ml of deionised  $\text{H}_2\text{O}$
- 2ml of the coloured reagent was then added and then 2ml of the buffered AMP buffer
- The sample was then mixed thoroughly
- 2.5ml of the solution was then pipetted into a cuvette, which was then tested using UV-vis with the absorbance (at the lambda max) utilised for further analysis.

## **II.9.2 Colourimetric test for phosphate**

Like the  $\text{Ca}^{2+}$  test, this was important to probe the bioactivity, degradation and calcium ion uptake studies

The method used for the analysis of phosphate was provided by Hanna Instruments. Which means that there was very little room for modification of the methodology besides the use of UV-vis in place of the portable Hanna instrument that was provided for this test.

### **II.9.2.1.1 Materials**

HI93713 Hanna instruments phosphate low range reagent.

### **II.9.2.1.2 Phosphate ion test procedure**

- The testing procedure used here required samples of 10ml.
- To these samples, the HI93713 reagent (provided as a powder by Hanna Instruments) was then added.

- The test procedure quoted 3min (by Hanna Instruments) for the complete dissolution of samples which was increased to 5min for the purpose of this experiments to aid comprehensive dissolution.
- After 5 min, 2.5ml of the sample was transferred to a cuvette for reading in the UV-vis. The lambda maxes was noted at 710 nm and 890nm.

### II.9.3 UV-vis testing for gentamicin

The test regime used for gentamicin was carried out using UV-vis. As gentamicin normally has a weak to a non-apparent absorption around UV, it was tested in conjunction with ninhydrin. This is a reagent which is used for the detection as well as the quantification of amino acids, peptides, proteins, ammonium salts and so on to produce a chromatic colour which was easily detectable in UV-vis. This is quite useful in probing gentamicin as the molecule carries primary and secondary amines (see Figure XII-1) which react with ninhydrin to produce a chromophoric compound (Frutos *et al.*, 2000). It was discovered by Siegfried Ruhemann (Harding and Warneford, 1916; Bottom, Hanna and Siehr, 1978; Friedman, 2004).

#### II.9.3.1.1 Materials

Ninhydrin (Sigma Aldrich).

#### II.9.3.1.2 Testing procedure

The gentamicin test conditions involved measuring out 2.5ml of the sample and adding 0.75ml of a 2.5mg/ml solution of ninhydrin that had been previously made up in phosphate buffer saline. The mixed colourless solution was then placed in a 95°C water bath and heated for 15min. It is during this step that the colour development began. The samples were then transferred to a cooler of ice for 15min and then to a cuvette for UV-vis analysis. The lambda max was read at 400nm (Frutos *et al.*, 2000) although there was another peak at 570nm, because the method used here was adopted from Frutos *et al.* (2000) and Ismail *et al.* (2016), 400nm was preferred (see calibration curve in section XII.5.1).

### II.9.4 Raman spectroscopy testing for gentamicin

#### II.9.4.1.1 Testing procedure

Here 0.02ml of the samples were placed on aluminium foil covered microscopic slide. The peak at 980cm<sup>-1</sup> was utilised as an indicator of gentamicin presence (see calibration curve in section XII.5.1). This peak was attributed to C-O-C stretching (Zaleski *et al.*, 2017).

## Chapter III Leaf Biomimicry via Sol Gel Synthesis

### III.1 Introduction

The field of biomimetics is diverse with boundaries that are difficult to define. Nature and its creatures have found novel ways to produce unique structures capable of utilising their surrounding resources to the best of their abilities. Current researchers now realise that they can take cues from nature in order to deduce solutions to a vast number of problems with which the human race is faced - whether these relate to energy harvesting or medical interventions.

Of these problems, the most concerning especially now seems to be with regards to energy. Such is the demand that it was estimated back in 2004 that about 15TW of energy was consumed, with 87% coming entirely from fossil fuels according to Krebs et al (2008), increasing to 35TW by 2020. Not only would the limited fuel sources be insufficient to cope with this increase, but other derived health and environmental issues would surely worsen respiratory illnesses, and global warming etc.

It makes sense that other alternative sustainable energy sources should be investigated as the next likely candidates to replace fossil fuels. Solar energy is being explored as the most promising candidate. It has been estimated that the amount of solar radiation incident on the earth surface is "in the range of terawatts" (Kalyanasundaram and Graetzel, 2010). In spite of this, solar energy as an alternative source is plagued with its own difficulty, mainly difficulty in obtaining the raw materials, and the limited conversion efficiency. Although the highest efficiency levels that have been recorded only account for about 25% (Krebs *et al.*, 2008), it is important to realise that accessing the sun's solar radiation is probably the only way forward in tackling the increasing energy hurdle that is being faced.

With biomimetics, it is possible to engineer materials, with enough control on the nanoscale level to affect the overall properties (whether optical, electrical or other). This would be useful, especially when considering photovoltaics and photocatalysts. By not just tuning the properties of the semiconductors through doping, could it be possible to affect things like electron tunnelling and recombination events in semi-conductors in order to improve the efficiency, while using biotemplates that have already been optimised by nature? Using templates which have been observed to have a specific function, it is highly likely, that with the right amount of modification its function could be spread to suit different applications. The author hopes to find a unique way of aiding our ability to harvest the energy that is so abundant around us. Therefore, it is an aim of this research (goal (i)) to consider and optimise the role of biotemplating in modifying the properties of titanium oxide (which already has an established role as a photocatalyst and as a photovoltaic cell component).

## III.2 Background

Before we can continue, we have to consider the structure of a leaf, which will be done in the following section, starting with a general overview of what a leaf structure is, the role of certain adaptive factors have in varying the overall morphology of a leaf and how this will come to affect the  $\text{TiO}_2$  replication process.

### III.2.1 Plants and their leaves

Photosynthetically capable eukaryotic plants have over eons evolved mechanisms to successfully harvest the sun's energy, turning it into chemical potential to sustain its life - with the help of their leaves. A leaf is a vital organ with an incredible assembly of features that direct and permit the conversion of solar energy into chemical energy, which can then be made available in a more accessible manner to be used to release energy and synthesise sugars of various complexities. Along with the aforementioned functions, the leaf structure regulates water evaporation on its surface, which in itself is linked to transpiration, an essential process that can be related to internal mass transportation in addition to a temperature control function (Cutler, Botha and Stevenson, 2008). Anatomically speaking, plants from a different environment possesses leaves with different structures, sizes, colours (all of which can be categorised); nevertheless, most leaves tend to contain certain features common in most eukaryotic plants. Below is a simple schematic of the cross section of a plant leaf:

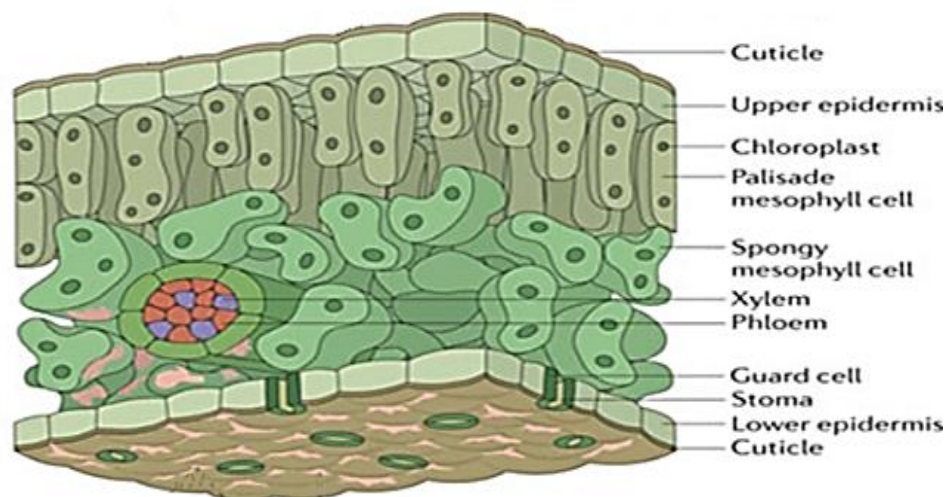


Figure III-1: Basic cross-section of a plant leaf (Vorholt, 2012).

The outermost covering of a leaf is usually referred to as a cuticle, which is a feature present in a variety of plants (it varies with environmental pressures: herbivores, ecological niches, water availability and light intensity). This feature undergoes modification to best suit the needs of the

plants arising from these selection pressures (Cutler, Botha and Stevenson, 2008), resulting in constituents and thickness that change accordingly. According to Cutler et al (2008), the thickness appears to be directly linked to the amount of water stress the plant is subjected to; thinner cuticles are particularly common when water stress is not a barrier.

The cuticle is a biopolymer of polyester called cutin, impregnated with integrated (intracuticular) waxes” (Bharat, 2010). It has a number of functions (reducing the loss of water and small ions, while preventing the ingress of molecules into leaf; anti-adhesive properties/self-cleaning; signalling both for insect recognition and cellular development at its surface; mechanical resistance against certain stress factors; maintenance of an optimum surface temperature (Bharat, 2010; Meyers and Chen, 2014)). It is the components of a cuticle that include cutan, pectin, polysaccharides, cutin and phenolics that contribute in whole to make the cuticle such a multifunctional organ. The cuticle’s hydrophobicity is thought to be derived from the epicuticular and intracuticular wax present in the cutin (Bharat, 2010). These waxes are made up of primary and secondary alcohols, fatty acids and aldehydes, of which (depending on the plant species) their combinations and amounts vary.

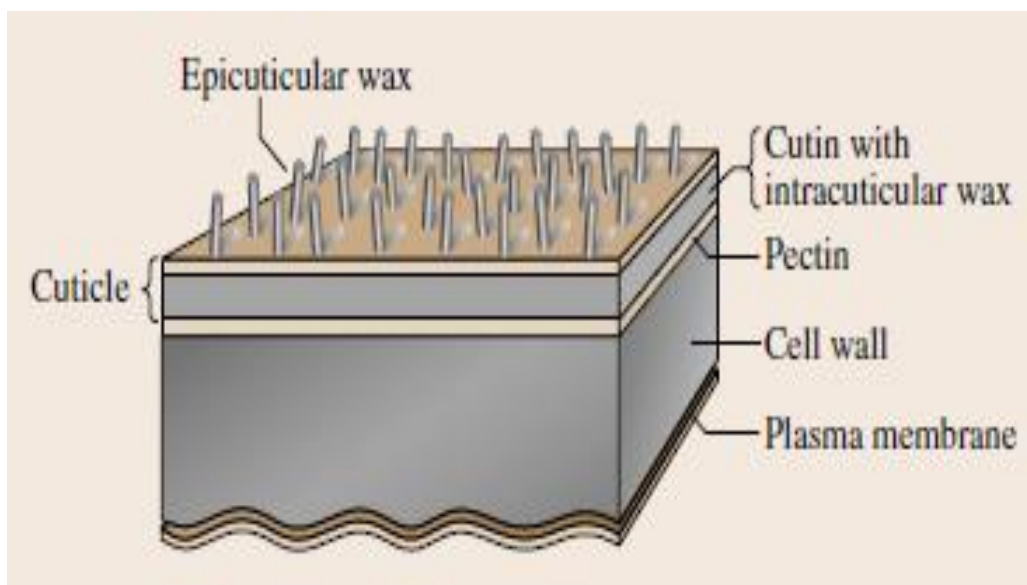


Figure III-2: Cross section of a plants cuticle membrane (Bharat, 2010).

Cuticles are in both terrestrial plants and aquatic plants albeit with a slightly different function to suit the environment. In hydrophytes (see III.2.1.2), they are thinner in submerged species while thicker in floating species (Ronzhina, Ivanov and P'yankov, 2010). This reduces the proliferation and growth of micro-organisms which would thrive due to the higher moisture levels of aquatic plants (Meyers and Chen, 2014). The cuticle aids in the absorption of CO<sub>2</sub>, creating a water-repellent surface that allows a better uptake of CO<sub>2</sub> in spite of its stunted permittivity in water

compared to air (Ronzhina, Ivanov and P'yankov, 2010).

It acts as a barrier, along with the waxes present, to control the flux of radiation that makes it to the plant interior reflecting some incoming radiation between 280nm to infrared: 400-700nm (Bharat, 2010). Phenolics that are present interact with harmful radiation reducing mutation in  $\pi$  bonded compounds (Jacobs, Koper and Ursem, 2007).

A natural leaf as a whole is essentially a 'machine' with the ability to capture solar energy. It accomplishes this as a result of certain morphological features that have been developed. In the case of both aquatic and terrestrial plants, their leaves tend to be relatively thin (albeit in the aquatic environment leaves tend to be thinner- even transparent at times (Liu *et al.*, 2013)). This thinness is an advantage when considering the plant's ability to absorb photons and transport substances (e.g. gas exchange and water transportation) required for respiration and photosynthesis (Liu *et al.*, 2013; Zhou *et al.*, 2013). This shortens diffusion distance in terms of gaseous exchange, as the stoma allows the exchange of CO<sub>2</sub> and O<sub>2</sub>.

Internally, diffusion of various gases occurs along a concentration gradient, through air spaces that already exist between the mesophyll cells- spongy and palisade cells, especially in the case of the spongy mesophyll (with surfaces having a very loose arrangement further making more surfaces free to interact with air) having an interspace larger than the mean free path of gaseous species (Zhou *et al.*, 2013). The palisade mesophyll acts as a guide (because of its elongated columnar morphology) allowing photon scattering; this continues in the spongy mesophyll where light is concentrated by 20x before passing into the chlorophyll (Zhou *et al.*, 2010). There, photosynthesis occurs. In higher plants, aquatic plants inclusive, chloroplasts are 4-8 $\mu$ m in diameter and number between 20-400 in a mature leaf cell (Kirk, 1994). In the presence of water and CO<sub>2</sub>, a series of reactions leads to the final photosynthetic products. Water enters the plant's system via the xylem, which also transports minerals; the photosynthetic products are transported via the phloem. The phloem and xylem make up the vascular bundle, their other functions providing some structural support and acting as light scattering surfaces for the deeper layers (Zhou *et al.*, 2010).

While most plants would ideally possess the above components and function, adaptation will cause some variation. The above description of plant anatomy applies to mesophytes, a specific category of plants having very little specific adaptation to dry or wet environments (Hall and Stern, 2012). As the plant species that will be employed in these experiments are not true mesophytes: *Rotala Rotundifolia* RR (hydrophyte) and *Eucalyptus camaldulensis* EC (mesophyte, with some xerophytic characteristics), it is necessary to expand on some of the structural adaptations that can occur in these chosen species.



### III.2.1.1 *Mesophyte with xerophytic characteristics*

Although mesophytes do not generally possess specific adaptation to a dry or wet habitat, they still show some variations depending on the family and whether they grow in xeric or mesic condition.

*Eucalyptus camaldulensis* have the features explicitly described above, as well as some xeric adaptation like having a thicker cuticle layer, numerous and sunken stomata, and rougher leaf surfaces (Hall and Stern, 2012).

### III.2.1.2 *Hydrophytes*

Hydrophytes may be defined as plants existing in a waterlogged habitat (D. a. Ronzhina and P'yankov, 2001). They are similar to terrestrial plants due to their common phylogenetics (D. A. Ronzhina and P'yankov, 2001); the difference in environment results in this deviation in both structure and function in order to adapt to the watery habitat.

As *Rotala rotundifolia* is an aquatic plant, it occupies a similar niche to a terrestrial plant albeit in a watery location. This location means that certain aspects of plant life that would normally have not been problematic in a terrestrial habitat become a problem in an aquatic surrounding. Whereas in a terrestrial habitat, the primary reason for evolution would have been dependent on maximising access to scarce resources, mostly water (Ronzhina, Ivanov and P'yankov, 2010); in an aquatic environment water is plentiful, thus the struggle would be to gain access to what would be deemed as scarce resources ( $O_2$ ,  $CO_2$ ,  $HCO_3^-$  and various other mineral substances) (Ronzhina, Ivanov and P'yankov, 2010). In terms of chemical composition, hydrophytes have had to reduce certain tissues associated with mechanical support and conduction by modulating their carbon composition. In order to achieve a low specific leaf weight with an increased ability to photosynthesise in the low light region, they preferentially proliferate chlorenchyma tissue over structural supporting tissue: sclerenchyma. They develop aerenchyma tissues (air-filled cavities) to alter densities of these leaves (D. A. Ronzhina and P'yankov, 2001). As such, hydrophytes have the majority of their chloroplast in the epidermis, compared to mesophytes where the opposite is the case. Hydrophytes tend to have a much higher mineral content to maintain osmotic pressure and to grow rapidly in order to absorb more light (Ronzhina, Ivanov and P'yankov, 2010).

## III.3 Aim

*Eucalyptus camaldulensis* and *Rotala Rotundifolia* will be considered as biotemplates for the production of useful titania phases and the ease at which nanoparticulate sizes are obtained. As such, the quality of the titania phase formed will be investigated, with reference to the rutile to

anatase phase balance in a bid to obtain a mix of titania polymorphs with an envisioned functionality as potential photocatalysts. Will EC or RR form the ‘right’ phases of titania? Will these phases bear any similarity or be better than commercial P25?

### III.4 Methodology

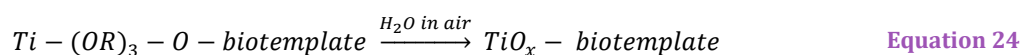
#### III.4.1 Sample preparation

Before the actual treatment of the biotemplate samples with the relevant titanium precursor and subsequent calcination, the following pre-treatment process was carried out to improve the chances of attaining replicas with the required titania polymorphs.

The pre-treatment process in question included, dewaxing, delignification and acid treatment as detailed below (& section II.1.2). Not all of the samples will be subjected to these treatments; the ones that are were to be pretreated and indicated.

##### III.4.1.1 Biotemplate and precursor reaction

Titanium isopropoxide, in this instance, is capable of forming intimate Ti-O-C linkages with the surface of the biotemplate material, thus creating an interface that consists essentially of the bonds between the titanium ion and the hydroxyl groups. It is



The interfacial sol-gel reaction between the alkoxide precursor and the biotemplate involves a hydrolysis- condensation reaction to form  $TiO_x$ -biotemplate (Equation 24), before calcination at  $600^\circ C$  to give  $TiO_2$  biotemplate residue (Equation 25) of EC and RR. TiBALD also follows a similar hydrolysis and condensation route, characteristic of sol-gel chemistry (see Figure III-3). The top reaction is a hydrolysis reaction between TiBALD and the OH groups present on the biotemplate (& tannic acid), and the second reaction is the condensation reaction which forms the polycondensate at the bottom. It is thought the presence of the lactate group/lactic, which is cleaved in the first reaction is partly responsible for the smaller  $TiO_2$  particulates formed (Anderson and Binions, 2016).

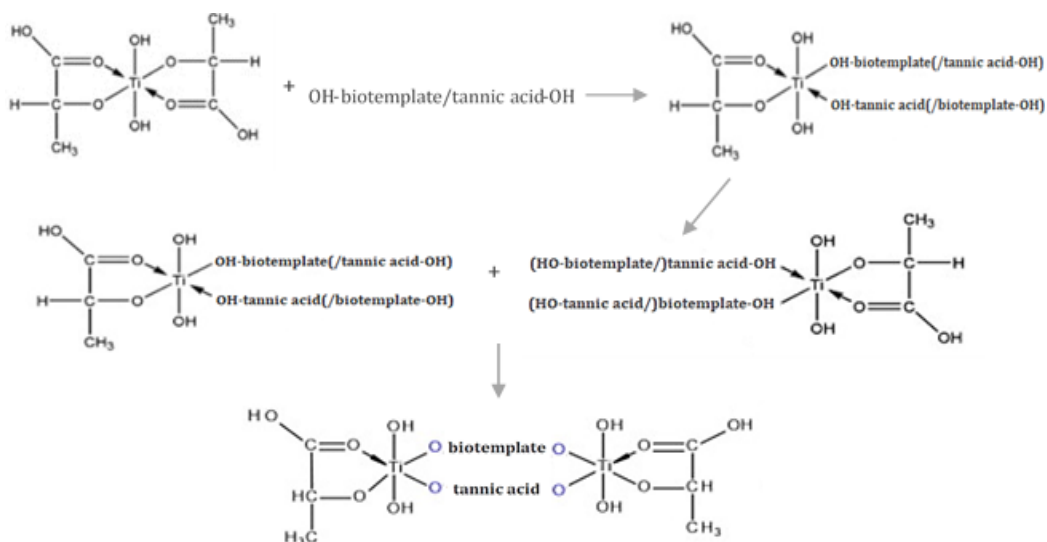


Figure III-3: Possible hydrolysis and condensation mechanism to form intimate Ti-O-biotemplate polycondensate before undergoing calcination to form  $\text{TiO}_x$ .

#### III.4.1.2 Dewaxing

Unfortunately, the replication process utilising *Eucalyptus camaldulensis* is affected by the presence of a robust cuticle layer coating the outer epidermis of the plant's leaf, effectively creating a barrier between the plant's epithelia cells and the replicating media (III.2.1). To try to diminish the effect of this barrier without completely altering the inherent surface morphology of the plant leaf, dewaxing was carried out.

Here, a two-step dewaxing process is carried out to destabilise and remove the cuticle membrane, starting with an organic solvent with a low polarity (hexane,  $\epsilon_r = 1.88$ ) and then a medium polarity solvent (ethyl acetate,  $\epsilon_r = 6.02$ ). Low polar organic solvents were used in this because of the components that make up this layer. As explained earlier (see III.2.1), they mostly consist of hydrocarbons, with cutin forming the majority of the component, followed by waxes and then other minor components like phenolics which make up these biopolymers. As a result of their organic nature, they would respond better to a low polarity organic solvent.

It was hoped that treating the samples with successively increasing polar organic solvents would minimise the effect of the cuticle membrane, making *Eucalyptus camaldulensis* more amenable to being successfully replicated by titanium isopropoxide.

- Dewaxing procedure:

Refer to II.1.2 for the dewaxing process

#### III.4.1.3 Delignification:

Delignification is usually carried out with bases such as "sodium, potassium, calcium and

ammonium hydroxide" (Alvira *et al.*, 2010). Sodium was chosen for the delignification agent because of its ease at being adapted for use in this experiment. As a delignification agent, NaOH works by causing localised swelling, increasing the internal surface of cellulose and decreasing the degree of polymerization and crystallinity, which provokes lignin structure disruption (Alvira *et al.*, 2010) and thus allow the solubilisation of lignin.

Treatment with the alkali leads to hydrolysis of ester or ether bonds that are present between lignin and cellulose through saponification (Ishiguro and Endo, 2015). These cleaved ester bonds might go on to participate in a trans-esterification reaction with the metal alkoxide used, creating more active sites on the leaf's internal structure. The delignification method here was a modified version of that used by Geng and Henderson (2012).

- Delignification procedure:

Refer to II.1.2 for delignification procedure

#### **III.4.1.4 Calcium and other cation leaching:**

Preliminary EDX analysis of the plant specimens showed that the leaves contained a variety of elements inherent to their biology. In the case of an untreated sample of Eucalyptus, although carbon accounted for a significant percentage of the overall leaf composition (see Table III-2) other elements such as calcium are known to be present.

The same could be said for RR although it had a slightly different percentage (see Table III-3).

To minimise any interference during the replication process from any of these elements, it was necessary to treat some of the samples with a weak acid for a short duration. In the natural environment, leaf leaching occurs fairly easily, mostly facilitated by the precipitation of some sort, which acts as a natural transfer pathway for cations back to the soil (Potter, 1990). Acid rain has been particularly exacerbated by human industrial activities, as such pollutants releasing  $H^+$ ,  $SO_4^{2-}$ ,  $NH_4^+$ , and  $NO_3^-$  decreases the pH of precipitation, resulting in enhanced leaching of minerals from the foliage (DeHayes *et al.*, 1999).

Using this as a basis, it was decided to treat the samples with acid at a pH of 4 for 30 min to reduce any further adverse effects on the plant leaf while maximizing the amount of mineral that would be leached from the plant in an effort to maximise the formation of Ti-O-C.

- Acid leaching procedure:

Refer to II.1.2 for leaching process

### III.4.1.5 Titanium precursor treatment and calcination process

Please refer to section II.1.3.1 for procedure

### III.4.2 Characterization Techniques

These biotemplates, before and after replication, were subjected to various characterization methods for the purpose of elucidating the changes occurring chemically, morphologically and elementally by the following methods: FTIR, TGA, SEM, XRD and EDX methods.

#### III.4.2.1 ATR-FTIR

The fresh samples had previously been lyophilised or oven dried (at 60°C); un-calcined samples were subjected to no further treatment. The final spectrum produced, was averaged over 40scans.

#### III.4.2.2 SEM

SEM in conjunction with EDX was used to study the morphology of the samples, as well as their elemental composition. Uncalcined samples, were usually desiccated in a lyophiliser for 12h, while the calcined samples underwent no further dehydrating process. Afterwards, they were placed on an SEM stub, which was covered with carbon tape. Finally, the samples were coated for a duration of 60sec with either a gold target or a silver target.

#### III.4.2.3 XRD (X-ray diffractometry)

Scans were conducted over the  $2\theta$  range of  $2^\circ$  to  $80^\circ$ , using a step size of  $0.09^\circ$ . For analysis, the samples were placed on a PMMA sample holder and then placed in the XRD.

#### III.4.2.4 TGA (Thermo gravimetric analysis)

The biotemplates were heated up to 600°C with a ramp rated of 10°C/min in air.

### III.4.3 Sample nomenclature

The samples in this section have the following designation

**Table III-1: Name of samples and their accompanying description**

<b>Samples</b>	<b>Description</b>
(RR or) EC only	Lyophilised EC/RR
EC (HCl[pH1])	Lyophilised EC, treated with HCl pH1
(RR or)EC (Lyo+TiPA)	Lyophilised EC, treated with 5mM TiPA
RR/EC (DW+TiPA)	Lyophilised EC/RR, dewaxed and treated with 5mM TiPA
EC (DW+DL+DI+TiPA)	Lyophilised EC, dewaxed, delignified, water added, before treatment with 5mM TiPA
EC (DW+DI+TiPA)	Lyophilised EC, dewaxed, water added and treated with 5mM TiPA. Calcined at 600°C
EC (DW+DL+HCl[pH4]+TiPA)	Lyophilised EC, dewaxed, delignified, treated with HCl[pH4] and then with 5mM TiPA
(RR or)EC (DW+HNO <sub>3</sub> [pH1]+TiPA)	Lyophilised EC/RR, dewaxed, delignified, treated with HNO <sub>3</sub> [pH1] and then with 5mM TiPA
EC (DW+DL+TiPA)	Lyophilised EC, dewaxed, delignified and then treatment with 5mM TiPA

## III.5 Results and Discussion

### III.5.1 TGA -Thermal analysis

TGA was carried out to help understand the ashing behaviour as a result of the different treatments the sample would be subjected to. Thermal analysis of all the samples was carried out at 600 °C, in air at a ramp rate of 10°C/min.

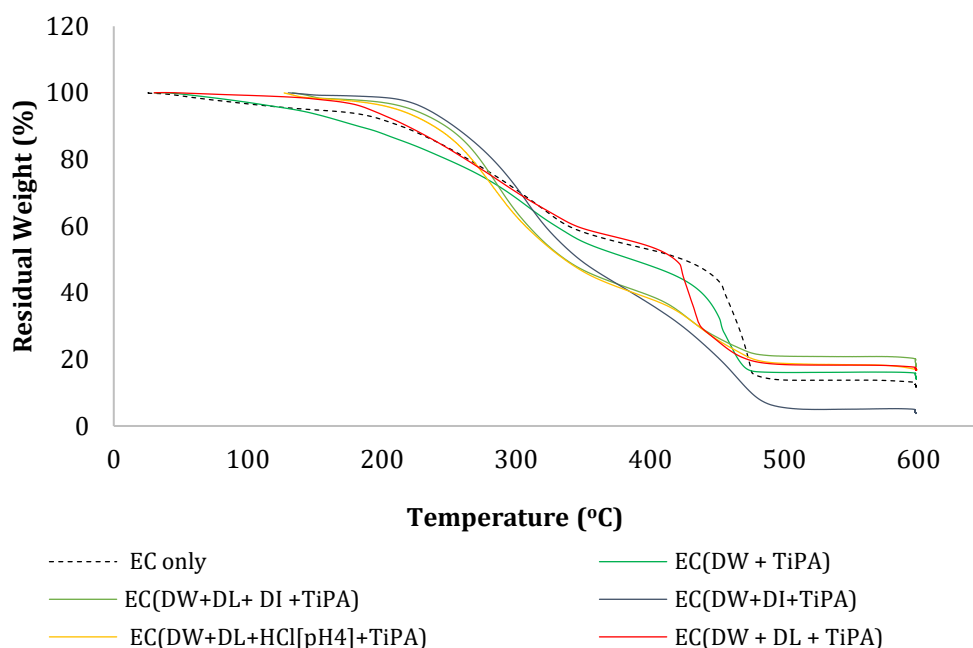


**Figure III-4: TGA thermographs of EC samples that had underwent different treatment process. They were heated to 600°C in air.**

From Figure III-4 it is clear that the heating profiles of the samples follow a similar pattern with a few differences that occur at  $\approx 200\text{-}300^\circ\text{C}$  and  $\approx 400\text{-}500^\circ\text{C}$ , all of which can be closely related to the untreated lyophilised eucalyptus leaf EC only. Between 200-300°C some of the TiPA- treated sample: EC (DW+DI+TIPA), EC (DW+DL+DI+TIPA), and EC (DW+DL+ HCl [pH4] +TIPA)- collectively group I - appear to show a more marked resistance to calcination in air at that temperature range as shown by the bowed-out shape. It should be mentioned that those samples have all undergone dewaxing and delignification. EC (DW+DI+TIPA) is the only one that has only been dewaxed without undergoing delignification. This is compared to the other samples: EC only, EC (DW+TIPA), and EC (DW+DL+TIPA). This group (group II) have more variety, with some samples undergoing no treatment (EC only) with others undergoing dewaxing EC (DW+TIPA), while EC (DW+DL+TIPA) underwent both dewaxing and delignification.

Beyond that temperature range, the samples appeared to show more resistance to the initial rise in temperature before the residual weight drops quite drastically just after 250°C; conversely, the other group undergoes a gentler drop. Between 300-400°C, the residual weight% of the samples

stabilises, and in the process the same group (EC only, EC (DW+TIPA), and EC (DW+DL+TIPA)) with the slower descent becomes thermally more resistant than the remaining samples. After 400°C, the residual weight % drops for a final time, stabilising around 450°C.

In the cases of the group I samples, just beyond 400°C, their descent is slow and gentle before it finally levels off just after 500°C until the thermal analysis concludes at 600°C. It is important to reiterate that these samples here had an additional step in their pre-treatment process. It could be inferred that this extra treatment, as well as having an effect on the final residual weight percentage left after calcination, had also actively altered the thermal behaviour, delaying mass loss events and minimising specific mass loss events along the temperatures.

From the final residual weight at the end of calcination, one can draw a conclusion about the stability of the samples. Here, the sample with the designation EC (DW+DL+DI+TIPA) could be considered the most stable, with a value of around 20%, this is followed by a cluster of samples including EC (DW+DL+TIPA) and EC (DW+DL+ HCl [pH4] +TIPA)- all of which show residual weight between 17-18%. This is then followed by EC (DW+TIPA) at around 15%, and finally the untreated sample coming in at 11% residual mass. EC (DW+DI+TIPA) is left with 5%.

It seems like the most stable of the samples were those that had undergone both dewaxing and delignification, with additional treatment to leach out more of the cations that might be present, using either water or nitric acid. These additional processes are essential especially in the case of Eucalyptus and its hardy cuticle layer. In dewaxing, the loss/reduction of the cuticle layer means that a more intimate contact can be established at the surface of the plant epithelia cell, improving the titanium loading of the structure just before it is calcined. Along with the dewaxing, the reduction of lignin is essential so that more of the ester bonds that were otherwise occupied between cellulose and lignin could be used in improving the TiO<sub>2</sub> replication process. This is perhaps why the samples have an improved residual mass percentage when compared to the untreated EC only. And this is an important indicator that the residual weight is a combination of the TiO<sub>2</sub> and the more robust mineral left behind of the biotemplate.

The sample EC (DW+DI+TIPA) has the poorest residual mass, less so than the EC only. Other samples had undergone extensive pre-treatments leaving them with stripped and bare surfaces to allow unhampered access to the precursor solution; EC (DW+DI+TIPA), having only dewaxing done, with the inclusion of deionised water might have created a condition that the majority of the reaction would have occurred in solution, rather than on the surface of the biotemplate. The majority of the titania species would end up being rinsed away, thus there would be less titanium compounds loaded in its structure - and a much lower weight percentage overall. The lack of a cuticle structure and deposition of titanium on its surface would result in a very low mass, which

might fall in the region of uncertainty of TGA equipment.

In the case of RR, the TGA profile (See Figure III-5) of all samples were similar to the EC profiles. There is in fact very little deviation from the shape with the sample pre-treatment (RR only), compared to those that have undergone various treatment modalities.

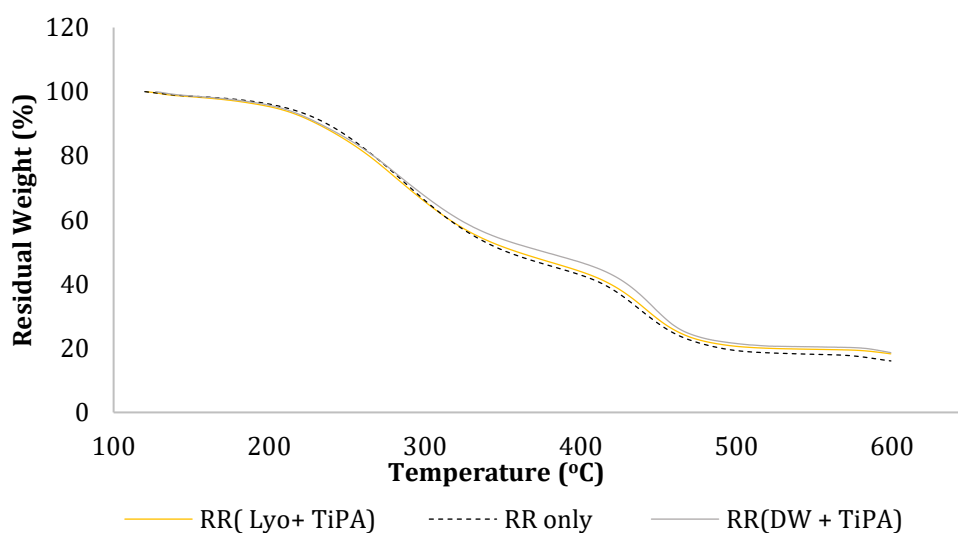


Figure III-5: TGA of different RR samples that had undergone different treatments. They were heated to 600°C, in air.

The main difference between *RR* and *EC* is residual weight (ash) content left over after calcination. It can be deduced that the aquatic *RR* naturally has a higher ash content than *EC* (compare Figure III-4 and Figure III-5). This is an adaptation by most aquatic plants to help maintain osmotic pressure within their environ, as well as in aid of colonising large portions of open water (discussed in section III.2.1.2). There is also the possibility that *RR* is simply better biotemplate encouraging the formation of  $\text{TiO}_2$ , hence reflected in the higher residual weight content after calcination.

Besides, it also appears that a dewaxed sample replicated using titanium precursor *RR* (DW+TiPA) produces a sample with a much higher ash or  $\text{TiO}_2$  content (17%) than one simply lyophilised (12%). It is possible that neglecting a separate dewaxing step results in it occurring simultaneously with replication and possibly in preference to deposition of titania onto to biotemplate, thus resulting in a lower titania loading. As such, it is a similar scenario as that seen for *EC*. The fact that *RR* (Lyo+TiPA) has a similar final residual mass to *RR* (DW+TiPA) serves as an indicator of the difference between its structural tissue and cuticle layer, compared to a terrestrial leaf like *EC*.



### III.5.2 Morphological characterisation:

The morphological analysis of EC and RR leaf samples were carried out using a scanning electron microscope (SEM) as well as elemental analysis using and energy dispersive X-ray spectroscopy (EDX).

#### III.5.2.1 Un-calcined samples

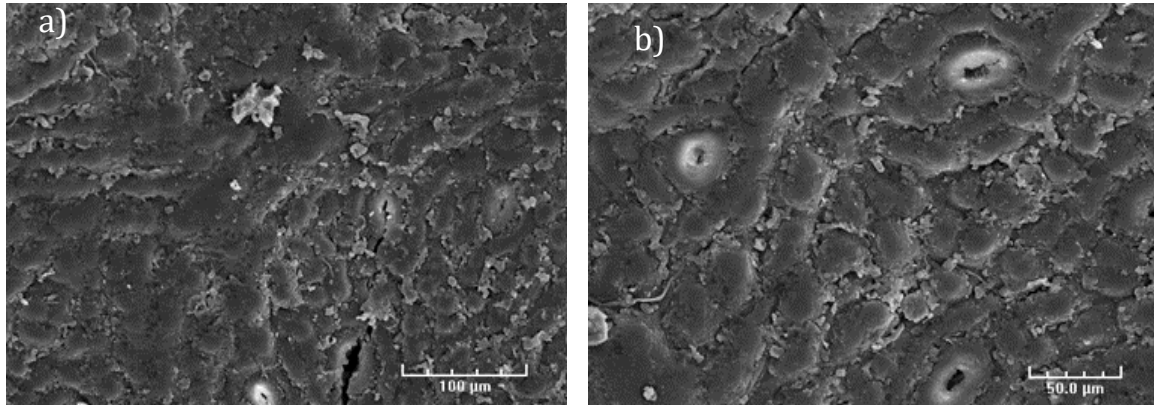


Figure III-6: SEM images of lyophilised EC leaf surface a) & b).

Here, the SEM images in Figure III-6 show the overall surface morphology of a *Eucalyptus camaldulensis* leaf that has been lyophilised. It shows features that are common to the specie and in general to most plants (stomata, papillae and waxes etc). Distinctively, the waxes are quite apparent on the adaxial plant surface, lending their roughness to the topography of the overall plant surface although the top of the stomata and the top of the papillae have been spared from its rough coverage. In between however, rough plate-like features can be seen occupying these spaces, which corroborates the theories of one of the different forms that can be assumed by the epicuticular wax. Figure III-7 is a magnified image of a stoma, showing its smooth surface immediately surrounding the guard cells.

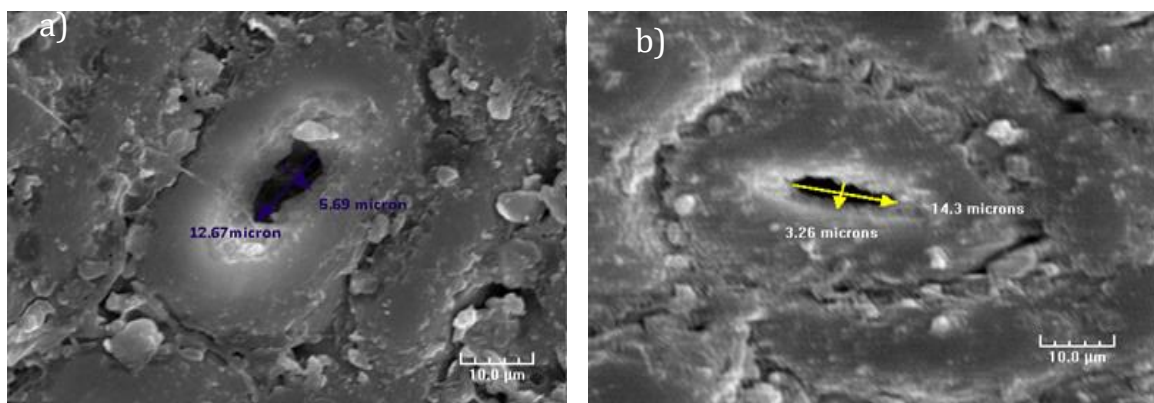


Figure III-7: SEM of lyophilised EC leaf showing the dimension of the stomatal opening a) & b).

The apertures of the stomata are fairly consistent in dimensions, maintaining a semi-open conformation (dimensions averaging  $\approx 12.08 \times 3.59 \mu\text{m}$ ). Lyophilising leaves the main features of the *EC* leaf as close to those in their natural environ. The same may also be said for the aquatic plant *RR* as seen in Figure III-8.

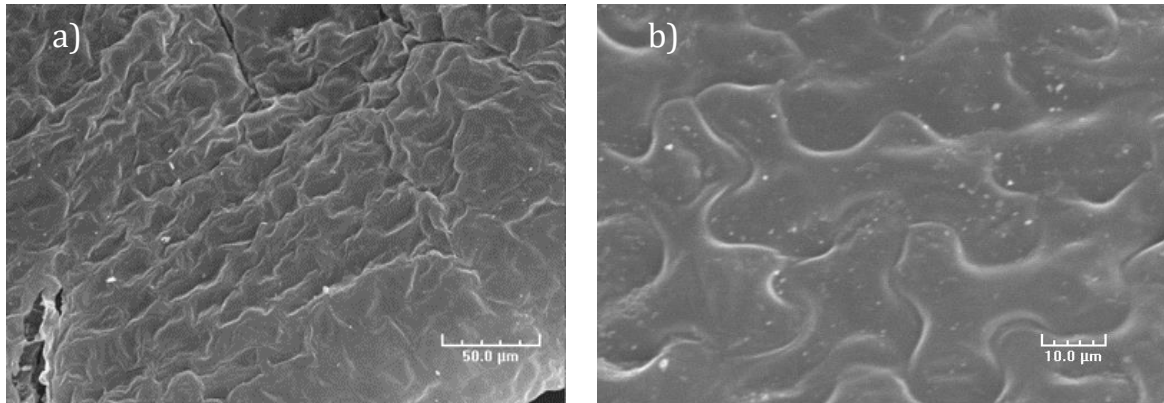


Figure III-8: SEM of lyophilised *RR* leaf a) & b).

Figure III-8 (a&b) provides a wider low magnification view of the surface of *RR* leaf. The folds on the surface of the system are likely due to natural cuticular folding of the epithelial cells that exist beneath the cuticle - resulting in unique patterns (Bhushan, 2009). In other plant species, the folds might be a repetitive pattern, those of *RR* seem to be without any particular order. It is quite apparent that the surface morphology of the *RR* leaf is different from its terrestrial counterpart. Its surface is much smoother, except for the obvious cuticular-folding giving the surface a wave-like structure. Another difference is that the stomata are found sitting on their surface, while those for *EC* (shown in Figure III-7) are sunken into the epidermis, compared to those seen in Figure III-9. The difference in environmental adaptation, specifically towards transpiration loss through the stomata, is less apparent in an aquatic environment. The stoma also appear to have smaller dimensions ( $6.05 \times 3.47 \mu\text{m}$ ).

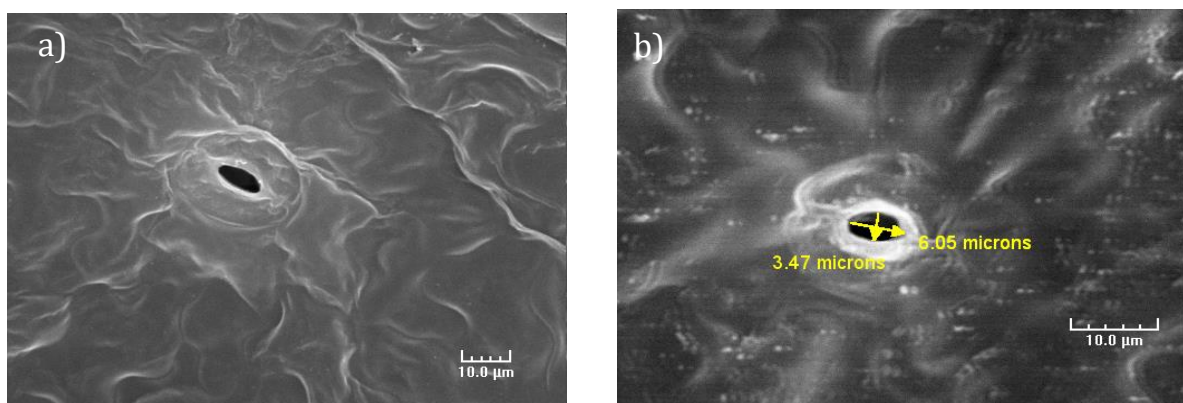


Figure III-9: SEM of lyophilised *RR* leaf surface showing a stomatal opening a) and its measured dimension b).

### III.5.2.2 Calcined samples

On calcining the samples, the overall appearance of the TiPA-treated samples are quite similar to their pre-calcinated states. This means that the  $\text{TiO}_2$  replication is dimensionally good. It is still possible to make out some of the features, after subjecting them to temperatures of  $600^\circ\text{C}$  in air (See Figure III-10).

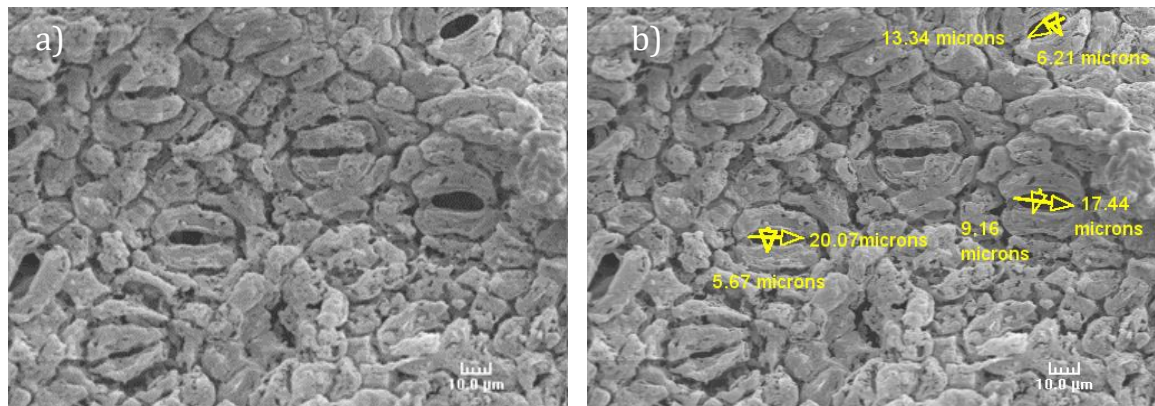


Figure III-10: SEM image of EC (DW+DL+TiPA) calcined at  $600^\circ\text{C}$  in air a) with measured dimension of some stomatal openings b).

Thus, the obvious features are still discernible are the  $\text{TiO}_x$  replicas of the papillae, with their boundaries now more obvious as the waxy coating has been oxidatively removed. Besides that, the previous smooth surfaces of the guard cells are no longer as smooth, with 'voids' appearing throughout their faces, most likely as a result of the high temperatures. The pores of the stomata remain recognisable although appearing distended (i.e. dimensions increased and now average  $\approx 16.25 \times 6.77 \mu\text{m}$ ). A close up of the stoma is shown in Figure III-11.

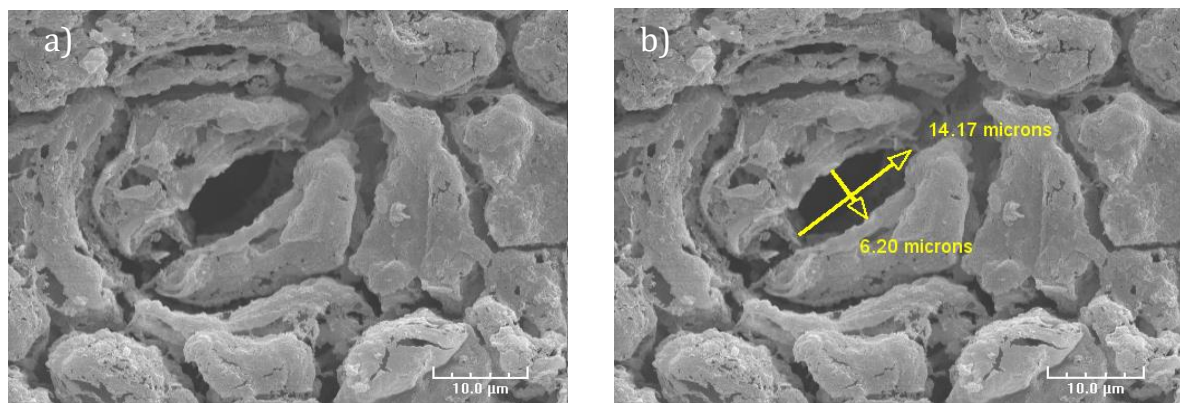
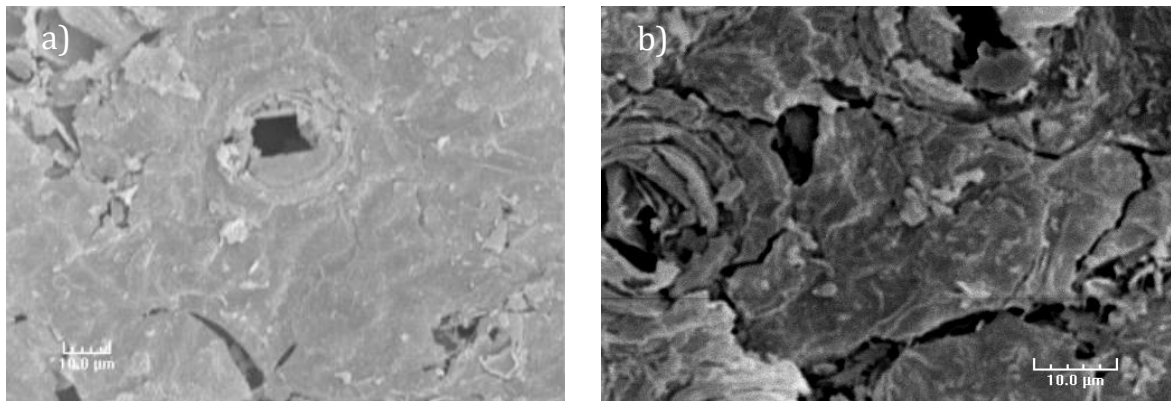


Figure III-11: SEM image of EC (DW+DL+TiPA) calcined at  $600^\circ\text{C}$  a) with measured dimension of some stomatal openings b).

### III.5.2.3 Other pre-treatment processes + calcination

Incorporation of other pre-treatment process can also affect the morphology as we will show in the coming section.

While dewaxing and opting to treat the sample only with water, in an attempt to remove the excess cations such as  $\text{Ca}^{2+}$ , this resulted in much poorer replicates (see Figure III-12).



**Figure III-12: SEM image of EC (DW+DI+TiPA) calcined at 600°C in air showing the surface and stomatal openings a) & b)**

Dewaxing and delignification, along with washing with water before the replication treatment, produced samples with much better and slightly defined features (see Figure III-13).

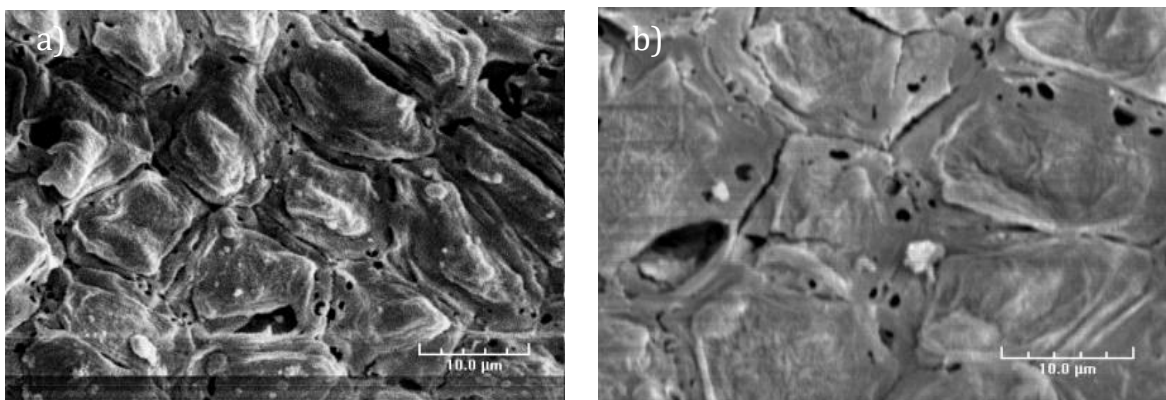


**Figure III-13: SEM image of EC (DW+DL+DI+TiPA) calcined at 600°C showing the leaf surface a) & b).**

HCl leaching of the samples (in an attempt to lower calcium content) along with a delignification process that employed the use of 2-propanol in place of water (in order to shorten the process) produced marginally clearer features. Figure III-14 shows missing papillae (revealing the inner anti-clinal walls of EC leaf) likely lost due to shear forces generated by the magnetic stirrer flea, on the softening tissue, during delignification.

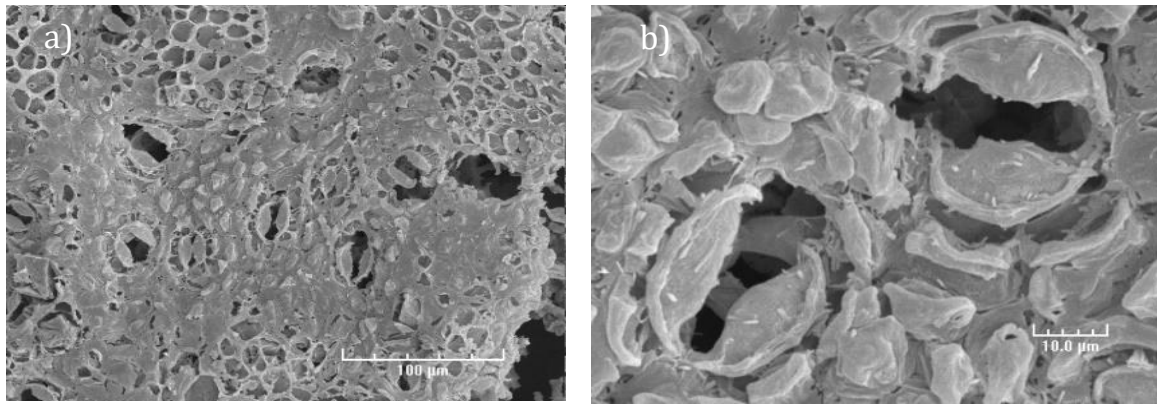


Figure III-14: SEM image of EC (DW+DL+ HCl[pH4]+TiPA) calcined at 600°C in air showing the anti-clinal wall interiors of EC leaf surface and the presence of stomatal openings a) & b).

The fragile nature of the samples might be due to the concentration of the replicating solution used. Increasing the alkoxide concentration from 5mM to a much higher 10mM, produced a more robust replica sample (see Figure III-15), with an almost perfect replication of the microscopical features of a typical EC leaf. At this point, the reader should remember the TGA residual weights which showed modest increase (from 11% to 20%) indicating TiO<sub>x</sub> overcoats.

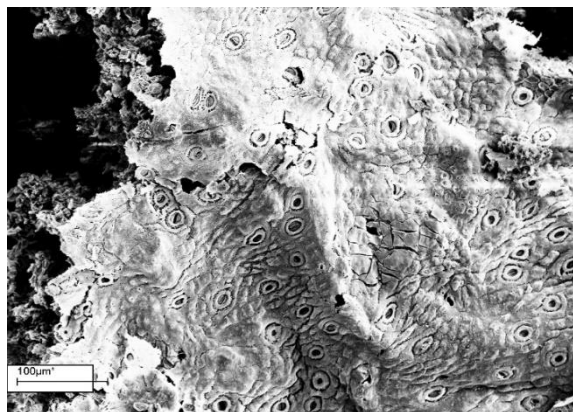


Figure III-15: SEM image showing a of EC leaf that had been delignified, treated with 10Mm TiPA solution only and subsequent calcined at 600°C.

Replicas of the aquatic plant *RR* (produced in the same infiltration manner) were a close approximation of the original non-replicated plant. The main difference between the replicas formed using *EC* and those formed using *RR* could be defined by the fragility of the samples. For example, in Figure III-16, the overall *RR* replica structure appears to be more fragile than produced using *EC* at the same TiPA concentration (5mM).

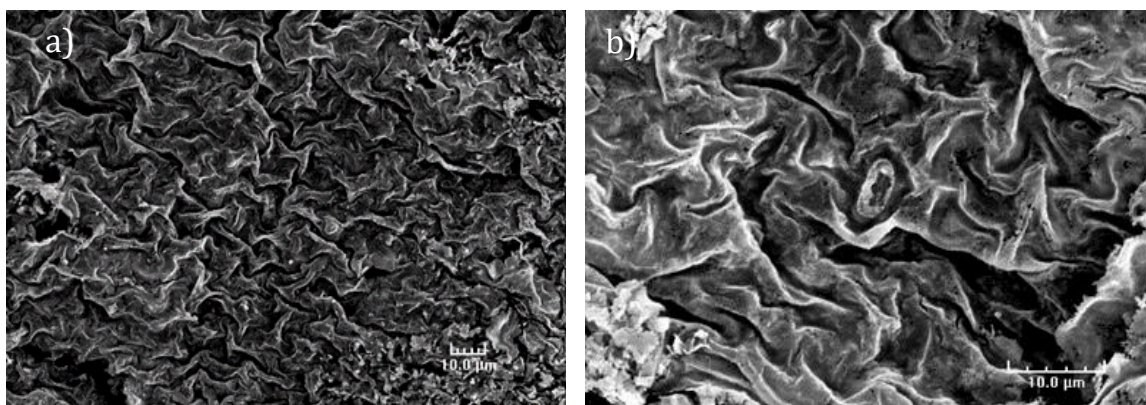


Figure III-16: SEM image of RR (DW+TiPA) calcined at 600°C, showing the preserved surface features a) & b).

This could be as a result of the overall thinness of the samples, as well as the composition of the leaf. EC (as well as most terrestrial plants) tend to have more structural components (as explained earlier), while hydrophytes mainly rely on water for structural support. This results in a plant with less of these structural components. In terms of replication, it could simply be a case of fewer barriers to contend with. As well as this, the fact that it has a reduced cuticle layer, compared to EC, could further enhance penetration of TiPA. Figure III-17 shows a close up on the RR stomata and their dimensions, which appear reduced in size compared to the initial dimension (6.05x3.47μm).

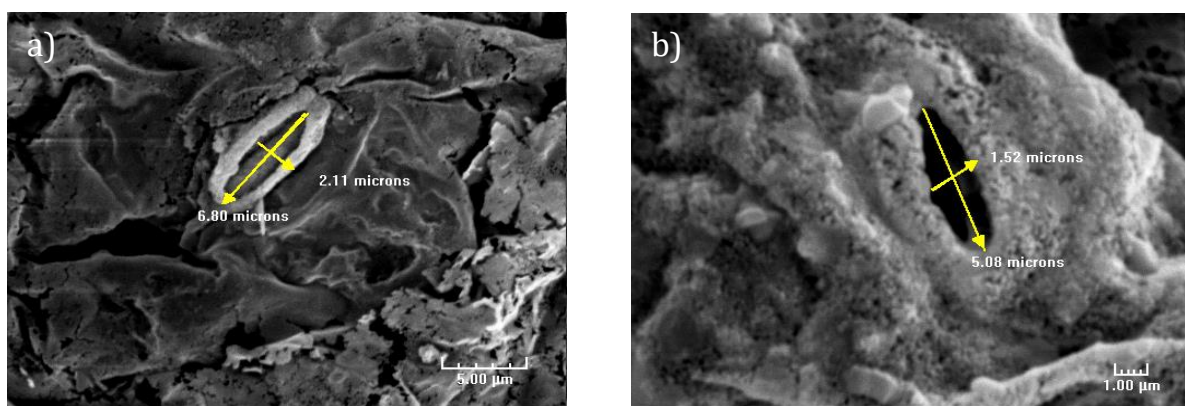


Figure III-17: SEM image of RR (DW+TiPA) calcined at 600°C, showing a close views of stomatal openings a) & b).

Clearly, the pre-treatment process has affected the surface of RR and EC, creating newer interfaces that will permit interaction with Ti precursor. This improved surface area (to volume ratio) is no doubt a cause of the increment in the residual weight of some of the samples that have undergone pre-treatment. Of course, one cannot discount the effect of chemical changes that would have made the surface more amenable to deposition with titanium. It remains to be seen the nature of the titania phases being formed.

### III.5.3 Compositional analysis

Using the EDX attachment on the SEM, it was possible to collect information on the elemental composition of the samples before and after they had been subjected to the various treatments (see Table III-2). All the samples listed below were calcined at 600°C (10°C/min), except the lyophilised samples (EC only and RR only).

**Table III-2: EDX derived elemental composition(at%) of EC samples. \* C was excluded as analysis was carried out on carbon tape.**

Samples	Ca (at%)	K (at%)	Mg (at%)	Na (at%)	O (at%)	Ti (at%)
EC Only	1.15	1.25	1.09	0.10	24.63	N/A
EC (DW + TiPA)	10.12	10.04	2.00	3.05	40.79	20.08
EC (DW +DI+ TiPA)	10.33	7.89	1.60	28.09	35.95	3.29
EC (DW+ DL+ DI+ HCl [pH 4]+ TiPA)	8.68	1.25	1.71	10.91	43.86	14.72
EC (HCl [pH1] + TiPA)	6.40	1.15	0.70	1.79	66.10	14.57

Oxygen makes up the next majority element, which again is to be expected seeing that the major components that make up a plant leaf (cellulose, chitin, hemicellulose, and lignin) all contain oxygen along with carbon in different combinations. The oxygen content appears to increase from 24.63at% in the untreated and un-calcined samples, to the highest level in EC (HCl[pH1] + TiPA (66.10at%). This trend seems to suggest that its increasing presence is linked to the also increasing percentage of titanium in the sample, which itself rose from 0at% to 20.08at%. It could be proposed that the oxygen here might be bonded with Ti in the formation of titanium oxide. Interestingly enough the sample with the lowest residual weight in TGA (EC (DW +DI+ TiPA)) has the lowest Tiat% content compared to the all the other samples which had higher residual weights and Ti at%  $\geq 14.0\%$  (Figure III-4).

Calcium (1.2at% originally) rose on overcoating. Its presence increases in spite of being subject to the various treatment process that would encourage its loss. Its presence however corroborates the results obtained from XRD where it constituted one of the major phases present in the replicas (see III.5.5 for results).

The other elements (K, Mg and Na) are bioactive trace elements. The atomic percentage of sodium in two of the samples (EC (DW+ DI+ HCl[pH 4]+ TiPA and EC (DW +DI+ TiPA)) is significantly higher (10.91at%; 28.09at%) as they had been delignified. It is likely that the rinsing process was inadequate in removing the excess amount of sodium. The other elements, magnesium and potassium, both remain below 2% in concentration.

In the case of RR, the percentage of oxygen is significant in the untreated sample, mirroring that of its terrestrial counterpart (EC).

**Table III-3: EDX derived elemental composition(%) of RR samples. \* C was excluded as analysis was carried out on carbon tape.**

Sample	Ca (at%)	K (at%)	Mg (at%)	Na (at%)	O (at%)	Ti (at%)
RR only	2.48	5.26	2.04	N/A	39.83	N/A
RR (HCl [pH1])	8.99	0.22	0.24	0.09	31.63	N/A
RR (Lyo+ TiPA)	3.36	9.11	2.28	1.28	32.92	1.35
RR (HCl[pH1] + TiPA)	1.09	0.17	0.18	0.31	53.69	34.94

Unlike EC, which was only able to achieve a Ti at% of 20.00at% at its highest, RR reached a value of 34.94at%. Again, like EC, the highest Ti loading seems to have occurred when there was some acidic pre-treatment. Meanwhile, the oxygen content of all the RR samples, remained fairly constant ( $\approx 34.79\%$ ), except for RR (HCl[pH1] + TiPA). In this case, the oxygen content jumps to just above 50at%, which gives the impression that its quantities is related to the titanium percentage (see III.5.5). Additionally, the calcium content decreases from levels seen in the untreated samples (from 2.48 at% to 1.09 at% respectively) to lower levels after infiltration and calcination. This is likely the reason why RR experienced an increase in residual weight (14 to 17%) for the TIPA treated samples RR (Lyo +TiPA) in TGA (see Figure III-5).

Mg content is quite responsive to any acid intervention. From a high of 2.04at% in a previously untreated sample, the percentage drops to levels below 1at% (0.24at% in the most extreme case). The same can be said for K, dropping from a maximum of 9.01at% to about 0.17at%.

Taking results from both sets of samples, it would seem that RR provided a better biotemplate especially in terms of loading with Ti-TiO<sub>x</sub>-TiO<sub>2</sub>. While EC seems especially resistant to the different forms of treatment that were administered, RR undergoing very little intervention was able to achieve titanium levels that were double that of those seen in EC. In addition, the presence of calcium, which seems to drive chemical reactions to favour the formation of calcite (seen in section III.5.5) rather than TiO<sub>2</sub>, is a lot less than in RR, which is a positive sign.

It is worth stating, that in spite of the acid treatment administered to the samples, both in EC and RR, the at% of Ca remained relatively unaffected in comparison to the other samples. Thus, it is likely that the improvements (brought on by an intervention with acid treatment), has less to do with cation leaching and more to do with the possible modification of groups present on the altered leaf surfaces.



### III.5.4 Infrared characterization:

#### III.5.4.1 Un-calcined samples

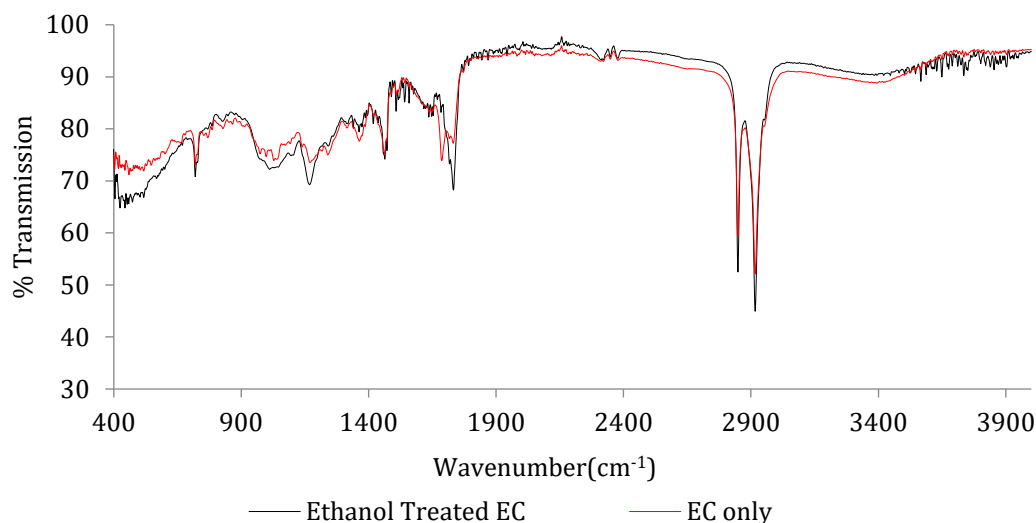


Figure III-18: FTIR spectra of lyophilised only EC and ethanol-treated EC samples.

The spectra for the lyophilised and ethanol-treated EC (see Figure III-18) exhibit a number of distinct bands highlighting the complexity of the compounds that make up the leaf. The broad peak around 3342cm<sup>-1</sup> and 3450 cm<sup>-1</sup> for lyophilised and ethanol-soaked EC respectively, suggests the presence of hydroxyl functional groups (O-H stretch, H-bonded) can be ascribed to tissue hydration, alcohols and phenols (Guzman, et al., 2014). The difference in intensity of the broad band might relate to the hydration of the tissue (Vázquez *et al.*, 2008). It is also likely that the cutins present in the plant cuticle will make a major contribution to this band (Heredia-Guerrero *et al.*, 2014). It is thus an indication that pre-treating the plant with ethanol (or other organic solvents) has the ability to remove from the plant leaf some of its cuticular content but not all (as the band is still present, though diminished).

Another prominent FTIR feature is the double sharp bands at approximately 2848cm<sup>-1</sup> and 2918cm<sup>-1</sup>, along with bands that appear around 1462cm<sup>-1</sup> and 719cm<sup>-1</sup>. They may relate to methylene found on long chain aliphatic hydrocarbon residues (also prominent in plant cuticles: cutin, cutan, waxes) (Heredia-Guerrero *et al.*, 2014). Bands around 1683cm<sup>-1</sup> and 1730cm<sup>-1</sup> are indicative of carbonyl bonds (C=O) in “dimerized saturated aliphatic acids” (Vázquez *et al.*, 2008). Stretches between 1650-1400 cm<sup>-1</sup> are usually common in aromatic phenolic compounds containing not just C=O functional groups and C=C, that may be an indicator of tannins (Guzmán *et al.*, 2014; Heredia-Guerrero *et al.*, 2014). The band at 1656cm<sup>-1</sup> can be attributed to amides from proteins (Ertani *et al.*, 2018). Between 1230-1153 cm<sup>-1</sup> are regions for C-stretching in esters and amide. The vibrations at 1161s cm<sup>-1</sup> is thought to be indicative of C=O ascribed to esters

present in cutin matrix (Kerr *et al.*, 2013; Heredia-Guerrero *et al.*, 2014) and amides (Ertani *et al.*, 2018). Smaller bands between  $1100\text{-}1000\text{cm}^{-1}$  (C-C or C-O) are linked to the presence of cellulose in leaves.

The spectra of samples pre-treated by lyophilisation or by chemical interventions, show that essentially the same functional groups that are characteristic of EC leaves remain active in spite of the different pre-treatment protocols. The most prominent of these vibrational intensities are those that can be easily associated with (phenols, carboxyls and carbonyls) major components of the plant's cuticle.

Concerning RR (Figure III-19), there are several bands that are absent/diminished: the methylene group arising from the aliphatic carbon ( $2848\text{cm}^{-1}$ ,  $2918\text{cm}^{-1}$ ,  $1462\text{cm}^{-1}$ ,  $719\text{cm}^{-1}$ ) prominent in in cutins. Along with those, the carbonyl bond for aliphatic acids ( $1683\text{cm}^{-1}$  and  $1730\text{cm}^{-1}$ ) linked to cutins are missing. Between  $1230\text{-}1153\text{cm}^{-1}$ , peaks linked to esters for amide and cutins are missing too.

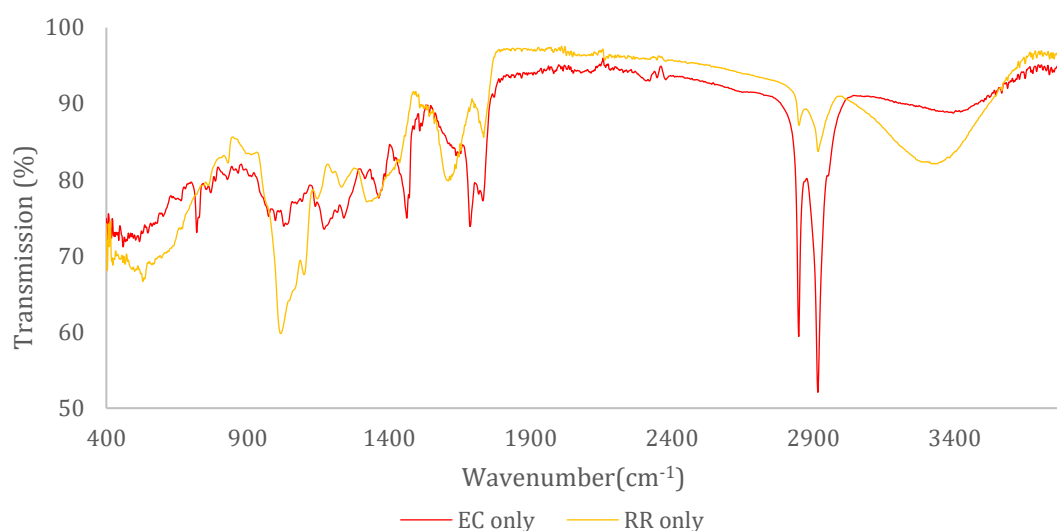


**Figure III-19: FTIR spectra of EC and RR after being lyophilised.**

The groups that are more prominent are  $1016\text{cm}^{-1}$ ,  $1097\text{cm}^{-1}$ ,  $1342\text{cm}^{-1}$ ,  $1436\text{cm}^{-1}$ ,  $1608\text{cm}^{-1}$ ,  $1734\text{cm}^{-1}$  and  $3323\text{cm}^{-1}$ . The band  $1016\text{cm}^{-1}$  and  $1097\text{cm}^{-1}$  are associated with cellulose; the region between  $1800\text{-}1200\text{cm}^{-1}$  (encompassing bands at  $1342\text{cm}^{-1}$ ,  $1436\text{cm}^{-1}$ ,  $1608\text{cm}^{-1}$  and  $1734\text{cm}^{-1}$ ) are associated with C=O vibration for cell wall, amide and lipids; and at  $3323\text{cm}^{-1}$ , the region is dominated by OH and NH, characterising the higher level of hydration and amide.

Although the spectra for EC and RR appear quite different, with EC dominated by the presence of cutins and membrane lipids (and RR containing more diverse groups), it is the author's opinion that this is due to the relative thickness of EC. One must remember that the cuticle membrane of

EC has been estimated as 2-5 $\mu\text{m}$  thick (Guzmán *et al.*, 2014). This is not a problem with RR, as IR can easily penetrate its thin cross section and its relatively sparse cuticle layer.

### III.5.4.2 Calcined samples

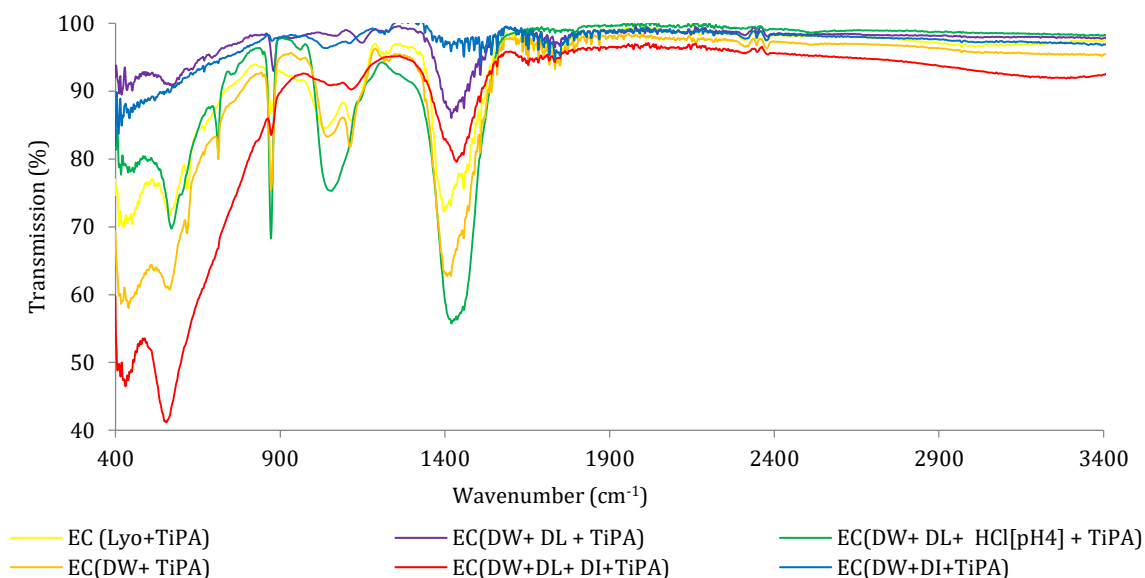


Figure III-20: FTIR spectra of EC samples after undergoing the various treatment processes, and calcination at 600°C.

Figure III-20 shows spectra collected for samples that were calcined to complete the replication process. The calcination process is an essential step in replication, which is meant to oxidatively remove the biotemplate, leaving just the inorganic  $\text{TiO}_2$  overcoat plus mineral phases replicating the hierarchal and porous structure of the leaf.

All of the samples regardless of their preparation methods appear to have undergone fairly significant changes as a result of the calcination process. The broad peak around 3342-3450 $\text{cm}^{-1}$  is not present in any of the samples indicating a reduction in the hydration/OH population of the leaf. The two double peaks that appeared around 2848  $\text{cm}^{-1}$  and 2918  $\text{cm}^{-1}$ , normally characteristic of methylene groups ( $\text{CH}_2$ ), have been suppressed. Along with this, the ester group at 1730  $\text{cm}^{-1}$  ( $\text{C}=\text{O}$ ) is less prominent compared to pre-calcination process as a result of the hydrocarbons oxidation/decomposition at high temperature in air.

In all of the samples (except for EC (DW+DI+TiPA)), a band of varying intensity emerges around 1396  $\text{cm}^{-1}$ ; this band would indicate the presence of C-H<sub>3</sub> and C-H<sub>2</sub> vibrations. They are sometimes found in protein/chitin/lipids samples and might also be related to residual organics (Kerr *et al.*, 2013). Perhaps EC (DW+DI+TiPA) does not exhibit this peak because it is water treated before its replication step.

Another divergence in the infrared signature of the samples is around the 1047-1144 $\text{cm}^{-1}$ . While

EC (Lyo+TiPA) and EC (DL+TiPA), show similar signatures in this same region, EC (DW+DL+DI+TiPA) and EC (DW+DI+TiPA) both had little or no perturbations at those wavenumbers. This is in contrast to the singular peak exhibited by EC (DW+ DL+ HCl[pH4] + TiPA). As the 1045-1144 $\text{cm}^{-1}$  region has also been attributed to Ti-O-C presence, this zone could either indicate the residual alkoxide trapped within the samples or the formation of a titanium-based compound with the carbon backbone of the leaf structure.

Between 700-719 $\text{cm}^{-1}$ , there is a small sharp peak (present in almost all of the samples) that may be linked to symmetric deformation of carbonates present in calcite. A second sharper peak at 870 $\text{cm}^{-1}$  is assigned to the asymmetric deformation of the same group (Gunasekaran, Anbalagan and Pandi, 2006).

Again, at around 619 $\text{cm}^{-1}$ , EC (Lyo+TiPA) and EC (DL+TiPA) have a peak forming. Its presence or rather lack is potentially linked to the delignification process, as these two samples are the only ones that have not undergone the process.

There is some evidence pointing to the presence of Ti-O-C. The band around 400-600 $\text{cm}^{-1}$  (Hou *et al.*, 2008) has been linked to Ti-O-Ti vibrations; He (2013) also mentioned that the same zone (although narrowing to 500-590 $\text{cm}^{-1}$ ) could be attributed to the presence of anatase in the replicas structure. If one went by these readings, then some of the samples: EC (Lyo+TiPA), EC (DW+DL+DI+TiPA), EC (DW +TiPA) show the emergence of a band around at 430 $\text{cm}^{-1}$  (along with a bigger band around 555 $\text{cm}^{-1}$ ). When all these samples were tested with XRD, peaks confirming the presence of titania in any form were absent. It is the author's opinion that the quantities of  $\text{TiO}_2$  were simply too small and were thus easily obscured by the other phases present. In fact, the only samples that have so far been able to show the presence of titania are those that had been extensively treated with a low pH acid (Figure III-21), which could be a matter of them crossing a concentration threshold (discussed further in III.5.5).

The spectra of acid-treated samples at first glance are quite similar to the previous samples (Figure III-20). On closer inspection, the 400-600 $\text{cm}^{-1}$  region is quite dissimilar. Whereas the spectra in Figure III-20 revealed a double peak in roughly the same height is seen, just as single prominent peak is seen in Figure III-21. This spectral region may be used as proof of titania formation, and the altered shape may be considered as a direct manifestation of Ti-O-Ti arising from titania or specifically anatase (He *et al.*, 2013). According to section III.5.5 this is indeed the case. The acid-treated samples also share quite a resemblance to P25 (see Figure III-22), which also has a similar shape as seen in literature (Martins *et al.*, 2016).

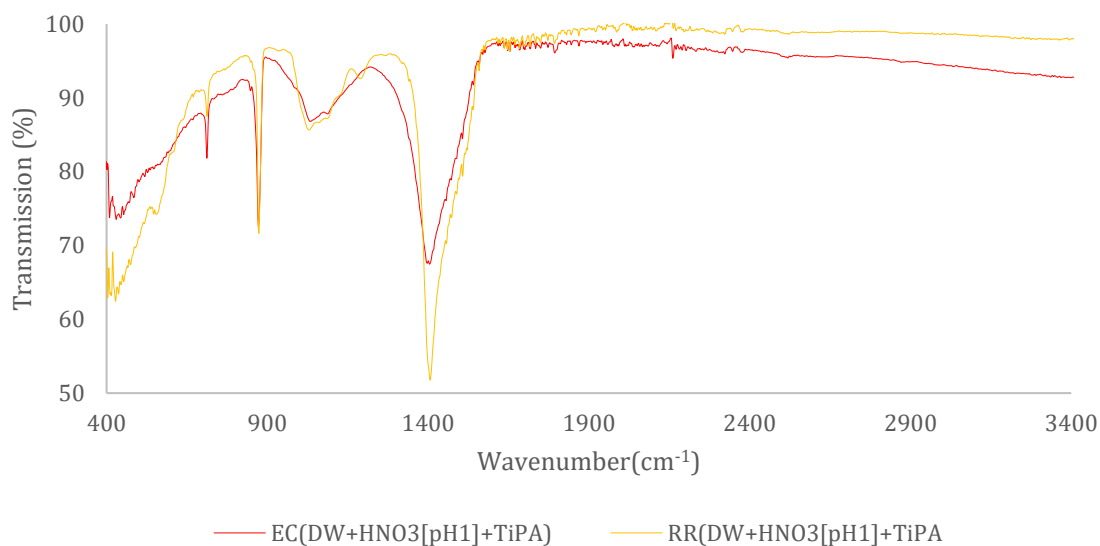


Figure III-21: FTIR spectra of EC and RR replicas having undergone extensive acid treatment; EC acid treated+ 5mM TiPA; RR acid treated + 5mM TiPA.

It seems apparent from FT-IR that there is some formation of titania and other titanium-based specie in the sample that had been treated with the titanium reagent.

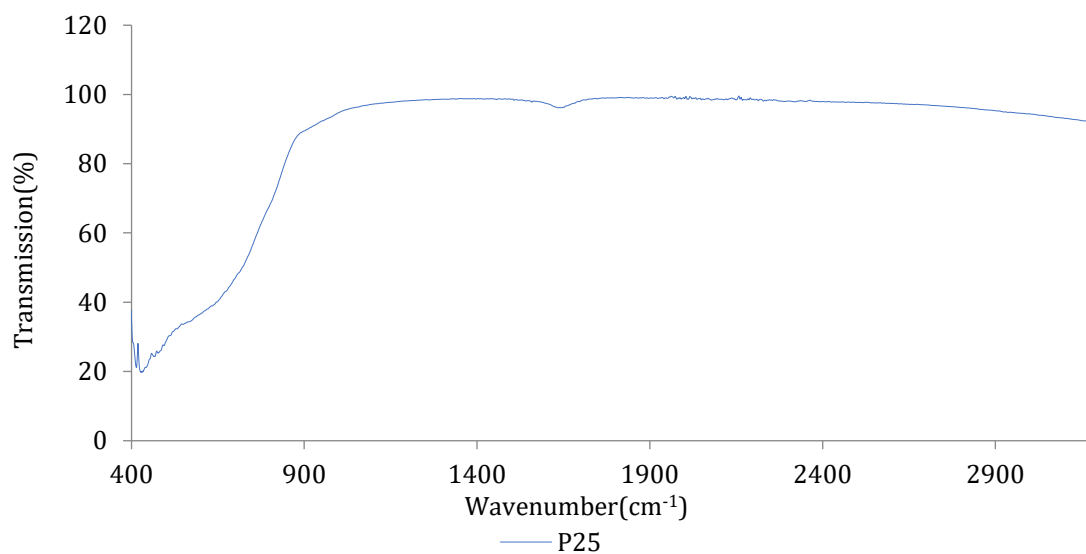


Figure III-22: Infrared spectrum of P25.

### III.5.5 Crystallographic characterisation of the calcined samples

XRD was chosen to help confirm the identity of the phases present in the replicas and how these compared to those that would otherwise be obtained from commercial TiO<sub>2</sub> sources (P25) and lab synthesised TiO<sub>2</sub> without a biotemplate (made by adding excess water to titanium alkoxide and the calcining at 600°C). All samples analysed here were calcined at 600°C. The composition and size of crystallites were estimated using Rietveld refinement (TOPAS software) on the line

profile of the samples by matching it with a mineral profile downloaded from the ICSD. Phase identification was carried out using a function of the “Diffrac Suit” phase identifier, it was possible to identify and confirm the identity of the crystalline phases present.

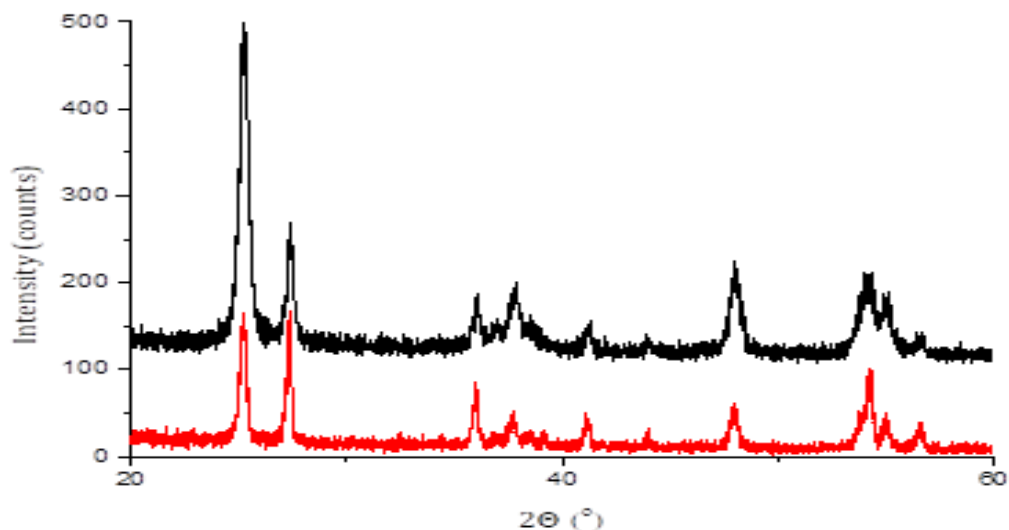


Figure III-23: XRD patterns of P25 (black) and lab synthesised TiO<sub>2</sub> (red).

In Figure III-23, the lab processed sample and P25 both have prominent peaks that are indicative of phases corresponding to the two main polymorphs of TiO<sub>2</sub>. In the case of P25 it was clear that there was a combination of peaks which indicated that anatase and rutile were present in the preparation. We know from the manufacturer (of P25) that this preparation would have approximately 70% anatase and 30% rutile (Ohtani *et al.*, 2010). The peaks at  $2\theta = 25.2^\circ, 37^\circ, 48^\circ, 53^\circ, 55^\circ, 62^\circ,$  and  $74^\circ$  were as a result of diffraction patterns occurring at the following crystalline planes respectively (101), (004), (200), (105), (204), (215), representing the elongated tetragonal unit cell characteristic of anatase. Rutile meanwhile has  $2\theta$  peaks occurring at  $27^\circ, 36^\circ$  and  $55^\circ$  which corresponds to (110), (101) and (211) respectively (Thamaphat, Limsuwan and Ngotawornchai, 2008). Both the lab synthesised and P25 had rutile and anatase present. Table III-4 contains the composition and estimates of the average size of crystallites in these samples.

Table III-4: % phase composition and the average crystallite sizes of P25 and a template free sample.

Sample	Anatase (%)	Crystallite size: Anatase (nm)	Rutile (%)	Crystallite size: Rutile (nm)
P25	78.49	22.1	21.51	32.9
Lab synthesised (template free)	58.22	36.4	41.78	64.2

While lab synthesised TiO<sub>2</sub> and P25 had spectra that were almost indistinguishable XRD profiles,

the same cannot be said for the leaf replica samples (see Figure III-24).

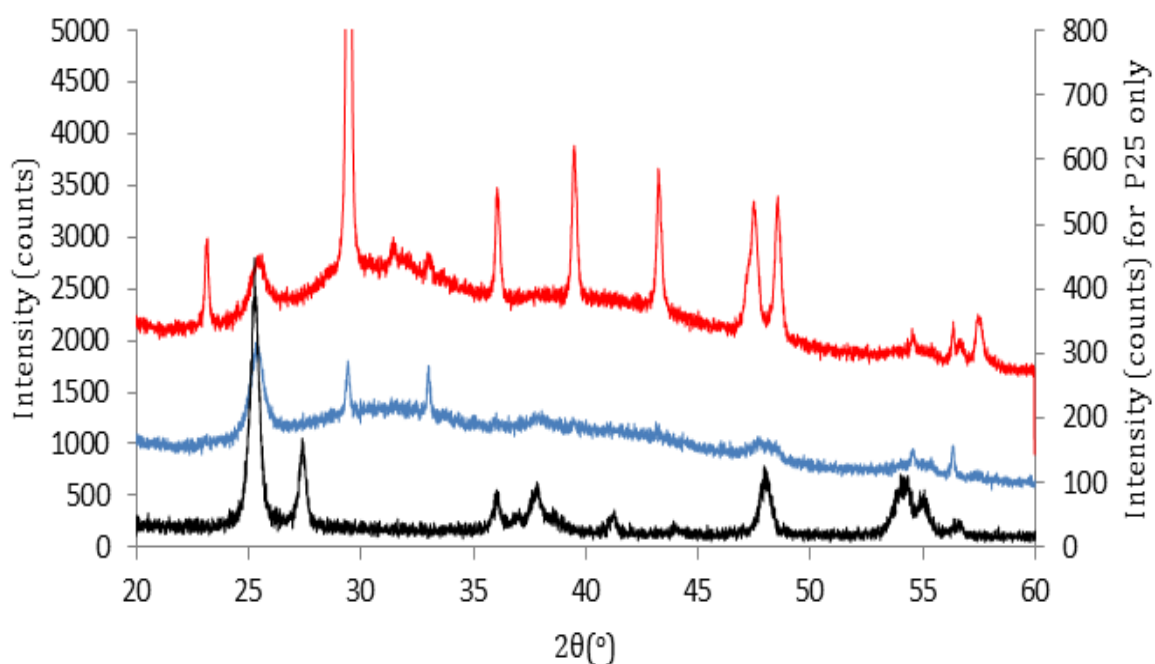


Figure III-24: XRD pattern of leaf replicates treated with acid: RR (DW+HNO<sub>3</sub>[pH1]+20mM TiPA) (blue), EC (DW+HNO<sub>3</sub>[pH1]+20mM TiPA) (red) and P25 (black).

Figure III-24 shows clearly that there are dissimilarities in XRD between all three samples. There are some common  $2\theta$  peaks overlapping at  $25^\circ$ ,  $38^\circ$ ,  $47^\circ$ ,  $54.5^\circ$ , which belong to anatase as mentioned above. The most prominent peak visible in all three of the samples is the small but broad  $2\theta$  peak at around  $25^\circ$  (a characteristic peak for anatase). Additional peaks seen in the RR and in the EC sample do not occur in the reference samples. This of course points to the presence of another phase which has grown as a result of the contribution from the leaf biotemplate. The additional phase was identified as calcite corroborating those of section III.5.4. Estimates of the size and composition are given in Table III-5. The % of calcite as well as its crystallite size is higher than for anatase.

Table III-5: % phase composition and the average crystallite sizes of the titania replica samples made using 20mM TiPA.

Sample	Anatase (%)	Crystallite size: Anatase (nm)	Calcite (%)	Crystallite size: Calcite (nm)
EC (DW+HNO <sub>3</sub> [pH1]+20mMTiPA)	12.5	18.3	87.5	83.8
RR (DW+HNO <sub>3</sub> [pH1]+20mM TiPA)	82.49	15.8	17.51	112.5

The presence of anatase is a positive in this replication process; unfortunately, the only samples that show the presence of anatase are those that have had extensive acidic pre-treatment before immersion into the actual titanium precursor; this may have removed some Ca<sup>2+</sup>. Other sample

that had not undergone this HNO<sub>3</sub> treatment did not display any characteristic XRD peaks of any titania polymorphs (likely as a result of the titania content being below the threshold of XRD detection). It is possible that small amounts formed signals that were easily obscured. It is also possible that the size of the anatase crystallites might have been too small.

It seems that the other pre-treatment processes were simply not effective at improving the yield of TiO<sub>2</sub>. Although the samples had been subjected to various treatment processes in an attempt to aid the formation of a viable titania overcoat, it is clear that a simple treatment with an acidic solution followed by immersion in the titanium precursor is all that is actually required (as in the case of EC (DW+HNO<sub>3</sub>[pH1]+TiPA) and RR (DW+HNO<sub>3</sub>[pH1]+TiPA)- the only successful samples). Cation leaching action of the acidic solution (evidenced in III.5.3), in addition to the alteration of the surface groups, may provide more binding sites for alkoxide interaction, improving the overcoating success. Additionally, the waxy layer was left intact, which may have contributed to the successful replication of specific samples. Further investigation of the best pre-treatment conditions will be described in III.5.5.1. This begs the question as to whether the simple removal of the excess cations from the leaf is behind the success, or if the low acidic pH might have caused a chemical or even physical change on the cuticle layer that created the optimal condition on the plant leaf.

#### ***III.5.5.1 Effect of pre-treatment conditions on the crystallinity of replicas formed***

From Table III-4 and Table III-5, it appears that the lab-synthesised template free sample and P25 contain more than one titania polymorph, which is not so with the biotemplated samples. In an attempt to improve the overall quality of the replica, or at least bring it as close to the photocatalytic benchmark (P25,) several aspects of the formation conditions were individually investigated to establish how the resulting replica's quality could be improved. The following factors were considered: the type of acid used, the duration of acid treatment, the calcination temperature and the type of titanium precursor utilised on the subsequent titania polymorph composition.

As RR has been shown to produce replicas with a more appreciable concentration of titania than EC, it will be used in preference to EC here.

The minimum XRD threshold limit of detection for a powder XRD setup is about 1wt% (Zhao *et al.*, 2004); thus it is possible that there is always a reasonable TiO<sub>x</sub> phase formed, but simply beyond the detection limit of XRD. For the moment, it will be assumed that if nothing has been picked up, then it is not present.

##### **III.5.5.1.1 Type of acid used**

The effect of the type of acid as part of the pre-treatment process before the eventual calcination



of the sample at 600°C appears to be crucial. It has been previously shown that EC samples which had not undergone an acid treatment process did not appear to form an appreciable amount of TiO<sub>2</sub>. The reluctance to form a suitable titania phase might have been due to the amount of cellulose and other structural tissue that make up a leaf tissue. In addition to the robust cuticle present in EC specifically, it appears that the presence of naturally occurring ions might be responsible for the low amount of TiO<sub>2</sub> produced.

To rectify this, an acid treatment step was included in the pre-treatment to aid in the titania formation step. It was soon found that the amount of TiO<sub>2</sub> produced was dependent on the identity of the acid used.

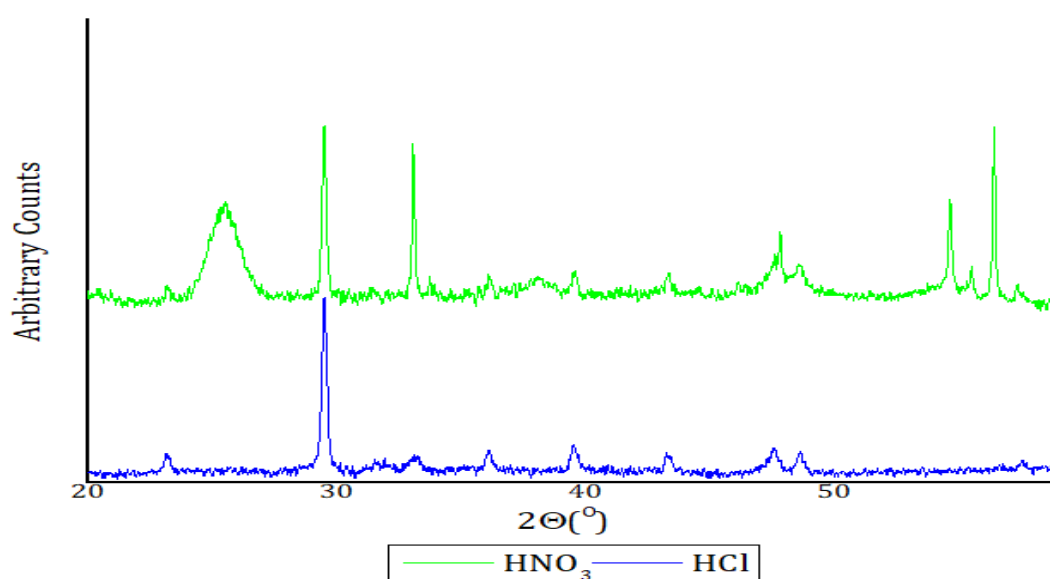


Figure III-25: XRD pattern of RR (DW+HNO<sub>3</sub>[pH1]+TiPA) and RR (DW+HCl[pH1]+TiPA). Calcination carried out at 600°C.

From Figure III-25, it is clear to see that there is quite a significant distinction between the XRD patterns obtained from the RR samples that have been treated with HCl or HNO<sub>3</sub>. What both of these samples have in agreement is their collective divergence from the XRD patterns collected for P25 and the lab synthesised sample (see Figure III-23). However, the replica sample made using HNO<sub>3</sub> is the only sample which contains anatase 2θ peaks around 25° and 37°. There are several other 2θ peaks previously listed and known to be identifiers of anatases, occurring at 47° and 54°, but their actual presence in the replica biotemplate samples are complicated/obscured by the presence of calcite.

Where HCl has been utilised, the identifier peaks of any useful titania polymorph, anatase and/or rutile, are missing (or perhaps lost in the background) with calcite being the only phase successfully detected. Rietveld refinement analysis by TOPAS suggests that indeed the more

successful sample containing a higher fraction of anatase was the sample which underwent the pre-treatment process using  $\text{HNO}_3$ . This makes a case for the continued utilisation of  $\text{HNO}_3$  in the future replication process.

### III.5.5.1.2 Duration of $\text{HNO}_3$ treatment

Since the type of acid utilised has been shown to go further than affecting the quality of titania formed, but the actual relative amount when compared to calcite after calcination, it stands to reason that the duration of acid treatment, using  $\text{HNO}_3$ , could possibly affect the quality ( $\text{TiO}_2$  crystallite size and composition).

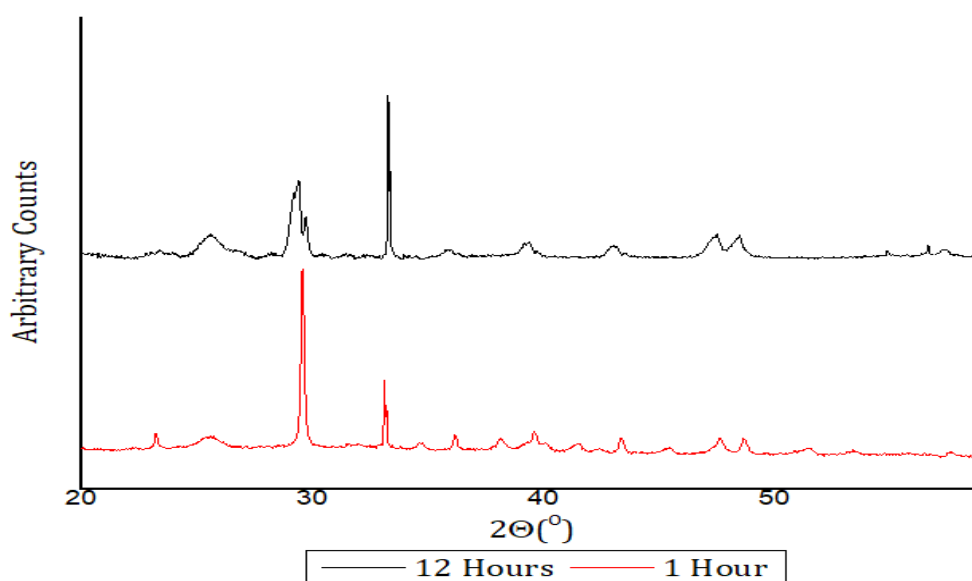


Figure III-26: XRD pattern of RR (DW+ $\text{HNO}_3$ [pH1]+TiPA) treated with  $\text{HNO}_3$  for 1h and 12h. Calcination carried out at  $600^\circ\text{C}$

Figure III-26 again illustrates the heterogeneous nature of the replica samples produced upon calcination is a composite of calcite, anatase and sometimes rutile (see Table III-6). From this table, it is quite apparent that increasing the duration of  $\text{HNO}_3$  enhances the formation of anatase. At 1h, about 10% of the replica formed is made up of anatase, with a majority of the samples comprising of calcite. At 12 hours, the percentage jumps to about 32% which seems to suggest that it is worth tuning the acid treatment period to improve the formation of anatase mainly. Rutile also appears at 1.6% ( $2\theta$  at  $27^\circ$ ); the amount is quite normal as the transformation from anatase to rutile, of pure samples, tends to occur between  $600\text{-}700^\circ\text{C}$  (Hanaor and Sorrell, 2010).

**Table III-6: % phase composition formed after calcination of RR samples that have undergone HNO<sub>3</sub> treatment at different durations (1h & 12h).**

Duration	Calcite (%)	Rutile (%)	Anatase (%)
1h	89.69	n/a	10.31
12h	66.30	1.69	32.01

The average sizes of the polymorphs are given in Table III-7. Although the size change is not so significant, anatase appears to grow by about 15%. Rutile only present for the sample treated for 12h is dimensionally larger than its anatase partner. The larger grain size, compared to anatase is thought to be a normal characteristic of rutile (Zhang *et al.*, 2014).

**Table III-7: Estimated average sizes of crystallites of the polymorphs of titania (nm) formed after the different acid treatment durations.**

Duration	Crystallite size: Rutile (nm)	Crystallite size: Anatase (nm)
1 h	n/a	11.9
12 h	17.1	13.7

### III.5.5.1.3 Calcination temperature

Keeping with the same pre-treatment condition (i.e. the dewaxing step followed by a 1h acid treatment step, the titanium precursor infiltration step) the final calcination temperature was varied in order to monitor how the presence of the biotemplate will affect the anatase to rutile transformation.

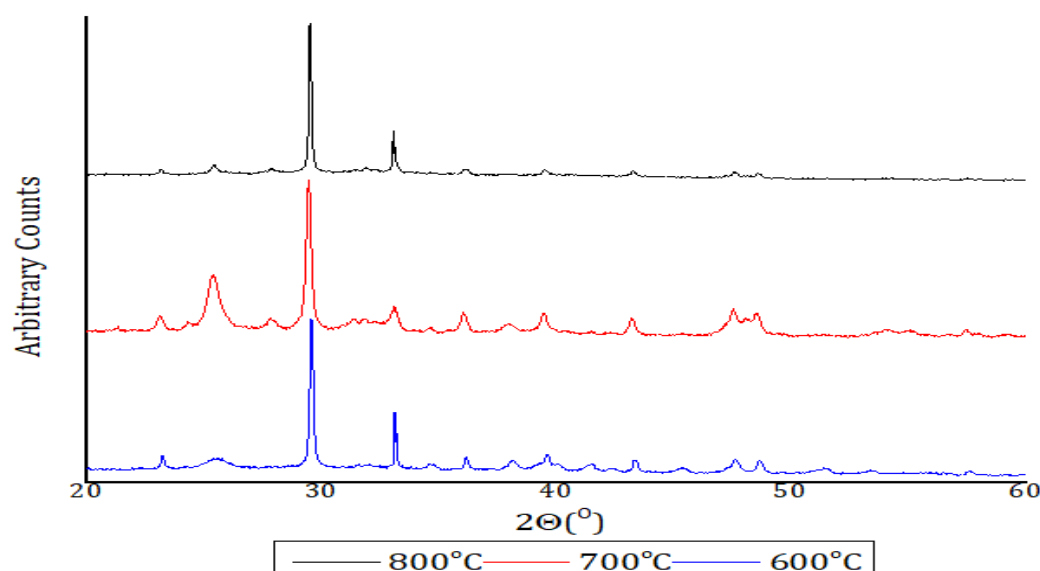


**Figure III-27: XRD pattern of RR (DW+HNO<sub>3</sub>[pH1]+TiPA) that have been calcined at increasing temperatures (600 °C; 700 °C; 800 °C).**

Figure III-28 shows the prevalent presence of the now familiar calcite phase (with 2θ angles at

23.0° (012), 29.4° (104), 31.44° (006), 35.9° (110), 39.4° (113)) in the overall replicas is not a fluke. Rietveld refinement of all the samples gives the estimated composition as seen in Table III-8. Calcite forms a majority component in the replicas, followed by anatase, and other minority phases (portlandite and rutile).

Increasing the calcination temperature from 600°C to 700°C, improves the % composition of anatase by an astounding ≈328%, the enhancement in the amount of anatase also brings with it the appearance of rutile. Relatively speaking, the amount of anatase against rutile is still quite low, with a ratio of ~1:15 (rutile: anatase).

**Table III-8: % composition of phases formed titania treated RR samples that have undergone calcination at different temperatures.**

Temperature (°C)	Calcite (%)	Rutile (%)	Anatase (%)	Portlandite (%)
600	89.69	n/a	10.31	n/a
700	48.39	2.97	44.17	4.47
800	71.84	6.75	21.41	NA

At 800°C, while the amount of anatase drops, its ratio to rutile is a lot better than at 700°C, achieving a value of 1:3 (rutile: anatase).

Observing the average crystallite sizes, as the temperature increases across all of the samples so does the estimated grain size. Both of the polymorphs appear to be affected by the temperatures increases.

**Table III-9: Estimated sizes of crystallites of the polymorphs of titania (nm) formed after calcination at different temperatures.**

Temperature (°C)	Rutile(nm)	Anatase(nm)
600	n/a	11.9
700	36.8	18.0
800	189.9	43.4

Increasing the calcination temperature appears to help hasten the transformation, leaving the replica with a better rutile to anatase ratio. However, the improvement in the ratio of anatase to rutile causes an undeniable increase in the grain sizes which would no doubt affect the positives that might have normally been resultant from obtaining nanosized materials. Not to mention the overall fraction of anatase that is being formed in the first place. A better means to achieve a balance of rutile to anatase that does not detrimentally affect the grain size, as well the relative amount of titania would be a better option.

#### III.5.5.1.4 Type of precursor utilised

Assuming that the amount/quality of titania formed is actually linked to the titania precursor utilised, two precursors will be considered, TIPA (which is the main titanium providing reagent

utilised in this section unless otherwise stated) and TiBALD.

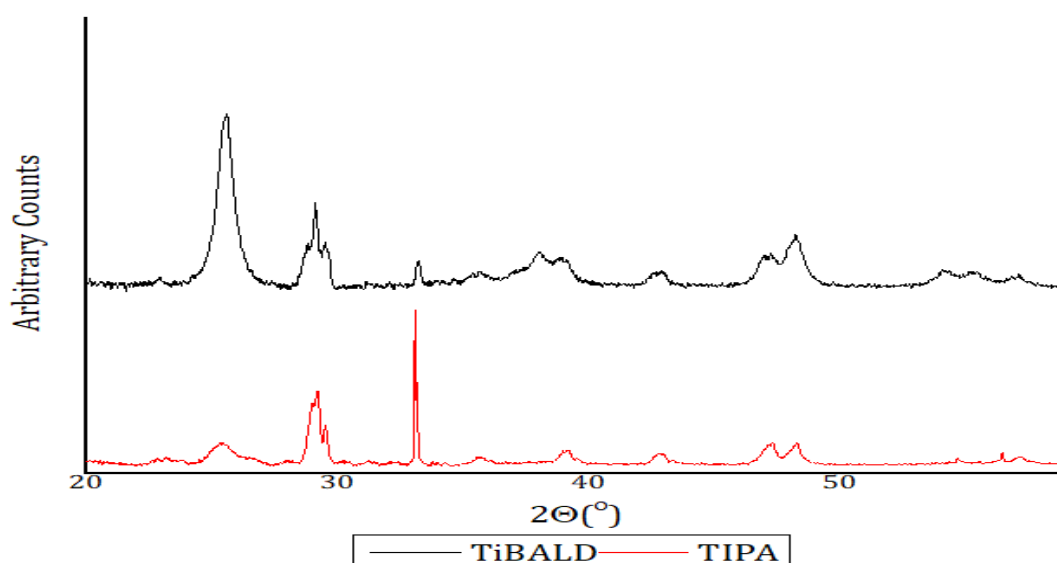


Figure III-29: XRD pattern of RR replicas that have been treated with different titanium precursors, TiBALD and TiPA. Calcination at 600°C.

Figure III-29 shows that the main  $2\theta$  peak associated with the presence of anatase, at  $25^\circ$  and  $37^\circ$ , along with  $2\theta$  associated with calcite. The percentage composition reported in Table III-10 shows that yet again calcite is present as quite a significant phase. The Ti reagents produced replica samples that do not contain portlandite; they do however contain rutile and anatase. Treatment with TiBALD appears to have promoted the formation of quite a substantial amount of anatase against rutile though the ratio is 1:14 (rutile to anatase). The other RR replica treated with TiPA has a poor rutile to anatase fraction (1:18; rutile to anatase). TiBALD produces a higher % composition of anatase (at 50.95%) against the 32.01% from TiPA.

Table III-10: % composition of phases formed after calcination of the RR replica samples that have been treated with different titanium precursors.

Precursor Type	Calcite (%)	Rutile (%)	Anatase (%)
TiBALD	45.46	3.63	50.95
TiPA	66.30	1.69	32.01

The average crystallite sizes of the polymorph fractions show in Table III-11, appear close to those obtained after calcination at 600°C.

Table III-11: Estimated sizes of crystallites of the polymorphs of titania (nm) formed on using the different titanium precursors.

Ti Precursor	Rutile(nm)	Anatase(nm)
TiBALD	15.7	12.5
TiPA	17.7	13.7

## III.6 Summary

### III.6.1 TGA

In terms of the thermal events observed by the samples as they are heated to 600°C, they all share a very similar thermograph. When heated from 20-120°C (a starting point to ensure only truly dried samples were analysed).

There WERE roughly two main thermal events that occur in EC only. The first of these is thought to be as a result of the breakdown of cellulose and hemicellulose (occurring between 226-326 °C). According to observation by Barneto, Hernández and Berenguer (2011), the region is broad due to a convolution of loss associated with hemicellulose at 294°C and cellulose at 328 °C. Following that, the next big step occurs around 513°C, associated with the decomposition/oxidation of lignin and char (Barneto, Hernández and Berenguer, 2011). Afterwards, there are no further thermal events up to 600 °C. Interestingly, only EC (DW+TiPA) follows this trend closely.

The other samples appear quite resistant up to 226 °C, before beginning to experience the first thermal events at 226-326°C where these samples appear to suffer more. The additional removal of lignin no doubt reduces its insulation; one can even see that the onset of the last event (480 °C) occurred over a larger range due to its loss.

Thus, while the samples have experienced different pre-treatment process prior to calcination, the actual principal thermal events still remain present, albeit with alteration in the thermal profile. The improvement in the ash content from EC only at 11% to 18% for EC (DW+DL+DI+TiPA), shows that the deposition of  $TiO_x$  ash constitutes about 5% -in the best possible case. All the other modified samples are 0-5%.

In RR, a very similar two-step degradation event is also happening. In the RR only sample, the main difference is in the degree of mass loss experienced around 476 °C. Rather than a steep loss, there is a gradual decrease which is due to the smaller amount of structural tissue that naturally occurs in RR. The treatment with TiPA (with pre-treatment: RR (DW+TiPA) and without: RR (Lyo +TiPA)) produced a similar ash content of about 21%, up by 1%. Of course, very little pre-treatment was carried out compared to EC.

### III.6.2 Electron Microscopy and elemental analysis

The micrographs highlighted the difference between RR and EC biotemplate. The presence of the robust cuticle layer, shown in Figure III-7, was a telling indicator of the difficulty of using EC as a template compared to RR (Figure III-9). Many pre-treatment processes were trialed to make the EC template more amenable to reaction with TiPA, which untreated resulted in the release of tannins that scavenged most of the Ti in the precursor solution. This ultimately led to a lower amount of  $TiO_x$  its surface. The effects of these pre-treatments are often deleterious to the

morphology of the EC leaf surface as seen in Figure III-12, Figure III-13 and Figure III-14. So, in spite of the perceived increase in the Ti content, as suggested by the higher ash content of EC (DW+DL+DI+TiPA), one cannot deny the arduous step taken to realise just 5% improvement. If the convoluted pre-treatment steps cannot be eliminated, such as in RR, then it would be best to abandon EC as a biotemplate sample.

The results from the elemental analysis also shows the improvement in Ti at% that was realised using RR rather than EC. The best sample RR (HCl[pH1] + TiPA) has a Ti content of 34at%, which is better than the best EC sample: EC (DW + TiPA), with 20at%. Again, this makes a case for using RR as a biotemplate for TiO<sub>2</sub> rather than EC, and this same problem might be encountered in using other terrestrial plants.

### III.6.3 Infrared characterisation.

Since RR is more efficient at taking up Ti reagents and possibly forming TiO<sub>x</sub> containing compounds, infrared characterisation was carried out. There is quite a significant difference in the FTIR spectra obtained before and after calcination. Before calcination, EC appears to consist mainly of chemical groups that may be linked to the presence of cutins, a major constituent of its cuticle in addition to waxes, phenolics and polysaccharides. This is evidenced by the presence of methylene groups ( $\nu_s$  CH<sub>2</sub> &  $\nu_a$  CH<sub>2</sub> and  $\delta$ CH<sub>2</sub>), at 2848 cm<sup>-1</sup>, 2916cm<sup>-1</sup>, 1462 cm<sup>-1</sup> and 719 cm<sup>-1</sup> which are prominent in the long aliphatic chains that make up cutins. Other groups were mentioned and briefly discussed in III.5.4.1: they include carbonyl groups (1683 cm<sup>-1</sup>, 1685 cm<sup>-1</sup> and 1730 cm<sup>-1</sup>) in saturated aliphatic acids. Also, carbonyl groups (as well as C=C) occurring between 1650-1400 cm<sup>-1</sup> were found in phenolic compounds associated with the presence of tannins. At 1161cm<sup>-1</sup> a band which can be ascribed to C=O was found in esters, again present in cutins.

After calcination, most of these functional groups have disappeared or undergone some transformation in all the replicas. Only the band at 719cm<sup>-1</sup> remained unchanged. Other than that, new bands that are prominent belong to carbonates at 879cm<sup>-1</sup>, Ti-O-C occurring between 1047-1144 cm<sup>-1</sup> and 1396 cm<sup>-1</sup> which were thought to belong to C-H<sub>3</sub> and C-H<sub>2</sub> that has originated Ti-reagent. All of these indicate that the organic fraction of the leaf have been transformed to high temperature residues, consisting of calcite and Ti containing compounds. And then when Figure III-21 is considered, the spectra of the replica samples (RR & EC (HNO<sub>3</sub> + TiPA)) appear more homogenous- with close similarities to that seen for P25 (Figure III-22).

### III.6.4 Crystallographic characterisation

Section III.5.5 confirms that after the calcination of the biotemplates, the final replicas consist of mostly calcite, followed mostly by anatase, and in some instances rutile and portlandite are also

present. It is worth reiterating that most of the samples, at least those that had undergone treatment without HNO<sub>3</sub> specifically showed no presence of any Ti containing phase in XRD. Which could be combination of the phases not actually being present, occurring in low concentration or due to the crystallite sizes. In addition to the results indicating the heterogeneous character of the replicas, the superiority of RR over EC as a biotemplate material is again shown here. Figure III-24 and Table III-5 both show that RR (HNO<sub>3</sub> + TiPA) produced an XRD pattern that shared a certain closeness in similarity with that of P25. Though it has foreign phases present (calcite), it was not as prominent as in EC (HNO<sub>3</sub> + TiPA). Additionally, RR (HNO<sub>3</sub> + TiPA) contained more anatase, compared to EC (HNO<sub>3</sub> + TiPA), not to mention the smaller size of the anatase phase.

XRD studies revealed the effect of pre-treatment and calcination conditions on the quality of replicas that can be obtained. Studying the use of HNO<sub>3</sub>, a longer treatment period improved the % composition of anatase and rutile. It was determined that increasing the calcination temperature above 600°C would improve the formation as well as the fraction of rutile: anatase presence (within a certain limit) but also increase the average crystallite size. The type of Ti precursor has some effect as well, with TiBALD producing a marginally better rutile: anatase ratio, coupled with a higher anatase amount compared to TiPA. The best ratio of rutile: anatase was at ~1:3 only occurring with a calcination temperature of 800°C.

It seems that the use of flora biotemplates always produces heterogeneous replicas on calcination. The pre-treatment process plays a significant role in the amount of useful TiO<sub>2</sub> phase formed (in addition to the blend of the TiO<sub>2</sub> phases and their average crystallite sizes).

### III.7 Conclusion

It is fair to conclude that replication as one promising route to engineer nano-scale materials is indeed a promising pathway. The experiments carried out, using the extremely complex plant leaf structure have shown that it is possible to build up intricate TiO<sub>2</sub> geometry using this biotemplate (and potentially any complex biomaterial) as a guiding building block. Not only was it possible to achieve a high degree of replication of the primary template, but it was also possible to build up these structures (replicas) with nano-scale crystallites as small as 15.8nm (in the case of RR (DW+HNO<sub>3</sub>[pH1]+20mM TiPA)), as was clearly demonstrated by the crystallographic results and electron micrographs. The fact that the materials formed had a high degree of crystallinity, in the case of both calcite and anatase, is an added bonus which shows that this method provides an attractive avenue in the context of engineering structures that may be assembled to a high degree of accuracy.



While the formation of calcite remains an issue, in the future one might be able to convert calcite and  $\text{TiO}_2$  in the replicas to  $\text{CaO}$  and  $\text{TiO}_2$  and then  $\text{CaTiO}_3$  perovskite. For the moment, no perovskite replica was seen at the modest calcination temperatures used here.

## Chapter IV Photocatalytic properties of the replica biotemplates

### IV.1 Introduction

Pollution is one of the more important problems currently affecting the health of the ecosystem and, directly or indirectly, the health of the human populous. Pollutants whether in the form of dispersed solids, gaseous molecular emission or liquid expulsions, can be emitted from industrial processes (ranging from clothing production, fuel extraction, heavy metal production, and even food production). All of these are responsible for the production of harmful pollutants with effects that can lead to various health and environmental problems. To date, one of the largest contributors of industrial waste is the one-use fashion/clothing industry, where the use of colourful dyes is ubiquitous. They impart lasting colours and hues of different intensity to clothing items: in the best-case scenario, these dyes are naturally occurring, benign and cheap; however, many dyes are synthetic and persistent. Certain groups of these dyes have been classified as not only being toxic, but carcinogenic. For example, a particular group known as azo dyes (further information in IV.3.2.1), which account for about 50% of dyes used in the textile industry (Karimi, Zohoori and Yazdanshenas, 2014) belong to this group. Not only do these hazardous chemicals cause problems for the industrial workers who handle them, they also cause far reaching complications when discharged to rivers, streams etc. with approximately 1-20% of these azo based-dyes thought to end up in waste water during the dying process (Karimi, Zohoori and Yazdanshenas, 2011). This could easily introduce them to the food chain of animals and subsequently taken up by connection humans.

Other pollutants such as surfactants and pharmaceuticals (antibiotics, antidepressants, anti-inflammatory, contrast agents and hormones etc) enter rivers, altering the food chain and affecting both human and environmental health (Schwarzenbach *et al.*, 2010). The excessive use of detergent in industrial processes (including decolouration and detoxification) is yet another important source of water pollution that has the potential to lead to serious health and environmental problems. Once these compounds have made their way into the water system, they can be quite difficult to breakdown. Considering azo dyes, their decolourisation under aerobic and anaerobic conditions is not straightforward. Anaerobically speaking, the azo bonds can be reduced ultimately resulting in aromatic amines which are toxic (genotoxic) and resistant to further break down (Gottlieb *et al.*, 2003a). Other decontamination processes exist and include: radical generation, physio-chemical treatments and anaerobic digestion (Gottlieb *et al.*, 2003b).

Above are just some of the examples of pollutants that need to be prevented from entering the ecosystem. Should the measures be inadequate, then a convenient and cheaper method needs to be found to render these pollutants safe. This is why semiconductors are currently being investigated to act as photocatalyst (I.1.5.1).

## IV.2 Aim

The aim of this part of the present research was to understand the catalytic characteristics of the titania-based bio-replicas from Chapter III, in the removal of water pollutants. In the previous chapter, the procedure surrounding the replication (as well as comprehensive morphological, structural and crystalline properties) were investigated to understand its functional properties. These replicas will be compared to commercially available alternatives (like P25) in pollution removal to obtain information on their chemical properties (especially catalytic performance).

At the end of this chapter, it was hoped that the catalytic properties of these biomimetic samples would be revealed. To this end, their properties (i.e. the adsorption edge, active sites, polymorphic composition and finally the rate constant  $k$  and TOF/TON will be investigated and used to comment on the abilities of the  $\text{TiO}_2$  replica samples (compared to commercial nanomaterial P25)).

## IV.3 Background

### IV.3.1 Surface reactions and adsorption

An important part of catalysis is surface reactions, which is dependent on active sites (see 1.1.7.2). One of the ways to determine the surface properties of a material is via probing its active site. In this instance, we shall be looking at the active sites in terms of acidity with certain tried and tested molecules: pyridine and acetone. Below are just some of the reactions that are likely to occur on the surface and how these may be seen to determine the activity of the materials surface.

$\text{TiO}_2$  photocatalytic activity is defined by the unique chemistry of titania, arising from its surface structure via the mixed ionic and covalent nature of bonds present in its metal oxide lattice. It is thought that the accumulated charge on its surface, partly formed as a direct consequence of its preparation method, affects the reaction of the catalyst with an adsorbate, seeing as the establishment of equilibrium between the Fermi level of the adsorbate and the catalyst is the main drive. Furthermore, many have found that besides the electronegativity of these adsorbates, their affinity for the  $\text{TiO}_2$  surface was also dependent on whether the  $\text{TiO}_2$  surface was “stoichiometric, reduced or oxidised”. These are properties which are ultimately summarised by what is known as the active sites.

In  $\text{TiO}_2$ , the control of acid sites on its surface is critical to the design of new effective heterogeneous catalyst with good emerging properties (De, Dutta and Saha, 2016). Different facets on the surface of  $\text{TiO}_2$  nanoparticles show different configurations and availability of  $\text{Ti}^{4+}$  cations and  $\text{O}^{2-}$  anions (Peng *et al.*, 2017). Any changes in this surface facets can introduce different  $\text{Ti}^{4+}$  and  $\text{O}^{2-}$  availability and reactivity.

To better understand the different adsorption sites, hosts of molecules have been found to interact with metal oxides in all the manners listed above. A number of oxides are already useful as catalysts, and some of the molecules mentioned are contaminants as well as probe molecules. Therefore, understanding the mechanism for adsorption is one step away from predicting the decomposition behaviour of these contaminants on the catalyst. As probe molecules, these adsorbates are quite useful in acting as methods to ascertain the “nature and the amount of acid centres on the surface of metal oxide materials” (Bezrodna *et al.*, 2003).

- Acetone

In the adsorption of acetone, the main acid site probed by acetone is the Lewis acid site. Usually, acetone adsorbs on the adsorbent by coordinating with the CUS. This can sometimes trigger a cascade of reactions resulting in the formation of enolates, and other decomposition products of acetone (Zaki, Hasan and Pasupulety, 2001) (see Figure IV-1)

- Pyridine

Pyridine is commonly used as a probe molecule to investigate the active sites on the surface of a metal oxide. It is able to show the nature as well as the number of acid sites that may be present on a metal oxide. Acid sites include Brønsted and Lewis acid centres (Bezrodna *et al.*, 2003) (see Figure IV-1). Used alongside IR spectroscopy, pyridine becomes a valuable tool in revealing the nature of the active sites present on a surface. It has the ability to be protonated by protons from the hydroxyl groups of the adsorbent, forming pyridinium ions that reveals Brønsted acid centres on the metal oxide (Zaki *et al.*, 2001). Also, its nitrogen pair can interact with the CUS of the metal oxide, thus showing Lewis acid centre (Zaki *et al.*, 2001). Pyridine can also form hydrogen bond with the metal oxide (Zaki *et al.*, 2001).

- H<sub>2</sub>O

While the other examples of adsorbates mentioned are artificially introduced to the metal oxide, water is one of the main molecules that are ubiquitous. Even in a highly controlled atmospheric environment, it is difficult to control its presence entirely. Its presence is seen as an attempt to reduce coordinative unsaturation (see I.1.5.3). Thus, the activities of most metal oxide catalyst are dependent on their interaction with water too.



(negative and positive) in the overall lattice of the mixed metal oxide. It makes this assumption by saying that the coordination numbers of the cations are maintained, while that of the oxygen anion holds true, only for the majority oxide. This method is able to predict the formation of new acid sites in about 90% of the cases (Kung, 1989); there are still inconsistencies which are down to the use of a unique coordination number. Some models consider the electrostatic potential of the substituting cation that has gone into the host matrix, depending on whether it is negative or positive would affect if it is likely to form Lewis acid sites or not.

### IV.3.2 Model Pollution Candidate (dyes)

To understand the photocatalytic abilities of the biotemplate TiO<sub>2</sub> samples with regards to their ability to degrade an azo dye (methyl orange). The degradation of these molecules will provide a realistic illustration of the potential application of for pollution control.

#### IV.3.2.1 Azo dye

Azo dyes represent an important chemical used in various industrial processes such as textiles, “in foodstuffs, paper and leather industries” (Chen *et al.*, 2008) and is also a frequent water pollutant. They include Trypan Blue, Ponceaus 3R, Citrus red, Sudan I and methyl orange etc. (Chung, 1983). Their metabolites (*N,N*- dimethyl-*p*-phenylenediamine) formed from the action of microbes, skin flora, intestinal bacteria etc, have mutagenic properties considered dangerous (Chung, 1983); hence the European Union has banned their use in goods like clothing, bedding, wigs etc, and any material that comes in contact with the skin (Puntener and Page, 2004).

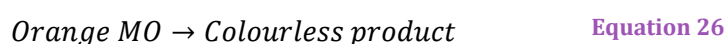
Methyl orange (shown in Figure V-1a) will be used as a model azo dye pollutant. Its photocatalytic removal will be investigated at neutral pH; this is entirely down to the conditions in which the aromatic amines are formed within the lower intestinal tract of mammals and in water treatment plants using of microbes (Amoozegar *et al.*, 2011).

### IV.3.3 Transformation kinetics estimation

Probing the photocatalytic activity of the TiO<sub>2</sub> replicas will be carried out through their interaction and removal of MO and TX-100 to provide information on the reaction rate constant, their turnover frequency (TOF) and deduce the effect of biotemplating. They can be used to compare the photocatalytic efficiency of different photocatalyst and so on.

The reaction rate constant is concerned with the rate of reaction and throughput (Gaya, 2014): basically the disappearance/appearance of a substance. Thus, in the case of the photocatalysis of a pollutant, one is concerned with the rate at which a given concentration of pollutant disappears.

For example, in the transformation/disappearance of an orange MO specie, see below



Another suitable measure of the true photocatalytic ability of a material is its turnover frequency (TOF). This is defined as the “number of product molecules formed per second ” (Serpone *et al.*, 1993) or per unit time (Gaya, 2014) in heterogenous photocatalysis. The TOFs of the biotemplates were to be compared with those for commercial P25.

## IV.4 Methodology

### IV.4.1 Photo-degradation

To access the photocatalytic/photo-degradative capacity, it was decided that the photo degradation of methyl orange will be used to probe and help compare the catalytic ability of the biotemplate replica with that of P25 as the model (control) catalytic material.

#### IV.4.1.1 Experimental setup

There are two distinct ways in which the samples will be prepared for the experiments: an immobilised method and a non-immobilised method. The immobilised method will be discussed in detail in Chapter V

**Non-immobilised state :** This is a simple and by far the most common form of assessing the photocatalytic ability during the process of dye degradation. Here,

- 0.25mg of catalyst was placed at the bottom of a cuvette
- The cuvette was then topped up with 2.5 ml of the 0.01mM MO solution
- To ensure optimum dispersion and MO adsorption of the samples, the contents of the cuvette were initially stirred and left for 12h to rest in the dark
- The samples were then ready for illumination with UV lamp at 365nm and 300W.

#### IV.4.1.2 Characterisation techniques

##### IV.4.1.2.1 UV-vis analysis of MO photo degradation

This was used to probe the response of MO as it underwent degradation in the presence of the photocatalysts. The lambda max was taken at 465nm and used to track MO's degradation and to derive other further parameters : rate constant and turnover frequency

- Rate constant and half-life calculations

The rate constants will be calculated using the transformation/disappearance of an orange MO specie, see below

The rate at which it disappears may be written following a differential rate law output, see below

$$r = \frac{d[MO]}{dt} = -k[MO]^n \quad \text{Equation 27}$$

In the above  $r$  is the rate of reaction,  $d[MO]$  is the change in the concentration of MO in  $\text{mol dm}^{-3}$ ,  $dt$  is the change in time,  $[MO]^n$  is the rate of reaction at a given order ( $n$ ).  $n$  can be anything from 0, 1, 2, 3 or non-integer, and  $k$  is the rate constant (Gaya, 2014). The units of the rate constant is dependent on the order of reaction ( $n$ ). As most photocatalytic processes tend to fall with the 0<sup>th</sup> and 1<sup>st</sup> order category, the 2<sup>nd</sup> and 3<sup>rd</sup> will not be discussed here. The 0<sup>th</sup> order is applicable to the surface processes only, with the concentration of the reaction having no effect on the actual rate constant ( $k$ ). The converse occurs with regards to the 1<sup>st</sup> order process. In the photocatalytic experiments, the rate constants were found to fall close to pseudo 1<sup>st</sup> order; therefore, the author will go ahead to show the derivation of the straight-line equation for the 1<sup>st</sup> order rate constant ( $k_1$  for  $n=1$ ).

with a 1<sup>st</sup> order reaction, one knows that the rate constant will change with changing concentration, thus integrating the differential rate equation (Equation 28) will give Equation 30 which is related to the equation of a straight line. Thus, the rate constant  $-k_1$  may be obtained by plotting a graph of  $\ln[MO]$  against time ( $t$ ), and its value is equivalent to the magnitude of the slope.

$$r = \frac{d[MO]}{dt} = -k_1[MO]^1 \quad \text{Equation 28}$$

$$\int_{[MO]_0}^{[MO]_t} \frac{d[MO]}{[MO]} = -k_1 \int_0^t dt \quad \text{Equation 29}$$

$$\ln[MO]_t = \ln[MO]_0 - k_1 t \quad \text{Equation 30}$$

Also, the half-life ( $t_{1/2}$ ) of a first-order reaction at time  $t$  and 0 may be derived as follows:

$$[MO]_t = \frac{[MO]_0}{2} \quad \text{Equation 31}$$

$$\ln[2] = k_1 t_{1/2} \quad \text{Equation 32}$$

- TOF determination

TOFs can be calculated as the number of molecules degraded in the presence of a UV source per second(s) per gram (g) of photocatalyst, versus molecules adsorbed (in the dark) per gram of photocatalyst. These gives the turnover frequency (TOF) with a unit of  $\text{s}^{-1}$ .



$$\frac{\text{Number of molecules degraded per gram of catalyst per second}}{\text{number of molecules adsorbed on a catalyst}} \quad \text{Equation 33}$$

Both the TOF and rate of reaction will be used throughout this chapter.

#### IV.4.2 Active site characterisation using FTIR

To prove the nature of the active site, the samples were exposed to several probe molecules. These include pyridine and acetone.

The TiO<sub>2</sub> samples were deposited on a glass slide and dried in an oven at 100°C. They were then stored in a sealed desiccator with the relevant probe molecule in a petri dish for 12h. The sample was tested on an ATR FTIR (spectrum was collected over 400-4000cm<sup>-1</sup> with a resolution of 4cm<sup>-1</sup> after carrying out 45 scans).

#### IV.4.3 TiO<sub>2</sub> phase characterisation using Raman spectroscopy

The TiO<sub>2</sub> samples were simply deposited on a glass slide with readings taken using a 534nm green laser, at 10% power. The integrated time for signal collection was at 10s, for 3 accumulations. The spectra of 3 random areas were collected to provide a suitable average.

### IV.5 Results & Discussion

Photocatalysis results will be collected using two main methods: a standard photocatalyst method, and a second method using some form of embedding as explained in the previous topic. In total, 4 calcined samples will be looked at here in addition to a control (P25)-they include the following:

#### IV.5.1 Photocatalysis: UV-vis results

The photocatalytic breakdown efficiency of the investigated samples against MO will be presented in this section. The following samples: P25, RR (HNO<sub>3</sub>pH[1]+TiPA), RR (HNO<sub>3</sub>pH[1]+TiPA) 5h, EC (HNO<sub>3</sub>pH[1]+TiPA) and EC (HNO<sub>3</sub>pH[1]+TiPA) 5h will be investigated. A first-order degradation model was applied here where A<sub>0</sub> is the starting UV-vis absorbance of MO, and A is the absorbance with changing time (in the presence of a UV source).

##### IV.5.1.1 P25 Control Sample

From Figure IV-2, it is quite clear to see the photocatalytic activity of P25 against the model pollutant MO gives a straight line with an estimated rate constant value of 0.004 min<sup>-1</sup>. In addition to that, the R<sup>2</sup> was found to be 0.9986 which indicates the suitability of the first-order rate of reaction model to fit the data acquired here.

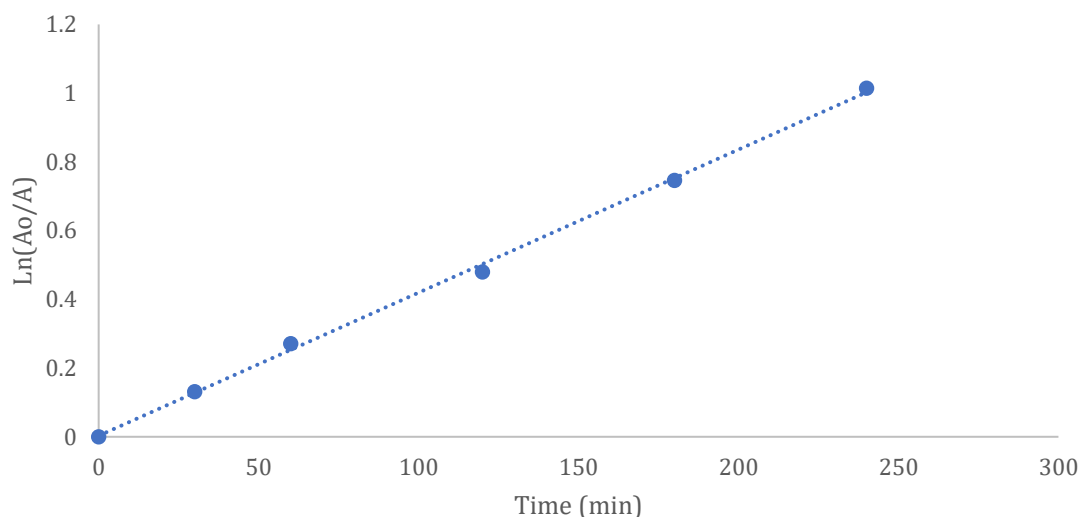


Figure IV-2: Photocatalytic breakdown of 0.01mM of MO in the presence of P25 at room temperature. Dose: 0.25mg of photocatalyst in 2.5ml of MO.

#### IV.5.1.2 EC-TiO<sub>2</sub> samples

The photo degradation of MO in the presence of EC (HNO<sub>3</sub>pH[1]+TiPA) is shown in Figure IV-3

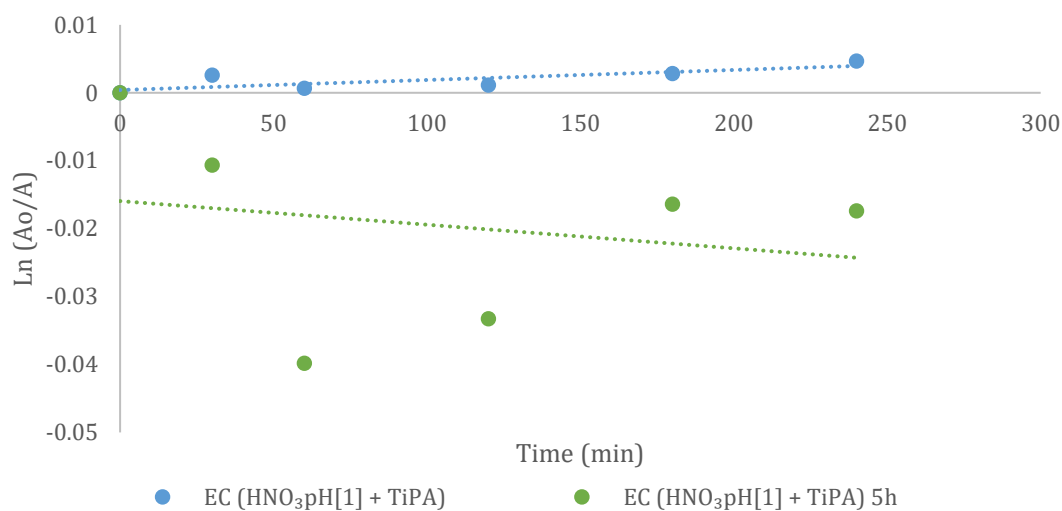


Figure IV-3: Photocatalytic breakdown of 0.01mM of MO in the presence of EC (HNO<sub>3</sub>pH[1]+TiPA) and EC (HNO<sub>3</sub>pH[1]+TiPA)-5h at room temperature. Dose: 0.25mg of photocatalyst in 2.5ml of MO.

It is clear that the samples concerned in Figure IV-3 are ineffective in degrading MO. No colour changes with the naked eye were apparent. Quantitatively speaking, the absorbance value (A) obtained directly from monitoring the lambda max (465nm) of MO (see Table IV-1) showed an even poorer degradative behaviour. Some near zero or positive absorbance changes were seen.

**Table IV-1: absorbance of the samples mentioned in Figure IV-3 at the  $\lambda_{\max}$  of the UV-vis spectra over 240min**

Samples	0 min	60 min	120 min	180 min	240 min
EC (DW+HNO <sub>3</sub> pH[1] + TiPA)	0.680	0.680	0.681	0.682	0.683
EC (DW+HNO <sub>3</sub> pH[1] + TiPA)-5h	0.657	0.684	0.685	0.687	0.688

It is possible that the exposure of the sample to UV might have simply resulted in the evaporation of the solvent to the atmosphere, concentrating the solution which resulted in an eventual increase in value. Whatever the case, as the experimental setup was similar to that of P25, the increase in absorbance rather than a decrease highlights the inferior crystalline property that was discussed in the section III.5.5. This is regardless of the protracted acid treatment period of between 5-12h.

#### IV.5.1.3 RR-TiO<sub>2</sub> samples

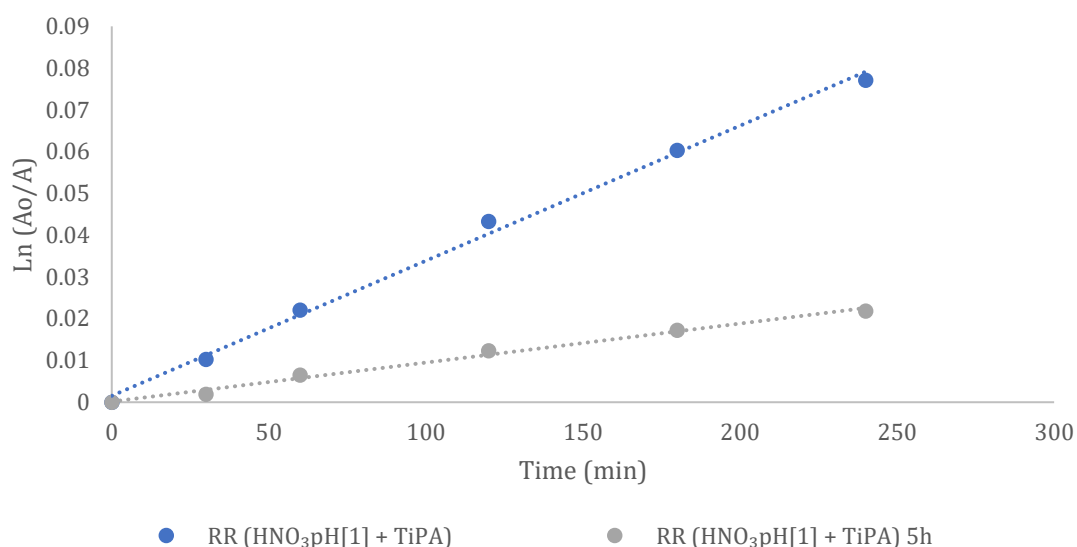


**Figure IV-4: Photocatalytic breakdown of 0.01mM of MO in the presence of RR (HNO<sub>3</sub>pH[1]+TiPA) and RR (HNO<sub>3</sub>pH[1]+TiPA)-5h at room temperature. Dose: 0.25mg of photocatalyst in 2.5ml of MO.**

The RR TiO<sub>2</sub> replicas fared better than those made using EC in terms of the photocatalytic breakdown of MO. Figure IV-4 shows that the data points fit the first-order reaction model, much better than when EC. The first-order rate constant for either samples were 0.0003min<sup>-1</sup> and 0.00009min<sup>-1</sup> for RR (HNO<sub>3</sub>pH[1]+TiPA) and RR (HNO<sub>3</sub>pH[1]+TiPA)-5h respectively. Their values are still lower than k<sub>1</sub> for P25 (0.004min<sup>-1</sup>).

It is possible to notice that the sample with the highest rate constant belongs to the control P25, followed by RR (HNO<sub>3</sub>pH[1] + TiPA), and RR (HNO<sub>3</sub>pH[1] + TiPA) 5h showing the least activity of all the tested samples. Taking all the lab prepared samples into context, it is unarguable that all

the successful biotemplated samples were those which were prepared using RR, unlike EC *that* had no successful replicas.

#### IV.5.1.4 TOF assessment

Using adsorption studies of the sample in the dark against the degradation rate of MO in UV TOF assessment was carried out. While Table IV-2 shows that the replica samples display the most adsorptive potential, in comparison to P25, their photocatalytic abilities are however poorer affecting the estimated TOF values, with P25 showing the best performance followed by RR (DW+HNO<sub>3</sub>pH[1] + TiBALD) and then RR (DW+HNO<sub>3</sub>pH[1] + TiPA). The results clearly show that the photocatalytic performance of P25 is greater than those of the replicas, in spite of its initial poor adsorption.

**Table IV-2: Calculated values of MO molecules adsorbed, degraded and the corresponding Turnover frequency.**

Samples	MO Molecules degraded (ns <sup>-1</sup> g <sup>-1</sup> )	MO Molecules adsorbed (ng <sup>-1</sup> )	TOF (s <sup>-1</sup> )
RR (DW+HNO <sub>3</sub> pH[1] + TiPA)	2.81 × 10 <sup>15</sup>	3.90 × 10 <sup>18</sup>	0.0007
RR (DW+HNO <sub>3</sub> pH[1] + TiBALD)	2.03 × 10 <sup>15</sup>	1.40 × 10 <sup>18</sup>	0.0014
P25	8.55 × 10 <sup>15</sup>	7.17 × 10 <sup>17</sup>	0.0119

#### IV.5.2 Composition: size and crystallographic phases

Crystallographic XRD analysis section in Chapter III. It was estimated that the replicas were composed of calcite and anatase while P25 had a mix of just anatase and rutile. Leaves, along with their adaptability means that depending on the environment on which they are cultivated, they have the potential to assimilate different forms of matter into their system for survival purposes: from the organic to inorganic. In inorganic matter, the presence of ions in their environment (in the cases of RR, both water and soil) means that they have different cations already assimilated into their system. It is these cations that then go ahead to form different phases, mostly in the form of calcite, alongside titania. Indeed, RR was found to contain about 17.51% of calcite (with 82.49% anatase – data in Table III-5). It is no wonder that such a huge discrepancy exists in the degradation of methyl orange as a function of the titania composition in P25 compared to a RR-replica. One could say that the results contained here could further corroborate the different literature research that has pointed to the fact that in terms of titania phases, anatase showed a better photocatalytic capability than any of the other titania polymorphs. Lutrell et al (2014) lists several reasons why anatase is the better photocatalyst than its other polymorphs, its indirect band conduction nature which reduces the possibilities of excitons recombination compared to the direct band conduction like that seen in rutile, the properties of the charge carriers (effective mass and their mobility across certain crystallographic planes), and its band gap.

Another possible reason for the low activity of the biotemplated samples against P25 are the particle sizes. Again, the XRD data in the previous chapter predicted that the leaf replicas contained an anatase phase with sizes from 15.8nm to 18.3nm after calcination. This is much smaller than the 25nm anatase particle size that had been measured for P25 (rutile 85nm) (Ohno *et al.*, 2001). Indeed, using Raman as an analytical technique to monitor the crystalline composition of the samples, result close to XRD were seen. Although Raman is not typically applied as a method to predict the particle sizes, the spectra below are nonetheless interesting as they appear to show the effect of diminishing particle sizing on the raman shift.

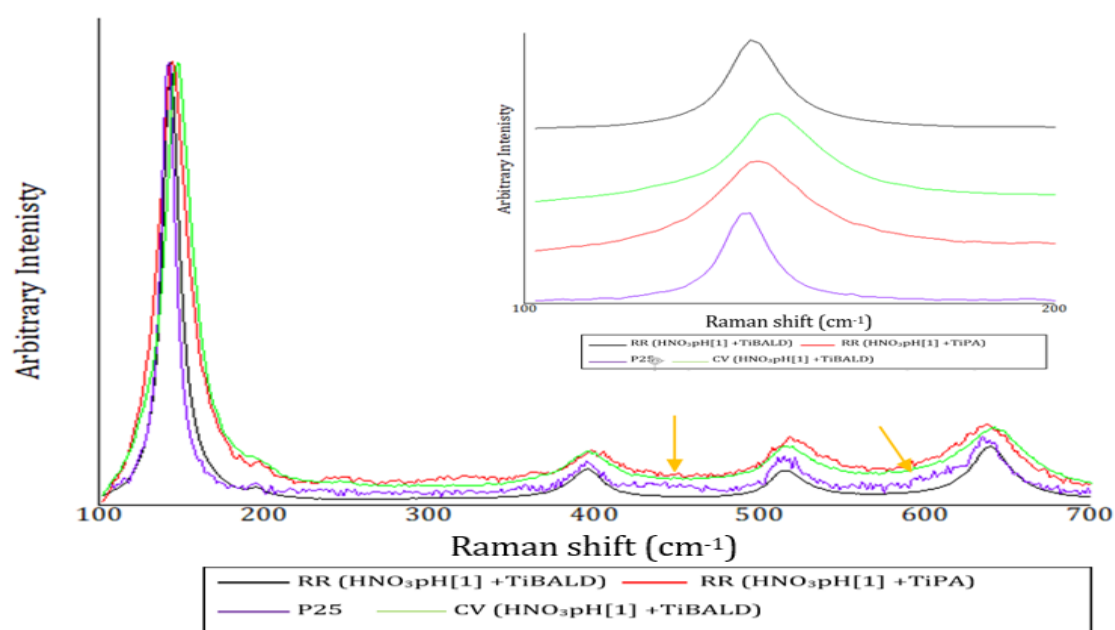


Figure IV-5: Raman spectra of titania replica samples and P25 showing anatase and rutile peaks. Inset is the reduced spectra showing one of the Raman active mode ( $E_g$ ) between 100-200 $cm^{-1}$ .

The spectra of all the samples in Figure IV-5 contain the main Raman shifts concerned with anatase. These are around 142-147 $cm^{-1}$ , 394  $cm^{-1}$ , 514  $cm^{-1}$  and 636 $cm^{-1}$  which are all values that are reminiscent of those found in literature (Zhang *et al.*, 2000; Tian *et al.*, 2012). Amongst all of the samples, it is only P25 that appears to exhibit growth of some rutile peaks (highlighted by the yellow arrows in the figure) occurring at around 441  $cm^{-1}$  and 610  $cm^{-1}$ . Again the values are close to those seen in literature (Ma *et al.*, 2007).

In Figure IV-5, it is clear that with respect to P25, all prepared replicas had shifted to a higher Raman shift (except RR (HNO<sub>3</sub>Ph[1]+ TiBALD)). Apparently, this is down to the particle size (Chang *et al.*, 2009), as the TiO<sub>2</sub> particle size decreases, there is a general shift to a longer Raman shift linked to a volume contraction occurring within the nanoparticles, ultimately increasing the force constant in the smaller interatomic spacing and shifting to a higher frequency occurs (Choi,

Jung and Kim, 2004).

In spite of the evidence pointing to the fact that smaller particle sizes have been achieved, it begs the question as to why the TiO<sub>2</sub> replica samples have a lower photocatalytic efficiency than P25. It is likely due to the presence of other non-catalytic phases towards MO e.g. the presence of calcite phase has been estimated to be about 17% to 83% depending on the original biotemplate used and pre-treatment process with average sizes between 83nm to 112nm. No doubt, its presence and most likely, the size of its crystallite has a less than synergetic effect on the photocatalysis. So, while P25 is composed of mainly anatase and to a smaller proportion rutile, this combination makes it an effective photocatalytic material; the same cannot be said for calcite, considering the size of its particulate (and the band gap energies as we will come to see).

#### **IV.5.3 Band gap consideration**

Calcite on its own is a well-known insulator that is utilised industrially in plastic, rubber and paper manufacturing. It is not known for its use as a catalyst most likely due to its wide band gap (between 4.95eV and 5.07eV, for indirect band gap, depending on the approximation method used). Experimentally, the value that has been observed at approximately 6.0eV (Medeiros *et al.*, 2007; Hossain *et al.*, 2009). These values are a numerical way of indicating the probable insulating factor the calcite phase has on the performance of the replica materials.

Figure IV-6 shows that P25 has an absorption edge closer to the visible, extrapolated to occur at 387nm using a linear fit of the linear region only, the replica appears to possess two linear regions (one was extrapolated to occur at approximately 315nm and the other closer to 275nm). The maximal absorption edge of the RR biotemplate replica samples appears to be closer to the UV region. The presence of a kink as well as the blue shift is another example of the difference between the replicas and the control P25, and perhaps a telling sign of the insulating phase(s) that exist in their structure. In fact, it is possible that the kink is due to one of these phases that have completely segregated from the replica. It would be interesting to know how calcite (and the other phases) are distributed in the replica material. Is there an even distribution (to a molecular level or are the phases distinct and separate) or is the titania phase is surrounded by a layer of calcite (or could it be the other way round?).

From spectra in Figure IV-6, the band gap energy was estimated using the Equation 10. The values obtained were 3.2eV for P25, and for RR a value of 3.9eV and 4.5eV was estimated.

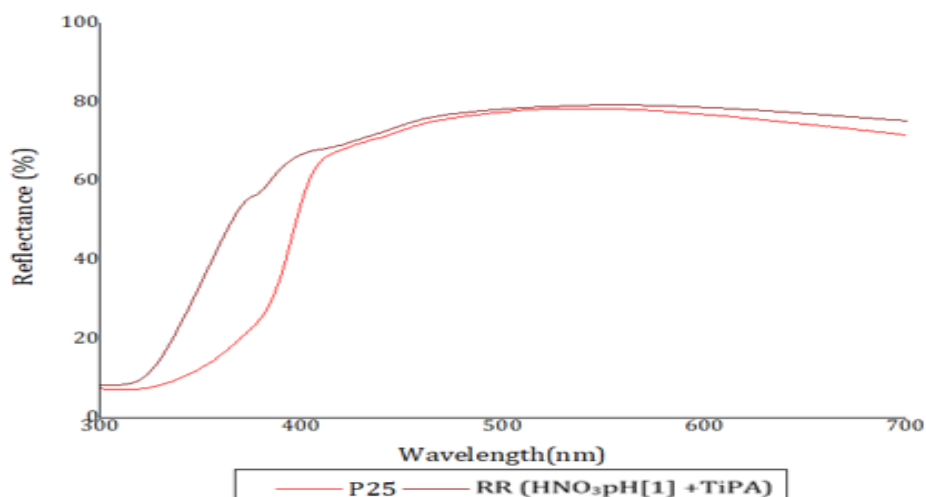


Figure IV-6: UV-vis spectrum showing the adsorption edge of P25 and RR (HNO<sub>3</sub>pH[1]+TiPA).

Clearly, the presence of the calcite, which is known to have a band gap energy greater than 4eV (Medeiros *et al.*, 2007; Hossain *et al.*, 2009) must be behind the higher value for the TiO<sub>2</sub> biotemplate replicas. The intimate combination of both phases must have resulted in a novel band gap structure that lies between that of pure calcite and pure titania.

It is becoming clear why the biotemplated samples have poorer photocatalytic efficiency, with a band gap that is dangerously close to being insulating. One then wonders whether this CaCO<sub>3</sub>-TiO<sub>2</sub> interaction changes the acid site surface concentration.

#### IV.5.4 Acid site analysis

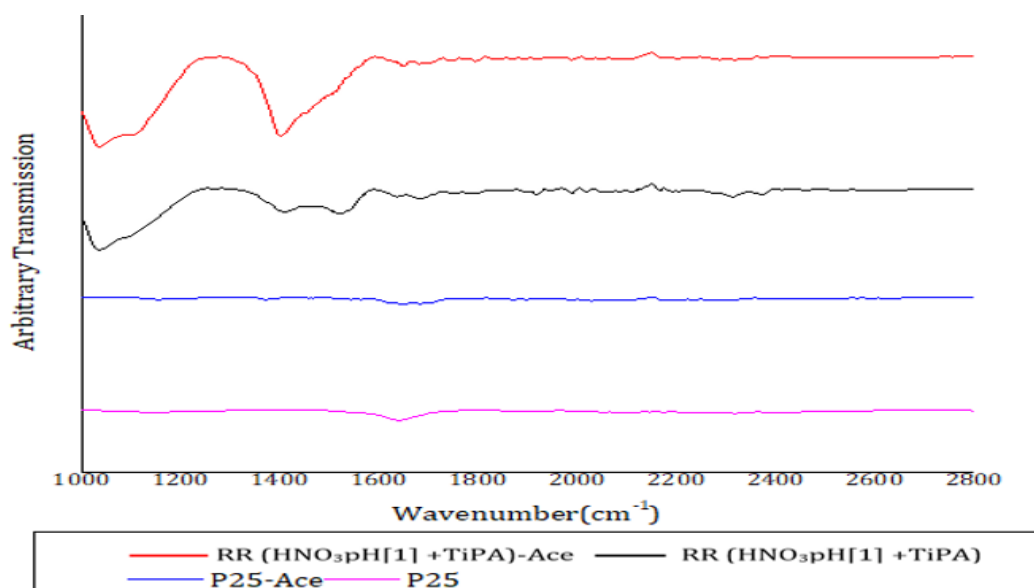


Figure IV-7: IR spectra of P25 and RR (HNO<sub>3</sub>pH[1]+TiPA) before and after exposure to acetone at room temperature (20°C) as P25-Ace and RR (HNO<sub>3</sub>pH[1]+TiPA)-Ace

Acid sites of P25 and the RR replicas were probed with the help of two probe molecules, acetone and pyridine at room temperature. Figure V-7 and Table IV-3 show the effect of samples that have been exposed to acetone at room temperature and atmospheric pressure. Before acetone exposure to the probe molecules, it is easy to see the difference in the spectrum of the replica sample and that of P25. Other than the ubiquitous bands representing Ti-O, Ti-O-Ti bonds at 400-700 $\text{cm}^{-1}$  (Table IV-3) that have been excluded from the FTIR spectra for either sample. The following bands have been flagged up to highlight the spectral difference between the RR  $\text{TiO}_2$  replicas and P25. These are mainly attributed to calcite.

**Table IV-3: IR assignment for RR (HNO<sub>3</sub>pH[1]+TiPA) and P25 (Coleyshaw, Crump and Griffith, 2003; Gunasekaran, Anbalagan and Pandi, 2006)**

RR replica ( $\text{cm}^{-1}$ )	Band assignments	P25( $\text{cm}^{-1}$ )
1103	$\nu_1$ - $\text{CO}_3^-$ stretching	-
1408	$\nu_3$ - $\text{CO}_3^-$ stretching	-
1517	$\nu_3$ - $\text{CO}_3^-$ stretching	-
1635	OH	1650
1798	$\nu_1$ and $\nu_2$ of $\text{CO}_3^-$	-

Table IV-4 lists the peaks that have emerged after exposure of the photocatalyst to acetone.

**Table IV-4: IR assignments of peaks emerging after adsorption of acetone on P25 and RR replica (M. I. Zaki *et al.*, 1999; El-Maazawi *et al.*, 2000; Zaki, Hasan and Pasupulety, 2001).**

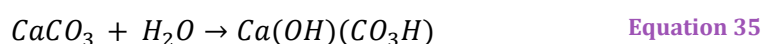
Observed acetone adsorption on RR replica ( $\text{cm}^{-1}$ )	Observed acetone adsorption on P25 ( $\text{cm}^{-1}$ )	Possible assignments
-	1369	$\nu\text{CH}$ (acetone/MSO coordination to Lewis site)
1402-1514	1535	$\nu\text{CH}$ , $\nu\text{C}=\text{C}$ (acetone/enolate coordination to Lewis site)
1659 and 1679	1645 and 1691	$\nu$ (C=O) (acetone and MSO to Lewis sites)

Starting with the adsorption on P25 of acetone, there is an immense difference in the spectra. Table IV-4 shows additional bands that may all be ascribed to the adsorption of acetone, including other possible condensation products (mesityl oxide(MSO), enolate, and diacetone alcohol (DAA)) that may arise from adsorption to Lewis sites (Zaki, Hasan and Pasupulety, 2001). It was found that acetone irreversibly adsorbed to Lewis acid sites ( $(\text{CH}_3)_2\text{C}=\text{O} \rightarrow \text{Ti}^{n+}$ ), with subsequent hydrogen abstraction by the ligand to form enolate type ions ( $\text{CH}_2(\text{CH}_3)\text{C}=\text{O}^- \rightarrow$



$M^{n+}$ ). Alternatively, proceeding to an aldol-condensation reaction that may lead to the formation intermediary DAA  $(CH_3)_2C(OH) - CH_2(CH_3)C = O \rightarrow M^{n+}$  and finally MSO  $(CH_3)_2C = CH - (CH_3)C = O \rightarrow M^{n+}$  (Zaki, Hasan and Pasupulety, 2001). For P25, the presence of the  $1369\text{cm}^{-1}$  band is possibly linked to the interaction of acetone with a Lewis acid site (Zaki, Hasan and Pasupulety, 2001). The same can be said for the broad band between  $1645\text{-}1691\text{cm}^{-1}$ ; additionally, this band is also linked to the formation of MSO that then interacts with a Lewis acid site. Finally, there is the peak at  $1535\text{cm}^{-1}$ , this has been ascribed to the presence of enolate/acetone coordination to an acid site. The fact that the intensities of these peak-associated with Lewis acid sites on P25- are quite low is to do with the apparent low surface activity of P25 (Wang *et al.*, 2006).

RR ( $\text{HNO}_3\text{pH}[1]+\text{TiPA}$ )-Ace does not have all the same bands present or bands at the same wavenumbers (Figure IV-7). It has bands at  $1110\text{ cm}^{-1}$ ,  $1402\text{-}1512\text{ cm}^{-1}$ , and at  $1659\text{cm}^{-1}$  and  $1679\text{cm}^{-1}$ .  $1110\text{cm}^{-1}$  is a vibration originating from the presence of calcite. This is to be expected as the replica sample has been proven to contain calcite as part of its majority constituent. The band at  $1402\text{-}1512\text{cm}^{-1}$  is linked to contributions from adsorbed acetone and enolates, coordinated to Lewis acid sites.  $1659\text{cm}^{-1}$  and  $1679\text{cm}^{-1}$  are thought to originate from adsorbed acetone and possibly MSO. An obvious difference seen in the wavenumbers of the  $\text{TiO}_2$  replicas from that of P25 might be a difference in the coordination of the adsorbed species to  $\text{Ti}^{4+}$  as well as  $\text{Ca}^{2+}$ . And seeing that the constituent of calcite has been seen to dwarf that of the titania in the replicas, acetone and its other species might be more likely to interact with calcite rather than titania. Thus, the shift, appearance and disappearance of some bands would be inevitable. Calcite has also been known to adsorb water dissociatively (see Equation 34)



leading to the presence of hydroxyl group and bicarbonate anions (Neagle and Rochester, 1990; Al-Hosney and Grassian, 2004) that can act as an H-bond donor and basic OH groups (Zaki *et al.*, 2001).

Pyridine can be used to tests for both Lewis acid sites and Brønsted acid sites, unlike acetone which is mainly geared to show mainly the Lewis acid sites.

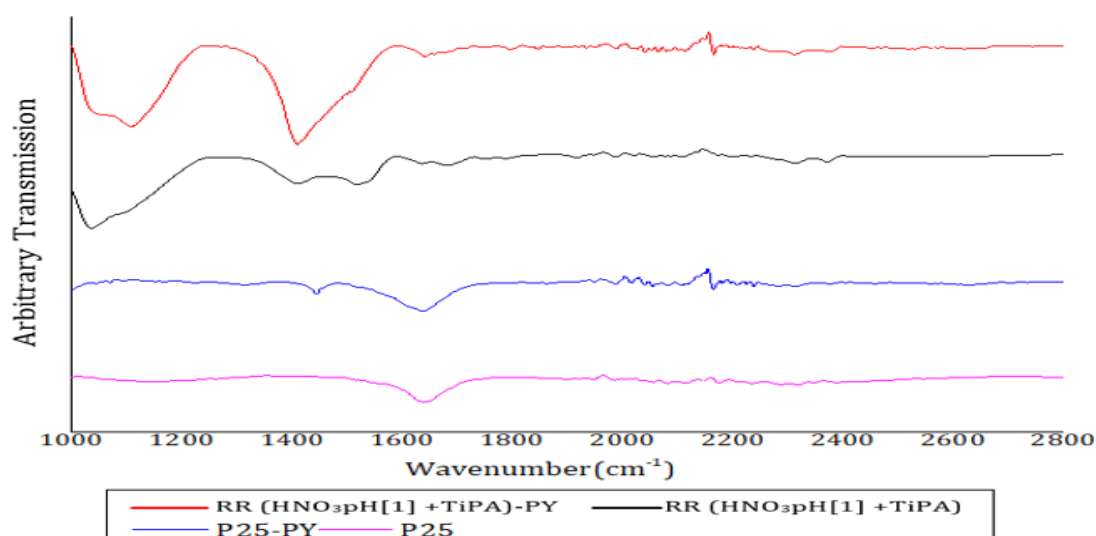


Figure IV-8: IR spectra of pyridine adsorption on P25 and RR (HNO<sub>3</sub>pH[1]+TiPA) before and after exposure to acetone at room temperature (20°C) as P25-PY and RR (HNO<sub>3</sub>pH[1]+TiPA)-PY.

Figure IV-8 and Table IV-5 shows the difference in the spectra after adsorption. While RR (HNO<sub>3</sub>pH[1]+TiPA)-PY shows complex changes (similar to that from acetone), P25 remains quite simplistic-but still relevant. In the case of Lewis acid sites, which according to the acetone probe are plentiful, one can see a sharp peak arise around 1448cm<sup>-1</sup> which indicates such a presence. In RR (HNO<sub>3</sub>pH[1]+TiPA)-PY, it is much harder to assign the broad looking composite peak at 1408-1514cm<sup>-1</sup> to the presence of a Lewis acid site, seeing as it is also present in Figure IV-7. Nonetheless, it could easily grow and be obscured by the two distinct peaks after treatment (i.e 1408 & 1514cm<sup>-1</sup>).

Table IV-5: IR assignments of peaks emerging after adsorption of pyridine adsorption ON P25 and RR replica (Bezrodna *et al.*, 2003; Wang *et al.*, 2006).

Observed pyridine adsorption (cm <sup>-1</sup> ) RR replica	Observed pyridine adsorption (cm <sup>-1</sup> ) P25	Possible assignments
1408-1514	1448	Lewis acid sites
-	1606	Lewis acid sites
1636	1639	Protonation of pyridine by Brønsted acid sites

Brønsted acid sites were no easier to ascertain; the possible assignment for this site is 1640cm<sup>-1</sup> for RR (HNO<sub>3</sub>pH[1]+TiPA)-PY is quite diminished, appearing to grow in favour of 1689cm<sup>-1</sup> in the PY free samples. In P25, the problem of distinguishing perturbation around this area is obvious, seeing as it already has appeared at 1650cm<sup>-1</sup>. The main difference that can be used to distinguish the contribution from pyridine is the shape. In untreated P25, the peak appears narrower, but

upon treatment, it seems to become broader as well as having a shoulder appearing at 1605cm<sup>-1</sup>. This convoluted band is thought to arise from interaction of PY with Brønsted sites, as well as Lewis acid sites (Bezrodna *et al.*, 2003).

In RR (HNO<sub>3</sub>pH[1]+TiPA)-PY, the variations in the wavenumbers could well be due to the interaction of the probe molecule with titania. But just like the adsorption of acetone, it is possible that rather than titania being perturbed only, calcite is likely participating as well.

The results from either of the probe molecules studies seemingly point to the presence of Lewis acid sites being the dominant active centres for P25. Further experiments will need to be carried out to confirm that the majority sites are mostly Lewis acid sites in addition to the strength of these sites; for the RR replica the situation is complicated. The presence of calcite has thrown in an extra uncertainty of the surface interactions that are seen with both pyridine and acetone. No doubt the difference in the spectra between P25 and the replicas shows that completely different surface interactions are at work and this might directly affect the interaction with MO and its degradative ability against it.

## IV.6 Summary

### IV.6.1 Photocatalysis

**Table IV-6: Calculated rate constants ( $k_1$ ) of only the successful photocatalyst samples after the degradation of 0.01mM of MO.**

Samples	$k_1$ (min <sup>-1</sup> )
RR (HNO <sub>3</sub> pH[1] + TiPA)	$3.00 \times 10^{-4}$
RR (HNO <sub>3</sub> pH[1] + TiPA) 5H	$9.00 \times 10^{-5}$
P25	$4.20 \times 10^{-3}$

From the table above, and the lack of EC replica data one can say that the better biotemplate for the use of synthesising a photocatalyst is RR. Since RR (HNO<sub>3</sub>pH[1] + TiPA) showed the highest potential, it is reasonable to say that its treatment process, which involved a prolonged treatment (12h) in a pH1 solution of nitric acid was effective in the creation of a viable TiO<sub>2</sub> replica. This was confirmed by the diffraction studies (III.5.5), showing an increased fraction of anatase against the formation of calcite. The other samples, formed from utilising EC as a biotemplate, displayed very little photocatalytic ability against MO. It is thought that along with the presence of its intrinsic cations, the presence of a hardy cuticle layer made it difficult to remove these ions. It did not help that this persistent cuticle, even after the elaborate pre-treatment process, was still robust and thus prevented the ingress of the Ti precursor. All of these factors caused a poorer formation of

anatase (against calcite) with calcite sometimes constituting 90% of the overall crystalline fraction. RR, with its thinner structure as well as thinner cuticle layer formed anatase a lot easier. No doubt this aided the samples produced from RR biotemplates to have better properties.

Although this author has endeavoured to maintain consistency in terms of where the starting biotemplates are sourced, it is obvious as with anything in nature that working without variables is simply impossible. This can affect the overall condition of the biotemplate, and their eventual transformation into a functional photocatalyst. Should these be overcome, there is the obvious fact that the best ratio for TiO<sub>2</sub> to promote photocatalysis is one that uses a combination of two specific polymorphs in a certain ratio (anatase and rutile) (Scanlon *et al.*, 2013; Luttrell *et al.*, 2014). The commercial P25 that was used here, is made up of anatase (70%) and rutile(30%). From the various XRD observation performed in the previous chapter, all the biotemplates (RR and EC) both favoured the formation of anatase alone. The only way to attain both polymorphs required temperature modification (detailed in section III.5.5.1). Certainly, the lack of a mix of TiO<sub>2</sub> polymorph in replicas would have also affected the photocatalytic efficiency of the biotemplated replicas utilised.

Another factor that would have also caused the lower rate constants in the samples is the calcite phase. This is to do with how it is in contact with titania as well as its size. XRD results carried out in the previous chapter showed that while the crystallite sizes of titania from the biotemplate were  $\leq 20$ nm in most cases, the size of calcite ranged between 83-112nm. Interestingly, Kaur and Verma (2014) utilised titania coated with calcite for their dye sensitive solar cells (DSSC) set up. They managed to keep the sizes even between both phases increasing their efficiency from 0.46%-1.44%. A larger calcite, assuming it is present as a coating around titania, might actually attenuate the incoming UV radiation to such an extent that the titania phase receives little to no light. And where it has managed to generate the necessary photo induced species, the bigger size of calcite might increase the distance these species have to travel to the surface, effectively increasing the likelihood of recombination. This problem is normally found in rutile, and is thought to be the reason behind its recorded low efficiency when used solely as a photocatalyst (Luttrell *et al.*, 2014). Yet again, this is another relevant factor that has impacted the efficiency obtained in the present TiO<sub>2</sub> replica photocatalytic studies.

Taking the aforementioned factors into consideration, it is clear why the replica samples might have exhibited lower rate constants than P25. Further insights into the composition, band gap and the active sites and how these would have come into play in affecting the efficiency of the biotemplated samples against that of P25 need to be obtained in future.

### IV.6.2 TOF assessment

The trend seen in TOF assessment was not so different from  $k_1$  analysis. Extra information was obtained for the extent of adsorption in the dark, which proved that the replica samples had superior MO uptake potential, but lower photocatalytic performance than P25. The lower TOF appears to something that was also seen in other TiO<sub>2</sub> biotemplates, where despite a higher uptake of MO the actual photocatalytic performance was still below that of P25 (Jaffer Al-Timimi *et al.*, 2016).

### IV.6.3 Composition size and crystallographic phases

The importance of having better composition of phases has been mentioned several times in this chapter. It has already been established that while anatase is an excellent photocatalyst on its own, the presence of rutile is necessary to have an improved photocatalysis efficiency. This criterion is displayed by P25, as confirmed by XRD results and Raman spectroscopy (as shown in Figure IV-5). Unfortunately, none of the biotemplated samples showed any titania phase other than that of anatase in the region between 100-700 cm<sup>-1</sup>. This would mean that whatever synergetic properties that would have otherwise been experienced by a titania-based photocatalyst (such as in P25) had rutile been present would have been missed out in the biotemplated replicas; resulting in the poor photocatalytic efficiency seen in IV.5.1.

### IV.6.4 Band gap consideration

Not only is the polymorphic composition of the photocatalyst an issue, but also the magnitude of the band gap is another problem that can affect the photocatalytic efficiency. Using the UV-vis, the band gap energy was estimated in section IV.5.3. From this, it was made apparent that the band gap of the biotemplate samples were worse than that of P25. P25 was estimated to have a band gap of 3.2eV while RR (HNO<sub>3</sub>pH[1]+ TiPA) was shown to have a value between 3.9eV and 4.5eV. The high value is probably as a result of the presence of calcite which has been estimated to have an indirect band gap of 4.9eV and a direct one of 6.0eV. Its presence would have had an effect, creating a value that appears to offer a compromise between titania and calcite. And although XRD and Raman have suggested that titania crystallites in the replicas are smaller than those seen for P25, it is likely that the lower band gap value usually seen in a nanoscale catalyst would only have come into play if the proportion was higher than that of calcite.

Indeed, the higher eV that has been approximated for the biotemplated samples shows that a higher energy source, or a lamp providing light deeper into the UV, is needed for better photocatalytic efficiency. It is no wonder that the biotemplated samples were slower in degrading MO with their wider band gap.

#### IV.6.5 Active site analysis

It appears that the band gap, the polymorphic composition of titania and the overall lower proportion of titania can be blamed for the lower photocatalytic efficiency seen in section IV.5.1. Another potential factor that should not be overlooked is the nature of the active sites (see section IV.5.4). Pyridine and acetone were utilised to ascertain the Lewis acid sites to Brønsted acid sites balance and hydrogen bond interactions. Probing using acetone predominantly showed just Lewis acid sites. In P25-Ace, although the peaks appeared quite small, they did occur at the same wavenumbers as those seen in literature (M. I. Zaki *et al.*, 1999; El-Maazawi *et al.*, 2000; Zaki, Hasan and Pasupulety, 2001). The same could not be said for RR (HNO<sub>3</sub>pH[1]+TiPA)-Ace, while it occurred in the specified region, the values were always deviated by a significant amount in comparison to P25-Ace. This led the author to believe that the surface reaction involves both titania and calcite; and seeing as calcite makes up a major proportion of the composite (in most instances), then the behaviour displayed by RR (HNO<sub>3</sub>pH[1]+TiPA)-Ace might be attributed to calcite mainly (if not alone).

The same conclusion can be drawn from the reaction with pyridine. Though P25-PY showed peaks proving the presence of Lewis and Brønsted acid centres at the wavenumbers seen in literature (Bezrodna *et al.*, 2003), RR (HNO<sub>3</sub>pH[1]+TiPA)-PY had peaks that appeared in roughly the same region. This might just be because the surface reaction with PY is dominated by calcite.

P25 results revealed active centres that are Lewis and Brønsted acid centres that are attributed to the presence of anatase and rutile. The same cannot be conclusively said for the TiO<sub>2</sub> based replica samples. The shift in the wavenumbers and the absence of some of the peaks mean that as a phase, calcite plays even more of a role in surface reactions than would have originally been assumed. If the FTIR results are to be attributed to solely calcite, then it would be possible that most of the surface interaction occurs first on calcite, with only a smaller proportion occurring on titania. This would be novel and lead a new character to replica photocatalysts. It explains why the bands that normally arise as a result of interaction with titania are always shifted or absent in the replica samples. If titania's interaction is as diminished (as the FTIR results suggest) then the compromised active centres could also be the cause of the poor photocatalysis.

If photocatalysis only occurs on titania, rather than calcite, then the active sites of calcite have to be completely occupied before any MO can get to the active site of titania. Even at that, it has to contend with the possibility that its own TiO<sub>2</sub> active site was partially blocked or occluded by calcite. Thus, whatever degradation of MO that occurs is a balance between how many active sites are available, and how many MO molecules can reach these.

## IV.7 Conclusion/future work

The aim of this chapter was to unravel the photocatalytic performance of the TiO<sub>2</sub> biotemplate replicas against commercial P25, using the polymorphic composition, adsorption edge, the active sites and the rate constants to aid in this comparison. P25 showed a better photocatalytic performance than the replica samples, but as we would come to find out the poor efficiency might have less to do with the actual titania present in the samples and more to do with the accompanying phase, calcite. However, the lack of rutile in the replica samples might also be a contributing factor and calcite blocking may be important. Certainly, one can see that the band gap values of the RR-TiO<sub>2</sub> replicas estimated (3.9eV and 4.5eV) are poorer than titania (3.2 eV for anatase and 3.0eV for rutile (Luttrell *et al.*, 2014)). With the active site analysis, almost the same conclusion can be drawn. Yet again, the surface activities with Ace and PY appeared to highlight the suppressed nature of titania that was present. This could only mean that calcite being present competed perhaps more favourably for molecules with titania.

Despite the mounting factors that point to the effect of calcite on the photocatalytic performance of the replicas, it is still outstanding that the samples RR (HNO<sub>3</sub>pH[1]+TiPA) and RR (HNO<sub>3</sub>pH[1]+TiPA)-5H were still capable of showing some positives at all. This could mean that while the presence of calcite is certainly problematic, it does not completely suppress the overall photocatalytic properties. Any future work should be centred on resolving the calcite in issue.

While the RR replicas were not able to show results that outperformed P25 one should keep in mind that it was possible to achieve a rate constant of  $3.00 \times 10^4 \text{ min}^{-1}$  (RR (HNO<sub>3</sub>pH[1] + TiPA)) following very simplistic processing conditions (no size optimisation of particle, no phase optimisation, no impurity screening etc.) in the presence of a prominent insulating phase.

## Chapter V Assembly of immobilised floating photocatalyst

### V.1 Introduction

The importance of pollution cannot be over emphasised: this is why so much effort is being put in to correct the imbalances created as a result of pollutants.

Specifically, in this chapter we shall be considering not only the effect of a photocatalyst on the pollutant in question, but also the manner in which the photocatalyst is exposed to the pollutant. This is a vital part of dealing with pollutants. Previously we considered pollutants in terms of those that are either accidentally or intentionally introduced into various water bodies. These included Azo dyes and surfactants. An important class of detergent is Triton-X100 (more in section V.5.1.1). It is a non-ionic surfactant used in the manufacture of cleaning agents, paints, coating and in the textile industry as “detergent, emulsifiers, wetting agents, solubilisers and dispersants” (Hegedús *et al.*, 2015). Triton- X100 breaks down only partially in anaerobic or an aerobic environ into products capable of causing damage to cell membranes and nervous systems once living organisms are exposed to them (discussed further in V.5). (Hegedús *et al.*, 2015).

Photocatalysts are one remedy to this situation.  $\text{TiO}_2$  when exposed to sunlight, or rather light of a specific wavelength is able to create electron-hole pairs which are capable of causing/hastening the breakdown of many of these pollutants. This property was exploited here, by using a model photocatalyst (P25) and a biomimetically-produced  $\text{TiO}_2$  to break down MO (see Chapter IV). It was discovered that using a loose photocatalyst, the rate constant that was achieved for P25 was  $\approx 0.0042 \text{ min}^{-1}$ .

While the efficiency of the photocatalyst may be improved with a structure able to fully utilise the light source. It would also be useful if it could be easily retrieved and reused with minimal impact on the surrounding environment (and inhabitants). This potential positive outcome will be considered now.

### V.2 Aim

Following on from the interesting results realised in Chapter IV, photocatalytic properties of  $\text{TiO}_2$  replica biotemplates immobilised in floating films will be investigated. Noting that the loose replica particulates generally have a much lower catalytic performance than P25, the improvement in their performance was sought through their immobilisation in PVAc and PVA films.

At the end of this chapter, it is hoped that the catalytic properties of the biomimetic samples



obtained, through the degradation of MO and TX-100, would be more favourable. In addition to that, it is hoped that one would be able to investigate the reusability of the film. Another important concept here would be the possibility of incorporating other substances in the film.

### V.3 Background

As we are already aware of catalyst and their surface properties that are responsible for their catalytic properties, we shall instead be considering the many forms in which photocatalysts exist, and how this affects their overall performance. Of course, maximum discretion will be paid to those that have been designed to float.

Indeed quite a lot of photocatalysts are used as fine powders in suspension, for the purpose of water treatment (Yao *et al.*, 2007; Marković *et al.*, 2018; Zhang, Li and Yang, 2018). The main issues that come from their use in this manner is recovery afterwards, which can be time consuming. In addition to that, the reusability of the photocatalyst is effectively lost seeing as recovery is difficult; all of this adds further monetary constraints as more photocatalyst has to be synthesised (Marković *et al.*, 2018). One also needs to consider the environmental implication of unintentionally introducing nanoscale materials, and the problems that this might generate in the environment. Indeed, one could replace a molecular pollutant with a particulate one. In addition, there is the effect of poor agitation which can reduce the performance of the photocatalyst. As such, immobilisation would allow the use and easy recovery of the material, but photocatalysts (specifically TiO<sub>2</sub>) are much more effective when used as slurries (Singh, P. K Singh and Mahalingam, 2015; Leshuk *et al.*, 2018). This is to do with better mass transfer and thus better overall contact with the pollutant, but then poor agitation decreases the access to air at the air-water interface which is just as important.

Immobilisation of the photocatalyst in a floating film is intriguing. In this way, one would be able to recover and reuse, thus making the water-treatment process more economically sound. In the design of an immobilisation structure for use in water treatment, it would make sense that this structure has the ability to float in an aqueous medium, as the photocatalytic reaction benefits from the presence of a source of light and oxygen. Consequently, a floating structure would be able to take advantage of optimal interaction with solar radiation better than if it were deeper in the aqueous medium; as this structure would exist at the interface between water and air, allowing the system to be more efficient regardless of whether the system is agitated or otherwise (Marković *et al.*, 2018; Zhang, Li and Yang, 2018).

To be a suitable immobilisation support, the support needs to be stable over time in an aqueous environment: pH stable and resistant to degradation. If it degrades, it needs to be nontoxic (Singh,

P. K Singh and Mahalingam, 2015), essentially imparting no changes in the chemical properties of the aqueous environment it will be placed in and still being air-permeable when needed. In addition to that, it needs to be easy to incorporate the photocatalyst phase. And finally, it needs to be optically transparent, thus reducing the possibility of attenuating the light intensity or photon flux that reaches the catalyst. Obviously, the support material needs to have a low density, at least lower than water, to enable it to remain afloat.

So far, there has been several attempts to produce a floating catalyst. The most popular methods involve the use of a template material that inherently has the ability to remain buoyant in an aqueous medium. The grafting of g-C<sub>3</sub>N<sub>4</sub> onto expanded perlite (EP) is an example of a photocatalyst synthesised by Zhang, Li and Yang (2018). Their system showed effective degradation potential against rhodamine blue, even after reusing the system 5 times. Its floating abilities was imparted by the light weight and porous expanded perlite. Again expanded perlite was used as a template for a TiO<sub>2</sub>/EP made by Xue *et al* (2016), which again showed enhanced activity in the decomposition of rhodamine blue when compared to just P25. Similarly, pumice was used to immobilised TiO<sub>2</sub> to create a floating photocatalyst which was able to degrade different dyes including methyl orange, acid blue and so on (Hayakawa *et al.*, 2001). Other researchers have relied on the templates produced from polymers to lend their samples floating abilities: they include the preparation of reusable polystyrene with TiO<sub>2</sub> supported on it which showed activity in the photo-assisted degradation of methylene blue under UV (Singh, P K Singh and Mahalingam, 2015). Polycaprolactone foam, prepared by supercritical foaming, was used to support TiO<sub>2</sub> (Marković *et al.*, 2018). They showed reusability over 3 cycles in the breakdown of acid orange and basic yellow. Besides polymers, hollow microbeads in the form of glass microbubbles (Leshuk *et al.*, 2018) and glass microbeads (Shi-Fu and Xue-Li, 2010) have been used to immobilise TiO<sub>2</sub> and were shown to decompose pollutants present in oil sands process affected water and ethylbenzene respectively.

#### **V.4 Photocatalyst immobiliser for consideration**

To address the problems associated with using photocatalysts in the form of slurries, the following polymers will be used as immobilising/support materials with the added feature of being able to float.

PVA seems to fulfil the majority of the properties required for an immobiliser. Unmodified, PVA has poor stability in water. It is prone to swelling with its tensile properties also diminishing (Figueiredo, Alves and Borges, 2008). The level of dissolution in water can be reduced by using crosslinkers to improve the entanglement of PVA chains, thus glutaraldehyde (GLA) will be used.

It will be paired with HCl to speed up the reaction (Figueiredo, Alves and Borges, 2008). Sodium alginate appears to share similar properties as PVA. It is hydrophilic, non-toxic, with intermediate solubility depending on its levels of crosslinkage, which can be controlled through the use of divalent cations.

Another immobilising material is PVAc, it is hydrophobic. It is derived from the polymerization of acetate amorphous monomers, via a free radical reaction to form a thermoplastic polymer (Figueiredo, Alves and Borges, 2008). It results in a UV transparent film, with better stability in an aqueous environment than PVA without crosslinks, with little dissolution and swelling observed over the course of the experimental process.

Polycaprolactone (PC) is an example of another hydrophobic polymer. It is degradable, but its degradable products are nontoxic (Sisson, Ekinici and Lendlein, 2013).

After assembly with TiO<sub>2</sub>, it was intended that the nanocomposite would float as films.

## V.5 Model Pollution Candidate (surfactant)

In addition to using MO, Triton X-100 will be used as another pollutant to test the photocatalytic ability of the floating films.

### V.5.1.1 Non-ionic surfactants

Non-ionic surfactants represents another important class of industrial detergents that can be used in the “processing of textiles, pulp and paper, recycled paper, paint and plastics” (Gomez *et al.*, 2011). Alkylphenol ethoxylates (APEO) are the most important and abundant surfactants (Sharma *et al.*, 2009). APEOs molecules (1,4-R- $\phi$ -(O<sub>2</sub>H<sub>4</sub>)<sub>n</sub>-OH) are made of hydrophobic alkyl unit (1,4-R), a benzene ring ( $\phi$ ) and ethoxy groups (O<sub>2</sub>H<sub>4</sub>)<sub>n</sub> which are hydrophilic. The ethoxy group have a distribution in ‘n’ (number of units in the chain).

APEOs are of particular concern due to their endocrine disrupting abilities. Their metabolites (nonyl phenol: NP, octyl phenol: OP, bis phenol A: BPA) are formed by the microbial cleavage of ethoxy units (EO) (Gomez *et al.*, 2011). These are prevalent in the effluent of waste water in plants, rivers, seas and ground water (Sharma *et al.*, 2009). They bind to human oestrogen and mimic natural hormones. They are also linked to increases in breast cancers, decline in sperm count and inducing early puberty in mice, etc (Sharma *et al.*, 2009).

Triton X-100 (Figure V-1b) is a suitable example of an APEO (Hegedús *et al.*, 2015). It undergoes only limited biodegradation in anaerobic and aerobic conditions, with pH having little effect on its rate or extent of degradation.

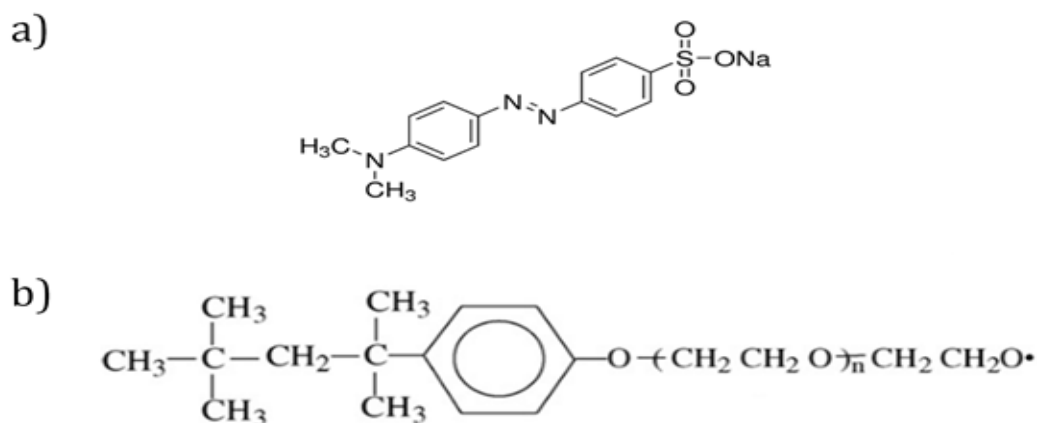


Figure V-1: Structural formula of methyl orange a); Structural formula of Triton X100, an APEO where n is an integer b) (Manhas et al., 2008; Haque, Jun and Jhung, 2011)

## V.6 Experimental technique and methodology

### V.6.1 Sample preparation

Two distinct methods were considered to immobilise the photocatalyst material:

- Single film:

Please refer to section II.2.1 and II.2.2 for more information on the preparation of PVAc and PVA only films

- Dual/asymmetric film:

Please refer to section II.2.3 for more information on the preparation on asymmetric films and their assembly

### V.6.2 Experimental setup for photocatalysis

- An uncovered polystyrene petri dish (90mm diameter) was filled with 8ml of 0.01mM MO.
- The already prepared films were then floated on the liquid and left-over night (12h)
- The samples (inside the petri dish) were subsequently irradiated with a UV lamp of 302nm (from above the petri dish)
- At various interval, 2.5ml of the liquid was collected for analysis within a UV-vis, and then returned

### V.6.3 Analytical instruments and conditions

#### V.6.3.1 UV-vis

This was used to probe the response of MO and TX-100 as they underwent degradation in the presence of the photocatalysts. Their lambda maxes were followed (465nm: MO; 223nm: TX-100) to track degradation and to derive their degradation rate constants.

#### V.6.3.2 SEM

Before analysis with SEM, all of the samples were freeze-dried for 12h. They were then placed on carbon tape on a SEM stub, where they were coated with an Au target for 60sec.

### V.6.4 Sample nomenclature

The samples in this section have the following designation

**Table V-1: Name of the photocatalytic film samples and their accompanying description**

<b>Sample</b>	<b>Designation</b>	<b>Description</b>
P25/PVAc	P25/PVAc	P25 embedded in PVAc film
P25/PVA	P25/PVA	P25 embedded in PVA film
B7AL 3VA/T0.5AL 2VA 7.5AC P25	AL/AC-P25	Base layer film: 0.7ml AL + 0.3ml PVA Top layer film: 0.05 ml AL + 0.2 ml PVA+ 0.75 ml PVAc (P25 embedded in the top layer)
B7AL 3VA 0.15TATi/T8PC 2AC P25	TATi/PC-P25	Base layer film: 0.7ml AL + 0.3ml PVA +0.015ml tannic acid infused sodium alginate Top layer film: 8mlPC+ 0.2 ml PVAc (P25 embedded in the top layer)
B7AL 3VA/T8PC 2AC P25	AL/PC-P25	Base layer film: 0.7ml AL + 0.3ml PVA Top layer film: 0.8ml PC+ 0.2 ml PVAc (P25 embedded in the top layer)
B7AL 3VA P25/T8PC 2AC	AL -P25/PC	Base layer film: 0.7ml AL + 0.3ml PVA (P25 embedded in here) Top layer film: 0.8ml PC+ 0.2 ml PVAc
B7AL-CV 3VA P25/T8PC 2AC	AL-CV-P25/PC	Base layer film: 0.7ml AL + 0.3ml PVA (P25 and CV embedded here ) Top layer film: 0.8ml PC+ 0.2 ml PVAc
B9AL 1VA/T8PC 2AC BLANK	9AL/PC	Base layer film: 0.9ml AL + 0.1ml PVA Top layer film: 0.8ml PC+ 0.2 ml PVAc
B9AL 1VA/T8PC 2AC P25	9AL/PC-P25	Base layer film: 0.9ml AL + 0.1ml PVA

		Top layer film: 0.8ml PC+ 0.2 ml PVAc (P25 embedded in the top layer)
B9AL 1VA P25/T8PC 2AC	9AL-P25/PC	Base layer film: 0.9ml AL + 0.1ml PVA (P25 embedded in here) Top layer film: 0.8ml PC+ 0.2 ml PVAc
B9AL-CV 1VA P25/T8PC 2AC	9AL-CV-P25/PC	Base layer film: 0.9ml AL + 0.1ml PVA (P25 and CV embedded here) Top layer film: 0.8ml PC+ 0.2 ml PVAc
B9AL 1VA 1CV-OIL/T8PC 2AC P25	9AL-CV-OIL/PC-P25	Base layer film: 0.9ml AL + 0.1ml PVA + CV in oil Top layer film: 0.8ml PC+ 0.2 ml PVAc (P25 embedded here)
B9AL 1VA/T0.5AL 2VA 7.5AC P25	9AL/AC-P25	Base layer film: 0.9ml AL + 0.1ml PVA Top layer film: 0.05 ml AL + 0.2 ml PVA+ 0.75 ml PVAc (P25 embedded in the top layer)
B9AL 1 VA/T8PC 2AC RR (HNO <sub>3</sub> pH[1]+TiBALD)	9AL/PC-RR(TIBALD)	Base layer film: 0.9ml AL + 0.1ml PVA Top layer film: 0.8ml PC+ 0.2 ml PVAc (RR embedded in the top layer)
B9AL 1 VA/TPC 2AC RR (HNO <sub>3</sub> pH[1]+TiPA)	9AL/PC-RR(TIPA)	Base layer film: 0.9ml AL + 0.1ml PVA Top layer film: 0.8ml PC+ 0.2 ml PVAc (RR embedded in the top layer)

## V.7 Results

### V.7.1 Photocatalytic degradation of MO degradation

In order to ascertain the film with the best properties, first the author had to investigate various curing conditions and film compositions to accomplish this. It emerged that film synthesis was easier than ensuring that the film was durable and capable of maintaining its shape after exposure to high UV conditions.

Thus, it is necessary to examine the photocatalytic conditions, especially with MO, and use this to draw some conclusions on the stability of the films and their usefulness (photocatalytic efficiency) when the photocatalyst were immobilized as nano-engineered.

A first-order degradation model was displayed by most samples when plotted.  $A_0$  is the starting UV-vis absorbance of MO (TX-100), and  $A$  is the absorbance with changing time (in the presence of a UV source).

### V.7.1.1 Effects of film composition- Single layer film

To begin with, the photocatalytic performance of P25 supported within a single polymer layer was investigated before any further investigation into the assembly of films with multiple layers. In Figure V-2, two samples were made containing similar amounts of P25 (0.25mg/ml) but on different support polymers: PVAc and PVA.

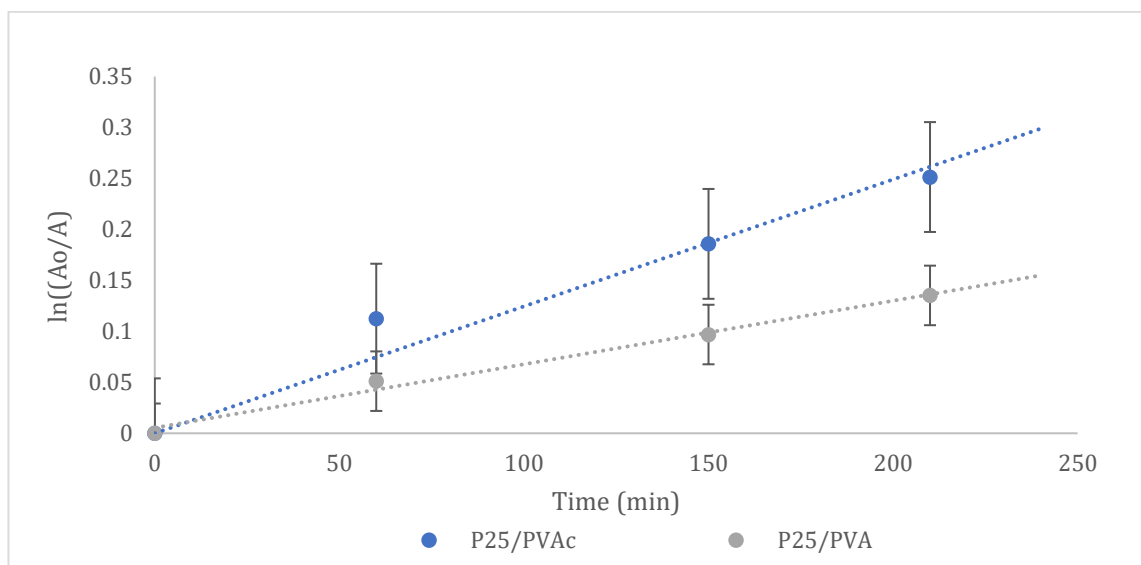


Figure V-2: Degradation of 0.01mM MO with single film supports containing P25 at room temperature (Dose: 0.25mg of photocatalyst in 8ml of MO).

The data points in both of the support polymers (PVAc and PVA) appear to fit the linear pseudo first-order model, with P25/PVAc showing the better performance of both of the samples in terms of their photocatalytic abilities. The following parameters were obtained from the curve above.

Table V-2: Calculated pseudo-first-order rate constants ( $k_1$ ), half-life  $t_{1/2}$  and  $R^2$  value of the single film support samples in Figure V-2 following their MO degradation abilities.

Samples	$k_1$ ( $\text{min}^{-1}$ )	$t_{1/2}$ (min)	$R^2$ value
P25/PVA	$3.0 \times 10^{-4}$	2310.49	0.985
P25/PVAc	$1.2 \times 10^{-3}$	577.62	0.956

The table above confirms P25/PVAc indeed has a superior performance to P25/PVA i.e there is a divergence in several orders of magnitude, according to the  $k_1$  constant, which is also reflected by the shorter half-life.

In Figure V-2  $A_0$  and  $A$  are the absorbance of the reactant at 0 time (hours, min, sec etc) and at  $t > 0$  respectively.

The half-life is 577min, in the case of P25/PVAc, is the time required for half of the MO present to undergo degradation, it is 4x faster than that witnessed for P25/PVA.

The result appears to show the P25 on the PVAc support is more efficient than when it is on PVA. Of course, this is most likely to do with the initial assembly process. In the assembly of P25/PVAc support, a thin film of PVAc is initially deposited which is then followed by deposition of P25 (dispersed in dichloromethane); P25 is left on the surface of the PVAc film, after the evaporation of the dichloromethane solvent. On the other hand, the sample made with PVA has P25 suspended in a dispersion of PVA solution. Thus, P25 is ultimately integrated in the PVA matrix. The difference between having P25 held only on the surface, as opposed to being part of a matrix is most likely the major cause of this photocatalytic difference, with an increased fraction of its active site blocked by PVA, possibly acting as a physical barrier to the dye reaching the photocatalyst surface. Of course, P25 in film-free suspension is better than immobilised in PVAc and PVA film (where  $k_1=0.0042\text{min}^{-1}$ , Table IV-6).

#### *V.7.1.2 Effects of film composition-Dual layer*

It is clear that depending on the position of P25 in relation to its supporting matrix, the overall photocatalytic efficiency can be significantly affected. In spite of this, there is still an attraction to casting P25 or other photocatalyst on a self-supporting matrix (PVA, PVAc or any other polymer matrix). Now, suppose the matrix functions as more than just a structure for support? Could it act as an extra surface to mop up pollutants, while positioning the photocatalyst in the optimum manner to utilise the necessary radiation to catalyse the degradation process? In addition to mopping up the pollutant, could the films also act as a medium to hold other molecules ( $\text{O}_2$ ) for the catalyst centre? Could such oxygen hasten a reaction that would otherwise proceed at an infinitesimally slow rate?

These questions necessitated the improvement of the films. The author therefore chose to move from earlier single layer films to those with multifunctionality and consisting of multiple layers with each layer having specific surface properties that would be amenable to different classes of molecules

This section attempts to address such a requirement through the investigation of a dual layer film. The intended design would have one layer of the film primarily consist of polymers that are more hydrophilic (comprising of a larger proportion of alginate to improve its stability in an aqueous environment and creating a matrix that would encapsulate water held molecules. This would allow the seeding of algae that would act as oxygen producers in addition to their natural remediation properties. The other layer would be more hydrophobic, providing floating potential, and would incorporate the photocatalyst, and for the purpose of buoyancy. When this dual-film was utilised in a body of polluted water, it was hoped that the hydrophobic layer would stay at the water-air interface, allowing the photocatalyst to have full access to sun radiation, while being bathed on the other half by the pollutant.



The intention will be to observe the effects of changing the composition of the two layers and how this will affect their photocatalytic efficiency as described.

For brevity, only two possible compositions of the base layer (hydrophilic) with respect to the changing composition of the top (hydrophobic) layer will be described.

#### V.7.1.2.1 Effects seen with a base layer of 7AL-3VA

Three samples will be investigated in this section with the same (7AL-3VA) base layer, except for one sample with designation TATi/PC-P25. Like the samples made using a single polymer support layer, the degradation profile was plotted using the pseudo-first-order model again (see Figure V-3 and Table V-3). It is clear that all the samples in question seem to fit quite well with the first-order model used. From the figure, one can already make out that the most successful sample with the higher  $k_1$  and lowest  $t_{1/2}$  appears to be AL/PC-P25 with the other two samples sharing similar performances, although their linearity is not uniform.

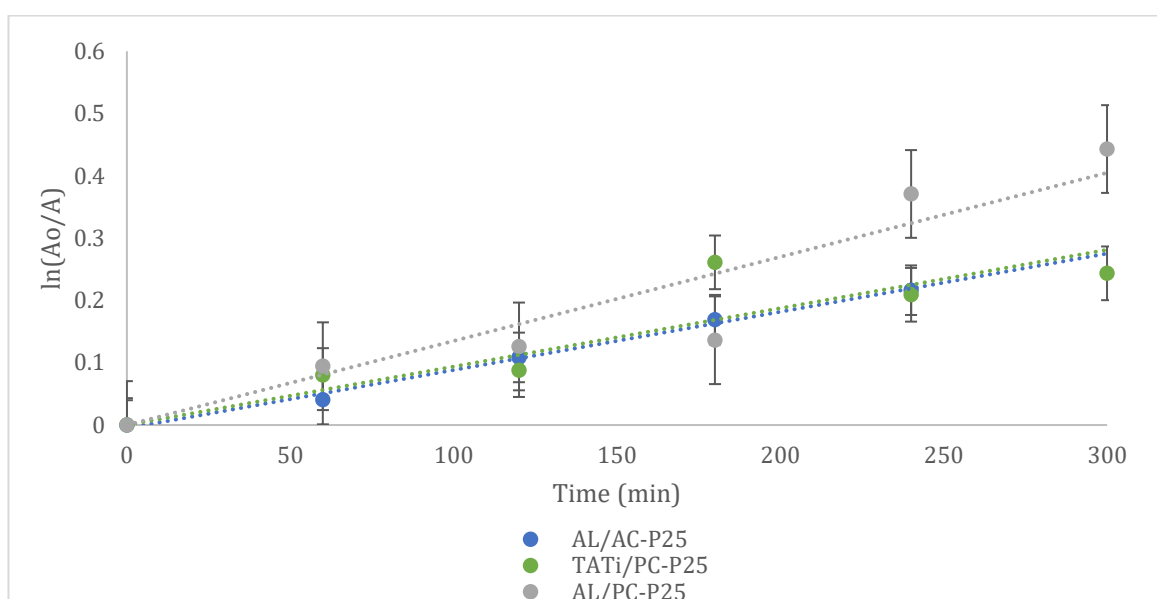


Figure V-3 Degradation of 0.01mM MO with dual-film support containing P25 at room temperature (Dose: 0.25mg of photocatalyst in 8ml of MO).

The sample AL/PC-P25 has a better performance than P25/PVAc from the single film system. Its  $k_1$  constant has an improvement of about 8.3% over that of P25/PVAc. The only other sample with a composition similar to the best samples, with the exception of an extra compositional component of the base layer TATi, has a lower degradation efficiency. This ultimately leads to a half time period that is 237min longer than it would have achieved otherwise. The last sample with designation AL/AC-P25, also has a similar degradation constant and half-life value.

**Table V-3: Calculated pseudo-first-order constant ( $k_1$ ), half-life  $t_{1/2}$  and  $R^2$  value of the samples in Figure V-3 following their MO degradation abilities.**

Samples	$k_1$ ( $\text{min}^{-1}$ )	$t_{1/2}$ (min)	$R^2$ value
AL/AC-P25	$9.0 \times 10^{-4}$	770.16	0.9931
TATi/PC-P25	$9.0 \times 10^{-4}$	770.16	0.9931
AL/PC-P25	$1.3 \times 10^{-3}$	533.19	0.8889

#### V.7.1.2.2 Effects seen with a base layer of 9AL-1VA

The photocatalytic performances of two samples were investigated in this section. The composition of their top layer was similar to those observed in the previous section, with a 7AL-3VA base layer.

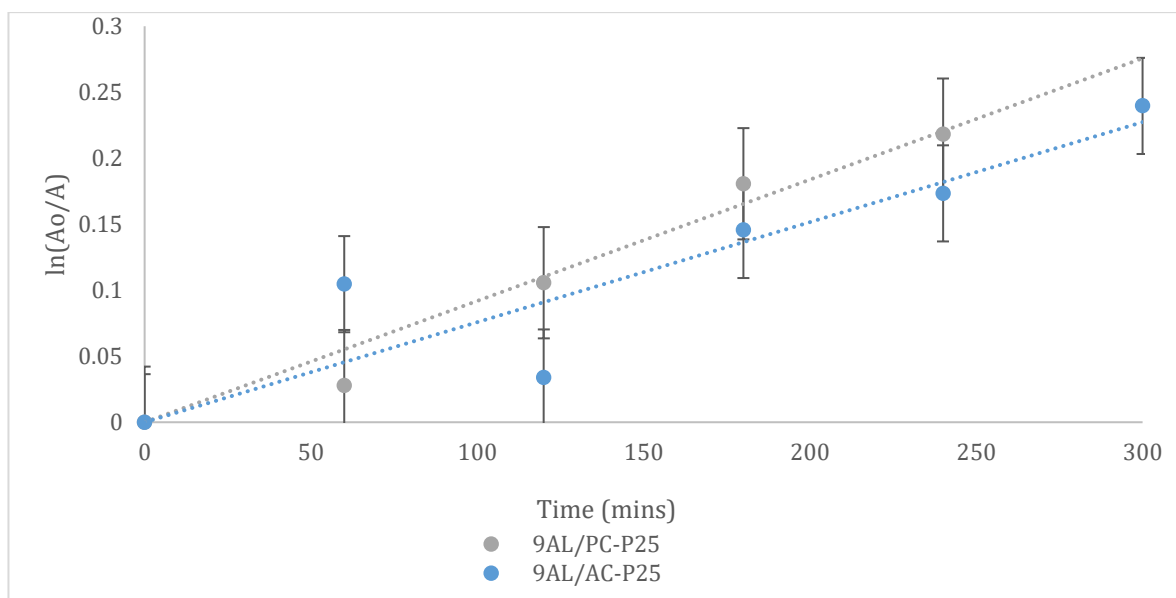


**Figure V-4: Degradation of 0.01mM MO with dual-films 9AL/PC-25 and 9AL/AC-P25 at room temperature (Dose: 0.25mg of photocatalyst in 8ml of MO).**

Again, the data points shown in Figure V-4 appears to fit quite closely to the linear first-order reaction model. Here, the sample 9AL/PC-P25 shows a superior photocatalytic behaviour than the sample 9AL/AC-P25 but lower  $k_1$  and  $t_{1/2}$  than Table V-3.

**Table V-4: Calculated pseudo-first-order constant ( $k_1$ ), half-life  $t_{1/2}$  and  $R^2$  value of the samples in Figure V-4 following their MO degradation abilities.**

Samples	$k_1$ ( $\text{min}^{-1}$ )	$t_{1/2}$ (min)	$R^2$ value
9AL/AC-P25	$8.0 \times 10^{-4}$	866.43	0.8261
9AL/PC-P25	$9.0 \times 10^{-4}$	770.16	0.9716

From the result of the parameters, as well as in the corresponding plot, one can conclusively say

that the sample 9AL/PC-P25 shows a better performance both in terms of its  $k_1$  constant, but also in terms of the correlation coefficient to the first-order model.

#### V.7.1.2.3 Blank sample

The results of the dual-layer samples have so far proven that their design makes them more efficient than if a single layer system was utilised (V.7.1.1). However, it was important to verify if the actual degradation of MO was in fact due to the influence of P25 (or if something else could be participating in the degradation of MO). This is especially important as several components of the dual-film, alginate and PVA, are known to swell in an aqueous environment. Thus, could they unwittingly be responsible for the disappearance of MO instead of P25? Figure V-5 shows us that the opposite is the case; the rate constant was negligible ( $-3.0 \times 10^{-4} \text{min}^{-1}$ ) increasing with time. A possible reason for this might have been due to the uptake of water by the hydrophilic polymer present, which could inadvertently have concentrated the MO dye solution. But that should not be the case, as this and all the other samples in this chapter were rested in the dye solution for 12h before the photocatalytic run began. Thus, any uptake of water should have already been concluded before the start of the experiment. It is possible that the apparent increase in MO concentration might be a function of scattering, caused by the breakdown of the films in the presence of the light source that might be increasing the crosslinks within the polymer; making the polymer chain inflexible while enhancing the likelihood of breaking apart (Mukherjee, Barghi and Ray (Mukherjee, Barghi and Ray, 2013).

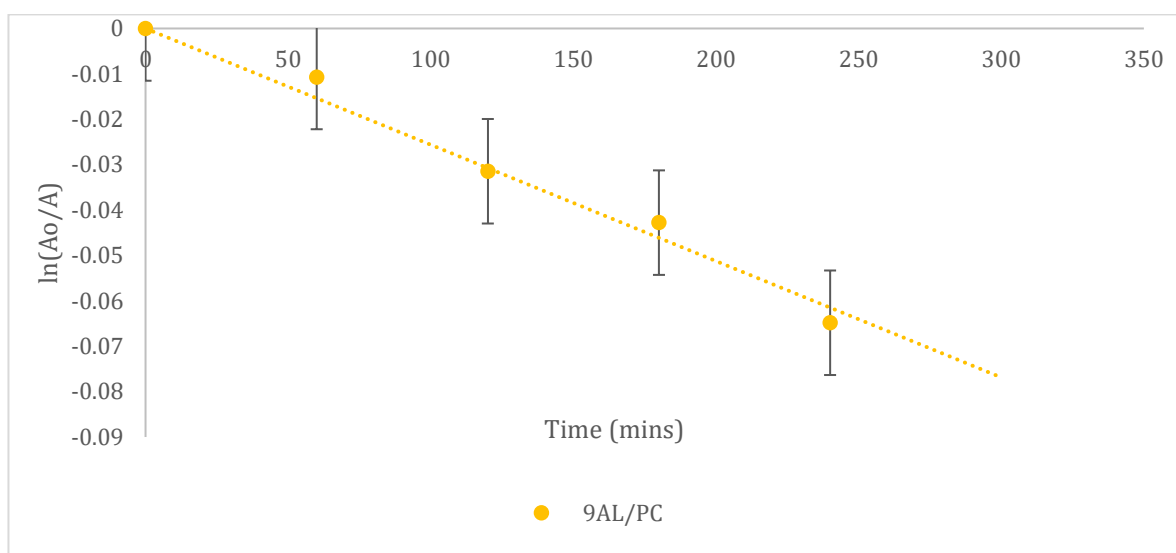


Figure V-5: Degradation of 0.01mM MO with dual-film 9AL/PC, containing no P25 at room temperature (Dose: no photocatalyst in 8ml of MO)

Whatever the case, one can decisively say that the photocatalytic performance seen in Figure V-2 and Figure V-3 are in reality much better, because the reduction in MO demonstrated by those

samples would have had to overcome scattering as suggested by the negative reading (Figure V-5), which are apparently intrinsic to the dual-film.

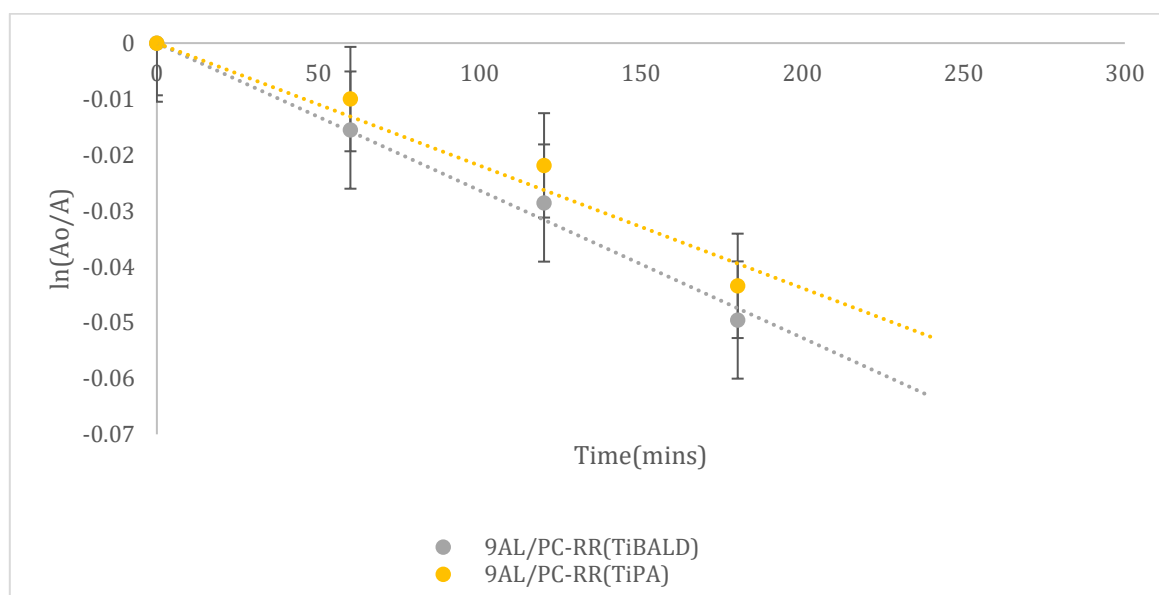
#### V.7.1.2.4 RR Replica samples

Figure V-6 shows the degradative behaviour of the TiO<sub>2</sub> replica containing dual-film samples which appear to have no effect on MO. The calculated rate constants are in Table V-5. Interestingly enough, the sample 9AL/PC-RR (TiBALD) has a similar rate constant as the blank sample from Figure V-5, which points to the fact that this sample truly had no photocatalytic abilities, within a dual-film support at least. However, 9AL/PC-RR(TiPA) has a higher rate constant (approximately 30% higher), which means that it does have some photocatalytic activity although  $k_1$  is still negative and not real. The value is vastly smaller than if P25 was used instead to give a positive  $k_1$ .

**Table V-5: Calculated pseudo-first-order constant ( $k_1$ ) of the RR-TiO<sub>2</sub> Replicas in Figure V-6 following their MO degradation abilities.**

Samples	$k_1$ (min <sup>-1</sup> )
9AL/PC-RR (TiBALD)	$-3.0 \times 10^{-4}$
9AL/PC-RR(TiPA)	$-2.0 \times 10^{-4}$

No doubt the factors that were discussed in section IV.6.1 are responsible for its lower properties.



**Figure V-6: Unreal/marginal degradation of 0.01mM MO with dual-film using the RR TiO<sub>2</sub> based replica samples at room temperature (Dose: 0.25mg of photocatalyst in 8ml of MO).**

#### V.7.1.3 Effects of the curing conditions

The curing conditions that will be considered are the crosslinking agents and time. With regards

to the curing/crosslinking agents utilised, one had to take into consideration the nature of the parts that made up the film before one could proceed.

As the hydrophilic portion of the film was going to consist primarily of PVA and sodium alginate, any crosslinking step had to fulfil the task of crosslinking these segments. Since the ideal composition of the film was found to contain a larger portion of alginate than PVA, the curing conditions were tuned more to facilitate the crosslinkage of sodium alginate. As explained in the experimental procedure,  $\text{CaCl}_2$  and amino-functionalised silica sol will be used as a method to enhance crosslinking.

#### V.7.1.3.1 Crosslinking agents

Therefore, in this section, the different crosslinkers alone, or mixed will be studied alongside their effect on the rate and extent of photocatalytic degradation of MO.

##### V.7.1.3.1.1 Calcium chloride as the crosslinking agent

Below is the degradation profile obtained for samples crosslinked using 1wt%  $\text{CaCl}_2$  as the main crosslinking agent. After the casting of both layers of the film, the dual-film was left in a petri dish filled with 1wt%  $\text{CaCl}_2$  for 12h. The catalytic behaviour of the three samples tested below are shown in Figure V-7 and Table V-6.

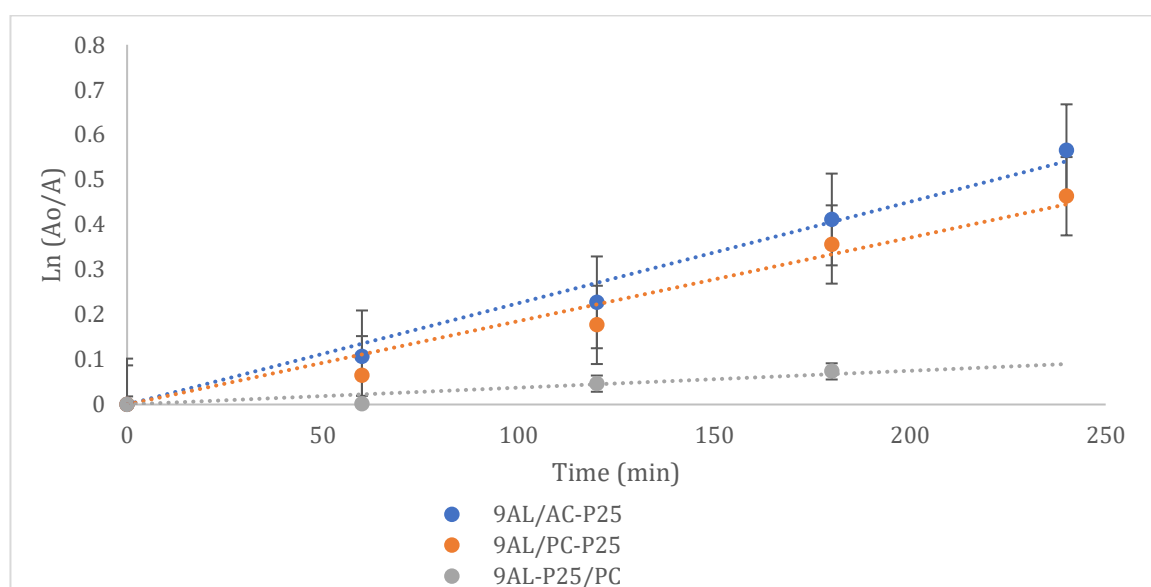


Figure V-7: Degradation of 0.01mM MO with dual-film support crosslinked with  $\text{CaCl}_2$  containing P25 at room temperature (Dose: 0.25mg of photocatalyst in 8ml of MO).

For simplicity, only samples with base layer 9AL 1VA were investigated, primarily because of their higher alginate content; thus, the use of  $\text{CaCl}_2$  would be expected to have a greater effect on their properties than if samples with the base layer 7AL 3VA were investigated. Figure V-7 shows that the sample with the best photocatalytic properties towards MO was 9AL/AC-P25, followed

very closely by the sample 9AL/PC-P25. The pseudo-first-order plot for both of these samples are extremely linear. The last sample 8PC 2AC has a similar chemical composition to 9AL-P25/PC, but Figure V-7 shows that their photocatalytic behaviours are quite contrasting. The main reason behind this is to do with the placement of P25. The successful sample, as with all the samples unless otherwise mentioned, had P25 present in the upper layer. The less successful sample instead had its P25 content within the bottom layer, the hydrophilic layer. This swap in position has completely changed its degradation behaviour, enough to have its  $k_1$  reduced to  $4.0 \times 10^{-4} \text{min}^{-1}$ .

**Table V-6: Calculated pseudo-first-order constant ( $k_1$ ), half-life  $t_{1/2}$  and R<sup>2</sup> value of the samples in Figure V-7 following their MO degradation abilities.**

Samples	$k_1$ ( $\text{min}^{-1}$ )	$t_{1/2}$ (min)	R <sup>2</sup> value
9AL/AC-P25	$2.3 \times 10^{-3}$	301.36	0.9481
9AL/PC-P25	$1.9 \times 10^{-3}$	578.21	0.9669
9AL-P25/PC	$4.0 \times 10^{-4}$	2746.53	0.8748

7.5AC 2VA 0.5AL P25 is by far the best sample, as the calculated half-life values in Table V-6 shows it is capable of breaking down 0.01mM of MO in 301min, which is considerably less than that seen for 8PC 2AC. This which took 2746min to break down i.e 9.11x longer than the best sample (9AL/AC-P25) and 4.75X longer than the second-best sample (9AL/PC-P25).

#### V.7.1.3.1.2 Amino functionalised silica crosslinking method

Figure V-8 and Table V-7 shows MO degradation data of films having the  $\text{CaCl}_2$ -curing step substituted with amino functionalised silica suggested by Pannier *et al* (2014). It involves the combination of the negatively charged alginate network and the positively charged amino-functionalised silica sol.

Again, only samples with the base layer 9AL 1VA will be considered here.

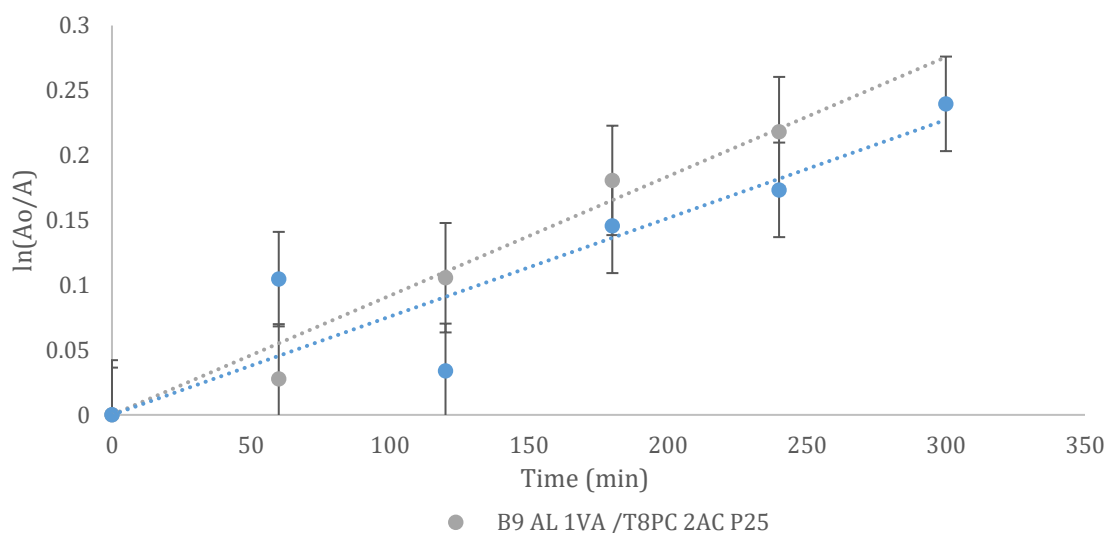


**Figure V-8: Degradation of 0.01mM MO with dual-film support crosslinked with amino silica sol containing P25 at room temperature (Dose: 0.25mg of photocatalyst in 8ml of MO).**

Figure V-8 shows the pseudo-first-order degradation behaviour of the samples crosslinked using an amino functionalised silica method. The errors are greater than in Figure V-7. Other than the earlier sample having a better fit with the pseudo-first-order model than this, there is also the estimated  $k_1$  constant which was by far superior to the constants seen in Table V-7. Thus, one assumes that the crosslinking agent has a tremendous effect on the efficiency of the photocatalytic breakdown of MO. No doubt, the effect of improving the overall stability of the majority alginate structure, seeing as the crosslinking agent was geared towards crosslinking alginate, has slowed down the reagent diffusion to the active site and the degradation rate in the case of 9AL/PC-P25 by about 65%, compared to when it was  $\text{CaCl}_2$  crosslinked; in the case of 9AL/AC-P25 there was a turnaround of 52% instead.

**Table V-7: Calculated pseudo-first-order constant ( $k_1$ ), half-life  $t_{1/2}$  and R<sup>2</sup> value of the samples in Figure V-8 following their MO degradation abilities.**

Sample	$k_1$ (min <sup>-1</sup> )	$t_{1/2}$ (min)	R <sup>2</sup> value
9AL/PC-P25	$9.0 \times 10^{-4}$	770.1635	0.9716
9AL/AC-P25	$8.0 \times 10^{-4}$	866.434	0.826

These results reflect the improved stability of the alginate portion of the dual-film (and by extension all of the film). The same method used to improve the stability of the “dots and film impregnated with *chlorella vulgaris*” (Pannier *et al.*, 2014). Usually, the breakdown mechanism of alginate that has been crosslinked by  $\text{Ca}^{2+}$  involves the disruption of the link with the screening of  $\text{Ca}^{2+}$  or chelation by another group; causing the osmotic swelling of its network and exposure/leakage of its contents. Thus the high  $k_1$  seen in Table V-6 (compared to the lower  $k_1$

constants from Table V-7) might be due to the breakdown of the inadequate alginate network releasing the photocatalyst from the film, freeing its active sites. The more stable samples here possess a network that undergoes very little attrition, meaning that the active sites of the catalyst remains occupied by the crosslinked polymer.

Thus, while the breakdown efficiency of the samples crosslinked with  $\text{CaCl}_2$  are quite attractive, the purpose of having a self-supporting structure capable of remaining unaffected as it retains its active agents (photocatalyst in this case) means that these samples here with their lower  $k_1$  are better. However, to have a dual-film capable of showing a high  $k_1$  without falling apart is still a goal. It is for this reason that samples were now to be made using a combination of  $\text{CaCl}_2$  and amino-functionalised silica sol to achieve the ideal dual-film.

#### V.7.1.3.1.3 Amino-functionalised silica and calcium chloride as crosslinking agents

The samples in this section have been crosslinked using different percentages of the crosslinkers. Starting with using 80%v/v of  $\text{CaCl}_2$  (1wt% concentration) and 20%v/v of the amino functionalised silica sol. The samples investigated had the same top layer (PC-P25), while having either of the base layers (AL ; 9AL )

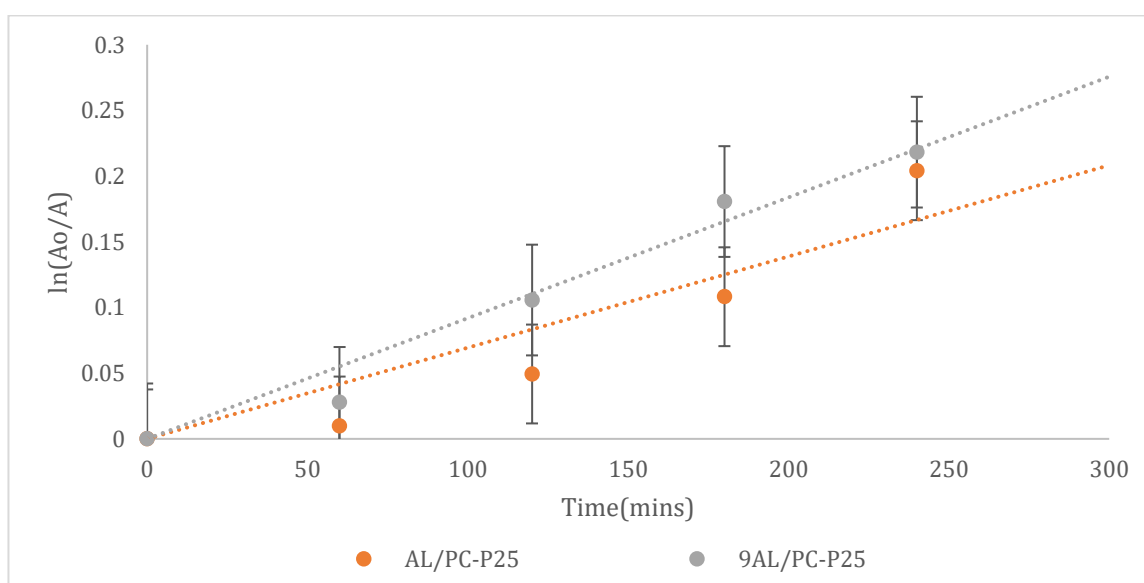


**Figure V-9: Degradation of 0.01mM MO with dual-film support crosslinked with 80%v/v  $\text{CaCl}_2$  and 20%v/v amino functionalised silica sol. Contains P25 at room temperature (Dose: 0.25mg of photocatalyst in 8ml of MO).**

Figure V-9 and Table V-8 shows some improvement over the samples that were simply crosslinked with amino functionalised silica (Figure V-8); at least in terms of scatter of the points. There however does not seem to be much of a difference in the  $k_1$  value, which shows that a more flexible and durable film can be produced by using both  $\text{CaCl}_2$  and amino-functionalised silica,



than relying on either/or of the curing agents.

**Table V-8: Calculated pseudo-first-order constant( $k_1$ ), half-life  $t_{1/2}$  and  $R^2$  value of the samples in Figure V-9 following their MO degradation abilities.**

Sample	$K_1$ ( $\text{min}^{-1}$ )	$t_{1/2}$ (min)	$R^2$ value
9AL/PC-P25	$9.0 \times 10^{-4}$	770.16	0.9716
AL/PC-P25	$7.0 \times 10^{-4}$	990.21	0.8638

Similarly, adjusting the curing condition to 60%v/v of  $\text{CaCl}_2$  (1wt% concentration) and 40%v/v of the amino-functionalised silica sol did not also appear to cause much of a significant improvement in the  $k_1$  value (Table V-9). Figure V-10 shows that the sample AL/PC-P25 has a similar degradation profile as when crosslinked with an 80% v/v - 20%v/v crosslinker mixture.

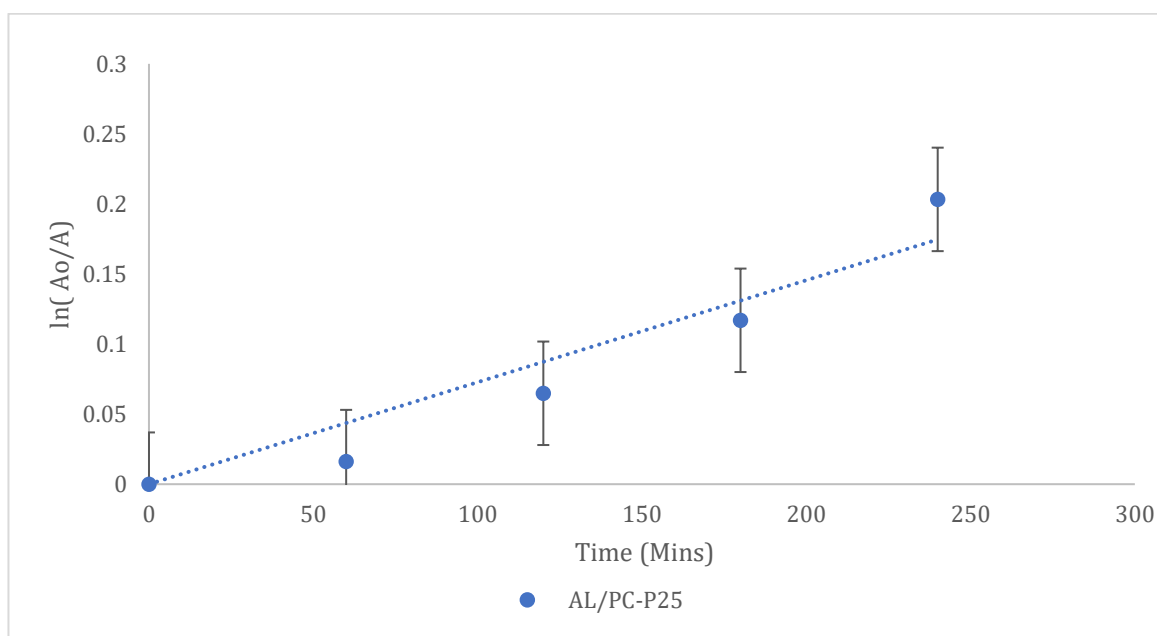


**Figure V-10: Degradation of 0.01mM MO with dual-film support crosslinked with 60%v/v  $\text{CaCl}_2$  and 40%v/v amino functionalised silica containing P25 at room temperature (Dose: 0.25mg of photocatalyst in 8ml of MO).**

It is becoming clearer that any act to improve durability of the film, whether through the use of just 20%v/v or 40v/v% amino-functionalised silica sol, will adversely affect the  $k_1$  obtained.

**Table V-9: Calculated pseudo-first-order constant( $k_1$ ), half-life  $t_{1/2}$  and  $R^2$  value of the samples in Figure V-10 following their MO degradation abilities.**

Sample	$k_1$ ( $\text{min}^{-1}$ )	$t_{1/2}$ (min)	$R^2$ value
AL/PC-P25	$7.0 \times 10^{-4}$	990.21	0.9165

In spite of this adverse effect on the  $k_1$  constant on the silica augmented samples, the possibility of recycling/reusing the dual-film multiple times becomes a possibility. In Figure V-11, the sample

AL/PC-P25 was used over the course of 2 days, with an efficiency that appeared to seemingly improve on the second day as shown in Table V-10.

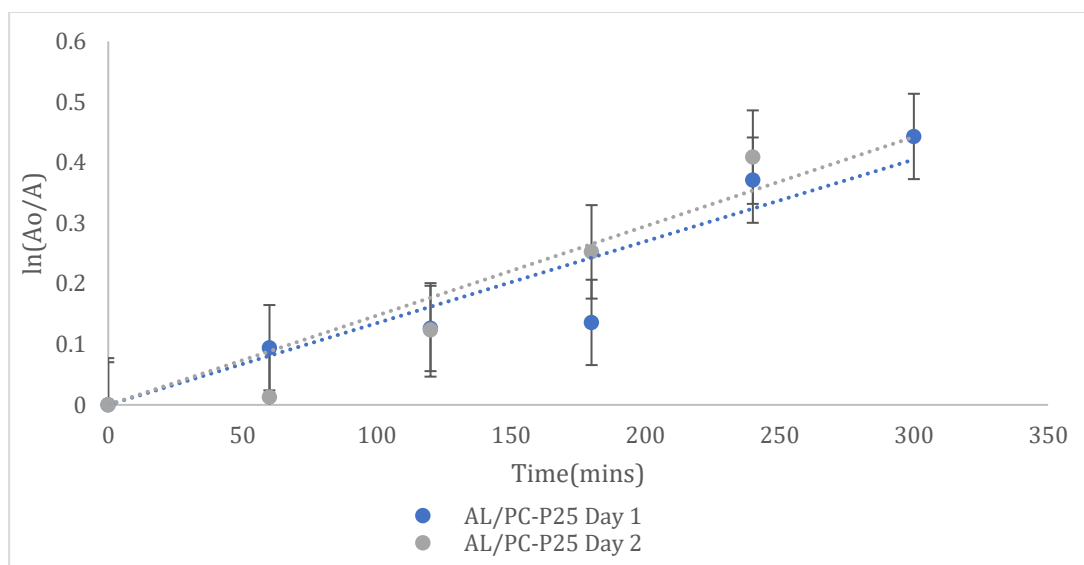


**Figure V-11: Degradation of 0.01mM MO with dual-film support crosslinked with 80%v/v CaCl<sub>2</sub> and 20%v/v amino functionalised silica over a two-day period. (Dose: 0.25mg of photocatalyst in 8ml of MO; at room temperature)**

The improvement in the  $k_1$  on the next day might be as a result of the onset of swelling brought on by the alginate network beginning to fail. There was no apparent physical attrition of the films, nor was there any physical sedimentation of P25 at the bottom of the petri dish at the end of the second day. This could mean that the film could still be reused for more photocatalytic sessions before complete disintegration of the alginate network occurred.

**Table V-10: Calculated pseudo-first-order constant ( $k_1$ ), half-life  $t_{1/2}$  and  $R^2$  value of the samples in Figure V-11 following their MO degradation abilities.**

Sample	$k_1$ (min <sup>-1</sup> )	$t_{1/2}$ (min)	$R^2$ value
AL/PC-P25 Day 1	$1.3 \times 10^{-3}$	533.19	0.8889
AL/PC-P25 Day 2	$1.5 \times 10^{-3}$	462.09	0.9013

### V.7.2 Results of the Photocatalytic degradation of Triton (TX-100)

This section will focus on the degradation behaviour of the dual support films on TX-100. All of the samples used for the degradation of TX-100 would have been crosslinked with 80%v/v of CaCl<sub>2</sub> (1wt% concentration) and 20%v/v of the amino functionalised silica sol as this was the crosslinker formulation that offered stability and reasonable photocatalytic ability of the dual films investigated so far.

### V.7.2.1 Effect of a blank dual-film on the photocatalytic removal of TX-100

Before the photocatalytic breakdown of TX-100 could be documented, it was necessary to carry out checks on a blank sample, i.e. a sample that contained the necessary compositional element minus the photocatalyst (P25). The sample 9AL 1VA/T8PC 2AC was used as a blank sample. Its degradation behaviour was plotted using the first-order model (Figure V-12). It showed negligible TX-100 removal.

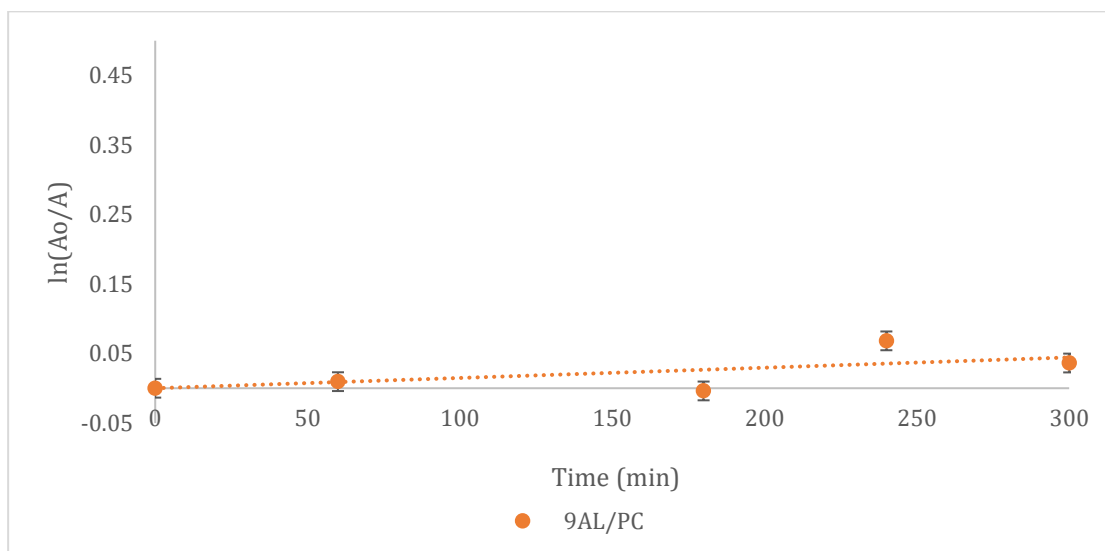


Figure V-12: Degradation of 0.01mM TX-100 with dual-film support in the absence of P25 at room temperature. Dose: no photocatalyst in 8ml of TX-100.

Therefore, one can conclude, that the photocatalytic abilities of the dual-film are negligible without TiO<sub>2</sub> guest particles .

Table V-11: Calculated pseudo- first-order constant ( $k_1$ ), half-life  $t_{1/2}$  and R<sup>2</sup> value of the sample in Figure V-12 following its TX-100 degradation abilities.

Sample	$k_1$ (min <sup>-1</sup> )	$t_{1/2}$ (min)	R <sup>2</sup> value
9AL/PC	$1.0 \times 10^{-4}$	6931.47	0.4393

### V.7.2.2 Effect of the dual-film composition on the photocatalytic removal of TX-100

Here, the effect of changing the base layer of the film was investigated, with two of the main formulations of base layers: AL-P25 and 9AL-P25. The top layer (PC) was kept constant for both. Figure V-13 and Table V-12 shows that after TiO<sub>2</sub> (P25) inclusion there is positive MO removal. It is clear that both of the samples show positive degradation results, compared to when the films were used without P25 (as seen in Figure V-12).

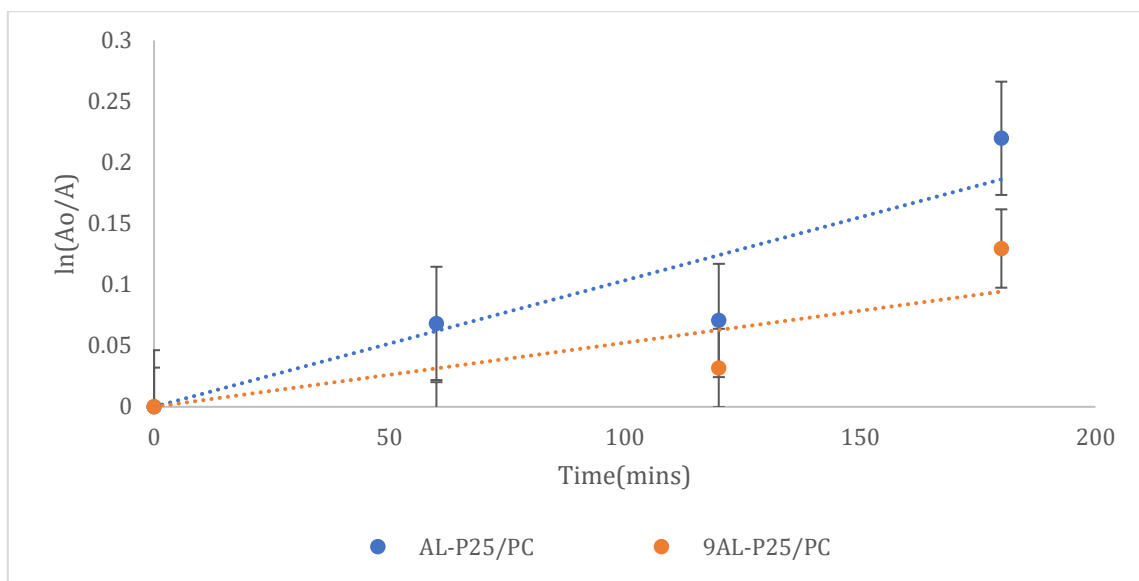


Figure V-13: Degradation of 0.01mM TX-100 with dual-film support containing P25 at room temperature. Dose: 0.25mg of photocatalyst in 8ml of TX-100.

AL-P25 appears to have superior properties compared to 9AL-P25. Table V-12 seems to suggest that their rate constant value increased by 100% in favour of the AL-P25 formulation. As such, its half-life is about half of the time it would have taken 9AL-P25 to break down the original concentration of TX-100.

Table V-12: Calculated pseudo-first-order constant ( $k_1$ ), half-life ( $t_{1/2}$ ) and  $R^2$  value of the samples in Figure V-13 following their TX-100 degradation abilities

Sample	$k_1$ ( $\text{min}^{-1}$ )	$t_{1/2}$ (min)	$R^2$ value
AL -P25/PC	$1.0 \times 10^{-3}$	693.14	0.844
9AL-P25/PC	$5.0 \times 10^{-4}$	1386.29	0.6689

### V.7.2.3 Effect of algae inclusion on the photocatalysis of TX-100

In this section, we begin to explore the potential of utilising the different composition of the dual-film layers, aside from providing buoyancy support and housing the P25. CV was introduced to the samples here, to be utilised as a producer of oxygen into the system to help spur the catalytic breakdown that might be slowed down due to a lack of dissolved oxygen in the system. The samples here are divided into two. In one half, P25 was incorporated into the bottom layer (in V.7.2.3.1) and in the other, it was instead assimilated into the top layer (V.7.2.3.2).

#### V.7.2.3.1 P25 on the bottom layer of the dual-film

Figure V-14 shows the degradation behaviour of samples that have CV incorporated in the bottom layer. Both of the samples in question AL-CV-P25/PC and 9AL-CV-P25/PC appear to follow the pseudo-first-order reaction model better than the samples seen in Figure V-14. Despite this, AL-CV-P25/PC offers a much better photocatalytic performance than the alternative samples, even

considering the fact that its rate constant had actual dropped with the addition of CV to the formulation (in Table V-13).

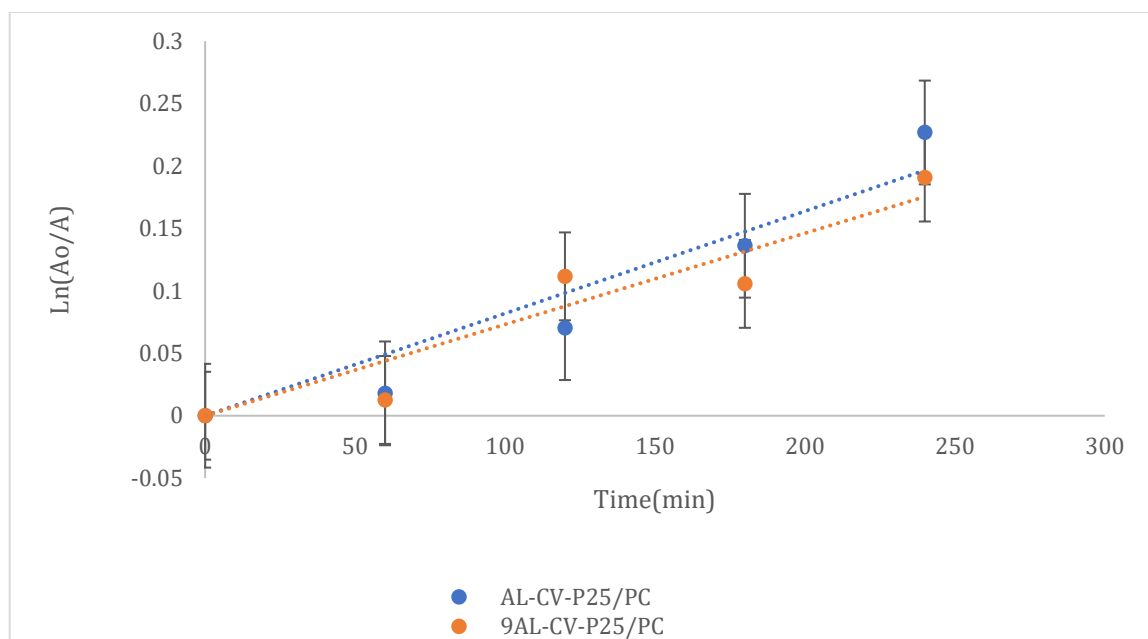


Figure V-14: Degradation of 0.01mM TX-100 with dual-film support containing P25 and CV at room temperature. Dose:0.25mg in 8ml of TX-100

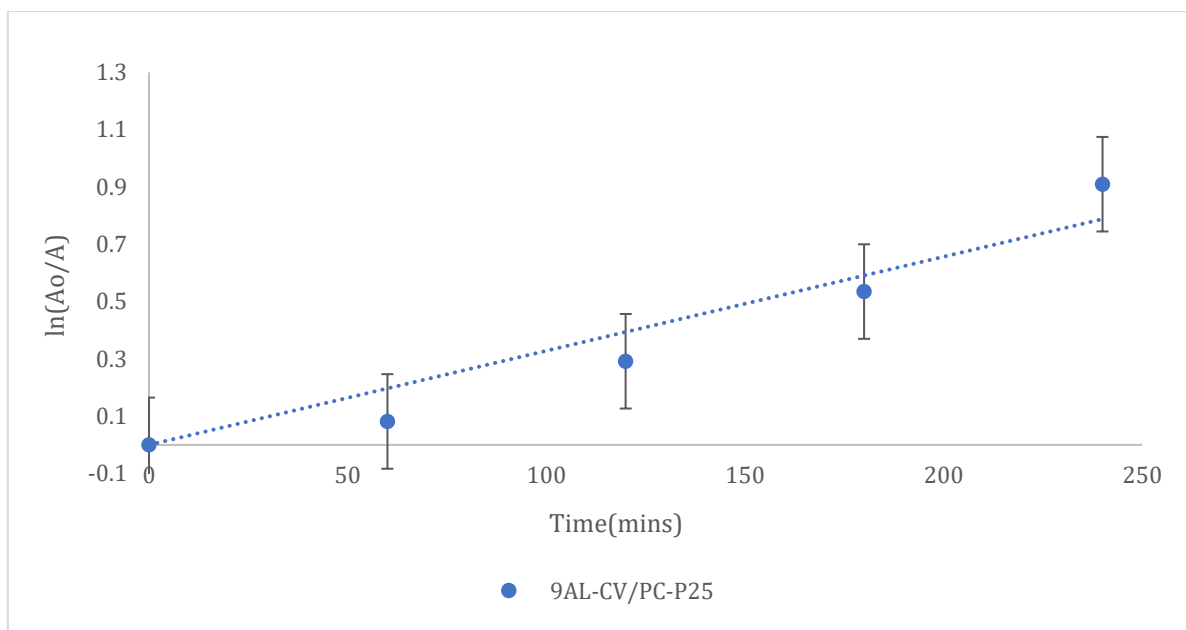
There are several improvements in Figure V-14 and Table V-13 brought on by adding CV overall:  $k_1$  of 9AL-CV-P25/PC going up by 40%.

Table V-13: Calculated pseudo- first-order constant( $k_1$ ), half-life ( $t_{1/2}$ ) and  $R^2$  value of the samples in Figure V-14 following their TX-100 degradation abilities

Sample	$k_1$ ( $\text{min}^{-1}$ )	$t_{1/2}$ (min)	$R^2$ value
AL-CV-P25/PC	$8.0 \times 10^{-4}$	866.43	0.9185
9AL-CV-P25/PC	$7.0 \times 10^{-4}$	990.21	0.9008

#### V.7.2.3.2 Inclusion of P25 on the top layer of the dual-film

The sample detailed in this section also has the CV content on the bottom layer, while P25 was contained on the top layer. The photocatalytic degradation of TX-100 by 9Al-CV/PC-P25 is shown in Figure V-15 and Table V-14. As with the other samples, a pseudo-first-order model is followed (except that the linear plot of  $\ln A_0/A$  versus  $t$  plot did not go through the origin which could mean an order other than 1).



**Figure V-15: Degradation of 0.01mM TX-100 with dual-film support containing P25 and CV at room temperature. Dose: 0.25mg in 8ml of TX-100.**

It should be noted that the best performance of all the samples studied can be seen in Figure V-15 and Table V-14. As this sample had P25 positioned on the top layer rather than the bottom, its position might be the cause of such a positive improvement in the rate of photo-degradation of TX-100.

**Table V-14: Calculated pseudo- first-order constant ( $k_1$ ), half-life ( $t_{1/2}$ ) and  $R^2$  value of the samples in Figure V-15 following its TX-100 degradation abilities**

Sample	$k_1$ ( $\text{min}^{-1}$ )	$t_{1/2}$ (min)	$R^2$ value
9AL-CV/PC-P25	$3.0 \times 10^{-3}$	210.04	0.9235

#### V.7.2.3.3 Effect of CV in sunflower oil inclusion of the photocatalysis of TX-100

The sample in this section had CV suspended in sunflower oil, before being cast into the bottom layer. Contained in Figure V-16 and Table V-15 is the degradation behaviour of the sample. It appears to be quite linearly following the pseudo-first-order model, with a good  $k_1$ .

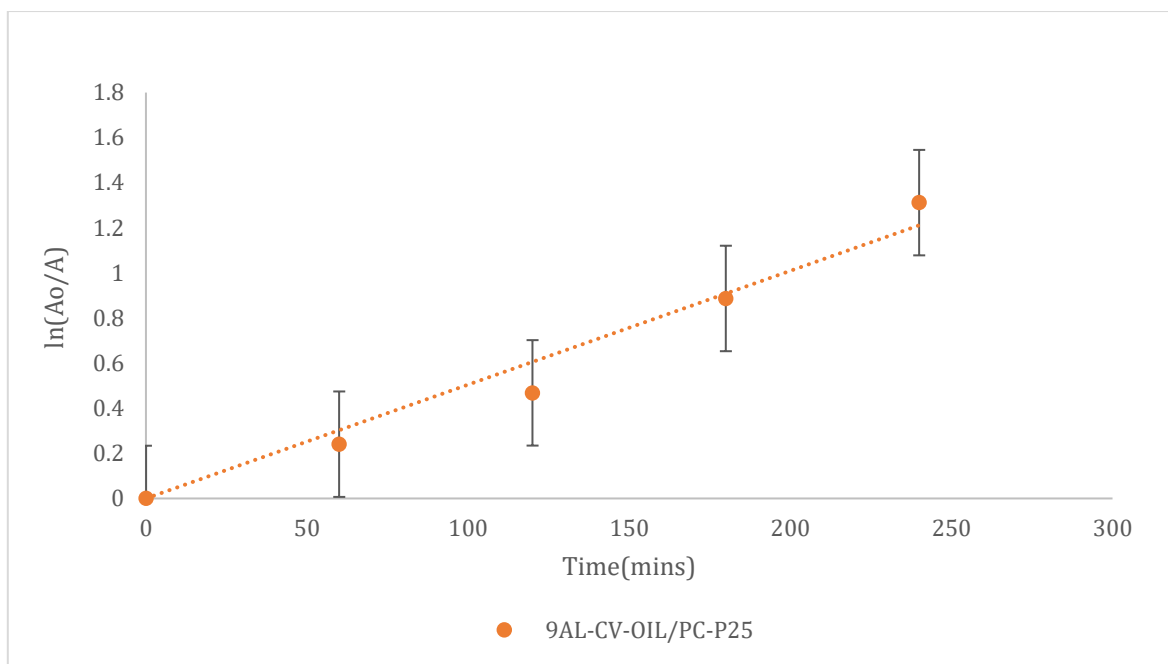


Figure V-16: Degradation of 0.01mM TX-100 with dual-film support containing P25 and CV in oil at room temperature. Dose: 0.25mg of photocatalyst in 8ml of TX-100.

It has a half-life of 138min.

Table V-15: Calculated pseudo first-order constant( $k_1$ ), half-life ( $t_{1/2}$ ) and  $R^2$  value of the samples in Figure V-16 following their TX-100 degradation abilities

Sample	$k_1$ ( $\text{min}^{-1}$ )	$t_{1/2}$ (min)	$R^2$ value
9AL-CV-OIL/PC-P25	$5.0 \times 10^{-3}$	138.62	0.9695

### V.7.3 Electron microscopy of dual-film samples

Following the assessment of the photocatalytic performance of the dual-film, this section will look at the morphological features of the film and perhaps help one gain a better understanding of how its morphology might have influenced the photocatalytic performance.

#### V.7.3.1 9AL/PC system

The blank film sample 9AL/PC will be studied. Micrographs of the top and bottom sides of the film can be seen in Figure V-17 below.

One can see that the top layer of the film (b) is smoother than the interesting web like network displayed by the bottom layer in Figure V-17a (and inset). The network likely reflects the majority alginate blend that comprises the bottom layer.

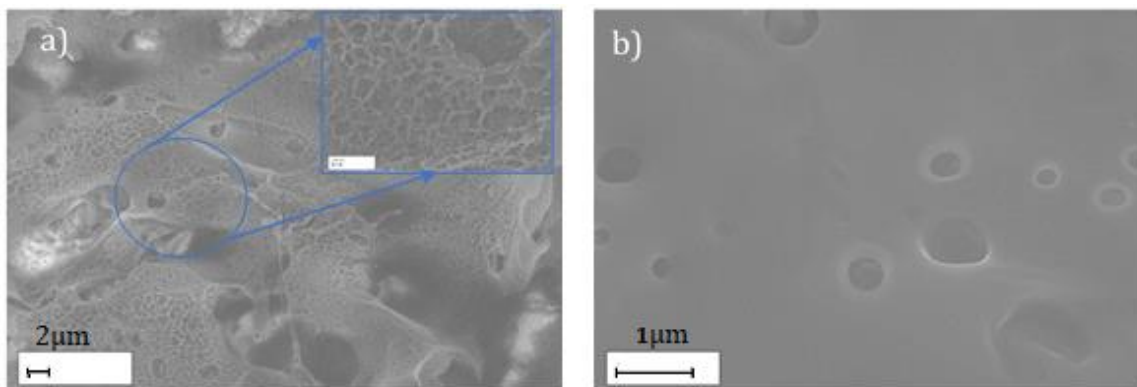


Figure V-17:SEM of the 9AL/PC dual-film system: the base layer a); and top layer b)

The interaction of the bottom layer with the glass slide, and the extended crosslinking might have prevented the network from collapsing in on itself, keeping it stretched out even in the wake of an enhanced interaction promoted by the different crosslinking agents utilised. Another important feature present, this time in the top layer, is the presence of pores that are dotted throughout its almost unblemished exterior. This might just be the effect of the solvent mix (DCM) evaporating at ambient temperatures. Not only do the pores appear in the top layer they also appear to extend through to the bottom layer.

The presence of the pores and open network means that the structure can display some permeability to gas as well as liquids. This is advantageous as  $O_2$ , necessary in the generation of radicals on the  $TiO_2$  catalyst surface, is readily available.

#### V.7.3.1.1 9AL/PC- P25

The incorporation of P25 into the top layer of the dual-film, is shown in Figure V-18. As we found in section V.7.1.3.1.1, the placement of P25 either in the bottom or top layer had an impact on the photocatalytic rate constant. The best sample had P25 in the top layer.

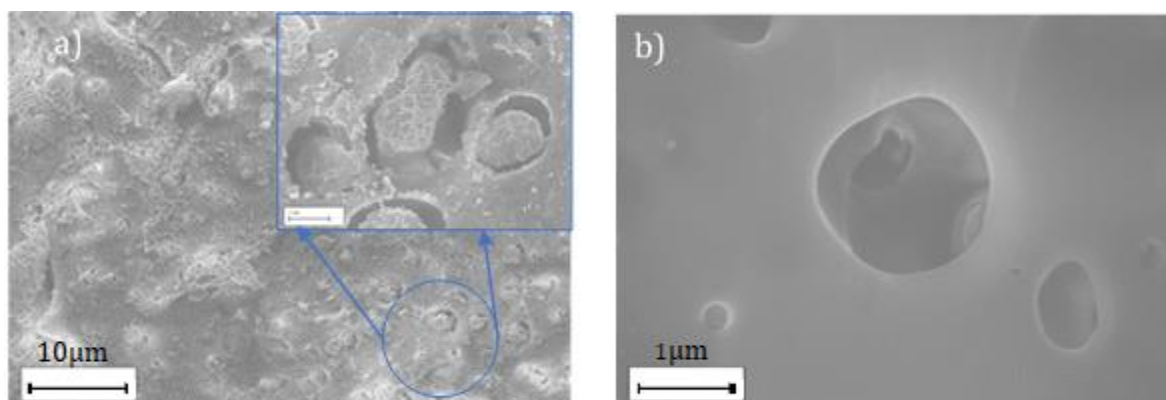


Figure V-18:SEM of the 9AL/PC-P25 dual-film showing the base layer a); and the top layer b)



Figure V-18a (& inset) shows that though P25 was incorporated into the top layer, it still appeared in the base layer. This is where the deposition process might have caused this interesting phenomenon in the highlighted circle from Figure V-18a. The casting process of the top layer and P25 was done directly onto the hydrophilic layer 9AL, which was first cast onto a glass slide. This means that the P25 fraction sank faster due to gravity, and with the action of the solvent (DCM) could go further as it partially dissolved the base layer, thus finishing in the base layer. Now, in the action of casting the top layer, the bottom/base layer would disperse around these raised edges of the slower dissolving top polymer layer and P25. This means that while P25 was incorporated in the top layer, it is now instead evident in the bottom and could actually interact better with the pollutant than if it was farther away in the top layer.

The top layer shown in Figure V-18b appear quite smooth, telling us that this is a particular feature of the primarily hydrophobic layer. It is not clear if there is intermixing of the layer which FTIR in V.7.4 also suggests.

#### V.7.3.1.2 9AL-CV-P25/PC

In Figure V-19, CV has been incorporated in the bottom layer along with P25. The presence of the spherical CV cells (Figure V-19a & inset) is apparent in the bottom section (in spite of the extensive rinsing processes to neutralise the effect of the crosslinking agents present, and any other unevaporated solvent).

The smoothness and voids of the top layer are also present here in Figure V-19b, as the formulation of that layer has not been radically changed. Some of the pores however appear to have been blocked by the CV cells (see the highlighted circle in Figure V-19b).

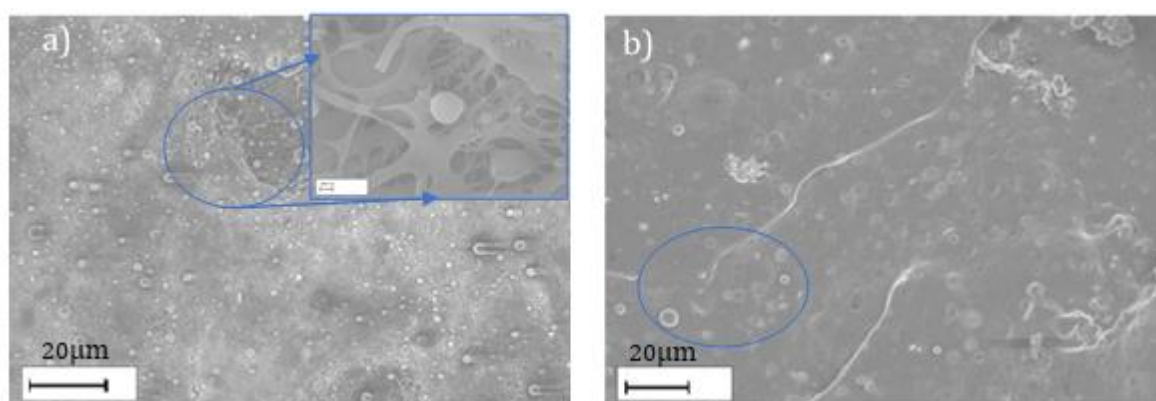


Figure V-19: SEM of the 9AL-CV-P25/PC dual-film showing the base layer a); and the top layer b)

#### V.7.3.2 AL/PC system

Other than a change in the blend proportion of the bottom layer, this dual-film system was assembled in exactly the same manner as in the previous section V.7.3.1.

#### V.7.3.2.1 AL/PC-P25

Quite similar to its corresponding partner in section V.7.3.1.1, the morphology of the assembled dual-film appears again to be broadly divided into two sections (see Figure V-20a & b). While the top layer pictured in Figure V-20b remain smooth, with cavities randomly present in (Figure V-20a) the expanded network structure of the bottom layer, P25 can still in obvious areas (see blue circle in Figure V-20a).

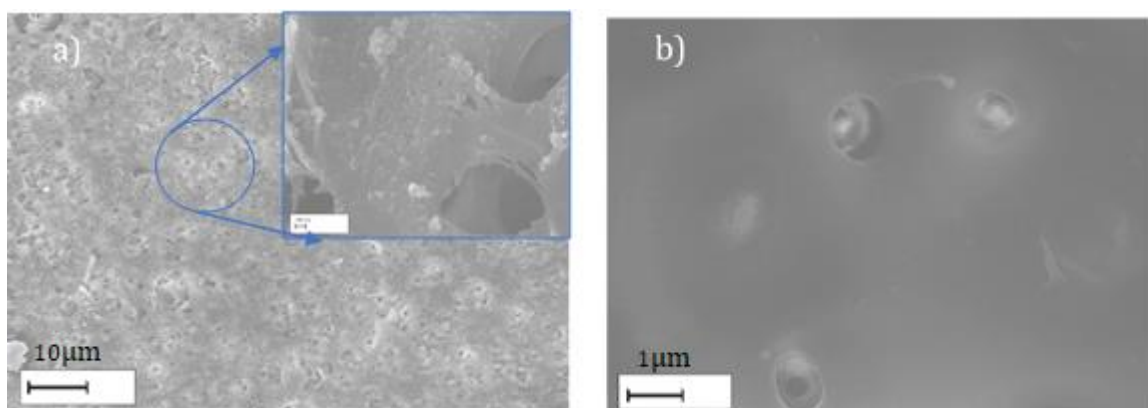


**Figure V-20: SEM of the AL/PC-P25 dual-film system's base layer a); and top layer b)**

The actual difference between this sample and its equivalent from V.7.3.1 shows us that the modification of the blend proportion in favour of more PVA is not superficially obvious. And perhaps this could explain why the improvement in the photocatalytic activity seen in sections V.7.2.2, V.7.2.3.1, V.7.1.2.1, V.7.1.2.2 are underwhelming.

#### V.7.3.2.2 AL-CV-P25/PC

The samples in Figure V-21 contains some CV in the bottom layer, along with a dispersion of P25. The CV content is easily discerned from Figure V-21a (& inset), appearing in clusters of multiple cells highlighted by the blue circle. On the top layer, shown in Figure V-21b, a same smooth exterior with pores spread over is surface, is again apparent. It appears that the formula modification had little to no visible effects on the morphology as suggested by the image above.

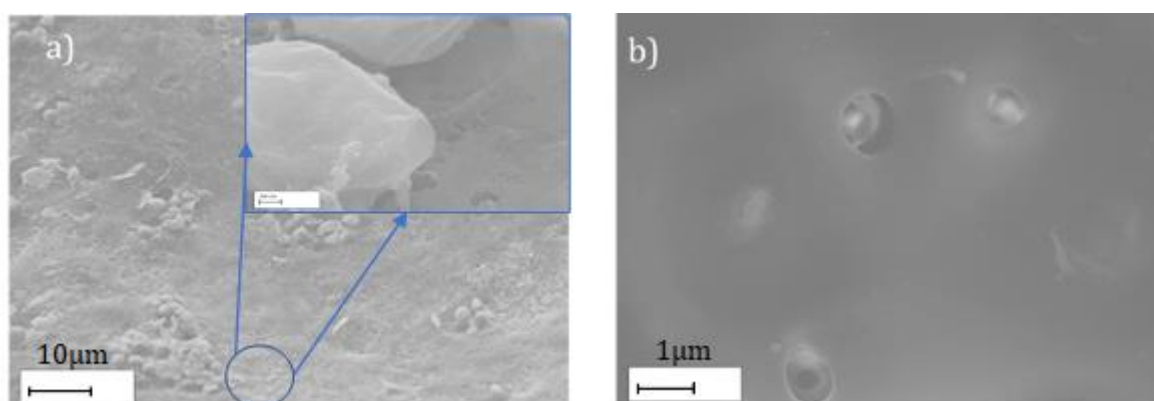


**Figure V-21: SEM of the AL-CV-P25/PC dual-film system showing the base layer a); and the top layer b)**

### V.7.3.3 Embedded RR replicas

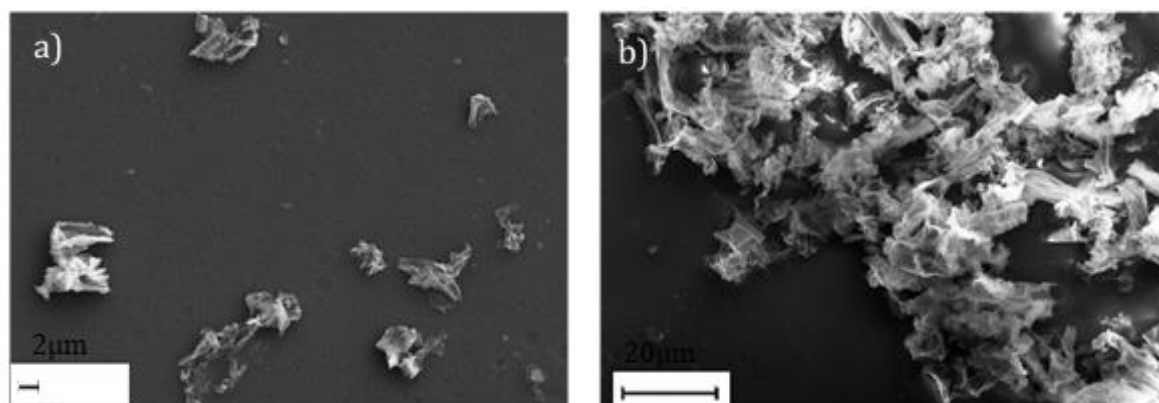


Figure V-22: SEM of embedded titania replica samples (a & b)

If one looks closer at the top-right corner of the SEM micrograph in Figure V-22a, one can observe that some of the replica is completely covered by the polymer. No doubt this would mean that some photocatalytic activity would be lost thanks to the complete immersion in the polymer, as more of the active site of the catalyst will be blocked. Also, in Figure V-22b, the overlap and accumulation of the replicas would also further reduce the activity as the pollutant and UV radiation might have penetration problems.

### V.7.4 Infrared analysis of the dual-film systems

As a further means of analysing of the identity of the films, bearing in mind that each of the dual layer is a blend, as well as to highlight the distinctiveness of each layer, infrared studies were carried out on two of the main samples. The samples utilised were devoid of the photocatalyst and CV to help simplify the spectrum produced.

Infrared was done by simply placing one side of the dual-film close to the ATR, and following this, a reading of the secondary side was also carried out in the same manner. The side/layer with the designation “Top” theoretically represents the PC fraction of the film, and the layer named “Base” belongs to AL.

Starting with AL/PC, in Figure V-23, the individual components of the dual-film seems to have allotted each of the layers a unique character, confirming that the distinctiveness of each layer has been maintained in the film assembly process.

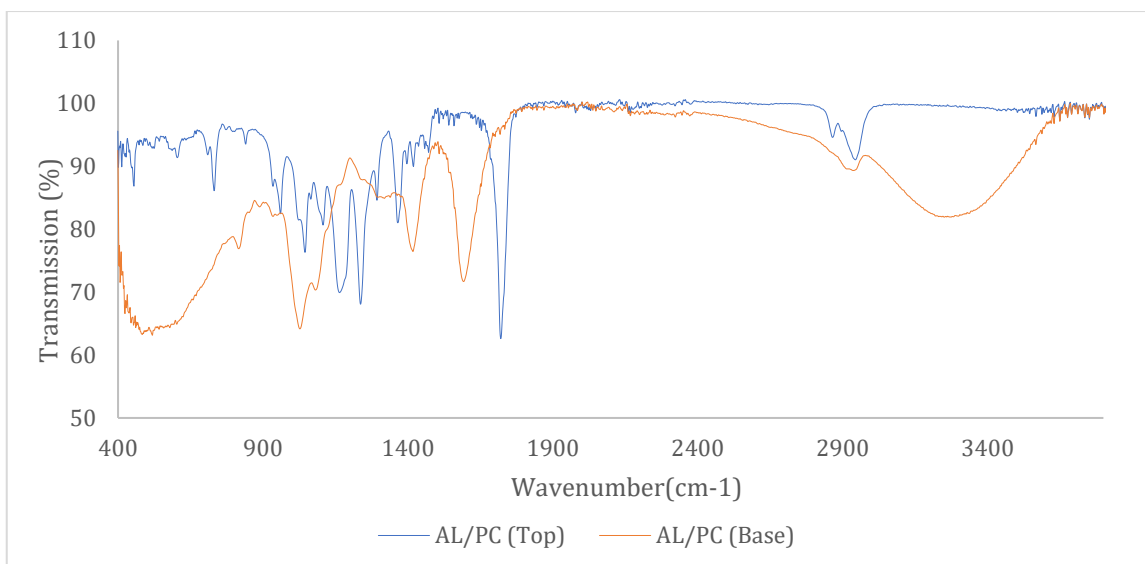


Figure V-23: FTIR spectra of AL/PC dual-film system's top layer and base layer.

As the top layer consists primarily of PC and AC, it is to be expected that the bands present in the figure above would be easily ascribable to PC. This is true, as PC has been shown to exhibit infrared bands as given in Table V-16:

Table V-16: IR band assignments for polycaprolactone (PC) (Elzein et al., 2004; Jung et al., 2015; Shkarina et al., 2018)

Wavenumber (cm <sup>-1</sup> )	Band assignment
1157	C-O and C-C
1170	C-O-C
1190	OC-O
1236	C-O-C
1293	C-O and C-C
1720	C-C and (=O)-O
2870 & 2960	CH <sub>2</sub>

The top side appears to consist solely of PC, judging by the presence of the bands which correspond to those found in literature (Elzein et al., 2004; Jung et al., 2015; Shkarina et al., 2018). Typically, the main characteristic peaks for PC tend to lie between 1000-1800cm<sup>-1</sup>, along with the two characteristic bands at about 2860 cm<sup>-1</sup> and 2960cm<sup>-1</sup>(Shkarina *et al.*, 2018). All of these bands are present meaning that the identity of the top layer has been preserved, with no palpable modification of its chemical groups.

The same can be said for its base layer, it contains peaks that are assignable to that of alginic salts (AL) (Leal *et al.*, 2008; Daemi and Barikani, 2012; Wang *et al.*, 2014). There is a broad band that lies between 3600-3000cm<sup>-1</sup> assigned to O-H that is hydrogen bonded. Then there is a relatively weak signal between 2850-2920cm<sup>-1</sup> belonging to aliphatic C-H. At 1593cm<sup>-1</sup> and 1417cm<sup>-1</sup> are

bands belonging to carboxylate ions: O-C-O, C-OH. 815  $\text{cm}^{-1}$  and 1022  $\text{cm}^{-1}$  are related to the mannuronic acid and the link that exists between it and guluronic acid residue. In spite of the bottom layer being made with some PVA, there appears to be no signal suggesting its presence.

**Table V-17: FTIR band assignments for Alginate (Leal et al., 2008; Wang et al., 2014)**

Wavenumber ( $\text{cm}^{-1}$ )	Assignment
815	C-H
1022	C=C, OC-OH
1078	C-O and C-C pyranose ring
1417	O-C-O
1593	O-C-O
2850-2920	C-H
3000-3600	O-H

In Figure V-24, the same scenario is repeated. Both the distinctiveness of the layers in addition to the fact that the spectra gives the impression that each layer is pure as observed. So, the increased fraction of AL in 9AL/PC appears to have caused almost no noticeable change in the IR signal of the dual-film.

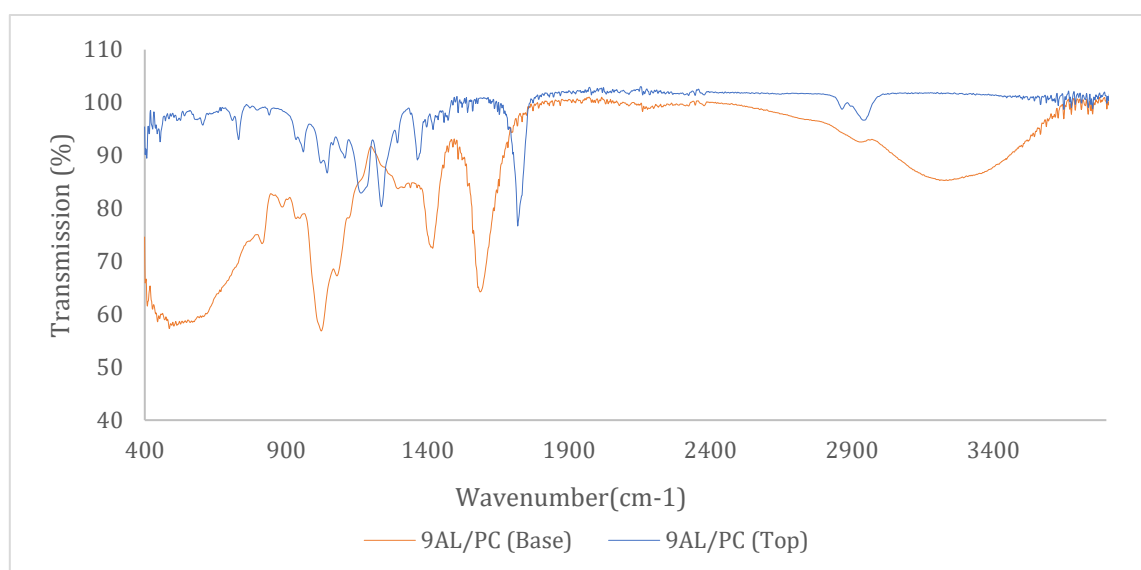


**Figure V-24: IR spectra of 9AL/PC dual-film system's top layer and base layer.**

## V.8 Summary

### V.8.1 Photocatalytic performance

#### V.8.1.1 Degradation of Methyl Orange (MO) by P25 supported floating films

The photocatalytic performance of the dual-film was demonstrated to be affected by several factors. These include the composition of the blends, the crosslinking conditions and the type of crosslinker used. Each of these affected the eventual breakdown of the 0.01mM of solution when

exposed to a UV lamp.

- Effects of film composition

Concerning the composition of the dual-film, the base layer was kept constant while the top layer was altered for easier monitoring. Only two main blends of the base layer were utilised 7AL and 9AL. In the former case, two blends for the top layer were considered; AC-P25 and PC-P25. The most successful of these was AL/PC-P25 which had a rate constant of  $1.3 \times 10^{-3} \text{min}^{-1}$ , compared to  $9.0 \times 10^{-4} \text{min}^{-1}$ . Switching the base layer to one with a higher alginate content, 9AL also resulted in the top layer of PC-P25 having a better rate constant value of  $9.0 \times 10^{-4} \text{min}^{-1}$  than the  $8.0 \times 10^{-4} \text{min}^{-1}$  of AC-P25. This might just be down to the composite stability.

- Effect of crosslinking conditions

In terms of the crosslinking conditions, two different crosslinkers were trialled,  $\text{CaCl}_2$ , amino functionalised silica sol crosslinking, and a mixture of both. Samples that had been crosslinked with  $\text{CaCl}_2$  showed far better photocatalytic efficiency. Indeed, 9AL/AC-P25 and 9AL/PC-P25 both had rate constants that were  $2.3 \times 10^{-3} \text{min}^{-1}$  and  $1.9 \times 10^{-3} \text{min}^{-1}$ . These are the best values that were obtained for any of the dual-film samples trialled. The reason, as previously discussed in section V.7.1.3.1.2 was down to the relatively weak stability of the  $\text{Ca}^{2+}$  crosslinked alginate salt. It is thought that the network is easily attacked, especially by chelating agents which can then remove  $\text{Ca}^{2+}$  from the network, encouraging swelling and distortion of the network (Mørch, Donati and Strand, 2006; Pannier *et al.*, 2014). This will ultimately lead to the release of the tightly bound photocatalyst that previously had most of its active sites covered by the alginate, ultimately resulting in an increase in photocatalytic efficiency. In addition to the improved MO breakdown, the leaking of the photocatalyst-alginate sediments is not entirely desirable especially when considering the toxic nature of nanoparticles.

Conversely, one can also see why the samples that have been crosslinked with the amino functionalised silica method consistently exhibited values that were lower than that crosslinked with  $\text{CaCl}_2$ . 9AL/AC-P25 and 9AL/T8PC-P25 this time crosslinked with amino functionalised silica had rate constants of  $8.0 \times 10^{-4} \text{min}^{-1}$  and  $9.0 \times 10^{-4} \text{min}^{-1}$ . The results serve as an indicator of how much more stable these films are to the  $\text{CaCl}_2$  crosslinked batch. Pannier and co (2014) thought that the stability was down to the strong interaction between the carboxylate group of the alginate network and the cationic group of the silica sol during synthesis, which upon condensation creates a reinforced network that now consists of silica and alginate. Because of this, there is less chance that the network will deteriorate, or suffer from widening pores and so forth. The photocatalyst will thus remain stuck in place, with most of its active surface hidden, improving the dual-film longevity but affecting its photocatalytic efficiency. Another downside to

using amino functionalised silica sol as a crosslinker was the fragile nature of the films.

To combat low efficiency of these films, mixing of crosslinkers was proposed to address this problem, while ensuring the films maintained their efficiency. A mix with 80%v/v  $\text{CaCl}_2$  -20% v/v amino functionalised silica sol, and 60% v/v  $\text{CaCl}_2$  – 40% v/v amino-functionalised silica sol. There was hardly any improvement to the level of just using  $\text{CaCl}_2$  alone in terms of rate constants with values of between  $7.0\text{-}9.0 \times 10^{-4} \text{min}^{-1}$  still occurring. The film here were more robust.

It appears that the dual-films are capable of demonstrating photocatalytic efficiencies as high as  $2.3 \times 10^{-3} \text{min}^{-1}$  and as low as  $4.0 \times 10^{-4} \text{min}^{-1}$  in terms of MO breakdown. However, obtaining the higher values required a sacrifice on the part of the films structural integrity as we saw while crosslinking with  $\text{CaCl}_2$  alone, whereas attempting to improve the integrity drastically decreased the photocatalytic efficiency. Clearly, the type of crosslinker used and the conditions is key to creating a dual-film with appreciable physical integrity and efficiency.

- Degradation of methyl orange (MO) by RR replica supported floating films

Finally, singling out the samples made with the replicas rather than P25, one can see that there was a drastic reduction in the rate constants compared to those discussed in the previous chapter. The drop in efficiency is partially affected by the morphology of the replica samples and their positioning on/in the film. Already one can rightly say that the replicas are self-supporting i.e. the titania phase is supported by the calcite phase. One can also see that P25 supported in/on the films had lost some of its efficiency, as opposed to if it was used as a loose powder. This may be linked to the blockage of some of its active sites. If P25 suffered such a reduction, then RR with its already compromised polymorphic and overall composition would be doubly affected as its “twice supported” surface would have more of its active sites covered. Perhaps, if it was morphologically similar to P25, then this issue would not have arisen.

#### ***V.8.1.2 Degradation of triton-TX100 by P25 floating films***

Against Triton-TX100, the films show some activity bearing in mind that the formulations were kept to AL/PC and 9AL /PC, with only the position of P25 and CV that were varied in this section. With regards to AL-P25/8PC and 9AL-P25/8PC from V.7.2.2, the rate constants were  $1.0 \times 10^{-3} \text{min}^{-1}$  and  $5.0 \times 10^{-4} \text{min}^{-1}$  respectively. The incorporation of algae in the form of CV within the base layer produced rate constants of  $8.0 \times 10^{-4} \text{min}^{-1}$  and  $7.0 \times 10^{-4} \text{min}^{-1}$  (for AL-CV-P25/PC and 9AL-CV-P25/PC). Yet again the AL/PC system seems to have proven more effective in the breakdown of the surfactant, compared to 9AL/PC system, a telling indicator of the superiority of one sample system over the other. It appears that the movement of P25 to the layer proved to be a positive in terms of the photocatalytic efficiency of the dual-film. The sample 9AL-CV-P25/PC was shown to have a rate constant of  $3.3 \times 10^{-3} \text{min}^{-1}$ , purporting to having caused an

improvement of about 371% with regards to all the systems made with 9AL/PC. Clearly, the repositioning of P25 was enough to cause such a substantial change. As we came to see and discussed in section V.7.3.1.1, the incorporation of P25 on the top layer still led to a deposition quirk where the photocatalyst was actually held out through openings into the bottom layer where it then had better access to the surfactant solution. It is thought that this was enough to improve the efficiency drastically.

The enhancement was also seen for 9AL-CV -OIL/8PC-P25, which had a rate constant of  $5.0 \times 10^{-3} \text{min}^{-1}$ . Clearly several mechanisms must be at work here. As well as the obvious photo-induced surface reaction between the photocatalyst and TX-100, it is possible that the oil present also had a reinforcing effect, and this might be in conjunction with CV. A separate experiment on CV growth, not included in this thesis, showed that the presence of sunflower oil caused the CV to undergo accelerated growth rate, within the first 5h. It is likely that this might have ramped up the production of dissolved oxygen within the system, creating more fuel to undergo reduction at the photocatalyst surface. The resulting products can then go on to break down more TX-100 molecules, accelerating its breakdown.

### V.8.2 Infrared spectroscopy

Infrared characterisation was carried out on AL /PC and 9AL/PC. Although each layer of the dual-films were made up of multiple components, as it turned out, IR spectroscopy was only able to pick just the peaks that pertained to the majority component of the films. The top layer only showed IR bands that belonged to groups that are standard in PC (see Table V-16). The homogeneity of the base layer were confirmed; both of which produced IR signals belonging to alginic salts.

Clearly, the film assembly and crosslinking process was not enough to drastically alter the characteristic of dual-film. In fact, it appeared that each layer still maintained its own distinctiveness.

### V.8.3 Scanning electron microscopy

The distinctiveness was expressed in section V.7.3. The micrographs showed the difference between the top and the base layer. The top layer consisting of the formulation 8PC 2AC was smooth, with the presence of voids believed to have been caused by the evaporation of the carrier solvent in the ambient atmosphere. The morphology of the top layer was common in all of the samples investigated: 9AL/PC, 9AL/PC-P25, 9AL-CV/PC, AL/PC-P25, AL -CV-P25/PC.

For the base layer, the fact that most of the samples essentially had a majority AL content compared to VA meant that the morphologies of the layers was also similar all round. In opposition to the top layer, the base layer had a network/web type morphology that was quite



stretched out. On the micrographs, there were certain areas that were clear of the network, Figure V-17a and Figure V-18a. This is because of the shrinking triggered during the crosslinking process. Since the layer was deposited in a solvent mix of acetic acid, certain segments would have embedded into the partially dissolved top layer. This imbedded part would constitute the stationary segment that does not have enough freedom to shrink, causing a stretched-out network, with at times patchy coverage.

Where P25 has been included in the samples, its presence does not elicit too much of a drastic change in the appearance of the film. For example, when it has been included in the top layer such as that seen in Figure V-18a, the particles can be seen to have gone through the top layer and into the base layer, away from the polymer/air surface, but in the polymer/pollutant interface. In the inclusion of P25 in the base layer, visualisation is a lot harder. In Figure V-19a and Figure V-21a, although it is possible to pick out some submicron particulates, that are not CV, it is harder to say if this is just part of the morphology of the base layer, or if it is P25.

The inclusion of CV also elicited minimal changes in the morphology. Other than the presence of these microorganism, the overall appearance of the dual-film structures were still consistent with the films having no CV in them.

## V.9 Conclusion

Several aims were set out in this section, the first of which was to formulate a film that could produce a result that was better than merely having loose particulates, such as that investigated with P25 dispersed in just a cuvette with MO. A spectrum of samples were trialled, the best of which had a rate constant of  $0.0023\text{min}^{-1}$ . Comparison between both experiments is not straight forward, as the first experiment utilised 0.25mg in 2.5ml of MO, while the samples here utilised 0.25mg in 8ml.  $0.004\text{min}^{-1}$  was the rate constant to be beaten, the value obtained here was half of this which is still quite reasonable; this is true considering that the pollutant amount increased by almost 4x, not to mention the effects of having a certain number of its active site blocked by the supporting polymer. But were we to attempt such a comparison then the following is assumed true:

In the case of the loose samples, 0.25mg of photocatalyst was dispersed in 2.5ml of MO, which is the same as 0.1mg/ml of MO. While for the film sample, 0.25mg embedded in a polymer was used to degrade 8ml of MO, which is equivalent to 0.03mg/ml of MO.

Since the loose sample has a rate constant of  $0.004\text{min}^{-1}$ , then by equivalency 1mg/ml could theoretically have a rate constant of  $4.0 \times 10^{-2}\text{min}^{-1}$ . In the same way, 1mg/ml of the film samples would have a rate constant of  $7.0 \times 10^{-2}\text{min}^{-1}$ .

The calculation shows that the film sample are far superior, but again this was if one uses the best

possible case scenario: sample 9AL/AC-P25, where crosslinking was done with CaCl<sub>2</sub> only (see section V.7.1.3.1.1). While one of the worst cases would yield a rate constant of  $1.0 \times 10^{-2} \text{min}^{-1}$  for 9AL-P25/PC, which is still quite appreciable.

The rate constant of the dual-films appears in certain cases to be better than that of the dispersed samples. Thus, the aim in terms of improving the dual-film design with a nanoengineered floating film has been accomplished. Also, in terms of creating a film that could be reused multiple times, Figure V-11 shows that it is possible to do just that. The rate constant across both days were even comparable.

The secondary aim for incorporating other substances in the dual-film besides the photocatalyst, CV, was successfully done. There may be some spin-offs into algal growth.

## Chapter VI Synthesis of hydroxyapatite hydrogel scaffold

### VI.1 Introduction

Following on from the synthesis of  $\text{TiO}_2$  and most importantly the effects utilising a biomimetic approach has had on its functionality, it was logical to apply a similar approach to the synthesis of a bone graft material, with a heavy emphasis on nano-scaling of hydroxyapatite and hierarchal structuring of the overall bone scaffold. The repair and management of bone injuries necessitates exploring alternative bone graft materials, seeing as both autografts and its more cumbersome counterparts (discussed briefly in section I.1.9) suffers from issues with limited supplies mainly, cost, immunogenic response, mortality of donor site, pain and surgical risks etc (Amini, Laurencin and Nukavarapu, 2012).

Bone grafts materials have included the use of ceramic based materials only (e.g. alumina ceramic, bioglass, and various calcium phosphate based ceramics (including HA) (Amini, Laurencin and Nukavarapu, 2012; Abou Neel *et al.*, 2016)), which have been trialled for use in bone repair. As is the case with most ceramics, although they have excellent strength in compression, their toughness and elastic moduli tend to make them more prone to failure (e.g. increasing the TTCP content in a TTCP/silicon composite decreased the resulting mechanical properties (Amini, Laurencin and Nukavarapu, 2012; Abou Neel *et al.*, 2016)). The same poor mechanical behaviour is experienced by porous bioglass as well (Su, Sanchez and Yang, 2012). A second category is referred to as hybrid materials. These are a combination of “two or more biomaterials” with the possibility of taking advantage of their different positives. It could be using copolymers (e.g. PLGA, PCL-PLGA, PLGA-PLLA, PCL PLA etc (Amini, Laurencin and Nukavarapu, 2012)), a blend of polymer that associate via van-der-Waals or other intermolecular interactions such as with PLGA and polyphosphazenes; or a polymer-ceramic composite taking advantage of the mechanical properties and the osteoconductive property of the ceramic, while addition aids in tailoring the overall mechanical and degradation as well (Amini, Laurencin and Nukavarapu, 2012). This is seen in scaffolds that are made of PLGA-PCL-HA (Hollinger, 2005). They are thought to have far superior osteoconducting properties compared to the use of pure polymers (Amini, Laurencin and Nukavarapu, 2012). According to Amini *et al.* (2012), the last two categories of bone graft materials are the “advanced hydrogels” and immune-modulatory biomaterial. The first of which utilises hydrogels (like PVA, collagen and gelatine), and the latter of which relies on the notion of including molecules (e.g. artificial ECM, thrombin peptide, prostaglandin etc) and adopting different morphological features that can manipulate the immunoresponse to allow tissue regeneration instead (Amini, Laurencin and Nukavarapu, 2012).

Here, as described (I.2) it was the author’s goal to adopt the ceramic-hydrogel composite approach, where it is hoped that the reinforcing and osteoconducting potential of apatitic calcium

phosphate, could work in conjunction with the mechanical tough matrix of the hydrogel. The method used to accomplish this was based on one previously developed (Taguchi, Kishida and Akashi, 1999). This involved the alternating immersion of hydrogels in an aqueous solution of (200mM) CaCl<sub>2</sub> for 2h at 37°C, followed by immersing the same polymer in a solution of (120mM) Na<sub>2</sub>HPO<sub>4</sub> again for 2h at 37°C. Depending on the amount of hydroxyapatite required, the number of cycles of immersion were varied to allow the formation and accumulation of calcium phosphate specie. One can also consider this method as being based on biomimicry, as the matrix is functionally similar to the vesicles where the initial formation of calcium phosphate nuclei occurs before deposition in osteoids-as in the formation of bone cells. In the same way, the porous and networked hydrogels resembles osteoid, with the necessary gaps to allowing the growth of blood vessels, the adhesion of cells, differentiation and possible osteogenesis of bone. In terms of nanotechnology, the matrix morphology causes the arresting of the calcium-phosphate nuclei in sizes that are nano-scaled in certain directions.

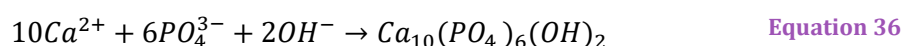
## VI.2 Aim

The main aim here was the development of a hierarchal bone graft scaffold, using the principles of biomimicry. Thus, this chapter will touch on the synthesis of the hydrogel matrix (which will serve as a synthetic equivalent of the vesicle for the concentration of calcium and phosphate ions) which will be supplied from the aqueous solution during the alternating immersion method. The hydrogel itself will be modified, with the use of glutaraldehyde and the inclusion of sodium alginate (see II.3.2 ) to improve its stability in an aqueous environment.

By the end of this chapter, the morphology of the composite, its chemical signature and the Ca/P ratio of the calcium phosphate species formed will be clarified.

## VI.3 Background Information

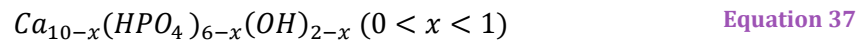
The relevant chemical reactions occurring are the wet precipitation of apatitic calcium phosphate, the crosslinking of PVA as well as sodium alginate. Wet chemistry of hydroxyapatite precipitation is the formation of apatitic calcium phosphate through a wet-precipitation route(González and Rodríguez, 2013)



The formula above provides a somewhat abbreviated summary of what is chemically occurring. We have earlier discussed the formation of a transient phase first, ACP (followed by OCP), that appears first upon precipitation before final transformation to HA.

The inclusion of carbonate was primarily to replicate CDHA (see Equation 37) (i.e. a calcium

deficient hydroxyapatite system) which is the type of apatite readily found in the body. As previously explained, the deficiency in calcium causes a charge imbalance which is known to be compensated for by carbonate substitution, protonation of phosphate. In this research, CDHA formation is guaranteed via the addition of a carbonate containing compound ( $\text{Na}_2\text{CO}_3$ ), interrupting the transformation of CDHA into the more stable HA.



Cross linked PVA is an important biomaterial with good mechanical resistance, biocompatibility and high hydrophilicity (Kamoun *et al.*, 2015). It is fairly popular in the biological field, as it has been used as artificial corneas (Xu *et al.*, 2008), repair of articular cartilage (Balgová *et al.*, 2013) and wound dressing (Kamoun *et al.*, 2015).

The dissolution of PVA granules in hot water leads to the formation of a PVA sol. It is the crosslinking of this that initiates the conversion from sol to gel consistency. The process can be accomplished in several ways: physical or chemical. The physical approach is an aging process often induced by thermal change, where the polymeric chains tangle amongst themselves, creating a physically entangled network. It usually done through a freeze-thaw sequence (Figueiredo, Alves and Borges, 2008). Chemical crosslinkage often uses glutaraldehyde as a means to immobilise the polymer chain and improved their elastic properties and durability in an aqueous environment.

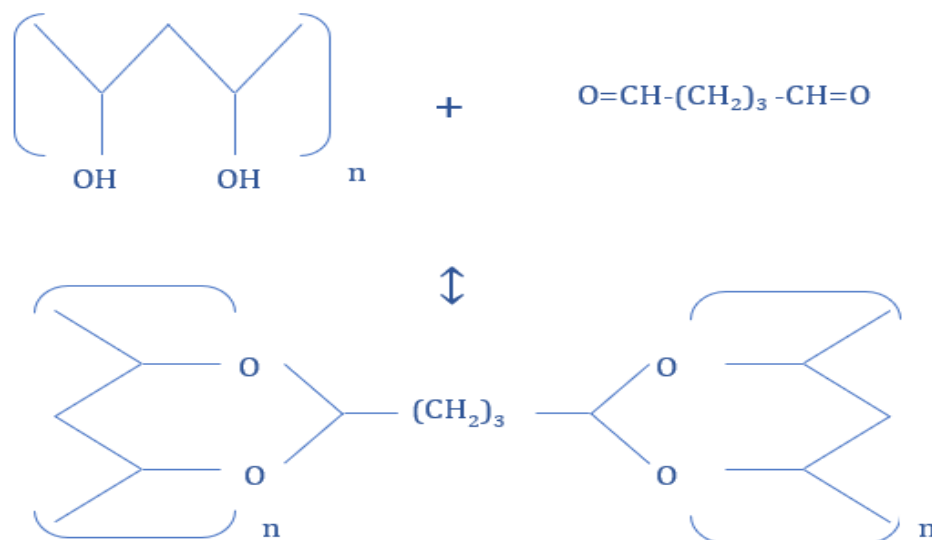


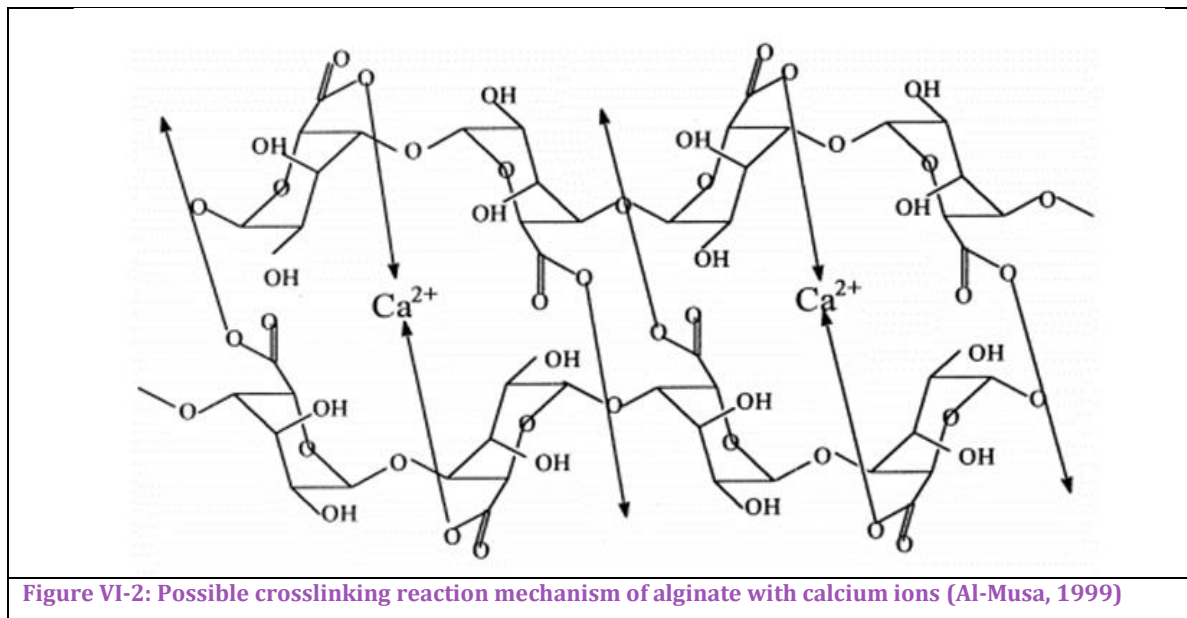
Figure VI-1: Crosslinking reaction mechanism of PVA and glutaraldehyde.

As the schematic suggests, PVA reacts with glutaraldehyde via the hydroxyl groups between both of them. This creates an acetal links between the glutaraldehyde and the polymer (Rudra, Kumar and Kundu, 2015). The reaction is usually carried out in the presence of an acid (e.g. HCl,  $\text{H}_2\text{SO}_4$ )

which catalyses the crosslinking .

While PVA shows good mechanical properties, and biocompatibility, it unfortunately shows poor “adhesive and mechanical fixation” to the surrounding body tissue, as a result of its “bioinertness” (Balgová *et al.*, 2013). This is where its use with hydroxyapatite, with excellent bioactivity, adhesion, appreciable mechanical properties (Sheikh *et al.*, 2010; Balgová *et al.*, 2013) and alginate, which is known to have better protein adsorption (Kamoun *et al.*, 2015), is useful; serving to enhance PVAs properties.

Alginate is a useful biopolymer that is obtained from brown seaweed and bacteria, with fewer ethical issues than gelatine. It is also biocompatible, hydrophilic and cheap to procure, with good protein adhesion (Kamoun *et al.*, 2015). It has wide usage in the medical field in wound dressing, drug delivery (Lin and Yeh, 2004). It unfortunately has poorer mechanical properties than PVA, suffering “poor shape definition and volume instability” (Turco *et al.*, 2009). It is built up of monomers of mannuronic acid (M) and guluronic acid (G), capable of forming region of G-only blocks, M-only blocks, or a mix of both (Mørch, Donati and Strand, 2006; Sun and Tan, 2013). It is a copolymer of both G units and M units (Al-Musa, 1999). Sols of alginate are able to undergo gelation through interaction with multivalent cations, involving crosslinking only the G blocks (seen in Figure VI-2) (Al-Musa, 1999; Du *et al.*, 2011). Metal ions that have been used to successfully crosslink alginate are  $\text{Ca}^{2+}$ ,  $\text{Ba}^{2+}$ ,  $\text{Al}^{3+}$  and  $\text{Sr}^{2+}$  (Al-Musa, 1999; Mørch, Donati and Strand, 2006).



The association of alginate, PVA can occur in any number of ways. The physical blending/mixing of the sols of the polymers causes some homogenisation on the larger scale between the alginate

and PVA domains. Crosslinking of PVA with glutaraldehyde, which increases the entanglement of the system, will indirectly cause a contraction of the PVA domains in/around alginate, improving the blend of the polymers and their resulting association. Finally, the wet chemical precipitation of apatite introduces  $\text{Ca}^{2+}$  into the system that can be utilised by the both alginate (as depicted above in Figure VI-2) and PVA through an interchain or intrachain link (Bonapasta *et al.*, 2002) as shown below in Figure VI-3.

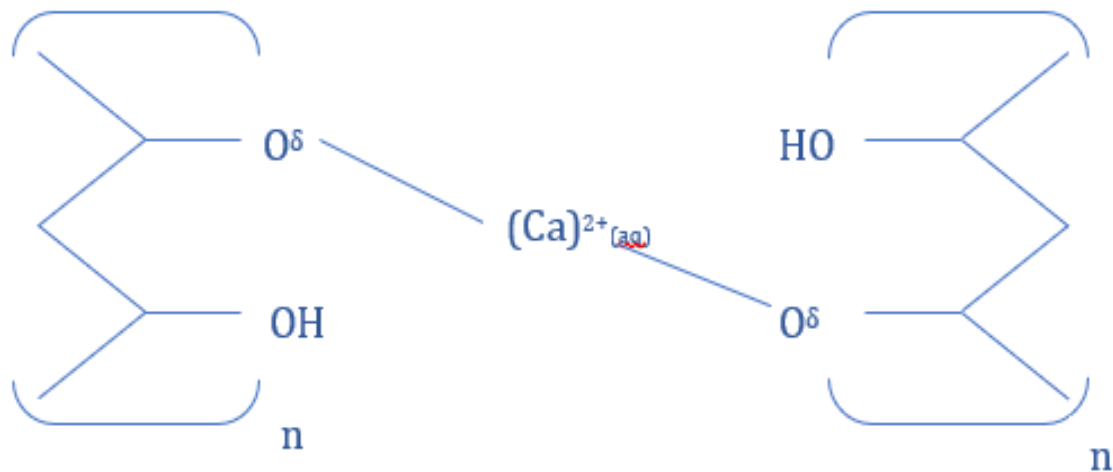


**Figure VI-3: Crosslinking reaction mechanism of PVA with calcium ion**

The added presence of nucleating hydroxyapatite growing with each layer can also serve to improve the interaction between all of the components present in the system.

Yet another dimension of biomimicry that could be included is the addition of tannic acid (TA). Tannic acids are a type of polyphenols which are found in variety of substances (tea, wine, chocolate (Lee *et al.*, 2015)). They are known for their ability to bind to a variety of surfaces, both organic and inorganic (Abouelmagd *et al.*, 2016). This ability has been exploited to coat a variety of substances, which can also be coupled with its “UV absorbing, radical scavenging and metal-ion complexation” capacity (Lee *et al.*, 2015). It achieves these due to the presence of numerous functional groups (see Figure VI-4). At neutral pH, TA takes on a negative charge that is due to the presence of galloyl groups which allows ionic interactions with other positive groups, while the presence of aromatic rings improves its interaction with hydrophobic molecules (Abouelmagd *et al.*, 2016). It has thus been used in the biomedical field to synthesise “mucoadhesive and biodegradable hydrogels” (Abouelmagd *et al.*, 2016), cytocompatible and corrosion resistant magnesium alloys for implants (Zhu *et al.*, 2017). It is currently being studied for use in the creation of shape-memory hydrogels, thanks to its ability to form numerous hydrogen bonds (Chen *et al.*, 2016). Its shows some promise in encapsulating cells for potential use as sensors

(Park *et al.*, 2014).

The presence of this plethora of hydroxyl groups can form the basis (along with alginate) to further stabilise the scaffold that will now be synthesised. It can form hydrogen bonds with the other compounds, as well as complexing with the  $\text{Ca}^{2+}$  present to create a more durable hydrogel scaffold.

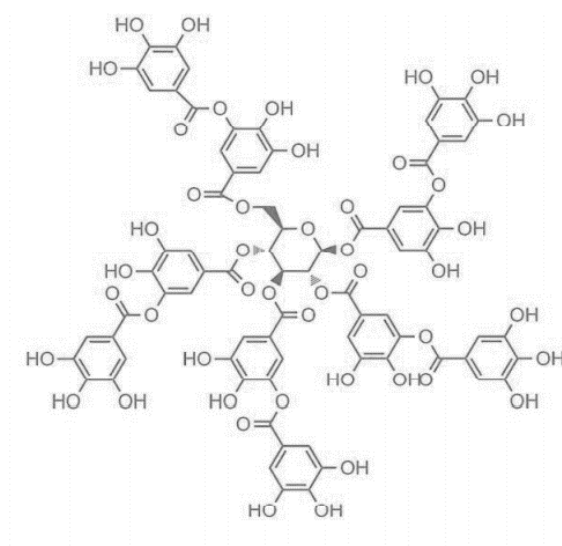


Figure VI-4: Structure formula of Tannic acid (Chen *et al.*, 2016)

## VI.4 Methodology

The method of sample preparation have been given in section II.3.1 for PVA only hydrogels, in II.3.2 for the hydrogel blends and in II.4.2 for the mineralisation of the hydrogel scaffolds.

### VI.4.1 Experimental setup for swelling properties

Hydrogel discs were dried at 37°C for 2 days to rid the discs of surface moisture. After drying, the dried samples are then weighed. This is considered their dry weight. Next, they are placed in a petri dish, this was subsequently filled with deionised water. The weight was measured after 24h.

### VI.4.2 Analytical instruments and conditions

The instruments and their conditions used in this section are listed below

#### VI.4.2.1 SEM

Before SEM analysis, all of the samples were freeze-dried for 12h, placed on a double-sided carbon tape on a stub and coated with an Au target for 60s.

#### VI.4.2.2 FTIR spectroscopy

Spectra were collected over 400-4000 $\text{cm}^{-1}$  with a resolution of 4 $\text{cm}^{-1}$  after carrying out 45 scans using an ATR accessory.



### VI.4.2.3 Raman spectroscopy

The samples were simply deposited on a glass slide and the measurements were done at 10% power. The integrated time for signal collection was at 10s for 3 accumulations. The spectra of 3 random areas were collected to provide suitable averaging.

### VI.4.3 Sample nomenclature

The samples were given the following designation shown in Table VI-1.

**Table VI-1: Name of the mineralised hydrogel samples and their accompanying description.**

Sample	Description
AL	80v/v% of PVA and 20v/v% sodium alginate
AL 15	80v/v% of PVA and 20v/v% sodium alginate, 15% glutaraldehyde
AL Ca	80v/v% of PVA and 20v/v% sodium alginate, immersed in 0.05mM Na <sub>2</sub> CO <sub>3</sub> for 1h
AL HA	80v/v% of PVA and 20v/v% sodium alginate, after mineralisation
PVA or PVA 30	100v/v% of PVA
PVA 15	100v/v% of PVA, 15% glutaraldehyde
PVA Ca or PVA 30 Ca	100v/v% of PVA, immersed in 0.05mM Na <sub>2</sub> CO <sub>3</sub> for 1h
PVA HA or PVA 30 HA	100v/v% of PVA after mineralisation
PVA 15 HA	100v/v% of PVA after mineralisation, 15% glutaraldehyde
TA	80v/v% of PVA and 20v/v% sodium alginate modified with tannic acid
TA 15	80v/v% of PVA and 20v/v% sodium alginate modified with tannic acid, 15% glutaraldehyde
TA Ca	80v/v% of PVA and 20v/v% sodium alginate modified with tannic acid, immersed in 0.05mM Na <sub>2</sub> CO <sub>3</sub> for 1h
TA HA	80v/v% of PVA and 20v/v% sodium alginate modified with tannic acid after mineralisation
TATi	80v/v% of PVA and 20v/v% sodium alginate modified with tannic acid and TiBALD
TA 15	80v/v% of PVA and 20v/v% sodium alginate modified with tannic acid and TiBALD, 15% less glutaraldehyde
TATi Ca	80v/v% of PVA and 20v/v% sodium alginate modified with tannic acid and TiBALD, immersed in 0.05mM Na <sub>2</sub> CO <sub>3</sub> for 1h
TATi HA	80v/v% of PVA and 20v/v% sodium alginate modified with tannic acid and TiBALD after mineralisation

To aid comparison, commercial samples (Bio-Oss® and nHAp) were utilised. Bio-Oss® is a bone substitute made by Geistlich. It is hydrophilic with unique topological features that have been shown to encourage bone formation (Wessing, Lettner and Zechner, 2017; Chappuis *et al.*, 2018). It is one of the more popular bone substitutes that are currently available on the market, primarily for dental application. It is utilised for the purpose of alveolar ridge management (i.e after teeth extraction in an attempt to prevent bone resorption around the ridge). Nano hydroxyapatite (nHAp) was obtained from Sigma Aldrich. Although this is also commercially available, it

functionally has not been especially designed for the purpose of use in medical applications.

## VI.5 Results

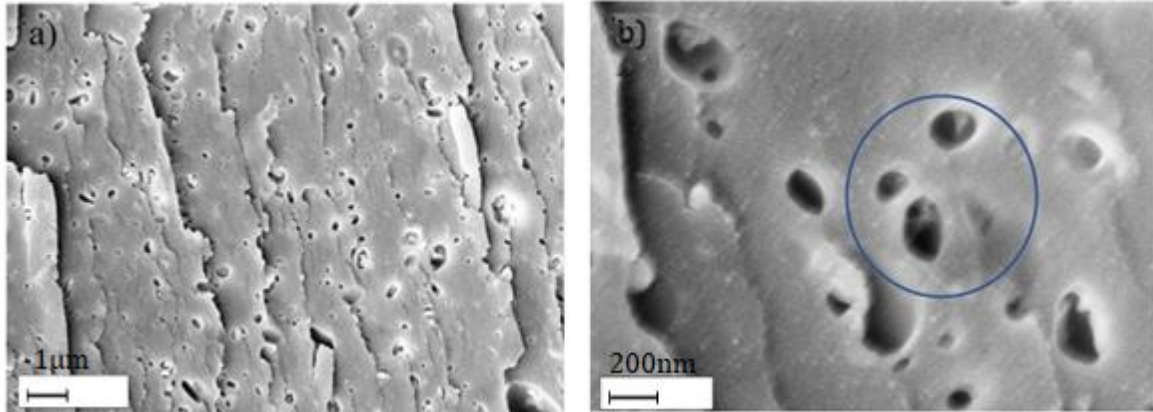


Figure VI-5: SEM of freeze dried PVA hydrogel before immersion in a CaP precursor solution (a & b)

Micrographs in Figure VI-5 shows the reader the appearance of freeze dried PVA samples before any modification. The surface morphology of PVA is not remarkable. The most important features obvious from (a&b) are the smooth surface, punctuated by hollows that are  $\leq 1\mu\text{m}$ . These hollows are not merely surface-only features, but are actually linked internally, forming networks of cavities/tunnels which allow the flow of substance through its structure.

Within the blue circle in Figure VI-5b, it is possible to make out an inner layer of the sample, with further voids present. This supports the assumption that a network of cavities may initially exist in the interior of the prepared PVA, thus allowing the flow and ingrowth of apatite-like materials. These would appear at the surface and internally too.

### VI.5.1 Non-carbonated method

This refers to a immersion method detailed by Taguchi *et al* (1998). The methodology described by this group involved an alternating immersion sequence, where a piece of crosslinked PVA was soaked in the precursor solution to enable the formation of hydroxyapatite. A breakdown of the methodology is given in section II.4.2.

### VI.5.1.1 PVA- hydrogel system after 2 alternating immersion cycles in CaP

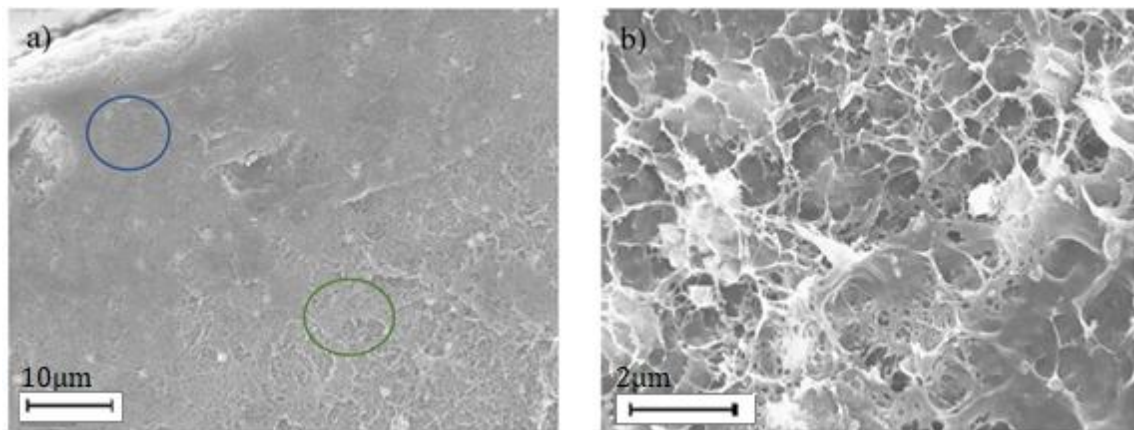


Figure VI-6: SEM of freeze dried of non-carbonated PVA-HA after 2 alternating immersion cycles in CaP precursor (a&b)

There is marked difference between the pure PVA sample and the modified sample as seen here in Figure VI-6. Most notably, the openness in the morphology of the samples seen in Figure VI-5 versus those in Figure VI-6 are worlds apart. While there seem to be sections where the sample looks fairly solid with little to no voids (see blue circle in Figure VI-6a), immediately next to that, the surface becomes more fibular (see green circle in the same Figure VI-6a and in Figure VI-6b).

The fibrils seem to either be as a consequence of the PVA swelling (due to the obvious difference in osmotic concentration between itself and the precursor solution, stretching out the PVA), or it is possible that the fibrils themselves are some form of calcium phosphate phase (which then go on to act as nucleation initiators to the more stable phases like hydroxyapatites).

If we move a step further, by increasing the number of alternating immersion cycles from 2 to 4, the micrographs in Figure VI-7 immediately become more complex, yet simpler to interpret. Here, along with the increased fibrillation of the surface morphology, one is immediately drawn to a bulbous like structure emerging outwards from the surface (Figure VI-7a & inset). This then resolves into a flower arrangement. It appears to consist of plates arranged around themselves, sometimes coincidentally growing out into a flower-like configuration (as seen in Figure VI-7b). One can now make a leap from what is occurring in Figure VI-6 to what is seen Figure VI-7.

### VI.5.1.2 PVA-hydrogel system after 4 alternating immersion cycles in CaP precursor

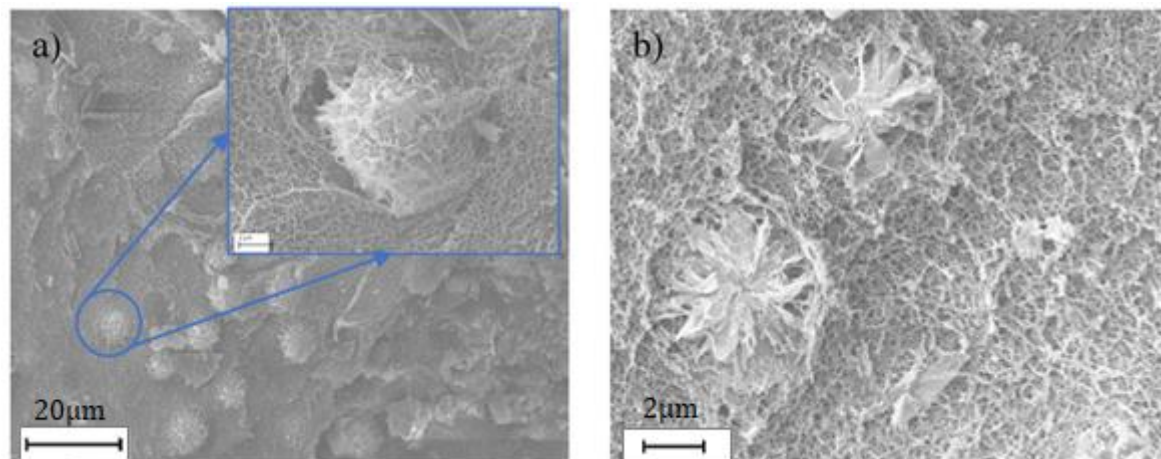


Figure VI-7: SEM of freeze dried non-carbonated PVA - HA after 4 alternating immersion cycles in a CaP precursor (a & b)

With the help of EDX results, as seen in Table VI-2 one can now gain a better picture of the elemental composition and most importantly, the ratio between Ca and P. Taking into account the elements present in the samples, the presence of carbon and oxygen are the least surprising in all of the samples (as these merely represent the original constituents of PVA itself).

Now, the other elements present include Ca, Cl, P and Na which one can directly link to the modification procedure that was carried out on them. The at% of chlorine and sodium were significant, as they ranged between 1.1 -16wt% for chlorine and 1-9.88wt% for sodium, but this may not be of surprise, as the samples were not rinsed between the alternating cycles.

The ratios of calcium to phosphate will be used as an important means of identifying the phase of calcium phosphate that is formed here. From the samples made with immersion terminated after 2 cycles, the Ca/P ratio does not exceed 0.67. This is even after taking reading at different spots, as seen in the EDX micrographs. It is possible that before a nucleation event can actually occur, a minimum ratio that has to be reached or surpassed; this is without mentioning the need for a surface to facilitate the calcium phosphate phase growth. This is possibly why in the sample made after alternating for 4 cycles, the incidence of surfaces with Ca/P ratios closer to CDHA (1.5-1.67) becomes more common. Perhaps the increased cycles boosts the probability of nucleating surfaces formation, along with the minimum amount of calcium and phosphate precursor absorbed/adsorbed in the PVA to allow the growth of apatitic calcium phosphate. The fact that we have an outward growth of the crystals from a common point (centre of the flower) could mean that the centre serves as a nucleating surface

**Table VI-2:EDX of non-carbonated PVA HA after 2 and 4 alternating immersion cycles in CaP precursor solution.**

2 alternating cycles		4 alternating cycles	
Selected area	Ca/P ratio	Selected area	Ca/P ratio
1	0.53	1	1.55
2	0.64	2	1.55
3	0.67	3	0.58

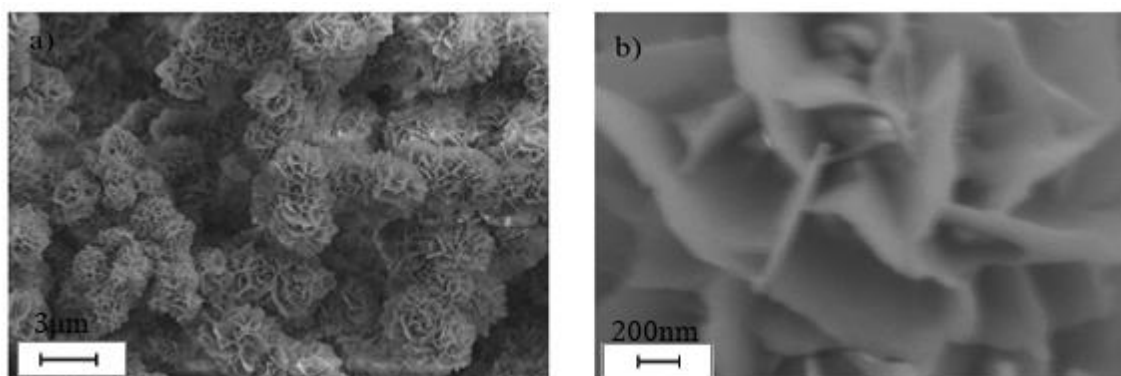
  

The SEM and EDX results seem to indicate that the formation of an apatite like substance is indeed possible using the alternating immersion method.

### VI.5.2 Carbonate-modified template hydrogels

Although the formation of apatitic calcium phosphate phases with Ca/P ratios closer to CDHA has been suggested by the EDX results as shown in Table VI-2, further modifications need to be carried out to encourage and increase the formation of apatites throughout the structure of the PVA samples.

#### VI.5.2.1 Carbonate-modified PVA hydrogel system after 4 alternating immersion cycles in CaP precursor



**Figure VI-8: SEM of freeze-dried carbonate-modified PVA -HA after 4 alternating immersion cycles in CaP precursor (a&b)**

The modification brought about by the inclusion of a carbonate step to the alternating procedure has already resulted in a significant change in the surface of the PVA in question. For one, the

presence of fibrils that would have otherwise been present (as seen in Figure VI-7a & b) has been completely obscured by apatite-like crystals (Figure VI-8) that are not as sparsely scattered compared to the original methodology.

In addition to the clustered presence of particulates of the apatite-like crystals on the surface of the PVA, it can also be deduced that the particulates have a different shape to those that are formed using the original literature derived methodology. While those formed from the carbonate modified PVA appear smaller, squat, with widths ranging from 400nm to 1000nm, those in Figure VI-7b on the other hand appear to be much longer. It might not be fair to attempt comparing these two samples, shape wise, as in either case, certain sections of the crystals are not visible. To elaborate, the micrographs of the samples in Figure VI-7b display the length and not the actual width (top) of the particulates, this is the opposite of Figure VI-8. So, while one can say the plate-like particulate aggregates are bigger or smaller, conclusively describing their shape/ratio might be problematic, and is something that would be better left for a more descriptive technique.

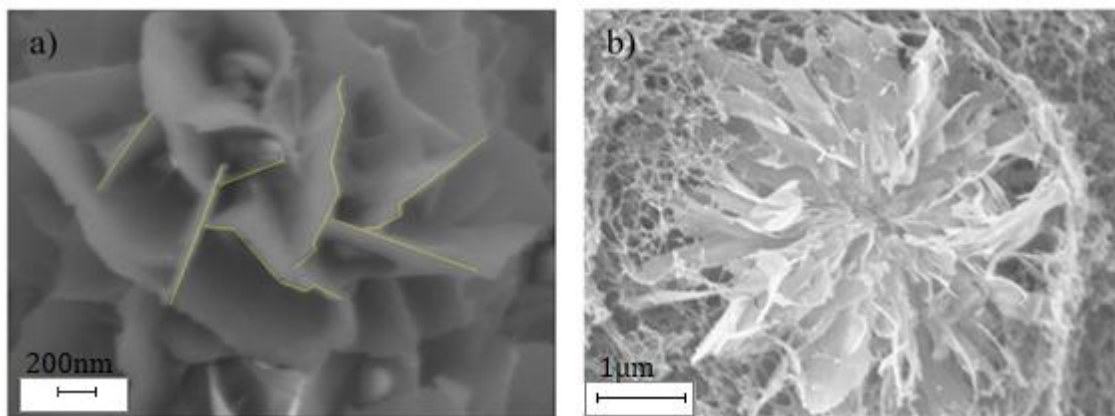


Figure VI-9: SEM showing the difference in shape and size between surface held particles on carbonate-modified and non-carbonate-modified PVA HA collected after 4 alternating immersion cycles in a CaP precursor solution.

#### *VI.5.2.2 Carbonate-modified PVA -hydrogel system after 8 alternating immersion cycles*

The same clustering observed in Figure VI-8 is again replicated in Figure VI-10 a & b. However, while the so-called flower bunches were easier to identify in the carbonate-modified 4 alternating cycle systems, the same cannot be said after increasing the number of alternating cycles to 8.

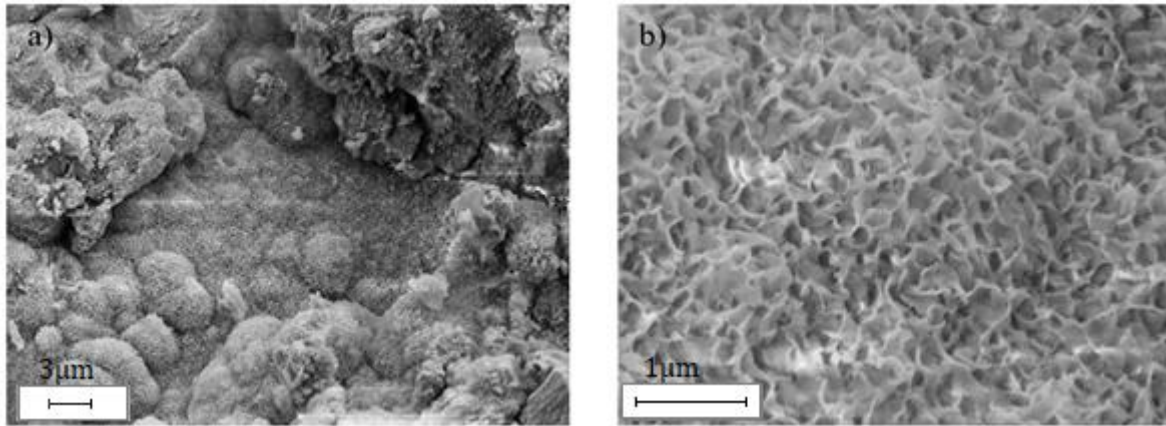


Figure VI-10: SEM of freeze-dried carbonate modified PVA -HA system after 8 alternate immersion cycles (a & b).

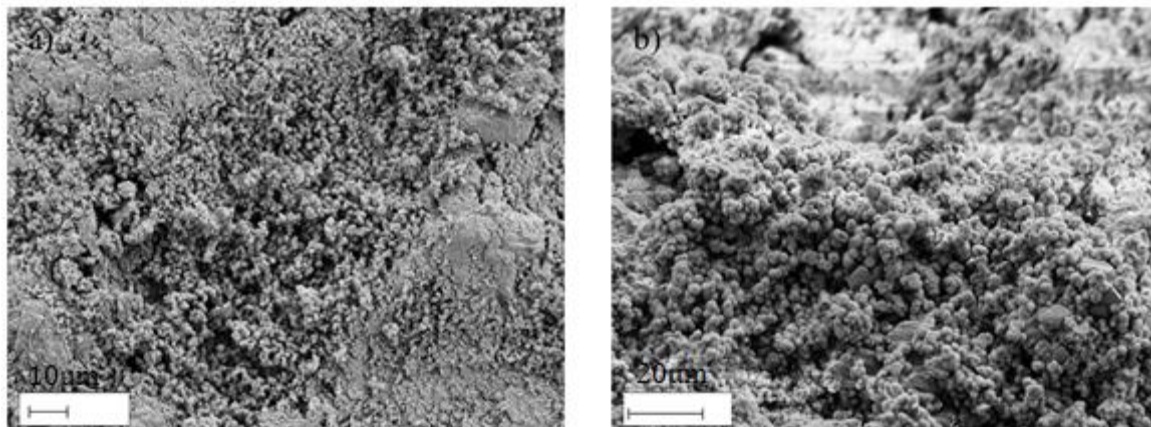
The surface now looks completely obscured; the flower-like structures seems to have completely disappeared. This is probably as a result of them growing out because of the increasing amount of precursor material deposited in each cycle. So, while at the start, their growth was more distinct, due to the marked difference between plain PVA surface and their conformation, the same can no longer be said now that almost every surface can act as potential point of nucleating. In the end we have a surface that is more homogenously covered with crystallites, but less distinct throughout.

Table VI-3: EDX of carbonate- modified PVA -HA system after 0,4 & 8 alternating immersion cycles

0 alternating cycles		4 alternating cycles		8 alternating cycles	
Selected area	Ca/P ratio	Selected area	Ca/P ratio	Selected area	Ca/P ratio
1	n/a	1	1.13	1	1.03
2	n/a	2	1.10	2	1.01

Unfortunately, no results for 2 cycles are included, so while it will not be possible to compare the ratio after 2 cycles (with Table VI-2), one can still achieve this by comparing the samples at 4 cycles instead. The Ca/P ratios calculated here appear to be much lower than those seen in the first system, of unmodified PVA. Instead of averaging ratios of  $\sim 1.55$ , we are instead seeing ratios of around 1.10-1.13 for 4 cycles and much lower after 8 cycles. It is possible that this drop in Ca/P between the samples after 4 and then 8 cycles is to do with the concentration gradient established between the precursor solution and the interiors of the samples. Taking heed from Watanabe et al (2008), they were able to show a trend where the ratio of Ca/P formation decreased as the number of deposition cycles increased. So, while they confirmed that the overall hydroxyapatite being formed increased between each alternating immersion cycle, the Ca/P did the opposite. Like their samples, it is likely that increasing the number of immersion cycles worked up to a point, but eventually the concentration gradient- which would normally have been higher outside the modified PVA systems- reverses causing the partial dissolution of the formed apatite like calcium phosphate; and this dissolution might eventually contribute to the downward shift in the Ca/P ratio and the perceived non stoichiometry exhibited with the EDX results.

### VI.5.3 Effect of changes in the crosslink density on the carbonate modified sample system



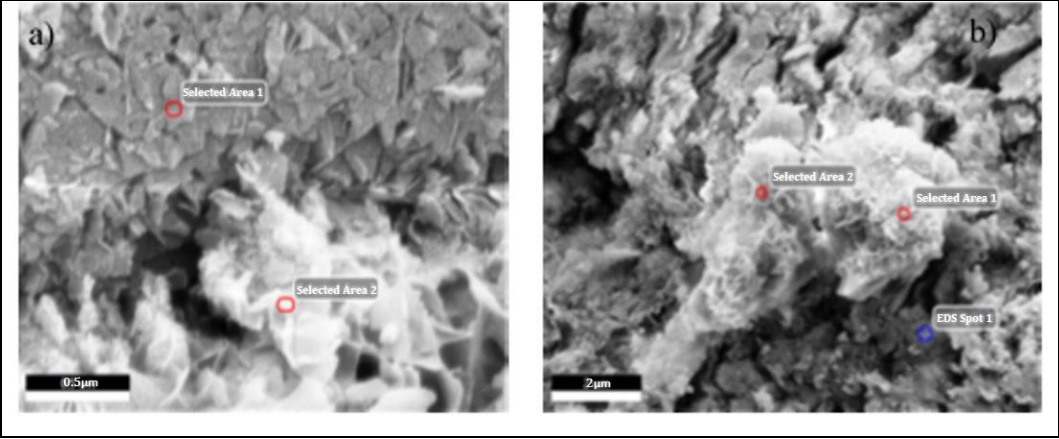
**Figure VI-11: SEM of freeze-dried carbonate-modified PVA 15-HA composite after 4 alternating immersion cycles (a&b)**

Changing the crosslink density of the sample is another mode of modification which was trialed. Here, the volume of glutaraldehyde was decreased to 15% rather than the usual 30% in order to change the density. Increasing the glutaraldehyde volume above 30% usually led to a final product with an extremely shrunken appearance, with the majority of the water excluded from its structure as well. Visually, there doesn't appear to be much of a difference between samples crosslinked at 15% glutaraldehyde and those at 30% glutaraldehyde (as seen in Figure VI-11a&b).



**Table VI-4: EDX of carbonate-modified PVA 15-HA composite after 4 and 8 alternating immersion cycles**

4 alternating cycles		8 alternating cycles	
Selected area	Ca/P ratio	Selected area	Ca/P ratio
1	n/a	1	1.44
2	1.30	2	1.05

The EDX reading (see

Table VI-4) seems to offer a slightly better method of differentiating between the crosslinkage densities employed with this system. Overall, there appears to be a marked increase in the Ca/P ratio than the samples made with 30% crosslinkage. It is unclear why the ratio is higher here, but it is possible that a number of factors might have contributed to the higher ratio; for example, less crosslinks means less sites for nucleation. And if there are less sites for nucleation then it potentially means that there is less instance of apatite like substance being formed, which in turn means that the concentration gradient between the inside of the PVA hydrogel system remains skewed to allow inflow of ions into the hydrogel; and all of this means that the stoichiometry of the apatite like particulates being formed remains more or less close to the CDHA examples mentioned in literature. Of course, this is all conjecture without anything other than the limited EDX results to work from.

#### **VI.5.4 Infrared characterisation of the carbonate modified samples with varying crosslinks density**

IR spectroscopy was carried out to characterise crosslinked PVA, before and after it had undergone the alternating immersion technique.

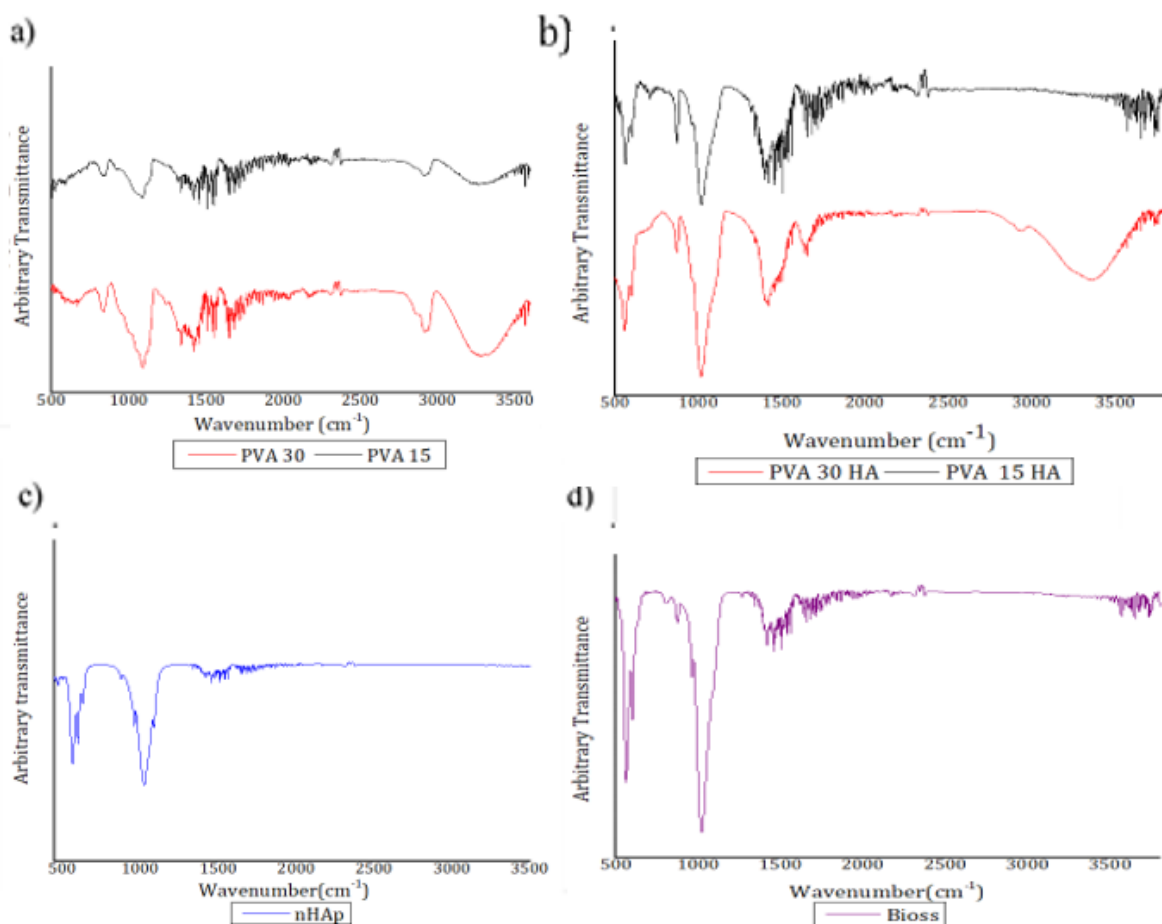


Figure VI-12: FTIR spectra of just PVA 15 and PVA 30 alone a); mineralised PVA 15 HA PVA 30 HA b); nanohydroxyapatite nHAp c); Bio-Oss® d).

Figure VI-12 contains the representative FTIR spectra of the crosslinked samples before and after mineralisation. From Figure VI-12a it is clear that the spectra of the two samples exhibit some similarities. This is expected as they are both crosslinked PVA samples, with only the level of crosslink altered by varying the amount of glutaraldehyde to achieve this. The characteristic bands that are normally ascribed to PVA samples are present. One of the major peaks is related to hydroxyl groups, seen from 3200-3600 $\text{cm}^{-1}$ . These are related to intermolecular and intramolecular hydrogen interactions by hydroxyl groups. Next to those is the duplet structure visible between 2800-3000 $\text{cm}^{-1}$ , which is related to the alkyl (methylene chains found in the aldehyde structure common to glutaraldehyde (Mansur *et al.*, 2008). In relation to these bands, there is the band around 1740 $\text{cm}^{-1}$  caused by C=O and C-O groups, that make up part of the acetate group present in PVA (from the initial polymerization process), but most likely from the unrinsed glutaraldehyde used in the preparation of the hydrogel. The band around 1400-1460 $\text{cm}^{-1}$  belong to methylene groups as well and the acetal bridges are around 1090 $\text{cm}^{-1}$  (Figueiredo, Alves and Borges, 2008; Mansur *et al.*, 2008).

**Table VI-5: FTIR band assignments of nHAp, PVA 15 HA and PVA 30 HA (Fathi, Hanifi and Mortazavi, 2008; Mansur *et al.*, 2008; Chavan *et al.*, 2010; Jastrzębski *et al.*, 2011)**

nHAp (cm <sup>-1</sup> )	PVA 30 HA (cm <sup>-1</sup> )	PVA 15 HA (cm <sup>-1</sup> )	Assignment
561	557	561	$\nu_4\text{PO}_4^{3-}$
597	597	597	$\nu_4\text{PO}_4^{3-}$
634			-OH
877	871	873	$\nu_2\text{CO}_3^{2-}$
974	958	958	$\nu_1\text{PO}_4^{3-}$
1016	1020	1018	$\text{PO}_4^{3-}$
1087			$\nu_3\text{PO}_4^{3-}$
	1097	1097	C-O-C
	1408-1458	1406-1458	C-H
1454			$\nu_3\text{CO}_3^{2-}$
	1498	1498	$\text{CO}_3^{2-}$
	1710	1710	C=O
	2900-2950	2900-2950	C-H
	3215 -3300		O-H

In Figure VI-12b, one encounters spectra of samples containing what may finally be confirmed as containing hydroxyapatite. Using a standard control sample of nano-hydroxyapatite purchased from Sigma-Aldrich (blue spectrum), it is possible to identify and relate the bands here to those visible in the mineralised PVA samples (PVA15 HA & PVA 30HA respectively).

Immediately, it is possible to see similarities in the bands present in the sample. In fact, the most prominent bands visible in all three samples visible in Figure VI-12b & c may be ascribed to the vibrational modes commonly found when phosphate groups are present. These are seen as a major band around 1016-1020 cm<sup>-1</sup>; followed by a band around 958-970 cm<sup>-1</sup> occurring on the shoulder of the band at 1016-1020 cm<sup>-1</sup>. It is thought that this band or at least its distinctiveness (sharpness) may be used as an indication of crystallinity of the sample (Hong *et al.*, 2006), seeing as the PVA15HA (black) and PVA30HA are lacking in the sharpness seen in the control sample (blue), one can assume that the sample made has a lower crystallinity.

Next to that is a series of smaller peaks at 557cm<sup>-1</sup> and 600cm<sup>-1</sup>, as specified in Table VI-5. We can see that although they are generated by phosphate, they are of a different vibrational mode than the bands mentioned in the preceding paragraphs. It is thought that these peaks supposedly represent the different position of the phosphate groups in the crystal lattice (Fathi, Hanifi and Mortazavi, 2008).

Another major set of bands identifiable in the two lab prepared samples, and to some extent in the control sample are the bands around 1400cm<sup>-1</sup> and 870-877cm<sup>-1</sup>. This band is thought to

belong to carbonates (Hong *et al.*, 2006; Fathi, Hanifi and Mortazavi, 2008). As these bands are sharper and a lot more obvious in the lab prepared samples, we can say that the hydroxyapatite-prepared is not pure, but carbonate-substituted hydroxyapatite. This may lend some justification as to why the calculated EDX ratios (Table VI-3 &

Table VI-4) were never 1.67 but were much lower. Fathi et al (2008) seem to indicate that these peaks ( $1400\text{cm}^{-1}$  and  $877\text{-}870\text{cm}^{-1}$ ) were a sign the apatite obtained was a “B-type carbonated apatite” This is substitution to replace phosphate ion rather than hydroxyl ions (Reyes-Gasga, Martínez-Piñeiro and Brès, 2012).

Finally, the presence of hydroxyl groups is shown by bands around  $3300\text{-}3500\text{cm}^{-1}$  and  $634\text{cm}^{-1}$ . According to infrared spectroscopy carried out, an apatite-like system has been formed, albeit with a carbonate substitution. It is very likely that the carbonate substitution is due to the initial treatment with  $\text{Na}_2\text{CO}_3$ , which was utilised in a bid to improve the formation of apatite. This has left the sample as a substituted apatite.

### VI.5.5 Raman of carbonate modified samples with varying crosslinks and increasing deposition cycles

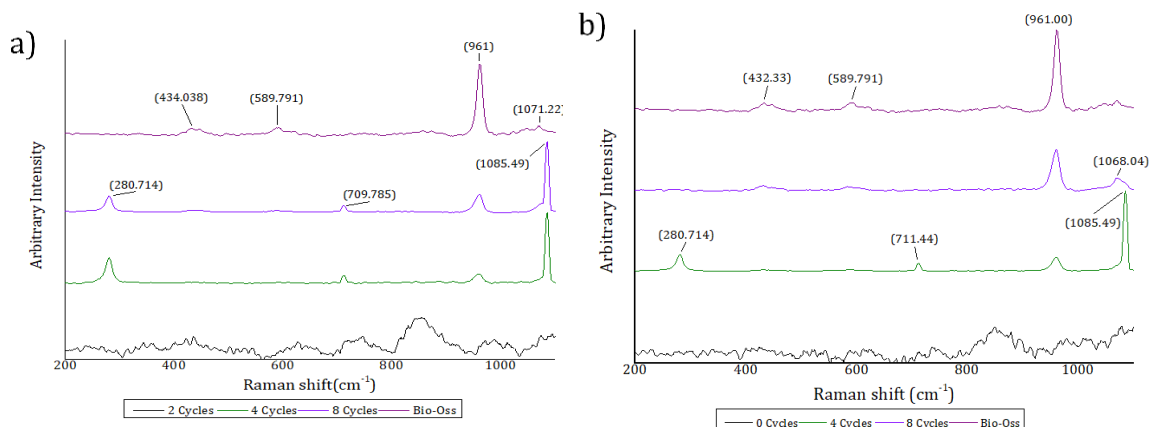


Figure VI-13: Raman spectra of Bio-Oss vs PVA 15 HA after 2, 4 & 8 alternating immersion cycles a); and PVA 30 HA after 0, 4 & 8 alternating immersion cycles b).

Another method used to ascertain and confirm the presence of hydroxyapatite was Raman spectroscopy. While it cannot be used to provide a quantitative reading on the amount of hydroxyapatite present, it may be used like FTIR for a qualitative understanding of the calcium phosphate phase formed in the laboratory prepared samples; allowing the comparison between them and the commercially-available control sample.

In Figure VI-13a & b, it is apparent that the spectra are dominated by the presence of the phosphate tetrahedra. The most obvious peak (at  $960\text{cm}^{-1}$ ) is one of the main identifiers of

hydroxyapatite and may be used to differentiate it from other calcium phosphate phases like TCP.

**Table VI-6: Raman spectra band assignment of Bio-Oss® and the mineralised hydrogel scaffolds (Gunasekaran, Anbalagan and Pandi, 2006; Khan et al., 2013)**

Bio-Oss (cm <sup>-1</sup> )	PVA 15 HA (cm <sup>-1</sup> )	PVA 30 HA (cm <sup>-1</sup> )	Assignments
	150 & 280	150 & 280	T(Ca, CO <sub>3</sub> ):
432-446	440	434	V <sub>2</sub> of PO <sub>4</sub>
588	586	586	V <sub>4</sub> of PO <sub>4</sub>
	711	711	V <sub>4</sub> of CO <sub>3</sub>
961	961	961	V <sub>1</sub> of PO <sub>4</sub>
1036			V <sub>3</sub> of PO <sub>4</sub>
1069	1069	1069	V <sub>1</sub> of CO <sub>3</sub>

Firstly, we can see that the samples at 0-2cycles have an almost unrecognizable spectrum. This is probably because the samples at that point consist of just PVA, and thus the signals that might normally be generated for PVA are actually outside the region under investigation (900cm<sup>-1</sup> to 1500cm<sup>-1</sup> (Gauthier *et al.*, 2004)).

On the 2<sup>nd</sup> cycle, the V<sub>1</sub> PO<sub>4</sub> band at ~ 960cm<sup>-1</sup> starts to emerge. It is not the most intense in the spectrum; this is the peak at 1085cm<sup>-1</sup> and it is common in both PVA 15 HA and PVA 30 HA. Another important factor to note is the actual position of the V<sub>1</sub> PO<sub>4</sub>; it occurs around 957cm<sup>-1</sup>. While this is not too important, the shift of the V<sub>1</sub> has been linked to the crystallinity of hydroxyapatite. In amorphous calcium phosphate (ACP) precipitation, it usually starts of around 950cm<sup>-1</sup>, and gradually moves to around 955cm<sup>-1</sup> (belonging to a transitional phase like OCP) before finally reaching 960cm<sup>-1</sup> at full crystallinity (Wang and Nancollas, 2008). We can see that even on the 8<sup>th</sup> cycle, in both samples, the V<sub>1</sub> PO<sub>4</sub> has just marginally grown while still remaining at the same position. It is possible that this is because of the low crystallinity that was hinted at by the infrared analysis, or an indication of the mix of the calcium phosphate phases formed.

Beside the V<sub>1</sub> PO<sub>4</sub>, we can see two other bands that are not obvious in the commercial sample (Bio-Oss), at 150cm<sup>-1</sup> and at 280cm<sup>-1</sup>. It is possible that these peaks are as a result of external vibrations of CO<sub>3</sub> arising from the CaCO<sub>3</sub> (Gunasekaran, Anbalagan and Pandi, 2006) – likely formed from the initial reaction of Na<sub>2</sub>CO<sub>3</sub> and CaCl- “translational modes of Ca<sup>2+</sup> and PO<sub>4</sub><sup>3-</sup> sub lattice and rotational modes of PO<sub>4</sub><sup>3-</sup> groups” (Khan *et al.*, 2013).

There is yet more emphasis on the manner of carbonate-substitution in the lattice. We see the band at 1069cm<sup>-1</sup>, present as a medium peak in Bio-Oss® and as a shoulder to the 1085cm<sup>-1</sup> band in PVA 15 HA. The presence of this band has been speculated to mean that the hydroxyapatite

formed is of the B-carbonate substituted variety, as similarly stated in FTIR analysis. Signifying that one (or more) of the sites commonly occupied by  $\text{PO}_4^{3-}$  in the apatite lattice has been replaced by carbonates (Khan *et al.*, 2013). If we were to refer to the band at  $280\text{cm}^{-1}$  and  $960\text{cm}^{-1}$  in the sample produced after 2 cycles and compare it to the sample obtained after 8 cycles (in both the PVA 15 & 30HA), we can observe that there is a marginal decrease in the peak at  $280\text{cm}^{-1}$  (with a simultaneous increase in the relative intensity  $960\text{cm}^{-1}$  as the number of alternating cycles increases). One can infer that the  $\text{CaCO}_3$ , might also act not just as a point of nucleation, but as a source of  $\text{Ca}^{2+}$  and  $\text{CO}_3^{2-}$  for the formation of hydroxyapatite.

Similar peaks are present in both PVA 30 HA and PVA 15 HA, as one would have expected as the formulation of the two systems are fairly identical. The only two variation would be in the 8<sup>th</sup> cycle, where the carbonate peak at  $1069\text{cm}^{-1}$  is reduced in PVA 30 HA (compared to PVA 15 HA) and  $V_1 \text{PO}_4$  is close to  $\sim 960\text{cm}^{-1}$ , which could potentially mean that the carbonate substituted apatite formed using the PVA 30 HA sample is more crystalline than its 15% counterpart.

While this is yet another confirmation of the formation of carbonate substituted hydroxyapatite, it does suggest that there are other phases present, like calcite, and other transitional calcium phosphate phases that contributes to the peak at  $1089\text{cm}^{-1}$  which has yet to be identified.

## VI.5.6 Effect of hydrogel composition

### VI.5.6.1 AL -hydrogel systems

As well as working with PVA as the main scaffolding material, attempts were made to expand on the use of PVA as a scaffold material for hydroxyapatite. PVA only has a finite level of modification which can be brought about mostly with the help of cross linkage, besides fundamentally changing the molecular weight or other intrinsic chemical properties. It is for this reason that alginate will be introduced to aid with not just its chemical properties, but in addition its mechanical and bioactive properties.

Following the preparation method, utilising carbonate modification that have been set out in the previous sections, the coming samples in this section were made in the same manner.

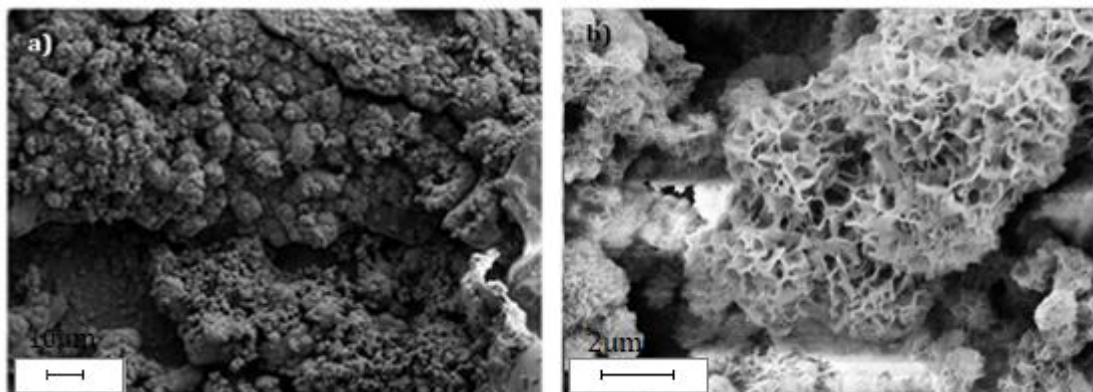


Figure VI-14: SEM of freeze-dried AL HA samples after 4 a); and after 8 alternating immersion cycles b)

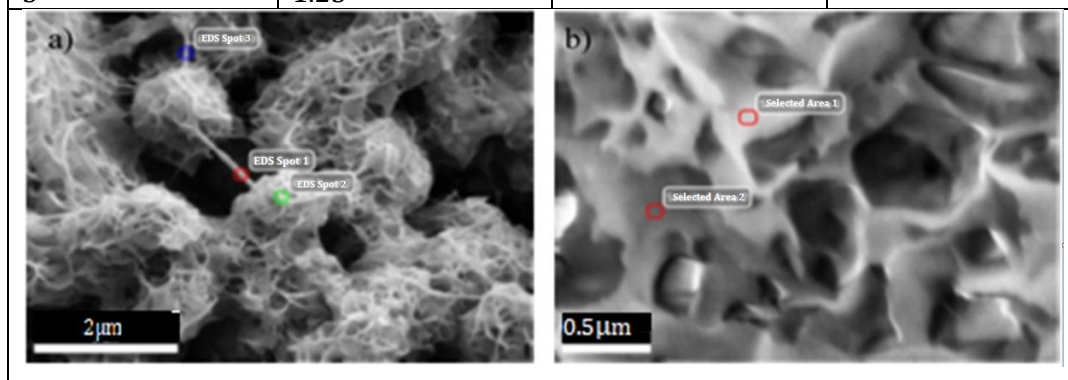
There does appear to be a significant difference in the morphology of the samples in these samples compared to the carbonate-modified PVA HA only samples. This is in reference to the actual shape. As one had discussed extensively in the previous PVA HA system, the shape that the confirmed substituted apatite like particulates assumed was in a flower like conformation. When examined closer, these aggregates were made up of petals-like plates, that is believed to be substituted hydroxyapatite crystal. While this was obvious then, in Figure VI-14 it is not the case. What is seen instead is an extremely porous spherical like structure.

In Figure VI-14b) after an increment in cycles from 4 to 8, the morphology of the samples begins to resemble the carbonate modified PVA HA system. But even then, there are still gaps which are now obvious in the bunches of crystals. It is possible that the initial porous spherical like structures were expanded parts of the hydrogel structure interspaced with some crystal deposition, possibly the calcium phosphate starting nuclei.

The samples here, as show in Table VI-7 have a better Ca/P ratio over PVA HA at cycle 4 (1.13-1.10). A similar behaviour with regards to the decrease in Ca/P ratio with increasing cycles is seen here as well. This seems to be standard behaviour for this methodology.

Table VI-7:EDX of carbonate-modified AL HA scaffold after 4and 8 alternating immersion cycles

4 alternating cycles		8 alternating cycles	
Selected area	Ca/P ratio	Selected area	Ca/P ratio
1	1.90	1	1.21
2	1.26	2	0.39
3	1.25	-	-



### VI.5.6.2 TA- AL -hydrogel systems

These samples have been modified through the addition of tannic acid into the hydrogel formulation. The preparation has been discussed in section II.3.2.3.

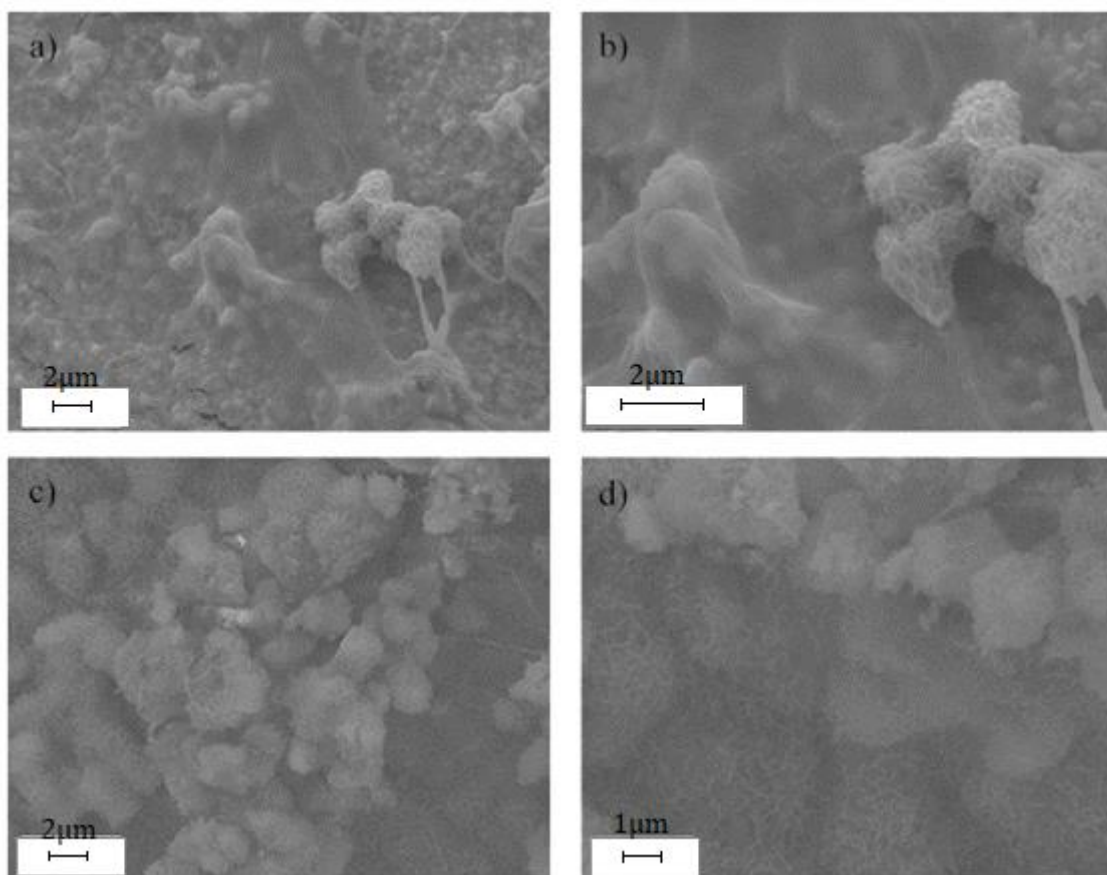


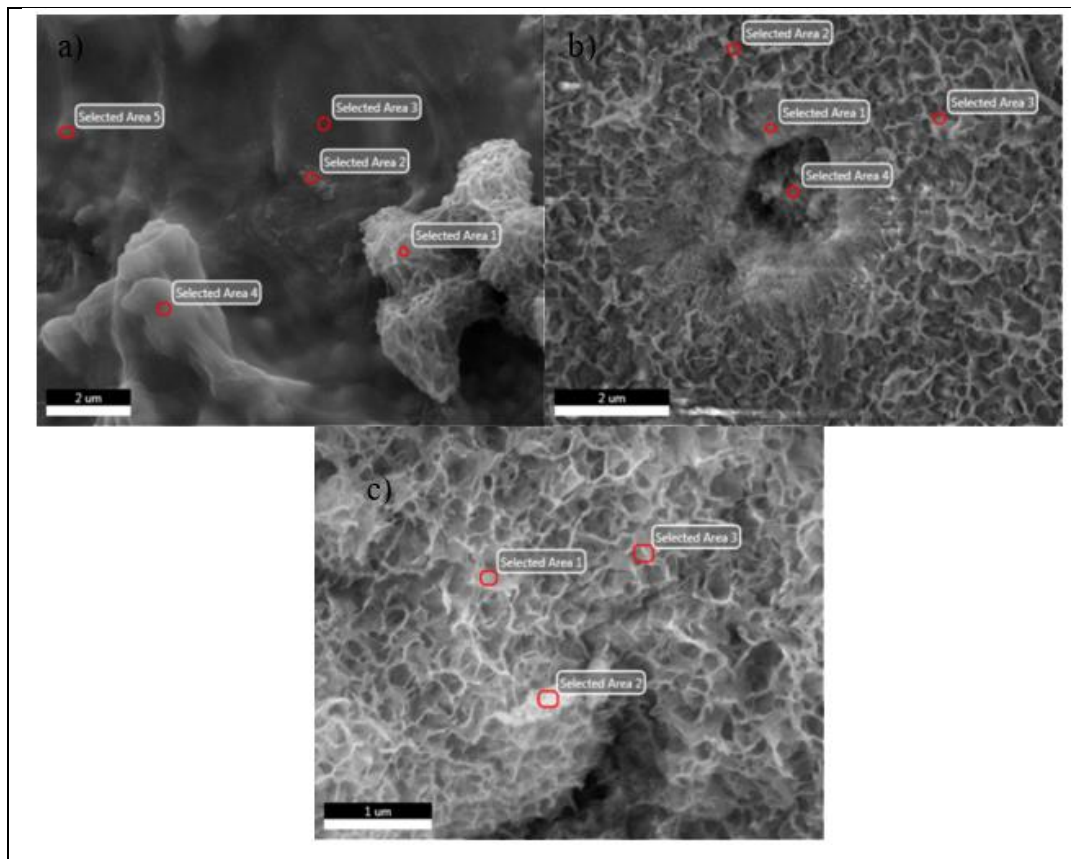
Figure VI-15: SEM of freeze-dried TA HA samples after 2 a & b); 4 c); and 6 alternating immersion cycles d)

In Figure VI-15 a-d similar features as one has come to expect in samples containing alginate: from the clusters to the interlocking blanket of platelets on the surface. Like the previous samples before this, the inclusion of tannic acid has not affected the morphology of the apatite-type crystals that are forming. At 2 cycles, the presence of the smaller clustered nuclei approximately 2µm across are more obvious, equally seen in Figure VI-8. Increasing the cycles, not only increases the sizes of these nuclei, but also the prevalence of the carpet like morphology - taking up more of the micrographs.

Table VI-8: EDX of carbonate-modified TA HA scaffold after 2,4 and 6 alternating immersion cycles.

2 alternating cycles		4 alternating cycles		6 alternating cycles	
Selected area	Ca/P ratio	Selected area	Ca/P ratio	Selected area	Ca/P ratio
1	2.01	1	0.35	1	0.48
2	1.55	2	0.34	2	0.58
3	1.18	3	0.37	3	0.33
4	1.59	4	0.37	-	-
5	1.56	-	-	-	-





EDX again reaffirms the difference in the Ca/P ratio (i.e. a drop in the ratio as the cycles increases which is an artefact of ionic concentration), which is the same as that seen in Table VI-3 & Table VI-7 at much higher cycles. One thing that however should be noted is the ratio achieved in these samples (Table VI-8) particularly after 2 cycles. There is a tremendous drop in the ratio across cycles 4 to 8 (0.33-0.58). The values are lesser than those estimated for the pure PVA samples, the PVA alginate sample, where the lower range were closer to 0.8 instead. This is the main difference that has been seen so far, and it is not clear if this is a function of the area that was chosen for EDX analysis, or if this is indeed due to the difference that has arisen from the addition of tannic acid. It is known that the inclusion of tannic acid has an interesting effect on the swelling property of hydrogel, effectively decreasing its swelling potential and thus the degradation properties. This might actually work to prevent the flow of the precursors through the sample, increasing the possibility of local concentration gradients. This would no doubt affect the nucleation and growth of the relevant apatite phases, and by extension their Ca/P ratio.

### ***VI.5.6.3 TATi-hydrogel systems***

The samples here have been synthesised through not just the addition of tannic acid, but the inclusion of TiBALD to the formulation. Further information is contained in section II.3.2.4

Figure VI-16(a-d) above shows us the now standardized morphology of apatitic growth on the surface of this polymer after 4 cycles. The inclusion of clusters of spherical nuclei in addition to blanket of upright platelets is again present in the micrographs. Figure VI-16a shows a combination of the different morphologies common amongst all the samples. Additionally, dense untextured block of particulates are visible (see blue circle in Figure VI-16a), they are likely the progenitor of apatite phases.

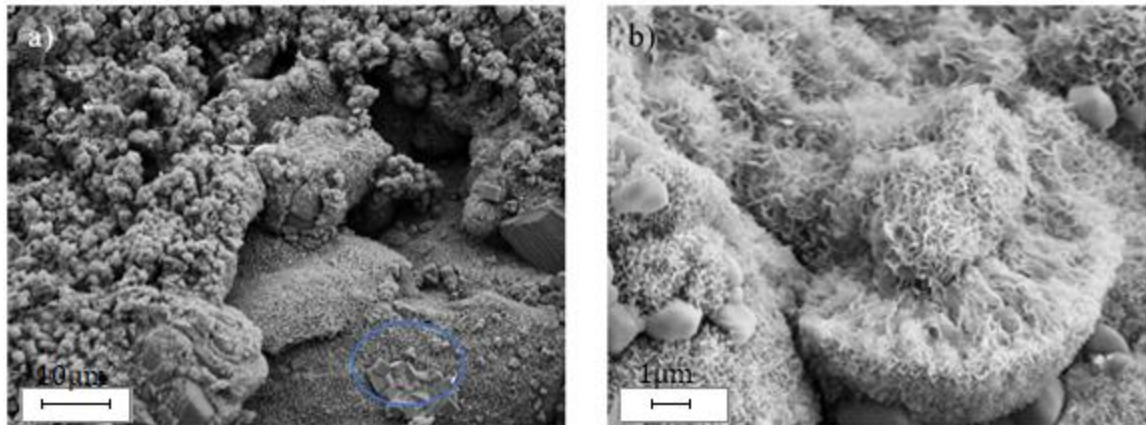
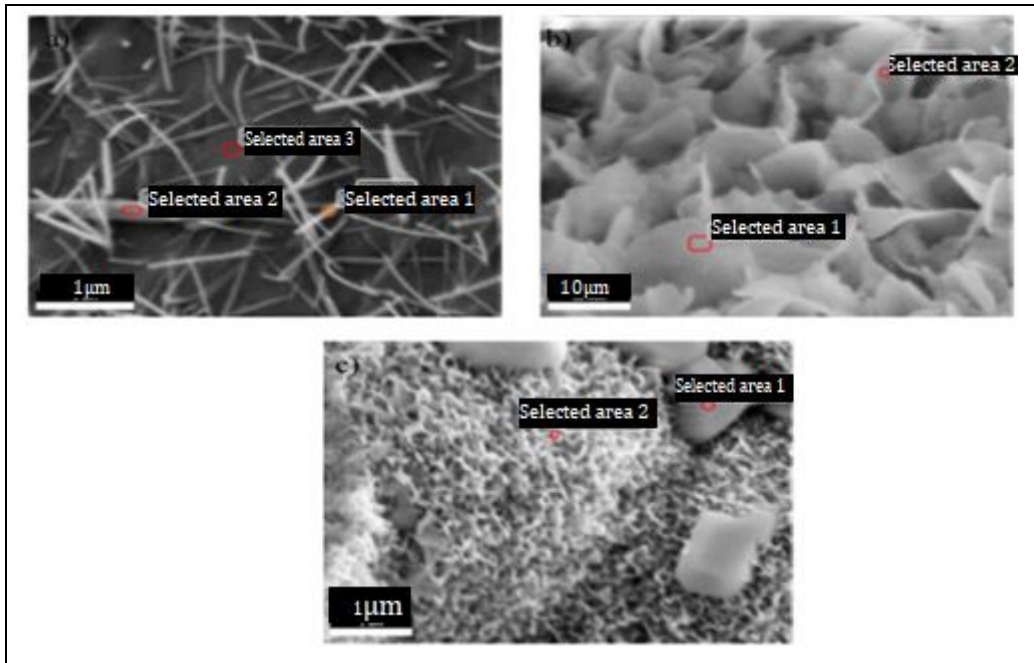


Figure VI-16: SEM of freeze-dried TATi HA samples after 4 a); and after 8 alternating immersion cycles b).

Increasing the cycles has little change on the morphology, other than the increment in the size of the clusters in Figure VI-16b. The most changes brought on by the increasing cycle treatment is their Ca/P ratio. The estimated ratios after 4 and 8 cycles are barely different with the increasing cycle time.

Table VI-9: EDX of carbonate-modified TATi HA scaffold after 0,4 and 8 alternating immersion cycles.

0 alternating cycles		4 alternating cycles		8 alternating cycles	
Selected area	Ca/P ratio	Selected area	Ca/P ratio	Selected area	Ca/P ratio
1	n/a	1	0.97	1	n/a
2	n/a	2	1.18	2	1.07
3	n/a	-	n/a	-	n/a
4	n/a	-	n/a	-	n/a



#### *VI.5.6.4 Spectroscopic analysis of the different samples with increasing cycle numbers*

Qualitative analysis using Raman spectroscopy confirms the formation of apatitic calcium phosphate, with certain substitution of carbonate. The main peaks common for hydroxyapatite, are seen in Bio-Oss®, occurring at  $430\text{ cm}^{-1}$ ,  $580\text{ cm}^{-1}$  and  $960\text{ cm}^{-1}$ , all of which are characteristic vibration for  $\text{PO}_4^{3-}$  seemingly giving indication of the position of phosphate ions in the different positions in a hydroxyapatite lattice. In addition to the phosphate vibration, Bio-Oss appears to be carbonate substituted, owing to the presence of a peak around  $1069\text{ cm}^{-1}$ . These peaks are also present in the lab synthesised sample, AL HA at 4 cycles and 8 cycles, albeit with lower intensity and a more enhanced peak for carbonate. It is worth mentioning that at the 4<sup>th</sup> cycle, the position of the  $V_1$  for phosphate is less than  $960\text{ cm}^{-1}$  which indicated that the crystallinity at lower cycle number is less, thus making this sample similar to PVA HA and PVA 15 HA.

The same scenario is seen for TATi HA where the clarity of the peaks, especially  $V_1$  becomes stronger as the immersion cycles increases. It is also carbonate substituted, just like all of the samples that have been synthesised.

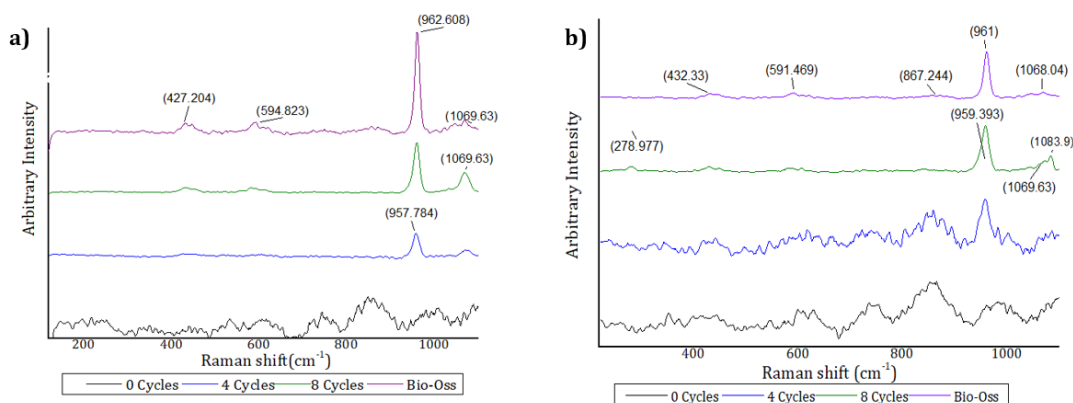


**Figure VI-17 :Raman spectra of Bio-Oss® at different alternating immersion cycles (0, 4 & 8) for AL HA a) and TATi HA b).**

The same as with the Raman spectra above, the spectra contained in Figure VI-18 show that the IR spectra of the samples are all similar to the PVA HA spectrum, as well as the spectra for pure hydroxyapatite (nHAp) and Bio-Oss®. The main bands are those that can be ascribed to phosphate vibrations at 958-970 cm<sup>-1</sup>, 1016-1020cm<sup>-1</sup> as well as other smaller peaks at 557cm<sup>-1</sup> and 600cm<sup>-1</sup>. Following these are the bands belonging to carbonates, which again occur around the regions 870-877 cm<sup>-1</sup> and 1400cm<sup>-1</sup>. The intensity of the carbonate bands in the samples, are again more than those seen in nHAp and Bio-Oss® (from Figure VI-12). This is a strong indication that regardless of the composition of the hydrogel backings, the actual apatite remains unaffected.

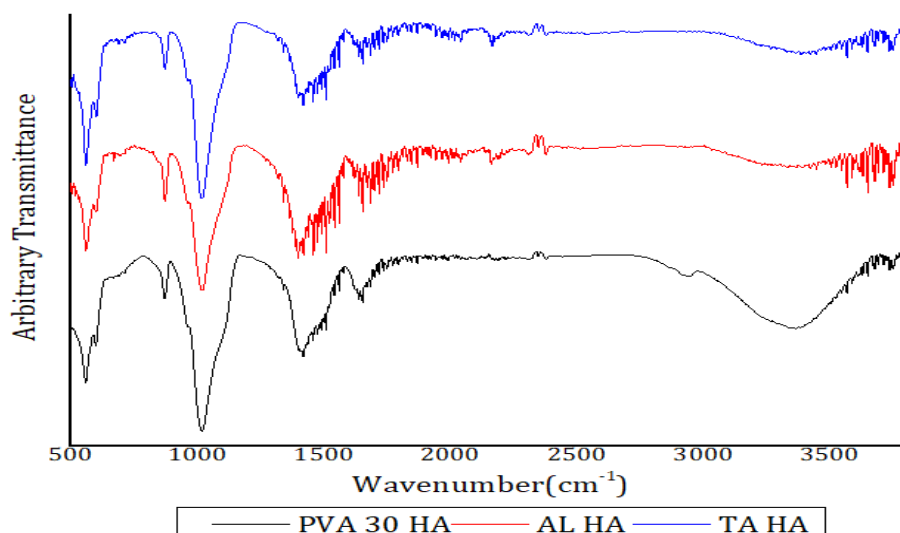


**Figure VI-18:FTIR spectra of PVA 30HA, AL HA and TAHA after 4 alternating immersion cycles in a CaP precursor solution.**

### VI.5.7 Swelling properties

The swelling properties of the hydrogel only samples in deionised water were tested giving the

following results

**Table VI-10: Swelling behaviour of the hydrogel only samples**

Duration (hours)	PVA (g)	AL-PVA (g)	AL-TA-PVA (g)	TATi-PVA(g)
0	0.356±0.003	0.337±0.002	0.333±0.001	0.335±0.010
24	0.863±0.003	0.713±0.013	0.729±0.020	0.735±0.050
% change	142±3	111±5	118±9	119±4

For the hydrogel-only samples in Table VI-10, all of the samples experienced an increase in their weight of above 100% of their original value. PVA underwent the most amount of swelling, followed by TATi-PVA, AL-TA-PVA and finally AL-PVA.

## VI.6 Summary

### VI.6.1 Non-carbonated samples

In this section, no carbonate was introduced into the system. The immersion it seems expanded the network structure of the PVA. Thus while they were more solid in Figure VI-5, solid and more fibril-like sections become more prevalent upon immersion (see in Figure VI-6) and this features becomes more obvious through chapter in relation to the many samples made. It is thought that immersion aided the expansion, and the actual growth of calcium phosphate in and on the fibrils keeps it upon, allow further deposition and growth. Increases in the apatitic calcium phosphate presence as the immersion cycles increases appear to be the norm (see Figure VI-6 and Figure VI-7), even EDX appears to show that before 4 cycles, the Ca/P ratios are nowhere near that of apatites.

### VI.6.2 Carbonated samples

The samples in this section had a carbonate step added in the synthesis of HA. The most obvious difference between the non-carbonated samples and those made with carbonate would be mainly down to the shape of the HA particulates that are visible on the electron micrographs. Whereas the uncarbonated samples above had particles that could be considered elongated, although still platelet shape. The carbonate samples are different in that they appear to be squatter. Although not all section of the samples are visible, their reduced dimension in contrast to the non-carbonated counterpart is impossible to miss especially if Figure VI-9 is taken into consideration.

In terms of the carbonated samples, increasing the immersion cycles does not necessarily appear to increase the Ca/P ratio. Instead as the immersion cycles jump from 2 to 8, the ratio experiences an ~8 % drop (see Table VI-3). This has been attributed to a shift in the concentration gradient between the interiors of the hydrogel and the immersion solution, where at a certain point a reversal in concentration gradient will occur causing a dissolution of the partially form apatites-

like calcium phosphate. This would be true especially for those that are closer to the solution, exterior of the hydrogel, as they would be immediately subject to the decreasing ionic concentration of the solution.

### **VI.6.3 Changes in crosslink density of PVA hydrogels and PVA HA**

The crosslink density was another parameter that was altered in the hydrogels. This involved changing the amount of glutaraldehyde present during the preparation/crosslinkage process.

The amount of glutaraldehyde was halved in the samples presented in section VI.5.3. In

Table VI-4 the samples showed some increase in their Ca/P ratio. The increase or rather stabilisation of the value might simply be caused by the more open network of the hydrogel.

Fewer glutaraldehyde in the system means that not all of the hydroxyl groups in PVA is involved in the acetal bridges formation. This allows the movement of the precursor solution easily through the interior, thus preventing the establishment of a concentration gradient, and apatite dissolution.

### **VI.6.4 Infrared analysis of PVA hydrogels and PVA HA**

The infrared spectra for the hydrogel only samples in Figure VI-12a) consist of bands that are normally present for crosslinked hydrogels. Bands at  $3200-3600\text{cm}^{-1}$  for inter and intramolecular hydrogen interaction. Then there is the band at  $1740\text{cm}^{-1}$  which is attributed to the C=O found in glutaraldehyde. The methylene groups were found around  $2800-3000\text{cm}^{-1}$  and then at  $1400-1460\text{cm}^{-1}$ , and finally the acetal bridges occur around  $1090\text{cm}^{-1}$ . All of these were present in the hydrogel only samples.

Some of the aforementioned bands were also present in the mineralised samples, but the bands that belong to HA dominated most of the spectra presented in Figure VI-12b. Two of these main bands occurred at  $1016-1020\text{cm}^{-1}$  and  $958-970\text{cm}^{-1}$ , both of which are contributions from phosphate groups in the HA lattice. The former of these are thought to indicate the crystallinity of the apatite lattice (Hong *et al.*, 2006). One can also use this as a distinction between the mineralised hydrogel and nHAp, seeing as the band in the lab purchased samples is not as symmetrical as that in nHAp. Then there are bands around  $557\text{cm}^{-1}$ , and  $600\text{cm}^{-1}$  again belonging to phosphate. Finally carbonate contributions at  $877\text{cm}^{-1}$  and  $1454\text{cm}^{-1}$  are present in both hydrogel sample and nHAp, but the latter of which is more prominent in the hydrogel samples. This is one major indicator that the HA produced in the hydrogels are carbonated-substituted and thus nonstoichiometric HA. This non-stoichiometry will have affected the Ca/P ratio in VI.6.2, VI.5.2 and throughout this chapter, lowering it from 1.67 (Fathi, Hanifi and Mortazavi, 2008).

### **VI.6.5 Raman of carbonate modified samples with varying crosslinks and increasing deposition cycles of PVA hydrogels and PVA HA**

The increasing complexity of the hydrogels, of varying crosslink density, were monitored as the immersion/deposition cycles increased from 0. At the start, 0-2 cycles, there was little in the way of any peak that would suggest the formation of any apatite phase. This changed once the cycle number reached 4 and above. Using the peak at  $960\text{cm}^{-1}$  (used as an identifier for hydroxyapatite), its presence grew with the increasing cycle number. Also, there was a positional shift (discussed in VI.5.5) which had to do with the crystallinity of the apatite lattice, and by extension the stoichiometry. The aforementioned peak for the mineralised hydrogel samples never quite becomes centred at  $960\text{cm}^{-1}$ , unlike Bio-Oss, this highlights the nonstoichiometric of its lattice and the possibility of ACP being prominent too.

Another prominent peak in the mineralised hydrogel samples occurs at  $1071\text{cm}^{-1}$ , belonging to carbonate. Although present in Bio-Oss, it is more obvious in the hydrogel sample. Additionally, peaks at  $280\text{cm}^{-1}$  and  $711\text{cm}^{-1}$  are also contribution from carbonate.

In addition to witnessing the increasing complexity of the samples with each cycle, the distinction between the mineralised hydrogel samples and the control samples is unmistakable. The contribution from carbonates, also seen in FTIR, shows that the HA grown in the hydrogels are carbonate substituted.

### **VI.6.6 Effect of composition changes on Raman and FTIR spectra**

Moving on from the PVA based hydrogels, further attempts were made to improve the scaffold to aid in improved addition of apatite onto the scaffold. This started with the use of alginate, with the starting premise that crosslinking of alginate, usually brought on by the introduction of divalent metal cations would act to improve the amount of apatite formed, in addition to possible improvement in the mechanical properties of the scaffold (discussed in section VIII.5.1). There is not much in the way of morphological differences that was expressed from the compositionally varied samples against the pure PVA samples. The only real difference that was in relation to the elemental composition. This was specifically seen for TA HA. The same sample was the only one to have shown Ca/P ratios that were drastically smaller after the first 2 immersion cycles, never exceeding 0.60. The only possible reasoning for this was due to the presence of tannic acid in the polymer blend, which is a known chelator of metal ions.

We see here that at least in terms of the morphology of the apatite crystals formed, there does not appear to be much in the way of difference between the samples. The ratio though is the main indicator, and this is only in relation to TA HA.

The FTIR spectra of the samples also show no immediate difference across the samples chemical

environment, specifically the bands associated with apatitic calcium phosphate. Again, this is another indication that changing the hydrogel composition does not necessarily affect the apatite grown within the hydrogels. At least, not changes that are immediately obvious using these spectroscopic techniques.

#### **VI.6.7 Swelling properties.**

The swelling properties overall are quite different from just pure PVA samples. The inclusion of alginate appears to have adversely affected the swelling abilities of the hydrogel, with all of their percentages dropping by 23-31%. The order of swelling being PVA> PVA-TATi>PVA-TA>PVA-AL.

### **VI.7 Conclusion/Future work**

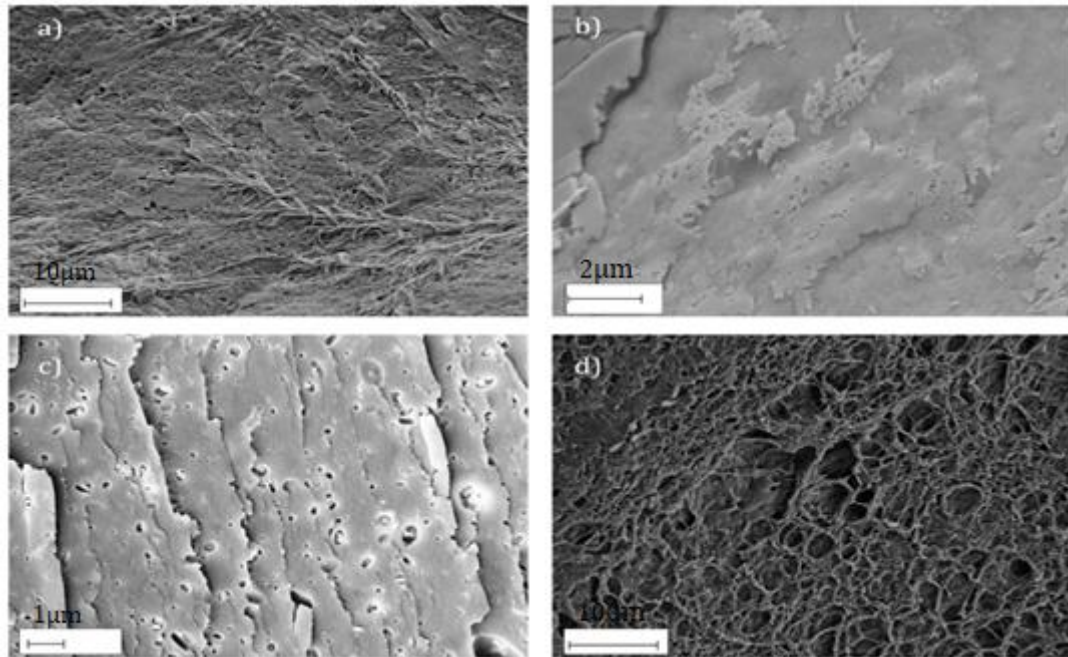
The aim of this section was concerned with the biomimetic synthesis of a mineralised hydrogel which can then find functional uses as a bone graft material. It is believed that this has been achieved through the nucleation and growth of apatitic calcium phosphate within the hydrogel matrix in much the same way as the growth occur within a living organism. The main ingredient in question have been vaguely provided. They include the precursor solution, which would normally be present within blood, plasma, granules, amorphous molecules or any similar medium that contains the precursor media (Meldrum and Cölfen, 2008). This is dependent on the complexity of the organism and the materials to be precipitated.

Next would be the compartment in which this mineralisation process takes place. In this experiment, this was in the form of the hydrogel matrix composed of PVA alone or blended with another molecule. In humans, osteogenesis occurs in vesicle, and in collagen fibrils. Other complex organism use matrices that are built from chitin, collagen, silk fibroin (Meldrum and Cölfen, 2008; Chen *et al.*, 2012). The whole point of these matrices within the living environment is to act as compartment where the concentration gradient of the ionic specie may be controlled to allowed deposition and growth to follow, not to mention acting as a sort of physical termination points of the precipitated. These compartments are usually equipped with ion pumps, with the ability to actively control the concentration gradient of ions, affecting nucleation and its growth rate. Also, certain macromolecules (amino acid etc) are present to provide extra control in the mineralisation process (Meldrum and Cölfen, 2008) as they have the ability to nucleate, direct, terminate as well select for the polymorphs that are being formed. This level of control, not to mention the presence of these very specific molecules are not present in this case. These particular functionalities are not present in this experiment, rather the diffusion of ionic species are passively controlled (Jeffryes *et al.*, 2008; Meldrum and Cölfen, 2008).

While some of these features are not present, the simple medium that has been produced with

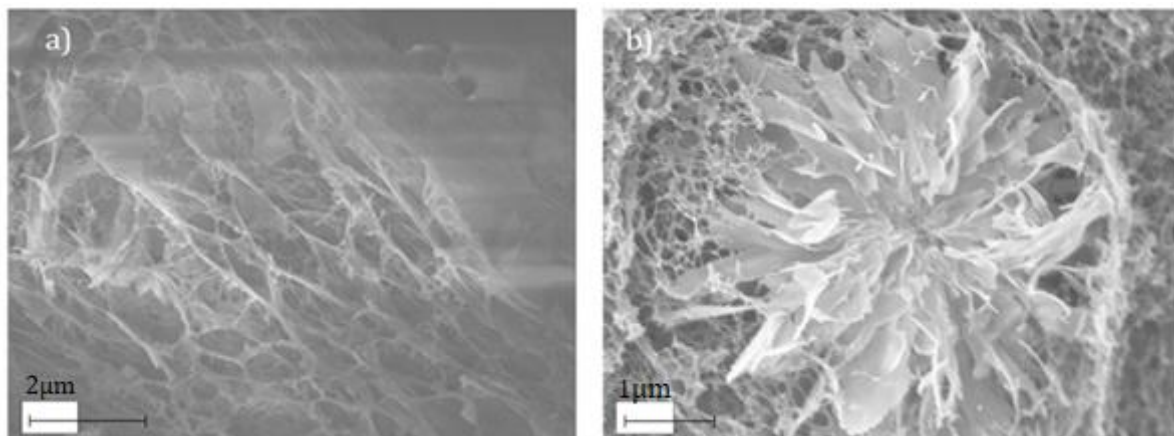


the aid of the hydrogel and the added precursor would serve as the necessary ingredients to allow the precipitation and growth of apatitic calcium phosphate. Indeed, in the Figure VI-19, it is clear to see the many irregular sites on the surface of PVA and its blends, which acted as favourable nucleation points for the precipitation of the crystals. This is in addition to the hydroxyl groups present and crosslinks that also acted as nucleation points.



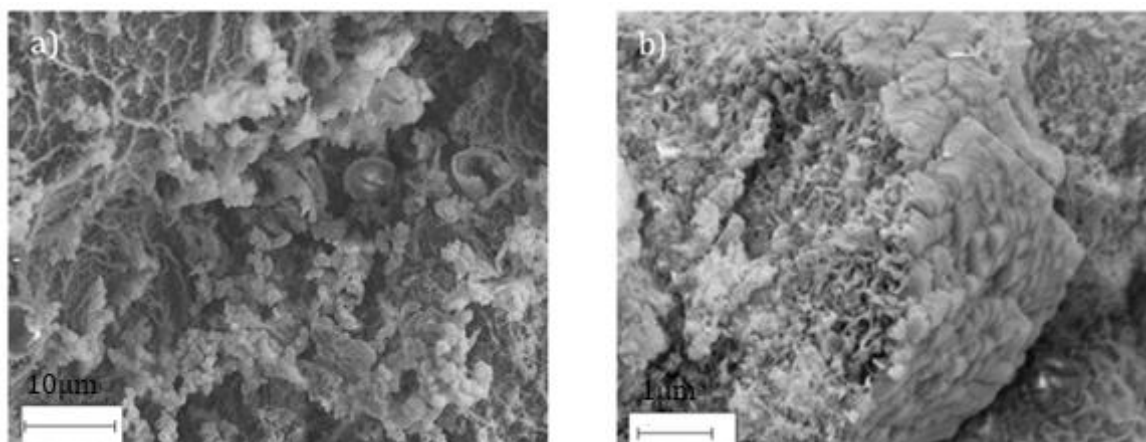
**Figure VI-19: Potential sites and irregularities for nucleation**

When immersed, the interconnected channels, network, pores act as physical compartments that allow a concentration gradient to be set up to allow the pairing of the calcium and phosphate ions. This increases the possibility of nucleation as would be allowed by thermodynamics and the relevant kinetics (Wang *et al.*, 2005). It is clear in Figure VI-20 that the expanded hydrogel network with fibrils acted as sites for the growth and confinement of the calcium phosphate crystals.



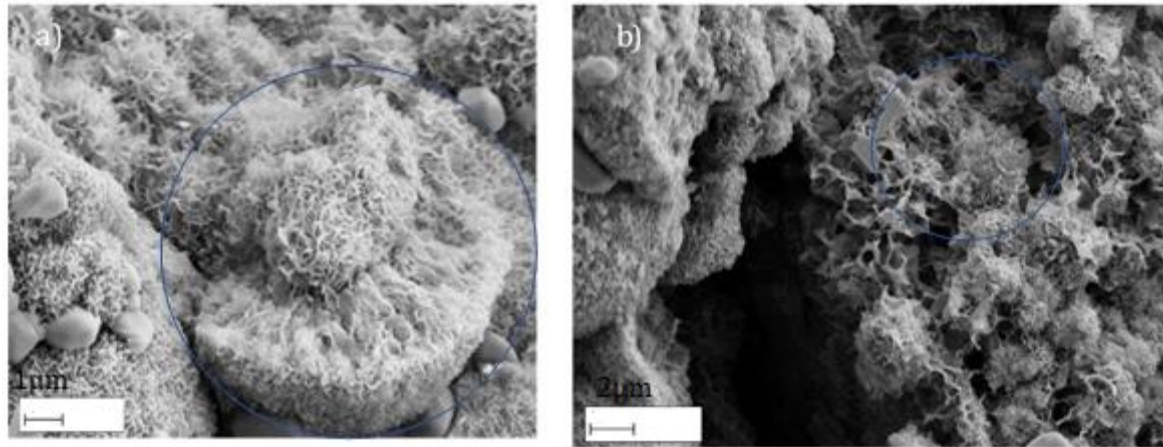
**Figure VI-20: Swollen hydrogel network showing deposition of early calcium phosphate crystals a&b).**

Figure VI-21 illustrates the matrix acting as both a nucleation site and a terminating boundary. In Figure VI-21a, it is possible to see tiny spherical nuclei at the centre of the micrographs. However, closer to the top left of that figure, tracks of high contrast regions maybe seen, further highlighting the preference of the nucleation even occurring at the irregularities of the hydrogel surface. Figure VI-21b show a great example of the hydrogel boundary acting as termination faces (centre-right), the crystals grow inward, or rather away from the boundary.



**Figure VI-21: Crystal growths controlled/terminated by the hydrogel boundaries.**

The crystals clusters themselves act as their own nucleation sites. Figure VI-22a shows a spherical crystal cluster forming the central region inside a halo of another bigger cluster. The same can be said for Figure VI-22b, within the blue circle, it is clear to see an open, partially formed cluster with smaller nuclei forming within the vacant spaces.



**Figure VI-22: Clusters behaving as nucleation sites**

While the control of macromolecules is not present in these samples, it appears that the aim of biomimetically-synthesising a hierarchal bone graft material has been achieved, with the necessary characterisation showing that the mineral phase formed are apatitic calcium phosphate. What remains is to probe their crystallographic properties, their mechanical properties, as well as their functionality in terms of biomineralization and drug uptake/release.

## Chapter VII Crystallographic properties of the mineralised hydrogel scaffolds

### VII.1 Introduction

This section concentrates on the crystallographic properties of the mineralised hydrogel scaffold that have been synthesised. Along with the attainment of apatite phase, the size of the crystallites and preferential orientation are parameters that are just as important which can have a pretty significant impact on the functionality of the overall scaffold. Starting with the attainment of the apatite phase, this is quite an important factor as the calcium orthophosphates family comprises of a large number of compounds, some with properties that render them impractical as materials in biomedicine (e.g. MCPM, MCPA and FA), as a result of their fast dissolution in an aqueous environment or the release of potentially dangerous by-products in vitro. Other phases like HA and TCP are more popular due to their biocompatibility and solubility properties (this is especially so with regards to HA). HA at least in the form of CDHA is readily found in-vivo which makes it the most likely candidate for drug delivery, bone substitution and other applications (Dorozhkin, 2011; Eliaz *et al.*, 2017). One cannot forget ACP, an extremely important calcium orthophosphate member, which is considered the precursor of all the other phases. In terms of biocompatibility, osteoconductivity and resorption, it is superior to HA and TCP (Zhao *et al.*, 2011). It is thought to be one of the first mineral phases formed in the osteoid during osteogenesis (Hollinger, 2005), making it more relevant than perhaps only the other phases.

The formation of apatite crystals that fall within the nanoscale is another factor that can improve the functionality of the synthesised scaffold. Macroscale HA can be at times problematic to utilise for bone regeneration due to their very low solubility. One way around this is through nanoscaling which can vastly improve this property (see section I.1.10). Additionally, there is the potential for increased interaction on the cellular level with cells that can foster osteogenesis, and the improved surface activity that can allow more efficient adsorption of drugs.

Another factor to watch out for is the preferential orientation. This property is intrinsically mixed with the shape of the crystal that is attained. Although this trait may seem innocuous, it has an effect on the mechanical and the reactivity of the sample. Mechanically, hydroxyapatite with a c-axis orientation has been found to be more wear resistant in the teeth of carp (Fu *et al.*, 2016); and in terms of chemical reactivity depending on which face develops, the surface charge which is exposed is different and can thus affect the reactivity of the samples (Aizawa, Matsuura and Zhuang, 2013).

These are some of the factors which can be probed using crystallography, and which can have important effects on the functionality and in turn the success of the mineralised scaffold.

## VII.2 Aim

In this subsection, the crystalline properties of the samples will be investigated for not just the purpose of establishing and confirming the identity of the phases that are formed but confirming the changes in the unit cell parameters of the mineralised hydrogel samples against several control samples that are commercially available. Also, it is hoped that the crystalline properties will shed some light on the functionality of these mineralised hydrogels, i.e. the dissolution and biogenic properties. In entirety, this section will look at the average crystallite size, the preferential orientation where possible, the shape of the crystallites, the effect of size and strain on the shape of the XRD peaks with the aid of WH plot.

## VII.3 Background

As we have extensively talked about the different phases of calcium phosphate and the advantages of having implants formed with apatite preferably, and if possible, in addition with ACP, OCP and TCP, we shall not touch on these phases any further.

Preferential growth of the crystal on the other hand is something that has only been briefly mentioned up to this point. To recap, the unit cell of hydroxyapatite has the following parameters  $a=9.84$ ,  $b=2a$ ,  $c=6.88$  for a monoclinic cell, and  $a=b=9.84$ ,  $c=6.88$  for a hexagonal cell (Eliaz *et al.*, 2017). Depending on where in the human body hydroxyapatite occurs, the c-axis can be oriented in different manners. For examples, in the bone, the c-axis is parallel to the collagen fibres that helps with its assembly, leading to the exposure of the a(b) face. In the human teeth on the other hand, the rod like prisms are arranged in bundles which are parallel to each other along the c-axis of hydroxyapatite -longitudinal direction of the enamel (Hanlie, Liyun and Tao, 2006; Li *et al.*, 2011; Aizawa, Matsuura and Zhuang, 2013; W. Wang *et al.*, 2013). The average size of the apatite crystal in bone has been estimated as being between 20-50nm lengthwise and between 12-20nm in width (Boskey, 2007), Kalia *et al* (2014) stated a similar dimension of between 15-200nm for the length and 10-80nm for the width. In teeth along the c-axis (longer length), it was estimated as 89.6nm in enamel and 30.9nm in dentine (Hanlie, Liyun and Tao, 2006); Abou Neel *et al.* (2016) estimated the size of dentine as being closer to 50nm lengthwise and 20nm in width, the size of enamel estimated as being closer to 100nm lengthwise with a width of 42nm by Reyes-Gasga *et al* (2015).

It was found that hydroxyapatite crystals, especially those that are artificially made, are often obtained in various morphologies (needles, plates or as just fine particulates (W. Wang *et al.*, 2013)). As needles or fibres, it is thought that the c-axis orientation is parallel to the long axis, thus leading to the exposure of the a(b) face, just like that seen in the long bones of humans

(Aizawa, Matsuura and Zhuang, 2013). As a platelet morphology on the other hand, the preferred orientation is along the a(b) axis with the c axis being the more developed face is parallel to the long axis. The platelet morphology is similar to that which is found in the human enamel, albeit occurring in bundles which then resembles rod (Aizawa, Matsuura and Zhuang, 2013). In the figure below, we see the electron micrographs of section of an enamel and a human femur such as that seen below

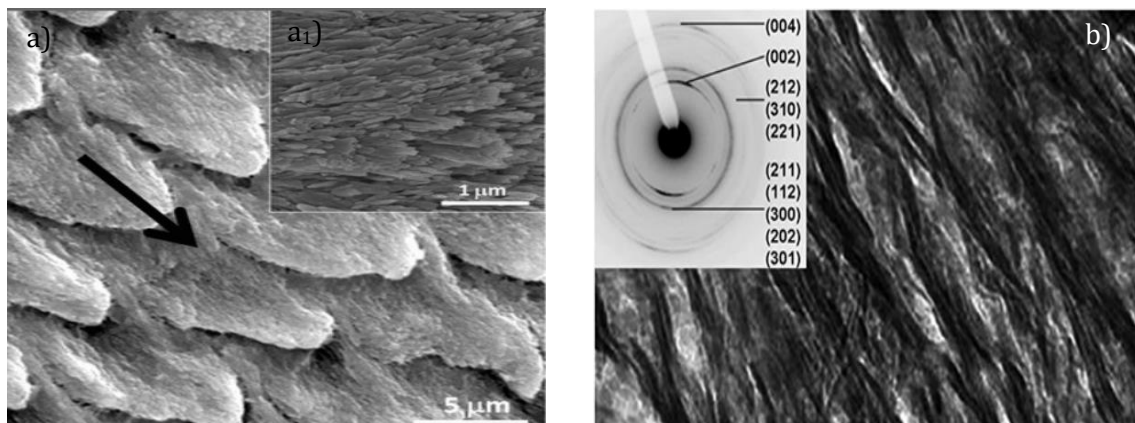


**Figure VII-1: (Li *et al.*, 2011) SEM images of an acid etched enamel showing the rod-like enamel crystal bundles a), insert shows magnified individual crystals a<sub>1</sub>); TEM of human femur showing dark contrast mineral lamellae with preferential c-axis orientation parallel to the long axis of the bone b) (Schwarcz, Abueidda and Jasiuk, 2017).**

As particulates, they tend to be characterised by a lack of a specific orientation, this morphology is not necessarily found in the human body. In the human body, the action of amino acids are thought to influence the shape of the apatite minerals that form. Amino acids like glutamic acid prevent supersaturation occurring in SBF, thus inhibiting the growth of apatite crystal completely (Li *et al.*, 2011). Aspartic acid was also shown to inhibit the growth of apatite crystals, this time because of their affinity for the c-face when grown in 38°C by Wang *et al.* (2013). They found that amino acids and other organic molecules had the ability to selectively adhere to certain faces, as a result of the charged nature of these faces i.e. adsorption of negative moieties on the a(b)face (c-axis) because it is calcium ion rich, and adsorption of positive moieties on the c-face because it is negatively charged due to the presence of phosphate and hydroxy ions (W. Wang *et al.*, 2013).

The shape of the apatite can be easily ascertained through the use of diffraction. This is because crystals having prominent c planes tend to give prominent diffraction peaks that coincide with the {00l} family of reflections, specifically (002) and (004) (Li *et al.*, 2011; Aizawa, Matsuura and Zhuang, 2013), thus a more pronounced peak with {00l} indicates that the sample is made with that specific orientation. Samples that are fibre like on the other hand have more intense peaks for the {h00} reflection family, thus (100), (200) and (300) (Li *et al.*, 2011; Aizawa, Matsuura and Zhuang, 2013). The strong presence of these peaks are indicators that majority of the samples

show this morphology, and orientation. As stated before, the isotropic nature of the particulates means that there is no reflection family that is particularly intense or not. Along with the phase of the calcium orthophosphate, the size of the crystallites, the preferred orientation can be determined using XRD, and TEM.

With XRD, Rietveld refinement process is extensively used. It is a method (using a least square approach) of minimising the differences between the XRD pattern that has been experimentally obtained against a theoretical/reference pattern (usually obtained from a well-maintained database like ICSD). It employs fairly substantial algorithms, in addition to emission and instrumental corrections (previously ascertained using a LaB<sub>6</sub> calibration standard) to reduce any external influence and thus characterise the contribution of the pattern from the sample alone. Outside the use of Rietveld refinement, the Williamson Hall plot may also be called upon to enable the estimation of the crystallite size, and the strain contribution to the diffraction peak shapes produced. It is a method that was developed by G Williamson and his student W Hall in 1953 (Williamson and Hall, 1953). “it differentiates the size induced and the strain induced broadening by considering the peak width as a function of 2θ” (Venkateswarlu, Chandra Bose and Rameshbabu, 2010). It is thought that the strain present in nanomaterials can affect the estimation of the size, particularly if the Scherrer equation is used as the sole form of size estimation.

Scherrer equation calculated the crystallite dimension using the following formula

$$D_v = \frac{k\lambda}{\beta_{hkl}\cos\theta_{hkl}} \quad \text{Equation 38}$$

where  $k$  is the shape factor which is constant at 0.9,  $\beta_{hkl}$  is the contribution due to the size of the crystallite measured at full width at half maximum (FWHM) in radians,  $\theta_{hkl}$  is the Bragg diffraction angle in degrees (°) and finally  $D_v$  is the mean size of the crystallites given in nm (Venkateswarlu, Chandra Bose and Rameshbabu, 2010).

In Williamson-Hall, the expression (Equation 38) is further augmented, where the broadening contribution is correctly assumed to be a sum of the size contribution and the strain contribution of the lattice (see Equation 39).

$$\beta_{hkl}\cos\theta_{hkl} = \frac{k\lambda}{D_v} + 4\epsilon\sin\theta_{hkl} \quad \text{Equation 39}$$

The above formula can be interpreted in a linear plot, where the slope of the plot gives the strain present in the crystallite, while the intercept gives the mean crystallite size (which is the mean

of the reflections that have been plotted).

TEM, HRTEM and SAED were used to obtain information of the apatite crystal.

## VII.4 Methodology

Sample preparation was elaborated in section II.4

### VII.4.1 Analytical instruments and conditions

The instruments and their conditions used in this section are listed below

#### VII.4.1.1 XRD

XRD was collected over the  $2\theta$  range of  $2^\circ$  to  $80^\circ$ , using a step size of  $0.09^\circ$ . For analysis, the scaffold samples was first sonicated. in a deionised water to collect the mineral content. The residue was drop cast on silicon wafer, which was used as the sample substrate/holder in the powder XRD.

#### VII.4.1.2 TEM

The samples collected in a similar as XRD were drop cast on carbon coated copper grids.

## VII.5 Results

### VII.5.1 XRD

This XRD section will be classified into 4 major parts based on the samples : Control samples, mineralised samples 4 cycles, mineralised samples 8 cycles, and heat-treated samples.

#### VII.5.1.1 Control samples

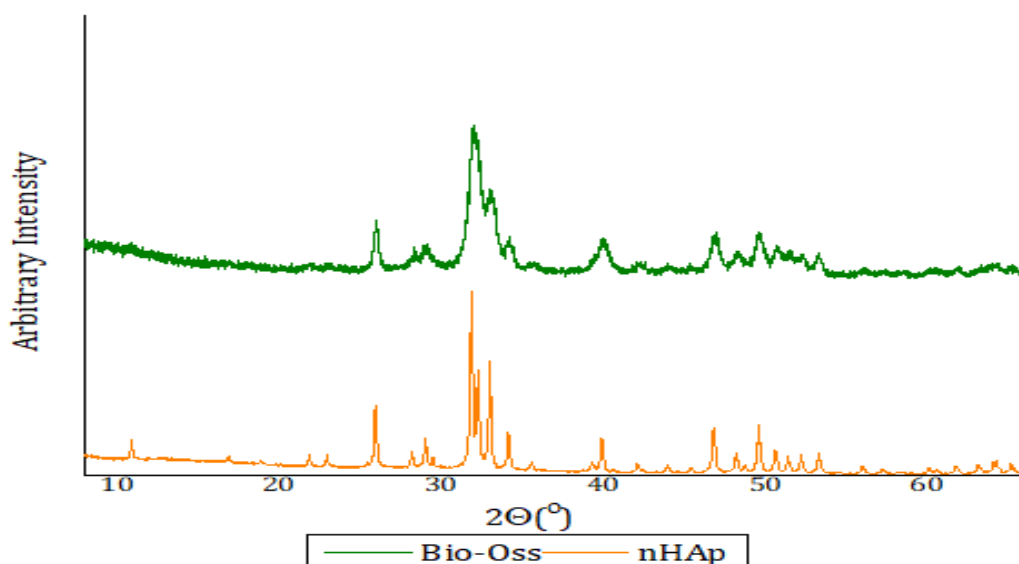


Figure VII-2: XRD diffraction patterns of Bio-Oss and nHAp.

Bio-Oss® is considered a benchmark dental bone substitute material; thus, comparisons against



the material would be a necessity for this study. The second control/model material is nHAp obtained from Sigma Aldrich, UK. It is assumed that they both would contain hydroxyapatite.

From the XRD pattern seen in Figure VII-2 one can clearly make out the similarities as well as differences between both of the patterns here. The main peaks are indicators of hydroxyapatite being present in both of the samples and occur at the following  $2\theta$  angles  $10.5^\circ$  (100),  $21.7^\circ$  (200),  $25.8^\circ$  (002),  $28.9^\circ$  (220),  $29.7^\circ$  (112),  $31.7^\circ$  (221),  $32.9^\circ$  (300),  $53.1^\circ$  (004) and many other reflections. The differences in the patterns visible in the above figure is not related to their compositional units as according to the preliminary phase identification using the “Diffrac suite EVA software” and a Rietveld refinement process using TOPAS, the vast majority of the peaks in question were all assignable to a monoclinic reference hydroxyapatite pattern obtained from the ICSD (PDF # 01-076-0694).

The similarity of the pattern and their confirmation with the appropriate Rietveld software seems to point to the possibility that the difference, mostly broadness of the peaks, is down to the size of the crystallite in question and possibly the percentage crystallinity in both samples. It is more than likely that Bio-Oss® has been specifically designed to have a reduced crystallinity for the purposes of ensuring active remodelling within the body. It is conceivable that this was done to improve the resemblance to bone in the body. The apatite structure in bone has been shown to be a mixture of ACP domains and poorly crystalline apatite. The presence of this amorphous to poorly crystalline phase make sense as evidence suggest that ACP has better osteoconductivity in vivo than hydroxyapatite and biodegradability; its intrinsic disorder structure makes it especially susceptible to reacting (resorption) with the necessary body fluid to precipitate apatite (Zhao *et al.*, 2011).

Of course, the difference could simply be a function of the mean size of the ordered crystallite which would then mean that Bio-Oss has a smaller crystallite mean size of 20nm while nHAp has sizes within the range of 216nm. The sizes of the samples were estimated using TOPAS where sizing was carried out using all the ordered peaks present and calculating their mean value: all of which were done using a double Voight peak modelling approach in addition to the corrections that have been previously mentioned, thus making the results closer to the real crystallite values.

The lattice constants of the unit cell are given in Table VII-1:

**Table VII-1: Lattice parameters of hydroxyapatite unit cell of samples estimated from Figure VII-2.**

Samples	a(Å)	b(Å)	c(Å)	Strain (dimensionless)
Bio-Oss®	9.44	18.75	6.88	0.04
nHAp	9.41	18.83	6.88	0.20

These unit cell parameters here are quite similar to the values shown for the hexagonal form as

“ $a=b=9.432(\text{\AA})$ ,  $c=6.881(\text{\AA})$ ” and the monoclinic form as “ $a=9.421(\text{\AA})$ ,  $b=2a$ ,  $c=9.881(\text{\AA})$ ” (Ma and Liu, 2009). The unit cell parameters when it comes to the discussion of hydroxyapatite are quite important, mainly due to the aligned nature of the mineral within the human tooth. Referring to the human enamel, the crystal appears to follow a specific direction vector in terms of its growth, thus depending on the section that is subjected to XRD analysis, certain peaks appear diminished or otherwise, which points to a certain preferential orientation/growth pattern of the mineral. According to Reyes-Gasga, Martínez-Piñeiro and Brès (2012) crystallites grow in human teeth enamel as prism like structures. As a result, the size fluctuates depending on if the estimate is done using the (002), (004) reflection and the (300), (200), (100) reflections. The {00l} reflections mentioned are presumed to coincide with the “c” axis of this prism, otherwise referred to as the length of the prism. The width of this prism is given by the {h00} reflections and these coincide with the “a” axis. The “b” axis is not important in the hexagonal context. In the monoclinic unit cell however, the “b” lattice parameter is double that of the “a” lattice and arises due to the arrangement of the OH groups. Hexagonal hydroxyapatite form has the OH group pointed in different direction, while in the monoclinic form, the opposite is the case (Ma and Liu, 2009). In the human teeth, the estimated size along the “a” axis is approximately 40nm, and along the “c” axis it is about 100nm (Reyes-Gasga *et al.*, 2015).

The elongated properties of the crystallite within the body is what sets it apart from the lab prepared samples. Having the crystallite aligned has been shown to be useful in a mechanical sense. This is why the human teeth have selective resistance to mechanical wear and fracture in certain directions (Bhushan, 2009; Fu *et al.*, 2016).

#### VII.5.1.1.1 WH-ISM(Williamson-Hall Isometric model) plots

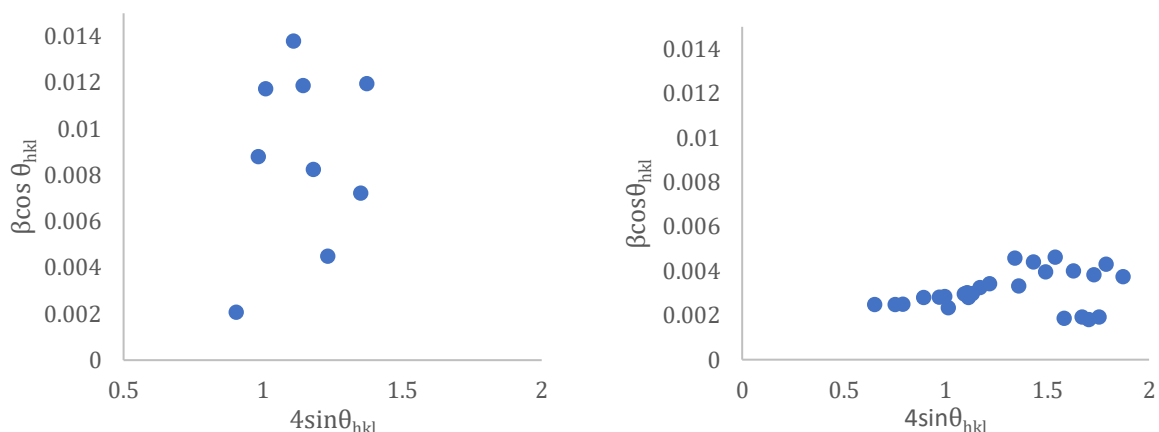


Figure VII-3: W-H ISM plots of Bio-Oss (left) and nHAp (right)

The first thing that one can see is that the plots are quite different. Bio-Oss® produced a plot with

a slope that appears undefined, this is in complete contrast to nHAp which seemingly has a cluster of points arranged sensibly around a linear trendline. Clearly, it would be easier to calculate the slope and the intercept of nHAp, while the other sample has a plot which makes deriving such information problematic. A value of 65.8nm is calculated from the intercept. And the strain present within the lattice is given from the slope at 0.0022 (no unit) which is fairly significant. The difference between the results obtained using this method and that from TOPAS seem to be fairly significant, but the following factors need to be considered.:

- Instrumental/emission correction: These are corrections that can be easily subtracted in TOPAS using the necessary calibration files that have been mentioned. It is not as easily done using the WH plot, so while the values here would be ultimately more accurate than Scherrer's method, it would still be considerably underestimated as the unnecessary broadness present in the XRD peak/pattern has not been properly deconvoluted to subtract the correction.
- The fitting model utilised; the methodology of fitting carried out for the purpose of the WH plot was done using Origin 9. Although created for data processing it is not necessarily geared towards the analysis of XRD patterns. As such the fitting models used would most likely be different from the macros that had been written exclusively for TOPAS which would be more suitable for cataloguing the shape of diffraction patterns (double Voigt approach). This no doubt created further over/under estimation of the peak width used. Most importantly, Origin 9 could only catalogue peaks that were "visible" to itself, in spite of the additional selection of the operator in identifying peaks. This is an approach which is completely different from TOPAS having the capability of using a reference matched pattern to search out and fit majority of the peaks. Thus, the absence of certain peaks would no doubt add additional errors in the estimation of the mean size.
- The peaks considered: this is an important factor and can greatly affect the size estimation. Depending on which peaks are used, with respect to their angles, certain errors can be realised. Peaks at low angles are apparently affected by flat specimen errors; peaks at higher angles are prone to distortions brought on by the dispersion of the radiation used to bathe the sample; peaks collected at medium angles are affected by the source of the X-ray and the "beam defining and receiving slits" (Burton *et al.*, 2009).

The following factors will have occurred in the following observations, no doubt to come, which would point to the difficulty in completely relying on the values obtained using WH-ISM plot.

Moving past the sizing and strain estimation, and returning to the shape of the plots, it is clear that they are quite different. Bio-Oss® shows a unique plot which at first glance one would easily misconstrue as error, but this is not so. It is here that we see the limitation of using the WH-ISM

plot while highlighting an important feature of Bio-Oss®. Other limitations like the necessity for no overlapping peaks and the assumption that broadening is only in the form of Lorentzian broadening no doubt cause some divergence in the real values (Girgsdies, 2015), but will be ignored for now. The shape seen for Bio-Oss® is as a result of anisotropy in the samples which is expected from the SEM micrographs in Figure VII-4b. While nHAp was observed to consist of particulates that were especially spherical in shape, thus quite isotropic Figure VII-4a, Bio-Oss® had no such morphology. Instead, it was shown to have a somewhat braided morphology, with well-defined parallel looking fibrils on its surface that interlocked in certain areas. It is possible that the fibrils were themselves individual crystallites, and this could be the origin of the anisotropy that we witness here in the WH-ISM plot.

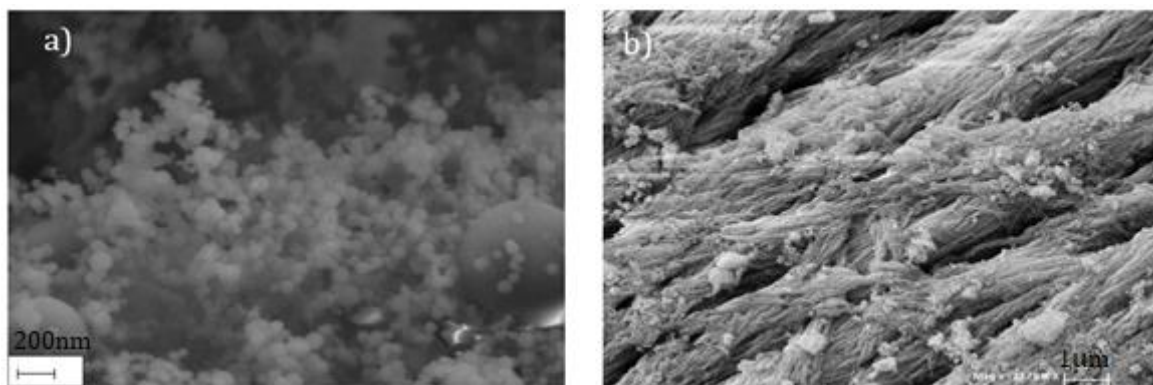


**Figure VII-4: SEM micrographs of nHAp a) and Bio-Oss® b).**

It is clear that while the WH -ISM plot is suitable in certain respects, mainly for isotropic material, it fails when the specimen in question adopts non-isotropic properties such as that seen in Bio-Oss®. Assuming the remaining samples are no more isotropic, one can expect to see the same issues with anisotropy, with the added limitations of the WH method.

#### ***VII.5.1.2 Mineralised samples obtained 4 alternating immersion cycles***

This section covers the first set of the mineralised samples which have undergone the immersion process in 4 cycles.

In the figure below, it is clear to see that the samples are quite different from the commercial samples. The peaks that would normally be attributed to the presence of apatite are not easily seen outside the broad area between  $2\theta = 29-34^\circ$ ; this covers the reflections (112), (221), (300) and (004). There are several reasons for the almost subdued presence of apatitic calcium phosphate in the XRD pattern below, and this is to do with the presence of another phase that has precipitated along with the phase of interest. It is calcite ( $\text{CaCO}_3$ ) with  $2\theta$  angles at  $23.0^\circ$  (012),

29.4° (104), 31.44° (006), 35.9° (110), 39.4° (113), 43.1° (202), 47.1° (024), 47.5° (018), 48.5° (116), 56.5° (211), 57.3° (112) and 58.0° (1010).

After the necessary search and match, Rietveld refinement was carried out again using TOPAS of the diffraction pattern in Figure VII-5.

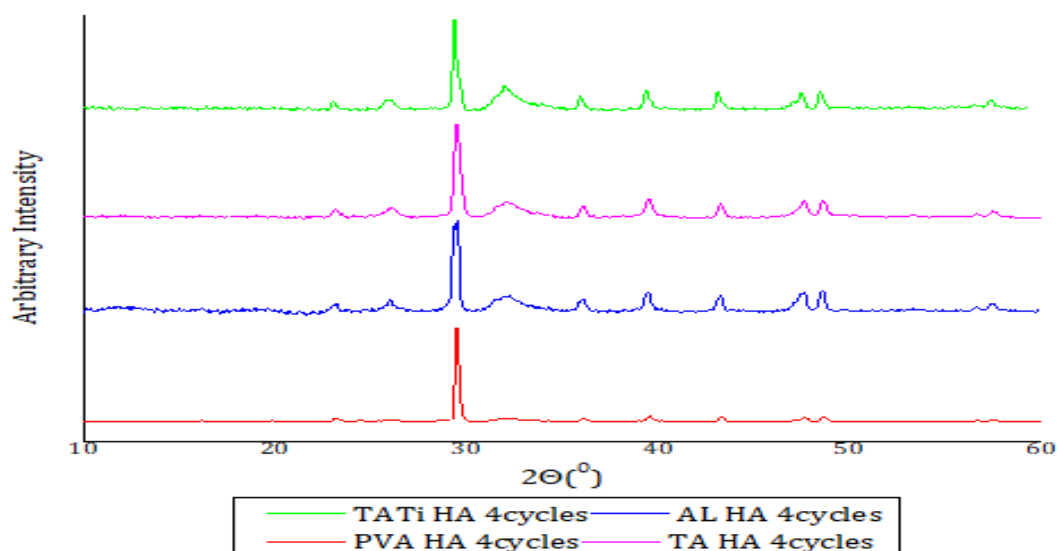


Figure VII-5: XRD patterns of AL HA 4 cycles, PVA HA 4 cycles, TA HA 4 cycles, and TATi HA 4 cycles.

The phase composition was given in Table VII-2:

Table VII-2: Percentage composition (%) of the phases present in the mineralised hydrogel samples(nm)

Samples	Hydroxyapatite (%)	Calcite (%)	Size(nm)
AL HA 4 cycles	44.68	55.32	14.4
PVA HA 4 cycles	41.57	58.43	19.3
TA HA 4 cycles	46.25	53.75	13.7
TATi HA 4 cycles	61.32	38.60	12.4

From the XRD pattern alone Figure VII-5, one would have assumed that the majority of the phase being formed would be anything but calcium phosphate, seeing as the more prominent peaks belong to calcite. This was most likely due to the crystallinity of the impurity phase, not to mention the sizes of their crystallites (ranging from 30-80nm), both of which contributed to a pattern that almost overshadowed the apatite in the mineralised samples.

In addition to the phase composition and size, it was also possible to extract information on the dimensions of the unit cells of the apatite formed, as well as some calculation of strain in the sample. The values are shown in Table VII-3

Table VII-3: Lattice parameters of hydroxyapatite unit cell for mineralised hydrogels in Figure VII-5 after 4

### alternating immersion cycles

Samples	a (Å)	b(Å)	c (Å)	Strain (dimensionless)
AL HA 4 cycles	9.32	19.22	6.85	0.33
PVA HA 4 cycles	9.58	18.53	6.87	0.15
TA HA 4 cycles	9.31	19.1	6.88	0.18
TATi HA 4 cycles	9.58	18.59	6.87	0.25

The unit cells shown in the above table are quite interesting. While the control samples show the “a” unit cell values of between 9.41-9.44(Å), with unchanging “c” unit cell values of 6.88(Å), the same cannot be said for the mineralised hydrogel samples. The “a” unit cell appears to have shrunken by about 0.9% for two samples (AL-HA 4 cycles and TA-HA 4 cycles), and on the other hand expanded by 1.4% for the remaining samples (PVA-HA 4 cycles and TATi HA 4 cycles). The change along the “c” unit cell is not quite as significant and will be disregarded, Now, considering the slight contraction in the “a” axis, this contraction (expansion) of the “a” axis might be as a result of substitutions occurring within the lattice. Apparently, substitution within the lattice is thought to affect the unit cell parameters. In the case of the “a” axis, substitution of the phosphates for carbonates is known to result in the contraction of the lattice (Hanlie, Liyun and Tao, 2006). This is most likely to do with the variation of the ionic radii of the species in question with carbonate having an estimated thermochemical radii of 178pm and phosphate with 238pm (Roobottom *et al.*, 1999; Lide and Haynes, 2010). Contraction of the “a” axis may also be facilitated by the substitution of calcium ion with smaller cations (Gamal, Al-Mufadi and Said, 2013). Ions such as Na<sup>+</sup>, Mg<sup>2+</sup> have been seen to cause contraction along the a-axis, as well as the c-axis. The substitution of Ca<sup>2+</sup> is the more unlikely scenario seeing as the c-axis for the most part appeared to remain unchanged (both in the control values and in the lab synthesised samples). Carbonate substitution makes the most sense and corroborates the findings from both FTIR and Raman spectroscopy, where several peaks and bands were found that suggested the presence of carbonates in the mineralised samples. In terms of “a”-axis expansion, again substitution might be behind the expansion of the apatite lattice. The replacement of phosphate, i.e. B-site substitution, can cause a contraction of the “a”-axis; however carbonate substitution of the hydroxyl group (A-site substitution) can cause an expansion of the axis (Yang *et al.*, 2013). Again, the differing ionic radii might be the cause; the fact that carbonates are larger than hydroxyl group can cause a significant distortion in the lattice along the “a” direction.

If the above scenarios are the case, then the samples produced are all carbonate modified hydroxyapatite. But the differing substitution sites of carbonate, whether via the A or B or AB site leads to the creation of apatitic crystal with varying crystallinity and solubility. Either A or B (or both) site substitution causes a change in the overall charge of the lattice which can be compensated through the creation of OH vacancies, in the case of A type substitution, or Ca and

OH vacancies in the case of the other type of substitution. In the case of A/B substitution, both instances are quite likely. The charge compensation and the initial substitution has been shown to affect the energy of the crystal. (Yang *et al.*, 2013). Samples with no substitution or exclusively B site substitution were known to be more stable, having lower crystal energies – a summation of “energy of valance and non-bond” with non-bond including: Van der Waals, electrostatic and hydrogen bond. What this means is that samples PVA HA 4 cycles and TATi HA 4 cycles could potentially be less stable than the remaining sample, assuming that carbonate substitution is the order of the day (Yang *et al.*, 2013).

#### VII.5.1.2.1 WH-ISM (Williamson-Hall Isometric model) plots

Figure VII-7 comprises the different WH-ISM plots of the mineralised hydrogel samples. It is immediately apparent that all of the samples have patterns that are similar to that of Bio-Oss®. This is to be expected as SEM images collected, recapped in Figure VI-8, showed that the particulates which were present in the matrix of the hydrogels had a specific crystal shape: as a cluster of platelets that radiated from a central source, growing outwards. One could clearly see from the shape of these crystals that they cannot be mistaken for being spherical, or any other shape close to it, thus they cannot be considered isotropic (see Figure VI-8).

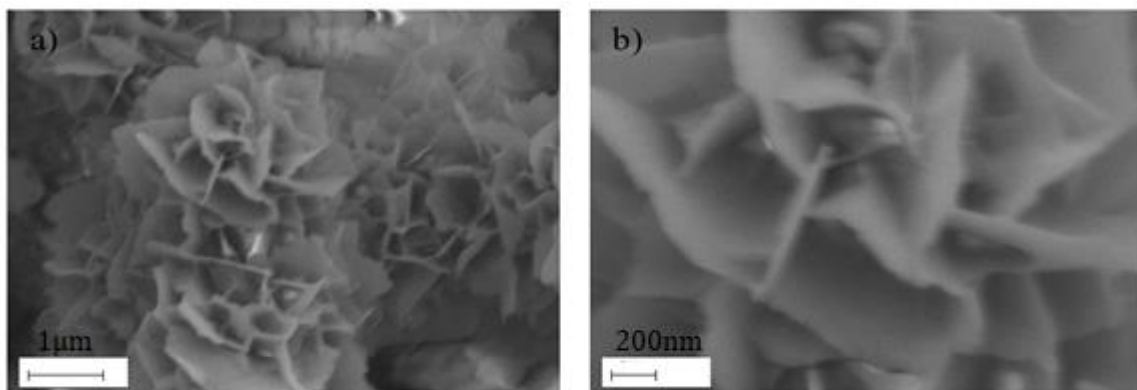


Figure VII-6: Carbonate-modified PVA HA obtained after 4 alternating immersion cycles (a & b)

They are quite the opposite of nHAp, which again like Bio-Oss® gives credence to why their WH-ISM plot does not contain points that can lie on a horizontal line, inclined or otherwise.

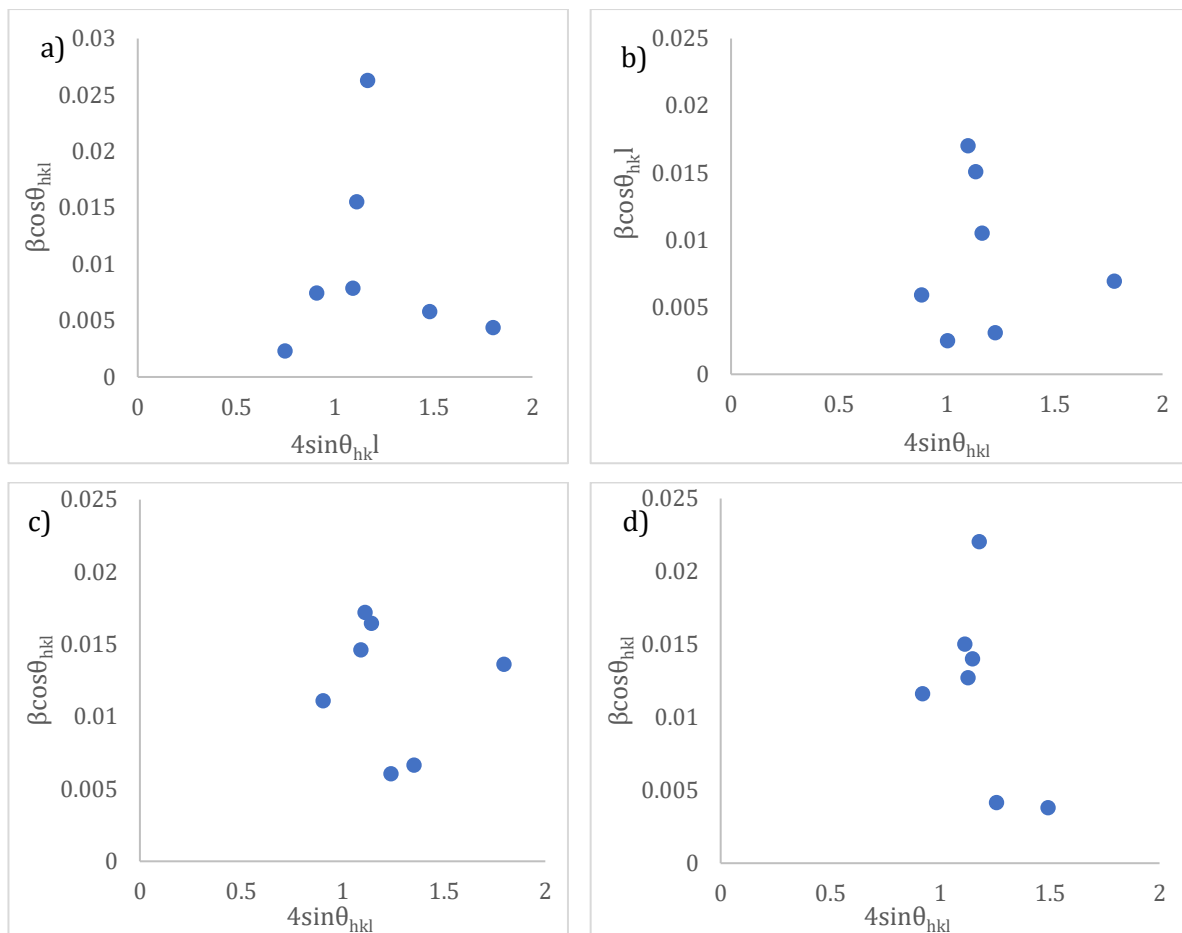
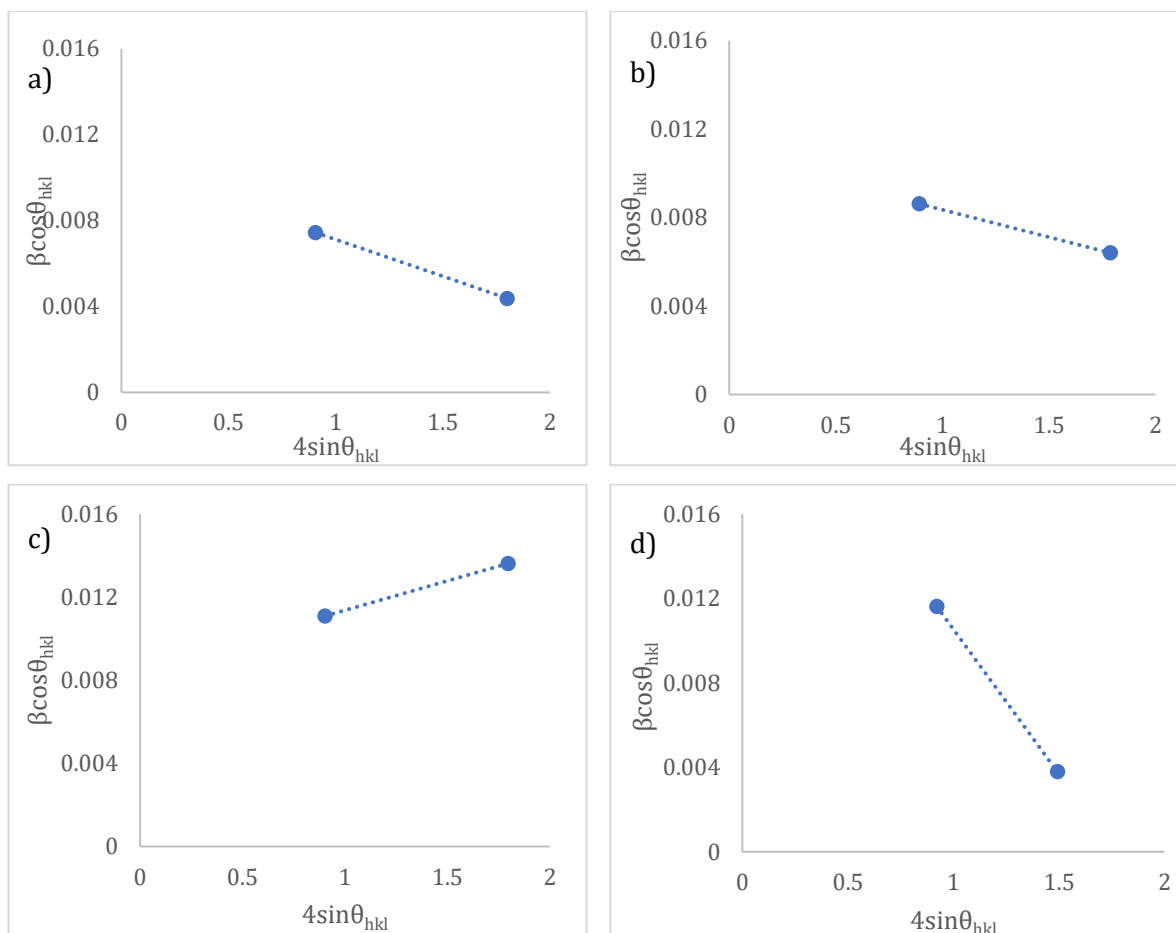


Figure VII-7: W-H ISM plots of AL HA 4 cycles a); PVA HA 4 cycles b); TA HA 4 cycles c); and TATi HA 4 cycles d).

The fact that the samples being synthesised have a platelet like conformation means that yet again the WH-ISM plot is not the best way to provide information on the crystallite size nor the strain present in the sample.

WH-ISM methodology is restricted to isotropic samples, but it is still possible to utilise families of certain reflection to help narrow down the size and strain contribution of the pertinent crystal faces (Reyes-Gasga *et al.*, 2015). Seeing as the apatite crystals in teeth and bone are fairly anisotropic, showing anisotropy mainly along the {001} and the {h00} reflection, for the c-axis and the a-axis respectively. It requires at least two members within each family to help with the estimation accuracy. This was done successfully for the {001} family, thus the c-axis or the length of the crystal, as shown in Figure VII-8.





**Figure VII-8: W-H ISM plots of selected reflections (0,0,2) and (0,0,4) for AL HA 4 cycles a); PVA HA 4 cycles b); TA HA 4 cycles c); and TATi HA 4 cycles d).**

The sizes that were estimated are shown in Table VII-4. These sizes estimated seem to be comparable, at least in the order of magnitude, with regards to those estimated using TOPAS. Either way, they are still significantly smaller than what would normally be present in the human tooth in the {00} direction, which is approximately 100nm (Reyes-Gasga *et al.*, 2015).

**Table VII-4: Crystallite sizes estimated using the WH-ISM plot of selected reflection (0,0,2) and (0,0,4) from Figure VII-8.**

Samples	Size (nm)	Strain (dimensionless)
AL HA 4 cycles	13.78	-0.03
PVA HA 4 cycles	13.40	-0.02
TA HA 4 cycles	17.02	0.02
TATi HA 4 cycles	5.98	-0.01

Also, the negative slope of some of the samples can be interpreted as samples having very little microstrain in their lattice (Langford and Cernik, 1991); thus the size calculated is closer to a real size.

There is no doubt that there is some error in this approximation, seeing as the actual reflections

used are limited (only two) and not helped by the difficulty in finding more reflection within the {001} family and the difficulty in resolving the peak areas accurately. Of course, it is possible that the values are real, the same as those calculated by TOPAS. One needs to keep in mind that TOPAS produces a mean value for size and strain. Thus, the contributions of the many crystal faces/reflections have simply been averaged, which means that it is possible that a significant portion of the faces- that are not exposed or consumed due to their high energy- are responsible for the values given by TOPAS. Using the WH-ISM method gives one the luxury of being selective of which face/family of reflections to concentrate, which would end up giving a result that could be anywhere in the distribution of sizes and strain, creating its own uncertainty. The only way around this problem is to increase the number of samples, in addition to using a different XRD scan setup i.e. WAXS and SAXS, to help pick up more reflection and thus families for improved estimation.

It is for this reason that the same methodology was harder to apply for the {h00} family due to the difficulty of finding peaks other than that for the (300) reflection.

### VII.5.1.3 Mineralised samples after 8 alternating immersion cycles in a CaP precursor

In this section, the samples were prepared in essentially the same manner as in section VII.5.1.2. While the previous section stopped at 4 immersion cycles, the mineralisation process in the following samples was carried out until the 8<sup>th</sup> cycle. One interesting feature that will become increasingly obvious in this section is the additional presence of halite (NaCl), along with calcite as the impurity phases.

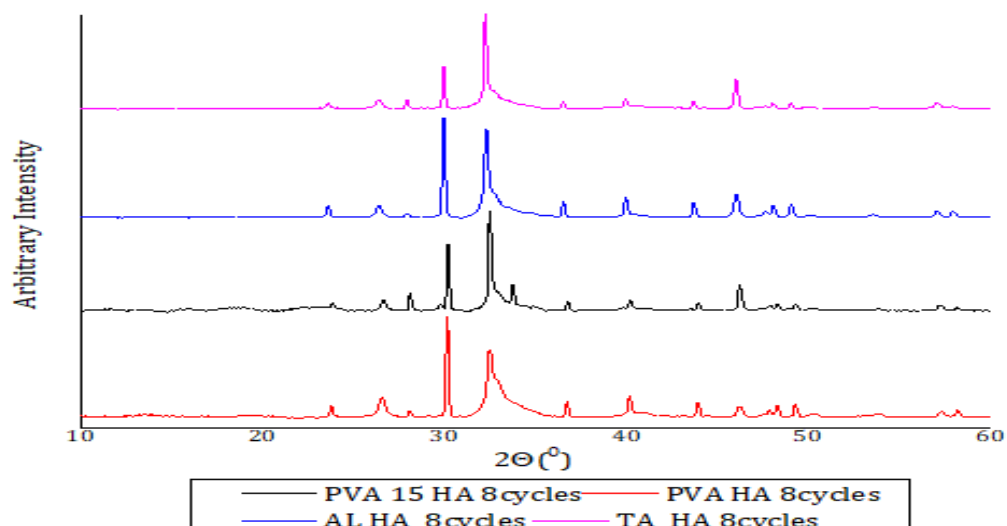


Figure VII-9: XRD pattern of AL HA 8 cycles, PVA HA 8 cycles, TA HA 8 cycles, and TATi HA 8 cycles.

In Figure VII-9 above, the extra peaks, as a result of halite are present at  $27.3^\circ$  (111),  $31.7^\circ$  (002)

45.4° (022), 53.9° (311) and 56.5° (222) in all of the samples. The most likely cause of this halite impurity is an inadequate rinsing step during one of the cycles. Section VII.5.1.2 and Table VII-2 shows that the main compositional phases that were discerned were due the apatite phase and calcite, unlike these samples. Remarkably enough, the percentage of apatite (see Table VII-5) that was picked up from the XRD pattern is much higher than that found in the samples obtained after 4 immersion cycles(see Table VII-2). The discrepancy might have simply arisen due to an increase in the cycle number. With each successive increase, the nucleation and eventual precipitation of apatite occurs with further nucleation points being offered by the new surfaces of the apatites that have also precipitated. In this same way, the presence of calcite, as well as the halite could act as a further surface that would allow the nucleation of further apatite crystals within the hydrogel. This could account for why the apatite in these samples are  $\geq 59.9\%$ . The lower calcite content may also be due to the increase in the successive cycles allowing solubilisation and eventual incorporation of the carbonate into the apatite lattice- creating the carbonate substituted apatite that have been hinted by FTIR, Raman and the lattice parameter previously reported in Table VII-3.

**Table VII-5: Percentage composition (%) of the phases present in the mineralised hydrogel samples and their mean size (nm) after 8 alternating immersion cycles.**

Samples	Hydroxyapatite (%)	Calcite (%)	Halite (%)	Size(nm)
AL HA 8 cycles	59.9	24.9	15.1	15.2
PVA HA 8cycles	69.7	22.9	7.2	15.8
TA HA 8 cycles	66.3	16.8	16.7	13.3

The sizes of the impurity crystallites were estimated to approximately  $\geq 120\text{nm}$  for calcite, and  $\geq 70\text{nm}$  for halite.

In addition to the phase composition and size, it was also possible to extract information on the dimensions of the unit cells of the apatite formed, as well as some calculation of strain in the sample. The values are show in the following table.

**Table VII-6: Unit cell parameters for the mineralised hydrogels after 8 alternating immersion cycles from Figure VII-9**

Samples	a (Å)	b(Å)	c (Å)	Strain (dimensionless)
AL HA 8cycles	9.31	18.93	6.89	0.27
PVA HA 8cycles	9.27	18.94	6.89	0.10
TA HA 8cycles	9.25	18.92	6.88	0.23

The unit cells shown in the above table are quite interesting. Compared to “a” unit cell parameter, the “a” unit cell given in Table VII-6 appears to have shrunken for all of the samples, showing a decrease of about 1.0-1.3%. The change along the “c” unit cell is again not significant and will be disregarded. Now, taking into account the slight contraction in the “a” axis: this contraction is

probably as a result of swapping phosphate for carbonates thus causing the shrinkage (Hanlie, Liyun and Tao, 2006). This is most likely in a similar manner as that shown for the samples made after 4 cycles. The difference in the ionic radii between the species involved is probably behind this (Roobottom *et al.*, 1999). Now, while in the samples made after 4 cycles the possibility of contraction of the “a” axis facilitated by the substitution of calcium ion with smaller cations (Gamal, Al-Mufadi and Said, 2013) was disregarded, largely due to a lack of a significant presence of other potential metal ions : in this instance, the occurrence of halite as a source of Na<sup>+</sup> increases the possibility that maybe such a mechanism might be in play along with carbonate substitution. Although carbonate substitution makes the most sense, the substitution of Ca<sup>2+</sup> could provide a mutualistic scenario even though the c-axis values remain similar in both the control values and in the lab synthesised samples. Perhaps the increment of the c-axis seen in Table VII-3 that was disregarded is actually representative of the real unit cell in the axis; and while a standalone phase like halite was not picked up in the estimation of phase composition, the possibility that the individual ions that made up the halite was simply incorporated, could partly explain the contraction in one axis and the expansion in the other.

The strain estimated in Table VII-6 is above 0.10 purporting to the possibility of internal strain within the lattice, which tends to be a function of the size of the crystallites. All the crystallites seem to fall within the nanoscale range.

#### VII.5.1.3.1 WH-ISM plots

Like the samples before this, Figure VII-10 shows that yet again the samples appear to possess anisotropic properties. This is not surprising, as the preparation methodology was similar to the samples in VII.5.1.2, and as such the particulates that were precipitated had a similar morphology to its counterpart made using only 4 cycles (see Figure VI-10).

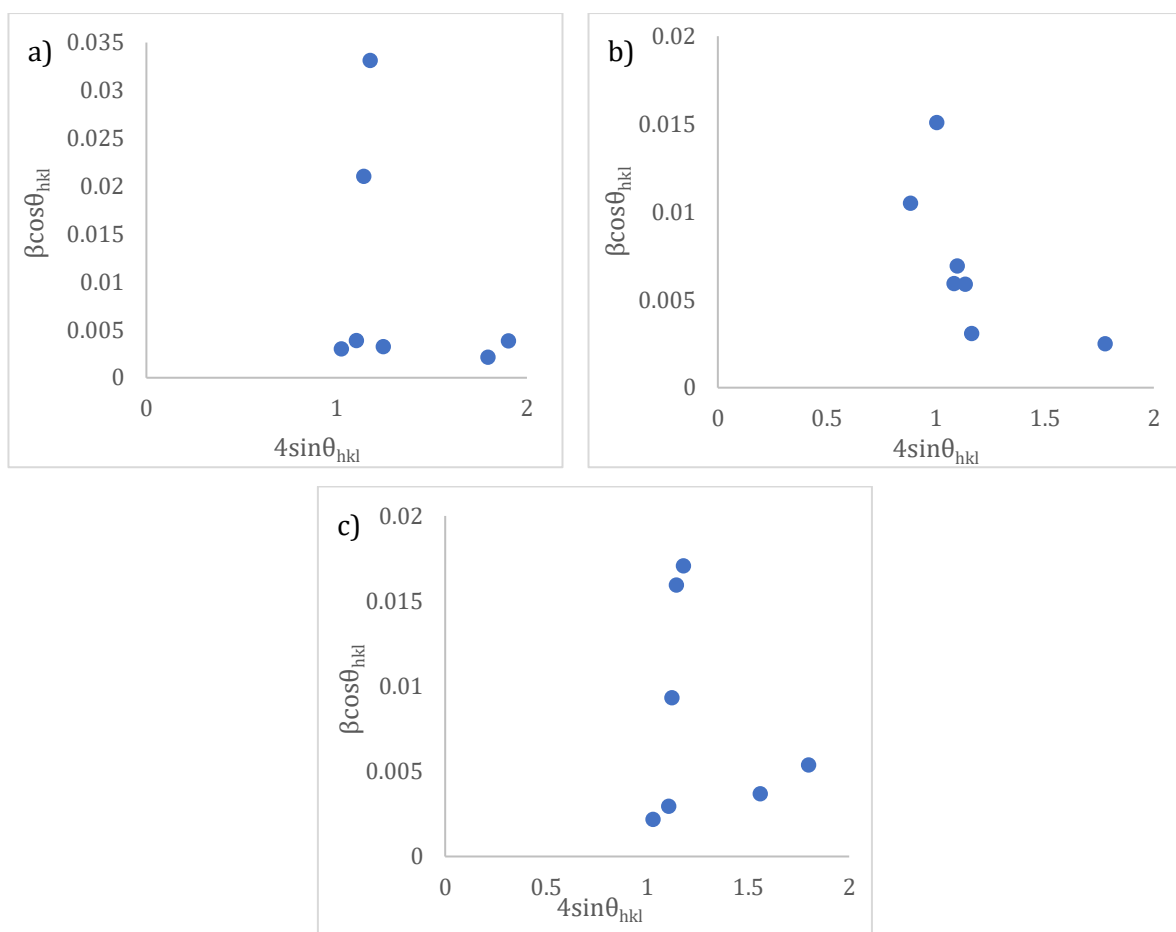


Figure VII-10: W-H ISM plots of AL HA 8 cycles a); PVA HA 8 cycles b); and TA HA 8 cycles c).

The main difference in the morphology is simply how crowded the cluster is, which is a function of the increased cycle number.

WH-ISM plot was then carried out using again two reflections from the {00} family, which can be seen in Figure VII-11.

Table VII-7 shows the increment in the dimension size of the crystallite compared to the previous samples (mineralised hydrogels at 4 cycles), and a drop in the order of magnitude of the strain within the lattice. The values here are different from those that have been calculated using TOPAS. Again, the negative slope of some of the samples can be interpreted as samples having very little microstrain in there. By the same reasoning of average number of reflections utilised, it is not entirely certain that the values given in the table below are real.

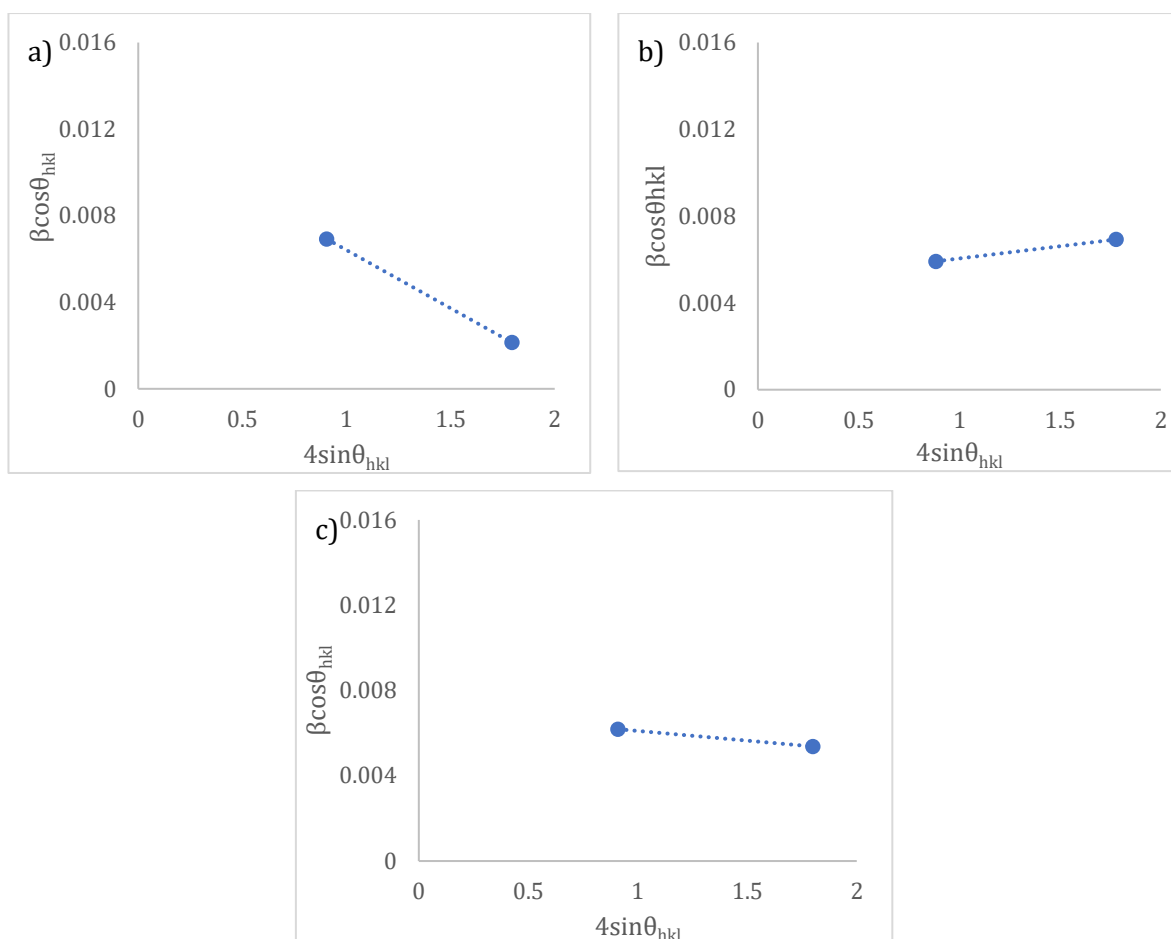


Figure VII-11: W-H ISM plot of selected reflections (0,0,2) and (0,0,4) for AL HA 8 cycles a); PVA HA 8 cycles b); and TA HA 8 cycles c).

Thus, the recommendation of an increased number of samples, in addition to different XRD setup, is necessary to improve the size and strain estimation especially as the peaks produced by the nanoscale apatite crystals are incredibly convoluted due to multiple peaks overlapping.

Table VII-7: Crystallite sizes estimated from the WH-ISM plot of selected reflection (0,0,2) and (0,0,4) in Figure VII-11.

Samples	Size (nm)	Strain (dimensionless)
AL HA 8cycles	12.26	0.005
PVA HA 8cycles	29.54	0.001
TA HA 8cycles	20.68	0.0009

#### VII.5.1.4 Heat treated mineralised hydrogel samples.

In this section, the mineralised hydrogel samples that had been previously produced were calcined in a box furnace at 800°C at a rate of 10°C/min for a duration of 1h in air, before cooling back to room temperature. One can already see that the diffraction patterns that have been presented in Figure VII-12 share very little resemblance to those in Figure VII-5 and Figure VII-9. Not only are the peaks produced sharper and more resolved than the broad and shallow lumps

previously seen, new peaks are also present in the pattern.

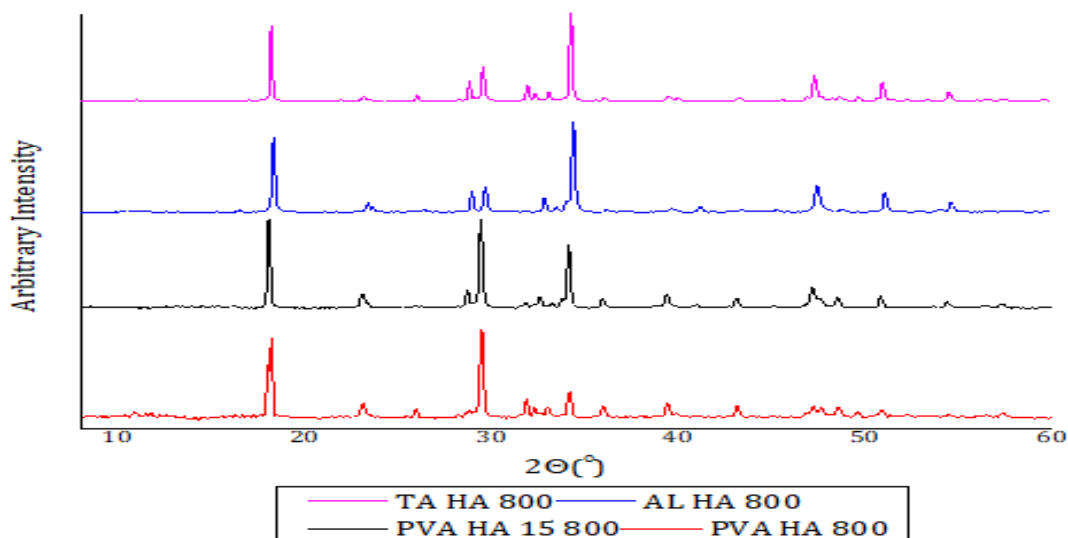


Figure VII-12: XRD pattern of the mineralised hydrogel scaffolds subjected to calcination in air at 800°C for 1h in air.

Phase identification and analysis show that the samples consist of three main phases: apatite, calcite and portlandite. The approximate composition of the phase produced is shown in Table VII-8.

Table VII-8: Percentage composition (%) of the phases present in the mineralised hydrogel samples and their mean size (nm) after calcination at 800°C from Figure VII-12.

Samples	Hydroxyapatite (%)	Calcite (%)	Portlandite (%)	Size (nm)
AL HA 800	17.40	31.11	51.47	91
PVA HA 800	32.27	60.09	7.63	65
TA HA 800	29.21	28.63	42.15	207
PVA 15 HA 800	5.85	67.85	26.29	59

Table VII-8 shows that the phases presented in the sample after calcination are dominated by the presence of impurity phases (calcite and portlandite) rather than the actual apatite. The presence of calcite is not surprising as it was also present before that; portlandite again is another mineral phase that has been shown to transform into apatite depending on the conditions. Its formation was probably facilitated by the rapid dehydroxylation of the “wet” apatite. The release of  $\text{OH}^-$  in the vicinity of any excess  $\text{Ca}^{2+}$  (probably substituted out to maintain charge neutrality in the nonstoichiometric apatite or any unreacted precursor) leads to a reaction with the formation of portlandite being a potential outcome (Fu *et al.*, 2018); increased temperature might have made this reaction more plausible, improving the mobility within the system. Otherwise, apatite according to Fu *et al.* (Fu *et al.*, 2018) has less solubility and is preferentially formed.

As to be expected the size of the crystallites increased with the heat treatment (800°C).

**Table VII-9: Estimated unit cell parameters for mineralised hydrogels after 8 alternating immersion cycles from Figure VII-12.**

Samples	a (Å)	b(Å)	c (Å)	Strain (dimensionless)
AL HA 800	8.84	18.62	6.81	0.00010
PVA HA 800	9.42	18.84	6.88	0.03
TA HA 800	9.42	18.82	6.88	0.005
PVA 15 HA 800	9.47	19.13	6.71	0.003

Moving on to the lattice parameters of the apatite phase, the “a”-axis for most of the samples, except AL HA 800, appears to fall close to the same value range as those that were initially recorded for the control samples. The temperature (and time) could have been enough to allow the arrangement of the unit cell and the expulsion and eventual decomposition of the impurities (carbonates especially into the atmosphere), creating a unit cell that is closer to a standard monoclinic apatite lattice. The very significant deviation of the “a”-axis in AL HA 800 is an indicator that the phase that was identified as apatite by the software is in fact something else. Any number of calcium phosphate phases with peaks that overlap with apatite might be the cause of this misidentification.

Although heat treatment improves the crystallinity of the sample, the trade-off appears to be a complete loss of the unique properties of the crystallites that would have otherwise persisted. The apatite crystals in the human body are not completely crystalline: they are nonstoichiometric with the inclusion of various “impurities” that imparts them with transient properties that allow them to be easily remodelled in a low temperature/interference environment. Increasing the crystallinity means that they lose this property that allows this ease of remodelling. This is not to mention the loss of the amorphous calcium phosphate phases, which are essential parts of the biomineralization process, acting as early precursors in most cases. So, while improving the crystallinity and possibly the mechanical properties are the aim for such heat treatment, the loss of properties that might affect the biocompatibility and osteoconductivity is something that ultimately might not be worth such pursuits.

Further analysis of this sample will not be carried out as the initial shape and nanoscale properties of the low temperature synthesis appear to have been lost through the addition of heat.

### VII.5.2 TEM

Along with diffraction studies, microscopy as well as some selected area diffraction (SAED) was done using TEM. The main reasoning behind using the additional technique was to allow a better visualisation of the particulates (specifically crystallites) in the cases where the samples have the right level of crystallinity to produce the necessary lattice fringes. The previous sections have shown that the crystallites produced using the hydrogel as the scaffold are not spherical in shape but have a specific directional anisotropy, just like the commercial sample Bio-Oss®. Thus, along



with giving a better visual idea of the shape of the crystallites, the sizes of the crystallites where possible can be roughly estimated using TEM- bearing in mind that only a limited population can be considered at a time, which would no doubt produce a very skewed sizing estimate. And finally, onto diffraction, powder XRD in principal is an averaging technique which can sometimes leads to obscuring certain pertinent information. In the previous sections, we saw that the apatite crystallite was made up of several reflections, which became harder to catalogue/index due to the nanoscale dimensions and their resultant effect on the XRD peaks. It is hoped that in using TEM, one might be able to get an idea of which face is the most prominent in all of the samples, in addition to how the dimensions of each face might be linked to the dimensions of the crystallites. To begin with, the control samples: Bio-Oss® and nHAp will be observed to see the morphology of their particulates and how this relates to the XRD results from the previous section and to the SAED that will subsequently be carried out in this section. Following that, analysis on the lab synthesised samples will be carried out.

#### **VII.5.2.1 Control samples**

In the Figure VII-13a & b) below, the polycrystalline nature of the Bio-Oss® is obvious. The particulates appears to be made up of crystallites with no specific orientation as seen in Figure VII-13b. Not only are they haphazard in the way they constitute the crystal aggregate visualised, they are no seen to be spherical in shape. Which confirms the results from WH-ISM plot, where the arrangement of the data points indicated that the sample not isotropic. Inset of Figure VII-13b shows the diffuse diffraction spot pattern which confirms the polycrystalline nature of the samples.

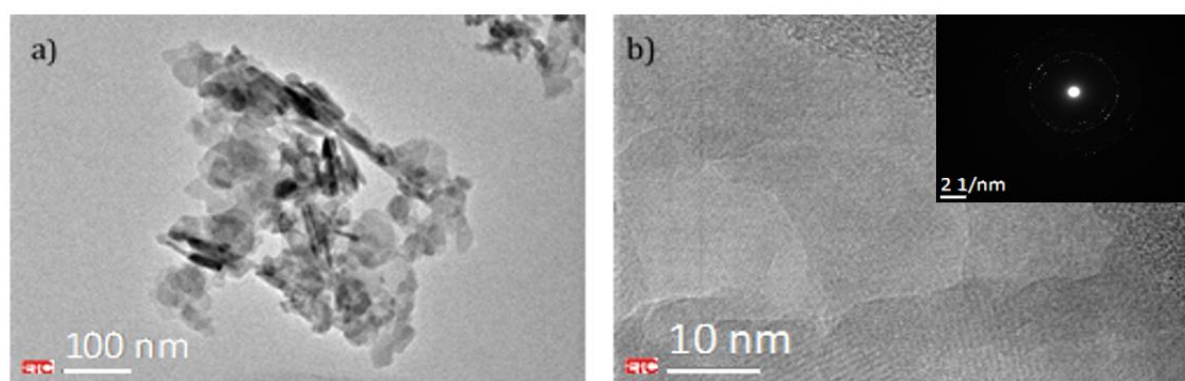


**Figure VII-13: a) TEM micrographs of Bio-Oss®; b) HRTEM showing lattice fringes of the crystallite aggregates in real space (Inset: SAED of the lattice fringes).**

With the aid of HRTEM images, the author attempted to use areas with prominent lattice fringes to estimate the d-spacing of the crystal faces. The calculation was not done using the SAED images owing to how diffuse some of the spots were. Instead, the distance between the lattice fringes that

were generated using HRTEM imaging mode was used to estimate the d-spacing. This of course had its own potential errors especially when concerning a polycrystalline material, due to the overlapping lattice fringes from crystals that might be in plane. Although not as problematic as using SAED, it does have its set of complications, as one will soon see. Many of the crystallites (that will be examined) do not exist alone, but rather with multiple overlaps that creates fringes with multiple criss-crosses.

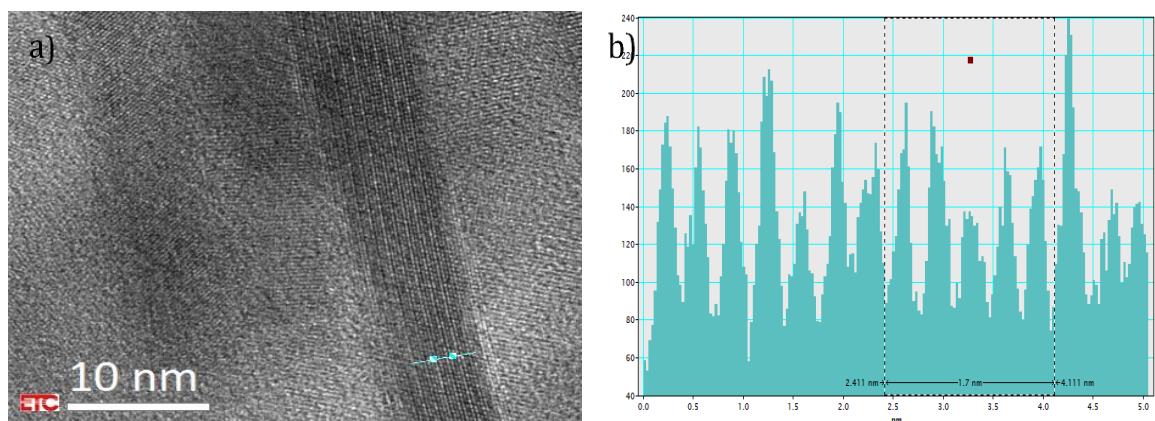


Figure VII-14: a) HRTEM of Bio-Oss®; b) and the estimated d-spacing from lattice fringes obtained from a).

An area with distinct fringes was picked as shown in Figure VII-14. A blue line was drawn perpendicular to the fringe lines; this gave an approximate d-spacing value of 0.34nm(3.4Å) after using the width of an average number of the fringes presented in Figure VII-14b. The d-spacing coincides with the (002) which as has been suggested by Reyes-Gasga *et al.* (2015) is supposed to coincide with the c-axis of the apatite unit cell, which is incidentally the longest length of the apatite “prism” that makes up the teeth. The images here provide a strong indication that the commercial sample is anisotropic. Thus it seems that most of the faces here are of the (002) plane belonging to the {00l} family which would make it plate like (platelet), and were it to be aligned the c-plane, a situation would be created where it would be similar to that of human teeth; Aizawa, Matsuura and Zhuang (2013) showed that plate shaped crystals has a preferred orientation along the a or b axis, which leads to the development of the c-axis. This might be the reason why the (002) plane was easily picked up, as it covered the most area.

A completely different scenario is observed when considering the other commercial sample, which is the nHAp. In Figure VII-15a-c, the differences are clearly easy to pick out. Starting with Figure VII-15a, the initial shape is quite different from that seen in Bio-Oss®. Instead of indistinct particulate shapes in Bio-Oss®, the sphericity of this sample is quite prominent. Picking out the individual particles are a lot easier.

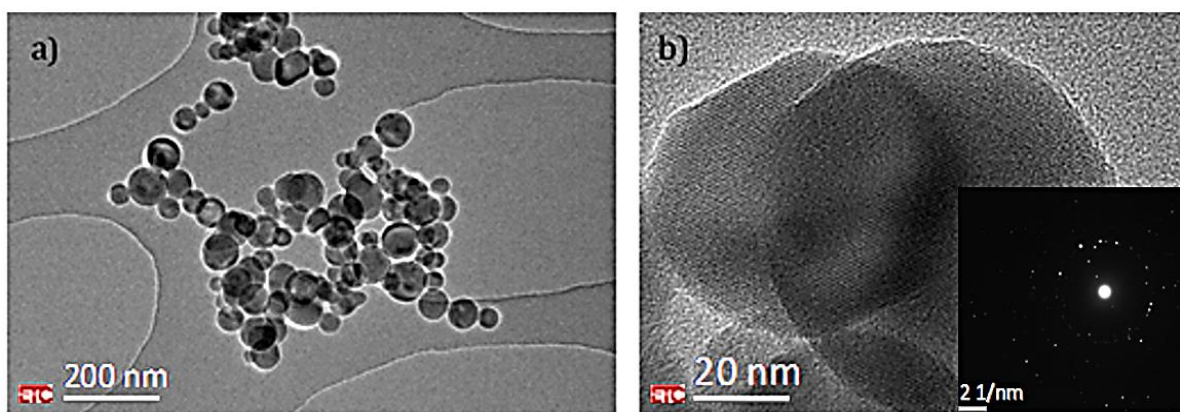


Figure VII-15: a) TEM micrographs of nHAp HRTEM showing lattice fringes of the crystallite aggregates in real space (Inset: SAED of the lattice fringes) b).

In addition to the samples being spherical, Figure VII-15b shows that each of these spheres appear to be monocrystalline from the HRTEM image. The lattice fringes are periodic with no imperfection visible at the chosen magnification. The fact that each of these spheres are monocrystalline made generating an SAED image with clear and discrete bright spots possible (Figure VII-15c). The spherical nature of the particles could mean that any number of the faces a or c face might be exposed to the surface. What is clear is that the spherical nature of this sample means that an equal distribution of faces is possible thus highlighting its isotropic properties.

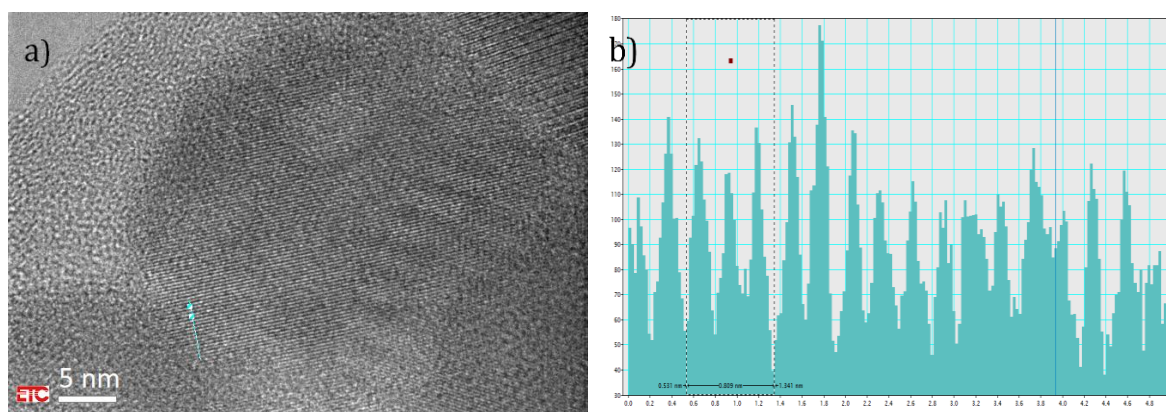


Figure VII-16: a) HRTEM of nHAp; b) estimated d-spacing from lattice fringes obtained from a)

Attempts were made to calculate the d-spacing again using a select number of the fringes to aid in the estimation of an average value. Although only a single figure for the lattice fringe width estimation was included, different areas were considered and most of them gave close to the same value, which is a d-spacing of approximately 0.27nm (2.7Å): this apparently represents the reflection at (300).

### VII.5.2.2 Mineralised hydrogels

Here, exploration of the differences in the apatite crystals that have precipitated with the different blends of hydrogels will be done. The samples PVA HA, AL HA, TA HA and TATi HA will be examined.

#### VII.5.2.2.1 PVA HA 4 cycles

What is immediately obvious in Figure VII-17a) is the shape of the particulates that have been picked up. They share absolutely no resemblance to the nHAp, which was suggested by the XRD pattern and additionally by the WH-ISM plot (where the anisotropy of this samples was highlighted). In terms of shape, it is obvious that the samples are not needle like in their morphology, eliminating the possibility that growth has occurred along the a-axis (over that of the c-axis) (Aizawa, Matsuura and Zhuang, 2013).

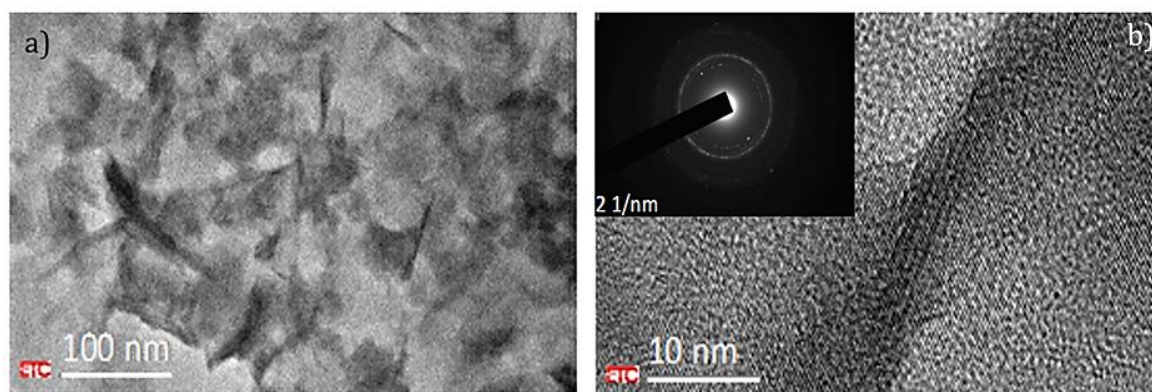


Figure VII-17: a) TEM micrographs of PVA HA 4 cycles; b) HRTEM showing lattice fringes of crystalline region in real space (SAED of the lattice fringes inset).

In the HRTEM image (Figure VII-17b), as well as the crystallinity of the samples being shown, the thinness of the crystals is obvious. This is highlighted by the dark fringed region at the middle, which suggest that that section is folded – a possible indicator of the thinness of the platelets. More of these dark regions are visible in Figure VII-17a, indicating the susceptibility of the platelet like structure to fold in on itself. This might also be the reason why the SAED produced a diffused pattern (inset of Figure VII-17b), in addition to the fact that the clusters are polycrystalline.

Estimation of the dimensions of the crystallites are not so easily done as the samples seem to overlap a great deal, so in this case perhaps TEM is not the best technique to look into the dimensions of the crystallites. Maybe in future more dilution and embedding of the samples may help to keep the crystals separate and easily catalogued.

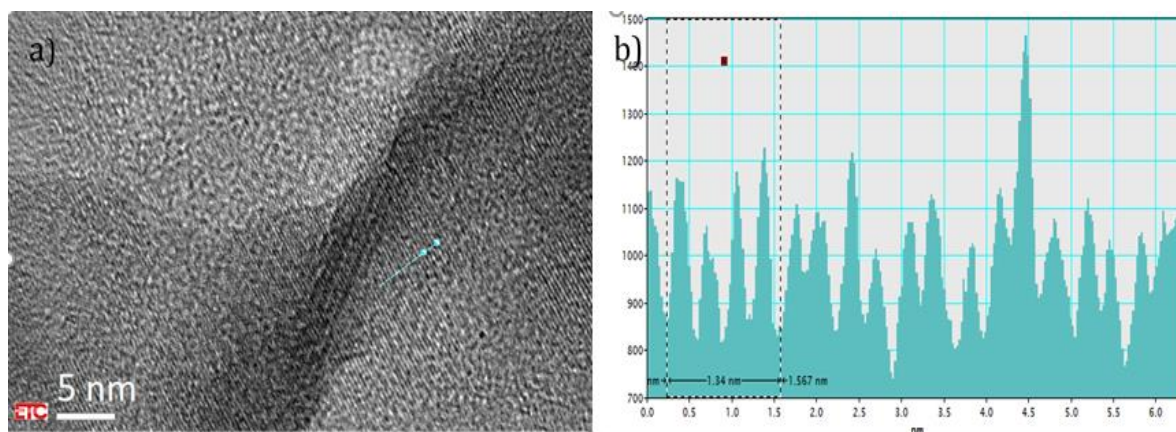


Figure VII-18:a) HRTEM of PVA HA 4 cycles; b) estimated d spacing from lattice fringes obtained from a)

The estimated d-spacing was calculated using the lattice fringes evident in Figure VII-18a. The value obtained was 0.335nm (3.35Å). This coincides with the (002) reflection of the apatite unit cell, which is related to the c-plane. This is a similar scenario to what was seen in Bio-Oss® where the most prominent plane of crystallites that were visible appeared to belong to that of the (002) reflection. Other reflections were much harder to estimate from the HRTEM images due in parts to the folded nature of the crystallites that were found and the overlap with other crystal. This could simply mean that again just like Bio-Oss®, the c-axis has been developed more in the crystal face in the direction of the a-axis, giving the platelet morphology. This is the same crystal shape that would normally be found in human teeth, albeit with more alignment.

#### VII.5.2.2.2 AL HA 4 cycles

Figure VII-19 a & b) reveals a similar situation to what was seen in the previous section VII.5.2.2.1. The shape of the particulates in Figure VII-19a share a similar morphology to those seen in Figure VII-17a. They are non-spherical, with a shape that suggest that they are closer to platelets yet again. They also appear to be quite flexible. This is apparent by the elongated darker streaks that are visible at the centre of the crystal clusters. No doubt these dark cluster areas are the folded portions of the platelets, as well as overlap from different crystals that are in plane. In Figure VII-19b, the overlapping sections are more apparent. Even though the fringes are evident, the overlap from the different crystals makes discerning fringes from a coherent area difficult. It does explain why yet again the SAED (inset of Figure VII-19b) of the crystals are distinct in some areas, but diffuse in others, thus expressing the polycrystalline nature of the AL HA samples. In essence it is similar to not just PVA HA, but also Bio-Oss®.

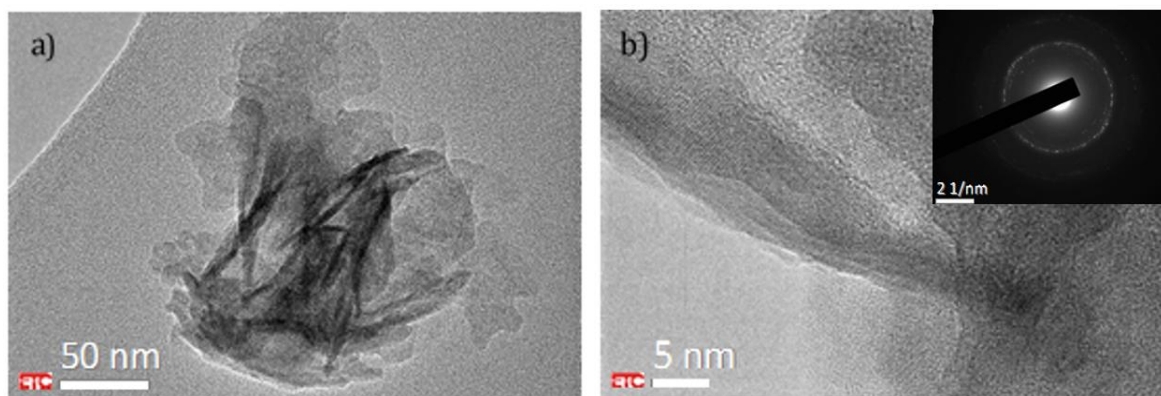


Figure VII-19: a) TEM micrographs of Al HA 4 cycles; b) HRTEM showing lattice fringes of the crystallite aggregates in real space (Inset: SAED of the lattice fringes).

In case there is any doubt to the multi-crystalline nature of the samples, the HRTEM image of one of the areas (shown in Figure VII-20a) contains several areas where the lattice fringes can be seen running in different directions. D-spacing approximation again returned with a value of 0.344 nm ( $3.44\text{\AA}$ ) after averaging the width over a select number of fringe peaks/intensities. This again coincides with the (002) reflection, lending some validation to the theory that the most developed face yet again belongs to that of the c-axis.

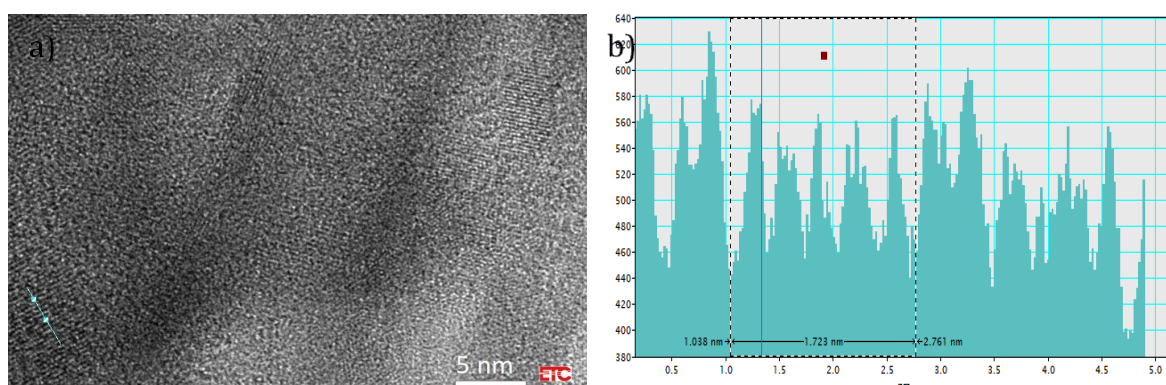


Figure VII-20: a) HRTEM of Al HA 4 cycles; b) estimated d spacing from lattice fringes obtained from a).

### VII.5.2.2.3 TA HA

The preparation done using tannic acid as an additional component is presented in Figure VII-21a & b. By now it is becoming apparent that the general conformation assumed by the apatite crystals in the hydrogels are platelet-like. Figure VII-21a shows the platelet like shape that has been seen in the previous lab-synthesised samples so far. The HRTEM image in Figure VII-21b shows us a twinned yet (highly periodic) crystal lattice of the particles. The SAED of the samples shown in inset gives a more accurate idea of the polycrystalline nature of the samples, which is similar to the circumstances that have been encountered so far.

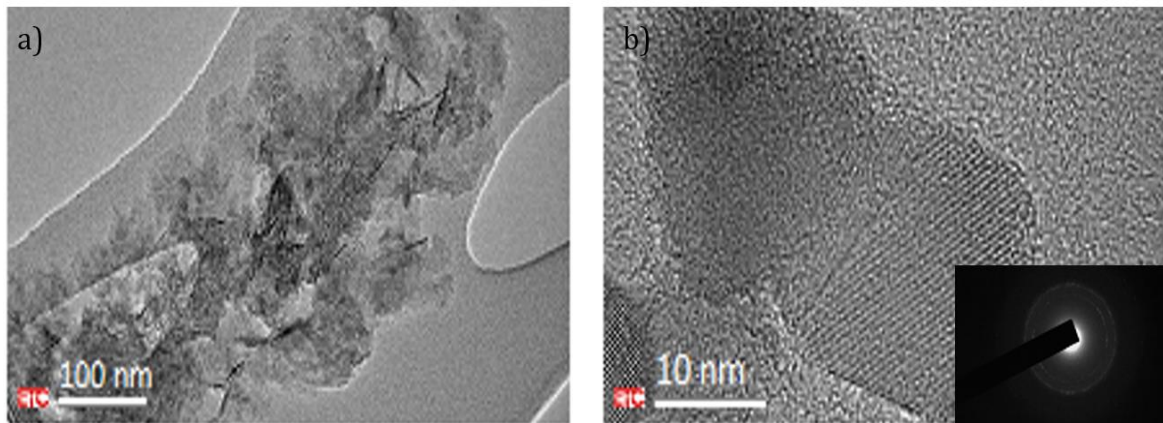


Figure VII-21: a) TEM micrographs of TA HA 4 cycles; b) HRTEM showing lattice fringes of a crystalline region in real space (Inset: SAED of the lattice fringes).

Using the HRTEM image, it was possible to estimate the d-spacing. Figure VII-22b shows the troughs and peaks that represent the dark and light areas of the lattice fringes from Figure VII-22a. the calculated d-spacing was approximately 0.348nm (3.48Å), belonging to the (002) reflection and by extension the c-axis. One can see that whether by some form of discriminatory coincidence, or an actual observation, the prominent faces of the platelets that are picked up in the lab synthesised samples yet again belongs to the c-axis, thus expressing some commonality amongst all the lab formed samples.

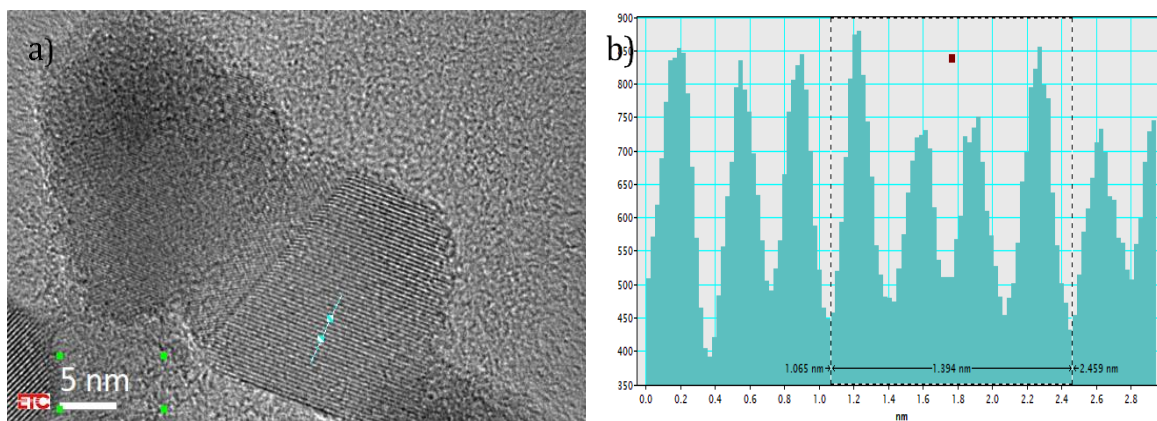


Figure VII-22: a) HRTEM of TA HA 4 cycles; b) estimated d spacing from lattice fringes obtained from a)

#### VII.5.2.2.4 TATi HA 4 cycles

Like the previous samples before TATi HA, the morphologies observed belong to that of a platelet (Figure VII-23a). This confirms that the particulates are not an isotropic sphere. Their crystallinity is not extensively different from the samples before this, judging from the HRTEM images (Figure VII-23b). Again, the overlapping of the samples, and the tendency of the samples-facilitated by their thinness to fold in on themselves has resulted in SAED that belongs to that of

a polycrystalline sample Figure VII-23b.

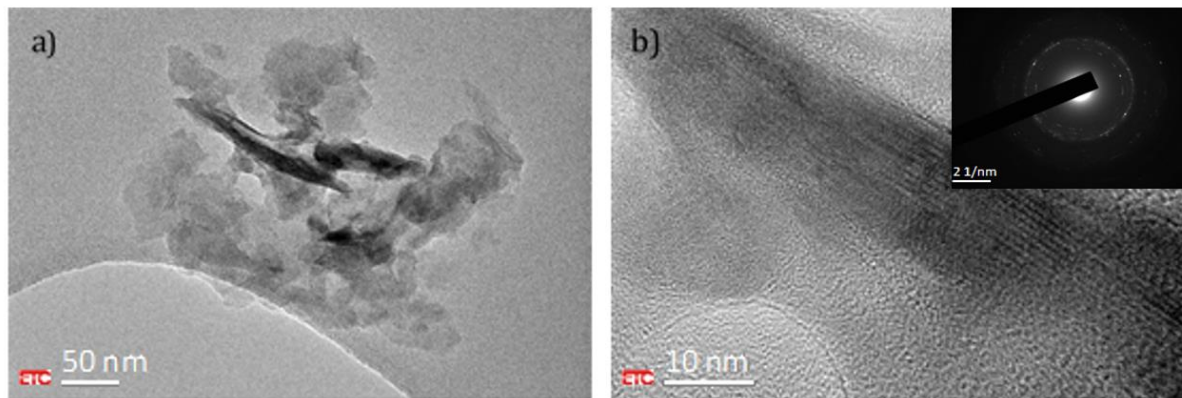


Figure VII-23: a) TEM micrographs of TATi HA 4 cycles; b) HRTEM showing lattice fringes of the crystallite aggregates in real space (Inset: SAED of the lattice fringes).

D-spacing averaging was carried out from the HRTEM image seen in Figure VII-24a, which resulted in a value of 0.341nm (3.41Å): representative (002) reflection. The (002) face appears to be responsible for the face of the crystal, suggesting the c-axis is the developed plane, while the preferred direction is thought to be along the a-axis.

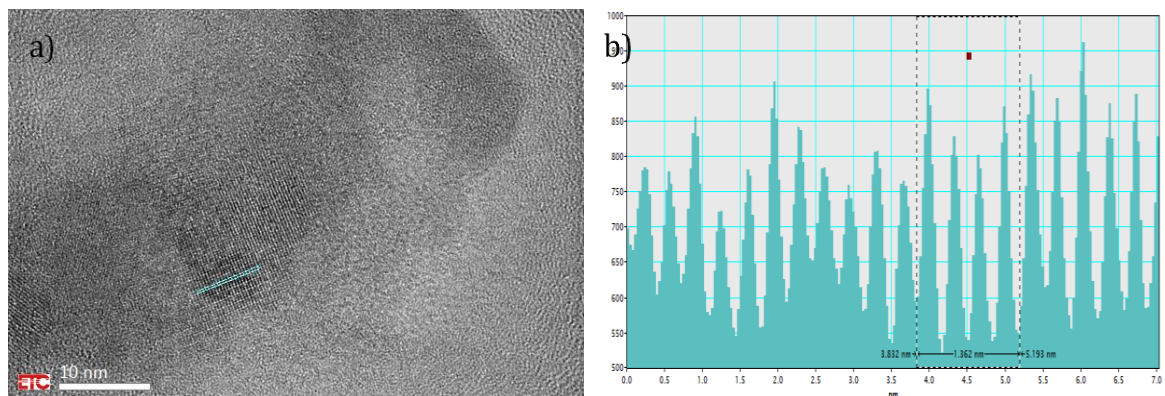


Figure VII-24: a) HRTEM of TATi HA 4 cycles; b) estimated d spacing from lattice fringes obtained from a)

## VII.6 Summary

This chapter has for the most part focused on diffraction and understanding the crystalline properties of the samples. Starting with the control samples and then going on to the lab synthesised, in order to find some commonality or differences that have resulted from the chosen synthesis conditions. As such, XRD was carried out on the samples, and from this the Williamson Hall method was performed on these samples in order to separate the contributions from the size and strain on the diffraction patterns that have been produced.



### VII.6.1 XRD & WH -PLOTS

From the XRD patterns of these mineralised hydrogel samples, as a result of the preparation methodology, the samples produced were not pure, which led to the inclusion of several other phases that showed up during the phase quantification. The impurity phases that were picked up belonged to calcite and halite and featured quite prominently in the XRD patterns. The chosen software, TOPAS, was able to demonstrate that in terms of the samples made after 4 cycles, the major impurity was calcite and in the major cases constituted  $\geq 50\%$  of the overall composition of the samples, with the apatite mineral phase coming up to  $\geq 41\%$  of the sample. While in the samples that have undergone 8 cycles, two of the impurity phases present were calcite ( $\leq 25\%$ ) and halite ( $\leq 17\%$ ). It was found that samples with more impurities had a higher composition of apatite at  $\geq 59\%$ , better than those made only with 4 cycles. This increment (discussed in VII.5.1.3) could simply be due to the higher number of cycles increasing the possibility of solubilisation of the  $\text{CO}_3^{2-}$  in calcite, and  $\text{Na}^+$  in the halite, which could both actively substitute into the apatite crystal. It seems that the increase in the number of cycles, as well as a more controlled rinsing step could result in a situation where not only is the apatite content changing, but the lattice constants too.

In terms of the lattice constants, we found that the lab synthesised samples all deviated from those that were calculated for the control samples, both of which had values that somewhat agreed with that found in the human teeth  $a=9.433 \text{ \AA}$  and  $c=6.896 \text{ \AA}$  for enamel and  $a=9.498$  and  $c=6.896$  for dentine (Hanlie, Liyun and Tao, 2006). These lattice parameters are quite important depending on which face is exposed; properties such as the biocompatibility, resolvability and absorption ability are affected (Aizawa, Matsuura and Zhuang, 2013; Yang *et al.*, 2013). This might be because depending on the axis/planes different ions are thought to dominate. For example, the c axis in stoichiometric apatites is dominated by the anionic groups, phosphates and hydroxyl ions, imparting a negative net charge to that face; in the case of the a-axis, it is mostly calcium rich and thus assumes a charge opposite to that of the c-face (Aizawa, Matsuura and Zhuang, 2013). Thus, any changes would no doubt result in some functional changes in the samples. In some cases, the lab synthesised samples appeared to contract along the a-axis in the cases of AL HA 4cycles, TA HA 4 cycles and all the samples after 8 cycles. The contraction as explained might be due to the replacement of phosphates for carbonates. The expansion on the other hand, seen in PVA HA 4 cycles and TATi HA 4 cycles, could be caused by the carbonate substitution for hydroxide. This apparent change in the unit cell can be related to the impurity phase composition spoken about in the previous paragraph, as the decreasing amount of calcite could be linked to its incorporation and eventual altering of the apatite unit cell. It is possible that in addition to the diminished sizes of the crystallites obtained via the lab synthesis method, the actual contraction means that the c-axis might be more dominant in the samples here.

The WH-ISM was the next important subsection. The main reasoning behind its use was to help separate the influence of strain present from the size and thus correctly estimate the size of the crystallites. In the course of subjecting the samples and their data to the WH-ISM method, it became increasingly apparent that the method was only relevant for a single sample. The sample in question was nHAp, and it was possible to calculate the size and the strain present in the sample. The other samples, including Bio-Oss® were more problematic to interrogate with this method. Why? Because the method was designed for samples that are isotropic i.e. uniformity of strain in all crystalline directions, nHAp falls into this category but the other samples are anisotropic instead. As a result of this, the plots of these individual samples had data points that were scattered, showing very little to no linear component. The main idea that can be extracted from the plots are indications that the crystallites are anisotropic.

In spite of this shortcoming in the use of WH-ISM, attempts were made to utilise only certain reflections, {h00} and {00l}, to estimate the size and strain. The reasoning for attempting the use of these reflections is mainly to do with how the apatite crystal is arranged within the body, and how the morphologies (and other properties: functional and mechanical) of the crystallites are seemingly dependent on the face that is exposed. Thus, by estimating the dimensions related to these reflections, one can get an idea of the average dimension of the crystallites, assuming that the c-axis is dependent on the {00l} reflection and the a-axis by the {h00}. Ideally this method would be more accurate with increasing number of reflections within the families quoted; however, the distinctiveness of the peaks (or lack) has a pronounced effect on actually finding the members of these families and estimating their areas correctly. For this reason, only the peaks from the {00l}, (002) & (004), were easily found and plotted, while for {h00}, only (300) was found, rendering the process for this latter's family immaterial. Another conjecture for the lack of members along the {h00} might simply be due to the morphology. We have extensively touched upon the fact that the samples produced here are plate like in shape, similar to those that were synthesised by Aizawa, Matsuura and Zhuang (2013). They successfully synthesised single crystals of apatite with different morphologies of which one of their samples, cHAp, was similar to those seen in the lab synthesised samples in this chapter. The XRD pattern that was collected by them showed that the reflection for the {h00} family, (300) & (100), were diminished, especially the (100). Thus, it was almost given that data would be easily collected for the {00l} family, due to the exposed face (as we have also seen in TEM micrographs).

In spite of the problems and limitations of the WH-ISM method, the sizes of the {00l} families were collected for both the samples after 4 cycles and 8 cycles. In the case of the 4 cycles, the changes between the TOPAS calculated and the WH-ISM calculated values were between 4.3-51% change; all the samples experienced a percentage decrease in the value from TOPAS to WH-ISM,

except for TA HA which had the only increase in size. In the 8 cycles mineralised hydrogels, there was a difference percentage difference between 19.3-86.9%, with AL HA 8 cycles showing the only decrease from TOPAS to WH-ISM estimates. The results are rather significant, but again the difference could be down to averages. TOPAS calculates the average of all the reflections which are present in its reference file, the WH-ISM method looked at only a single family (containing only two members). Thus, it is expected that the differences in size would be significant. It is not possible to say how accurate the estimates for the WH-ISM method are, because only two members were used, but as previously discussed in VII.5.1.2.1, more samples and a different XRD mode would improve resolution and possible accuracy of the dimensional calculation.

### VII.6.2 TEM

The results from TEM were quite insightful. What was seen provided evidence that two morphologies were being dealt with (a spherical and platelet type morphology). The lab synthesised samples and Bio-Oss® were shown to be truly platelet like, with the most prominent crystal face belonging to (002). nHAp, was the only sample that showed a different reflection, (300), when its d-spacing was calculated. The results seem to suggest that the c-axis is the most extensive face in the lab synthesised samples (and Bio-Oss®), while that of nHAp (due to its isotropic properties) could easily have featured any reflection. As much as the observation provided by TEM directs one to the anisotropic nature of the lab synthesised platelets and the prevalence of the (002) reflection on its surface, one needs to be wary of the extremely selective nature of TEM – a bias introduced by the operator- and extremely low sampling number.

Unfortunately, due to the overlapping nature of the crystallites and the difficulty in picking out their terminating edges, estimating the dimension of the crystals was not easily done. Thus, relying on XRD for the size estimate is the best option so far.

### VII.7 Conclusion

After interrogating the crystalline properties of the mineralised scaffold, the following outcomes have been realised:

- The mineralised scaffolds appear to be made up of a composite of phases that include hydroxyapatite, calcite, and halite. The lower cycled samples (4 cycles) have calcite in most cases as the majority element, followed next by hydroxyapatite. The higher cycled samples have hydroxyapatite as the majority element, followed by the calcite and then halite (see Table VII-2 and Table VII-5).
- The sizes of the hydroxyapatite crystallites of the mineralised hydrogels(4 and 8 cycles inclusive) were estimated as being between 12.4-19.3nm, using Rietveld refinement (see

Table VII-2 and Table VII-5). PVA HA 4 cycles was the biggest and TATi HA 4 cycles was the smallest sized crystallites.

- TEM and WH-PLOT confirmed the anisotropy of the crystallites, meaning that their dimension change depending on the plane. They were seen to be platelet shapes with TEM (Figure VII-17 to Figure VII-24) and (see Figure VII-7 and Figure VII-11).
- Their preferred growth appeared to be along the {001} plane. This was seen by the preferred development of reflection for the {001} family over the {h00} family in most of the XRD patterns. Also, the repeated occurrence of the d-spacing (0.341nm) that coincided with the (002) reflection in TEM was further confirmation that the c-face was the most extensive.
- The cell parameter of all the lab synthesised samples deviated from pure hydroxyapatite values. The contraction of the a-axis was the more prevalent change, which has been linked to carbonate substitution for phosphate. This is in line with what has been seen from FTIR and Raman spectroscopy. Only two samples underwent expansion, PVA HA 4 cycles and TATi HA 4 cycles, making them unstable with a higher likelihood to transform.
- The overall strain estimation for the samples were higher on average, as provided through the Rietveld refinement, rather than through the estimates with WH-Plot. In spite of that, the average size of crystallites remained unaffected when estimated using Rietveld and compared to those using WH-plot. Other than the errors associated with the limited faces used for the WH-plot estimation, the possibility of smaller and more unstable crystallites contributing to the higher strain estimate should not be ignored, Afterall, due to the intentional selection of the crystallites faces that are likely to be the biggest, their internal stresses would always be smaller (Table VII-7 and Table VII-4).

The mineralised scaffold consist of an adequate amount of CDHA: being more reactive and better osteoconductive (Yang *et al.*, 2013), with a shape that is common in the human body, as well as nanoscale proportions, thus making these samples potentially useful in the biomedical field as bone graft substitutes.

## **Chapter VIII      Mechanical and thermal properties of the mineralised hydrogel scaffolds**

### **VIII.1 Introduction**

This chapter is dedicated to the investigation of the thermal properties as well (as the mechanical properties) of the hydrogel, with and without the inclusion of hydroxyapatite. Also, it was anticipated that at the end of this chapter, the thermal properties of the pure hydrogel, as well as the composite material, would provide valuable information which maybe be used to further understand the overall properties of the samples produced and what this would mean in terms of their use as a bone graft scaffold material. While functionality in terms of uptake/release based on the hydrogels' interaction with MB, MO and AA (Chapter X) and its bioactivity in contact with SBF (Chapter IX) are related more to its surface reactivity, it is hoped that an investigation into the thermal and mechanical properties would help understand the physical manifestation of the scaffold composite as a whole.

### **VIII.2 Aim**

The aim is to understand the physical properties of the scaffold. To begin with, the mechanical properties in relation to the compressive strength and the elastic modulus will be ascertained and used to compare against all of the neat hydrogel samples, and the composite samples; afterwards, the thermal properties will be determined using TGA and DSC.

### **VIII.3 Background**

As previously discussed in section I.1.9, in order for scaffolds to be considered as suitable bone graft agents, they need to have suitable biocompatibility. Hydroxyapatite, PVA and alginate are all considered biocompatible components alone; and in combination it is probably unlikely that the feature will change. Next, they need to be bioactive, while hydroxyapatite has been proven to be bioactive (Pan and Xiong, 2009), alginate and PVA on their own will not form bonds with the surrounding tissue in the body thus they are more bioinert in comparison to hydroxyapatite (Balgová *et al.*, 2013); the utilisation of both the hydrogels and the mineral helps satisfy this criteria. Then there is stability of the material in-vivo: PVA and alginate have intermittent stability affected by their level of crosslinkage, thus giving them some temporal durability that would allow the infiltration of tissue into their mesoporous structure. The further presence of hydroxyapatite will allow cellular attachment that can improve the rapid development of meaningful bone structure. There are surface properties like wettability and surface reactivity,

satisfied by the hydrogels and hydroxyapatite. And finally, there are the mechanical properties. This is quite an important criterion, especially so as the main function of bone is to support load; thus, the material needs to have some mechanical resilience in its role. There would be no point of a bone graft scaffold having excellent biocompatibility, bioactivity, surface properties and stability if it fails as soon as it has been implanted in the body. Thus, it needs to be proven to fulfil its criteria as a mechanical support, which is admittedly just as vital as it being able to provide an environment necessary for cell attachment and proliferation, as well as osteogenesis.

## **VIII.4 Methodology**

Sample preparation was described in section II.4 for the mineralised and II.3 for the non-mineralised hydrogels.

### **VIII.4.1 Analytical instruments and conditions**

The instruments and their conditions used in this section are listed below

#### **VIII.4.1.1 Compression testing**

The samples were tested on a Hounsfield mechanical testing machine at room temperature between 21-26°C at 60% humidity. An approach speed of 5mm/min was used during the experiment with a load cell of 10N. The elastic modulus of compress (E) for three different portions of the stress-strain curve and the stress ( $\sigma$ ) at 50% strain were calculated from the force against extension curve produced. The calculation of these mechanical parameters would have to be obtained over an average of 2-3 samples to foresee possible sample variations.

The samples for mechanical testing were prepared in a similar manner as previously stated in the methodology section. The main difference was a change in the volume cast. This was done for the purpose of achieving hydrogel samples with adequate thickness to allow successful testing on the mechanical testing machine. The resulting samples had a circular shape, of diameter 0.034-0.035m. and thickness of 0.004-0.0045m. The mean mass of the samples were maintained at ~ 4.305g. Before testing, all the samples would have been immersed in deionised water for 24h, to allow complete saturation. Before the test, excess moisture was then wicked away using filter paper before weighing and then mechanical testing.

#### **VIII.4.1.2 TGA**

Samples for TGA studies were heated from room temperature to 520°C at a heating rate of 10°C/min under N<sub>2</sub>.

#### **VIII.4.1.3 DSC**

The samples were initially cooled from room temperature to -50°C/min, and then heated through

to 150°C at a rate of 10°/min. The samples were cooled to -50°C and then heated again to 350°C at a rate of 5°C/min. DSC was carried out in N<sub>2</sub>.

## VIII.5 Results

### VIII.5.1 Compression testing of the scaffolds

As part of the characterisation analysis carried out, the synthesised hydrogel samples were subjected to compression as a means to understand their mechanical properties, and which could ultimately have an effect on their future application. But before this, the pure hydrogel samples will be compared against each other, to observe how the effects of blending might be manifested in terms of their mechanical properties; following this, the effects of mineralisation, if any, will be tested via compression.

#### VIII.5.1.1 Hydrogels only

Only PVA hydrogels and the resulting blends will be discussed here : AL, TA and TATi, besides PVA.

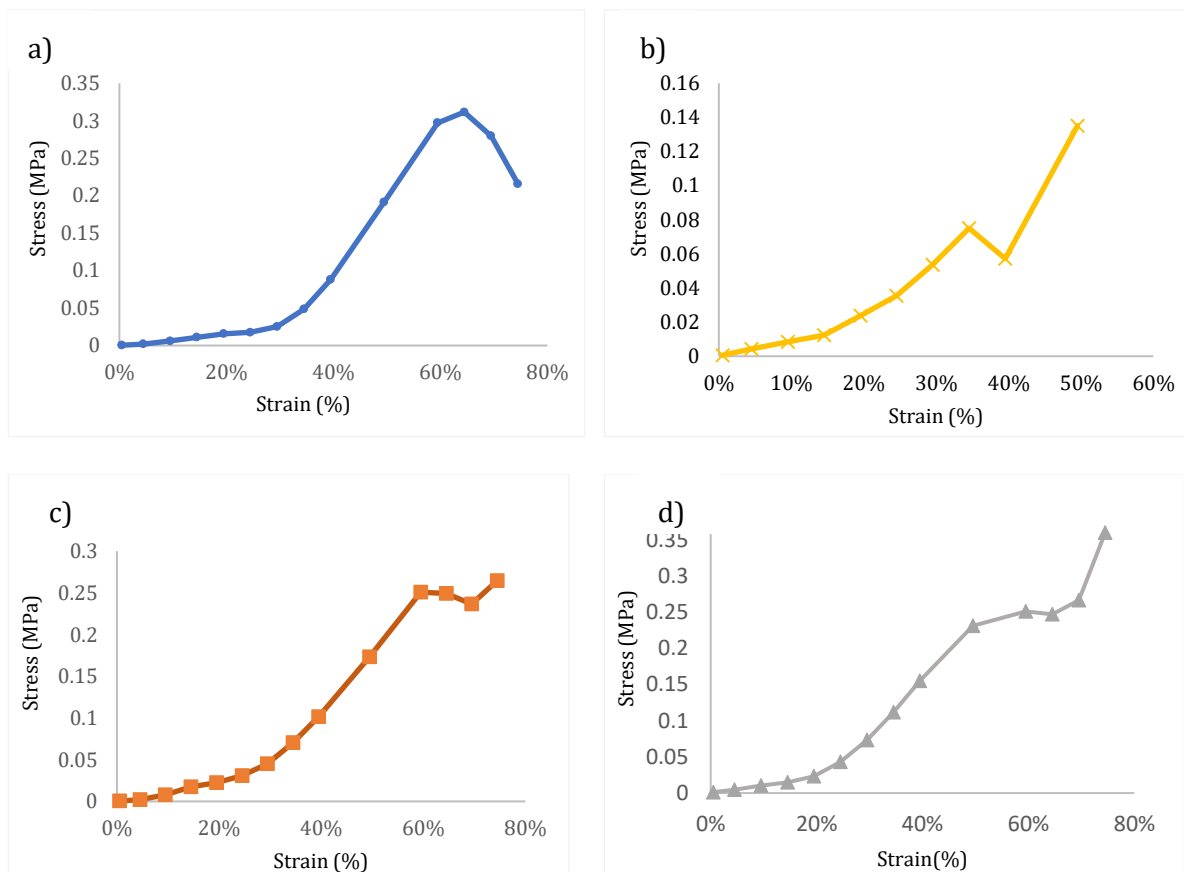


Figure VIII-1 Average stress-strain behaviour curves of PVA hydrogel and its blends a)AL; b) PVA; c) TA; and d)TATi

It can be concluded from Figure VIII-1 that the behaviour of all the hydrogels present a relationship that is roughly exponential, which is testament to the viscoelastic behaviour that is a normal denominator in the majority of hydrogels. This behaviour is true at least to 50% strain, after which some of the samples begin rupturing; as such the resulting stress-strain curve no longer follows an exponential fit.

It is thought that the viscoelastic properties of the hydrogels are due to a combination of the crystalline and amorphous section of the hydrogels (Pan and Xiong, 2009). To recap, crosslinking has the ability to affect the amorphicity of the hydrogels (Rudra, Kumar and Kundu, 2015). Here, as the crosslink density reached a certain value, the amorphicity increased and in tandem the crystallinity of the sample decreased. As such, depending on the overall crystallinity of the PVA hydrogel and its blends, certain regions of the stress-strain curve will be affected. The amorphous region of the hydrogels contribute towards the elastic modulus and the elongation to break; as load is applied to the hydrogel, the amorphous polymeric chain attempts to realign itself in the direction of the force, and once aligned the polymer is considered hardened. The micro-crystalline segments are thought instead to be responsible for the strength of the material (Gonzalez and Alvarez, 2014). Depending on how weak and defective the crystal (within the semi crystalline section) of the hydrogels are, failure of the sample might either be due to the slippage of the chains leading to thinning and rotation of the crystals (common in crystals that are defective). Should the crystals be more cohesive and thick, then cavitation usually sets in first (in the amorphous region) as deformation within the crystals itself is energy intensive (Pawlak, Galeski and Rozanski, 2014).

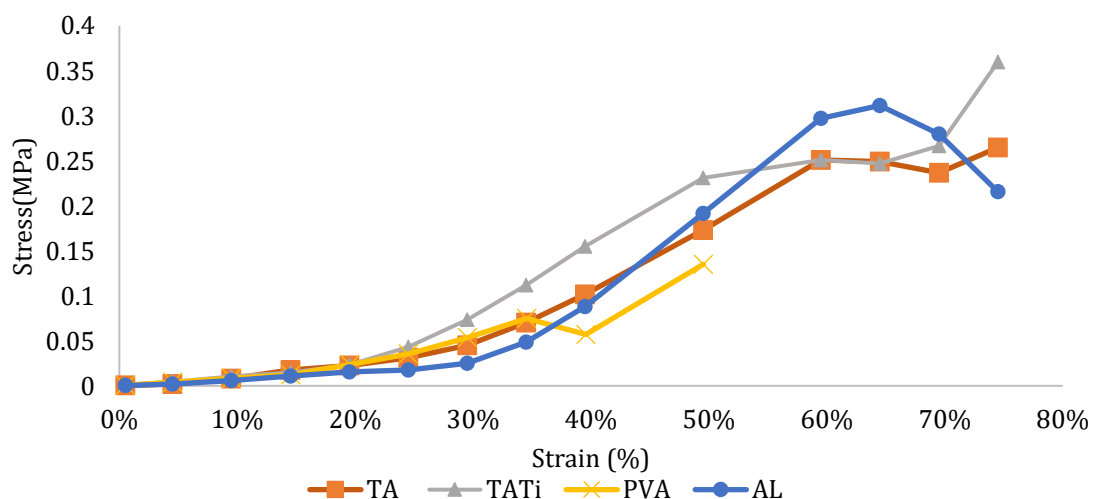


Figure VIII-2: Combined stress-strain behaviour curves of the hydrogel samples



As well as being viscoelastic, all the samples within the stated 50% strain are almost identical to one another (see Figure VIII-2). The similarity might just be due to the PVA hydrogel contributing to that region seeing as it makes up the majority of all the samples. Afterwards there is some divergence in the stress-strain curve. The behaviour at higher strain, being associated with the crosslinks and the crystalline region, is visibly different as all the samples tested have a different composition that most likely crosslinks in a different manner as opposed to if they were purely made of a single polymer.

Estimation of the elastic modulus and the compressive strength at 50% is presented in Table VIII-1. The elastic modulus was estimated from the initial stress-strain portion of the strain curve of all the samples. The gradient of that region was the resultant modulus. The sample with the highest ability to resist deformation appears to be TA, having a value of 0.14MPa, followed by TATi, PVA and AL. The values here are closely similar to those of a healthy articular human cartilage, which has estimated moduli values that fall within 0.1MPa and 2MPa. (Almarza and Athanasiou, 2004; Chen *et al.*, 2016). Bear in mind that the values from literature were usually collated over a range of % strain, rather than calculated from just the initial linear portion; as such the compression strain induces the modulus changes as well, exponentially in some instances like running (Li *et al.*, 2016). This shows that the samples, at least TA, could be used to satisfy such a function, at the lower spectrum of low load bearing like “walking and cantering” (Pan and Xiong, 2009).

The stress at 50% and 75% strain are also listed in the table below They all seem to have very similar stress at around 75% strain, which confirms that all the hydrogels share fairly similar properties.

**Table VIII-1: Average elastic modulus of compression (between 0 -10%strain) and the stress at 50% strain\* at 75%strain#**

Samples	E (MPa)	$\sigma$ (MPa)*	$\sigma$ (MPa)#
PVA	0.083	0.13	0.21
AL	0.081	0.19	0.21
TA	0.143	0.17	0.26
TATi	0.103	0.23	0.35

The modulus of the samples increase with increasing compression ratio, which is a behaviour common in human cartilage (Li *et al.*, 2016). Thus, depending on the loading stress, it is clear that all the samples have the potential to resist the increasing stress as ascertained from the modulus seen in Table VIII-2. The mineralised samples all experience increases; AL going up by 12.3x, TATi by 8.07x, PVA by 5.4x, and TA by 4.8x. All the increases experienced still keeps them in line with

the average modulus experienced by the articular human cartilage (Li *et al.*, 2016).

**Table VIII-2: Average elastic modulus of compression at 0-10%\* strain, at 20% -30%~ strain and at 30-45%# strain**

Samples	E(MPa)*	E(MPa)~	E(MPa) #
PVA	0.083	0.299	0.455
AL	0.081	0.096	1.003
TA	0.143	0.224	0.689
TATi	0.103	0.501	0.814

### VIII.5.1.2 Mineralised hydrogels

Only the samples that have undergone 4 alternating immersion cycles in a CaP precursor will be considered. Just like their non-mineralised counterpart, the samples in this section also appear to have stress-strain curves that indicate their viscoelastic properties: this is in spite of the mineralisation of the hydrogels (Figure VIII-3). The most obvious difference is the presence of the 'hump'. The non-mineralised samples have this hump positioned close to or above 50%, which is not the case as seen in Figure VIII-3- with the exception of PVA HA. In the mineralised samples, it was seen at ~50% strain. The most likely explanation for this shift in the hump might be due to the availability of free volume and free water in the hydrogel. The mineralisation of the hydrogels means that the otherwise unoccupied free volume such as pores, voids and other imperfections are no longer unoccupied. So, while in the nonmineralized samples, the slow compression of the hydrogel allows the realignment of the polymer chain of the amorphous region, enabled by the free space provided by the open network of the hydrogel the same cannot be said for the water present in these voids. Were these spaces to be otherwise occupied with something less pliant than air, the compression will be halted much earlier on, hence the movement in the hump from a higher strain value to a much lower strain value (Pan and Xiong, 2009). The arrangement of the polymer chain will be delayed, and so will the flow of water (if there is any present within the network) outside the network whose presence is also thought to aid the flexibility of the hydrogel (Ma *et al.*, 2009; Gonzalez and Alvarez, 2014). It likely that Ca<sup>2+</sup> from the apatite type minerals has bonded with the hydrogel via the hydroxyl groups in PVA (and in the sodium alginate), as well as the link forming between the hydroxyl groups present on the hydrogels and the apatite type crystals. These additional links work to improve the resilience of the samples, also the physical occlusion caused by the mineral could account for the shifted hump and possibly other mechanical properties (Pan and Xiong, 2009).

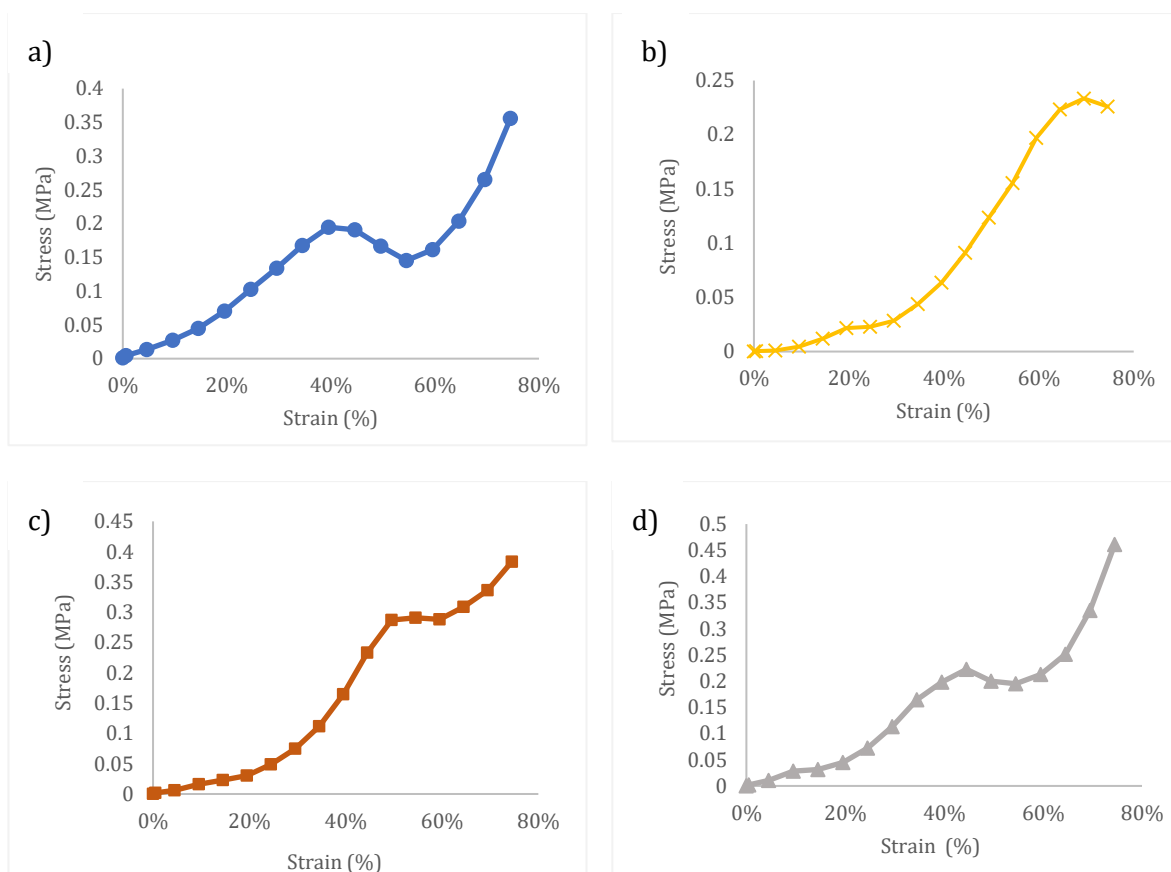


**Figure VIII-3 Average stress-strain behaviour curves of the mineralised hydrogels a) AL HA; b) PVA HA; c) TA HA; and d) TATi HA.**

The combined chart in Figure -VIII-4 highlights the similarities as well as the differences between the prepared samples. Their initial phases, at least up to 20% strain is closely similar, but then PVA HA shows a lower resistance to deformation to the applied stress than the other samples. At lower stress, it deforms by 45% strain when stressed with 0.09MPa. This is in contrast to the other samples: these samples required stresses of about 0.16MPa before they were deformed by 45% strain. Then most notably is the hump region: TATi HA and AL HA both exhibit this slowdown, which might be due to their increased level of mineral deposition, or their poor swelling ratios, which would all contribute to hamper the rearrangement of the amorphous section and cause premature hardening. TA HA sees its hump occurring closer to 50% strain, and then finally PVA HA near 70% strain. Perhaps this is an indication of the PVA having a more open network, and thus more free space to still be deformed before the mineral contents are then stressed, or it might have less mineral content of all the other samples. A resolution to the amount of mineralisation could be offered through gravimetric analysis in the coming section.

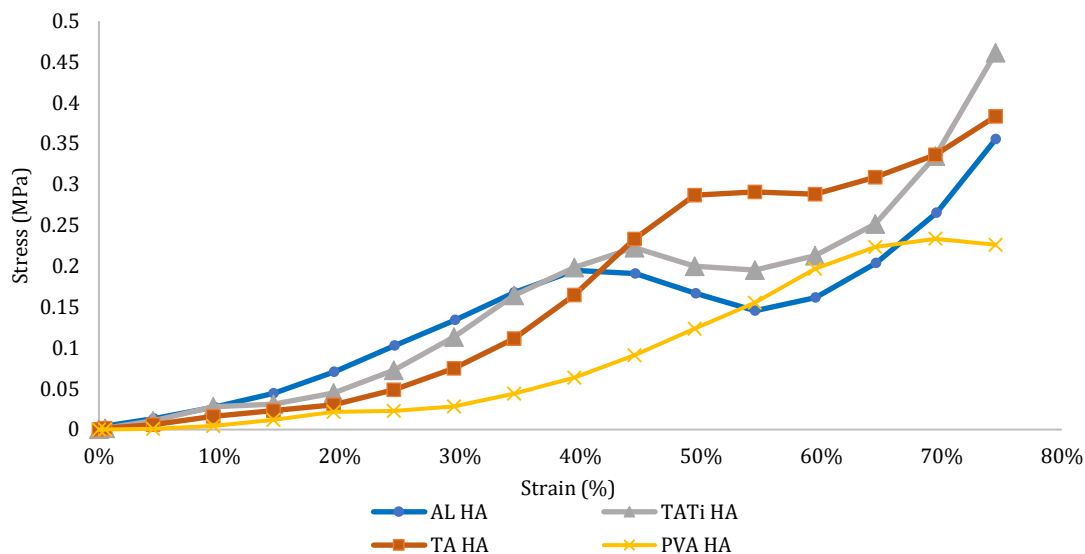


Figure -VIII-4: Combined stress-strain behaviour curves of the mineralised hydrogel samples.

Quantitative analysis of the curve (Table VIII-3) shows that the elastic modulus of the mineralised samples are higher than those calculated for just the plain samples, in some case accounting for more than a 2x increase over the unmineralized samples. The stress at 50% strain is not excessively different but the values for 75% strain for all the samples show a marked improvement. This is an indication that the mineralisation has more of an effect on the elastic modulus and then at the final stress required for deformation at 75% strain. As previously explained, this might be down to a possible physical occlusion and/or molecular interaction.

Table VIII-3: Average elastic modulus of compression (between 0 -10%strain) and stress at 50% strain\* at 75%strain#

Samples	E(MPa)	$\sigma$ (MPa) *	$\sigma$ (MPa)#
PVA HA	0.13	0.12	0.22
AL HA	0.28	0.16	0.35
TA HA	0.15	0.28	0.38
TATi HA	0.28	0.20	0.46

In Table VIII-3, the samples with the highest moduli are AL HA and TATi HA, with PVA HA having the least modulus of all the samples. The highest stress experienced by the samples at (75% strain) was again experienced by TATi HA, followed by TA HA and then AL HA.

**Table VIII-4: Average elastic modulus of compression at 0-10%\* strain, at 20% -30%~ strain and at 30-45%# strain**

Samples	E(MPa)*	E(MPa)~	E(MPa) #
PVA HA	0.138	0.111	0.415
AL HA	0.288	0.636	0.606
TA HA	0.158	0.527	1.056
TATi HA	0.286	0.683	0.725

The modulus of the mineralised samples increases with increasing compression strain ratio, just like their unmineralized counterpart and like human cartilage. Thus, depending on the loading stress, it is clear that all the samples have the potential to resist the increasing stress as ascertained from the modulus seen in Table VIII-2. The mineralised samples all experience rises, TA HA going up by 6.6x, PVA HA by 3.0x, TATi HA by 2.5x and AL HA by 2.1x. In spite of the mineralisation, the increases still in line with the average modulus experienced by the articular human cartilage. While mineralisation does seem to augment the initial elastic modulus response of the hydrogel, it still keeps the resistance to mineralised hydrogel samples similar to what would normally be required for cartilage.

### **VIII.5.2 TGA of the hydrogels (and mineralised scaffolds)**

Thermogravimetric analysis was used as a technique to evaluate the thermal stability of the synthesised polymers. Following the thermograms produced from TGA, it will be possible to study several thermal events such as evaporation/dehydration, degradation due to breakage of the main polymer chain and the possible difference in mineral contents of the mineralised hydrogels.

To begin with, the thermal behaviour of the starting polymer materials (pure PVA and pure sodium alginate) will be looked into first. Knowing what to expect from their original precursors, the events of the synthesised polymers could be better put in perspective. Thus, any event that is unaccounted for could be easily detected.

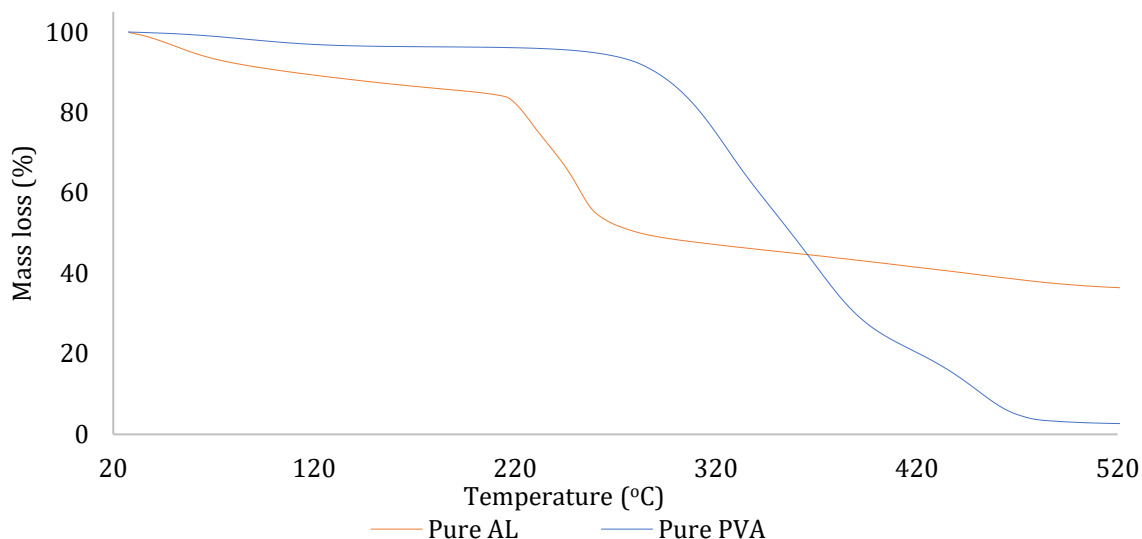


Figure VIII-5: TGA thermograms of pure sodium alginate (AL) and pure PVA in a nitrogen atmosphere.

From Figure VIII-5, one can see that the thermal behaviour of the two polymers are quite different. Starting with AL, there is a rapid loss in mass between 20°C to around 77°C which is more than likely as a result of the dehydration of the samples. Soares *et al.* (2004) observed dehydration occurring from 28°C to 177°C in the different alginic salts. Following that, the mass stabilises until 220°C, where a more drastic mass loss is observed (a 30% loss occurs). This is part of the decomposition process of sodium alginate and has been seen to continue up till 520°C (Soares *et al.*, 2004). It can be attributed to the carbonisation of the samples. Following this event,  $\text{Na}_2\text{CO}_3$  precipitates.

Pure PVA has a different profile. There is the initial dehydration peak, which goes up to 120°C. Very little mass is lost between that temperatures 20-120°C. The mass stabilises until about 280°C. This marks the start of a huge mass loss event, that slows down at 407°C (after about 70% mass loss). This event is associated with the formation of polyene (Figueiredo, Alves and Borges, 2008). The mass of the PVA drops further around 450°C which has been stated to be caused by the breakage of the main polymer backbone (Figueiredo, Alves and Borges, 2008) and then the mass remains constant till the end of the run. From this, it is clear that there are at least three main thermal events that define the behaviour of PVA under thermalgravimetric analysis.

#### VIII.5.2.1 Effect of glutaraldehyde on the gravimetric behaviour of the polymers.

Following the initial analysis of the starting component of the polymers, we can see that in the figure below, the synthesised hydrogel samples appear to possess a thermal profile that is quite similar to that of PVA rather than AL. This is not surprise seeing that PVA still makes up a larger proportion in the blends, constituting about 80v/v%.

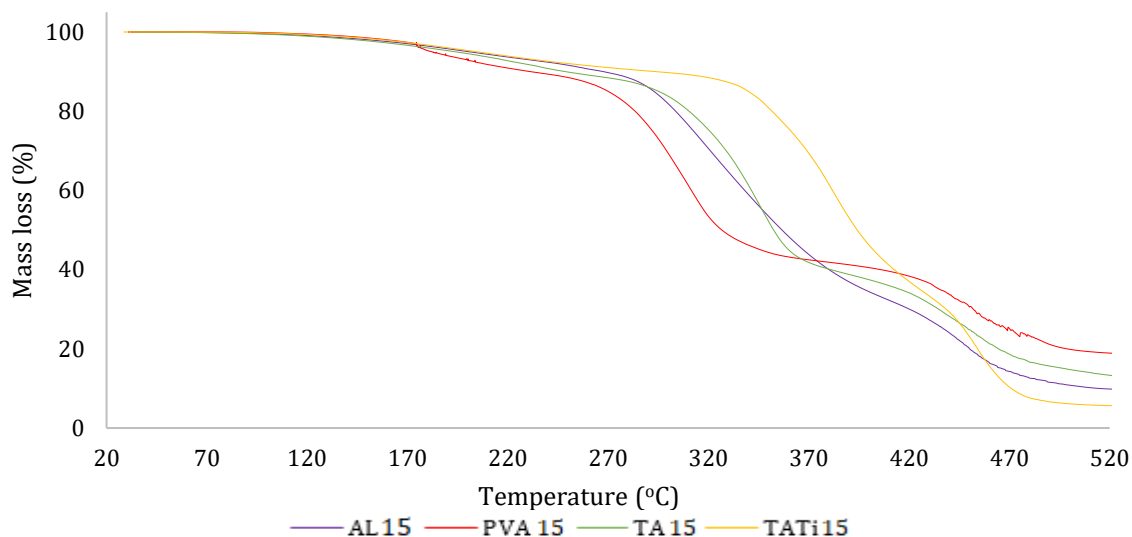


**Figure VIII-6: TGA thermograms of the PVA 15 hydrogels and its blends crosslinked with a low amount of glutaraldehyde (15%), in nitrogen.**

In Figure VIII-6, all of the samples appear to be stable up till 170°C, having very similar profiles. Afterwards, there is some divergence, of which the most apparent is PVA15. It begins to rapidly lose mass around 270°C, which is much earlier than the other 3 samples. This most likely due to the formation of polyene (following the loss of acetic acid). The other samples do not experience this drop until 290°C (for AL15 and TA15), while TATi15 only begins losing mass around 339°C. This event is probably the most telling sign about the inclusion of sodium alginate fraction into the overall polymer preparation. Though PVA15 visibly stabilises around 340°C, the other samples do not appear to experience this delay. TA15 shows some slow down around 377°C, it is however not as apparent as in PVA15. AL15, almost like TATi15 shows almost a continuous mass loss until the end of the run. PVA15 starts losing mass around 430°C until it ends with a final mass of about 19wt%. This is followed by TA15 with a final remaining mass of 13wt%, AL15 at 10wt% and final TATi15 at 6wt%. In general, although PVA15 suffered the most loss in the first half of the thermographs, it was still the only sample with the most content left. It also seems to suffer the most from dehydration, and acetic acid break down, while the others were more than likely to suffer full chain scission: probably an artefact of the complex network between AL15 chains and PVA15 chains. Their entanglement might have been enough to resist thermal vibration at the relatively low temperatures, but the more multifaceted entanglement might have given little room for a more efficient transfer of energy through the network (chain slippage) and the tighter bonds might have worked to pull the stable network apart, by breaking the bonds (Guirguis and Moselhey, 2012). It is possible that a lower glutaraldehyde amount can be used along with a tannic acid to achieve a similar property.

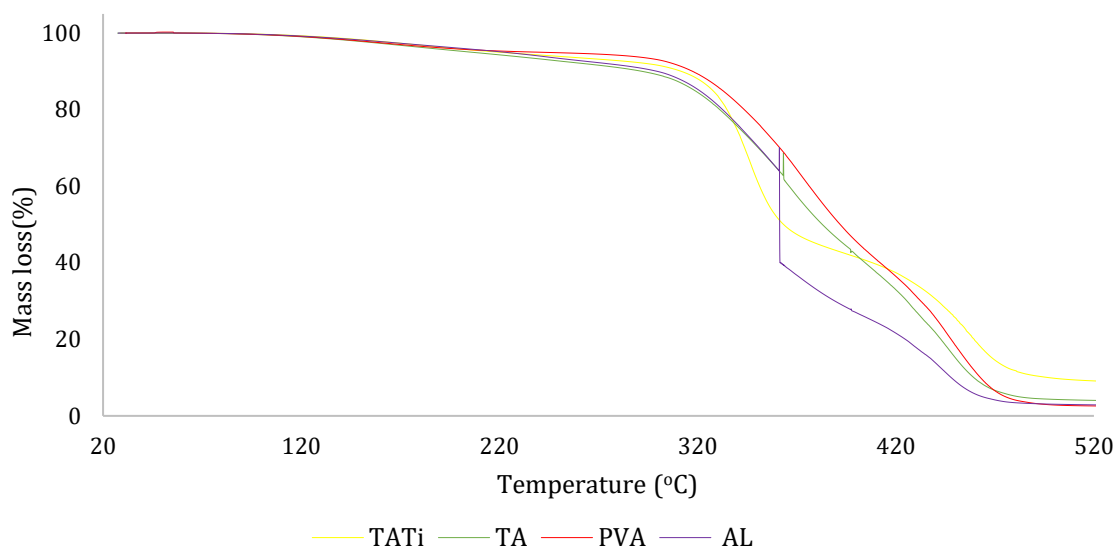


**Figure VIII-7: TGA thermograms of the PVA hydrogel and its blends crosslinked with a higher amount of glutaraldehyde (30%), in nitrogen.**

Interestingly enough, in Figure VIII-7, which shows the thermal behaviour once the amount of glutaraldehyde has been increased, it is clear to see that the profile at least for PVA and TA has smoothed out considerably, contrary to what was shown in Figure VIII-6. The different stages normally associated with pure PVA is lost in these samples. TATi profile remains similar. Compared to the others, one would assume that it actually had more PVA in its composition because it possesses the characteristic degradation steps associated with PVA in its profile. All of the samples show an initial mass loss beginning around 300-305°C. PVA and TA, show a continuous loss until a stabilisation at 477°C, where there were then left with 2.5wt% and 3.5wt% respectively. AL was left with 2.8wt%, while TATi was left with 9.1wt%.

The author believes that the lower residual mass content could be linked to the level of crosslinks ironically. Just like TATi in Figure VIII-6, the elevated number of crosslinks might have reduced the ability of heat energy to propagate through the polymer chains. This led to chain scission rather than slipping, creating smaller polymer fragments that are more susceptible to volatilisation. Consequently, less crosslinks means larger-fewer volatile fragments are left behind. The results here yet again highlight how the TATi could possibly reduce the amount of glutaraldehyde introduced into a system.

#### **VIII.5.2.2 Effect of mineralisation cycles on the gravimetric behaviour of the polymers.**

As the polymer samples were prepared with the higher amount of glutaraldehyde concentration, a similar smooth profile seen in Figure VIII-7 is also seen in Figure VIII-8. All the samples are uniform up till about 100°C, at which point they begin to diverge. The main mass loss still occurs around the same temperature 300-310°C. TATi HA again is the only one that shows very



discernible degradation stages in its thermal profile. It stabilises around 360°C, before dropping again closer to 420°C. The last drop is replicated across all of the samples. The final residual mass is about 17.5wt% for TATi HA and AL HA, 16.3wt% for TA HA and finally 12.6wt% for PVA HA.

The most likely reasoning for the other samples having a slightly higher residual mass than PVA HA is probably due to the additional chelating effect of sodium alginate and tannic acid. These substances are known chelators, with a particularly high affinity for metallic ions. In a network containing sodium alginate which is particularly dependent on metal ions- mainly divalent cations for the purpose of crosslinking- it is likely that as well as the formation of apatite at pores/imperfection in the PVA network, the presence of the chelating sodium alginate network (and tannic acid) would also act as extra nucleating sites that would encourage the formation of more apatite like nuclei all over the substrate.

Thus, the more nucleation sites, the better the likelihood of having more appreciable growth of the inorganic mineral within the polymer substrate.

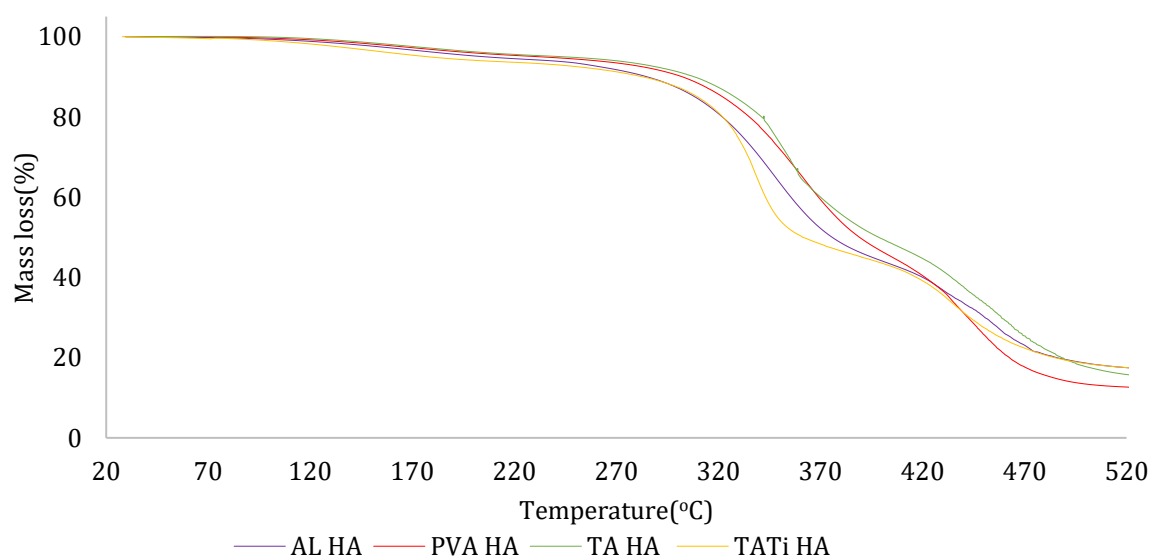


**Figure VIII-8: TGA thermograms of the mineralised PVA hydrogel scaffolds and its blends after 4 alternating immersion cycles, in nitrogen.**

It appears that increasing the immersion cycle (8 cycles) process serves to increase the residual mass amount left behind and further smooth out the thermal profile of the polymer samples. The thermographs in Figure VIII-9 exhibit diminished degradation steps, thus ending with a thermal profile that is significantly more linear. Some of the events, specifically the elimination of acetic acid seems to have shifted to a lower temperature, from about 305°C (in the 4 cycle samples) to 255°C. It is not clear why this has started earlier: it might just be exaggerated more due to the minerals inclusion, which have their own differing heat capacities, depending on which particular

crystalline phase might be present at any one time. Also, the effect of the polymer having prolonged contact with the aqueous calcium phosphate precursor solution, might lead to accelerated polymer degradation. It could be a combination of these events causing this lower temperature shift. Either way, the residual mass is an indication that deposition of the mineral is a success, and that increasing the cycle time can effectively increase its proportion within the polymer.

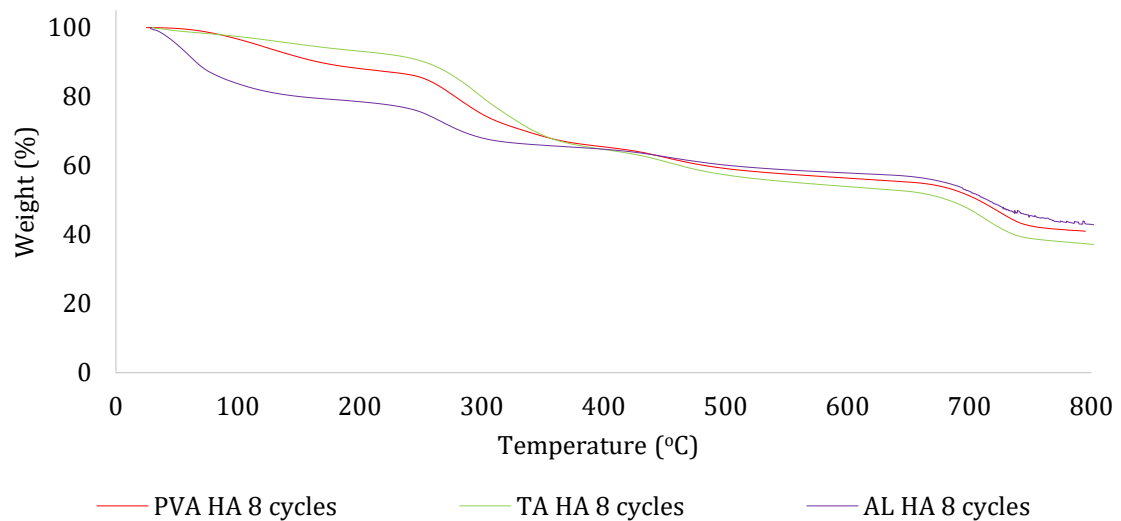


Figure VIII-9: TGA thermogram of the mineralised PVA hydrogel scaffolds and its blends after 8 alternating immersion cycles, in nitrogen.

### VIII.5.3 DSC

Before any further analysis can be carried out, the individual polymers need to be first analysed to understand their thermal properties before any modification.

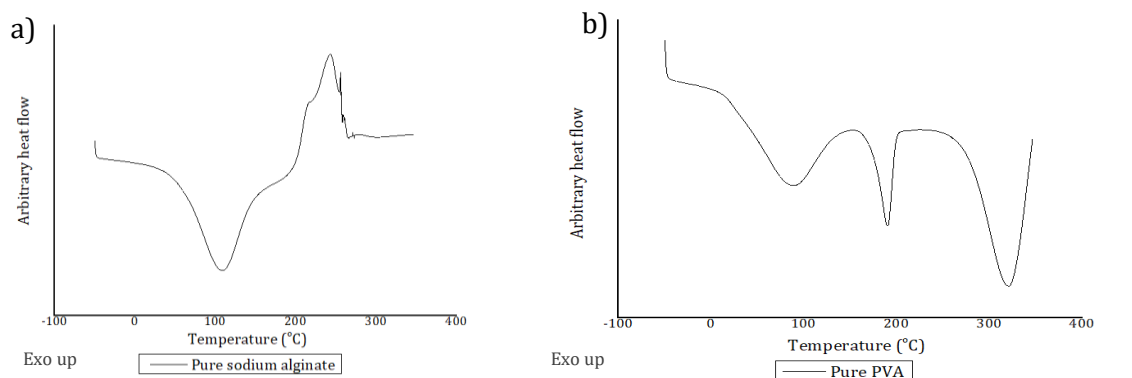


Figure VIII-10 : DSC curves of pure sodium alginate (AL) and pure PVA.

In terms of the thermal properties of pure AL Figure VIII-10a, very little seems to be occurring in

the DSC curve. There appear to be two events of interest occurring in the thermogram. The first of the events is centred around 100°C, but actually begins much earlier close to 40°C, may be associated with the dehydration of sodium alginate. This occurs in a similar area to those quoted for sodium alginate by Soares *et al.* (2004). The next thermal event, which occurs as an exothermic peak may be assigned to the decomposition of sodium alginate, is centred around 242°C and this value is in line to that quoted by Soares *et al.* (2004), where decomposition was observed to begin around 140°C-600°C when a heating rate of about 5°C/min was used. This is thought to be due to carbonisation of the organic samples, resulting in a release of energy.

Pure PVA appears to feature a more diverse thermal profile. The first broad peak just like that seen in Pure AL can be assigned to endothermic dehydration of the sample: evaporation of water trapped in the structure of the samples, which is centred around 88°C. This evaporation of water associated with the hydrophilic groups of the PVA is believed to be responsible (El-Hefian, Nasef and Yahaya, 2010). In addition, the fact that it is centred close to 88°C is an indicator that the peak also encompasses the glass transition temperature of PVA, which is thought to occur between 50-60°C (Pshezhetskii *et al.*, 1990; Guirguis and Moselhey, 2012). Following that, there is another sharper endothermic peak, which likely signifies the melting point of the samples: it occurs around 200°C (Gonzalez and Alvarez, 2014). Above 300°C, degradation of the pure sample begins, which is similar to that stated in literature (Gonzalez and Alvarez, 2014). It is an intensive endotherm, signifying the substantial amount of energy required to break down the chemical bonds present in a PVA polymer. There is no clear peak indicating transition within the amorphous phase of pure PVA, which suggests that the amorphous region has been masked or no amorphous region is present. It is most likely the former case.

#### **VIII.5.3.1 Hydrogels only**

The following section focuses on the thermal properties of the different hydrogel specimens that have been synthesised. Other than the specimens that have been crafted from a blend of different components, we shall be paying specific attention to the effect of increasing the crosslinking percentage specifically on the T<sub>g</sub>, and the water content of the samples-which may be ascertained from the enthalpy of evaporation from the DSC curves and where possible the melting point if applicable.

To start with, in Figure VIII-11 a & b below, one can see that the two sub figures display two very interesting thermal events. In Figure VIII-11a, a clear peak between 40-55°C is seen in two samples (at 48°C for TA15 polymer and at 51°C TATi15). These signify a transition within the amorphous portion of the prepared samples. Its shape means that it cannot be wholly assigned to the glass transition temperature, as glass transition temperature is characterised by a step change in the heat flow culminating in a slight shift in the baseline and with nothing as drastic as

a peak (Leng, 2013). It is more akin to an enthalpic relaxation thermal event: here a small peak occurs at the top of the glass transition temperature obscuring the traditional glass transition shape (Gabbott, 2008). This is a norm in materials that carry some form of stress, usually induced in its production. As a result, around the glass transition, they absorb energy and thus molecules assume a more relaxed configuration. Heating tends to anneal the samples, lowering the enthalpies of these stressed regions (Gabbott, 2008), not to mention move the transition to a lower temperature. In the samples that show a perceptible transition (TA 15 and TATi 15), their temperatures are higher than the glass transition temperature normally quoted for PVA samples cast from an aqueous solution at about 35°C (Sarti and Scandola, 1995). The two other samples both appear to show some slight depression, at temperatures much closer to ambient temperature, which might be because these samples carry no residual stress.

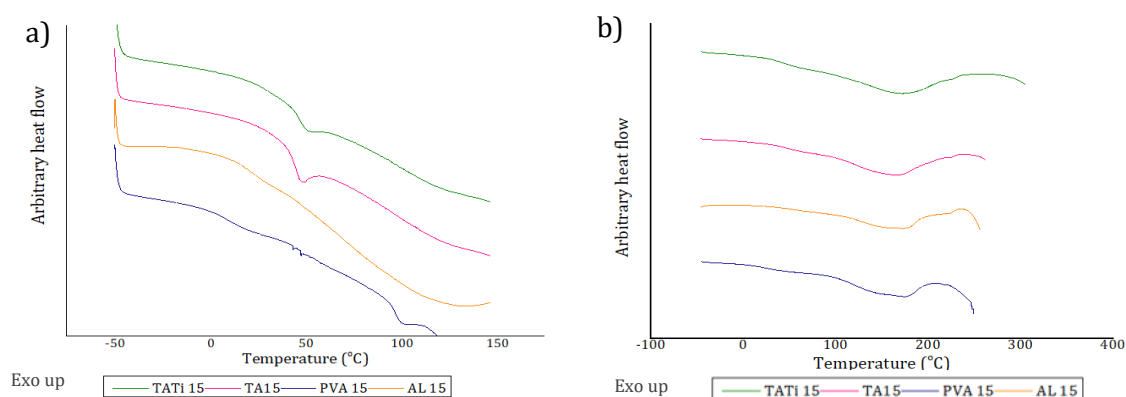


**Figure VIII-11 : DSC curves of PVA (15) hydrogel with low glutaraldehyde content and its blends a) 1<sup>st</sup> run - 50 to 200°C; b) 2<sup>nd</sup> run - 50 to 280°C**

Following the first heating regime, the second regime (Figure VIII-11b) contains fewer peaks belonging to the relaxation enthalpies. This is most likely due to annealing from the 1<sup>st</sup> run relieving the stress in the samples, diminishing any subsequent peaks. In the second run, the peak also shifts to a lower temperature, which again points to a relaxation process occurring (Sarti and Scandola, 1995). In Figure VIII-11b, the other thermal history that can be observed is another endothermic dip in the thermogram. This falls in the temperature range that would suggest dehydration/water loss from the sample had begun to occur. Unlike the pure samples (both pure PVA and pure sodium alginate in Figure VIII-10 a&b), the peak is not well defined, and covers a wider temperature range. This is actually an interesting change in the manner in which water is held within the relatively complex cast polymer sample. The fact that it occurs over the wider range means that there are probably multiple adsorption sites (possibly a multiple layer situation) with different activation energies. As such water would have a different affinity depending on the site, making the adsorbed water molecule more likely to leave at different

temperatures depending on where exactly they are adsorbed.

Quantitative evaluation of the evaporation enthalpies and the glass transition enthalpies derived from (Figure VIII-11a & b) are shown in Table VIII-5. In addition, the estimated water content was also calculated using the following formula:

$$(\%)H_2O = 100 \frac{\Delta H_{evap}^e}{\Delta H_{evap}^t} \quad \text{Equation 40}$$

The formula (Equation 40) includes quantities for the experimental enthalpies of water vaporization ( $\Delta H_{evap}^e$ ) from the different samples and the theoretical enthalpy of vaporization of water ( $\Delta H_{evap}^t$ ).  $\Delta H_{evap}^e$  is calculated from the DSC curves through the integration of heat flow (mW) over a specific period of time (seconds).  $\Delta H_{evap}^t$  is the theoretical standard value for the heat of vaporisation of water which has been measured at 2257J/g (Lide and Haynes, 2010).

**Table VIII-5: Values for the enthalpy of evaporation and enthalpic relaxation associated with glass transition from Figure VIII-11a & b.**

Samples	Transition enthalpic relaxation (J/g)	Evaporation enthalpy (J/g)	Water content (%)
AL 15	0.44	304	13.4
PVA 15	1.40	112	4.9
TA 15	7.68	373	16.5
TATi 15	3.40	241	10.6

From the enthalpies associated with relaxation around glass transition point. It is clear that the samples with the lowest enthalpic relaxation value were made with AL (blended with 20% sodium alginate). However, in the opposite direction, the sample blended with TA (20% sodium alginate with Tannic acid) has the highest enthalpy for glass transition. The remaining samples, PVA and TATi seem to fall in between the aforementioned samples. The enthalpy of evaporation calculated from Figure VIII-11b for the broad evaporation zone does not mirror the transition enthalpies, suggesting that these quantities might be independent. The same can be said for the % water content. What is clear from the table and their values given, is that the simple action of blending different polymer constituents can have a drastic effect on the ability of the resulting polymer to hold water. The PVA hydrogel, which was made without any other addition has the lowest amount of water content, and only the inclusion of sodium alginate, with the other iterations (explained in the methodology) has led to a  $\geq 5\%$  in their ability to hold water.

Assuming the crosslinking density was increased through the mere action of increasing the

amount of glutaraldehyde during the solution casting of polymers, the following DSC curves (Figure VIII-12) give us an idea of the effect on the thermal properties.

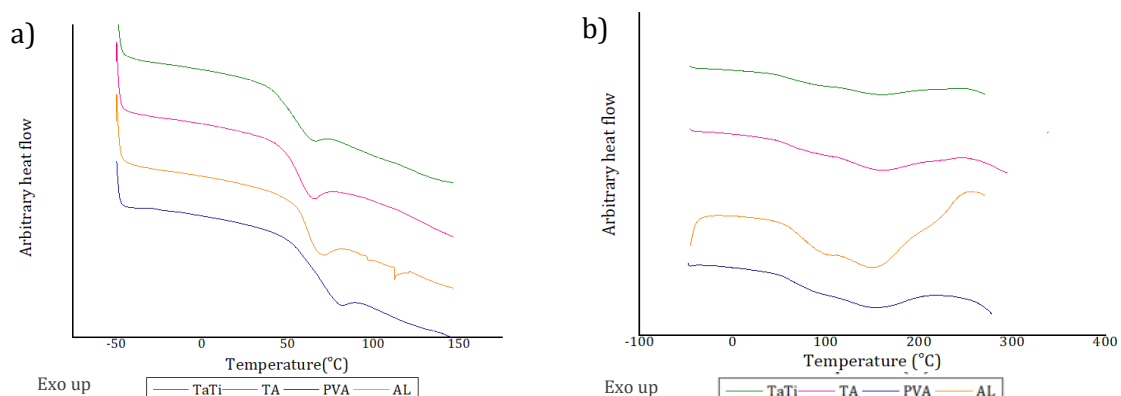


**Figure VIII-12 : DSC curves of PVA hydrogel and its blends, made with double the amount of glutaraldehyde a) 1st run -50 to 200°C; b) 2nd run -50 to 280°C**

The most obvious changes apparent in Figure VIII-12a are the fact that all the polymer blends have a very obvious transition enthalpic relaxation peak compared to the previous DSC curves. PVA polymer has a transition that occurs at the highest temperature (81°C), while the remaining samples have their transitions within the range of 65-71°C. This change might not be so significant, but such a difference in the transition temperature might be a necessity in reducing the processing cost for extruding such polymers. Also, TATi and TA now appear to have experienced general increases in their transition temperature, which puts them within a range where a sudden loss of their physical properties within ambient temperatures is avoided. With the higher amount of crosslinking facilitated by the increase in the amount of glutaraldehyde, it is possible to see the advantages not just from a processing perspective, but also the use of products containing such polymers and their blends over ambient temperatures.

Quantitative analysis of the DSC curves were carried out on the samples, which are displayed in Table VIII-6. While all of the samples have experienced an increment in the glass transition enthalpies, their enthalpies of evaporation have fallen when compared to their counterparts with half the amount of glutaraldehyde. The likely explanation is due to the degree of crosslinking caused by the increased amount of glutaraldehyde. The introduction of glutaraldehyde consumes the -OH groups present in the polymer, as the crosslinker forms a branch with the -OH groups on both edges of the glutaraldehyde at the carbonyl sides/acetyl sides (Rudra, Kumar and Kundu, 2015). This branch is otherwise known as an acetal bridge. The increasing amount of the crosslinker results in the formation of more of these acetal bridges. These result in more space between the PVA chains which then makes organisation into a sensible crystal configuration less probable (Figueiredo, Alves and Borges, 2008). By the same reasoning, more amorphous regions

are suddenly more likely, resulting in the more prominent glass transition peaks in the samples. Another important effect of this crosslinkage, is the consumption of the -OH groups of the PVA. This Affects the hydrophilicity of the samples and its ability to draw in water. In addition to the acetal bridge, which can affect the swelling of the network it contributed in making, affecting the swelling of the overall polymer. The reduced hydrophilicity can also act to reduce the overall water content (see in Table VIII-6) of the polymer.

**Table VIII-6: Values for the enthalpy of evaporation and enthalpic relaxation associated with glass transition**

Samples	Transition enthalpic relaxation (J/g)	Evaporation enthalpy (J/g)	Water content (%)
AL	9.00	152.31	6.78
PVA	6.06	95.69	4.23
TA	11.06	170.00	7.59
TATi	6.80	94.69	4.19

The reason that the water content is not as affected in the other samples (TA and AL) could be as a result of the hydrophilicity supplemented by AL, and it not being affected by the crosslinker- glutaraldehyde. However, TATi does have a similar water content to PVA. This is probably due to the addition of the titanium precursor, which has not doubt been consumed by the tannic acid dispersed in the sodium alginate (AL); thus, reducing the hydrophilicity as well.

### VIII.5.3.2 Mineralised hydrogels obtained from immersion in CaP precursor.

The samples here have been further processed to encourage the formation apatite type crystals, acting as a substrate. From Figure VIII-13a & b one can see the effect on the DSC thermogram on the growth of apatite type crystals within the polymer host.

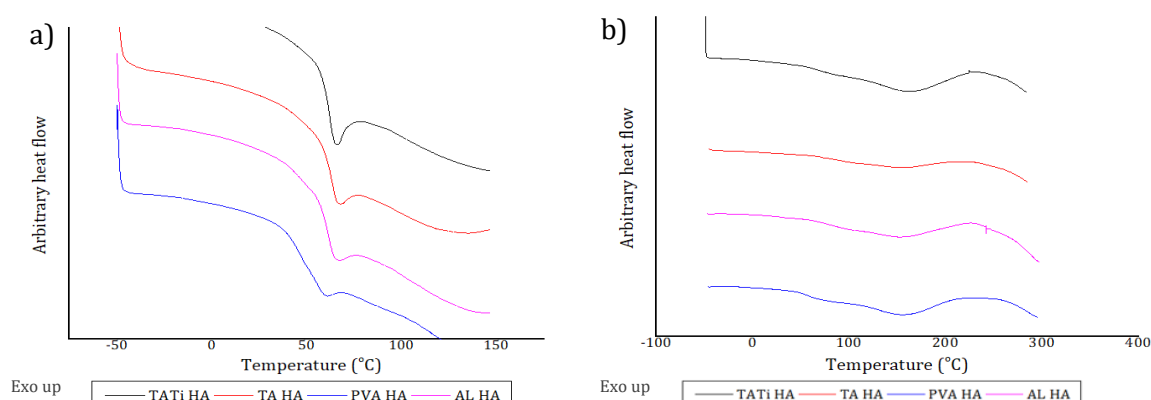


**Figure VIII-13 : DSC curves of the mineralised PVA hydrogel and its blends a) 1<sup>st</sup> run -50 to 200°C; b) 2<sup>nd</sup> run -50 to 280°C**

Figure VIII-13a shows the glass transition relaxation peaks with more of a pronounced endothermic dip than the mineral-free samples. In addition to that, the glass transition temperatures for all the collective samples now occur between 60-67°C, the lowest of which belong to PVA HA, at 60°C while the other samples are centred around 66-68°C.

In the Figure VIII-13b, the characteristic broad peak associated with the evaporation of water from the sample is again apparent. It occurs over more or less the same range (45-200°C).

Quantifying the results of the DSC curves produced the values of the enthalpies for evaporation and glass transition which are shown in the table below.

**Table VIII-7: Values for the enthalpy of evaporation and the enthalpic relaxation associated with glass transition from Figure VIII-13a & b.**

Samples	Transition enthalpic relaxation (J/g)	Evaporation enthalpy (J/g)	Water content (%)
AL-HA	8.24	101.37	4.49
PVA- HA	6.34	124.39	5.51
TA-HA	6.93	82.28	3.64
TATi-HA	9.26	137.28	6.08

The relaxation transition for the samples here have almost identical value to those calculated without the addition of apatite-like crystals. From these results (Table VIII-7), one may infer that the treatment process to produce these minerals have had very little effect at least in terms of the overall amorphous domains that are present in the samples under investigation. The stress induced whether as a result of synthesis or simply due to ageing is a common factor in all of the samples.

The enthalpies of evaporation remained generally consistent with those having no mineral inclusion. There is some increment and some reduction, with PVA HA and TATi HA experiencing increases in the vaporisation enthalpies of water. Meanwhile, the other two samples mentioned showed a drop in their vaporisation enthalpies.

In the previous sections, the increment of glutaraldehyde could be ascribed as the cause of this change in the evaporation/dehydration properties of the samples; the thermal properties with these mineral enriched samples might not be easily explained by the presence of glutaraldehyde (at least not completely). It is possible that several reasons might be behind these changes.

There is the effect of the mineral inclusion, and the consequence of its own inherent affinity for water absorption on the enthalpy of evaporation. It is known that apatite (i.e. hydroxyapatite, substituted hydroxyapatite) and other phases of calcium phosphate have their own abilities to



take up water. These minerals have different type of water either surface adsorbed water, which is merely adsorbed on the surfaces of hydroxyapatite; or bound internal water that tend to occur within the lattices of calcium phosphate minerals. In ACP, water is thought to occur within the interstices of so called “Posner clusters”, accounting for close to 20% of the overall ACP mineral (Wang and Nancollas, 2008; Dorozhkin, 2011). In apatites, usually substituted apatites like CDHA, the lack of stoichiometry caused by the deficiency of  $\text{Ca}^{2+}$  causes a charge imbalance which can be offset via the inclusion of water, through the protonation of  $\text{-OH}^-$  ion and  $\text{PO}_4^{3-}$  in the vicinity closest to the lack (Dorozhkin, 2011). Thus, some form of water is always guaranteed.

There is also the effect of the changing network of one portion of the polymer blend. While PVA HA has only crosslinked PVA to contend with as the main substrate. The other samples containing sodium alginate (TA-HA and AL-HA) begin their own crosslinking through the introduction of  $\text{CaCl}_2$  during the alternating immersion process. Thus, a wet precipitation process (for the formation of apatite) occurs in congruency to the crosslinking of the relevant sodium alginate moieties. The resulting network becomes more complex, ejecting more water due to the shrinkage caused by the complexation of sodium alginate. This decreasing free volume within the polymer blends will no doubt affect the volume of apatite that would otherwise grow within the pores in the polymer network. There is also the possibility that  $\text{Ca}^{2+}$  that would have been freely available for the wet precipitation process is now used up for crosslinking. This situation might also be why TATi-HA has experienced an increase, just like PVA HA, as both are the only substrates that had completed their crosslinking early on; the inclusion of the water adsorbing mineral within their network can only work to increase the % water content.

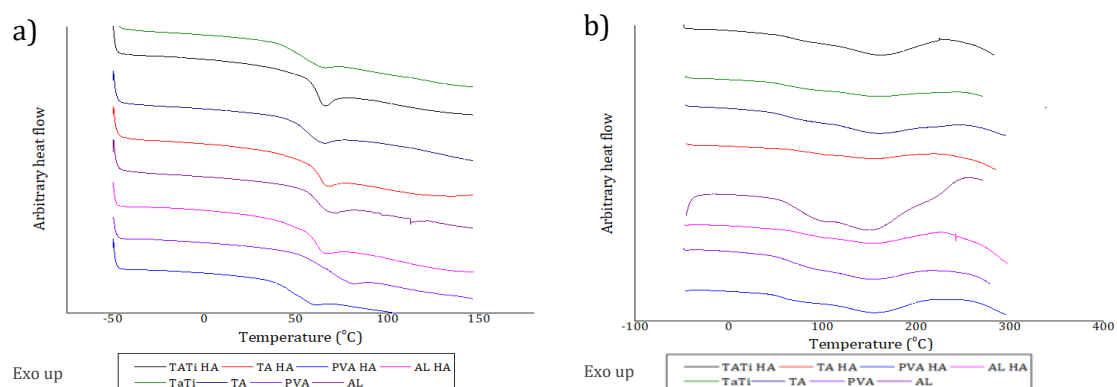


**Figure VIII-14 Mineralised hydrogels versus un-mineralized hydrogels a) 1<sup>st</sup> run -50 to 200°C; b) 2<sup>nd</sup> run -50 to 280°C.**

Combining the results of the mineralised and non-mineralised polymer substrate (see Figure VIII-14a&b) the differences (at least in reference to the shape of the glass transition temperature and its temperature shift) are more apparent when comparing both samples on a single graph. As

discussed, and calculated, it is now possible to observe the changes in the transition brought on by the mineralisation process, with the  $T_g$  peaks having a greater dip in the endothermic direction in the mineralised product, than spreading outward. Figure VIII-14b covers the region where evaporation occurs, visually the differences are a lot more difficult to pick out.

## VIII.6 Summary

### VIII.6.1 Compression testing of the hydrogels (and mineralised scaffolds)

- Hydrogel-only samples

In reference to the pure hydrogels, the stress-strain graphs are believed to be affected by the crystallinity and amorphicity of the hydrogel. The amorphicity is linked to the elastic modulus and the elongation to break, as explained in VIII.5.1.1. The compressive strength is thought to be related to the crystal domains of the hydrogel, apparently occurring when the polymer chains have reached their maximum extension and begin pulling on these crystal domains. Putting further stress will cause either slippage of these chains, or cavitation of the amorphous region causing rupture.

For the most part, the stress-strain behaviour of all the hydrogel only samples: PVA, TA, TATi and AL, are all identical up till the strain at 50%. As this is to do with the amorphous regions of the hydrogel, the majority of which is contributed by PVA, thus PVA and its polymer chains dominate this area.

In compressing past 50% strain, divergence in their behaviours begins to occur. It is at this point that the presence of crosslinks and the composition of the different hydrogel blends comes to play. Compared to a sample like PVA, that is compositionally homogenous; the other samples with their differing polymer blend could make it difficult for the polymer chains to attain full extension i.e. assuming PVA is still responsible for the majority of the blend's properties, the addition of polymer, poorly mixed or not, would cause stress to propagate through a different pathway as it attempts to travel through the cross section of the sample. Before the polymer chain in the amorphous section attains full elongation present in the majority hydrogel, the polymer chains of the minority hydrogel (alginate and its derivatives) will need to have reached its full stretch. The TA and TATi would be at an advantage over the other samples because of the presence of tannic acid. Its numerous hydroxyl groups allows the formation of temporary intrachain crosslinks within alginate, and interchain crosslinks with PVA as well. Also, the easy breakage of the hydrogen bonded crosslinks provides an easier path for energy dissipation (Chen *et al.*, 2016), thus pushing elongation to break further in these samples; one can also not ignore the contribution to the tensile strength provided by the increase hydrogen bonding.

In spite of this, most of the hydrogels have similar stresses (at 75% strain) between 0.21-0.26MPa, although TATi consistently had the highest stress at 50% and then at 75%, followed by TA, AL and PVA respectively (see Table VIII-1). The difference is likely to do with the levels of crosslinks. The elevated mechanical properties of the hydrogels blended with AL and TA, can be linked back to the additional sources of hydroxyl groups that the alginate and tannic acid would have provided in the blends. PVA would theoretically have a finite amount of interchain linkage, less so than if it has the hydroxyl-rich tannic acid or alginate included. Also, the elastic modulus increased in most of the blends, specifically TATi and TA, regardless of the regions that were used for this analysis (see Table VIII-2).

- Mineralised samples

The stress-strain properties of the mineralised hydrogels are different from their nonmineralized counterparts. The likely variance is associated with the changes in free volume (pores, voids, channels), water present in the scaffold material and additional crosslinkage (discussed in VIII.5.1.2). The lack of free volume as a direct of occupation by the apatite minerals, creates a denser scaffold which means that it is unable to undergo the same amount of deformation it would otherwise have experienced in its unmineralized form. The amount of water provides further resistance to deformation as the denser network means that it is more difficult to escape the stressed surface (Ma *et al.*, 2009). Of course, there is the added crosslinkage that has now been augmented by ionic interaction between the hydrogel (both alginate and PVA) and calcium ions. All of these are responsible for the general increase in the mechanical properties of the mineralised hydrogel over its nonmineralized counterpart.

Nevertheless, Figure -VIII-4 shows that all of these samples experienced different stress-strain behaviour. This is further confirmed in Table VIII-3 and Table VIII-4. As, PVA HA has the lowest stress at 50% strain and at 75% strain of all the hydrogel, and TATi HA experienced that highest stress at 75% strain, while TA HA's was best AT 50% strain. Also, the elastic modulus yet again reflects the poorer performance of PVA HA, with values that were consistently lower than the other gels through the compressive test. The same explanation with regards to the requirement for the majority hydrogel amorphous region to elongate may be applied here.

## VIII.6.2 TGA of the hydrogels (and mineralised scaffolds)

- Hydrogel only samples

The hydrogel only samples, which have been crosslinked with a lower amount of glutaraldehyde, appear to have adopted a thermal profile similar to PVA only samples, as a direct result of PVA making up the majority of the scaffold contents (see Figure VIII-6). The main benefits of adding sodium alginate and tannic acid looks to be in the delay of the thermal events linked to the breakdown of the polyene backbone. While in PVA15 hydrogel only, the events commence around

270°C, in AL15 and TA15 it begins at 290°C, and much later for TATi15. Although PVA15 eventually ends up with the largest amount of residual mass at 520°C, one cannot ignore the benefits of having a polymer blend that remains workable and stable at a much higher temperature in terms of processing. It can have an effect on manufacturing conditions such as processing temperature, viscosity and ability to attain more intricate architectures.

The increase in the amount of glutaraldehyde in Figure VIII-7 appears to have changed the thermal trend in the hydrogel-only samples. Significantly, all of the samples have their initial mass loss delayed to >300°C, although TATi appears to be the only one with less stability because mass loss occurs earlier than it would have with less glutaraldehyde. In addition to delayed mass loss, the final residual weight recorded for all of the samples have dropped to below 5% (only TATi remains closer to its original value). It is possible that the decrease could be due to the more efficient transmission of heat energy through the scaffold, facilitated by the denser hydrogel, lack of pores and voids, as well as the increased crosslinking. A more open network like sample (made with less glutaraldehyde) means more voids, hence more inclusion of air spaces, which are worse conductors of heat than the polymer. This serves to delay the volatilisation of the analysed samples.

- Mineralised samples

In the mineralised samples, only a single glutaraldehyde volume was maintained for all of the samples (i.e. the higher volume). Figure VIII-8, shows the thermal behaviour of the mineralised samples that have been subjected to a 4 cycle treatment of calcium phosphate precursors. Their thermograms bear some similarity to the samples shown in Figure VIII-7, primarily with the late onset of mass loss and the almost featureless thermographs of the samples. As explained in VIII.5.2.2, the increased residual weight may be linked to the precipitation of the calcium phosphate minerals within the body of the hydrogel matrix. The calcium phosphate minerals are simply more stable at higher temperatures with completely different heat capacities and are more likely to remain after the organic component (e.g. hydrogel) has long since degraded into their volatile by-products. PVA HA ends up with the least amount of residual mass, with the other blends performing much better. The increased crosslinks/entanglement points have most likely contributed nucleation points for apatite deposition and growth.

Increasing the cycle number from 4 to 8 resulted in increased nucleation and deposition events of calcium phosphate phases, which ultimately increased the amount of residual weight left after 520°C. There residual mass increased from  $\leq 20\%$  for the mineralised hydrogels to just around 60%. This increment in mass, reflects the more mineralised micrographs that were seen in SEM analysis.

### VIII.6.3 DSC of the hydrogels (and mineralised scaffolds)

- Hydrogel-only samples

The hydrogel samples made with a lower volume of glutaraldehyde in Figure VIII-11a appear to show some glass transition events, with the two samples that consisted of tannic acid (TA15 and TATi 15) showing the more apparent transition temperature step coupled with an enthalpic relaxation peak. PVA 15 and AL 15, barely showed any perceptible peak around 40-55°C. Figure VIII-11b showed the second run of the DSC analysis; here none of the samples appeared to display any transition event, mainly due to the annealing on the first run. The other significant event (dehydration/water loss) were around 200°C to 300°C, with enthalpies and the water content shown in Table VIII-5. It appears that PVA 15 had the lowest water content, reflected by the evaporation enthalpy calculated, as well as a transition enthalpy. TA 15 on the other hand had the highest of all the values.

Increasing the amount of glutaraldehyde caused some change in the DSC curve (see Figure VIII-12a). For one, all of the samples now had a distinctive transition enthalpic relaxation peak, which had shifted to higher temperatures  $\geq 65^\circ\text{C}$ . As explained in VIII.5.3.1, this is linked to the levels of crosslinks, making the formation of crystal domains less likely, thus increasing the amorphous character of these hydrogel samples which makes the transition peak more prominent. The increased crosslinking means amplified consumption of hydroxyl groups and less hydrophilicity of the samples, this is reflected in the diminished peak for evaporation in Figure VIII-12b. This is why PVA and TATi are more affected with respect to their water content (see Table VIII-6). The lack of alginate donating further hydroxyl groups for PVA and the use of a titanium precursor in the case of TATi used up the available hydroxyl group. Also, the increased amount of unconsumed hydroxyl groups in AL and TA means an increase in the probability of hydrogen bonding, preventing the assembly of the polymeric chain into a sensible crystalline domain, increasing the samples amorphicity over PVA and TATi.

- Mineralised samples

Mineralisation was not carried out on samples with a lower volume of glutaraldehyde. Figure VIII-13a&b shows that the DSC curve of the first run resembles that from Figure VIII-12a&b. Any difference are reflected better in Table VIII-7. Here, PVA HA and TATi HA both appear to have a better water content, in opposition to what their individual hydrogel's constituents had in Table VIII-6. Their increase could be explained by the presence of a calcium phosphate phase (which as explained in VIII.5.3.2) always has some form of water presence (surface and lattice), thus contributing to the enthalpy of evaporation. In the case of TA HA and AL HA, the presence of  $\text{Ca}^{2+}$  could have easily restarted the crosslinking process, occurring in tandem with the wet precipitation, resulting in the consumption of hydroxyl groups and hydrophilicity. Now, TATi HA

has the highest water content, followed by PVA HA, AL HA and then TA HA.

## VIII.7 Conclusion

The main aim of this chapter was to examine the mechanical properties for the neat hydrogels and mineralised hydrogel scaffolds.

- Amongst all the hydrogel samples, TA had the highest modulus between 0-10% strain. TATi had the highest between 20-30% . AL had the highest at 30-45% strain
- With regards to the stress, TATi reached the highest stress at 50% strain and then at 75% strain
- After mineralisation, AL HA had the highest modulus between 0-10% strain, TATi HA had the highest between 20-30% and TA HA had the highest between 30-45% strain. PVA HA showed the lowest moduli at all strain range examined (see Table VIII-4)
- TATi HA, and TA HA showed impressive compression stress values at 50% strain and 75% strain, respectively. PVA HA showed the lowest values amongst all the samples (see Table VIII-3)

From the results obtained, it appears that the mechanical properties of the hydrogels and mineralised hydrogel scaffolds benefited more from good choice of blending properties. Indeed, the samples made with TATi HA and TA HA have the most promising mechanical properties amongst the mineralised samples, making them suitable scaffolds for low-load bearing areas, such as use as bone grafts, as well as showing some relevancy for the replacement of human cartilage.

In the thermal sense, using TGA the effect of crosslinking and blending on the thermal events on the hydrogels, before and after mineralisation were investigated.

- Neat PVA 15 has the highest amount of residual mass at the end of the TGA run; however, TATi 15 showed the most resistance to mass loss between 300-350°C
- At higher glutaraldehyde content, TATi has the highest residual mass at the end of the run. The increased crosslinker content improved the resistance of all the samples extending their resistance to about 300-350°C
- In the mineralised samples, TATi HA and AL HA had the highest residual mass for the samples processed through 4 cycle. At 8 cycle, AL HA 8 cycles showed the highest residual mass although TA HA 8 cycles exhibited the most resistance to mass loss between 20-300°C

Clearly there is something to be gained through crosslinking and blending in terms of resistance to mass loss at high temperatures. At low crosslinking volume TATi 15 showed the most promise

for high temperature stability. Increasing crosslinking makes all the samples resistant, but TATi leaves behind more residue after the TGA run. For the mineralised scaffolds, TATi HA and AL HA are suitable after 4 cycles of immersion.

Finally, in terms of DSC one can see how the different hydrogels now have different hydrophilicity and amorphicity. TATi-HA appears to show extensive hydrophilicity (Table VIII-7), highlighting the potential for its use in-vivo use. As a neat hydrogel, TA seems to display the highest water content. In terms of the transition enthalpies that can be linked to the sample amorphicity, AL and TATi HA have the highest values which indicates that these samples are less crystalline than the other samples.

## **Chapter IX Bioactivity and degradation of the mineralised hydrogel scaffold**

### **IX.1 Introduction**

Following on from the synthesis and subsequent characterisation of the morphological and thermal properties of the hydrogel, its blends and upon mineralisation of the samples- not to mention the uptake thermodynamic and kinetics of the hydrogel- the next logical step was to probe a potential functional application route. This route will involve focusing on the bioactive properties of the hydrogel, i.e. its ability to remodel in the face of being placed within a biological system, in addition to its dissolution properties. It is hoped that from this study, one will be able to approximate the behaviour of the synthesised hydrogels in the presence of a pH (7.4) and a compositional equivalent environ (SBF and PBS). Will the hydrogels (mineralised and otherwise) behave more as a reservoir for ions for the environ? Will they behave more as a scaffold that instead will allow the deposition of ions from the environ onto itself? Comparison will be carried out using Bio-Oss® which is a commercially available bone remodelling/substitute currently utilised within the dental field.

### **IX.2 Aim**

Thus, the overall aim of this thesis chapter would be to probe the ability of the hydrogels (with and without mineralisation) to remodel or otherwise in the face of being placed in a simulated setting closer to what occurs within the human body (SBF & PBS), at a pH of 7.4 and temperature of 37°C. And before this, a short experiment will be carried out to follow the initial uptake of the Ca<sup>2+</sup> and phosphate ions onto the neat hydrogels, to monitor the natural affinity of the hydrogels to mineralise in the presence of the necessary calcium/phosphate precursors. These specific set of tests will be carried out at room temperature. The resulting samples formed will be characterised using FTIR, XRD and SEM to analyse the effect of this bioactivity evaluation on the morphological, chemical and crystalline structure of the samples.

### **IX.3 Background**

Evaluation of the bioactive potential, biocompatibility and toxicity studies are all standard tests that need to be carried out before a material can be implanted within the body. A mineral like hydroxyapatite, which makes up a significant composition of the body's bone tissue, as has been shown in the previous chapters, is easily synthesisable outside vivo condition with characteristics that mimic those that would normally be made within bone tissue. But while these lab synthesised



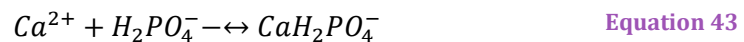
apatites appear in terms of crystallinity and lattice constants, to be closely similar to the body's own apatite, it remains to be seen whether these synthesised samples would react in the same manner. The manner in question, would be the ability to undergo biomineralization just as it occurs within the body, although the body systems has several other agents in the form of bone remodelling biomolecules (cells and proteins), as long as the synthesised calcium phosphate phase has the ability to precipitate calcium phosphate on its surface.

The bioactivity of the material stems from this biomineralization process. In certain regards, foreign materials that are usually placed in the body tend to cause the formation of a capsule of fibrous tissue around the material. Isolating the materials from the body, decreasing its interaction with the body and rendering it fairly close to inert with respect to the body (Kokubo and Takadama, 2006). However, calcium phosphate has the quality of not causing this immunogenic response. It instead has the ability to precipitate calcium phosphate onto the surface, especially when in contact with the necessary active agent; in the body, this would be the blood plasma (Kim *et al.*, 2004; Wang *et al.*, 2005; Kokubo and Takadama, 2006) which has the necessary pH and ion concentration to facilitate bone formation. The calcium phosphate, usually taking the form of an apatite that forms the necessary anchoring point, allows the connection of this (foreign) bioactive material with living tissue. This makes it not just bioactive, with regards to its ability to form bone, but is also osteoconductive in its ability to bond via the surface with living bone with no direct intervention.

To assess this bioactive property, it would be necessary to replicate the conditions that would normally allow the formation of bone in the body but in a lab setting. This property was seen in several bioactive glass ceramic samples in the presence of a pH7.4 Tris-HCl buffered solution over a period of time (Ogino, Ohuchi and Hench, 1980; Kokubo and Takadama, 2006). They displayed the formation of a calcium phosphate film on their surface in spite of the ionically deficient buffered solution. Further improvements on this method, from the initial use of an acellular simulated body fluid by Kokubo *et al.* in 1989 (Kim *et al.*, 2004), led to the development of several SBF formulations with compositions that were made to follow that of blood plasma. Further improvement in characterisation techniques, led the better identification of the calcium phosphate phases that were being formed. There are several recipes that have been created from the initial method, which lacked  $\text{SO}_4^{2-}$ , where the  $\text{Cl}^-$  and  $\text{HCO}_3^-$  have been varied e.g. c-SBF, n-SBF, r-SBF (Kokubo and Takadama, 2006). These bioactive tests proved the formation of suitable calcium phosphate phases in vitro, which correlated positively with the in vivo studies. Ceravital<sup>®</sup> glass-ceramic when implanted in rabbit tibia was shown to produce a layer of carbonated hydroxyapatite, a positive outcome that was initially confirmed by the bioactive invitro test (Ohtsuki *et al.*, 1991), while Bioglass<sup>®</sup> was revealed to bond directly with bone, after being

confirmed to do so in vitro in the presence of SBF (Kokubo *et al.*, 1990).

With this justification of using SBF, it is thought that the actual formation of bone on the surface, especially on immersion, assuming the calcium phosphate phase is HA, begins via the revelation of the negative surface of the hydroxyl and phosphate group. The charge originates as a result of the isoelectric point. This lies between 5-7 which is a little lower than the pH of the solution of SBF (Kim *et al.*, 2004). Through an electrostatic process,  $Ca^{2+}$  in the solution are attracted onto the negative surface. This quickly forms amorphous calcium phosphate (ACP) on the surface, surmounting the initial negative charge. The phase forms first mainly as a kinetic consequence, with the ions in question having a strong attraction to one other (Dorozhkin, 2012a). The net positive charge begins to mop up the phosphate ions present in the solution. Wang *et al.* (2005) list several association/dissociation reactions, with the following having the highest constants  $K$ , which gives an argument for the interaction between calcium and phosphate ions over the other possible ions present in the solution.



The ACP phase act as precursors which precede the formation of more thermodynamically stable phases like HA and OCP. The transformation proceeds through any of these means, which could be the dissolution of ACP and then re-precipitation, reorganisation of the internal structure, formation of crystalline structure either within or on the exteriors of the ACP and self-aggregation coupled with surface transformation etc (Dorozhkin, 2012a). Wang *et al* (2009) attempted a possible summary using theirs and different findings to do with ACP transformation. They claimed that calcium and phosphate ions cluster, forming the initial ACP mass. At numerous sites in the clusters, the calcium and phosphate ion pairs take up more ions from their surroundings, forming the initial crystal domains/nucleation sites. The uptake of the ions from the surrounding, allows the growth of the domains, and the subsequent release of hydrated protons affects the density and thus mechanical strength of the compromised cluster. These then collapses, revealing the crystals. The crystals that have formed can now act as further nucleation sites, with their very high surface energies, which rapidly induce further precipitation with a marked drop in pH (Wang *et al.*, 2009; Dorozhkin, 2012a).

## IX.4 Experimental technique and methodology

The sample preparative conditions have been mentioned in section II.3.

### IX.4.1 Analysis conditions

Three aspects of the hydrogels will be studied. They include:

- 1 Uptake and release of calcium and phosphate ions: The calcium ion and phosphate ion uptake of neat hydrogel (blends included) will be monitored. For the  $\text{Ca}^{2+}$  uptake, an immersion solution of  $\text{CaCl}_2$  with a  $\text{Ca}^{2+}$  concentration of approximately 260ppm was utilised as the probing solution. 20mg of the hydrogel was immersed in 10ml of the  $\text{Ca}^{2+}$  rich solution (260ppm). This was carried out at room temperatures of between 18-20°C. Readings were collected periodically at 0, 2, 4, 24, and 28 h using the o-cresolphthalein complexone calcium method and UV-vis (the preparation and methodology of use was discussed in section II.9.1).

For phosphate ion uptake, 20mg of the neat hydrogel (blends) was placed in 10ml of the phosphate ion rich source with a concentration of approximately 20ppm. This was carried out at room temperatures of 18-20°C. Readings were collected at 0, 2, 4, 16, 20 and 32 h. They were characterised with the UV-vis using the modified molybdenum blue methodology as provided by Hanna instruments.

The concentration of the calcium (260ppm) and phosphate (20ppm) ion rich source for these tests was derived from the concentration used for the preparation of the mineralised samples stated, which was 50mM for  $\text{CaCl}_2$  and 13mM for  $\text{Na}_2\text{HPO}_4$ . The concentration was dropped to 5mM and 1.3mM respectively to reduce the possibility of signal saturation.

Estimation of calcium ion in 5mM (0.005M) of  $\text{CaCl}_2$ :

Converting 55 mM to ppm first,

$$\begin{aligned} & 0.0055 \times 147 \\ & = 0.808 \left( \frac{g}{mol} \right) \\ & = 808.5 \text{ (ppm)} \end{aligned}$$

Therefore, the estimated amount of calcium ion is 5mM of  $\text{CaCl}_2$ :

$$808.5 \times \left( \frac{40}{147} \right) = 219 \text{ ppm}$$

Estimation of phosphate ion in 1.3mM (0.0013M) of  $\text{Na}_2\text{HPO}_4$

$$0.0013 \times 141.96$$

$$= 0.1845 \left(\frac{g}{mol}\right)$$

$$= 184.5(ppm)$$

Therefore, the estimated amount of phosphate ion present in 1.3mM of Na<sub>2</sub>HPO<sub>4</sub>

$$184.3 \times \left(\frac{30}{141}\right) = 39.2ppm$$

The main discrepancy between the calculated amounts and the actual prepared/measured amount is more than likely due to human error and possibly instrumental variation.

- 2 Bioactivity studies: While the principle of detection of calcium and phosphate ions is done in a similar manner as that for the uptake studies above, the premise and experimental setup is different. The reasoning for this test as previously pointed out is to study the bioactivity of the mineralised hydrogels and monitor their behaviour within a pH 7.4 SBF which has the following composition (see Table IX-1) :

**Table IX-1: Composition of simulated body fluid (SBF) (Vasilescu *et al.*, 2011)**

Salts	Amount (g) per litre
NaCl	7.99
NaHCO <sub>3</sub>	0.35
KCl	0.22
K <sub>2</sub> HPO <sub>4</sub>	0.22
MgCl <sub>2</sub> . 6H <sub>2</sub> O	0.30
CaCl <sub>2</sub>	0.27
Na <sub>2</sub> SO <sub>4</sub>	0.07
Tris Base buffer	6.05

3mg of the mineralised hydrogel samples were placed in 5ml of SBF, within a closed container, which was then placed in an incubator having a temperature maintained at 37°C. The samples were kept agitated at 70rpm for a duration of 100h. Samples were retrieved periodically and tested using the appropriate calcium ion and phosphate ion detection method. After each retrieval, an equal amount of SBF was topped up to maintain roughly the same solid-liquid ratio. Phosphate ion was not replenished after each reading but after 2 days, and 4 days.

- 3 Dissolution studies: The same experimental methodology carried out for bioactivity was replicated in this section. The only difference as dictated by the premise of this study was swapping the SBF for PBS instead, as this section was not concerned with the remodelling of the mineralised hydrogels, but rather the absolute dissolution within the body.

3mg of the samples was placed in 3ml of the PBS, with pH 7.4. It was carried out over a period of 30 days, with tests on the sample carried out weekly. After each retrieval, an equal amount of PBS was topped up to maintain roughly the same ratio of solid-liquid through the duration of the experiment.

## IX.5 Results

### IX.5.1 Calcium ion and phosphate ion uptake

#### IX.5.1.1 Calcium ion uptake

In this section of the results, the uptake of calcium and phosphate ions will be studied. With  $\text{Ca}^{2+}$  (Figure IX-1), it is clear to see that there is an overall reduction in the  $[\text{Ca}^{2+}]$  solutions analysed. Starting with a standard solution of 260ppm  $\text{Ca}^{2+}$  at 0h, each of the hydrogels appear to adsorb  $\text{Ca}^{2+}$ , some more than others. The least sorbing sample of all the samples appears to be PVA Ca, followed by PVA, AL, TATi and finally TA. After the 0h mark, all of the samples appear to uptake about 2% at least of the calcium, which improves in some of the samples. At the final hour of measurement, although there has been fluctuations, there is a net reduction of 3% for PVA Ca, 8% for PVA, 11% for AL, ditto TATi and finally TA has a reduction of 14% in the overall solution concentration of  $\text{Ca}^{2+}$ .

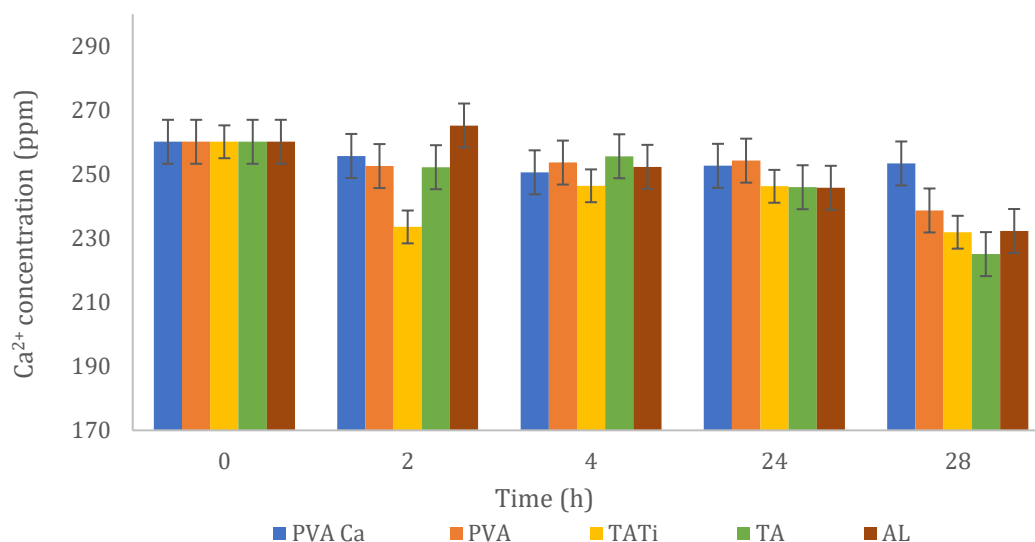
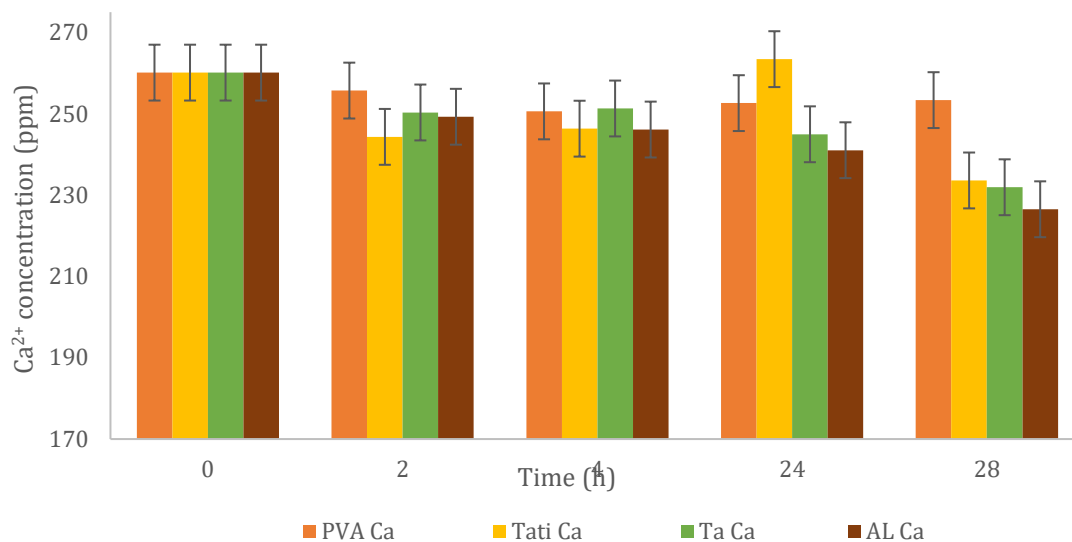


Figure IX-1: Calcium ion uptake behaviour of the hydrogels over a 28h period at room temperature. (Dose: 20mg of hydrogel in 10ml of 260ppm  $\text{Ca}^{2+}$  solution).

With regards to the order of the mineralisation process (i.e whether starting with  $\text{CaCl}_2$  or  $\text{Na}_2\text{CO}_3$ ) there generally does not seem to be a significant difference in the sample behaviour. Therefore, all of the samples in Figure IX-2 still appear to take up  $\text{Ca}^{2+}$ . After the 28h period, TA

Ca, TATi Ca, both end up sorbing about 11% of the  $\text{Ca}^{2+}$  from the solution, AL Ca with 13%. All of the aforementioned appear to be better than PVA Ca which peaks at 3%  $\text{Ca}^{2+}$  uptake. One could speculate that if the alternating process was increased from 1h to 28h, there might be a marginal gain in the  $\text{Ca}^{2+}$  content, this however sacrifices the time (as the preparation for one cycle has been extended). The most efficient sample in terms of sorbing  $\text{Ca}^{2+}$  appears to be TATi Ca.



**Figure IX-2: Calcium ion uptake behaviour of the hydrogels, previously treated with sodium carbonate for 1 h, over a 28h period at room temperature. (Dose: 20mg of hydrogel in 10ml of 260ppm  $\text{Ca}^{2+}$  solution).**

Whether considering the samples that have been treated first with  $\text{Na}_2\text{CO}_3$  (Figure IX-2) or not (Figure IX-1), it is possible that increasing the immersion period to longer than 24h might benefit the uptake of  $\text{Ca}^{2+}$ . However, the increase in time might not be a worthwhile process. At  $\leq 2\text{h}$ , the uptake amount is reasonable, and seems to be similar at 4h and 24h too.

#### **IX.5.1.2 Phosphate ion uptake**

Similarly, with  $\text{Ca}^{2+}$  uptake, there appears to be a positive sorption of phosphate ion by the hydrogels (Figure IX-3). There seems to be an uptake of close to 5ppm from the phosphate-rich solution. The most interesting development here is the fact that PVA (unlike  $\text{Ca}^{2+}$ ) showed the best uptake at least within the first 2h, although afterwards the uptake fluctuated. The remaining samples took up a similar amount to PVA, but at different points throughout the experimental window. At 32h, AL is the least sorbing sample, only taking  $\approx 19\%$  of the phosphate, this is followed by TA (26%), PVA (27%) and PVA Ca (29%) and finally TATi (30%). It should be mentioned that at 2h the order of uptake of phosphate ion is closer to PVA > PVA Ca > TA > TATi > AL.

Just like with  $\text{Ca}^{2+}$ , there appears to be overall a better uptake efficiency with an increasing time

period. If one were to indeed increase the cycle time, the turnover amount per cycle would be longer, which is not entirely realistic for an industrial manufacturing process.

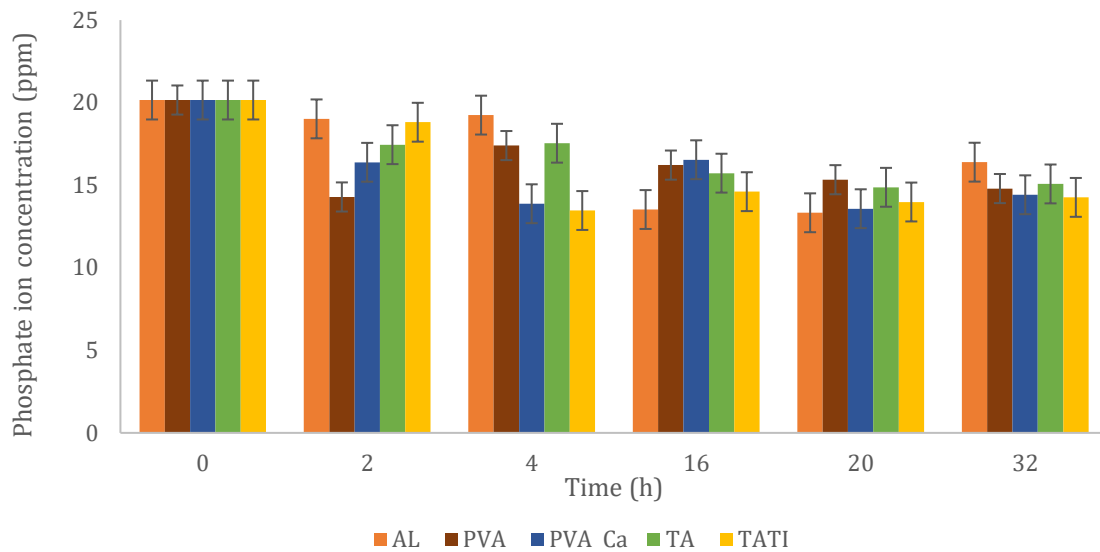


Figure IX-3: Phosphate ion uptake behaviour of the hydrogels, over a 32h period at room temperature. (Dose: 20mg of hydrogel in 10ml of 20ppm solution).

## IX.5.2 Bioactivity studies using colourimetric analysis

The bioactivity of the samples were studied by following the fluctuation of calcium and phosphate ions in SBF. It should be noted that the concentration of  $Ca^{2+}$  and phosphate ions in the solution are 103ppm and about 45ppm. This because SBF has salts containing the respective ions as part of their composition, exactly as would be found in the human body. Fluctuations in the concentrations of  $Ca^{2+}$  and phosphate ions will be analysed (in addition to the changing pH) to obtain the fullest picture of what the mineralised hydrogels are capable of eliciting within such a simulated environment.

### IX.5.2.1 Calcium ion ( $Ca^{2+}$ ) monitoring

Figure IX-4 depicts the changing  $Ca^{2+}$  concentration of SBF with increasing time interval while in contact with the different mineralised hydrogel samples, Bio-Oss® and nHAp.

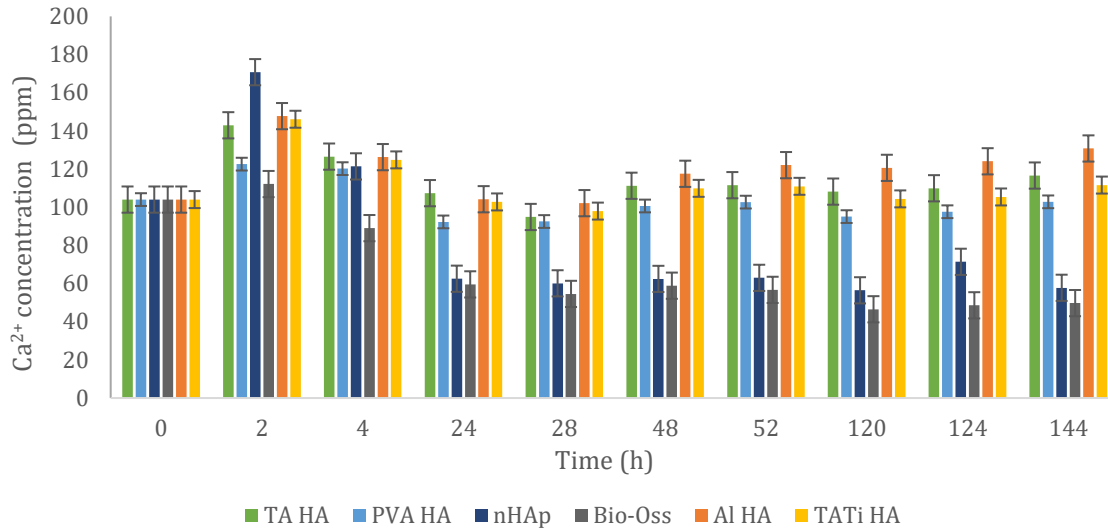


**Figure IX-4: Bioactivity evaluation of the mineralised hydrogels (HA) and the commercial samples following the changing concentration of calcium ion in the immersion the test media (Dose: 3mg of mineralised hydrogel in 5ml of SBF (pH 7.4) at 37°C).**

It appears that within the first 2h, all of the samples experience a fairly significant increase in  $Ca^{2+}$  concentration within their corresponding SBF media. The most significant increase was produced by nHAp which appears to yield closer to 60% more  $Ca^{2+}$  than the other samples; next to it is TA HA with a 30% increase in the calcium concentration. AL HA and TATi HA appear to release an extra 40%. PVA HA gave an extra 17% extra. Finally, Bio-Oss barely releases a further 7% into the SBF solution.

Following the initial rapid release, the amount of  $Ca^{2+}$  released into the solution decreases. The number of  $Ca^{2+}$  dropped the most drastically with nHAp and Bio-Oss®. nHAp returns to almost normal following the drop, Bio-Oss® instead drops by about 15%. It drops in total by 43% and then remains fairly static. nHAp falls as well, to a value closer to 40%. The other lab synthesised samples have fairly consistent values, barely dipping by 12% from the original SBF concentration. Interestingly enough, it is only PVA HA that experiences a net drop in  $Ca^{2+}$  concentration, with respect to the original SBF concentration. The other samples however do not show this reduction and instead with the number of  $Ca^{2+}$  hovering above what was initially present in the SBF fluid at the start in true dynamic equilibrium. At the final observation (144h), the SBF media of Bio-Oss® has a deficit of 53% (49.7ppm), nHAp 45%(57.5ppm), PVA HA of 2% (102ppm). The remaining samples TA HA AL HA and TATi HA all sustain values above that of the initial  $Ca^{2+}$  concentration in SBF (with increases of 12% (116ppm), 44% (130ppm) and 7% (111ppm) respectively).

The results show that all the hydrogel samples, except for PVA HA, favour the release of calcium



ions rather than sorption of the ions, like nHAp and Bio-Oss®. There are several possibilities that might explain this difference between the purchased samples and the hydrogel samples.

Starting with the phase concentration. This is an important parameter, as the XRD studies have shown that the purchased samples are not only made up of mostly hydroxyapatite, they are also highly crystalline. Hydroxyapatite has been shown to be one of the most stable calcium phosphate phases present. Apparently it has a solubility at 25°C of ~0.0003 mg/ml (Dorozhkin, 2011, 2012b), which makes it extremely difficult to dissolve easily. It is only logical, at least in the case of Bio-Oss® that its dissolution would be quite low and slow, hence rather than its SBF media experiencing a high Ca<sup>2+</sup> release during its studies, it instead has a net decrease, meaning that we have a situation where precipitation rather than dissolution is occurring. Also, although nHAp had an initial increase, most likely due to increased surface areas to volume ratios of its nanosized particles (≤200nm) which encourages such a rapid dissolution, even in spite of the stability of hydroxyapatite (Fathi, Hanifi and Mortazavi, 2008). The hydrogel samples are not highly crystalline nor are they completely composed of hydroxyapatite as the majority calcium phosphate phase. The inclusion of carbonate during the synthesis, and the supersaturation of the calcium/phosphate precursor encouraged the precipitation of hydroxyapatite phases that are non-stoichiometric. This means that the crystals formed are impure, substituted or deficient hydroxyapatite which are known to be less stable with a solubility of ~0.0094mg/ml (Dorozhkin, 2011, 2012b). There is the possibility of precipitating other calcium phosphate phases like MCPM, DCPD, OCP, TCP which have 18mg/ml, 0.0088mg/ml, 0.0081mg/ml, 0.0025mg/ml respectively (Wang and Nancollas, 2008; Dorozhkin, 2011, 2012b). Any of these phases, as well as amorphous calcium phosphate phase (with estimated solubility of ≥25 mg/ml (Dorozhkin, 2012a)) are easily formed, and their variable solubility would likely contribute to the net increase in the Ca<sup>2+</sup> concentration seen in Figure IX-4.

In addition to the possible calcium phases present, one needs to consider the composite nature of the mineralised hydrogels. They are after all made up of a hydrogel matrix with a deposition of an inorganic calcium phosphate growth. While this cannot account for the increasing net calcium concentration of most of the mineralised hydrogels, it does explain why it would remain closer to the initial SBF calcium ion concentration. The hydrogel would technically not participate as much in the sorption, especially when an equilibrium has been set up. And if it did participate, it should have resulted in a decrease in the calcium ion concentration in the corresponding SBF media of the mineralised sample, as was witnessed in the uptake of calcium during the uptake studies in IX.5.1.1. But as SBF is more isotonic than deionised water (with the dissolved CaCl<sub>2</sub>), instead of an uptake, a release would be the likely outcome in such an ionically balanced solution (SBF).

### IX.5.2.2 Phosphate ion monitoring

In (Figure IX-5), one can see the changes in the concentration of phosphate ion through 100h monitoring period. Notably, the trend is a lot more difficult to pick up compared to  $\text{Ca}^{2+}$ . In this case, it will be easier to take the reading at 36h and at 72h. At these periods, more SBF was added to replenish the amount of SBF left to maintain the solid- liquid ration. There seems to generally be a reduction in the amount of phosphate ion that is released into the SBF media, Bio-Oss® within the first 36 h experiencing the most erratic release pattern. It does end up with 18ppm detected; AL HA ends up with 8ppm. The other two samples TA HA and PVA HA sport negative values, perhaps due to the unsuitability of the phosphate detection method to measure below a certain threshold. The mineralised hydrogels might have taken up the majority of the phosphate ions in their SBF media.

All the samples were again replenished after the 36h period. This explains the notable increase in the phosphate ion concentration being picked up. It decreases again across all of the samples, with the lowest amount encountered at 72h. Here Bio-Oss® has a detectable amount of 16ppm (close to its reading at 36h), PVA HA at 38ppm, TA HA at 13ppm and AL HA having a negative reading. After this reading, the SBF amount was replenished.

The final reading at 100h shows a net reduction in the number of phosphate ion in the SBF media, relative to the starting concentration. TA HA at 33ppm, Bio-Oss® at 29ppm, AL HA 17ppm and finally PVA HA at 11ppm. There seems to be a general drop in the concentration of phosphate ion present in the SBF, which all points to the possibility that the drop could be due to the phosphate ions being taken up by the commercially-purchased sample and the mineralised hydrogels.

This trend (Figure IX-5) suggests that the mineralised hydrogels are indeed bioactive, with a possibility that deposition of phosphate ion onto the scaffold is preferred over dissolution.

The results of bioactivity so far have been conflicting. On one hand, there appears to be what might be a net uptake of phosphate ions by the mineralised substrate. This runs in the opposite direction to what is occurring in the  $\text{Ca}^{2+}$  bioactivity where  $\text{Ca}^{2+}$  is being released into the SBF than is taken up. It is not entirely clear why such readings are so contradictory. Usually, if dissolution was the main process, then there should be an increase in the ion concentration of both elements into the solution, and if it is deposition, then the opposite should occur. It is possible that this contradictory behaviour might be because the phosphate ion, in the form of phosphate, is quickly being scavenged by something else. Indeed Vasilescu *et al.* (2011) and (Fathi, Hanifi and Mortazavi (2008) instead of using UV -vis as a detected method, utilised plasma optical emission spectroscopy and atomic absorption spectroscopy which are able to avoid the problem of the interested ions being unavailable to the detection probe molecule.

As the results for  $\text{Ca}^{2+}$  and phosphate ion concentration are not exactly conclusive, when considered together, other tests might need to be done such as gravimetry, pH analysis, FTIR and XRD.

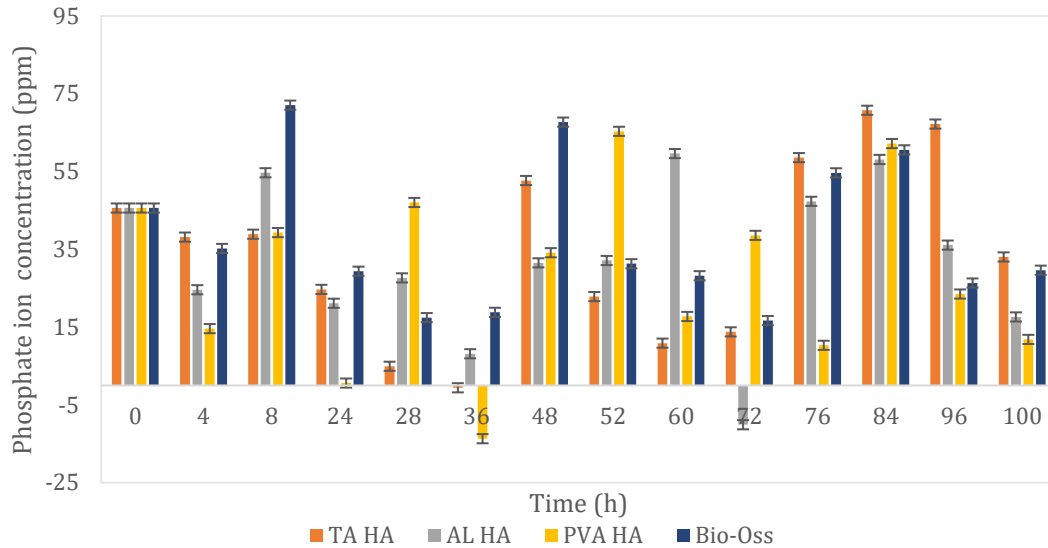


Figure IX-5: Bioactivity evaluation of the mineralised hydrogels (HA) following the changing concentration of phosphate ion in the immersion the test media [Dose: 3mg of mineralised hydrogel in 5ml of SBF (pH 7.4) at 37°C].

As the phosphate test reagent was supplied (by Hanna Instruments) in powder that had to be dissolved to produce a colour, retrieving the powder fully from the sachet and ensuring uniform dissolution was difficult.

### IX.5.3 pH of the sample during the bioactivity studies

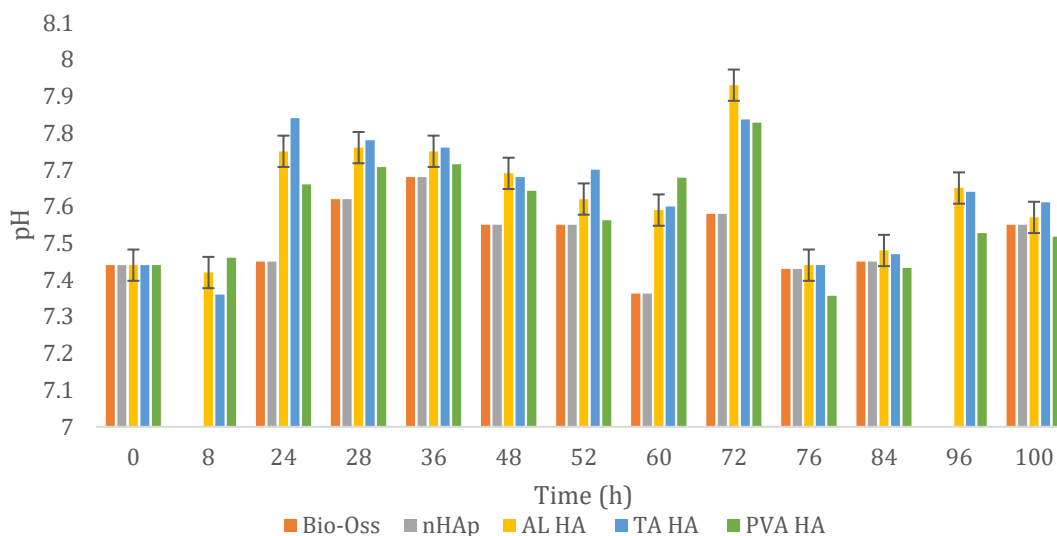


Figure IX-6: Bar chart showing the changes in the pH of the SBF test media across the 100h period

The pH of the samples fluctuate in the range of 7.3-7.9 (Figure IX-6). Starting at a pH of 7.4, from 0 h, the pH of the commercially-bought samples remain stable over a 24h period before they experience a jump afterwards to pH 7.6. The lab synthesised samples do not experience this, but they peak quite rapidly at 24h, with TA HA showing the most increase at 7.84, followed by AL HA at 7.75 and finally PVA HA at 7.66. The mineralised hydrogels fall slowly, until another infusion of simulated body fluid was added after the 52h. Meanwhile, the commercial samples, after reaching their zenith at 36h, drop until the 60h (to 7.36). All the samples reach their secondary peak values after 72h (when more SBF was added). At that point, all of the mineralised hydrogels' pH is  $\geq 7.8$ , while the commercial samples only reach pH 7.6. All their values again drop to around pH 7.4 from the 76<sup>th</sup> h to the 84<sup>th</sup> h. Upon which the last infusion of SBF cause a further rise in pH.

Interestingly enough, all of the samples elicit pH values that remain above 7.4, so although the lab synthesised samples appear to have the higher pHs compared to the commercially available samples, the general conclusion is that the pHs of all the samples are higher than the original SBF solution. This means that a dissolution process is not dominant after the initial 8h period. From that point on, the process that seems to be the most favourable, judging from the high pH (especially in the mineralised hydrogels) is the deposition. According to Vasilescu *et al* (2011), the high pH observed in their bioactivity studies on scaffolds - based on different calcium phosphate phases- was down to the deposition of  $\text{Ca}^{2+}$  and phosphate ions which illustrated a bioactive behaviour. The same behaviour is seen in the mineralised and commercial samples as demonstrated by the high pHs. Possibly, the higher pH value in the mineralised samples points to a preference for deposition on the lab synthesised samples, compared to a slightly more mixed character of dissolution and deposition in the commercial samples.

The result here supplements that from phosphate ion monitoring, seeing as more phosphate was lost from the SBF solution. It is however in contrast to the results from  $\text{Ca}^{2+}$ , whose results suggest resorption instead.

#### **IX.5.4 Gravimetric analysis of the samples before and after bioactivity studies**

Weighting the samples appears to give a straightforward result (Table IX-2). For one, in all of the samples considered, there appears to be an increase in weight of the specimens,

The positive value for the mass change indicates that there is an increment in mass after the bioactivity studies in SBF. Although this reinforces the fact that deposition seems to occur, supporting the results of the phosphate ion results which showed uptake IX.5.2.2, it does not necessarily support the results of the calcium ion studies in section IX.5.2.1 which points to resorption. Again, it is possible that whatever is being deposited is actually not calcium based but phosphate based.

**Table IX-2: Values of the mineralised hydrogel samples before and after bioactivity studies after 334h immersion in SBF. \*sample was lost**

Samples	Initial Mass(mg)	Final mass (mg) after 334h	% Mass change
TA HA	3.1	3.7	19.3
PVA HA	3.2	4.1	28.1
nHAp	3.1	*	*
Bio-Oss	3.1	3.9	25.8
AL HA	3.1	3.8	22.5
TATi HA	3.0	3.4	13.3

### IX.5.5 Infrared spectroscopy of the samples before and after bioactivity test

Infrared spectroscopy was carried out on all samples before and after the bioactivity studies to follow any chemical changes. Previous infrared studies on the mineralised hydrogels have shown that the main markers for calcium phosphate, specifically apatitic calcium phosphate, is the presence of bands that are usually ascribed to phosphate groups (VI.5.4 & VI.5.6.4). These occur around  $560\text{cm}^{-1}$ ,  $590\text{cm}^{-1}$ ,  $970\text{cm}^{-1}$ ,  $1016\text{cm}^{-1}$  and  $1087\text{cm}^{-1}$ , that are all clearly visible in Figure IX-7 and Figure IX-8. Even before immersion in SBF, the mineralised hydrogels share similarities with the commercially purchased HA samples. However, the differences in the shape of the phosphate-assigned peaks along with their relative height is a testament to the difference in the symmetry of the apatitic-type crystals that precipitate on and within the hydrogels. After immersion in SBF, all of the samples in Figure IX-7 and Figure IX-8 do not appear to show much difference in these peaks. It is therefore quite difficult to differentiate the normal variation that are standard from scan to scan when using FTIR, versus the actual changes that may have arisen as a result of the sample interactions with SBF for such a significant period of time.

Consider the next prominent groups, which would be the carbonates. The peaks that are assigned to these groups can be found at  $871\text{cm}^{-1}$ ,  $1462\text{cm}^{-1}$  and  $1418\text{cm}^{-1}$ , that are understood to signify carbonate substitution at the B -sites, while  $1512\text{cm}^{-1}$  arises due to substituting into the A sites of phosphates ions within the apatite crystal (Fathi, Hanifi and Mortazavi, 2008). This group is observable in Figure IX-7 and Figure IX-8. It is here that some difference arises between the samples before and after they have been treated with SBF. The pretreated samples appear to have peaks around  $1418\text{-}1502\text{cm}^{-1}$ .

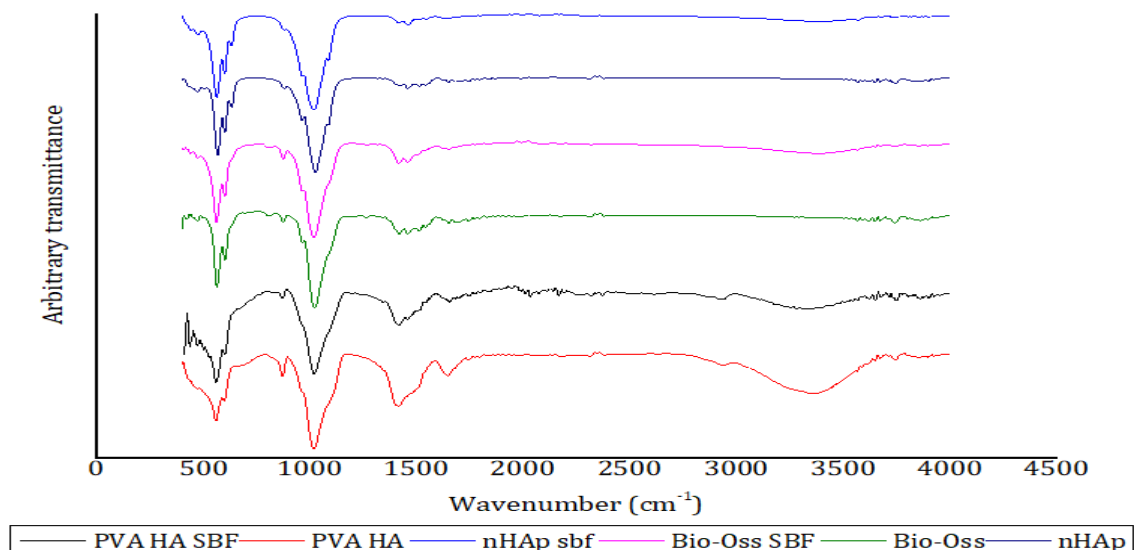


Figure IX-7: Infrared spectroscopy of commercial purchases samples (Bio-Oss® and nHAp) and PVA HA before and after the bioactivity studies in SBF (pH 7.4) at 37°C over 334h.

After treatment, quite a significant reduction occurs in the integrated area of this peak with regards to PVA HA SBF, AL HA SBF and TA HA SBF. (Figure IX-8). This reduction in the IR carbonate region is also visible in Bio-Oss and nHAp, in spite of them having an initially more reduced carbonate region (see Figure IX-7). Just as important is the band at 867cm<sup>-1</sup> that has decreased in size in all the lab synthesised mineralised samples.

This might be the explanation for why the phosphate ion amount in SBF is reducing in IX.5.2.2. Fathi, Hanifi and Mortazavi (2008) as well as Elliott, Holcomb and Young (1985) have stated that 871 cm<sup>-1</sup> can be attributed to a phosphate group. This band (and its overlap with that for carbonate) might be the explanation for the perceived uptake of phosphate into the mineralized hydrogel. If the original synthesis resulted in the production of carbonate substituted apatitic calcium phosphate (as suggested by Figure IX-7 and Figure IX-8) exposure to a reservoir of phosphate (in the form of SBF) would result in the replacement of the carbonate already present in its lattice in place of phosphate. Thus, at the 'A and B' site, there might simply be a swapping of one ion for the other. This would account partly for the increase in the mass of the hydrogel, as the phosphate group (molecular mass of 94.9g/mol) is heavier than carbonate (60.1g/mol).

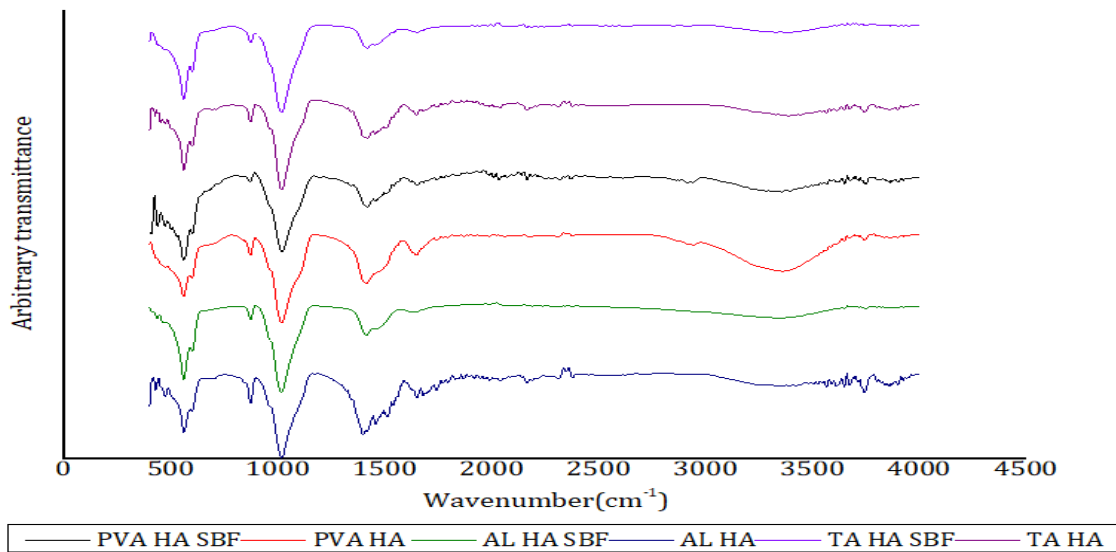


Figure IX-8 Infrared spectroscopy of mineralised hydrogels scaffolds before and after the bioactivity studies in SBF (pH 7.4) at 37°C over 334h.

Besides the phosphate and carbonate groups which are normally present, another signature group of apatitic calcium phosphate is the hydroxyl group, found close to 3200-3500 $\text{cm}^{-1}$  and 634 $\text{cm}^{-1}$ . After immersion in SBF, the peak around the 3200-3500 $\text{cm}^{-1}$  appears to grow more in intensity than the commercially purchased samples, Bio-Oss® and nHAp. It does not grow in the mineralised hydrogel samples. It might just be a case that hydrogels are more responsive to drying than a specimen made of pure calcium phosphate, like Bio-Oss® and nHAp.

#### IX.5.6 X-Ray diffraction of the samples before and after bioactivity studies

Infrared observation in the previous section appears to conclude that an apatitic phase is still present within the mineralised-hydrogel fractions that have been tested. Suggesting that the apatitic phase is undergoing some form of transition which is heralded by the possible swapping out of the carbonate phase for phosphate phases. Thus, it possibly transforms the apatite phase present to something closer to a more stoichiometric hydroxyapatite; it is just as likely that a different phase is mineralising as well. With these changes occurring, the initial crystal symmetry of the apatitic calcium phosphate formed would undergo changes that can be evaluated using diffractometry. Hence, this section will attempt to look at the possible changes in crystalline phase formed. Will the deposition process that has been suggested through the gravimetric analysis and phosphate ion colorimetry be reflected with XRD patterns?

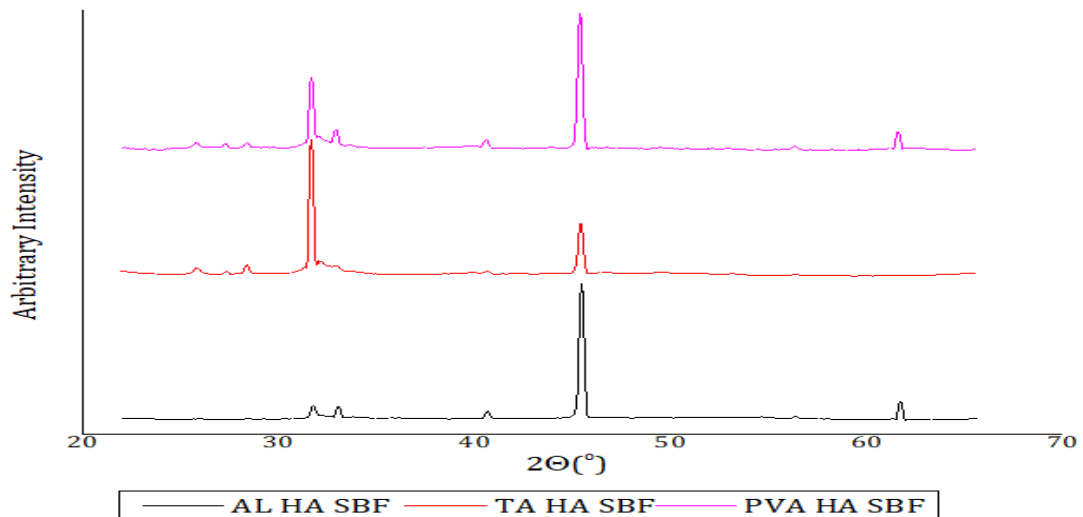


Figure IX-9: XRD patterns of the hydrogel samples after their bioactivity evaluation in SBF (pH 7.4) after 334h

The XRD patterns displayed in Figure IX-9 appear to show several peaks that are common in all of the samples. These peaks can be seen at  $2\theta$   $37^\circ$ ,  $31^\circ$ ,  $45^\circ$  and  $56^\circ$  (Fontana, Schefer and Pettit, 2011). These are characteristic of NaCl. It is reasonable that this forms as the SBF fluid used for the evaluation of bioactivity contains sources of sodium ion and chloride ions. The prominence of the NaCl peaks gives the first impression that this phase is the only phase present, but a closer inspection and comparison with the samples that have not undergone this evaluation (Figure IX-10) shows that this is misleading.

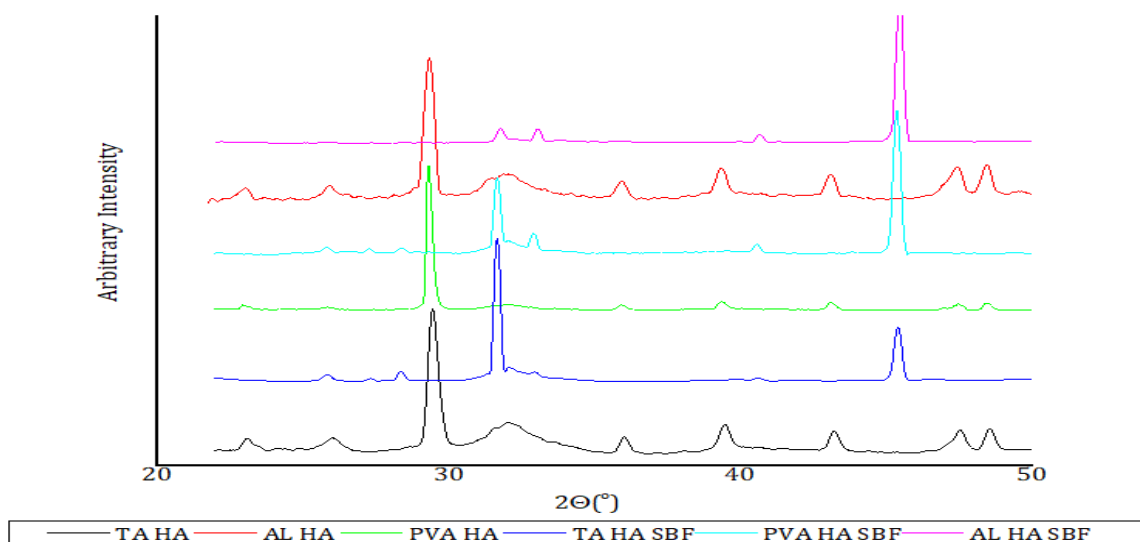


Figure IX-10: XRD patterns of the mineralised hydrogel scaffolds before and after their bioactivity evaluation in SBF (pH7.4) after 334h.



In Figure IX-10, a comparison of the before and after diffraction pattern helps show us that there are several peaks which overlap between the before and after samples. The peak in question occurs at  $2\theta$   $25^\circ$ ,  $28^\circ$ ,  $32.9^\circ$ ,  $53^\circ$ , which correspond to hkl indices (002), (220), (300) and (004) (Elliott, Mackie and Young, 1973). In addition to these, the indices at (112) and (211) occur around  $30$ - $31^\circ$  similar to the same  $2\theta$  angle ( $31^\circ$ ) of salt. The aforementioned peaks have been catalogued from monoclinic hydroxyapatite by Elliott, Mackie and Young (1973). While it is possible to confirm the presence of apatitic calcium phosphate, the overshadowing presence of NaCl makes it difficult to discern the presence of any other phases.

### IX.5.7 Electron microscopy of the samples before and after bioactivity studies

Following on from the gravimetric, colourimetric and infrared studies, electron microscopy was utilised to follow the bioactivity and specifically the morphologies of the following: Bio-Oss®, PVA HA, AL HA, TA HA, and TATi HA. This was to observe the changes in the sample surface as a result of SBF immersion.

For Bio-Oss® without immersion in SBF (Figure IX-11a) SEM shows the untreated surface has a unique fibril like morphology. There appear to be several strands that are bunched together, running in parallel. In certain places, when they run into other similar parallel strands, they twist into a sort of braid before continuing on to transverse the surface of the samples. In addition to these organised strands, there are larger particulate pieces that are scattered over the surface, which are most likely not compositionally different. They might have simply broken off from the strands.

After the bioactivity studies Figure IX-11b, SEM revealed the formerly textured surface has now been covered with a much smoother outer coating. It is possible that this smooth coating is a new layer which has arisen from the deposition of calcium phosphate onto its surface.

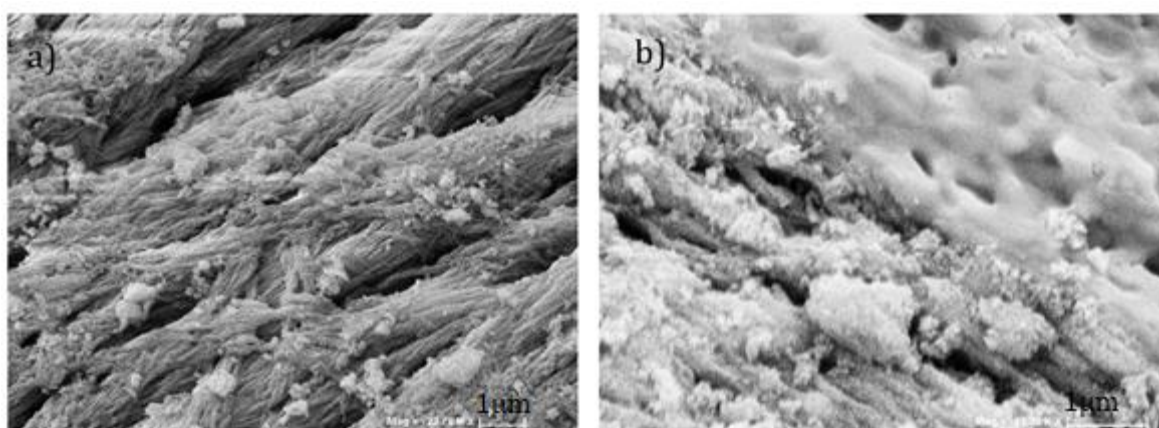
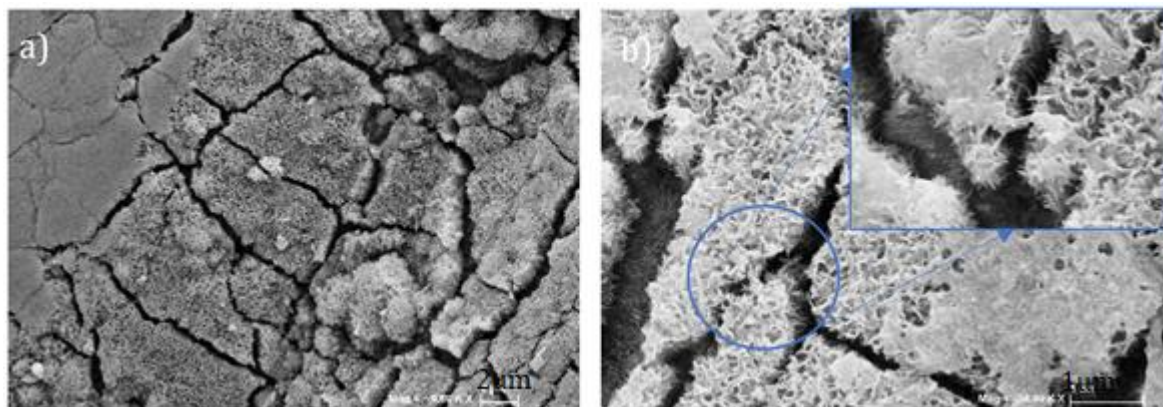


Figure IX-11: SEM micrographs of Bio-Oss® before a); and after bioactivity evaluation test b).

EDX analysis of this sample before and after the bioactivity series reveals that there is a drop in the Ca/P ratio after the SBF immersion. Before the treatment, the average Ca/P ratio obtained after spot analysis at random areas in the samples returned a value of  $\sim 1.56$ , which is a ratio that is consistent with that of a calcium deficient hydroxyapatite (Dorozhkin, 2011). After SBF, the ratio tumbles lower to about 1.18; this value is reminiscent of amorphous calcium phosphate (Dorozhkin, 2011), which may be considered a precursor phase that is capable of transforming to any one of the possible crystalline phases present, given time and the necessary thermodynamic drive. Using these results as a model, it seems that phase formed is most likely amorphous.

Figure IX-12a & b shows the surface morphology of PVA HA after SBF treatment. Besides the difference in the original morphologies from Bio-Oss<sup>®</sup>, there seems to be certain areas that have a smooth covering over the distinct interlocking plates. It appears that the possible route for growth is through a deposition of this thin layer of calcium phosphate as shown in the circle in (Figure IX-12b). The spikey protrusion seen inset of Figure IX-12b is another manifestation of the possible precipitation that is occurring on the sample.



**Figure IX-12: SEM micrographs of PVA HA scaffolds after the bioactivity evaluation test (a & b).**

The EDX analysis of this section produces a Ca/P value that do not stray far from those that have been estimated pre SBF treatment. The Ca/P ratio is between 1.20-1.23.

The surface of AL HA (see Figure IX-13) appears to be somewhat different from those illustrated in Figure IX-12. This sample is characterised by the presence of tiny bunches of apatitic type crystal nuclei that are scattered over the surface of the mineralised substrate. They appear to be made of the same material that blankets on which they sit. As the mineralised hydrogel samples are known to display this sort of growth, even before SBF treatment, it is not entirely certain if the SBF process is the cause of the apatitic crystals nuclei or if these are just features that have remained stable through the bioactivity process. Again, one can see the smoother surface

(indicated within the blue circle in Figure IX-13b). Like the two other samples that have been previously examined, this seems to be the only indicator of the samples undergoing morphological changes triggered by their immersion in SBF.

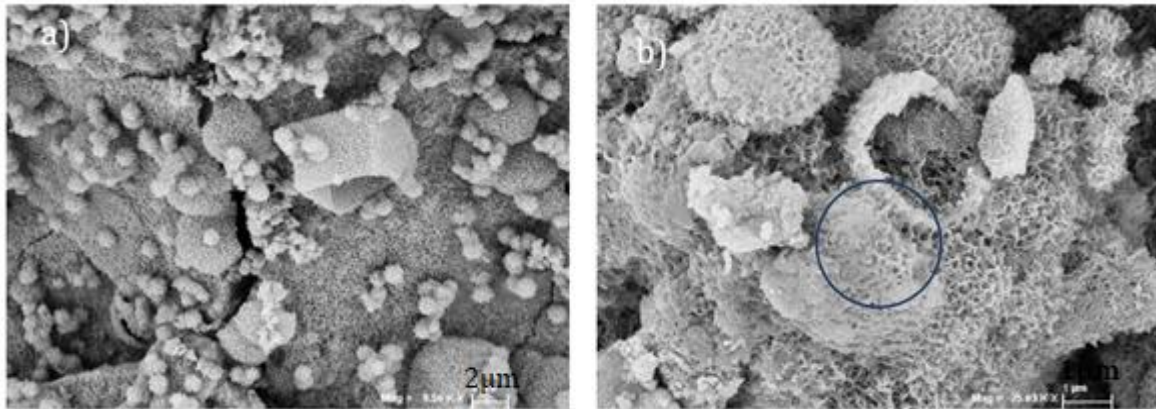


**Figure IX-13: SEM micrographs of AL HA after the bioactivity evaluation (a & b).**

It is conceivable that (just like the other samples) this phase that is mineralising on the surface is not strictly hydroxyapatite but could be a combination of calcium phosphate and together with the many ionic nuclei that might deposit on the surface. This might be why the average Ca/P ratio of this sample was lower (at 1.45).

The TA HA sample, just like AL HA and PVA HA, appears mostly undisturbed (Figure IX-14). The same presence of the smooth surface that could most likely be due to the mineral deposition accelerated through bioactivity is here, although not as prominent as the others. In Figure IX-14b two different coloured circles have been highlighted to indicate one texture that is most likely characteristic of the mineralisation caused by the SBF treatment (seen within the blue circle). In the red circle on the other hand, one can see a section that is much smoother and is probably a stretched-out part of the hydrogel appearing almost translucent as well.

EDX analysis estimated that the Ca/P ratio across the sample averaged at around 1.20-1.81. No doubt the wide range of Ca/P ratio is likely due to the ease of precipitation of a number of calcium phosphate phases at the slightly elevated temperature.

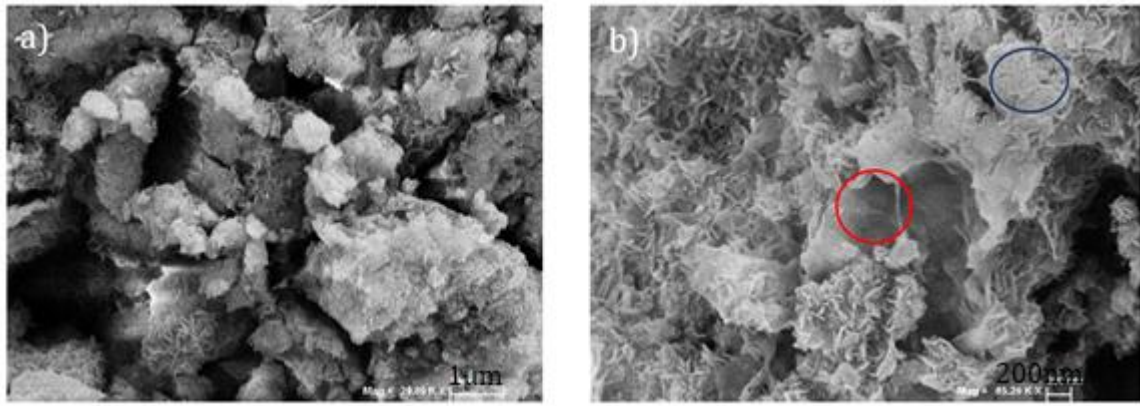


Figure IX-14: SEM micrographs of TA HA after the bioactivity evaluation test (a & b).

TATi HA appears to have the most intact surface. There are portions which seems to have a cohesive coating of the apatitic crystal, and then next to that there is again to the ubiquitous coating that is characteristic of SBF induced deposition on the surface; this is highlighted by the blue circle seen in Figure IX-15b which was then magnified (see inset of Figure IX-15b).

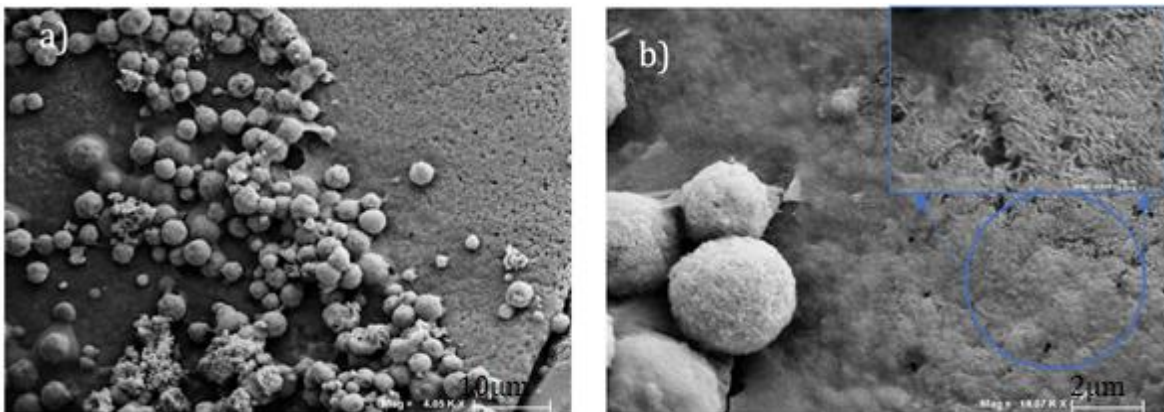


Figure IX-15: SEM micrographs of TATi HA after the bioactivity evaluation test (a & b).

EDX reading across TATi HA showed that its Ca/P ratio is about 1.19.

Although sporting different morphologies, it is clear that all of the samples investigated so far show the prevalence of non-apatitic calcium phase Ca/P ratios after their SBF treatment. This treatment process led to the formation of phases that are closer to ACP, rather than pure hydroxyapatite.

## IX.6 Degradation studies

Degradation studies were used to monitor the stability of mineralised hydrogel samples within PBS at 37°C over a period of about 30 days. In Figure IX-16 one needs to first consider the upper

scale of the y-axis ( $\text{Ca}^{2+}$  concentration). The limit seen is 15ppm; this indicates that the amount of calcium ion that is actually released over the duration of the monitoring period is quite low. Most of the samples, except for TATi HA on the 18<sup>th</sup> day, do not appear to release more than 5ppm of calcium ion into the PBS solution. This slow dissolution of the mineralised HA, as well as Bio-Oss<sup>®</sup> shows how similar their dissolution properties are, making them suitable for instances where they would be used within a similar in-vitro environments.

It is worth noting that the prevalence of the negative values, especially ongoing from midway through the experimental window, is merely to do with errors generated from the sparse concentration of calcium ion that is being released. This methodology, using the o-cresolphthalein complexone calcium detection method appears to be less efficient once the ppm drops to below the 20ppm mark (Hokazono *et al.*, 2009).

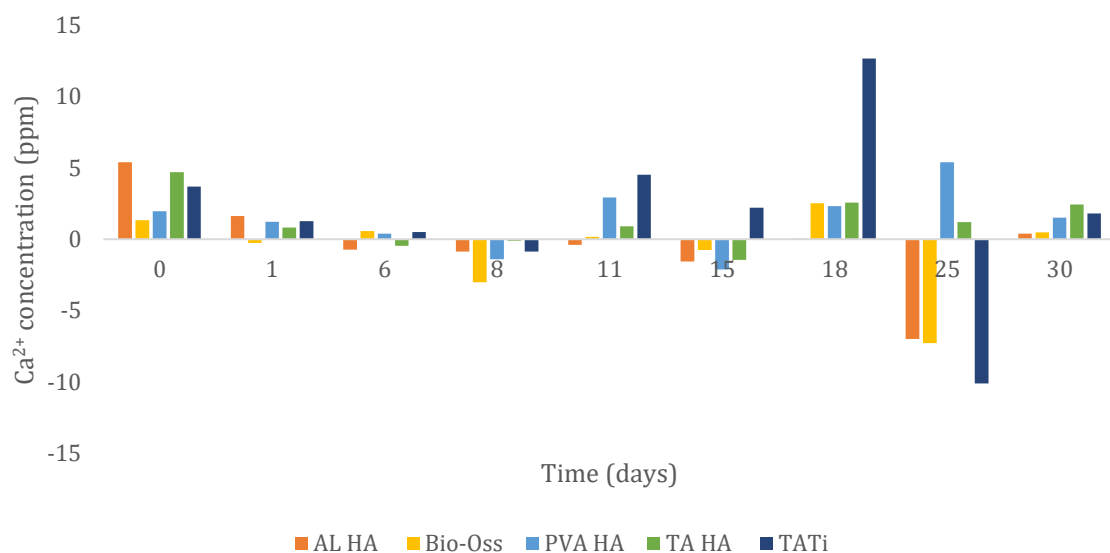


**Figure IX-16: Degradation studies of the mineralised hydrogel scaffolds and Bio-Oss<sup>®</sup> over a 30-day period. [Dose: 3mg of mineralised hydrogel in 3ml of PBS (pH 7.4) at 37°C].**

## IX.7 Summary

From the uptake studies, the dissolution tests and finally the bioactivity assessment of the hydrogel samples (mineralised and otherwise) compared to the commercially available samples, it is clear to see that the hydrogel-based systems are quite dynamic and responsive.

- Uptake of calcium and phosphate ions

Following the uptake studies of  $\text{Ca}^{2+}$  and phosphate ions on the neat hydrogel samples, it was revealed that the hydrogel samples are not inert and are able to sorb these ions onto their surface and into their interiors. In the case of  $\text{Ca}^{2+}$ , the results show that they are able to take up just over 20ppm of  $\text{Ca}^{2+}$  into their systems (after 28 h); TA showing the best results. Short term, < 1h, they

are able to take up just under 8ppm. Carbonating the samples first did not seem to cause any significant improvement, or otherwise, in the ability of the hydrogels to adsorb the ions onto their system; AL Ca looks to have benefited the most here. This proves, that whether  $\text{CaCl}_2$  is added first or  $\text{Na}_2\text{CO}_3$ , the number of  $\text{Ca}^{2+}$  that is sorbed into the system is not remarkably affected. In terms of phosphate ion, uptake stagnates around 5ppm. The overall amount of uptake by the samples fluctuates until they eventually stabilises at 32h. Either way none of them sorb more than that.

It is their ability to sorb these ions that have facilitated the mineralisation of apatitic calcium phosphate into the hydrogel matrix, especially when using an alternating cycle process (detailed in the experimental methodology section) to build up the amount of precipitated mineral.

- Bioactivity studies

Testing the bioactivity of the mineralised material gave interesting results. While the amount of  $\text{Ca}^{2+}$  released into the SBF media increased for all of the samples (IX.5.2.1), the same could not be said for the amount of phosphate ion, which decreased instead (IX.5.2.2). This is quite conflicting especially if one observes that the commercial sample decreased on both fronts. As earlier mentioned, a reduction/uptake in the number of ions would point to a deposition/mineralisation process, while a release of the ions into the test media means the opposite. Additionally, to the phosphate ion result, the gravimetric results also point to the addition of mass, as all of the samples experienced a net mass increase of more than 10% in all cases (IX.5.4), where PVA HA showed the highest increase in mass afterwards. The pH also suggest a bioactive process where precipitation rather than dissolution is the order of the day. Only FTIR and XRD give results that are inconclusive, with FTIR merely confirming that an exchange in the carbonate/phosphate site is occurring, with phosphate seemingly replacing the carbonates as suggested by the reduction in transmittance of the bands (around  $1418\text{-}1502\text{cm}^{-1}$ ) that are common for carbonates, at the 'A' and 'B' sites within an apatite crystal (IX.5.5). Then there is the examination of the diffraction patterns of the samples, before and after they had undergone the SBF test. Other than the added presence of NaCl which was detected in great abundance in all of the spectra, there does not seem to be any suggestion of whether deposition is occurring or not.

Taking into account the outcomes of all the add-on characterisation, besides the initial colourimetric ion monitoring, it might appear that the mineralised hydrogels are not only bioactive but appear to favour the depositional side of biomineralization rather than resorption. Of whether more apatitic crystals are formed as the precipitate, it is not clear. However, going back to the  $\text{Ca}^{2+}$  monitoring test, which is the only test to give a blatant contrary resolution to the deposition process, several aspects were touched upon: the crystalline properties (including the

phases of calcium phosphate present and their inherent solubility), the overall crystallinity of the phases and the possibility that the apatite present might be substituted/calcium deficient. In addition, there is the composite nature of the samples. All of these provide some probable reason for why this release could occur. One possibility that could have resulted in this release is the fact that some of the calcium present might not have strictly been bound in the calcium phosphate lattice, whether as an apatite or otherwise. Maybe, during the initial mineralisation of the hydrogel, some of the  $\text{Ca}^{2+}$  went into the hydrogel matrix and actively crosslinked it. Bonapasta *et al.* (2002) (VI.3). It is also able to form interchain connections by linking two PVA chains using available O atoms. With this in mind, it is plausible that in the progression of the bioactivity test, that degradation of the hydrogel (in spite of the crosslinks (chemically or ionically linked)) would contribute to the increase in the  $\text{Ca}^{2+}$  colourimetric signal. The same can be said for the other hydrogel blends containing alginate, which itself crosslinks via divalent metal ions. It is also possible, that the release of the  $\text{Ca}^{2+}$  is actually an exchange process with any other ion that could easily fulfil the bonding property. Thus, the higher number of  $\text{Ca}^{2+}$  reported in section IX.5.2.1 might not actually signify a release of the  $\text{Ca}^{2+}$  from the calcium phosphate phase, rather the hydrogel matrix. Furthermore, this misleading release could very easily distract one from a deposition process that could be occurring. This reasoning easily falls in line with the evidence for deposition that was discussed in the above-mentioned paragraph. Another possibility could be a substitution of  $\text{Ca}^{2+}$  for  $\text{Na}^+$  and  $\text{Mg}^{2+}$  (both of which have been known to occur in the apatite lattice (discussed in sections VII.5.1.2 and I.1.8)). It might also explain why the calcium phosphate phase had a fairly low Ca/P ratio, since the presence of these cations have been known to stabilise ACP phase for longer. Indeed, their ionic radii ( $\text{Mg}^{2+}$ : 89pm and  $\text{Na}^+$ : 139pm) allows an easier replacement of  $\text{Ca}^{2+}$  (134pm) (Lide and Haynes, 2010; Eliaz *et al.*, 2017).

Assuming that deposition is occurring all of the samples, it is expected that the deposition would be due to the precipitation of calcium phosphate phase. Indeed, SEM characterisation, along with EDX seemed to point to the fact that the newly-formed coating was primarily made of calcium and phosphate. This is in addition to the other apatite-looking structures, like the interconnected clusters some forming into tightly packed spheres, but mostly as blankets that covered the surface of the hydrogels. The fact that the ratios calculated fell lower than the ratio common to hydroxyapatite showed that the new coating was more than likely made of carbonated hydroxyapatite, or even calcium deficient hydroxyapatite. As has been mentioned, these calcium phases have a lower ratio than hydroxyapatite. Other phases that could easily lower the Ca/P ratio that were estimated are OCP and DCPD. Both of these samples are well known to precipitate fairly quickly in aqueous solution (Wang *et al.*, 2005). Viewing the act of precipitation as something that is either thermodynamically favoured or kinetically favoured, Wang *et al.* (2005) calculated that in terms of the driving force (Gibbs free energy), which is dependent on the

supersaturation, the most likely phases to be precipitated from SBF—regardless of the compositional variation—was hydroxyapatite, followed by OCP. This is especially so when the pH is 6.3. And above the aforementioned pH, carbonated hydroxyapatite was calculated with lower  $\Delta G$  values, making it more thermodynamically feasible to precipitate than hydroxyapatite. CDHA however had a  $\Delta G$  value similar to OCP (Wang *et al.*, 2005).

Other than thermodynamics, kinetics also plays an important role in determining which phase nucleates first. It is affected by  $\Delta G$  and more importantly by the kinetic factor ( $K$ ).

$$K = K'P \quad \text{Equation 44}$$

where  $K'$  is a constant and  $P$  is the probability that “the appropriate ion units of Ca-P will meet” (Wang *et al.*, 2005). The kinetic factor  $K$  is majorly affected by the probability the ions in solution would meet to form a calcium phosphate association. OCP was shown to have the highest nucleation rate, followed by HA. CDHA and carbonated apatite are better than hydroxyapatite (Wang *et al.*, 2005).

It appears that in terms of thermodynamics and kinetics, OCP would be the most likely calcium phosphate phase to form, with an almost equal probability of HA, CDHA and carbonate hydroxyapatite also forming. It is no wonder that the recorded calcium phosphate had Ca/P ratios of 1.2-1.5. Any number of these phases formation might be just as feasible. Interestingly enough, the XRD pattern for the samples after SBF treatment could just as easily belong to any of these phases. While all the apatites share almost similar patterns especially the non-stoichiometric apatites, OCP own similarity (to the apatites) is coincidentally due to resemblance arising from the “alternative stacking of apatitic layers” of its lattice (Drouet, 2013). The occupation of ions in its lattice are in very comparable positions, making it difficult to discern from nanosized apatites especially as, all of their XRD patterns overlap strongly. In addition, when you have contaminants like NaCl, with a strong presence in the diffractogram, differentiating all these nanocrystalline phases apart becomes even more difficult.

With all of this evidence, it is clear that deposition is the order of the day. This is not to discount the fact that they cannot act as a reservoir of excess calcium. From the crosslinks break down, the hydrogel has the ability to interact with an ion-rich aqueous medium and change not just its surface morphology but its chemical characteristics as well. The mineralised hydrogel has qualities that makes it similar to the commercially available sample in certain respects, which means that they can be considered, albeit with some modification to function as bioactive tools within the medical world.

## IX.8 Conclusion & future works

Following the aims that had been stated out at the start of this chapter, which were to probe the



bioactivity of the samples created in relation to immersion in a simulated body environment (i.e. SBF and PBS), the following were the outcomes.

- Starting with, the uptake of  $\text{Ca}^{2+}$  and phosphate ions by the neat hydrogels was carried out showing the affinity of the hydrogels to uptake. TA displayed the greatest uptake of  $\text{Ca}^{2+}$ , while AL Ca showed the highest uptake for a sample previously treated with carbonate. As for phosphate uptake, TATi Ca showed the best uptake capacity.
- After an extended immersion in SBF (144h at 37°C), deposition of  $\text{Ca}^{2+}$  and phosphate ions were discovered to be the most likely event to occur in all of the prepared mineralised-hydrogel scaffold material. This is in spite of the hydrogel themselves apparently release some of the adsorbed/absorbed ion into the solution in some of the cases. In any case:
  - o PVA HA seemed to release the least number of  $\text{Ca}^{2+}$ , while AL HA caused the greatest  $\text{Ca}^{2+}$  increase. Again, a likely effect of the hydrogel alone.
  - o Phosphate ions were less conclusive (see IX.5.2.2), due to the unreliability of the test kit causing numerous negative reading, but the end results showed that PVA HA again took up the most phosphate ions. While TA HA was shown to take up the least amount of phosphate ions.

The uptake of both phosphate and calcium ions, which was also confirmed by other complementary analysis (pH, gravimetric reading, XRD, SEM and FTIR) showing apatitic-type depositions along with other bioactive calcium phosphate phases, are indicators of the bioactive properties of the mineralised hydrogel scaffold.

- Immersion in PBS for 30days showed that the mineralised hydrogel scaffolds were quite stable, releasing very little amount of calcium ions that never exceed more than 5ppm, mirroring Bio-Oss®. This stability can be taken advantage of for the purpose of drug loading.

It is clear that the samples investigated indeed have properties that would make them active in a biological context, with properties that are not far off from that of Bio-Oss®, making them suitable for use as possible bone graft alternatives that are stable enough for drug loading.

## Chapter X Sorption kinetics of the mineralised hydrogel scaffolds.

### X.1 Introduction

So far, we have investigated the synthesis of mineralised scaffold, its bioactivity, mechanical and thermal properties. Another property of the mineralised hydrogels is its ability to act as a drug delivery agent. We have talked about the scaffold material as something that could be utilised in vivo as primarily a bone graft material, with other derivative purposes such as an articular cartilage replacement or drug loading. In terms of drug delivery or indeed any purposes that would require the implantation of the scaffold in the body, one important necessity that has only been briefly touched upon is the need for an infection free implantation. Infection could easily cause implant failure, affecting patient recovery time in the process. Thus, if the scaffold material can serve a dual-purpose of halting infection through the release of drugs, then it would be considered an added bonus in the use of a scaffold material. Most importantly, this property can be expanded past the loading and release of infection controlling drugs, to the possibility of introducing other molecules to satisfy various functions from “cell/growth factors” (Dorati *et al.*, 2017), chemotherapy agents (Sharpe *et al.*, 2014), anti-inflammatory drugs (Dorati *et al.*, 2017) and anti-oestrogen drugs (Vallet-Regí, Balas and Arcos, 2007) etc.

### X.2 Aim

With the above in mind, the aim of this chapter will be devoted to studying the possible use of the mineralised scaffold as a potential drug delivery platform. This will be achieved through the monitoring of the its drug uptake behaviour: equilibrium studies, adsorption kinetics and thermodynamics. The behaviour of the hydrogel alone (and after mineralisation) will be ascertained to understand the effects of mineralisation on the mineralised hydrogel scaffold ability to take up various model drug molecules. They include methyl orange, methylene blue and ascorbic acid.

### X.3 Background

To be an effective drug delivery platform, a material needs to be effective in sorbing the molecule in the first place, which should then be followed by a suitable release profile at the target site. Ideally, the material needs to be able to provide some form of protection for the drug in question, until the point in time it is released (Sharpe *et al.*, 2014). The release of the molecule needs to be

controlled, preferably at a slow rate. A high initial burst is likely to cause more harm than good, especially in the case of antibiotic release in an implant site, as this might cause recolonization of the site with bacteria after the antibiotic agent has run out leading to further infection. Similarly, if the drug release is too sluggish, infection at the implant site can also set in (Sun and Tan, 2013). The use of effective drug delivery platforms provides some advantage over traditional parenteral and oral administration of drugs as these tend to require very high doses to kill bacteria. This is so in the treatment of osteomyelitis using oral antibiotic: the high dose of antibiotics used can sometimes lead to “systemic toxicity, renal complication, liver complication” which often requires expensive hospitalisation, caused in parts by the low penetration ability of the drugs used in the first place (Porter, Ruckh and Papat, 2009; Dorati *et al.*, 2017). A drug delivery mechanism that can suitably deliver drugs (whether low molecular weight drugs or large biomolecules) can effectively bypass the problem of toxicity, and low penetration (Sun and Tan, 2013); avoiding the saw tooth release profile of traditional drug administration (Vallet-Regí, Balas and Arcos, 2007).

As we have discussed previously, different materials may be called upon for bone graft purposes. From synthetic polymers (like PLA, PC, PVA, PMMA) to more natural polymers that bear some similarity to extracellular matrix (e.g. alginate, silk, hyaluronic acid, fibrin etc), ceramics (like hydroxyapatite, TCP, bioglass and so on) and composites. These materials have the ability to sorb/release various molecules in their own respect. We know that the use of these materials individually carries various drawbacks (mechanical, adhesive and production of degradative by-products) that would affect the success of the implant. Thus, having a hybrid scaffold, such as the mineralised scaffold prepared here could fulfil the purpose of releasing molecules, in addition to its other function as a bone graft material, which will no doubt decrease the risk of failure of the implant in the in-vivo. These composite systems have the ability to combine the benefits of their individual components (Dorati *et al.*, 2017).

So far, the most popular material used for the treatment of infection is a PMMA cement or beads impregnated with gentamicin, which have been shown to release a sustained level of the antibiotic (Dorati *et al.*, 2017). Unfortunately, because of the high polymerisation temperature requirement for PMMA, most of the antibiotics used have to be high temperature resistant or they would degrade. This limits the antibiotic selection pool to gentamicin, amikacin and streptomycin. Another issue, is the poor degradation of PMMA and the immunological response that it elicits in the body, which means the PMMA often has to be removed surgically (Vallet-Regí, Balas and Arcos, 2007; Dorati *et al.*, 2017).

In this chapter, the author intends to study the sorption ability of the scaffold material when exposed to different probe materials and then gauge how the modifications carried out on the mineralised hydrogel scaffolds will affect their ability to uptake and release these molecules.

## X.4 Methodology

Sample preparation was elaborated in section II.3.

### X.4.1 Analytical instruments and conditions

#### X.4.1.1 UV-vis analysis

The changing concentration of the pH7.4 solution for the following probe molecules:

- MB: MB is a cationic/basic molecule which could be considered the opposite of MO. It has an RMM of 319g/mol and belongs to a class of molecules called azo dyes (and toxic just like MO). A representation of MB is shown in Figure X-1.
- MO: This is an anionic/acidic molecule, with an RMM of 327g/mol. It is also an azo dye. Further information on it may be found in section IV.3.2.1.
- AA: This is a water-soluble molecule. It is a strong antioxidant as it is capable of reducing nitrogen and free oxygen species (Moreira *et al.*, 2014). A representation of the AA molecule is shown in Figure X-1.

These can all be probed with UV-vis.

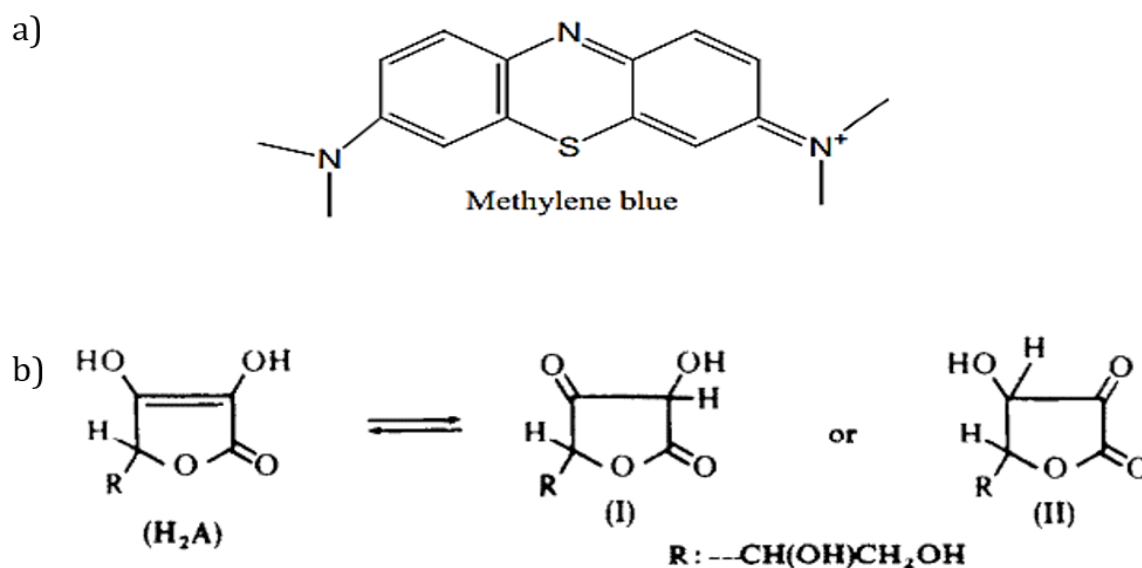


Figure X-1: Molecular formula of methylene blue a); Ascorbic acid and its tautomer's b) (Ogata and Kosugi, 1970; Haque, Jun and Jhung, 2011)

#### X.4.1.2 SEM

The samples were lyophilised and then placed on a double-sided carbon tape on an SEM stub, where they were coated with an Au target for 60s.

### X.4.1.3 Experimental setup

1. Effect of contact time: The experimental procedure involved placing 3mg of the solution of the desired adsorbent in a sample bottle containing 3ml of the desired probe molecule (0.015mM of MB; 0.005mM of MO; 0.014mM of AA) of a specified concentration. Monitoring was carried out at 0, 10, 30, 50, 70, 110, 140 and 200min, by pipetting 0.75ml of the liquid phase into a micro cuvette and then collecting the absorbance reading at the lambda max of the specific probe molecule (660nm for MB, 260nm for AA and 465nm for MO).
2. Effect of concentration: The experimental procedure here followed similar steps as the aforementioned experiment. The only difference was the use of a different starting concentration (0.003mM, 0.008mM and 0.015mM). Only MB was used in this section.
3. Release studies: Here, the previously loaded samples were again measured into a sample bottle and then topped up with 3ml of PBS solution (pH7.4). The samples were placed in a water bath at 37°C and agitated at 70rpm, to replicate physiological conditions. Observation followed the same scheme as detailed in #1. Only MB was used in this section.

### X.4.2 Samples nomenclature

The samples studied here were given the following designation

**Table X-1: Name of the hydrogel samples (before and after mineralisation) after uptake of AA, MO and MB and their accompanying description.**

<b>Samples</b>	<b>Description</b>
AL AA	AA sorbed by AL
AL MO	MO sorbed by AL
AL MB	MB sorbed by AL
PVA AA	AA sorbed by PVA
PVA MO	MO sorbed by PVA
PVA MA	MB sorbed by PVA
TA AA	AA sorbed by TA
TA MO	MO sorbed by TA
TA MB	MB sorbed by TA
TATi AA	AA sorbed by TATi
TATi MO	MO sorbed by TATi
TATi MB	MB sorbed by TATi
Bio-Oss AA	AA sorbed on Bio-Oss®
Bio-Oss MO	MO sorbed by Bio-Oss®
Bio-Oss MB	MB sorbed by Bio-Oss®

Ascorbic Acid	AA
Methylene Blue	MB

## X.5 Results

### X.5.1 Uptake behaviour of MB

#### X.5.1.1 Hydrogels only

PVA only hydrogels are bound to be affected by processing process (such as crosslinking, blending with other polymers or the growth of calcium phosphate and so on), for this reason that the contents of this chapter will attempt to construct a narrative between the neat polymers and those that have been used to grow calcium phosphate within them. It is only by understanding the role of the polymer on its own that one could attempt to predict the behaviour of the calcium phosphate grown within the polymer, without going through any additional separation procedure.

As such, in this section, the sorption behaviour of the prepared hydrogel samples will be considered. The effect of the contact time, the concentration and time on the sorption behaviour of the different polymer types will be elucidated. It is hoped that at the end of this whole endeavour, the adsorption kinetics as well as the thermodynamics will be clarified.

##### X.5.1.1.1 Effect of Contact Time

Figure X-2 shows the effect of contact time on the sorption behaviour of the different permeations of the polymer systems used. In the chart below, the quantity  $q$  is used, this is calculated using the following formula

$$q = \frac{(C_o - C_e) \times V}{W} \quad \text{Equation 45}$$

where  $q$  is the sorbed amount (mg/g);  $C_o$  and  $C_e$  is the concentration of probe molecule solution at the start and at equilibrium (mg/l);  $V$  is the volume of the solution in litre and  $W$  is the weight of the adsorbent (g). One can easily pick out a trend  $q$  increasing with time for MB. This starts off quite rapidly, nearing saturation after the 20min mark, but is not saturated even at 200m. Although the reading is stopped after 200min, the uptake increases in the sequence PVA AL-TATi (1.03mg/g) > PVA AL-TA (1.371mg/g) > PVA-AL (1.499mg/g) > PVA (1.737mg/g).

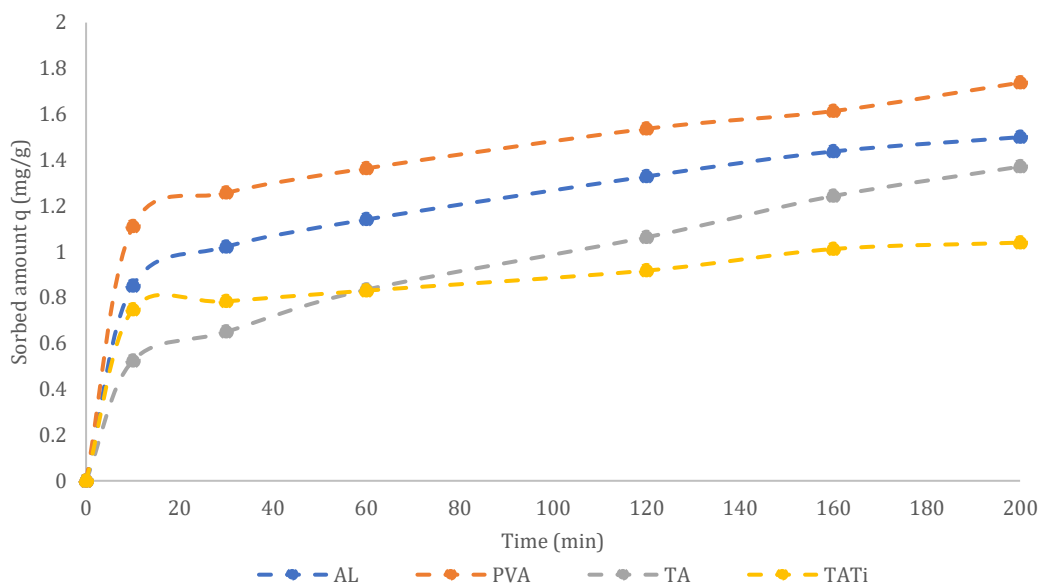


Figure X-2: Effect of contact time on the MB sorption capacity in the different hydrogel samples (pH=7.4, dose= 3mg/ml; temperature=20°C; MB concentration 0.015mM)

#### X.5.1.1.2 Effect of Concentration

The effect of varying concentration on the adsorption capacity of the adsorbent was examined. Figure X-3 contains four separate charts documenting the behaviour of the four different polymers used when exposed to MB of different concentrations.

The trends in all the charts appear to remain consistent. From the lowest concentration (0.003mM) to the highest (0.015mM), the polymer samples appear to uptake MB fairly rapidly at the initial stages (very obvious at the higher concentration), followed by a much slower uptake capability, no doubt likely due to the active sites being mostly occupied. The lowest concentration across both of the samples are again similar, but uptake here seems to increase until the experiment termination, which most likely is due to the higher proportion of adsorption sites compared to adsorbates concentration; thus, saturation never truly occurs.

From the charts (Figure X-3), we can clearly see the uptake mechanism is not uniform across all the samples, but the adsorbed amounts at t=200min is also different.

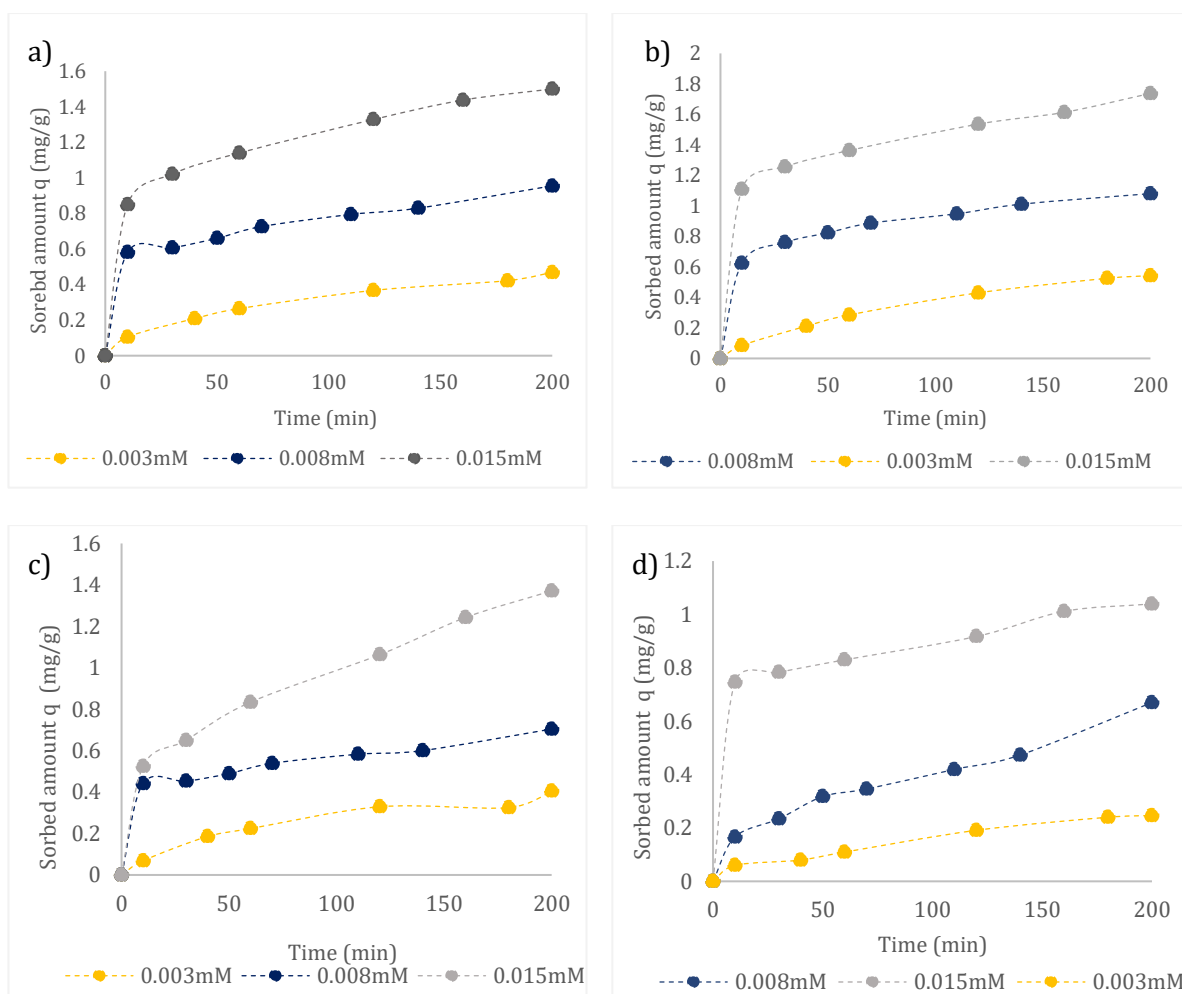


Figure X-3: Effect of the initial concentration of MB against contact time for the different hydrogel samples: AL a); PVA b); TA c); TATi d). (pH=7.4, dose= 3mg/ml; temperature=20°C)

Compare for a moment the amounts taken up at 200mins, Table X-2 shows that at 200min PVA seemingly having the highest  $q$  at the different concentration over all of the polymers, followed by AL, TA and finally TATi.

Table X-2: Sorbed amount  $q$  of the hydrogels across the different concentrations at  $t=200\text{min}$

Samples	0.003mM (mg/g)	0.008mM (mg/g)	0.015mM (mg/g)
AL	0.469	0.955	1.499
PVA	0.543	1.080	1.737
TA	0.404	0.704	1.371
TATi	0.246	0.670	1.039

#### X.5.1.1.3 Adsorption isotherm fitting of the hydrogel samples

Using the experimental data obtained for sorption of MB over different concentrations, it was



then possible to fit the data obtained using the linear form of the Langmuir isotherm (Equation 46) as seen in Figure X-4.

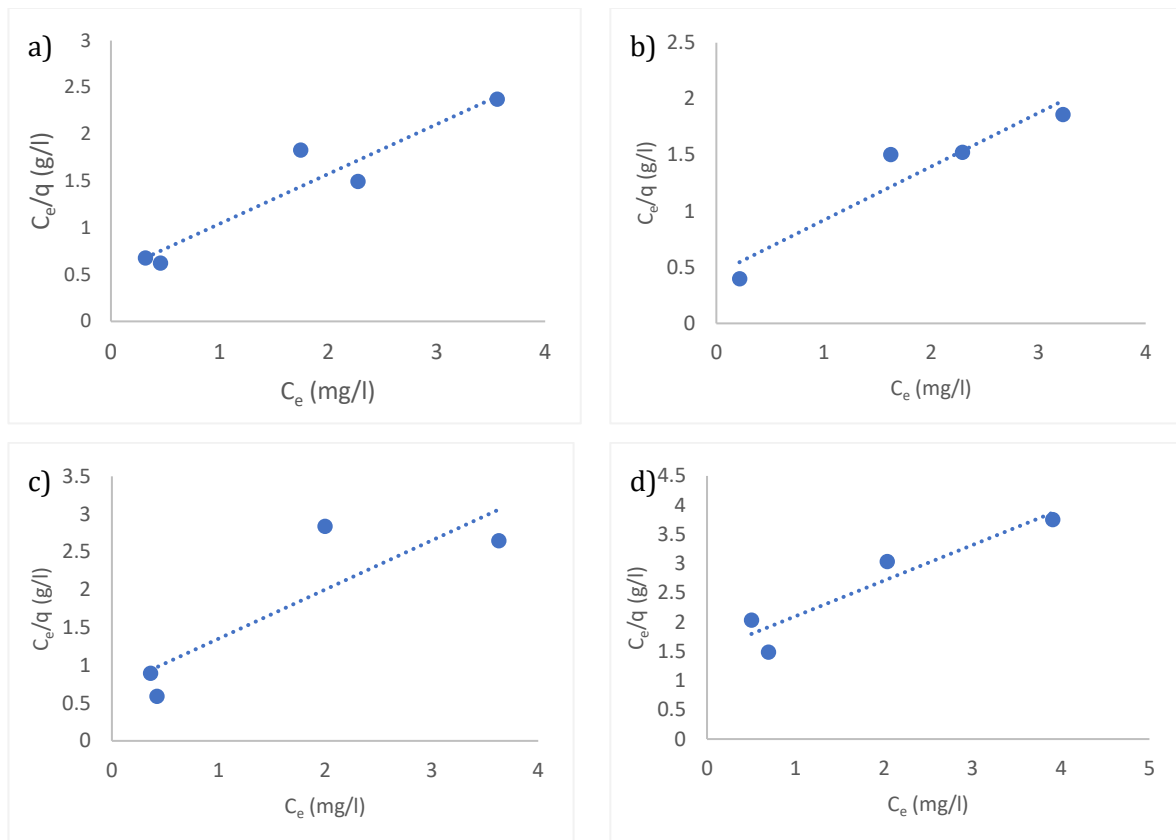


Figure X-4: Linearised Langmuir-isotherm obtained over the different concentrations of MB at room temperature (20°C) for the hydrogels: Al a); PVA b); TA c); TATi d).

From the plots in Figure X-4 it was then possible to deduce the saturation uptake  $q_L$  and the Langmuir constant ( $K_L$ ) (as well as the  $R^2$  values). Sorption data was also analysed using the linear form of the Freundlich's model (Equation 47). Both models have their own limitations, and neither is expected to be obeyed for MB sorption by the hydrogels. Rather, the behaviour of the samples might show attributes common from either or both models.

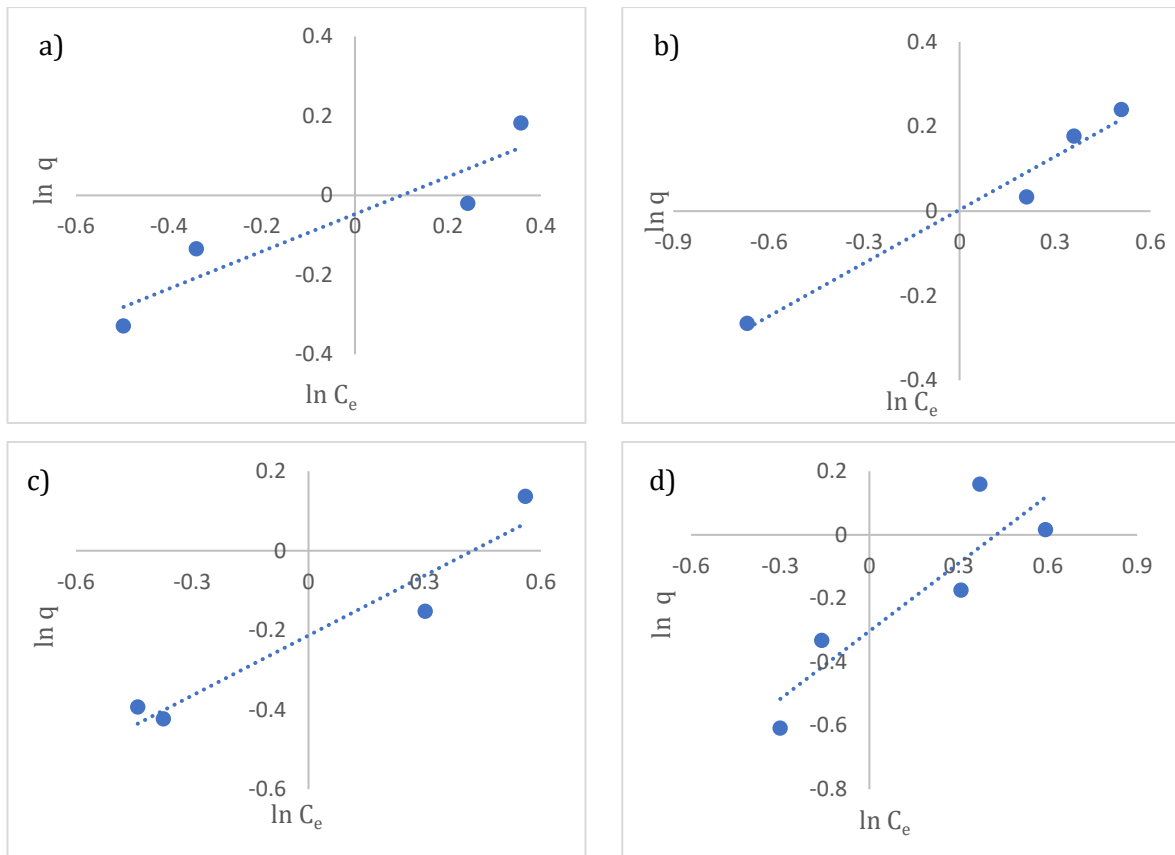


Figure X-5:Freundlich isotherm analysis over the different concentrations of MB at room temperature (20°C) for the hydrogels: Al a); PVA b); TA c); TATi d).

In Table X-3, several parameters have been mentioned,  $q_L$ , and  $K_L$  for Langmuir isotherm model, and  $K_f$  and  $1/n$  for Freundlich model.  $q_L$  is the maximum adsorption capacity (mg/g),  $K_L$  is to do with the rate of adsorption (or the energy of adsorption), which according to Equation 46 are obtained from the intercept and gradient respectively.  $K_f$  is related to the distribution coefficient of the dye on the sorbent surface (or rather the attachment capacity of the adsorbent),  $1/n$  is a measure of the extent of adsorption at the surface (heterogeneity of a surface); they are calculated from the intercept and gradient respectively using Equation 47 (Nasuha, Hameed and Din, 2010; Gong *et al.*, 2013).

$$\frac{C_e}{q} = \frac{1}{q_L K_L} + \left(\frac{1}{q_L}\right) \cdot C_e \quad \text{Equation 46}$$

$$\ln q = \ln K_f + \left(\frac{1}{n}\right) \cdot \ln C_e \quad \text{Equation 47}$$

The  $R^2$  values reflect the data scatter obtained from using both of these isotherms. It is an effective statistical model that gives one a preview of how close or not the values are to an ideal model, in this case the linear form of the adsorption models. As we can see, the  $R^2$  values obtained using either models are fairly comparable and so one cannot use this to discriminate between the two

models. For the Langmuir model,  $q_L$  for the PVA hydrogel (at room temperature) is the highest amongst all the samples, followed by AL, and then TATi and TA. While the  $q_L$  and  $K_f$  are not necessarily equivalent, PVA has the greater Freundlich sorption capacity over the other samples, AL follows PVA as the next efficient sorbing substrate, having the values of the constant in between PVA and the lower efficiency substrates. The last two (TA and TATi) depending on which isotherm model is consulted, take the last position.

**Table X-3: Isotherm parameters obtained for the different hydrogel samples using Langmuir (Figure X-4) and Freundlich models (Figure X-5).**

Sample	Langmuir parameters			Freundlich parameters		
	$q_L \frac{mg}{g}$	$K_L \frac{l}{mg}$	$R^2$	$K_f (\frac{mg}{g}) (\frac{l}{mg})^{-\frac{1}{n}}$	$\frac{1}{n}$	$R^2$
AL	1.88	1.04	0.90	21.27	0.46	0.86
PVA	2.09	1.08	0.90	322.58	0.41	0.97
TA	1.53	0.92	0.74	4.69	0.50	0.92
TATi	1.64	0.40	0.88	3.30	0.71	0.79

Each model has a specific criterion which encompasses the behaviour of the samples that best fit. For examples, the Langmuir model describes the situation for monolayer adsorption (Belhachemi and Addoun, 2011). Langmuir asserts that upon adsorption onto the adsorbent surface in a uniform homogenous manner, the adsorbed molecules remain unreactive with their neighbours. And another limitation, is the fact that the model also proposes that the surfaces of the adsorbent is finite, and thus at a certain point saturation will occur (Belhachemi and Addoun, 2011; Haque, Jun and Jhung, 2011). This is of course the antithesis of the Freundlich model, which supports multilayer heterogeneous adsorption (Belhachemi and Addoun, 2011). For the moment it appears that such analysis is useful to compare different sorbents.

#### X.5.1.1.4 Adsorption kinetics of the hydrogel sample

The sorption kinetics of MB for the samples were investigated using the pseudo-second-order model. It is mathematically expressed as follows:

$$t/q_t = 1/k_2 q^2 + (1/q) t \quad \text{Equation 48}$$

$k_2$  is the pseudo-second-order rate constant which now can be obtained by interpreting Equation 48 as a plot of  $t/q_t$  against time  $t$ . It is equivalent to “slope<sup>2</sup>/intercept” of the straight line obtained

from the plot (see Figure X-6).

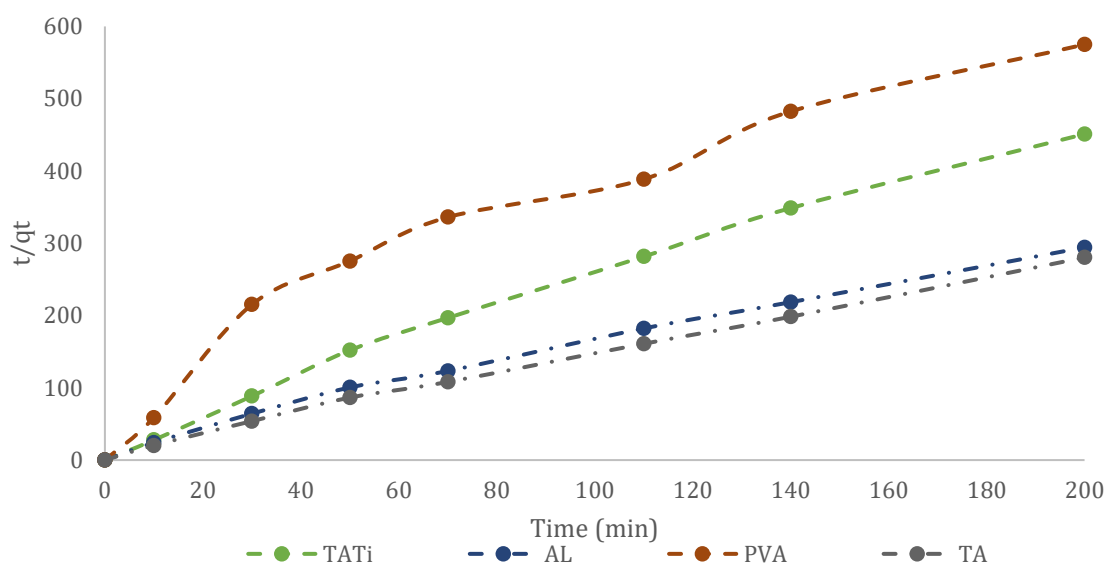


Figure X-6: Pseudo-second-order kinetics for the adsorption of MB on the hydrogel samples at room temperature (20°C).

The relevant parameters ( $k_2$  and  $R^2$ ) were extracted from Figure X-6, and then presented in Table X-4.

Table X-4: Kinetic parameters for the adsorption of MB onto the hydrogel samples at room temperature (20°C).

Samples	$k_2$ (g mg <sup>-1</sup> min <sup>-1</sup> )	$R^2$
AL	0.083	0.9939
PVA	0.051	0.9292
TA	0.13	0.9989
TATi	0.17	0.9939

The  $R^2$  values for the majority if not all of the samples were  $\geq 0.99$ , excluding PVA was most satisfactory. Even at that, the  $R^2$  was slightly better than those of the pseudo-first-order kinetic model. This serves as an indicator that in describing the kinetics of all of the samples prepared, pseudo-second-order kinetic behaviour would be the best descriptor/fit.

### X.5.1.2 Mineralised hydrogels

The previous section was centred on the adsorptive behaviour of the hydrogel only samples, now attention is drawn to the uptake behaviour of the mineralised samples in the presence of MB. As such, the effect of contact time, concentration and temperature will be investigated. At the end of this, the data collected will be used to find the sorption isotherm and kinetics models that best describe the uptake behaviour of the mineralised hydrogels, while collecting the necessary

thermodynamic parameters to further improve the understanding of the mechanism in action behind their behaviour.

#### X.5.1.2.1 Effect of Contact time on the mineralised sample uptake behaviour

With the untreated samples ( Figure X-2) where two main trends were obvious: i.e. a rapid uptake first stage followed by a slower approach to saturation stage where little to no adsorption seems to occur. Now with the mineralises samples, again MB uptake is fast within the first 20mins and then slows (Figure X-7).

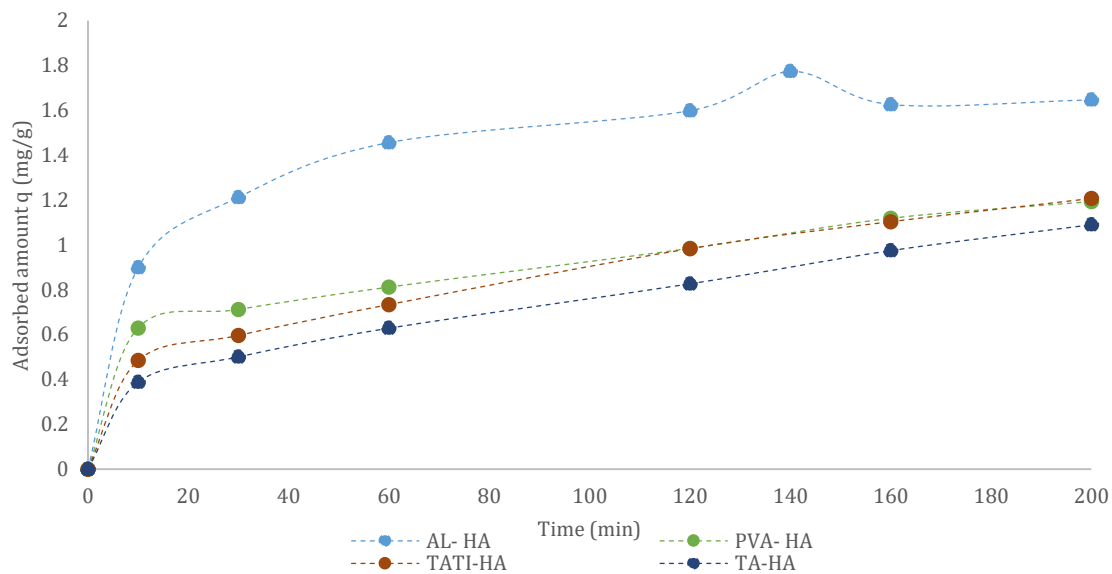


**Figure X-7: Effect of contact time on the adsorption capacity of MB on the different mineralised hydrogel scaffolds (pH=7.4, dose= 3mg/ml; temperature=20°C; MB concentration 0.015mM)**

In addition to the different adsorption character, the system that previously had the better adsorptive capacity of MB has given way to an AL based system: AL-HA; it adsorbed the highest amount at about 1.646mg/g. PVA-HA and TATI-HA are in competition for the second best adsorption capacity, both of which adsorbing 1.193mg/g and 1.206mg/g respectively. TA-HA had the least adsorbing potential in the course of the 200min at 1.089mg/g. One needs to know the uptake by HA to make full assessment.

#### X.5.1.2.2 Effect of Concentration on the uptake behaviour of the mineralised hydrogels

Figure X-7 shows the effect of solution concentration on MB sorption by the mineralised hydrogel. Aside from the initial rapid uptake, none of this samples appear to show a true saturation stage (stagnation never seems to occur).

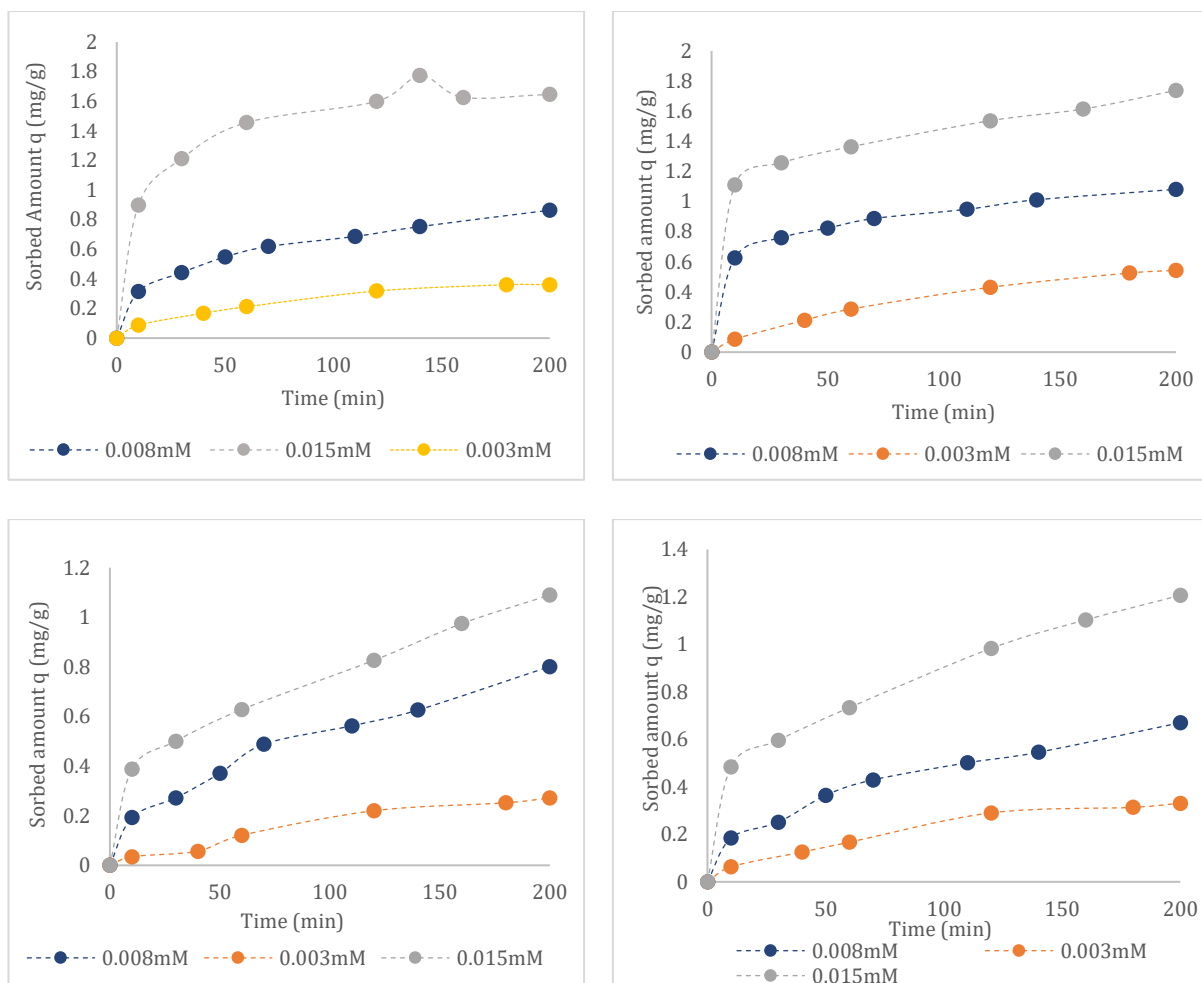


**Figure X-8: Effect of the initial concentration of MB against contact time for the different mineralised hydrogel scaffolds: AL HA a); PVA HA b); TA HA c); TATi HA d). (pH=7.4, dose= 3mg/ml; temperature=20°C)**

The amount of the MB sorbed by the mineralised hydrogels at 200min is shown ( Table X-5). ALHA adsorbs the most amount across all of the concentration, followed by PVA HA and TATi HA and finally TAHA.

**Table X-5: Sorbed amount q of the hydrogels across the different concentration at t=200min, from Figure X-8.**

Samples	0.003mM (mg/g)	0.008mM(mg/g)	0.015mM(mg/g)
AL HA	0.360	0.863	1.646
PVA HA	0.302	0.640	1.193
TA HA	0.271	0.801	1.089
TATi HA	0.331	0.670	1.206

Comparing Table X-2 and Table X-5 again shows that mineralisation causes an increase in the MB uptake by some hydrogels (AL HA > AL), and a decrease in uptake by others (PVA > PVA HA) and intermediate effects in others (TA, TA HA, TATi, and TATi HA). What is important is that mineralisation is not blocking MB uptake.

### X.5.1.2.3 Adsorption isotherm fitting of the mineralised hydrogels

The experimental data obtained for the sorption of MB over different concentrations was fitted using the Langmuir isotherm model for a better understanding of the samples' sorption behaviour (Figure X-9).

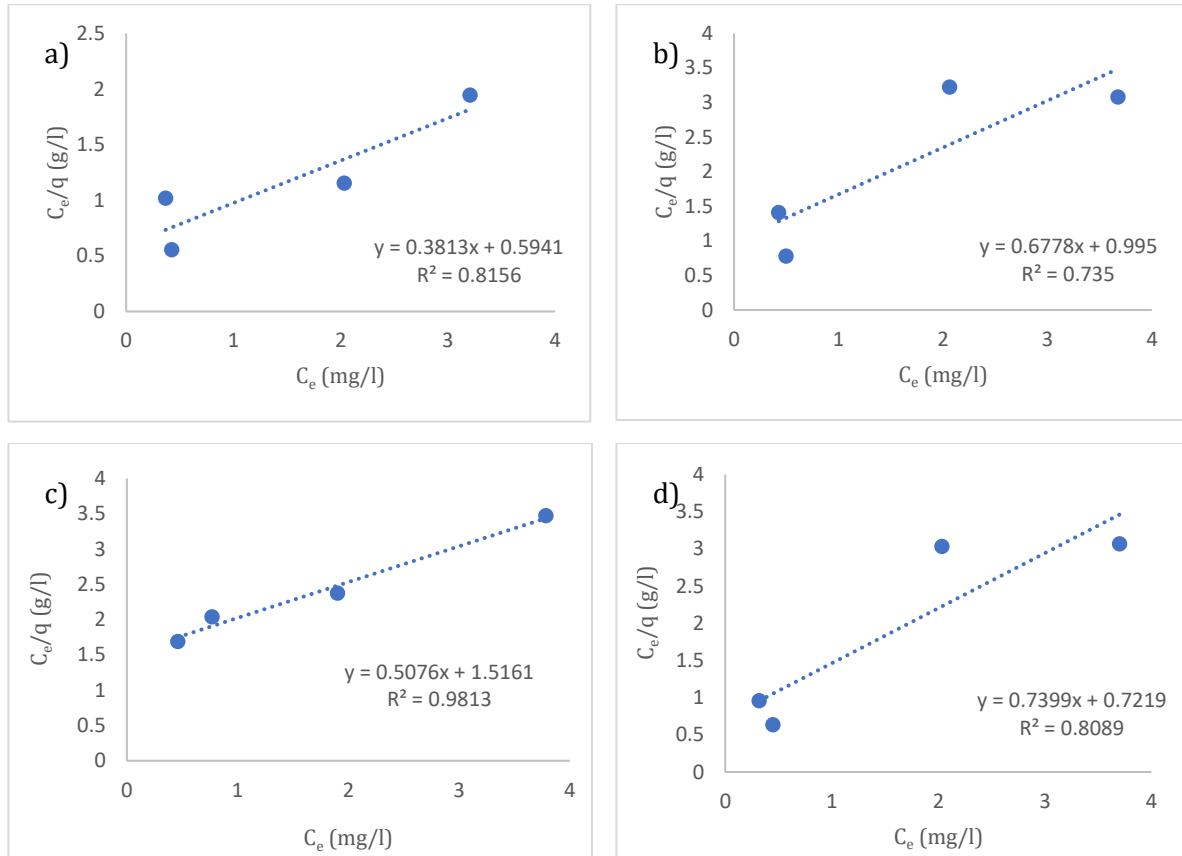


Figure X-9: Langmuir isotherm of the mineralised hydrogel scaffolds obtained over the different concentrations of MB at room temperature (20°C) for Al HA a); PVA HA b); TA HA c); TATi HA d).

Using the plots in Figure X-9, Langmuir constants and their corresponding  $R^2$  values were calculate (see Table X-6). In addition, fitting was carried out using the Freundlich model (Figure X-10 and Table X-6).

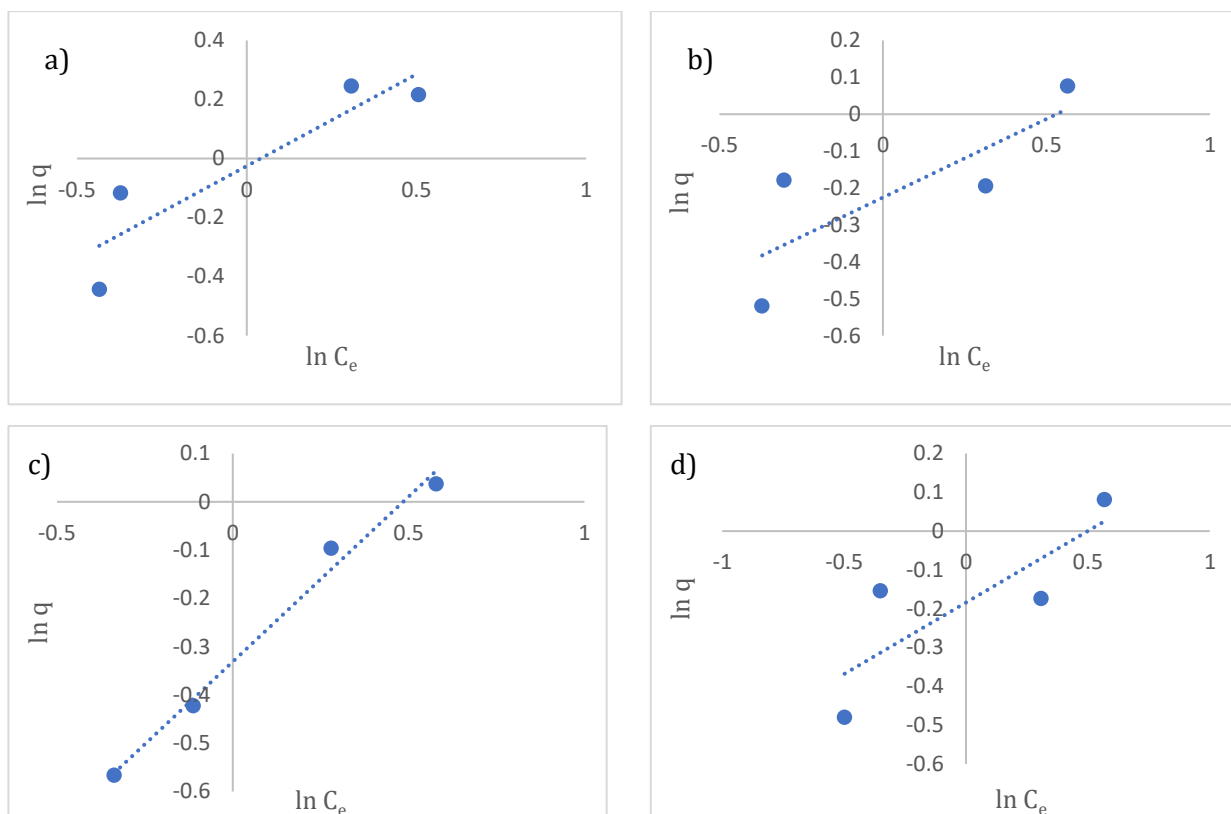


Figure X-10: Freundlich isotherm of the mineralised hydrogel scaffolds obtained over the different concentrations of MB at room temperature (20°C) for : Al HA a); PVA HA b); TA HA c); TATi HA d).

From Table X-6 (and making a comparison to the data in Table X-3) one can say that from  $q_L$  values, MB sorption is not drastically reduced or increased by mineralisation. One can also say that neither Langmuir and Freundlich models are better for analysing MB uptake by mineralisation. Table X-6 contains the parameters derived from Langmuir and Freundlich models, the  $R^2$  values here are collectively lower than those calculated from the hydrogel only samples. This could point to the possibility of another sorbing process occurring in these mineralized samples.

Table X-6: Isotherm parameters obtained for the mineralised samples using Langmuir(Figure X-9) and Freundlich models (Figure X-10).

Sample	Langmuir parameters			Freundlich parameters		
	$q_L \frac{mg}{g}$	$K_L \frac{l}{mg}$	$R^2$	$K_f (\frac{mg}{g}) (\frac{l}{mg})^{-\frac{1}{n}}$	$\frac{1}{n}$	$R^2$
Al HA	1.71	1.29	0.73	10.27	0.49	0.73
PVA HA	1.47	0.68	0.73	4.43	0.42	0.64
TA HA	1.97	0.33	0.98	3.01	0.68	0.98
TATi HA	1.45	0.98	0.75	6.23	0.41	0.70
Bio-Oss	1.03	1.44	0.92	4.54	0.25	0.40



The author suggested MB uptake needed to be measured for HA alone. Table X-6 shows exactly this data. The  $q_L$  data for Bio-Oss is measurable and so in mineralised hydrogels one may be measuring MB uptake by the hydrogel and HA and the interfaces that exists between the two.

#### X.5.1.2.4 Adsorption kinetics of the mineralised hydrogel samples

Like the un-mineralised sample, the kinetics of adsorption was also investigated from the isotherms obtained at room temperature. The pseudo-second-order model shown in Figure X-6 were interpreted.

The relevant parameters from each of the models ( $k_2$  and  $R^2$ ) have been summarised in Table X-7.

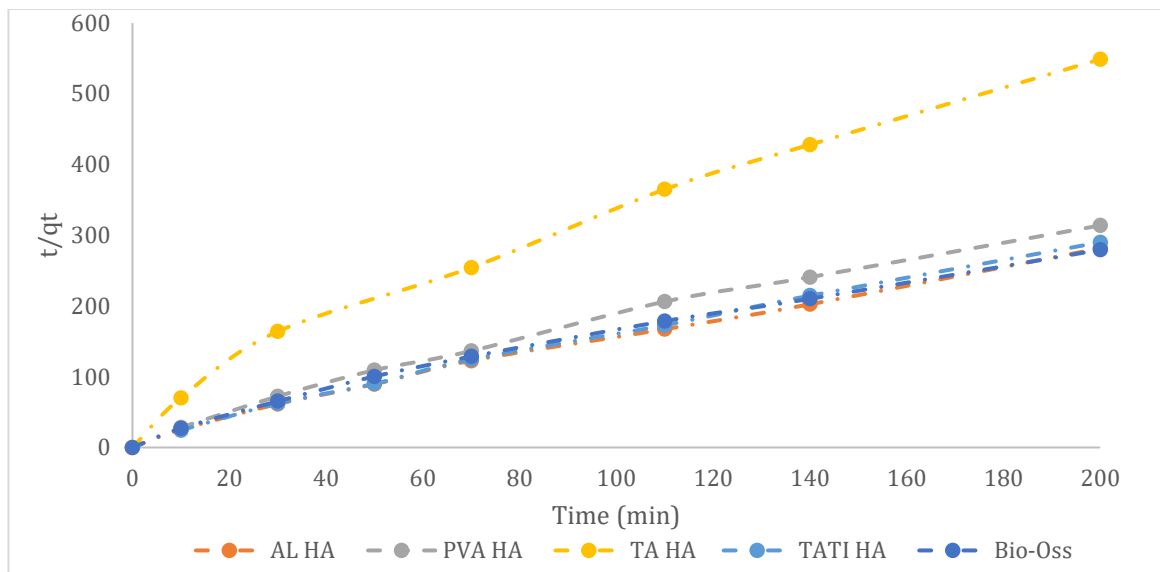


Figure X-11: Pseudo-second-order kinetics for the adsorption of MB on the mineralised hydrogel samples (& Bio-Oss) at room temperature (20°C).

Some  $k_2$  were raised by mineralisation, others were depressed, but not to zero. This is not surprising since the  $k_2$  value for a nano hydroxyapatite specimen like Bio-Oss alone was significant. Here we have a nanocomposite where both components sorb MB.

Table X-7: Kinetic parameters for the sorption of MB onto the mineralised samples at room temperature.

Samples	$k_2$ (g mg <sup>-1</sup> min <sup>-1</sup> )	$R^2$
AL HA	0.081	0.9957
PVA HA	0.078	0.9893
TA HA	0.081	0.9870
TATi HA	0.095	0.9962
Bio-Oss	0.093	0.9836

The  $R^2$  values for the majority if not all of the samples were  $\geq 0.99$ , which shows that the pseudo-second-order model was useful in describing the behaviour of the mineralised hydrogels as well.

### X.5.2 Release behaviour of MB from mineralised and unmineralized hydrogels

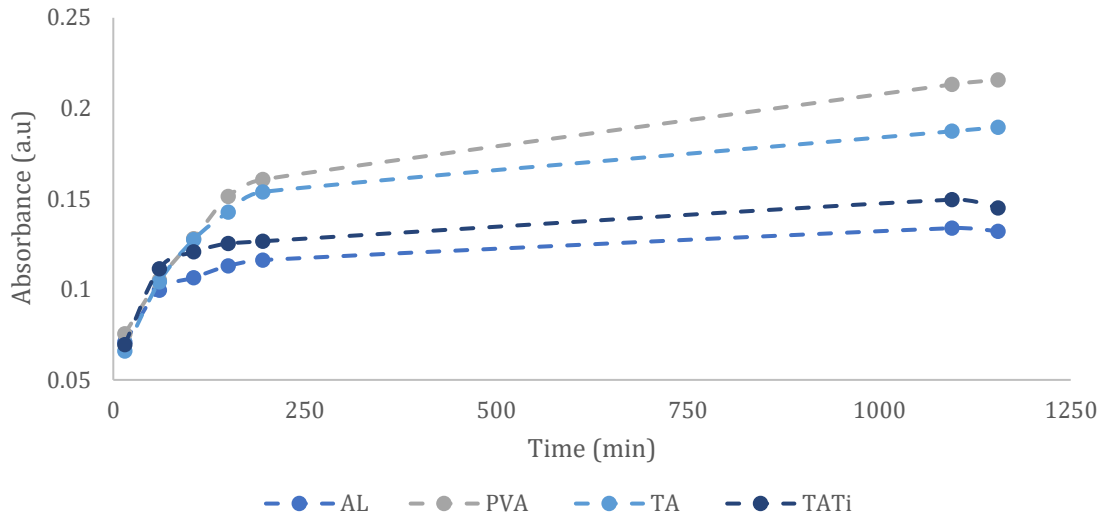


Figure X-12 : Release profile of MB from the hydrogel samples (PBS, pH=7.4, dose= 3mg/ml; temperature=20°C).

Following the uptake of MB, its release by the hydrogel only samples is shown in Figure X-12. All of the samples possess a significant but slowing release of MB over the first behaviour within the first 120min. Just like trends that was shown in Table X-2, PVA seems to again be quite prolific in releasing its content, mirroring its sorptive capacity.

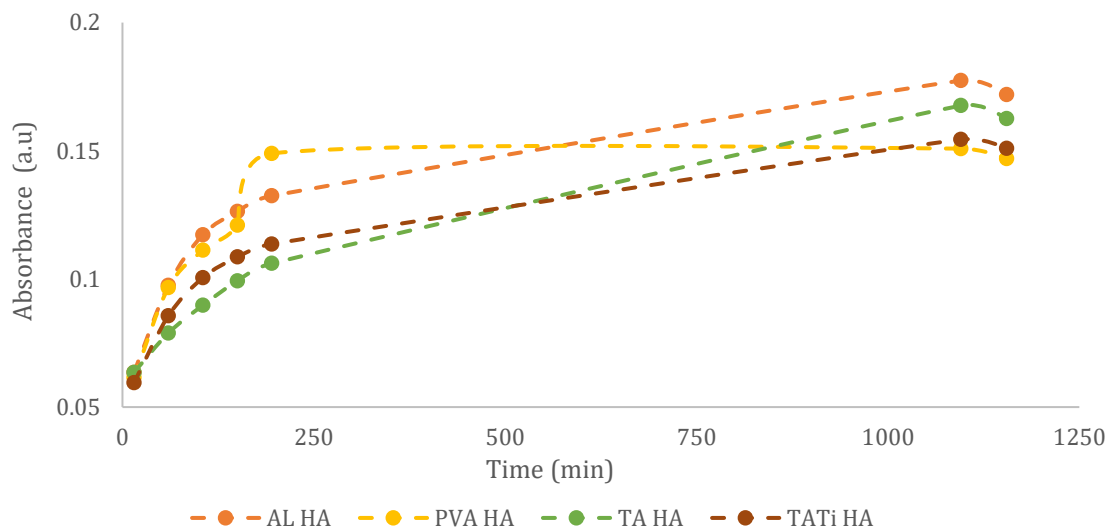


Figure X-13: Release profile of MB for the mineralized hydrogel samples (PBS, pH=7.4, dose= 3mg/ml; temperature=20°C).

The mineralised-hydrogel samples seem to follow a similar release profile and trend as the hydrogel only sample. Here, AL HA is the best sample, followed closely by the tannic acid modified samples (TA HA and TATi HA) and then finally PVA HA. It appears that HA overcoating did not cause hinderance of MB uptake or release.

### **X.5.3 Uptake behaviour of other probe molecules**

While MB was subjected to a comprehensive data analysis in order to its sorptive behaviour, the upcoming probe molecules will not be subjected to such an extensive undertaking. MO was a large, charged adsorbent (opposing charge to MB). AA was included in this study to account for its antioxidant potential and its inclusion in many drug preparations to preserve the longevity of the main active ingredient, especially in instances where the active ingredient suffers irreversible damage due to oxidation (Moreira *et al.*, 2014).

#### **X.5.3.1 Methyl orange (MO) uptake**

In Figure X-14 it is possible to observe the behaviour of the non-mineralised sample in the presence of MO. Notwithstanding the lower concentration of the adsorbent utilised for this observation, the uptakes are very different for MB seen in Figure X-3. The sorbed amount from the best samples is smaller than the least sorbing sample from Figure X-3 (0.24mg/g : TATi); in spite of the longer observation time (300min) and lower concentration used. MO and MB are of opposite charge but of similar size, so it appears electrostatic interactions drive the MO-MB uptake by the nonmineralized hydrogels.

The sorbed amounts of MO never exceeds 0.05mg/g for the best sample (TA) and 0mg/g for the worst sample (AL); the natural sorptive capacity of the hydrogel samples for MO is less than that of MB. This most likely means that the adsorptive process in this instance is affected by the presence of a charged component. The same behaviour is seen in the mineralised sample Figure X-15.

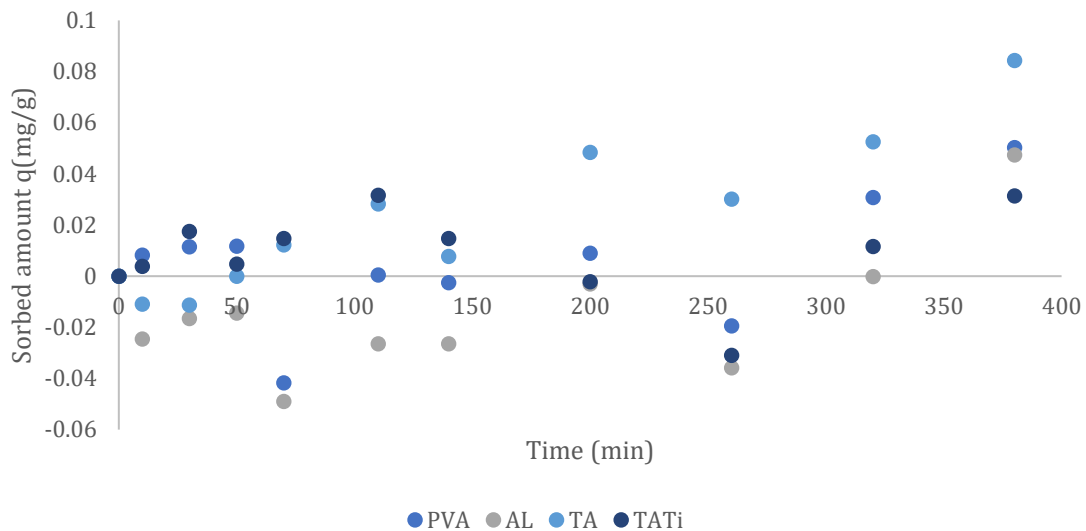


Figure X-14: Effect of contact time on the MO sorption capacity of the different hydrogel samples (pH=7.4, dose= 3mg/ml; temperature=20°C; MO concentration 0.005mM)

The amount adsorbed by the mineralised hydrogel samples never seems to exceed 0.029mg/g for TATi HA and AL HA, which were the best samples. The mineralisation process could not improve the negligible uptake of MO.

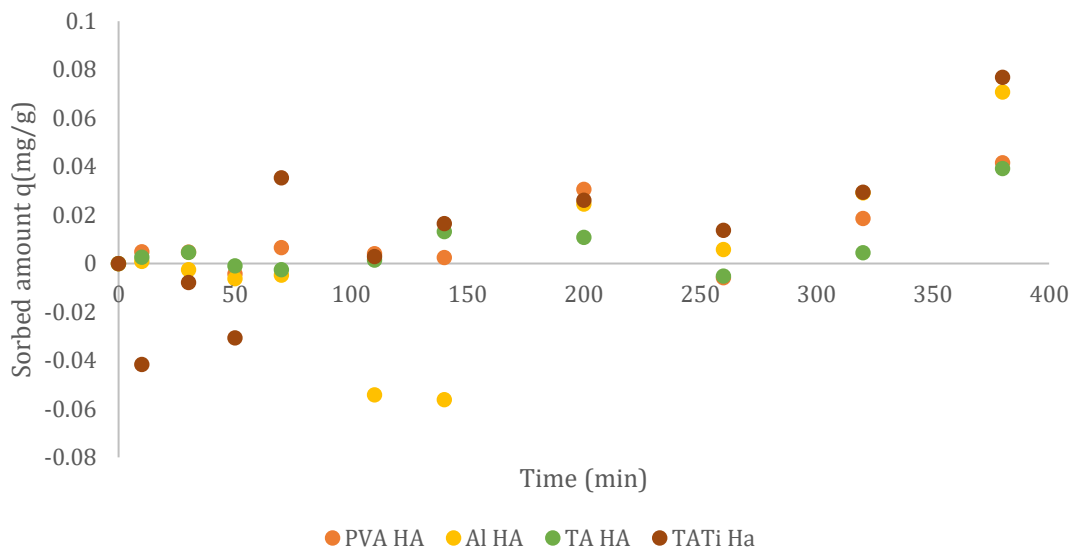


Figure X-15: Effect of contact time on the MO sorption capacity of the different mineralised hydrogel scaffolds (pH=7.4, dose= 3mg/ml; temperature=20°C; MO concentration 0.005mM)

### X.5.3.2 Ascorbic acid uptake

The third probe molecule used in adsorptive studies for the prepared hydrogels and their mineralised partners was AA. Figure X-16 shows the uptake behaviour of AA with respect to

increasing contact time.

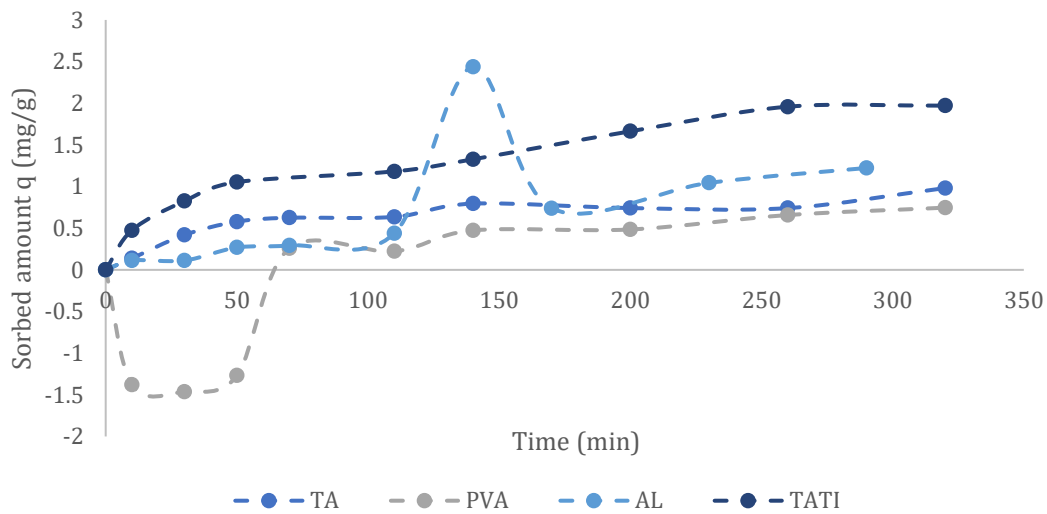


Figure X-16: Effect of contact time on the AA sorption capacity of the different hydrogels (pH=7.4, dose= 3mg/ml; temperature=20°C; MO concentration 0.014mM).

Figure X-16 shows that the adsorptive behaviour of the hydrogel samples is improved. In terms of individual adsorptive capacity of the hydrogels, Figure X-16 demonstrates the superior adsorptive performance of TATi (1.66mg/g), with PVA (0.48mg/g) being its inferior partner. The results are in direct contrast to those that were seen in Figure X-2 where their positions were exchanged.

The results here, along with the those obtained for MO proves that the hydrogels have a selectivity in what they are most likely to uptake.

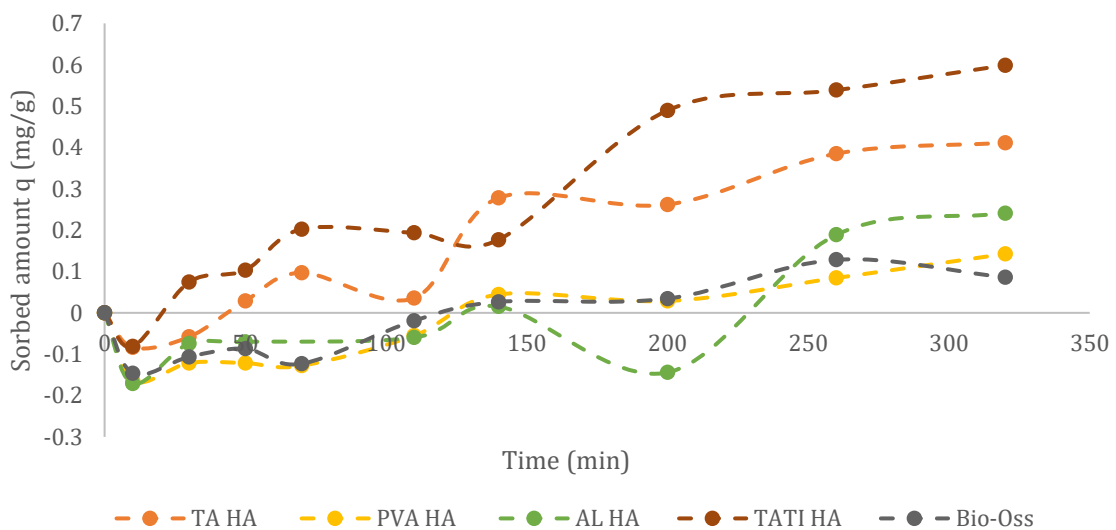


Figure X-17: Effect of contact time on the AA sorption capacity of the different mineralised hydrogels (pH=7.4, dose= 3mg/ml; temperature=20°C; MO concentration 0.014mM).

The sorption of AA for the mineralised hydrogels are reasonable (Figure X-17) from 50min onwards. Again, TATi HA shows the highest uptake at 0.48mg/g. It is possible that the negative values are due to the amounts of AA used in this experiment.

Overall, there is a drop in the collective sorptive capacity of AA compared to the mineralised samples. And so, mineralisation appears to affect AA uptake.

#### X.5.4 Comparison of sorption across all samples

In this section, we shall attempt to compare the extent to sorption of all the samples, and deduce the area occupied by each MB, MO and AA, in the hydrogels.

Before going on, the geometric surface area of the 3mg hydrogel samples was ascertained by measuring the thickness ( $\approx 0.94\text{mm}$ ), width ( $\approx 1.55\text{mm}$ ) and length ( $\approx 2.17\text{mm}$ ) using the surface area formula of a rectangle

$$\text{Surface Area} = 2(LT) + 2(TW) + 2(LW) \quad \text{Equation 49}$$

where L is the length, T is the thickness and W is the width. The average surface area of a 3mg piece of the present hydrogel sample was calculated as  $\approx 82.16\text{mm}^2$  (or  $8.21 \times 10^{19} \text{pm}^2$ ), and the data was averaged over 10 samples.

The estimated number molecules of 0.015mM of MB, 0.005mM of MO and 0.014mM of AA in 3ml solution was calculated using the following formula

$$= \text{Avogadro's number} \times \text{concentration} \times \text{volume} \quad \text{Equation 50}$$

Avogadro's number is  $6.0 \times 10^{23}$ , the concentration is in moles and the volume is in L.

**Table X-8: Estimated number of molecules in 3ml of starting solution**

Adsorbate molecule	Number of molecules
MO	$9.0 \times 10^{15}$
MB	$2.7 \times 10^{16}$
AA	$2.5 \times 10^{16}$

The number of molecules sorbed on the 3mg sample piece is estimate using Equation 51

$$\begin{aligned} &\text{Number of adsorbate adsorbed} \quad \text{Equation 51} \\ &= \% \text{Uptake} \times \text{number of molecules in 3ml starting solution} \end{aligned}$$

From the value obtained, the area covered by the adsorbing molecules is estimated using the

relationship below

$$\text{Area per sorbing molecule} = \frac{\text{Surface area of sorbent}}{\text{number of sorbate molecules sorbed}} \quad \text{Equation 52}$$

The value obtained from Equation 51 and Equation 52 are shown in Table X-9.

The project area occupied by each MB molecules has been reported as  $1.35 \times 10^6$ - $1.97 \times 10^6$  pm<sup>2</sup> (Graham, 1955; Hang, Thompson and Brindley, 1970). As the area estimated below appear be on the same order of magnitude or lower than those stated in literature, it appears that the surface adsorption might be the dominant process, along with absorption is occurring with respect to MB uptake. It is likely that MB is adsorbed on the exterior surface, the surfaces of pores, voids and also absorbed. Interestingly, the area occupied by each MB in the mineralised hydrogels is similar to Bio-Oss.

**Table X-9: MB molecules sorbed per unit area (pm<sup>2</sup>) on the sorbent surface**

Samples	q <sub>o</sub> (mg/g)	q (mg/g)	% Uptake	Number of MB molecules sorbed	Area of sorbed MB MB/pm <sup>2</sup>
PVA	4.90	1.73	35.39	$9.55 \times 10^{17}$	$8.60 \times 10^6$
PVA HA	4.90	1.19	24.31	$6.56 \times 10^{17}$	$1.25 \times 10^6$
AL	4.90	1.49	30.55	$8.24 \times 10^{17}$	$9.96 \times 10^6$
AL HA	4.90	1.64	33.54	$9.05 \times 10^{17}$	$9.07 \times 10^6$
TA	4.90	1.37	27.93	$7.54 \times 10^{17}$	$1.09 \times 10^6$
TA HA	4.90	1.08	22.20	$5.99 \times 10^{17}$	$1.37 \times 10^6$
TATi	4.90	1.03	21.17	$5.71 \times 10^{17}$	$1.44 \times 10^6$
TATi HA	4.90	1.20	24.58	$6.63 \times 10^{17}$	$1.24 \times 10^6$
Bio-Oss	4.90	0.93	18.99	$5.12 \times 10^{17}$	$1.60 \times 10^6$

Moving on now to the uptake of MO (Table X-10) and also bearing in mind the MO and MB have fairly similar volumes (Wang *et al.*, 2016) of  $34,500 \text{ pm}^3$  and  $31,000 \text{ pm}^3$ . From estimation by Wang *et al.* (2016) estimated that the area occupied by MO on their Wheat biochar (BC-4-700) was closer to  $1.62 \times 10^7$ -  $3.36 \times 10^7 \text{ pm}^2$ . It appears that most of MO is being taken up in hydrogels and mineralised hydrogels occupy similar areas.

**Table X-10: MO molecules adsorbed per unit area (pm<sup>2</sup>) on the sorbent surface**

Samples	q <sub>o</sub> (mg/g)	q (mg/g)	% Uptake	MO molecules adsorbed	Area of adsorbed MO/pm <sup>2</sup> (nm <sup>2</sup> )
PVA	1.36	0.009	0.66	5.94 × 10 <sup>15</sup>	1.38 × 10 <sup>8</sup>
PVA HA	1.36	0.031	2.24	2.02 × 10 <sup>16</sup>	4.07 × 10 <sup>7</sup>
AL	1.36	-0.003	-0.22	-1.98 × 10 <sup>15</sup>	-4.15 × 10 <sup>8</sup>
AL HA	1.36	0.024	1.80	1.62 × 10 <sup>16</sup>	5.08 × 10 <sup>7</sup>
TA	1.36	0.048	3.55	3.19 × 10 <sup>16</sup>	2.57 × 10 <sup>7</sup>
TA HA	1.36	0.011	0.79	7.13 × 10 <sup>15</sup>	1.15 × 10 <sup>8</sup>
TATi	1.36	-0.002	-0.16	-1.45 × 10 <sup>15</sup>	-5.66 × 10 <sup>8</sup>
TATi HA	1.36	0.026	1.91	1.72 × 10 <sup>16</sup>	4.77 × 10 <sup>7</sup>

Ansari, Alizadeh and Shademan (2013) estimated that the area occupied by AA on adsorption onto silica gel/PANI composite was closer to 3000pm<sup>2</sup>. Larger areas occupied are seen in Table X-11.

**Table X-11: AA molecules adsorbed per unit area (nm<sup>2</sup>and pm<sup>2</sup>) on the adsorbent surface**

Samples	q <sub>o</sub> (mg/g)	q (mg/g)	% Uptake	AA molecules adsorbed	Area of adsorbed AA/nm <sup>2</sup> (pm <sup>2</sup> )
PVA	2.436	0.48	19.90	5.02 × 10 <sup>17</sup>	1.64 × 10 <sup>6</sup>
PVA HA	2.436	0.03	1.17	2.96 × 10 <sup>16</sup>	2.78 × 10 <sup>7</sup>
AL	2.436	0.74	30.33	7.64 × 10 <sup>17</sup>	1.07 × 10 <sup>6</sup>
AL HA	2.436	0.02	0.77	1.95 × 10 <sup>16</sup>	4.21 × 10 <sup>7</sup>
TA	2.436	0.74	30.45	7.68 × 10 <sup>17</sup>	1.07 × 10 <sup>6</sup>
TA HA	2.436	0.26	10.74	2.71 × 10 <sup>17</sup>	3.03 × 10 <sup>6</sup>
TATi	2.436	1.66	68.26	1.72 × 10 <sup>18</sup>	4.78 × 10 <sup>5</sup>
TATi HA	2.436	0.49	20.09	5.06 × 10 <sup>17</sup>	1.62 × 10 <sup>6</sup>
Bio-Oss	2.436	0.03	1.41	3.56 × 10 <sup>16</sup>	2.31 × 10 <sup>7</sup>

Overall it seems that the hydrogel, mineralised hydrogels and Bio-Oss all samples synthesised have the ability to sorb and release MB, MO and AA, where the molecules occupy expected areas.



## X.6 Summary

### X.6.1 General uptake behaviour and selectivity of the different probe molecules

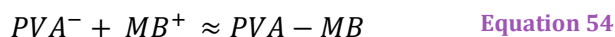
The sorption behaviour of the hydrogels (pre and after mineralisation) is measurable even when one considers the slight differences in the hydrogel blends used, not to mention the different probe molecules that are utilised.

With regards to the sorptive profile of all the hydrogel, mineralised hydrogels and Bio-Oss samples, the pattern assumed seems to be dependent on primarily the probe molecules that are utilised.

It is clear that MB is sorbed most extensively amongst all of the probe molecules that have been tested. This is most likely due to the positive charge that it assumes in an aqueous environment (Belala *et al.*, 2011) at a  $pK_a$ , greater than 0.04 (Chowdhury and Saha, 2012); and MB is completely ionised. As the experiment was run at a pH of 7.4, it is assumed that the charge of the dye would be positive during the experiment. An electrostatic interaction might be responsible for facilitating its sorption. The aqueous medium doubly affects the surface of the mineralised hydrogels involved in these experiments. It has been stated that apatites or more specifically hydroxyapatites have an isoelectric point that falls within the range of 5-7 (Kim *et al.*, 2004). The MB solution used throughout this experiment was adjusted to have a pH of 7.4, which lies just outside the isoelectric range suggested. As such, the negative groups on its surface would be revealed (carbonate ions and phosphate ions). Ultimately the summation of a net negative surface (adsorbent) and the positively charge dye molecules sets up an electrostatic attraction which leads to a favourable adsorption process (see Equation 53)



In addition to the groups of the mineralised phase being deprotonated, it is also possible that the hydroxyl group within the hydrogel also undergoes ionisation, similar to the hydroxyl group in the mineral. If/when this happens, a similar sorption process facilitated by electrostatic exchange would exist, working concurrently with the sorption on the mineral surface (see Equation 54).

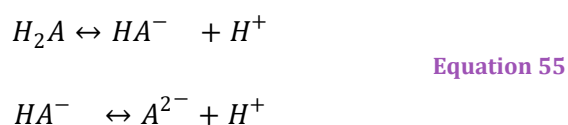


The strength of interaction affects the type of uptake isotherm seen.

In most of the samples, the same behaviour or order of uptake was followed during the subsequent release process. As strong sorption should result later in a weakened release; clearly this is not always true. The only sample that behaved differently was the hydrogel AL.

- Uptake behaviour of AA

The uptake behaviour of AA is essentially the same process seen in MB. AA is quite reactive and especially unstable in aqueous solution. It tends to exist as a combination of its neutral form, but easily dissociates into its charged form, ascorbate mono-anion ( $HA^-$ ) and subsequently into di-anion ( $A^{2-}$ ). In the scheme below  $H_2A$  is the neutral AA:



The aforementioned forms can all be interrogated in the presence of UV. Thus, decomposition from the neutral form of ascorbic acid to its other forms can be followed by observing the change in lambda max (243nm for AA) where  $\pi \rightarrow \pi^*$  transition within the C=C bond is responsible. In the case of the dissociated form, the transition is a  $n \rightarrow \pi^*$  which occurs at a much longer wavelength (red shift) (Ogata and Kosugi, 1970). The dissociation is affected by the solution's pH and the solvent in question. The use of a buffered solution has the ability to stabilise the neutral form of AA for longer as it allows the establishment of an equilibrium between the neutral and the charged forms (see Equation 55).

The above suggests that it is fairly easy for the charged/dissociated form to persist within an aqueous solution, especially in an unbuffered solution. It is probable that the uptake at least in the case of the mineralised-hydrogel was hampered by this charge. One can see that at  $t=0$ , the uptake was marginal or negative (most likely error caused by the extremely low uptake amount). After 30min, the samples began to exhibit a positive AA (Figure X-17). This might be due to some partial neutralisation (screening the negative charge of the surface) and protonation from the dissociated AA fragment (allowing the subsequent uptake of the AA). A lack of bulky anions in the hydrogel might explain why uptake occurred easily, to a high extent.

In both the mineralised and non-mineralised-hydrogel sample, TA (HA) and TATi (HA) seem to have exhibit stronger sorption possibly due to tannic acid and its PKA.

Finally, AA may break down into other forms that do not show up in UV-vis (although that would mean that the estimated uptake is erroneous).

- Uptake behaviour of methyl orange

Methyl orange was the only probe molecule with a very negligible uptake by all the mineralised-hydrogel samples, with the uptake capacity never exceeding 0.04mg/g (and 0.06mg/g in the hydrogel-only cases); It is assumed that this is down to the negative charge of the anionic MO dye

molecule which contains a sulfonic acid group (sulfonate) (Huang *et al.*, 2017). The anionic charge of this group, along with the negative charge of apatite groups on the surface leads to net repulsion of the dye specie barring it from sitting on the apatite surface. A similar scenario was reported by Jensen (1977), who showed that several dyes: sunset yellow, amaranth, indigo carmine etc, all of which containing sulfonic groups showed little uptake by neat hydroxyapatite, unless it was pre-treated by chlorohexidine.

As both MO and AA have anionic charges in an aqueous media, why is AA shown to be preferentially taken up instead of being repulsed like MO? As MO is quite stable, compared to AA, it is more than likely that AAs natural instability in an aqueous media might ultimately lead to its break down rather than uptake.

### **X.6.2 Equilibrium studies of MB on the samples**

Equilibrium studies were carried out on all the samples. Neither Freundlich model nor Langmuir model were especially appropriate (as defined by their  $R^2$  values). PVA and TA had data that was better fitted by Freundlich's model, while TATi and Al adhered more to Langmuir's model. Considering their mineralised counterpart, all of the samples had higher  $R^2$  when Langmuir isotherm was used to fit the models.

The sorption behaviour of the mineralised hydrogels compared to that of the hydrogel only samples suggests that the majority of MB uptake was the responsibility of the hydrogel. This is because all the mineralised samples, with the exception of TA HA, showed a decrease in the maximum uptake capacity (9.04% for AL H), 29.66% for PVA HA and 11.58% for TATi HA; TA HA went up by 28%). It is not yet clear why the blended samples did much better than PVA HA. Possibly, the blending process (i.e. homogenising) of the two polymers could have easily created more surfaces (voids, pores) that would be available to sorb the MB even after mineralisation. With the alginate samples,  $\text{OH}^-$  and carboxyl groups could participate in the sorptive process.

### **X.6.3 Kinetics of MB on the samples**

Pseudo second order kinetics model gave the best fit for the samples data. The close adherence to this model means that formation of chemical bonds/links was the rate limiting step.

### **X.6.4 Adsorbate area**

The results from section X.5.4 on the areas occupied by MB, MO and AA molecules highlights the fact that MB sorption, is not restricted to only surface but also occurs in the voids, pores and channels that make up the hydrogel structure (mineralised or not). Sometimes sorption may have been on the scaffolds alone.

## **X.7 Conclusion**

The aim here was to probe the uptake capacities of the different molecules: MB, MO and AA, as a

means to predict the possible use of the scaffolds as drug delivery systems. This was successfully undertaken. The following things were discovered

- PVA hydrogel on its own had the highest uptake capacity of MB, followed closely by AL (see Figure X-2). It also appears to possess the highest subsequent release rate.
- After mineralisation, AL HA was shown to have the highest uptake capacity of MB (Figure X-7); there was a general drop in uptake capacity when compared to its pre-mineralisation counterpart. AL HA also displays the highest release rate of MB.
- TA hydrogel on its own still had the highest uptake capacity of MO, having the most consistent trend (Figure X-14). All the other samples displayed erratic trends. It also shows a very high MB release capacity.
- After mineralisation, TATi HA and AL HA were shown to have the highest uptake capacity of MO (Figure X-15).
- TATi hydrogel on its own had the highest uptake capacity of AA, followed closely by AL (Figure X-16).
- After mineralisation, TATi HA had the highest uptake capacity of AA (Figure X-17).

From these results, it does seem that neat hydrogel and the mineralised-hydrogel scaffold have appreciable uptake capacities that could be used in drug delivery. However, the type of drugs would affect the amount that could be taken up. Positively charged molecules (like M)B show maximum uptake capacity, with PVA and AL HA proving to be good candidates for such an endeavour. If the therapeutic drug consisted of negatively charged molecules, their uptake and delivery will be better served if TATi HA (and AL HA), and TA are the host matrices used. To enhance the uptake ability of negatively charged molecules, further modifications might be required.

In terms of release of MB, the host matrix may define if release is fast/short lived or slow/long lived, it depends on if a fast release of a more sustained release is required. Neat PVA and TA hydrogels both show the most promise, as well as most of the mineralised-hydrogel samples. For a much slower release rate, TATi and AL would be the more suitable options. Clearly the addition of alginate and tannic acid are enough to change the adsorption and release properties of the samples here.

Lastly, some molecules were seen to be sorbed on Bio-Oss.

## Chapter XI Microspheres

### XI.1 Introduction

We have previously touched on the use of templates for the purpose of affecting the morphology, size and possibly the properties of functional materials that are grown on these. This chapter extends the synthesis of the calcium phosphate-based scaffold on bio and hydrogel templates, to a situation where synthetic microspheres are evaluated as suitable scaffold materials for the purpose of obtaining apatitic calcium phosphate for bone graft material with drug delivery capabilities.

The methodology developed in chapter (II.3) was extremely promising for the development of rather bulky scaffold material; unfortunately adapting it for the synthesis of much smaller, intricate structures might prove quite difficult. This has necessitated the need for a different synthesis route which will focus on the production of a biodegradable microsphere that could potentially be self-assembled into any shape depending on the purposes intended. The added presence of a more precise particle size, means a better control of the surface to volume area, which can in turn affect the packing of these spheres, the mechanical strength of the scaffold as a whole, and their ability to allow a sustained drug release (Hossain, Patel and Ahmed, 2015). This is perhaps better than relying on the almost random generation of pores in the hydrogel scaffold systems that has so far been developed.

Here, PLA microspheres were utilised as the template material for the purposing of obtaining a suitable bone graft material.

### XI.2 Background

PLA is a polymer that has the formula below:

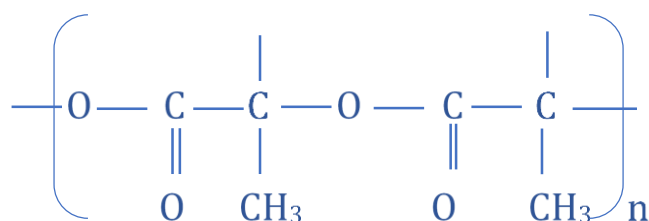


Figure XI-1: Structural formula of poly (L-Lactic acid)

PLA is easily produced by the fermentation of sugars and starchy materials, making its raw materials easily sourced (Pan and Inoue, 2009). It is a biodegradable polymer with adequate mechanical properties (tensile strength 65MPa and modulus of 3GPa (Tábi, Hajba and Kovács, 2016)). It is also non-cytotoxic, making it a useful material for biomedical applications (Dorati *et al.*, 2017). Its mechanical, thermal and degradation properties are usually affected by the crystallinity of the polymer. For biomedical applications (such as use as a scaffold material, or a drug delivery device), the mechanical and degradation properties are paramount, making the crystallinity of the polymer an essential factor that needs to be considered (Pan and Inoue, 2009).

The crystallinity can be affected by the type of isomers present. PLA is isomeric. It can exist as P-D-lactide (PDLA) or P-L-lactide (PLLA) or as a combination of both (PDLLA). Thus depending on whether the pure isomers are used or a mixture, the chance of obtaining stereoregular polymers with a high level of crystallinity will obviously be affected; with polymers made using PDLLA being generally amorphous (Pan and Inoue, 2009). Another factor that can affect the crystallinity of the PLA samples is the processing conditions. Usually melt, solution or cold crystallisation (Pan and Inoue, 2009) are used. Under normal conditions these lead to the production of  $\alpha$ -form PLA. The  $\beta$ -form manifests through stretching of the  $\alpha$ -form at high temperatures usually from hot-drawing of melt or solution spun PLA. The  $\gamma$ -form is developed through crystallisation on a hexamethylbenzene substrate (Pan and Inoue, 2009; Tábi, Hajba and Kovács, 2016). Of all the possible forms that can crystallise, the most stable and easily obtained is the  $\alpha$ -form, which has a helical packing conformation (Lizundia, Landa and Sarasua, 2011). An abundance of the  $\alpha$ -form has been seen to have a positive effect on tensile and flexural strength (and modulus) (Tábi, Hajba and Kovács, 2016). Unfortunately, its slow crystallisation kinetics often means that a more disordered  $\alpha'$ -form is the result instead. It is characterised by a lower packing density with poorer mechanical properties as well. Dissolution/degradability of PLA is also affected by crystallinity. Higher levels of crystallinity tends to slow down hydrolytic attack (i.e. the disruption of its ester bond (Tsuji and Ikada, 1998)). Usually, the packing of the crystals takes the form of highly organised spherulites which are composed of organised lamellae, interspaced with an amorphous region- made up of the ends of the polymer chains. Hydrolytic attack or even an enzymic cleavage tends to begin within the amorphous region, causing a reduction in the ordering of the system (Tsuji, Mizuno and Ikada, 2000). Consequently, increasing the percentage crystallinity reduces the number of amorphous regions, slowing down degradation, affecting drug release kinetics (Makadia and Siegel, 2011) and uncontrolled resorption of the template with premature loss of mechanical strength.

One downside of using PLA within the body, whether as just as scaffold or drug delivery vehicle

is its hydrophobicity. This property means that it is usually aggregated and is rapidly cleared from the body (Makadia and Siegel, 2011; Abdul Hamid, Tham and Ahmad, 2018). Several ways to improve its hydrophilicity use intentional hydrolysis (with HCl and NaOH), coating (with materials like albumin, gelatine etc.) that can alter the charge and hydrophilicity, and the copolymerisation with more hydrophilic polymers (Makadia and Siegel, 2011; Dorati *et al.*, 2017; Abdul Hamid, Tham and Ahmad, 2018). Another downside to the use of PLA is the formation and accumulation of lactic acid as a degradation product, which can trigger inflammatory effects in the surrounding area. Another downside is the problem of a rapid initial drug release profile that is often seen (Bee *et al.*, 2018).

Microspheres have been prepared through various methods. PLA/PLGA, containing the drug gentamicin sulphate (GC), has been prepared using spray drying and solvent evaporation (Prior *et al.*, 2000). Alginate-based microspheres containing stem cells were synthesised and incorporated into hydrogels utilised for bone regeneration (Sun and Tan, 2013). GC was again loaded in PLA-PEG via a double emulsion solvent method, with the presence of PEG seen to improve GC drug loading over 3 months due to its hydrophilicity (Dorati *et al.*, 2017). One method to improve the hydrophilicity of PLA incorporated the use of hydrolysis with NaOH and the subsequent biomineralization of the porous microspheres in SBF (17d) to form hydroxyapatite (Shi *et al.*, 2011). Shi *et al.* (2011) were able to demonstrate that human osteoblast cells adhered to the porous microspheres' exterior. A biomineralisation process using SBF to first obtain small apatite nuclei that were then attached to PLA microspheres, and immersed in SBF (7d) was used by Tabe, Hibino and Yao (2007), to obtain PLA covered with hydroxyapatite.

Therefore, from literature, it appears that the preferred method involves the use of co-polymers, hydrolysis and surface roughening to improve the hydrophilicity of PLA. Then, where hydroxyapatite was finally included, the authors use SBF over an extended period of time. Here, the author will attempt to form apatitic calcium-phosphate coated microspheres within a shorter period of time, without the need for surface roughening or forced hydrolysis, while incorporating biomimetic principles.

### **XI.3 Aim**

The aim of this section will be to optimise the development of microsphere bone graft material with a drug loading and release capability. Thus, this chapter will touch on the process of synthesising these microspheres, while considering the effects of surfactant concentration and composition. It is also to optimise the process of coating the microspheres encapsulating drugs (GC and AA), and the effect on the PLA matrix properties.

At the end of this chapter, the effects on the morphology and crystallinity of the PLA microspheres, as a result of surfactant modification, surface coating and drug loading, will be clarified.

## **XI.4 Methodology**

The procedure for preparing the microspheres (PLA PVA MS, PLA PVA-AL MS, PLA PVA-AL-TA MS, PLA PVA-AL-TATi MS) were described in section II.5. The coating procedure with CaP and TiO<sub>2</sub> may be found in sections II.7.2 and II.7.1 respectively. The preparation of the drug core is found in section II.6.

### **XI.4.1 Analytical instruments and conditions**

#### **XI.4.1.1 SEM**

Before analysis, the samples were dispersed onto a microscope slide and dried at 40°C for 3-4h. They were then placed on double sided carbon tape on a stub and coated with an Au target for 60s. Image J was used to estimate the sizes of the microspheres.

#### **XI.4.1.2 DLS**

The samples here were dispersed in deionised water. The results were averaged over 10 runs.

#### **XI.4.1.3 TEM**

The samples in this section would have been prepared for TEM analysis in two different way:

- i) suspended in deionised water and then drop cast onto a carbon-coated copper grid, or
- ii) they were set in a medium-hard resin and microtomed to produce slices of the microsphere's cross section they were also deposited onto a carbon-coated copper grid.

Characterisation used 200kV as the accelerating voltage used (unless otherwise stated).

#### **XI.4.1.4 XRD**

Crystallographic characterisation was undertaken over the 2θ range of 2-80° at a scan rate of at least 0.003°/min. The samples were drop cast onto silicon wafer (Si reflection around 32-33°) might be at times visible in the diffraction patterns.

#### **XI.4.1.5 FTIR spectroscopy**

A spectrum was collected over 400-4000cm<sup>-1</sup> with a resolution of 4cm<sup>-1</sup> after carrying out 45 scans.

#### **XI.4.1.6 DSC analysis**

The specimens were first cooled to -50°C, and then with a heating rate of 10°C/min, the samples were heated through to 250°C. Upon reaching that, they were then cooled back to 23-27°C with



the same ramp rate. Carried out in N<sub>2</sub>. All of the samples were hermetically sealed in an Al pan. All the data were individually processed using Origin 9 pro.

#### XI.4.2 Sample nomenclature

The samples were given the designations shown in Table XI-1.

**Table XI-1:Name of the microsphere systems and their accompanying description.**

<b>Samples</b>	<b>Description</b>
PLA PVA MS	Microspheres made using PVA as a surfactant
PLA PVA AL MS	Microspheres made using PVA + sodium alginate as a surfactant
PLA PVA AL TA MS	Microspheres made using PVA + tannic acid-infused sodium alginate as a surfactant
PLA PVA AL TATi MS	Microspheres made using PVA + Ti crosslinked tannic acid-infused sodium alginate as a surfactant
PLA PVA MS/CaP (TiO <sub>x</sub> )	Coated with CaP (or TiBALD)
PLA PVA AL/CaP (TiO <sub>x</sub> )	Coated with CaP (or TiBALD)
PLA PVA AL TA/CaP (TiO <sub>x</sub> )	Coated with CaP (or TiBALD)
PLA PVA AL TATi/CaP(TiO <sub>x</sub> )	Coated with CaP (or TiBALD)
Gent core PLA PVA MS	Gentamicin (GC) core microspheres
Gent core PLA PVA MS/CaP(TiO <sub>x</sub> )	Coated with CaP (or TiBALD)
AA core PLA PVA MS	Ascorbic acid core microspheres
AA core PLA PVA MS/CaP(TiO <sub>x</sub> )	Coated with CaP (or TiBALD)

## XI.5 Results

### XI.5.1 SEM

#### XI.5.1.1 Pure PLA-PVA samples

Figure IX-12 shows the micrographs of pure PLA PVA samples. They appear to be spherical, with very little size inhomogeneity. Their sizes range from between 2.63µm to 17.25 µm (with a mean of 6.41 µm±3.04).

Furthermore, their surfaces are quite smooth, containing little to no features, which might suggest the incorporation of some of the surfactant. As it appears from the surface, these microspheres are continuous-uniform spheres of the same substance (PLA).

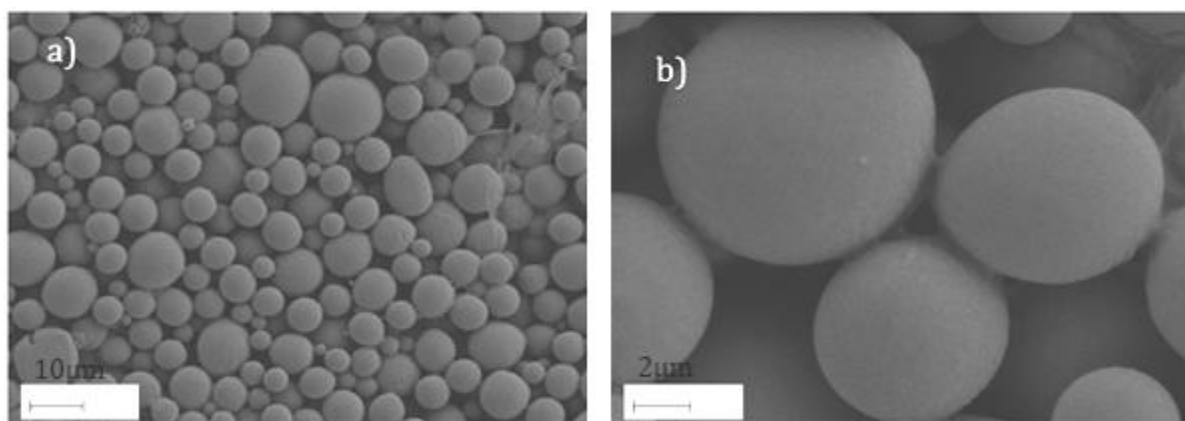


Figure XI-2: SEM micrographs of PLA PVA microspheres (a & b)

#### XI.5.1.1.1 Effects of varying PVA surfactant concentration

In order to optimise the morphological properties of the microspheres (MS) (i.e. their sphericity), the surfactant PVA concentration was altered to improve the chances of obtaining uniform microspheres in a series of synthesis iteration. Specifically, PVA concentrations of 1%, 2%, 5% and 10% were trialled to ascertain the optimum surfactant concentration for future use.

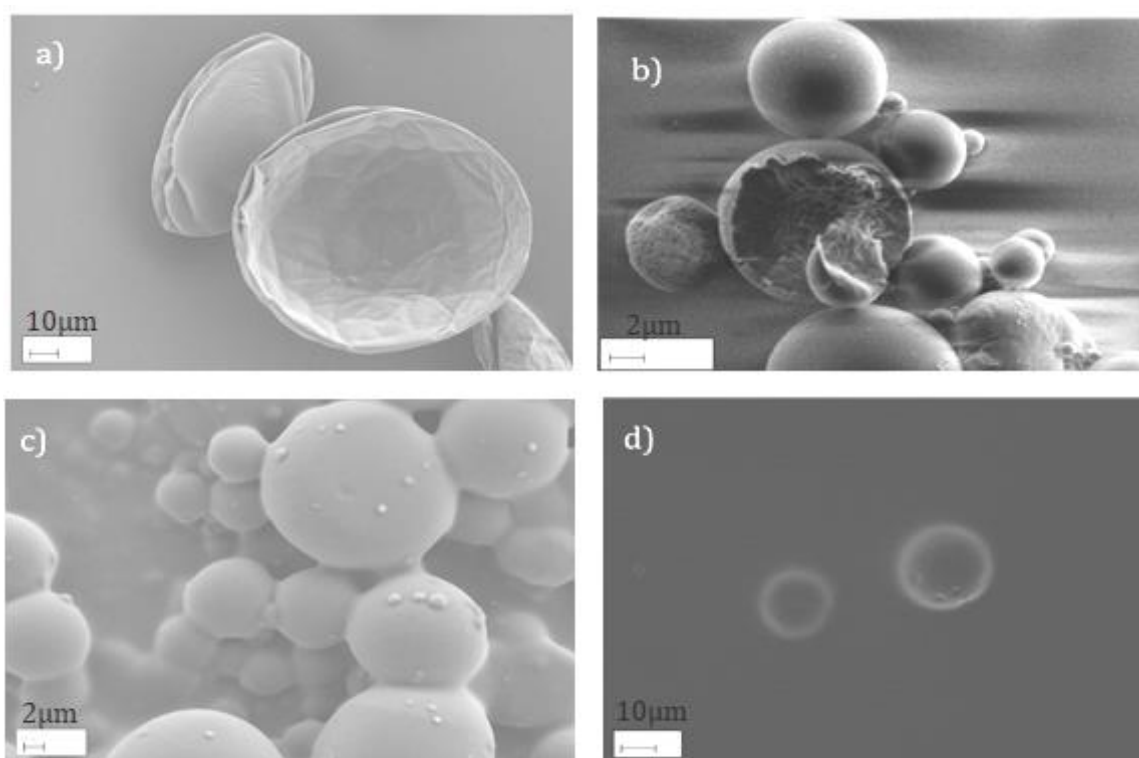


Figure XI-3: SEM micrographs of PLA PVA microspheres (MS) samples that have been synthesised with different PVA surfactant concentration. 1% a), 2% b), 5% c) and 10% d).

It is clear that lowering the surfactant concentration leads to the production of very thin particles

that appear sickled and bowl shaped (see Figure XI-3a), rather than full and plump, like the subsequent samples. Figure XI-3b & c obtained with 2% and 5% appear to be fully-formed microspheres, but in terms of quality the sample produced using 2wt% PVA is more microsphere like than the sample made with 5wt% PVA concentration (Figure XI-3c). At 5wt%, the particles are no longer distinct but appear bulky and aggregated with bridges seen connecting the necking particles. The samples formed at 10wt% were the most problematic, not only were they more difficult to emulsify with the organic phase, but the final rinsing step was quite difficult due to the difficulty of separating the formed particles from the viscous surfactant. As a result, a significant portion of the particles formed were lost while rinsing. Hence, it appears that the best PVA concentration was 2%

#### XI.5.1.1.2 Effects of modifying the surfactant composition

Further modification of the microspheres was attempted through changing the composition of the surfactant used: by mixing in sodium alginate, tannic acid and in some case TiBALD.

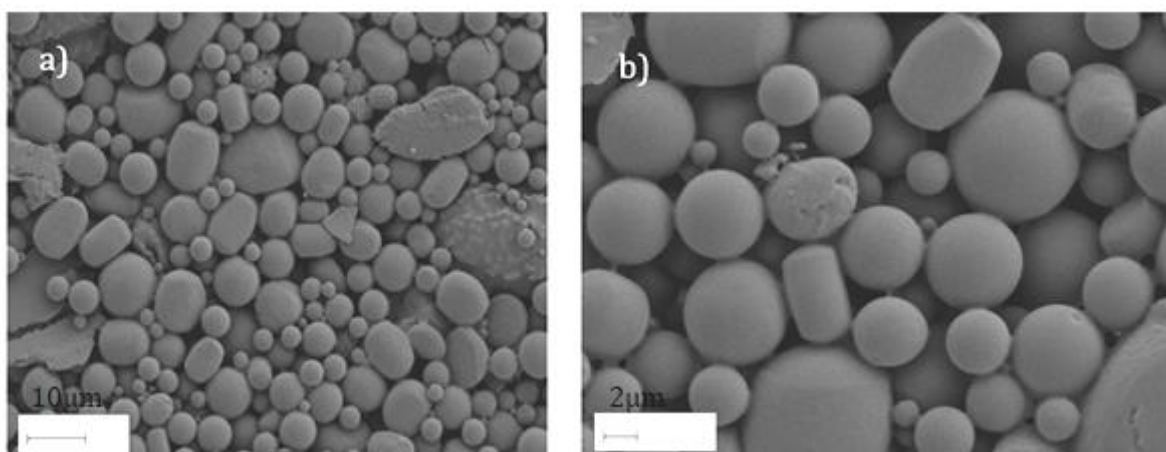


Figure XI-4: SEM micrographs of PLA PVA-AL microspheres (MS) samples made by modifying the PVA surfactant + sodium alginate formulation (a & b).

The sample in Figure XI-4 was made through the pre-addition of 20v/v% AL to the surfactant. It is possible to make out that this slight modification of the surfactant composition has led to the production of microspheres that are less spherical and more cylindrical in nature. It is more than likely that the wetting properties of the surfactant has been completely changed by the addition of AL. Their sizes now ranged from 2.57µm to 11.74 µm (with a mean of 5.23 µm ±2.25). This surfactant modification was thought to not be beneficial as the resulting microspheres deviated from a spherical shape.

Now the author used a PVA-alginate-tannic acid-surfactant blend.

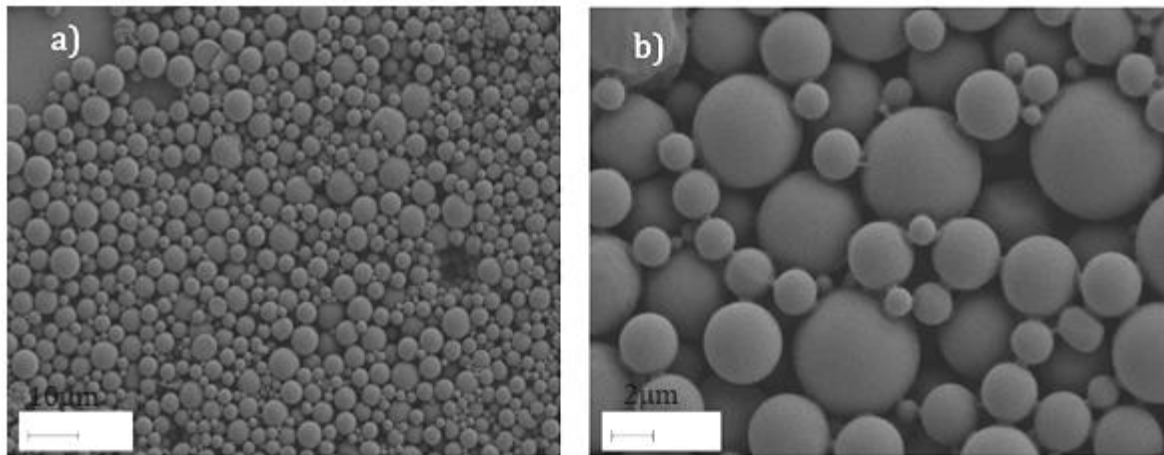


Figure XI-5: SEM micrographs of PLA PVA AL-TA MS made from tannic acid infused sodium alginate +PVA surfactant formulation (a & b).

Unlike the samples seen in Figure XI-4, here in Figure XI-5 the samples are much closer to the ideal spherical shape. Like before, the possible reasoning for this transition in shape is most likely down to the difficulty in forming surfaces through control of oil-water interfacial tensions during a solidification process. Unfortunately, the oil water tension could not be measured here in the time available. In the case of the samples formed with AL, the particles deviated more from the spherical ideal compared to these samples which might actually be due to the poor wetting potential of the surfactant mixture (and possibly viscosity). The addition of AL was not completely successful at this, but the subsequent addition of tannic acid (TA) must have improved the wetting properties to ensure that the samples seen in Figure XI-5 are closer to a spherical shape. They have sizes from 1.27  $\mu\text{m}$  to 6.52  $\mu\text{m}$  (with a mean of 3.44  $\mu\text{m} \pm 1.36$ ).

Now the author used a PVA-alginate-TATi surfactant blend in the hope that this would further improve the microspheres size distribution and shape.

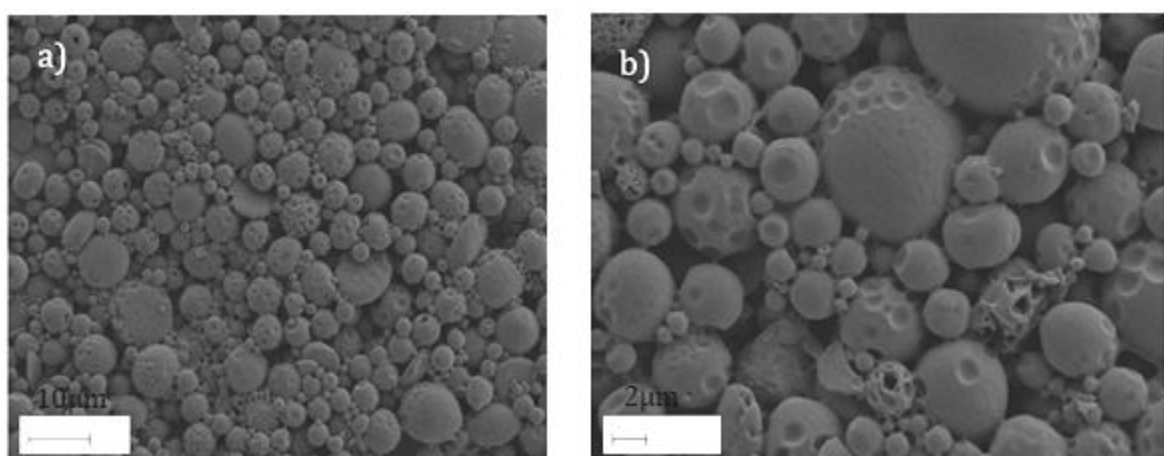


Figure XI-6: SEM micrographs of PLA PVA-AL-TATi microspheres (MS) made from titanium crosslinked tannic acid-infused sodium alginate + PVA surfactant formulation (a & b)

First it can be said that the PVA-AL-TATi surfactant derived samples presented in Figure XI-6 are as close to spheres as those seen in Figure IX-12 and Figure XI-5. But it is clear that their surfaces are dimpled for reasons that are not entirely clear as the synthesis condition was similar to the other samples (i.e. the mixture of the oil phase and the pre-prepared water phase (containing the surfactant)). The only difference was the addition of the titanium precursor in the form of TiBALD -which is known to be quite hydrophilic, after mixing had already begun. This reagent has its own density and surface energy, which would no doubt affect the already established sum of surface energies and oil-water interfacial tension of the added 20v/v% AL-TA and 80v/v% PVA surfactant. In addition, there is the chance that TiBALD has simply imprinted on the still soft PLA particles that are on the edge of solidification. Their sizes range from between 1.09 $\mu\text{m}$  to 9.72  $\mu\text{m}$  (with a mean of 4.13  $\mu\text{m} \pm 2.16$ ).

It is quite evident that through the simple act of surfactant modification, whether through the concentration, or the composition (and by extension wetting properties) one can tune the size, shape and overall surface morphologies of the final MS products. It is not entirely certain if the precise average sizes produced change, but there seems to be a trend towards smaller MS diameters with some surfactant modification.

#### ***XI.5.1.2 PLA-PVA coated samples***

As the PLA-PVA MS substrate has been optimised through surfactant concentration and compositions, it can now be used as a template for coating using different coating agents.

The CaP-coated samples are illustrated in Figure XI-7. It is clear that the samples in Figure XI-7(a-b) have an appreciable and uniform covering of their exteriors by what is most likely CaP. Although there are portions that appear uncovered, overall most of their surfaces do seem to be intimately covered with spikey foreign protrusions on their surfaces. PLA PVA-AL-TA however is not as consistently covered as the other two samples with its coating having a preference for covering portions where the microspheres are necked together. It is possible that even after the surfactant has been rinsed away (perhaps not completely), it might have altered the surface properties of the microsphere. Could the chemical groups of the microspheres have been altered or is there more amiss? Perhaps more can be made clear in the coming sections dealing with chemical characterisation techniques (EDX is used later on these samples in XI.5.1.4).

#### XI.5.1.2.1 CaP coating

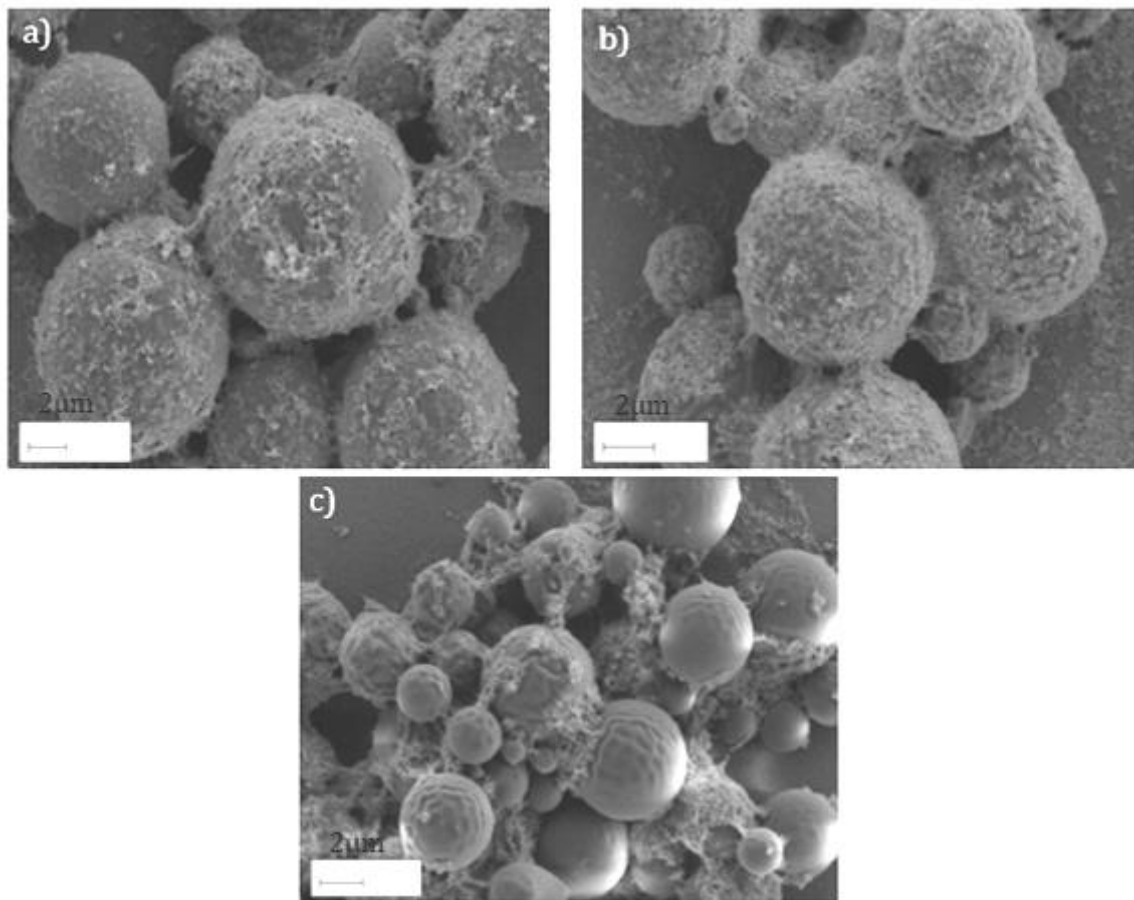


Figure XI-7: SEM micrographs of CaP coated samples of PLA PVA MS/CaP a); PLA PVA-AL/CaP b); PLA PVA-AL-TA/CaP c)

#### XI.5.1.2.2 TiO<sub>x</sub> based coating

A noticeable sign of TiO<sub>x</sub> was much harder to pick up visually in the samples shown in Figure XI-8. It was erroneously thought that the little features on the surfaces of the microspheres in Figure XI-8a-d might have something to do with Ti but EDX picked up no Ti in the elemental analysis. The tiny features had similar elemental composition as the bigger MS particles they covered, which probably means that the smaller particulates might simply be debris formed during the initial synthesis process which adhered to the microsphere surface.

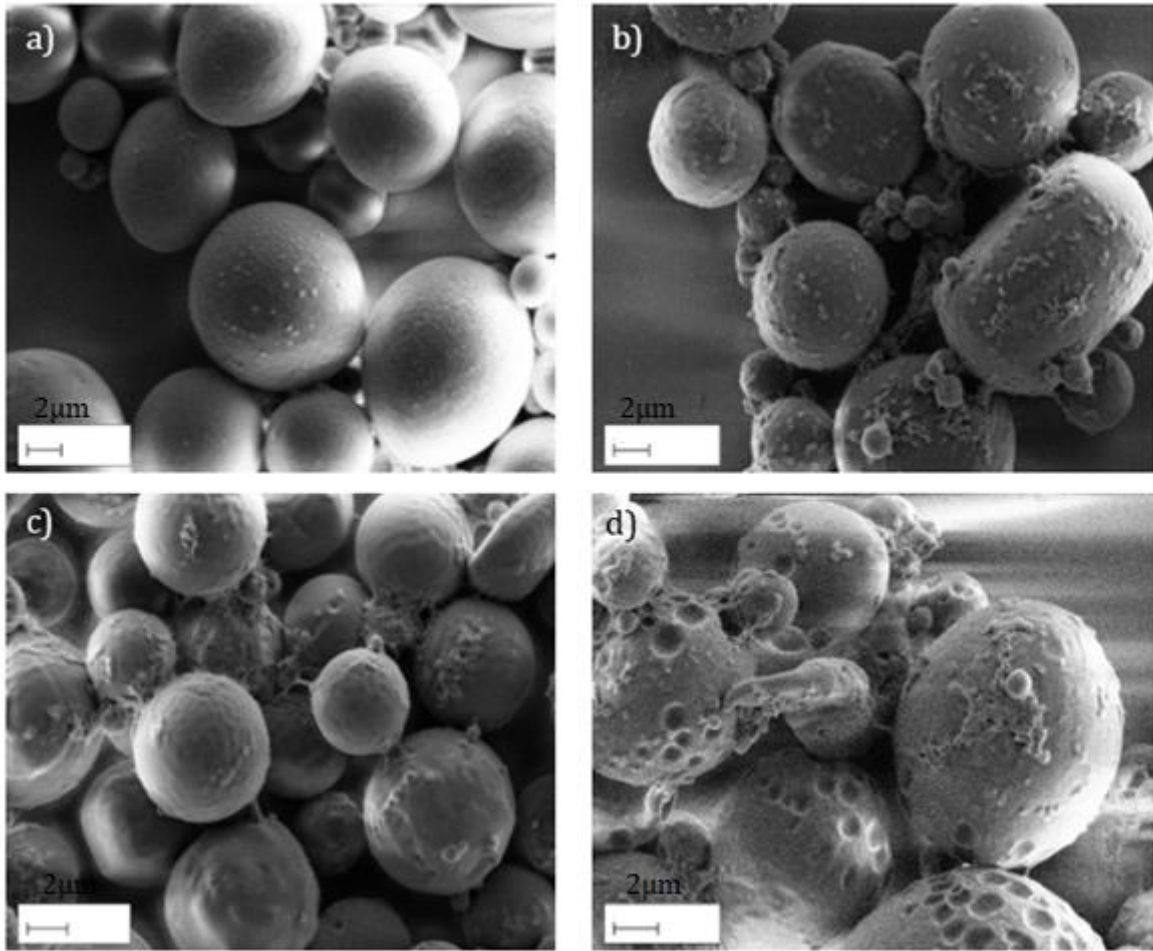


Figure XI-8: SEM micrographs of titanium coated samples of PLA PVA MS/TiO<sub>x</sub> a); PLA PVA-AL/TiO<sub>x</sub> b); PLA PVA-AL-TA/TiO<sub>x</sub> c); PLA PVA-AL-TATi/TiO<sub>x</sub> d).

Coating with CaP seems to be the most conclusive and comprehensive, at least in comparison with TiO<sub>x</sub> coating. The author does believe that TiO<sub>x</sub> occurs, but is not visible on the SEM micrographs, as the TiO<sub>x</sub> coated samples had a yellow colouration compared to the pure of CaP coated MS.

#### *XI.5.1.3 Drug core encapsulated samples*

For drug loading, the samples were prepared in a completely different manner (as explain in the methodology section (II.6)) such that the PLA forms a wall around a core centre that is filled with the relevant drug.

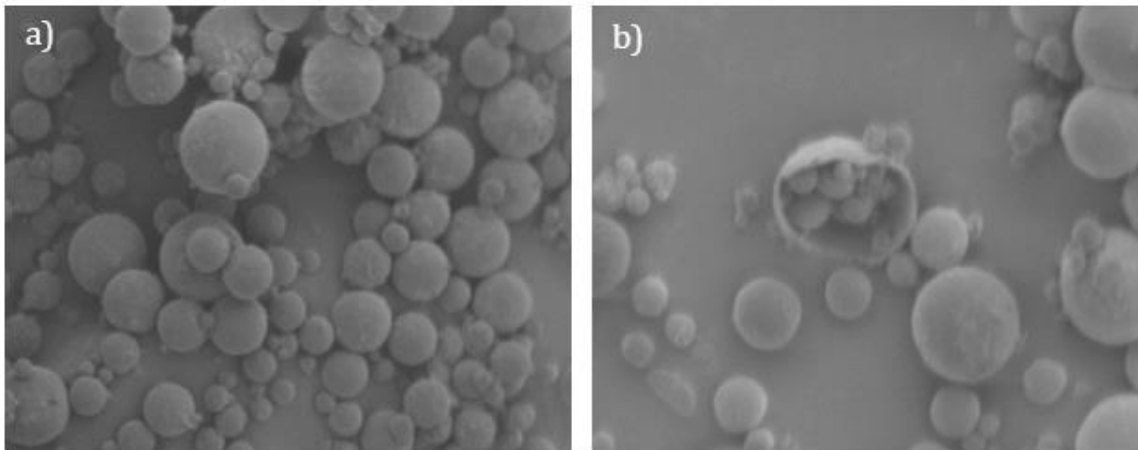


Figure XI-9: GC drug core encapsulated PLA PVA MS (a & b)

The samples in Figure XI-9 are GC drug core encapsulated samples that resemble the MS previously shown in Figure IX-12 in terms of their shape and inhomogeneity of their size. Most interestingly, Figure XI-9b shows a broken hollow microsphere housing other smaller sized microspheres. This is vastly different from Figure XI-3b that was solid through its cross section. It is expected that the drug core samples would be hollow; Figure XI-9b confirms this. They had sizes in the range 3.27-18.24 $\mu\text{m}$  (with a mean of 8.15  $\mu\text{m} \pm 3.27$ ).

Replacing GC with AA gave particulates that are sometimes spherical, and at other times almost completely flattened (see Figure XI-10a). Not only have they lost their shape (sphericity), but the external surface is quite rough and uneven. No doubt, as touched upon earlier in sections XI.5.1.1.2, the presence of AA (a complex antioxidant molecule) interacts and modifies the oil-water interfacial tension at the water-oil and possibly the water/oil boundary. The ability to form microspheres has thus been affected, resulting in a state where some of the particles formed appear to be 1D spheres (flattened). Whatever the cause, AA is affecting the MS produced.

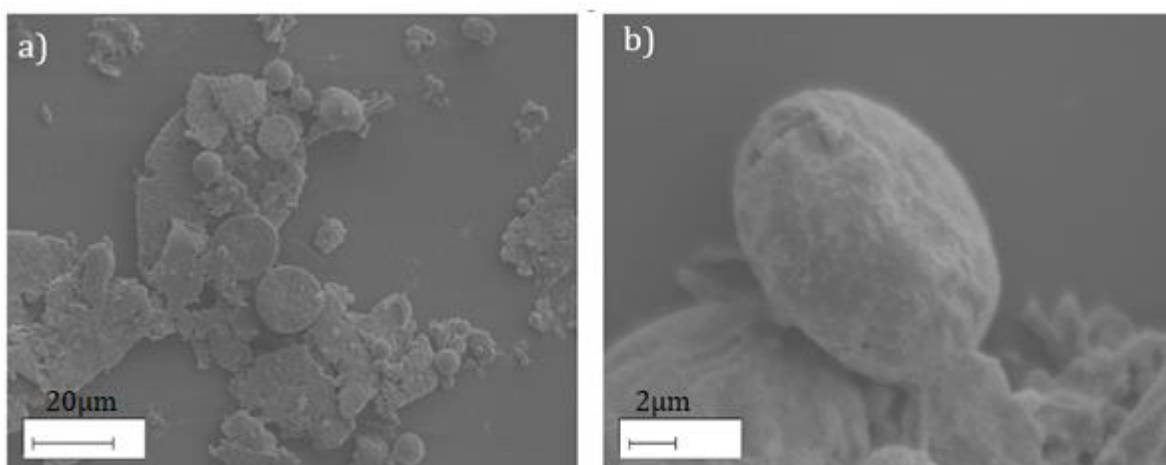


Figure XI-10: AA drug core encapsulated PLA PVA MS (a-b)



The average size of the AA cored samples was 9.04  $\mu\text{m}$  (with a range of between 5.56-16.48 $\mu\text{m}$ ). It seems that the drug cored samples were larger than the regular PLA PVA microspheres.

#### XI.5.1.3.1 GC core encapsulated samples with coating

The sample made using AA were not coated because the inclusion of AA resulted in porous particulates that would probably have little/no drug load. GC core-encapsulated microspheres were coated with CaP. Just like the samples with no drug cores, the CaP coating appears to be quite consistent in its coverage through the whole sample (see Figure XI-11).

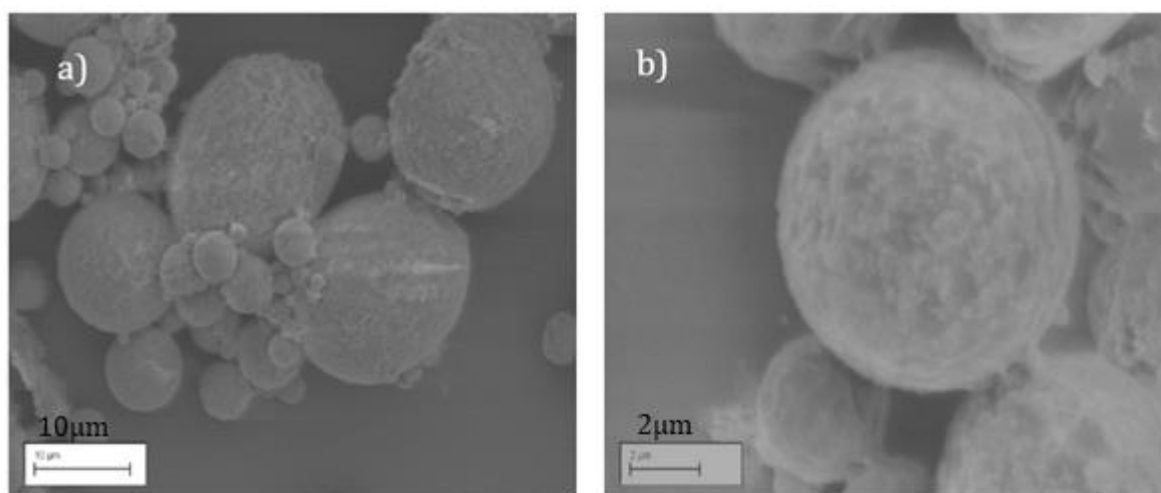


Figure XI-11: GC core encapsulated PLA PVA MS coated with CaP (a & b)

In addition to the good CaP coating, modifications with Ti precursor was also carried out on some of the samples. Again (just like its non-cored equivalent) the presence of any tangible feature showing the presence of titanium is absent. This cast further doubt on whether or not the coating process with titanium is actually successful.

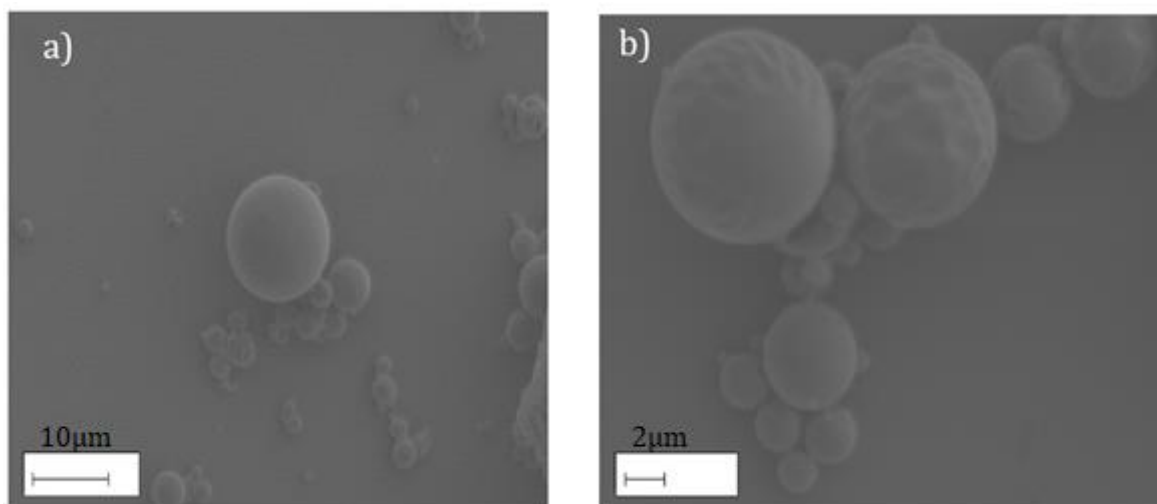


Figure XI-12: GC core encapsulated PLA PVA MS coated with a Ti precursor (a & b)

#### XI.5.1.4 EDX

Elemental analysis was carried out on the PLA PVA MS systems and the GC-cored microsphere. The results are presented in the table below:

Table XI-2: Table showing the average elemental composition of PLA PVA MS systems and GC core PLA PVA systems.

Samples	Ca (at%)	P (at%)	Ca/P	Ti (%)
PLA PVA MS	n/a	n/a	n/a	n/a
PLA PVA MS/CaP	31.26	5.2	11.58	n/a
PLA PVA-AL/CaP	35.21	2.53	13.95	n/a
PLA PVA-AL-TA/CaP	34.2	1.82	19.23	n/a
GC PLA PVA MS	n/a	n/a	n/a	n/a
GC PLA PVA MS/CaP	29.45	4.5	7.01	n/a

The presence of Ca and P on the coating layer was confirmed using EDX point analysis on different areas of the samples listed in Table XI-2; they are normally not present in the unmodified/uncoated microspheres. While the presence of Ca and P are positive indications that the coating with CaP was successful, the calculated ratios of Ca/P are not entirely encouraging. The ratios here bear no resemblance to that of the different calcium phosphates mentioned in literature (Dorozhkin, 2011, 2012a). There are several possible reasons for this: the analysis method is not suitable; the phases being formed might have nothing to do with calcium orthophosphates. Thus, the only other way would be to attempt another elemental analysis method to find the elements present and their approximate composition. It is partly for this reason that TEM was utilised as described later.

### XI.5.2 DLS

The average size derived from DLS measurements are given in Table XI-3.

**Table XI-3: Average microspheres dimensions in nm**

Sample	Average sizing/nm (PDI width)
PLA PVA MS	4310 (5267)
PLA PVA-AL MS	3710 (3390)
PLA PVA-AL-TA MS	3563 (2082)

As a result of the polydisperse nature of the microspheres produced, the results returned from using DLS might not be the most accurate, due in part to the omission of contributions from the smaller particulates. There is also the possibility of the much larger particles physically blocking the signal from the much smaller microspheres, further skewing the average. The inclusion of the polydispersity index (PDI) width was done to highlight the size ranges distribution of the samples tested. While it appears that the modified surfactants produced slightly smaller samples, the uncertainly resulting from the polydisperse nature of the samples makes one hesitant to conclusively say that one synthesis method produces smaller microspheres over the other. Nevertheless, the sizes in Table XI-3 appear to fall within the range noted in SEM.

### XI.5.3 TEM

Further studies on the morphology of the microspheres was carried out using TEM. With the limitations in resolution of SEM hampering the ability to pick some fine features, especially in the case of the samples that had been externally modified, it was decided the TEM would be attempted. Several analytical outcomes will be expected other than just a study of the surface morphology of the sample, i.e. crystallinity determination of the coating layer (and perhaps the PLA MS), thickness of the coating surface, cross section through the entire microspheres and additional EDX on the samples.

### XI.5.3.1 PLA PVA MS

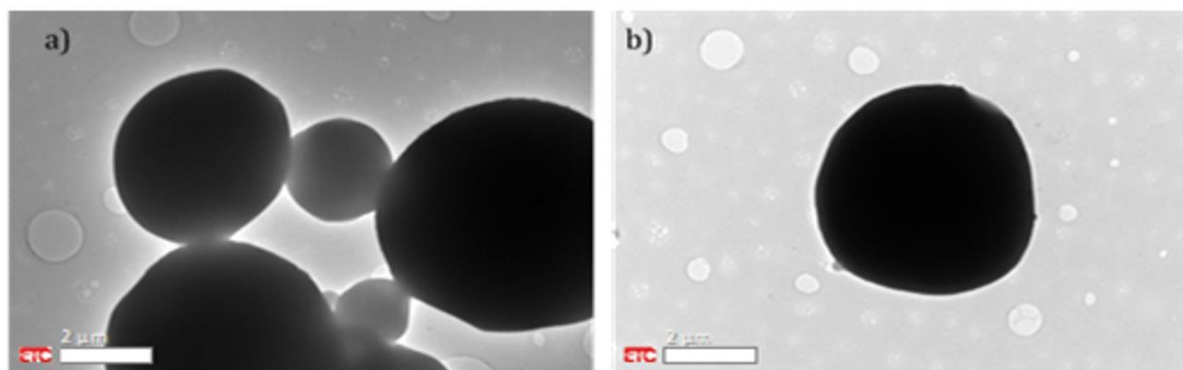


Figure XI-13: TEM of PLA PVA MS drop cast on a carbon coated copper grid (a & b)

In Figure XI-13 we can see individual microspheres. As suggested by SEM, the microspheres do seem to be roughly spherical in shape, with some irregularities (see Figure XI-13a). Using the limited population seen in the aforementioned figures, it may be estimated that they range in sizes from just under 2  $\mu\text{m}$  to about 5  $\mu\text{m}$ . Of course, only a small number of microspheres have been captured by TEM here, which happens to fall within the range of the estimates from SEM micrographs and DLS analysis.

#### XI.5.3.1.1 Externally-coated microspheres

Although SEM did appear to confirm the presence of a layer consisting of CaP, it was not possible to ascertain how thick or rather how uniform was the layer formed over the microspheres. Using TEM, it was hoped that it would be possible to tell if the CaP layer was distinct from the PLA surface, or if there was any sort of intermingling transition zone between the termination of one layer and the beginning of another layer.

##### XI.5.3.1.1.1 CaP-coated PLA PVA Microspheres

The micrographs in Figure XI-14 were obtained from drop cast samples of PLA PVA MS coated with CaP. Compared to the images seen in Figure XI-14, it is clear that the smooth curvature of the spherical microsphere surface has been replaced with jagged protrusions. This new feature is most likely linked to the coating of CaP that it was hoped had formed on the exterior of the microspheres.

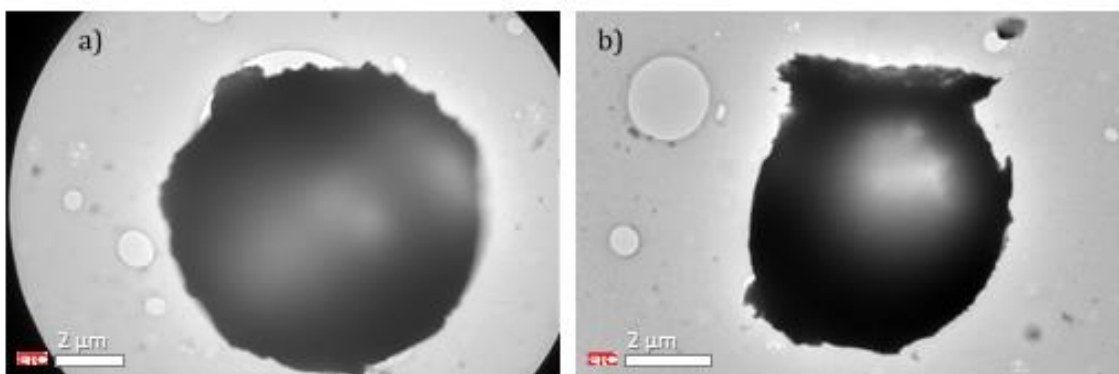


Figure XI-14: TEM micrographs of PLA PVA MS that have been coated with CaP and drop cast on a carbon coated copper grid (a & b).

Moving from the drop cast samples for the microtomed samples, we can turn our attention to the cross section of the microspheres. In Figure XI-15a-b, which provides a lower magnification view, it is possible to see that there indeed seems to be a fine continuous layer of CaP formed on the exterior of the microspheres (the mottled oval shapes). Although the coating layer appears continuous, there are regions where the layer seems to spawn almost hazardously away from the surface. Moving our attention to Figure XI-15a & b, which are magnified micrographs of sections of the CaP wall, it is obvious that the wall is crystalline in nature. This is exactly what the author hoped would be the outcome of her work. Now turn to the interiors, they appear unaffected, resembling those of the PLA-PVA MS that have been untreated. Figure XI-15a-b displays a patterned centre, some areas with a light colouration, while others mostly dark. Assuming this is not any form of aberration, it is possible that these regions maybe be directly linked to the potential mixed crystalline nature of the microsphere.

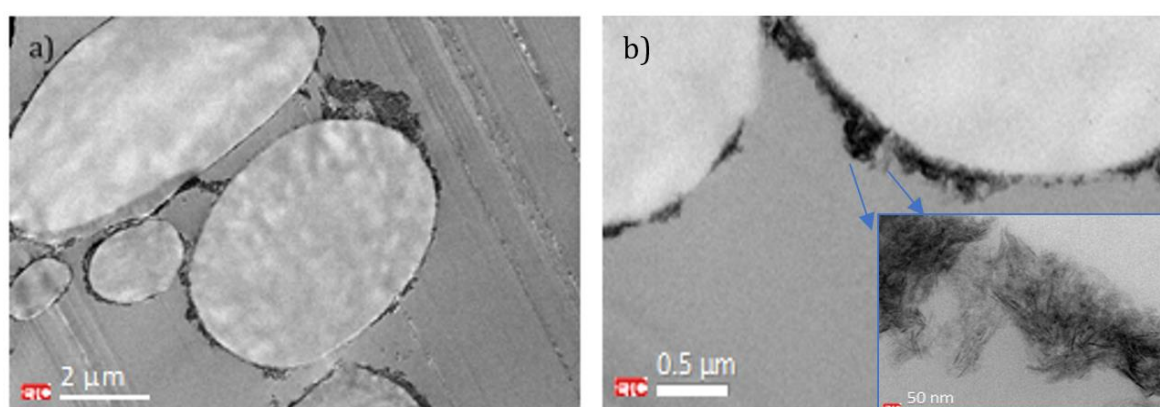


Figure XI-15: TEM micrographs of PLA PVA MS coated with CaP (a & b). The microspheres have been embedded in resin and microtomed to produce thin cross section.

A closer inspection of surface in Figure XI-15b (& inset) shows that the crystalline region is composed of electron-dense regions that appear darker than the surrounding portions. These

dark regions appear as elongated spindles with no particularly preferred orientation, although closer to the surface they do seem to preferentially follow the curvature of the microsphere. HRTEM images of this region (as shown in Figure XI-16a) reveal the lattice fringes on the atomic level of the spindle like structures. It was then possible to produce fast Fourier transform (FFT) from this observed fringe to reveal diffraction spots (as seen in Figure XI-16b). This would aid in the estimation of the relevant d spacing. A value of 3.671/nm was obtained (which is a significant figure for a calcium phosphate phase, i.e. hydroxyapatite). The evidence: d spacing as well as the shape of the crystalline region, points to the possibility that hydroxyapatite might just be formed as the preferred phase on the microspheres. If this were so, then the estimated d spacing (3.671/nm) might actually represent the width (300), contributing to the *a*-axis of an apatite crystallite, making the plane (002) perpendicular to that specific region (300) affect growth of the crystal in the *c*-axis (Jevtić *et al.*, 2008). Not only are some of the samples crystalline, they also seem to exhibit an individual anisotropic morphology similar to that found in human teeth (enamel), where the crystals seen there have a preferential growth direction: in the *c* axis direction (Kuśnieruk *et al.*, 2016).

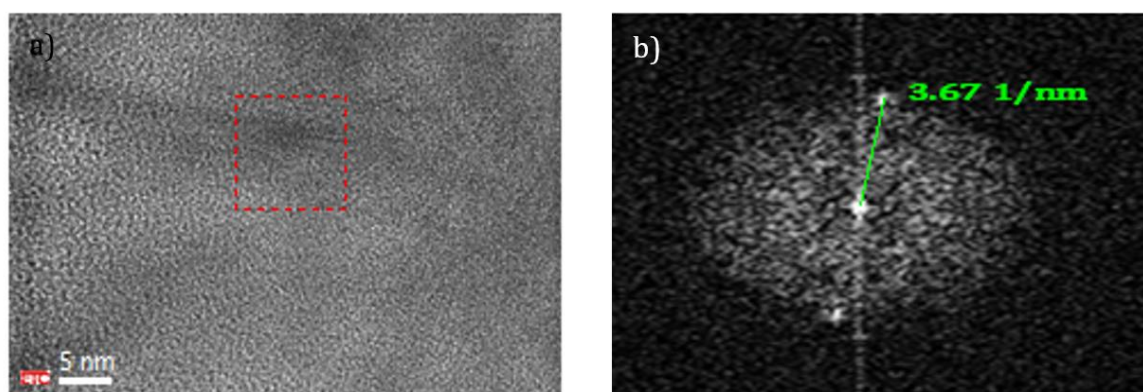


Figure XI-16 a) HRTEM displaying lattice fringes in real space; b) FFT image derived from the region highlighted in a).

### ***XI.5.3.2 GC-core Microspheres***

Just like the samples seen for the pure PLA-PVA microspheres with no drug core, we can see that the samples here also appear to be spherical (see Figure XI-17). Their diameters seem to range from between 0.5 $\mu$ m to 2.5 $\mu$ m. Again, this is not a conclusive size range as only a limited number of MS has been counted.

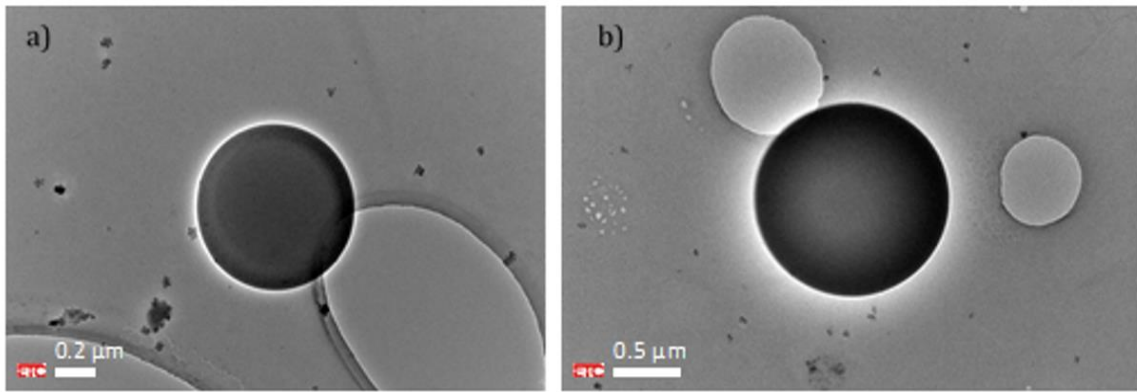


Figure XI-17: TEM micrographs of GC core PLA PVA MS that have been drop cast onto a carbon-coated copper grid (a & b).

In Figure XI-18, we can see the main distinction between this microsphere system and the samples prepared without a drug core. In Figure XI-18a most of the microspheres (but not all) are not fully solid but appear to consist of two distinct regions: an inner core and an outer ring of varying thickness that appears to depend on the size of the particle. The largest particle has an outer ring with a wall width of  $1\mu\text{m}$ . Two smaller spheres having walls that are closer to  $0.5\mu\text{m}$ . The walls appear marbled compared to the interior; this could suggest that completely different substances or perhaps phases are predominant in either of the two phases. It is possible that the exterior is made up of just PLA (albeit compressed) and thus more “crystalline” than that seen in the PLA PVA MS. It is not possible to say for sure what the interior core conclusively is; possibly it could be PVA (that has found its way enveloped inside the PLA) or it could be just the drug GC. It is unlikely it is a combination of the two as the interior appears homogenous with no visual irregularities, in terms of contrast at least.

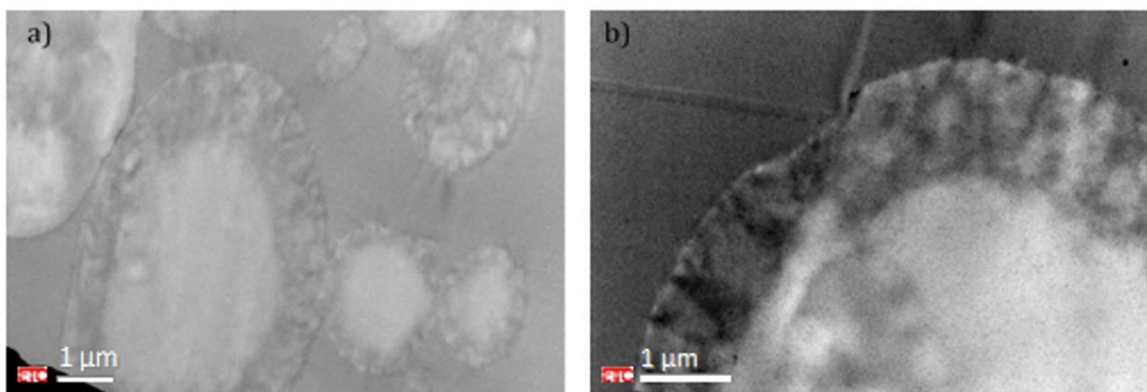


Figure XI-18: TEM micrographs of GC core PLA PVA MS cross sections (a & b)

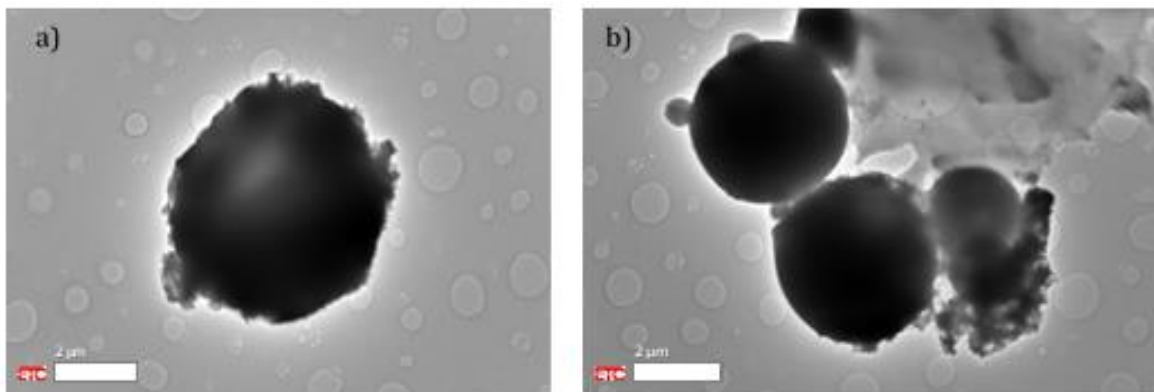
#### XI.5.3.2.1 Externally coated GC core samples

Here, the samples considered have had their exteriors modified with either CaP or  $\text{TiO}_x$  to attempt

production of an inorganic casing for GC-core PLA microspheres. As with the plain samples, SEM images showed positive results in that the samples that had been treated with CaP precursors (same as with EDX). Those that had undergone treatment with a Ti precursor showed some positives.

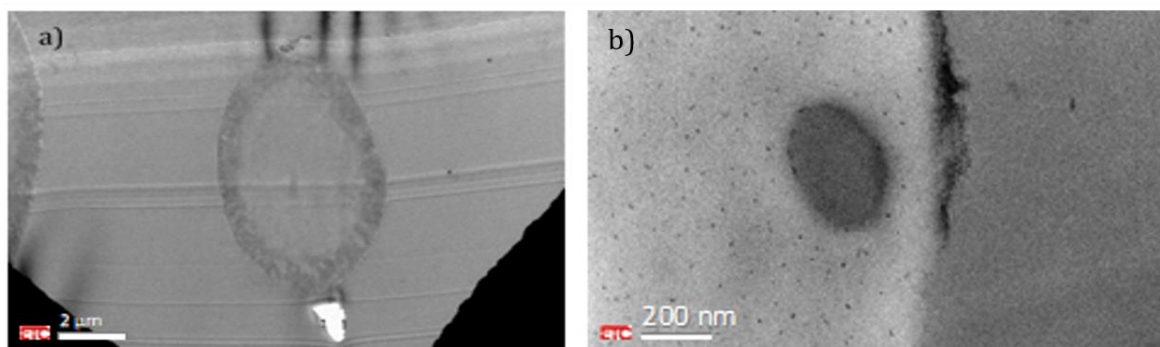
#### XI.5.3.2.1.1 CaP coated GC -core PLA PVA Microspheres

Figure XI-20a & b (again similar to its plain PLA PVA MS counterpart) shows the beginning of inorganic CaP outcrop emerging from the otherwise smooth surface of the GC-core PLA PVA MS surface.



**Figure XI-19: TEM micrographs of GC core PLA PVA microsphere coated with CaP drop cast on carbon coated copper grids (a & b).**

Imaging the cross-section images ( Figure XI-20) confirms the presence of a CaP growth. That the coating is not as extensive, as its non-cored counterpart, is just an artefact of the preparation process (i.e. the normal immersion time was reduced to half to mitigate the possibility of GC escaping during the coating process). Figure XI-20b shows the patchy coating layer on this sample's surface, with what may well be elongated CaP spikes. It was not possible to obtain diffraction rings as the region of interest was quite small.



**Figure XI-20: TEM micrographs of cross sections of GC core PLA PVA microsphere coated with CaP (a & b)**

#### XI.5.3.2.1.2 TiO<sub>x</sub> coated GC core PLA PVA Microspheres

This sample showed no positive outcome in SEM. However, TEM in Figure XI-21 does finally



prove that there is something nucleating on the external surface. The drop cast of the microspheres appear to have acquired a dense and rough exterior. While the previous samples with a CaP coating have a much more extensive growth, sometimes ruining the spherical silhouette, the coatings on this sample are rather more “intimate”.

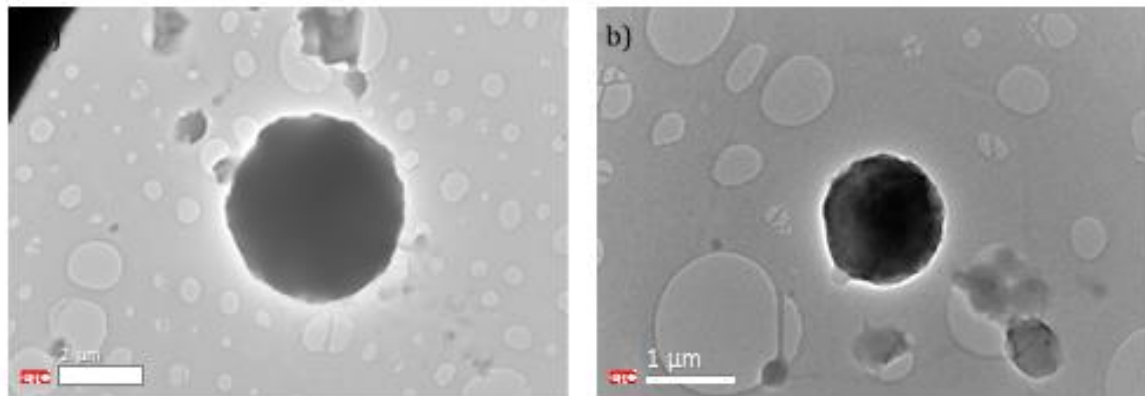


Figure XI-21: TEM micrographs of GC core PLA PVA microsphere coated with titanium drop cast on carbon coated copper grids (a & b).

Therefore in Figure XI-22, it is now more obvious why the TiO<sub>2</sub> coating appears more “intimate”. The layer width is thinner 20nm (see inset of Figure XI-22b), while CaP coating of 100-200nm thickness were seen in PLA PVA MS CaP (at its thickest).

In terms of crystallinity, HRTEM images generated contained no distinguishable lattice fringes and thus it was not possible to obtain any diffraction rings that might suggest the crystalline nature of the sample. This is likely due to the lack of any crystalline domains in the coating.

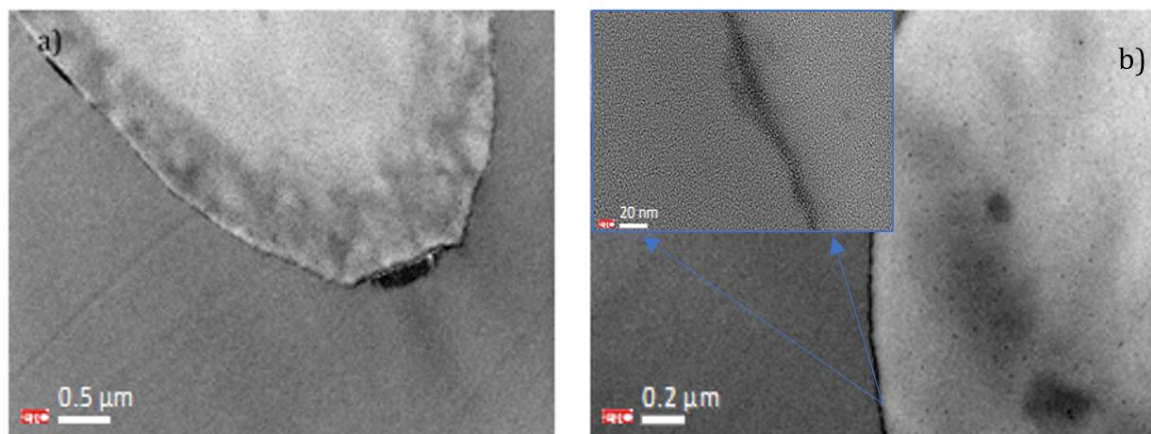


Figure XI-22: TEM micrographs of cross sections of GC core PLA PVA microsphere coated with titanium (a & b).

### *XI.5.3.3 Elemental composition of coated and uncoated microspheres*

EDX was carried out on all samples. While EDX on both TEM and SEM follows fairly similar

principles, the position/arrangement of the samples in the electron beam results in different elemental estimation. The author is inclined to believe the results obtained using TEM. Why? Because the position of the sample in TEM means that the majority (if not all) of the sample in question lies in the path of the electron beam. Thus, maximum interaction with the electron beam occurs; unlike the SEM where only the surface actually interacts with the electron beam, meaning that there is more inaccuracy.

Unless otherwise stated, EDX is carried out on only the samples that have been drop cast onto the carbon coated copper grid. For this reason, a copper peak was almost always present that was ignored. Carbon was much harder to decipher, seeing as PLA contained carbon, but realistically the peak was generated from PLA alone.

**Table XI-4: Table showing the average elemental composition (at%) of the different microsphere samples using EDX as part of a TEM set up.**

Samples	C (at%)	O (at%)	Ca (at%)	P(at%)	Ti (at%)	Na (at%)	Cl (at%)	Ca/P
PLA PVA MS/CaP	76.94	13.2	2.05	1.85	N/A	3.10	0.47	1.16
PLA PVA MS	92.70	6.13	N/A	N/A	N/A	N/A	N/A	N/A
GC Core PLA PVA MS/CaP	81.06	11.72	3.00	1.98	N/A	1.9	0.4	1.41
GC Core PLA PVA/TiO <sub>x</sub>	93.22	4.27	N/A	N/A	0.15	N/A	N/A	N/A

Table XI-4 gives the elemental composition of the different samples. They all seem to consist of effectively the same amount (i.e. before coating) of carbon (>70at%) and oxygen (>4at%) which formed the majority element of each sample. The sample that has been coated with Ti precursors seems to consist of no greater than 0.15at% of Ti when EDX was done on its exterior wall. While the amount is low, it is not a surprise as Figure XI-22 proves how thin the coating of titanium actually is.

The sample coated with CaP did seem to show a significant amount of Ca and P content which ranged in value for PLA PVA MS from 1.8-2.6at% for Ca and from 1.6-2.5at% for P; in the case of GC-core PLA PVA MS this ranged from 0.2-9.7at% for Ca while P showed a range from 0.2-6.1wt%. The average calculated ratios for PLA PVA MS and GC core PLA PVA MS were 1.16 (with a range of 0.90-1.58) and 1.41 (with a range of 1-1.58at%) respectively. The earlier hypothesis that the crystalline regions (seen in Figure XI-16 and Figure XI-20) might actually be representative of hydroxyapatite are backed by the Ca/P ratios. The calculated ratio seems to fall in line, at least at

the upper end, with a calcium deficient hydroxyapatite at 1.5 (Dorozhkin, 2012a), while the lower range (of the calculated ratio) could possibly be attributed to the amorphous calcium phosphates (Zhao *et al.*, 2011). The evidence from the FFT, micrographs and now EDX seem to point to the likelihood of apatite being the majority crystalline phase formed in addition to amorphous calcium phosphate. It is entirely possible that other calcium phosphate phases could be present, seeing as EDX is fairly discriminatory with regards to the test population.

#### **XI.5.4 XRD of the microspheres**

##### **XI.5.4.1 PLA PVA Microspheres**

###### **XI.5.4.1.1 Uncoated samples**

The main  $2\theta$  peaks attributed to PLA are  $12.14^\circ$  (101),  $14.66^\circ$  (010),  $16.55^\circ$  (200/110),  $18.80^\circ$  (203) and  $22.16^\circ$  (210) (Masaki *et al.*, 2008; Lizundia, Landa and Sarasua, 2011; Tábi, Hajba and Kovács, 2016). The two high  $2\theta$  peaks:  $16.55^\circ$  and  $18.80^\circ$ , and the  $2\theta$  signal at  $22.16^\circ$  can be attributed directly to poly lactide (Amirian *et al.*, 2013; Teng *et al.*, 2015). They are thought to be generated from the crystalline region of PLA- most likely due to the  $\alpha$  helical conformation that PLA is known to sometimes assume (Chakoli *et al.*, 2011). Chen *et al.* (2014) seems to think that the peaks corresponding to (200/110) and (203) are a result of contributions from  $\alpha$  and the  $\alpha'$  crystalline phases of PLA; while the peak for (210) and (010) are linked to the presence of  $\alpha$  which is the more stable crystalline form of PLA.

Although the systems appear similar, the PLA PVA AL MS and PLA PVA AL TA MS both show  $2\theta$  peaks at  $14.6^\circ$  and  $22.10^\circ$  which are absent in the PLA PVA MS. In PLA PVA MS the  $2\theta$  peak at  $18.8^\circ$  appears pointed but in the other samples, it is much broader, perhaps this is a direct result of the crystallite size differences caused by the various surfactant composition. SEM has showed the altered morphology and shape of the PLA PVA-AL MS (seen in XI.5.1.1.2), which could mean that the crystalline configuration of this sample has been affected. It seems likely that PLA PVA-AL MS and PLA PVA AL TA MS both contain the more stable  $\alpha$  crystalline form of PLA judging by the presence of the  $2\theta$  peaks around  $22^\circ$  and  $14^\circ$ .

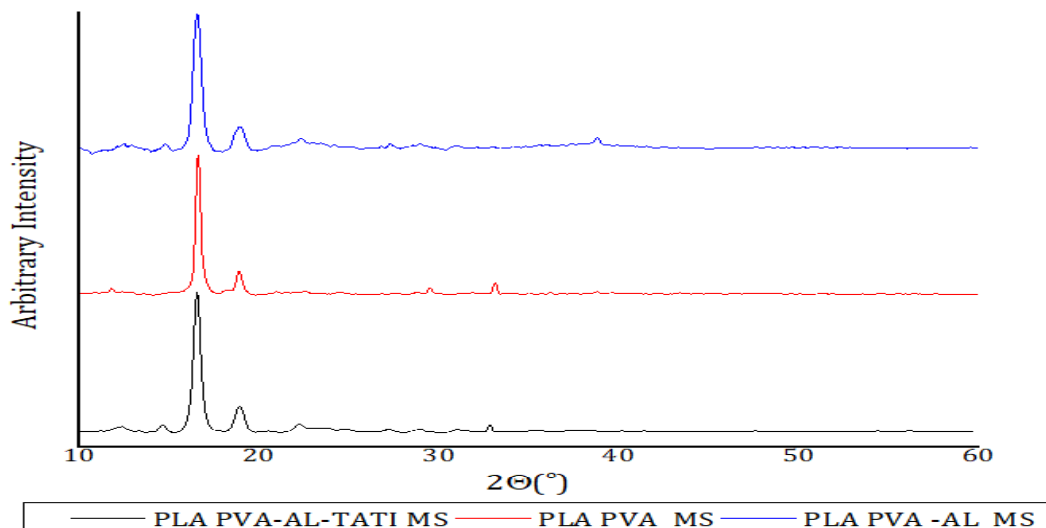


Figure XI-23: XRD patterns of PLA PVA MS, PLA PVA- AL MS, and PLA PVA-AL-TATI MS

#### XI.5.4.1.2 Coated samples

- Ca/P coated samples

The samples were made following the initial synthesis and subsequently a post-processing procedure to coat them in CaP.

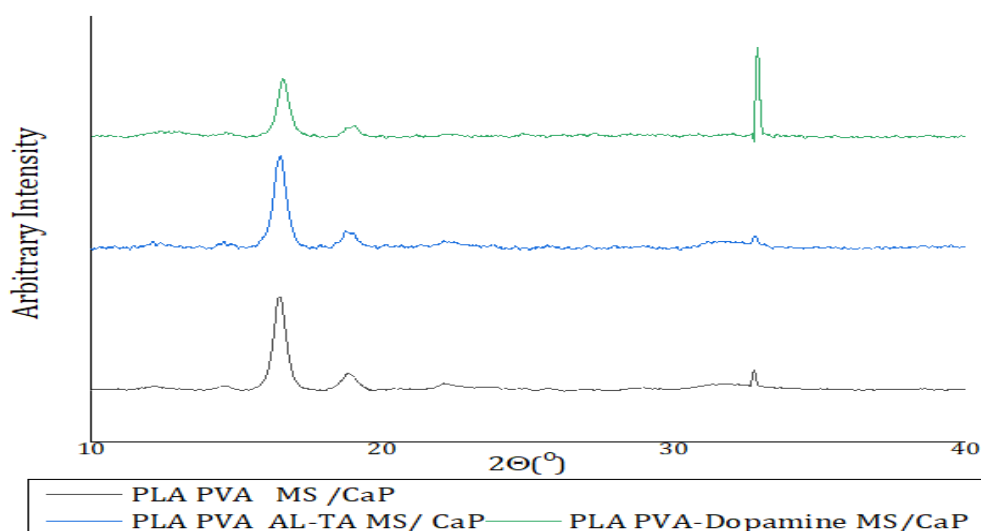


Figure XI-24: XRD patterns of PLA microsphere systems coated with CaP

The diffraction profiles shown for the CaP coated samples in Figure XI-24 are all quite similar. There however does seem to be a  $2\theta$  peak centred around  $31^\circ$  that is not present across all of the samples, only appearing for the PLA PVA MS/CaP and PLA PVA AL TA MS/CaP and not the sample dopamine sample. Perhaps the presence of this reflection is the first indication showing the appearance of a CaP-based exterior. It is broad, and generally featureless which might be due in

part to its amorphicity; the broadness might also be due to the nanoscale nature of the apatitic calcium phosphate (seen from TEM characterisation).

Other than this, the  $2\theta$  peak around  $18^\circ$  appears to be much broader in these coated samples, than in the uncoated samples (see Figure XI-23), suggesting a possible change in the crystallinity of these samples. There is also a reduced presence of peaks denoting the presence of the more stable form of PLA.

- $\text{TiO}_x$  coated samples

The samples coated using a Ti reagent were also examined with XRD. Just like the samples coated with CaP, the diffractograms in Figure XI-25 seem to only contain the characteristic peaks for PLA. Yet again, the peak attributed to the (203) reflection appears broader in these samples. As TEM suggested that the  $\text{TiO}_x$  is about 20nm, it makes sense that XRD shows no feature for anything other than PLA.

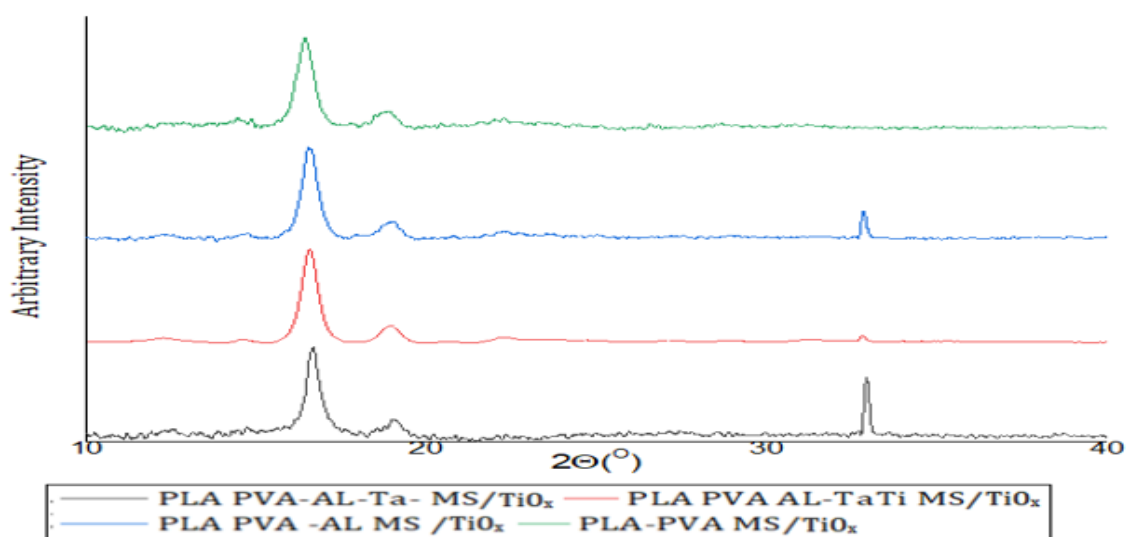


Figure XI-25: XRD pattern of PLA microspheres coated with TiBALD reagent.

#### XI.5.4.2 Drug core microspheres

The method of preparation for these samples has been presented in the experimental methodology section. The diffractograms are presented in Figure XI-26.

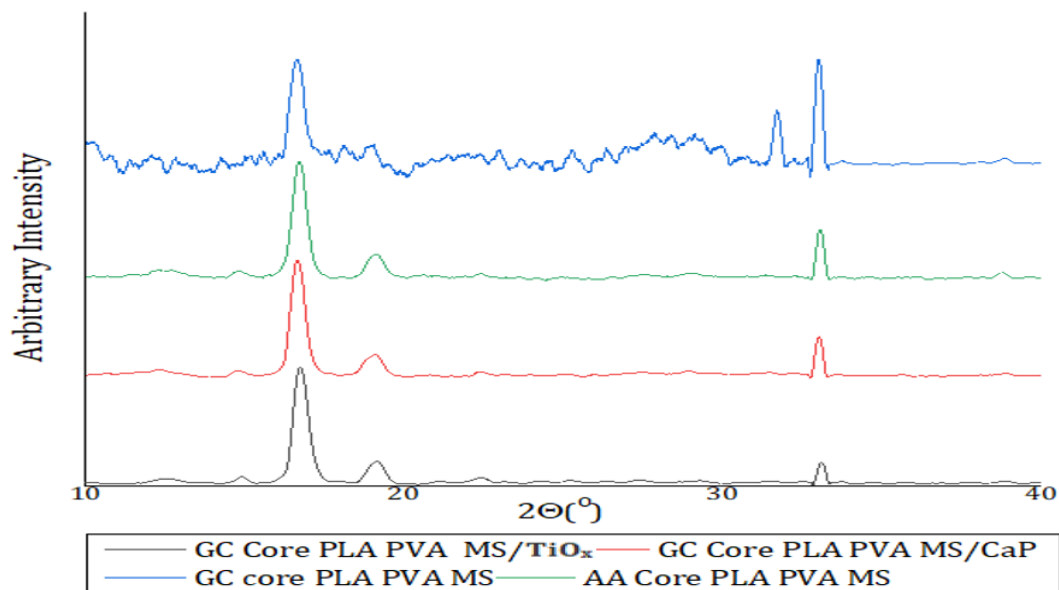


Figure XI-26: XRD patterns of drug core encapsulated PLA microspheres.

Again, all the samples examined in Figure XI-26 contain the ubiquitous peaks found in PLA (in addition with those from the support silica wafer). They appear similar to the microspheres that have undergone a coating process. There is no obvious indication of drugs being present.

#### XI.5.5 FTIR

Infrared studies were carried out on the microspheres systems in an attempt to compare the effects of using different surfactants, surface coating and drug encapsulation on the chemical signature of the microspheres. FTIR spectra underwent post processing i.e. base correction and normalisation of the percentage transmission. Where the shape of the peak was required for comparison purposes (i.e. the peak area and height) the normalised data was subjected to a peak analysis using the Lorentzian function to fit the peaks. All of these were exclusively carried out on "Origin 9".

### XI.5.5.1 PLA-PVA Microspheres

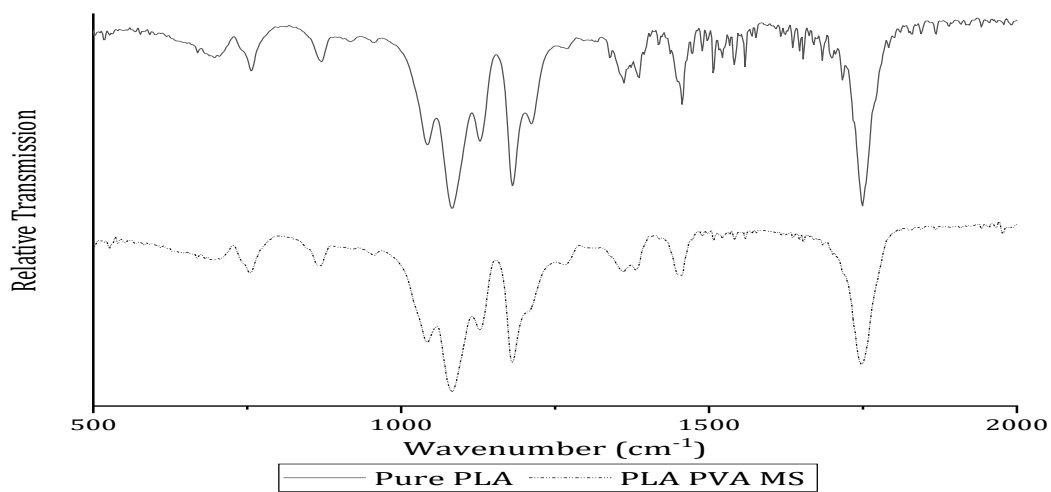


Figure XI-27: FTIR spectra of pure PLA powder and PLA-PVA Microspheres

Table XI-5 contains the infrared bands and their PLA assignments of (Kister *et al.*, 1995).

Table XI-6: FTIR Wavenumbers of Poly(L -Lactic acid) and their assignments (Kister *et al.*, 1995)

PLA powder (cm <sup>-1</sup> )	Assignments
695	$\gamma$ C=O
760	$\gamma$ C=O
870	$\gamma$ C-COO
920	$r$ CH <sub>3</sub> + $\nu$ CC
956	$r$ CH <sub>3</sub> + $\nu$ CC
1043	C-CH <sub>3</sub>
1082	$\nu_s$ COC
1128	$r_{as}$ CH <sub>3</sub>
1180	$\nu_{as}$ COC
1209	$\nu_{as}$ COC
1267	$\delta$ CH + $\nu$ COC
1361	$\delta$ CH + $\delta_s$ CH <sub>3</sub>
1381	$\delta_s$ CH <sub>3</sub>
1452	$\delta_{as}$ CH <sub>3</sub>
1747	$\nu$ C=O

The infrared spectra collected for pure PLA powder and the laboratory-synthesised PLA-PVA microspheres shown in Figure XI-27 appear to be fairly similar, almost identical. At a glance, little difference can be picked out; indeed, they both appear to contain the same peaks, occurring at similar wavenumbers.

From the aforementioned spectra, it appears that the most prominent groups observable are those that are consistent with carbon rich groups. The peak at  $1750\text{cm}^{-1}$  can be ascribed to the C=O bond which points to the presence of ester groups that are common in PLA chains. The next noticeable peaks occur around the  $1030\text{-}1130\text{cm}^{-1}$  region. Here, there is a sharp central peak occurring around  $1080\text{cm}^{-1}$ . Kister *et al* (1995) and Amirian *et al* (2013) have ascribed this peak to the symmetrical vibrations which are in part due to the coupling associated with C-CO-O -again of the ester bond. It is also linked to the stretch at  $1180\text{cm}^{-1}$  (and  $1215\text{cm}^{-1}$ ), which is as a result of the asymmetrical vibration of the ester link. On either side of the peak centred at  $1080\text{cm}^{-1}$ , there are two peaks with one occurring close to  $1040\text{cm}^{-1}$  and the other at around  $1130\text{cm}^{-1}$ . The former is ascribed to the stretching of the C-CH<sub>3</sub> bond, and the latter belonging to the rocking mode of the same bond. The peaks occurring between  $1500\text{-}1300\text{cm}^{-1}$  can also be linked to the CH and CH<sub>3</sub> vibrational modes at about  $1361\text{cm}^{-1}$ ,  $1381\text{cm}^{-1}$  and  $1452\text{cm}^{-1}$  (Kister *et al.*, 1995; Amirian *et al.*, 2013; Yuniarto *et al.*, 2016). The bands appearing from  $1000\text{cm}^{-1}$  to  $700\text{cm}^{-1}$  are medium to weak bands. The appearance of relatively weak stretches at  $950\text{cm}^{-1}$  and  $920\text{cm}^{-1}$  are assumed to be due to the rocking of the CH<sub>3</sub> modes and the vibration of the  $\alpha$ -helical PLA backbone (Kister *et al.*, 1995; Yuniarto *et al.*, 2016). The band at  $873\text{cm}^{-1}$  is thought to be associated to the C-OO bond stretching of the repeat unit. The band at  $920\text{cm}^{-1}$  is used as an indicator of the level of crystallinity of PLA (Kister *et al.*, 1995). Their presence generally means that the polymer in question has semi crystalline characteristics, while their suppression or absence may be due to the increasing amorphous character of PLA under investigation; along with this band, several bands ( $1210\text{-}1268\text{cm}^{-1}$  and  $1740\text{-}1770\text{cm}^{-1}$ ) have also been utilised as indicators to study the crystalline properties of PLA (Meaurio, López-Rodríguez and Sarasua, 2006). Finally, peaks at  $756\text{cm}^{-1}$  are associated with the in plane bending of C=O, while  $695\text{cm}^{-1}$  is associated with out of plane bending.

The first thing that may be deduced from the spectra is the absence of peaks that might be characteristic of PVA. This shows that the emulsifying process for the production of the MS was successful in only creating microspheres where the main constituents was PLA, with little to no PVA being left behind after the acquired microspheres were rinsed after the emulsifying process.

#### XI.5.5.1.1 PLA-PVA microspheres prepared using different surfactant compositions

Following the assignment of IR spectra of the purchased PLA powder and lab synthesised PLA-PVA microspheres, it has already been established that there is very little difference between the



lab prepared system and the purchased powder as far as their chemical signature is concerned.

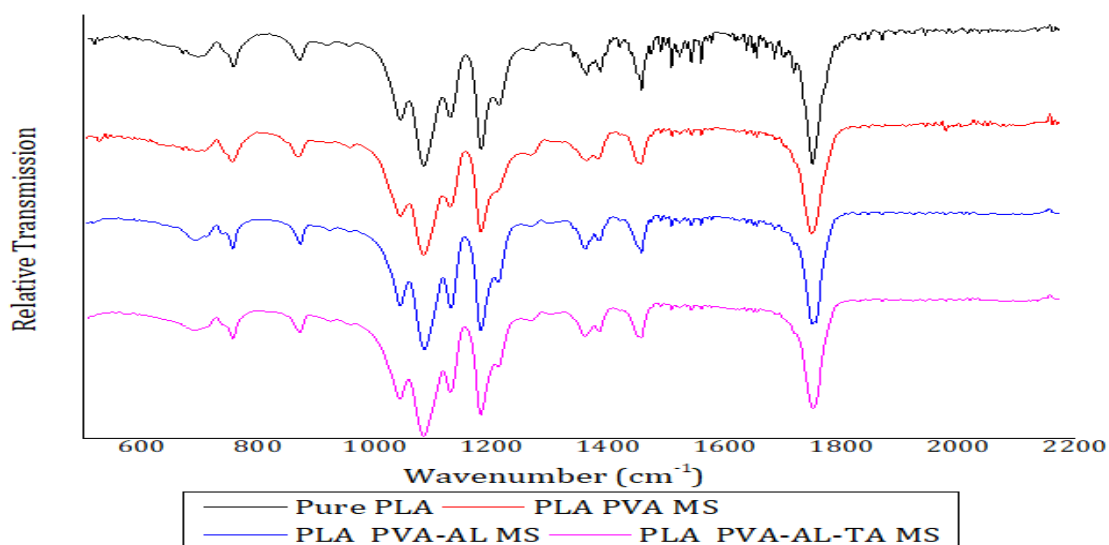


Figure XI-28: FTIR spectra of PLA-PVA microsphere systems prepared with different surfactant compositions

Figure XI-28 suggests that any modification brought about by such changes are not obvious. Indeed, the same signature peaks that were noted for the pure PLA sample and the PLA-PVA MS sample are reflected here again. Not only are the main peaks present, their wavenumbers also remain unchanged. The only observable differences are at 1180cm<sup>-1</sup> and at 1211cm<sup>-1</sup> (both of which have been linked to vibrations due to the ester link), where they both indicate some changes in the overall crystallinity of samples. The use of different surfactants appear to cause changes in the sample crystallinity.

### *XI.5.5.2 Externally-modified PLA-PVA microspheres*

#### *XI.5.5.2.1 CaP modified samples*

The samples were coated with the reagent solution containing Ca<sup>2+</sup> and phosphate ions, in a proportion that would facilitate the formation of hydroxyapatite.

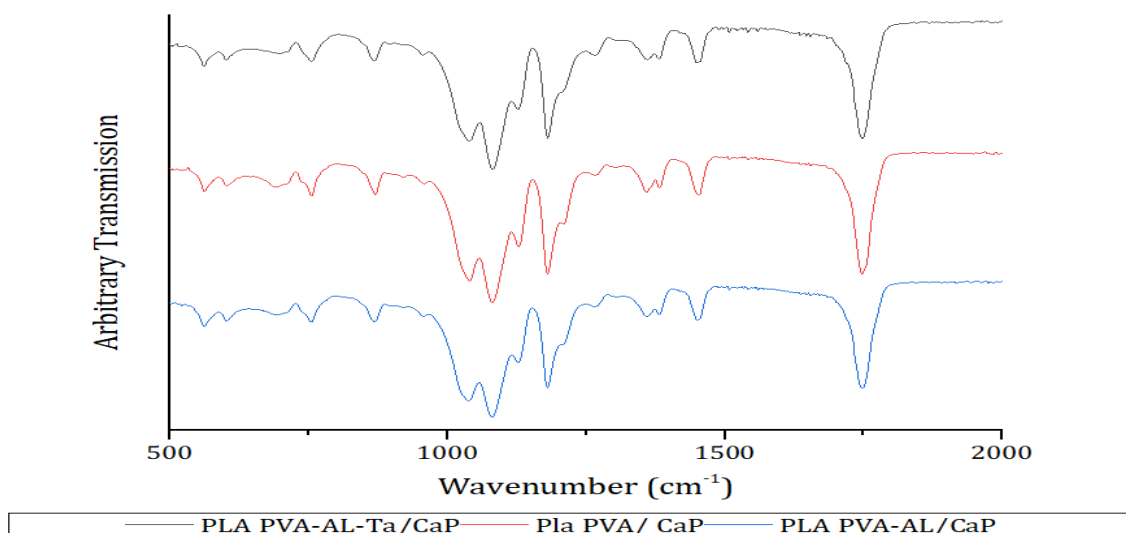


Figure XI-29: FTIR spectra of PLA PVA microsphere systems coated with CaP.

The only perceptible difference in the spectra after coating is seen in the regions between 560-600 $\text{cm}^{-1}$  and between 1040-1130 $\text{cm}^{-1}$ . In the former, two peaks (560 $\text{cm}^{-1}$  and 600 $\text{cm}^{-1}$ ) are both assignable to the bending of O-P-O for phosphate ion vibrations (Jastrzębski *et al.*, 2011). They indicate the presence of hydroxyapatites. They are absent from the PLA-PVA MS IR spectrum, which means that they are not native to normal PLA. Their ratios (560/600) are similar to Bio-Oss® (Table XI-7).

Table XI-7: Ratio of normalised peak heights at 561 $\text{cm}^{-1}$  and 601 $\text{cm}^{-1}$  using an internal reference \* calculation out without an internal reference.

Samples	560/1083	600/1083	560/600	Internal reference
Bio-Oss®	0.682*	0.324*	2.104*	N/A
PLA-PVA MS	N/A	N/A	N/A	0.701
PLA-PVA MS/CaP	0.171	0.095	1.800	0.728
PLA-PVA-AL MS/CaP	0.209	0.128	1.632	0.695
PLA-PVA-AL-TA MS/CaP	0.163	0.088	1.852	0.728

There is some deviation, with sample PLA-PVA-AL MS/CaP showing a reduction of more than 14%, and the other with a 11% increase.

In this region 1000-1130 $\text{cm}^{-1}$ , the main peaks of interest would be those at 1022 $\text{cm}^{-1}$ , 1040 $\text{cm}^{-1}$  and 1130 $\text{cm}^{-1}$  (and 1083 $\text{cm}^{-1}$  and 1382 $\text{cm}^{-1}$  as the internal references). These bands, 1040 $\text{cm}^{-1}$  and 1130 $\text{cm}^{-1}$ , had been previously assigned to C-CH<sub>3</sub> and  $r_{as}$ CH<sub>3</sub>, respectively (see XI.5.5.1.) First,

the ratios of peak height ratios will be deconstructed, then the peak areas will be considered.

It is possible to observe notable differences between the pure PLA -PVA MS system and the other systems that have been coated. There is a difference in the heights between 1040 cm<sup>-1</sup> and 1130 cm<sup>-1</sup>. Ratios were calculated (Table XI-8). The ratios of PLA -PVA MS (1.330) and its CaP (1.359) coated counterpart are not as significant as those seen for PLA -PVA-AL MS/CaP (1.547) and PLA -PVA-AL-TA MS/CaP (1.437). The peak height for the uncoated sample system (see Figure XI-28) start off fairly equal, but upon coating, asymmetry apparently grows.

**Table XI-8: Ratio of normalised peak heights at 1040cm<sup>-1</sup> and 1130cm<sup>-1</sup> using an internal reference.**

Samples	1040cm <sup>-1</sup> /1083 cm <sup>-1</sup>	1130 cm <sup>-1</sup> /1083 cm <sup>-1</sup>	1040/1130	Internal reference
PLA-PVA MS	0.50	0.38	1.33	0.70
PLA-PVA MS/CaP	0.56	0.41	1.36	0.73
PLA-PVA-AL MS/CaP	0.55	0.36	1.55	0.69
PLA-PVA-AL-TA MS/CaP	0.51	0.35	1.44	0.73

This asymmetry is not just limited to the height, but more importantly the width of 1040cm<sup>-1</sup> peak. It was thus treated as a compound peak, and deconvoluted. Two peaks emerged at 1022cm<sup>-1</sup> and at 1040cm<sup>-1</sup>. The new peak (here at 1022cm<sup>-1</sup>) is thought to belong to phosphate vibrations, it is used to indicate the presence of hydroxyapatite.

**Table XI-9: Ratio of normalised peak areas at 1022cm<sup>-1</sup> and 1040cm<sup>-1</sup> using an internal reference (1382cm<sup>-1</sup>).**

Samples	Area (1022cm <sup>-1</sup> /1382cm <sup>-1</sup> )	Area (1040cm <sup>-1</sup> /1382cm <sup>-1</sup> )	1022/1040	Internal reference
Bio-Oss®	121.77	N/A	N/A	N/A
PLA-PVA MS	N/A	16.79 (6.55)	N/A	2.56
PLA-PVA MS/CaP	10.28 (4.33)	16.45 (6.93)	0.63	2.37
PLA-PVA-AL MS/CaP	11.70 (4.51)	16.98 (6.87)	0.66	2.47
PLA-PVA-AL-TA MS/CaP	10.65 (4.53)	15.59 (6.61)	0.69	2.36

It seems that PLA-PVA-AL-TA MS/CaP might elicit more of a growth of the phosphate group when compared to the others.

#### XI.5.5.2.2 Titanium modified samples

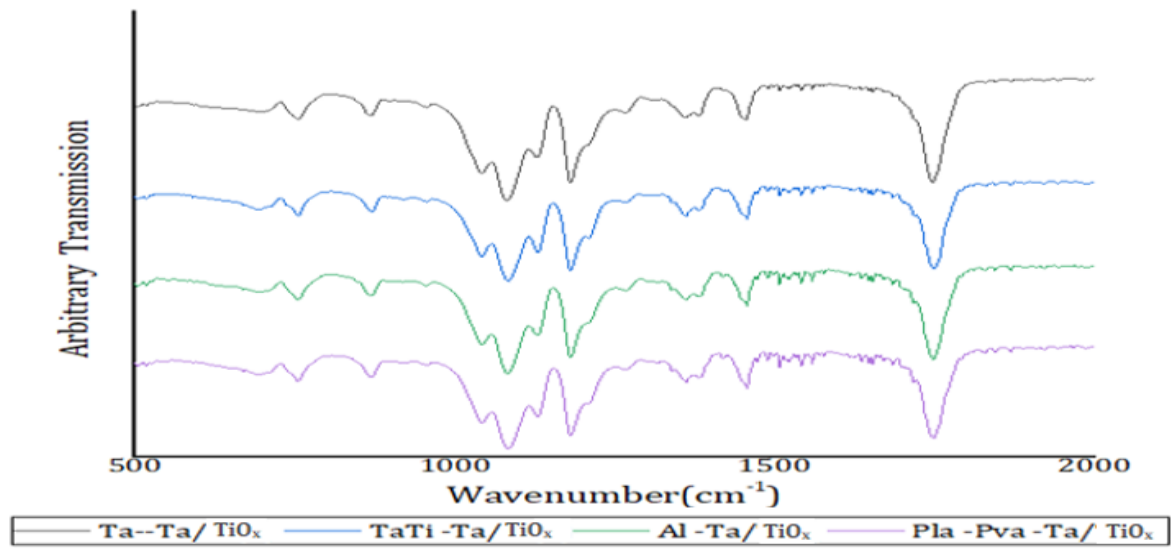


Figure XI-30: FTIR spectra of PLA PVA systems coated with TiO<sub>x</sub>.

Unlike the CaP coated samples, the titanium coated samples have negligible differences to indicate the presence of any perturbation of the bonds as a result of the addition of Ti reagent. Although this gives the impression that titanium coating was unsuccessful, TEM suggest otherwise.

#### XI.5.5.3 Drug core samples

The samples here already have drugs encapsulated in their core during their preparation including gentamicin sulphate (GC) and ascorbic acid (AA).

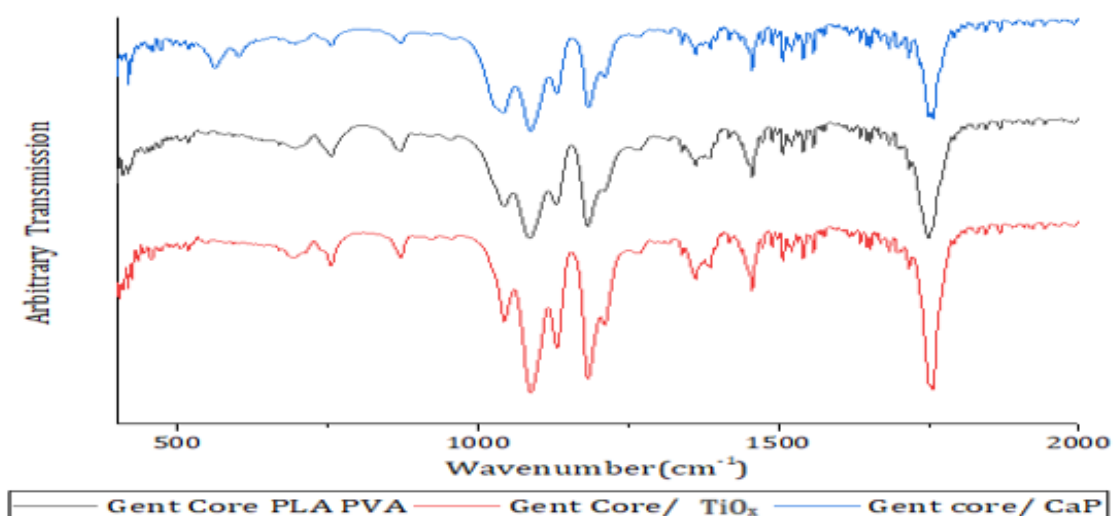


Figure XI-31: FTIR spectra of GC core encapsulated samples, with and without external coat.

The spectra of the gent core systems appear quite similar to the samples containing no drugs. From Figure XI-31, the only differences that may be picked out are those that appear standard to the plain microsphere systems. Of course, the CaP coated sample has the extra peaks associated with phosphate vibrational bands ( $560\text{ cm}^{-1}$ ,  $600\text{ cm}^{-1}$  and  $1020\text{ cm}^{-1}$ ). A similar trend is seen for the AA core system in Figure XI-32, however for the AA core CaP sample, the extra peaks associated with phosphates were absent.

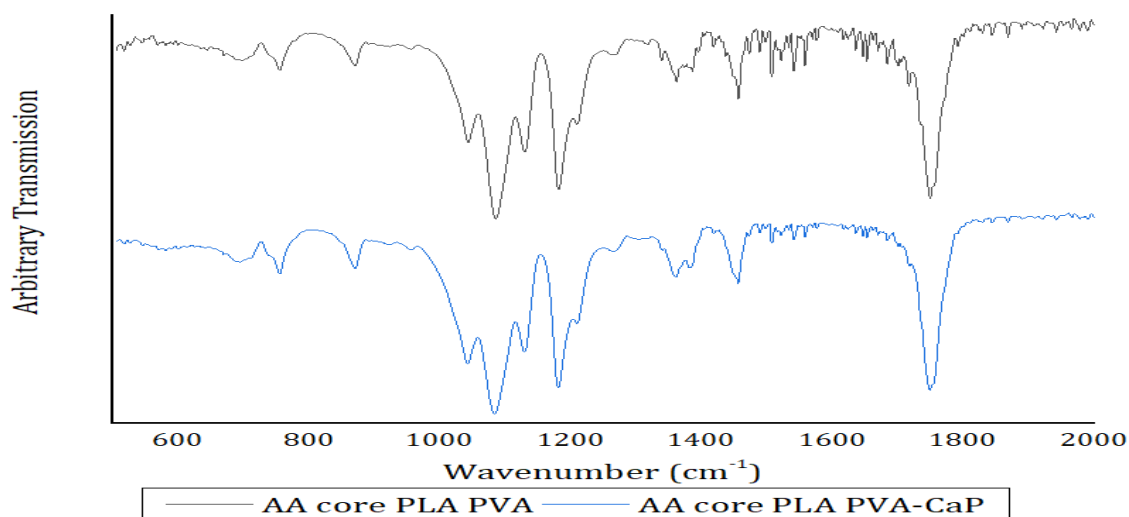


Figure XI-32: FTIR spectra of AA core encapsulated samples, with and without externally modification.

To help decipher the differences between the drug-core sample systems, the region between  $1040\text{--}1128\text{ cm}^{-1}$  will be used (Figure XI-31).

Table XI-10: Ratio of normalised peak heights at  $1040\text{ cm}^{-1}$  and  $1130\text{ cm}^{-1}$  using an internal reference.

Sample	$1040\text{ cm}^{-1}/1089\text{ cm}^{-1}$	$1128\text{ cm}^{-1}/1089\text{ cm}^{-1}$	$1040/1128$	Internal reference
AA Core PLA PVA	0.416	0.476	0.873	0.793
AA Core PLA -Ta CaP	0.56	0.48	1.16	0.72
GC-AA Core PLA PVA	0.57	0.49	1.14	0.75
GC Core PLA PVA	0.56	0.46	1.21	0.71
GC Core PLA -Ta $\text{TiO}_x$	0.42	0.55	0.77	0.81
GC Core PLA -Ta CaP	0.59	0.46	1.27	0.73

Using the ratios of the 1040 and 1130 $\text{cm}^{-1}$ , it appears that the encapsulation method or the drugs themselves have had an effect on the crystallinity of the polymer microsphere. Thus, the calculated height ratio for 1040/1128 are a lot smaller than those calculated in Table XI-8, with a difference of about 8.5% between a plain PLA PVA MS and that of a GC core PLA-PVA sample (and 34% for AA core PLA-PVA MS). This is of course not as small as that seen for GC Core PLA -Ta Ti $_{(x)}$  that is an even smaller with the GC core system at a ratio of 0.7. As these peaks are associated with CH<sub>3</sub> backbone in the polymer, it is likely that the crystallinity of the microspheres are greatly affected.

#### XI.5.5.4 Comparison of crystallinity across all samples

The relative crystallinity of the samples produced may be elucidated from IR data as previously mentioned (see XI.5.5.1). The main peaks used to identify sample crystallinity are the peaks around 1180-1280 $\text{cm}^{-1}$  and 1750-1780 $\text{cm}^{-1}$ .

- Regions 1180-1280 $\text{cm}^{-1}$  (C-O)

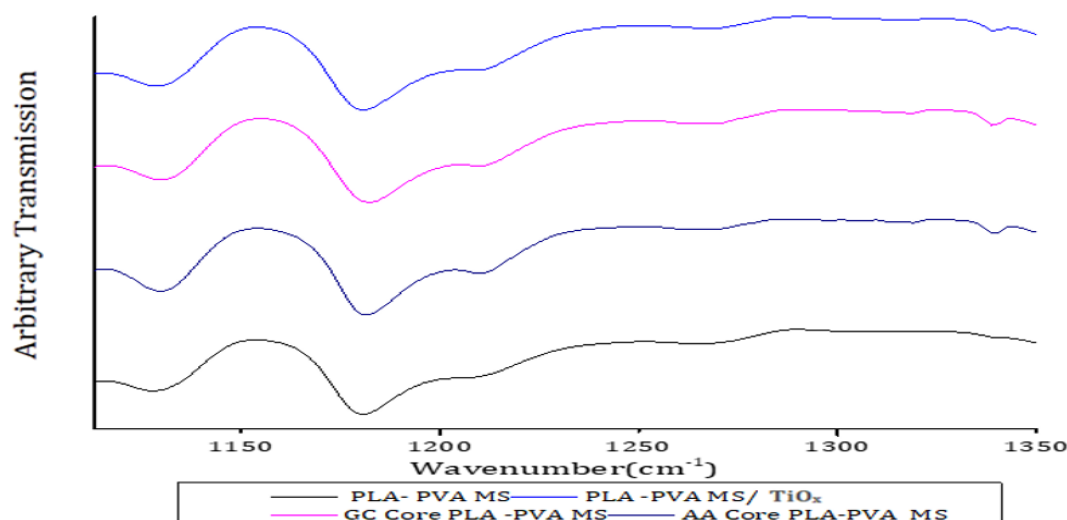


Figure XI-33: FTIR spectra showing regions 1100-1350 $\text{cm}^{-1}$  of PLA-PVA MS; PLA-PVA MS-T $_{(x)}$ ; GC-core PLA-PVA MS; and AA core PLA-PVA MS.

The bands 1180 $\text{cm}^{-1}$  and 1211 $\text{cm}^{-1}$  are the main bands of interest here. Deconstructing these peaks in the PLA -PVA sample, it is fair to say that the peak at 1180 $\text{cm}^{-1}$  is the most distinct of the two peaks (with the band occurring around 1211 $\text{cm}^{-1}$  being much weaker); it looks more like a shoulder than a separate peak in this spectral region. After some post-synthesis treatment, the peak at 1211 $\text{cm}^{-1}$  no longer appears as weak and indistinct as in the PLA-PVA spectra. Rather, it is resolvable and appears more as a distinct peak in the other samples.

The increasing distinctiveness of all the samples (except for PLA-PVA MS and PLA-PVA MS/TiO<sub>x</sub>)

appears to indicate that encapsulation has an effect on the crystallinity of the samples. The same goes for coating of the sample with CaP, judging from the spectra (Figure XI-34).

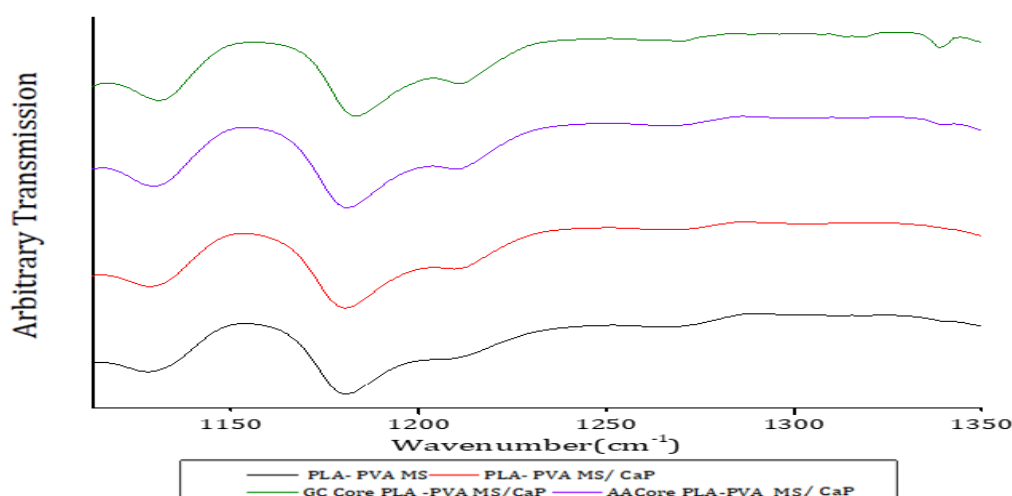


Figure XI-34: FTIR spectra showing regions 1100-1350 $\text{cm}^{-1}$  of PLA-PVA MS; PLA-PVA MS/CaP; GC-core PLA-PVA MS/CaP; and AA core PLA-PVA MS.

The inclusion of the Ca and P containing precursors might interact with the PLA helical structure. Indeed the band at 1182 $\text{cm}^{-1}$  and that at 1212 $\text{cm}^{-1}$  represent C-O ester stretches parallel and perpendicular to the helix axis (Meaurio, López-Rodríguez and Sarasua, 2006). There is a possibility that AA and GC might interfere with the normal conformation of these groups, as with CaP coating. This is probably why the peak at 1212 $\text{cm}^{-1}$  is seemingly splitting off with decreasing intensity. Meaurio, López-Rodríguez and Sarasua (2006) said that PLA samples with increasing crystallinity (whether from melt or cold crystallisation) experience splitting/growth of narrower peaks around 1195 $\text{cm}^{-1}$  and 1216 $\text{cm}^{-1}$ ; this might explain why the samples seen in Figure XI-34 have the peaks around 1212 $\text{cm}^{-1}$  that are increasingly more distinct.

- Region 1650-1850 $\text{cm}^{-1}$  (C=O)

The region between 1650-1850 $\text{cm}^{-1}$  is attributed to the carbonyl C=O stretch and also contains some crystallinity indicators, as seen in Figure XI-35. The evolution of the broad peak around 1760-1750 $\text{cm}^{-1}$  in amorphous samples is shown here, while more crystalline samples possess narrow peaks that have been recorded to split, occurring between 1758 $\text{cm}^{-1}$  and 1767 $\text{cm}^{-1}$  in melts or at 1760 $\text{cm}^{-1}$  in cold crystallized samples (Meaurio, López-Rodríguez and Sarasua, 2006). PLA-PVA MS samples (Figure XI-35) have a more centralised symmetrical peak at 1747 $\text{cm}^{-1}$  which is different from the samples that have a CaP-coating (having a non-symmetrical peak as well as a peak around 1757 $\text{cm}^{-1}$ ). Further changes can then be witnessed in the CaP-coated drug

core samples (AA core, GC core). In the case of the AA-core PLA PVA CaP coated sample, the peak appears narrower, while still showing evidence of a split at  $1749\text{cm}^{-1}$  and  $1757\text{cm}^{-1}$ . This is also reflected in the GC-core PLA PVA CaP coated sample.

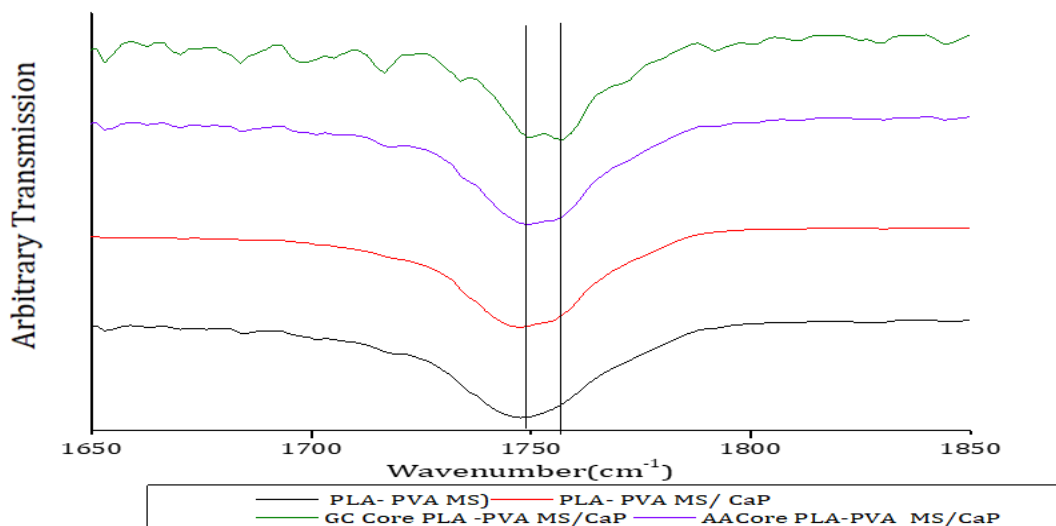


Figure XI-35: FTIR spectra showing regions  $1650\text{-}1850\text{cm}^{-1}$  of PLA-PVA MS; PLA-PVA MS/CaP; GC-core PLA-PVA MS/CaP and AA core PLA-PVA MS/CaP

In Figure XI-36, the titanium coated and PLA-PVA MS samples show similar spectra. The drug-core samples show evidence of band narrowing and splitting, similar to the coated sample seen in Figure XI-35. Clearly, any changes to crystallinity of the microspheres appear to occur upon coating or encapsulation.

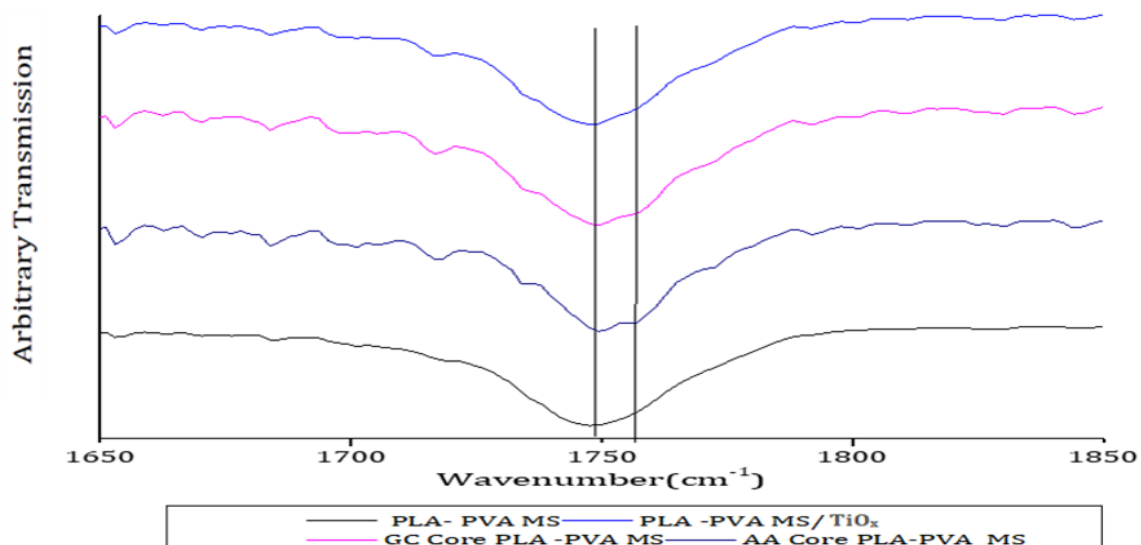


Figure XI-36: FTIR spectra showing regions  $1650\text{-}1850\text{cm}^{-1}$  of PLA-PVA MS; PLA-PVA MS-TiO<sub>x</sub>; GC-core PLA-PVA MS and AA core PLA-PVA MS



## XI.5.6 DSC

The author hoped that these properties would help in highlighting the difference between the microspheres that have been synthesised and provide a more in-depth understanding of the differences in the stabilities and crystallinities of the samples produced. With this information, it was hoped one might be able to apply the trends here to real life applications.

### XI.5.6.1 PLA PVA MS

Here, we make a brief comparison between the formed PLA PVA microspheres and the commercially obtained PLA powder.

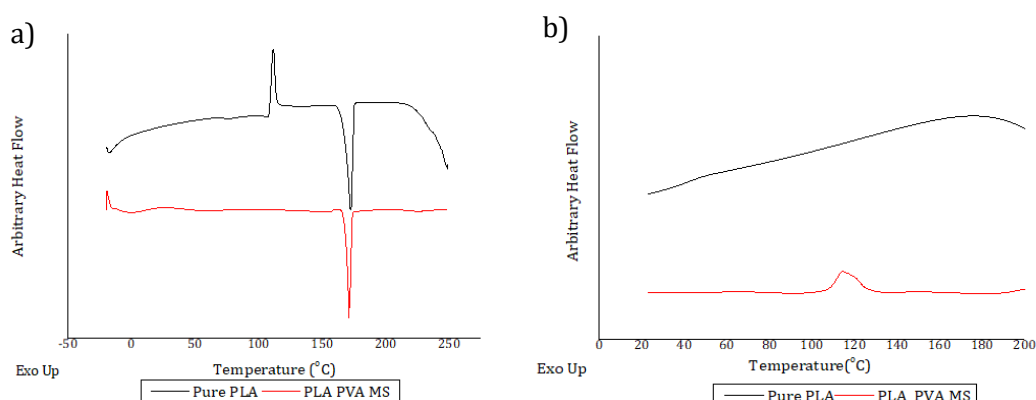


**Figure XI-37: DSC curves of Pure PLA and PLA PVA MS showing their a) heating run from -50 to 250°C; b) cooling run from 250 to 20°C. Carried out N<sub>2</sub>**

The main features that can be seen in the heating regime in N<sub>2</sub> of the DSC (Figure XI-37a) is the endothermic melting point which in both samples occur at 170°C (PLA PVA MS) and at 172°C (pure PLA). These lie within the melting range for PLA between 130-190°C (Zhao, Wang and Yang, 2005; Meaurio, López-Rodríguez and Sarasua, 2006; Chakoli *et al.*, 2011). One of the most obvious differences between both of the samples is the presence of the exothermic crystallisation peak at 111°C, again similar to those previously seen (Ke and Sun, 2003). This is due to a rearrangement of the polymer chains/cold crystallisation of a mixture of the  $\alpha$  and  $\alpha'$  occurring (Tábi, Hajba and Kovács, 2016). One can see that just before the onset of that peak, there is a minor endothermic peak, most likely the T<sub>g</sub> of the PLA. It is possible that the increased freedom of movement of the polymer chains as a result of the extra input in energy, allowed the rearrangement of the polymer chains. This is absent in PLA PVA MS which means that the sample has already undergone significant crystallisation during synthesis, which would also explain why a T<sub>g</sub> is missing, as with a cold crystallisation peak. Another important difference is the drop off of the heat flow around 200°C for the pure PLA samples. It looks like degradation has begun to occur. This feature is missing in PLA PVA MS. The enthalpy of melting for PLA PVA MS was calculated as 57.9J/g, almost comparable to pure PLA. It can thus be said that while there is some difference between the two

of these, the closeness of their enthalpies displays their common nature.

In the cooling regime b), nothing of interest occurs which is an indication that degradation in fact did occur around 200°C during heating. PLA PVA MS does show a wide exothermic peak centred at 115°C (although beginning to emerge at 128°C), indicating crystallisation of certain domains have begun to occur. It is interesting to note that while the peak for crystallisation in the pure sample was sharp, here the shape is broader.

The enthalpy of crystallisation is measured as 31.47J/g for the PLA PVA MS (compared to 19.97J/g for pure PLA)

#### *XI.5.6.2 Effects of surfactant composition on the thermal properties of PLA PVA MS systems*

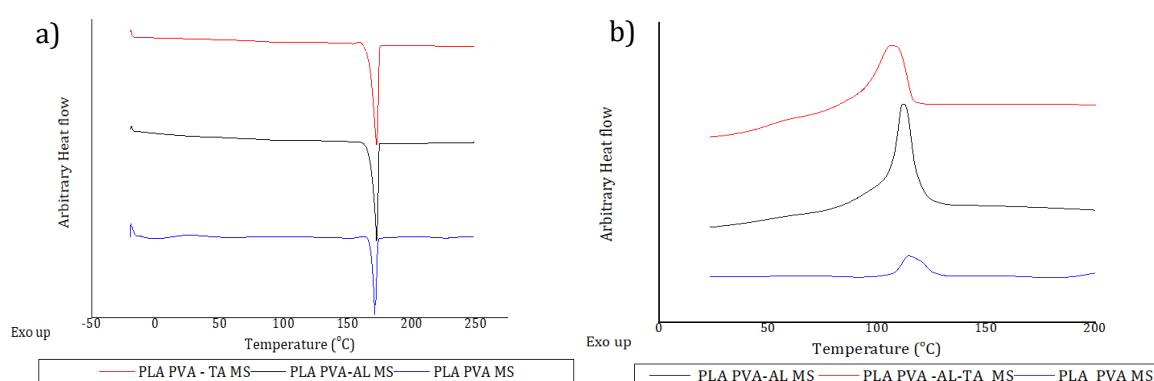


**Figure XI-38: DSC curves of PLA PVA MS, PLA PVA AL MS and PLA PVA TA MS showing their a) heating run from -50 to 250°C; b) cooling run from 250 to 20°C. Carried out N<sub>2</sub>**

Comparison between PLA PVA MS and the samples made using the different surfactant composition is undertaken here: PLA PVA MS, PLA PVA AL MS and PLA PVA TA MS. Starting from the heating regime (Figure XI-38a), it appears that all of the samples share a similar thermal event i.e. they all only undergo melting at roughly the same temperature between 170°C and 172°C. Moving onto the cooling regime, the differences become obvious. Not only is there a difference in the shape of the peak associated with crystallisation, the onset temperature of crystallisation also appears to be different for all of them. PLA PVA AL has a peak which is very similar to that associated with pure PLA, with the addition of a crystallisation temperature which occurs at 112°C. PLA PVA MS as previously mentioned has a maximum crystallisation temperature at 115°C. PLA PVA TA MS appears to have a peculiar crystallisation peak, having a maximum at around 110°C unlike PLA PVA AL MS and in part PLA PVA MS.

The enthalpies of melting for the samples here were calculated as 55.3J/g and 59.48J/g for PLA PVA -AL MS and PLA PVA-AL-TA MS respectively. All the MS systems have lower values than that of pure PLA. This is logical in the light of their spherical nature that would allow an optimum

transfer of heat through their structure than that of pure PLA. The enthalpies of crystallisation were estimated as 40.13J/g and 9.83J/g respectively (against PLA PVA MS at 31.47J/g).

### XI.5.6.3 Effect of surface coating on the thermal properties of PLA PVA MS systems

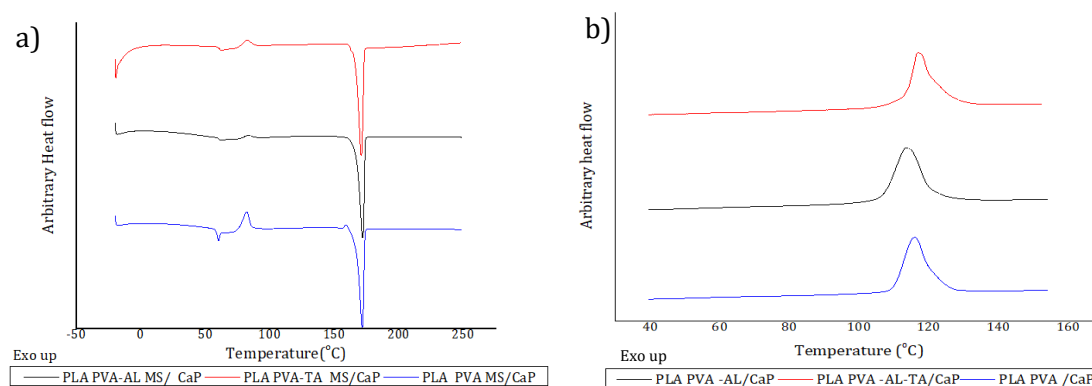


Figure XI-39 : DSC curves of PLA PVA MS/CaP, PLA PVA AL MS/CaP and PLA PVA TA MS/CaP showing their a) heating run from -50 to 250°C; b) cooling run from 250 to 20°C. Carried out N<sub>2</sub>

Therefore, coating of the sample has resulted in the appearance of new features occurring on heating of all the samples (this is beside the melting peak which again remains unaffected). These new features are present between 50-80°C: one is endothermic (centred around 60°C) and the other is exothermic (centred 80°C). The position of the endothermic peak is similar to those in literature (48°C and 59°C) (Ma, Jiugao and Wang, 2006; Chakoli *et al.*, 2011; Teng *et al.*, 2015). The exotherm indicates cold crystallisation is occurring in the samples; it is at a much lower temperature than that seen for the reference pure PLA pellet, suggesting that it is mostly  $\alpha'$  that is forming. The presence of this feature serves as some form of reassurance of the results that were extensively touched upon in FTIR (XI.5.5.4) and in XRD (XI.5.4). Syazwan and Sasaki (2018) have linked the presence of the more stable  $\alpha$  phase to the (210) reflection in XRD analysis. They explain that the shift of the (200/110) peak might also be an indication of both  $\alpha$  and  $\alpha'$  being present. In FTIR, Syazwan and Sasaki (2018) also seem to link the emergence of 1749cm<sup>-1</sup> splitting and 920cm<sup>-1</sup> as indicators of the more stable  $\alpha$  phase, and the band around 918cm<sup>-1</sup> as a possible pointer to the less stable polymorph of PLA.

The enthalpies of melting were calculated as 39.9J/g, 47.7J/g and 64.3J/g for PLA PVA MS/CaP, PLA PVA-AL MS/CaP and PLA PVA-AL-TA MS/CaP respectively. The former two samples appear to have experienced drops in their melting enthalpies as a result of coating (difference of 18J/g and 8J/g), while the latter had an increment in its melting enthalpy of 5J/g.

The enthalpies of crystallisation were calculated as 30.4J/g, 39.8J/g and 56.57J/g for PLA PVA MS/CaP, PLA PVA-AL MS/CaP and PLA PVA-AL-TA MS/CaP respectively. Unlike previously, the former samples experienced very little decrease while PLA PVA-AL-TA MS/CaP experienced an

increase of 47J/g.

Overall coating might have some effect on melting, but this does not really transfer to the enthalpies of crystallisation (for the exception of PLA PVA-AL-TA MS).

#### *XI.5.6.4 Effect of drug core loading on thermal properties*

The samples that have been covered in this section would have been made with a drug core during their synthesis process. The thermal properties of these samples will also be compared with their counterpart MS systems.

Their DSC profiles (Figure XI-40a) show that their melting points are unaffected by the inclusion of drugs (AA, GC and GC-AA) in their interiors. It would appear that the PLA encapsulating the drug has not necessarily undergone any significant event that would shift its melting point significantly. All the samples do however seem to show the possible cold crystallisation into  $\alpha'$ , which is likely due to hydrolytic action (of the drugs during Ms solidification) preventing a more complete crystallisation during synthesis.

In the cooling regime (Figure XI-40b), though crystallisation of the AA-core PLA PVA MS and GC-core PLA PVS MS begin around the same temperature (120°C), the same cannot be said for GC-AA core PLA PVA MS where its crystallisation starts around 117°C instead. Ignoring the shift in the drug cored samples, it is clear that the shape of their crystallisation peaks are quite different from drug free PLA PVA MS which began with a gentle slope and then peaked at a 116°C (see Figure XI-37). The other samples have a much steeper onset which then gently slopes off, over a longer range than all the drug free samples. It is likely that the broad shape is an indication of the scission of the polymer chain occurring, thus increasing (and adding a lower limit) to the PLA molecular weight distribution. This means a wider and lower temperature range is required to begin the crystallisation of the shorter and more mobile chain fragment; this same phenomenon was observed by Jaafar *et al* (2017), albeit with injection moulded PLA pieces. One can deduce that the drug-encapsulated samples have an abundance of crystallites covering a larger size range than the unloaded samples.

No evidence of the drugs' presence could be seen in the DSC curves.

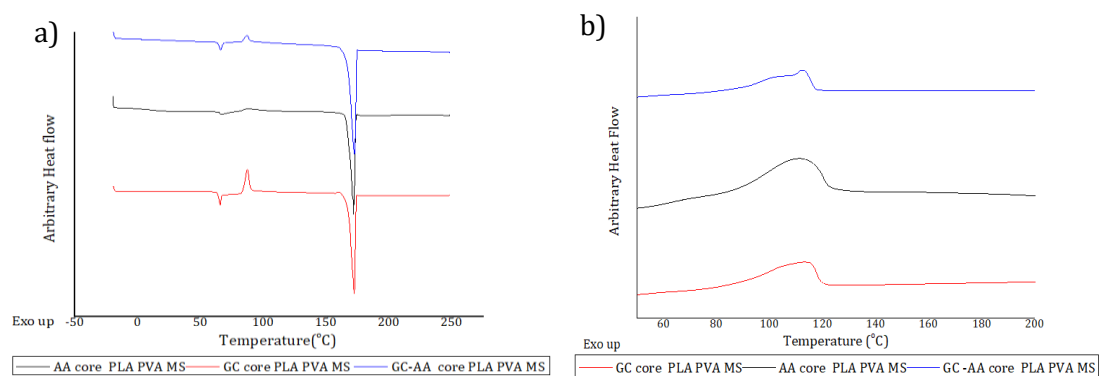


**Figure XI-40 : DSC curves of GC-Core PLA PVA MS, AA-core PLA PVA AL MS and GC-AA core PLA PVA MS showing their a) heating run from -50 to 250°C; b) cooling run from 250 to 20°C**

Interestingly enough, the enthalpies of melting were not as affected by this different synthesis process. The drug core sample had enthalpies of 55.3J/g, 53.2J/g and 59.8J/g, for AA core, GC core and GC AA core PLA PVA MS systems. The enthalpies of crystallisation were calculated as 17.6J/g, 14.12J/g and 24.33J/g. which are for AA-core, GC-core and GC-AA core PLA PVA MS systems respectively. Their crystallisation enthalpies are more varied than the melting enthalpies. It is more than likely that the nature of the encapsulated drugs have had a more severe/permanent effect on the assembly of the PLA substrate during the synthesis process, and thus directly affected the nucleation and growth of the crystalline domains in the PLA PVA substrate.

## XI.6 Summary

### XI.6.1 Electron Microscopy

#### XI.6.1.1 SEM

From the images obtained from SEM, it was clear that the method used to achieve microspheres led to the formation of smooth solid spherical particulates, after finding the optimum surfactant concentration. Varying the composition of the surfactant had an effect on the shape of the microsphere, as well as on the surface finish. The inclusion of alginate in the surfactant composition caused the formation of oblong microparticles along with microspheres (see Figure XI-4). Adding tannic acid and alginate was less disruptive than using alginate alone, although some of the microspheres appeared connected by minute bridges (see Figure XI-5). The addition of Ti precursor caused the surface to dimple extensively (see Figure XI-6). This as explained was either down to the viscosity of the surfactant, or the change in the wetting properties due to the different surfactant compositions.

Coating with CaP showed appreciable formation of surface calcium phosphate, confirmed by EDX. Only the samples coated with Ti showed no actual visual presence; the same goes for the EDX

analysis which was negative.

The GC-drug encapsulated samples appeared to be hollow and not solid, although they still maintained their spherical shape (Figure XI-9). Loading with AA was less successful. The micrographs showed completely flat microspheres in the worst case, or spheres with flattened characteristics. The surface finish of the drug encapsulated samples was also affected (Figure XI-10).

#### **XI.6.1.2 TEM**

TEM confirmed the formation of solid PLA microspheres for the PLA-PVA systems (see Figure XI-15). On the samples coated with CaP, a visible layer of CaP about 200nm thick was visible around the spheres' perimeter. The d-spacing value noted could be attributed to (300) reflection for HA.

The GC-drug encapsulated sample appeared to comprise of a homogenous core sphere, encapsulated by an outer ring with a different contrast. The striation on the outer wall suggests that it might be a material of different crystallinity, possibly higher due to the abundance of darker contrast regions (Figure XI-18). The CaP coated samples like the drug free system possessed a layer of CaP needles, whose presence were confirmed with EDX, possessing a ratio close to that of calcium orthophosphate compounds.

Interestingly, the Ti coated had a subtle coating, which was missed on SEM but appeared to be less than 20nm wide (Figure XI-22) in TEM. Unfortunately, the dimension made deduction of crystalline fringes difficult. EDX did however confirm the presence of Ti, along with C and O(see Table XI-4).

#### **XI.6.2 XRD**

All the microsphere systems appeared quite identical, with only reflections that originated from PLA. This confirmed the success of the emulsion preparative process and the complete removal of the PVA and modified-PVA surfactants (Figure XI-23). However, the samples made with modified surfactants appeared to contain the more stable  $\alpha$  PLA phase.

After coating of the samples with CaP (Figure XI-24) and Ti (Figure XI-25), very little change to the XRD patterns could be picked out. The sample coated with CaP showed a very broad  $2\theta$  peak around  $31^\circ$ , which could possibly be a reflection that attributed to HA, because PLA has no known reflection in that region. Other than that, the coated samples appeared to show a broadening of the peak around  $2\theta = 18^\circ$ , which is known to belong to the less stable  $\alpha'$  crystalline phase of PLA. In addition, a reduction in the intensity of  $2\theta$  peaks at  $14^\circ$  and  $20^\circ$  could mean that  $\alpha'$  crystalline PLA phase is more dominant now. This could be because of the plasticizing effect of  $H_2O$  during the coating process as well as some hydrolytic action on the crystalline chain ends and free

amorphous zone of the polymer by the salt precursors (Tsuji, Mizuno and Ikada, 2000). As the hydrolytic action on PLA leads to an increase in the density of carboxyl groups and hydroxyl groups, from ester hydrolysis, these groups can interact with the metal salts, further eroding the PLA matrix.

The same appears to go for the drug-encapsulated samples. The peak around  $18^\circ$  looks to be rounded with a loss of the  $\alpha'$  crystalline peaks, suggesting some change in the crystallinity of PLA caused by loading drugs.

### XI.6.3 FTIR

The spectra of pure PLA pellets and the microspheres show very little difference in term of the bands' presence as see in Figure XI-27 and Figure XI-28. The results from these confirms yet again that the microspheres are wholly made of PLA, with no interference from the emulsifying surfactant. However, some perturbation of the peaks at  $1180\text{cm}^{-1}$  and  $1211\text{cm}^{-1}$  is seen, which are thought to indicate changes in a sample's crystallinity.

Upon coating the samples with CaP, in addition to native PLA peaks, FTIR confirmed the presence of the phosphate bands ( $560\text{ cm}^{-1}$  and  $600\text{ cm}^{-1}$ ) that are often used to signal the presence of apatitic calcium phosphate. Using the ratios calculated for 560/600 (Table XI-7), it appears that the ratios are similar to those seen for Bio-Oss<sup>®</sup>. Several factors including the type of apatite formed, and the preparation conditions might have affected the ratios. Further analysis of these ratios was used to highlight the differences between the coated microsphere samples were carried out (Table XI-8 and Table XI-9) to look at the changing height ratios of the peaks at  $1040\text{cm}^{-1}$  and  $1130\text{cm}^{-1}$  and area ratios of the deconvoluted peak  $1040\text{cm}^{-1}$ . Both of which highlight the asymmetry caused by the presence of phosphate groups introduced during the coating. The sample coated with Ti did not seem to show any real changes that could be followed.

Moving on to the drug-core coated samples, the introduction of drugs seem to have caused an effect on the PLA matrix (as shown by the  $1040\text{cm}^{-1}/1128\text{cm}^{-1}$  ratios calculated in Table XI-10). The ratios were all lower than (Table XI-8) for the drug free samples. This suggests that the presence of the drugs has had an effect on these bands, which is likely a manifestation of the conformation taken up by the group C-CH<sub>3</sub> ( $1040\text{ cm}^{-1}$ ) and CH<sub>3</sub> ( $1130\text{ cm}^{-1}$ ) groups in response to hydrolytic breakdown or other rearrangement.

Comparing all the samples highlights the changes that coating and drug loading has caused compared to the drug free sample, which has a low crystallinity as suggested by the lack of peak splitting at  $1750\text{cm}^{-1}$  in Figure XI-35 and Figure XI-36. The coated samples, except PLA PVA MS/TiO<sub>x</sub>, have bands in various stages of splitting and asymmetry, pointing to a change in crystallinity. XRD points to an evolution towards  $\alpha'$  (for the drug encapsulated and coated

samples), it is conceivable that the samples are becoming increasingly crystalline (albeit into a less stable form). No doubt, the plasticising effect of being placed in a liquid for a long period could have contributed to chain motion in the matrix. This along with chain scission of the ester links, and autocatalytic reaction by the terminal links carboxylic groups, could be responsible for the evolving crystallinity (Tsuji, Mizuno and Ikada, 2000; Alexis, 2005).

#### XI.6.4 DSC

DSC (Figure XI-37) shows that the levels of crystallinity in the reference PLA are different from the synthesised PLA PVA MS microspheres. The reference samples appears to undergo cold crystallisation around 111°C, which was absent in the microsphere system, suggesting that synthesis of the microsphere allows their extensive crystallisation of the samples. The melting point temperature is similar for both samples, highlighting their chemical commonality. However, the reference suffers degradation soon around 250°C (seen by the drop in heat flow in Figure XI-37a) causing the lack of a crystallisation peak (Figure XI-37b). PLA PVA MS underwent no degradation and crystallises upon cooling.

Despite a change in the composition of the surfactants used, the melting point temperature remains roughly the same (170-172°C) for the samples in Figure XI-38a. The crystallisation temperature ranges between 110-116°C for all of the samples.

Coating of the samples with CaP added a transition endotherm and a cold crystallisation exotherm to all samples (Figure XI-39a), coinciding with those found in literature. The presence of the cold-crystallisation peak suggests that the coating process has resulted in a change in the crystallinity of the samples (which confirms the evidence seen from XRD (see section XI.5.4.1.2) and FTIR (see section XI.5.5.2)). After the heating run, the polymer chain now have enough energy to allow reorganization of the PLA chain; hence the presence of a similar crystallisation peak (Figure XI-39b). The fact that the  $T_c$  is higher here (~ 117°C) than in the uncoated samples is likely to do with the presence of the CaP mineral, which in addition to its higher temperature stability might have migrated through the softened samples, allow better temperature distribution and resilience.

The inclusion of the drugs left the melting temperature unaffected; however, the samples in Figure XI-40a again contained the peaks pertaining to glass transition and cold crystallisation, signifying the same scenario that has caused these peaks appearance for coating, are replicated here again. On cooling, as shown in Figure XI-40b, the crystallisation peak is again present at a similar temperature, but this time, the peaks appear stretched out. The hydrolytic process occurring here is likely more severe than simply coating, as drug encapsulation occurred during synthesis, rather than as a post modification reaction. Clearly, the loading of drugs has had quite



an effect on the crystallinity of the samples.

## **XI.7 Conclusion**

The chapter was primarily aimed at the development of microspheres and drug encapsulated microspheres, which were then coated with an apatitic calcium phosphate. Microscopy (XI.5.1 and XI.5.3) confirms the formation of solid mostly spherical microspheres, and GC-encapsulated microspheres with what appears to consist of a core sphere surrounded by an exterior wall.

The crystallinity of the samples, along with their morphology, appears to be a property that undergoes quite a degree alteration. It appears that drug-free samples contain the more stable  $\alpha$  form, which is absent in PLA PVA MS (see Figure XI-23). However, upon coating with CaP and titanium, the presence of the  $\alpha$  form decreases, or rather, the  $\alpha'$  form grows (Figure XI-25 and Figure XI-26). This change in crystallinity is manifest in FTIR analysis, with the splitting of the peak around  $1750\text{cm}^{-1}$ , known to be coupled with increasing crystallinity, being more evident in the coated samples (see Figure XI-34 and Figure XI-35). FTIR also confirms the presence of CaP on the microspheres as seen in SEM (Figure XI-7) and TEM (Figure XI-15). The presence of titanium was more elusive but confirmed in Figure XI-22. Also, the drug encapsulated samples showed a change in crystallinity which was seen again in Figure XI-35 and Figure XI-36.

It is clear that the methodology used here to obtain microspheres, with and without drugs, was successful, and the means to coat them was also positive. It remains to see what the effect of the changing crystallinity might have on the sample in terms of drug release. Whether the microspheres can also self-assemble to colloidal crystals remains to be seen in the future.

## Chapter XII Drug (GC) release of the prepared microsphere systems

### XII.1 Introduction

The synthesis of PLA PVA microsphere systems has been investigated along with effects caused by using different surfactant concentrations, the coating process, as well as encapsulation. We have seen that besides the change in the morphology, the other main property to change is the crystallinity. One way to investigate the effects of these designed properties on the microspheres is through their drug release. A study of this is important as it gives one a better understanding of how these microspheres would function as drug delivery vehicles while in in-vivo, additionally offering some insight into their degradation (and long-term stability). As discussed, a drug delivery system needs to be able to release its payload in a sustained manner over a designated period of time. This is especially important if it is going to be utilised in conjunction with bone graft or other bone regenerative treatments, where an infusion of antibiotic, growth factors, proteins and other molecules may be required at the implant site. Specifically their use with antibiotics, as orthopaedic surgeries carry a 4.3% infection risk (Guo *et al.*, 2013). The release profile is quite important in order to prevent systemic toxicity and patient discomfort (Chung and Chung, 2001).

This investigation therefore probes the release of GC, which is an important antibiotic utilised in orthopaedics because it is able to treat a wide range of infections (Dorati *et al.*, 2017). Here GC is introduced to the microspheres as either an adsorbed or an encapsulated specie. GC subsequent release will be followed using Raman spectroscopy.

### XII.2 Background

Gentamicin is a broad spectrum antibiotic, usually included in implants as a means to halt infection (Guo *et al.*, 2013). Its widespread use is no doubt assisted by its low cost, high temperature stability and low pathogen resistance (Guo *et al.*, 2013). Its use is plagued by problems associated with its low bioavailability: mainly because it is sequestered into lysosome that then reduces its activity (Dorati *et al.*, 2017). Another problem with GC is its persistence. It is known to accumulate in the renal cortex and can cause nephrotoxicity if its dosage is not closely monitored. Besides nephrotoxicity, GC is also known to cause ototoxicity because of its ability to induce free radical formation. It makes sense that a more measured approach to introduce GC, or any other drug that might be equally harmful, in a controlled manner should be sought after.

One way to achieve this is through the use of host polymeric microspheres. These would normally function by releasing the drugs through controlled-diffusion, and/or the degradation/erosion of the polymeric matrix (Makadia and Siegel, 2011).

The use of microspheres to uptake and release GC is quite popular. GC drug delivery systems have been made out of bioactive glass, hyaluronic acid, chitosan, PMMA, PLGA, PLA and hydroxyapatite (Chung and Chung, 2001; Guo *et al.*, 2013; Dorati *et al.*, 2017; Abdul Hamid, Tham and Ahmad, 2018). However, these materials themselves are affected by problems with hydrophobicity, poor stability in an aqueous environment and inertness.

Some questions present themselves. Through the surface deposition of CaP layers, as shown in the previous chapter, will the samples that have been obtained display a better drug release pattern? Would the presence of the CaP layer improve or make worse the uptake of cationic GC? With the complications of nephrotoxicity and ototoxicity associated with GC (Dorati *et al.*, 2017), would it be possible to introduce AA which has been shown to protect humans against GC induced nephrotoxicity (Mal *et al.*, 2012; Moreira *et al.*, 2014)?

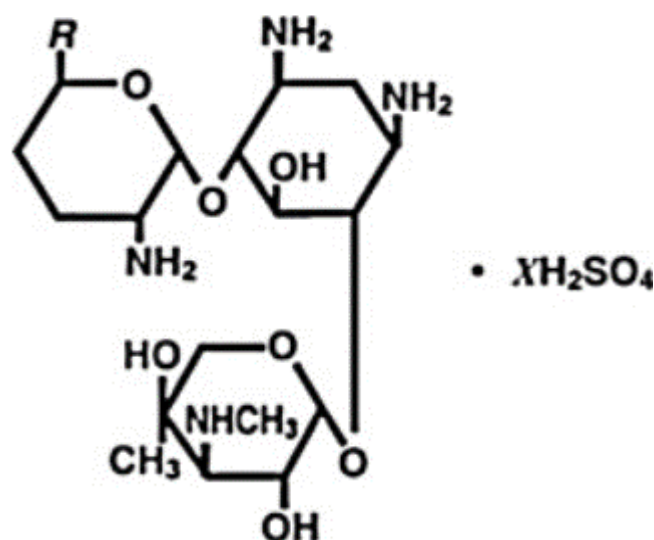


Figure XII-1: Molecular structure of gentamicin sulphate (Radhakumary and Sreenivasan, 2014)

### XII.3 Aim

The main aim of this chapter will be to probe the drug release functionality of the synthesised samples. This will involve monitoring the GC drug release pattern of microspheres on which the drug is adsorbed or encapsulated in. The samples with CaP coating will also be compared to establish whether the CaP over-coating is advantageous or not.

By the end of this chapter, a comprehensive understanding of the microspheres release profile and the associated changes in their morphology and thermal properties will have been investigated and discussed, with an aim to establish the potential use of these microspheres as drug-releasing bone-graft substitutes.

## **XII.4 Methodology**

Sample preparations were described in section II.6 for the drug encapsulation procedure for GC and AA. Surface adsorption of the drug and its release is described in XII.4.1.

### **XII.4.1 Experimental setup**

- Drug surface loading/adsorption :
  - 5mg of the microspheres was placed in sample bottle
  - 5ml of 10mM of the drug solution was added.
  - The samples were left for 12h with agitation
  - Raman readings were done by collecting 0.02ml of the supernatant and analysing
  - Surface loaded MS were collected and dried at 40°C in an oven 5h
- Drug release
  - 5mg of the encapsulated (and drug-adsorbed samples) were placed in 1.5ml of Tris buffer solution in a 37°C incubator, with agitation of 70rpm
  - Raman readings were done by collecting 0.02ml of the supernatant and analysing
  - reading were carried out twice daily
  - 0.02ml of Tris was added back to keep the volume the same

### **XII.4.2 Analytical instruments and conditions**

#### **XII.4.2.1 Raman spectroscopy**

Raman spectroscopy measurements was carried out using 10% power. The integrated time for signal collection was at 30s, for 3 accumulations, 5x objective. The spectra of 3 random areas were collected to provide a suitable average. 0.02ml of the supernatant was simply deposited on an aluminium covered glass slide for readings.

#### **XII.4.2.2 SEM**

Before analysis, the samples were dispersed onto a microscope slide and dried at 40°C for 3-4h. They were then placed on carbon tape on a SEM stub, where they were coated with an Au target for 60sec.

#### **XII.4.2.3 DSC analysis**

All of the samples were sealed in a hermetic pan made of aluminium. The specimens were first cooled to -50°C, and then with a heating rate of 10°C/min in N<sub>2</sub>, the samples were heated through to 250°C. Upon reaching that temperature, the specimen were then cooled back to 23-27°C with the same ramp rate. All the data obtained were individually processed on Origin 9 pro.

## XII.5 Results

### XII.5.1 Drug surface loading and release studies

#### XII.5.1.1 UV-vis and Raman spectroscopy

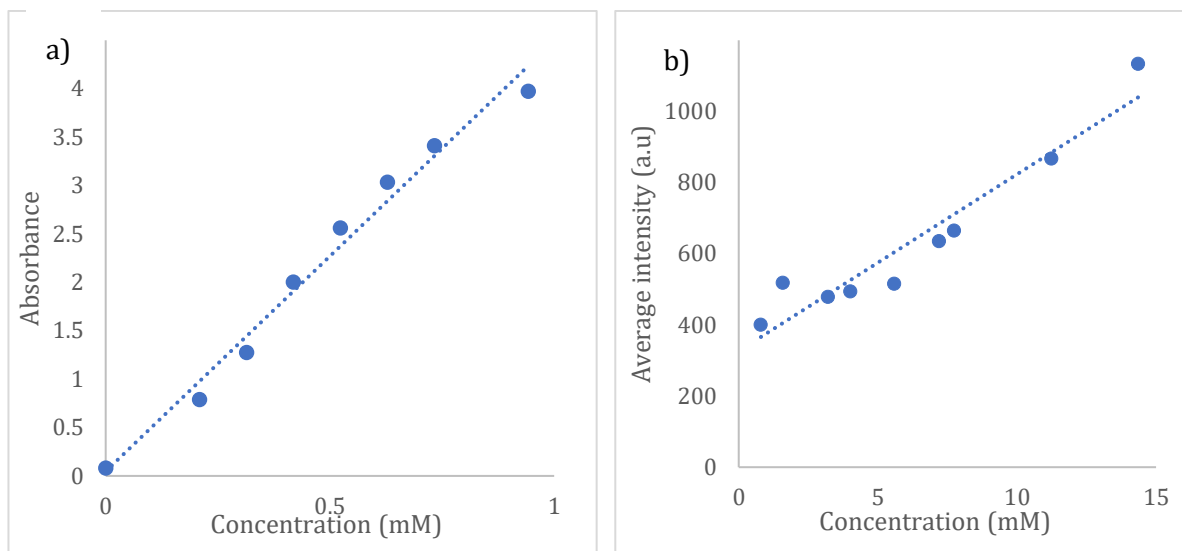


Figure XII-2: Calibration curve of gentamicin sulphate using UV-vis spectroscopy a); Raman at  $\approx 980\text{cm}^{-1}$  b)

Drug uptake and release of GC may be monitored using UV-vis spectroscopy; however this requires treatment with ninhydrin to create an intermediate compound that is detectable in visible light (Frutos *et al.*, 2000). The UV-vis method has an upper and lower threshold of 1mM and 0.2mM respectively. GC loading and release can be followed using Raman spectroscopy (Zaleski *et al.*, 2017).

Raman was chosen as one of the chief analysis systems due four reasons.

- i. The speed compared to the UV-vis. While the latter required at least 20min to instigate and colourise the GC present in the buffered medium, Raman spectroscopy took less time with the possibility of completing a sample reading within 5s.
- ii. This is to do with post processing of the samples, Raman spectroscopy required no post processing to analyse GC, while the UV-vis method required a reaction with ninhydrin to produce the coloured intermediate. Raman probed GC unchanged (rather than coupled with ninhydrin).
- iii. This is to do with the probe quantity required for analysis. UV-vis required a larger amount that could maintain the volume ratio between gentamicin to ninhydrin (5ml :1.5ml) that would demand a larger ratio of microspheres to liquid to ensure that that the minimum threshold for drug detection could be attained in all of the samples. Raman was therefore an attractive analysis method since as it required as little solution (0.02ml) for an accurate

enough reading.

- iv. Raman could be used to easily detect a wide range of between 0.7mM to 14mM of gentamicin, which falls in the clinically relevant range (2-4mg/ml equivalent 5-10mM) (Zaleski *et al.*, 2017).

### **XII.5.1.2 GC drug loading studies**

A measurement of GC uptake was attempted. Unfortunately, due to the high concentration of the loading solution, the changes in concentration of the loading solution impossible to follow using Raman.

### **XII.5.1.3 GC release studies**

Seeing as the loading profile of GC into the non-cored PLA PVA MS systems was not followed, the GC release profile will be studied instead as a means of comparing the efficiencies of GC release amongst all of the samples taking part in this study.

#### **XII.5.1.3.1 GC release in PLA PVA MS system with varying surfactant composition**

The first thing that will be noticed is the presence of negative GC concentration at 0mM. This is an artefact of the fluctuating Raman signal that has been averaged over 3 spot areas, not to mention the added complication that the actual drug release studies were carried out in a buffered solution rather than the deionised water as used during the calibration (Figure XII-3).

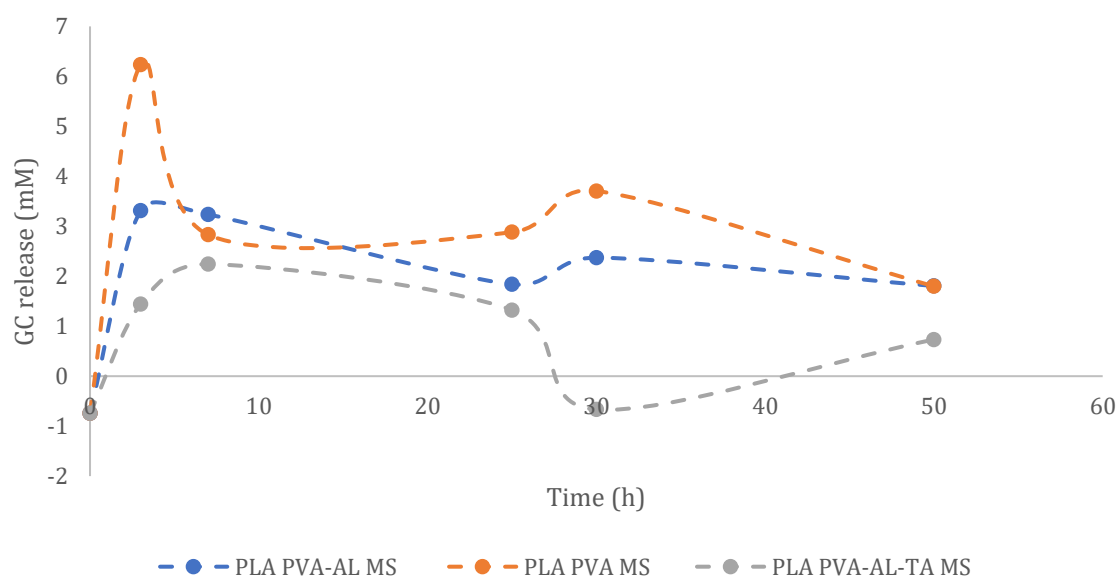


**Figure XII-3: GC release from PLA PVA MS systems with time. Dose: 1mg of microspheres per ml of TRIS-HCl buffer (pH7.4) at 37°C over 50h.**

Two of the samples in Figure XII-3 (PLA PVA-AL MS & PLA PVA MS) appear to have experienced quite a substantial initial burst of GC within the first 3h (3.3mM & 6.2mM). This is most likely due

to the drug molecules that were just superficial held on the surface of the host. This burst was not seen in PLA PVA-AL-TA MS which showed a fairly modest GC release of just about 1.4mM with a gradual reduction of accumulated drug to about 0.7mM (accounting for 49% drop in released GC in the solution), when the experiment was then terminated. PLA PVA-AL MS exhibited a similar drop in released GC concentration of about 47%, while PLA PVA MS registering the most drastic drop (~ 70%).

These results suggest that the systems created here by the author do seem to have some form of appreciable drug loading and release properties, judging by the initial release in addition to the sustained maintenance of an appreciable raman signal across the 50h monitoring period. This potential is substantial. While the initial high release behaviour of two of the systems could be problematic, owing to the known toxicity of gentamicin, the persistence of the elevated release over the 50h period might be useful in a situation where a high sustained release at a specific drug site is required. One may in future be able to nanoengineer out the initial fast GC release. PLA PVA-AL-TA MS has a very interesting behaviour in GC release. Although it releases the least amount of GC compared to the other systems, it does have a smoother release that is consistent. This behaviour would make it an ideal drug release device. Although care needs to be taken in terms of the area of implantation, seeing as the persistency of PLA (i.e. its slow degradation) in addition to the degradative product could create further problems at the site of use.

#### XII.5.1.3.2 Drug release studies in PLA PVA MS/CaP system with varying surfactant composition

Just like the samples in the previous section, the starting concentration starts below the 0mM mark (see Figure XII-4). But no sample (including Bio-Oss®) show significant GC release to the buffer solution.

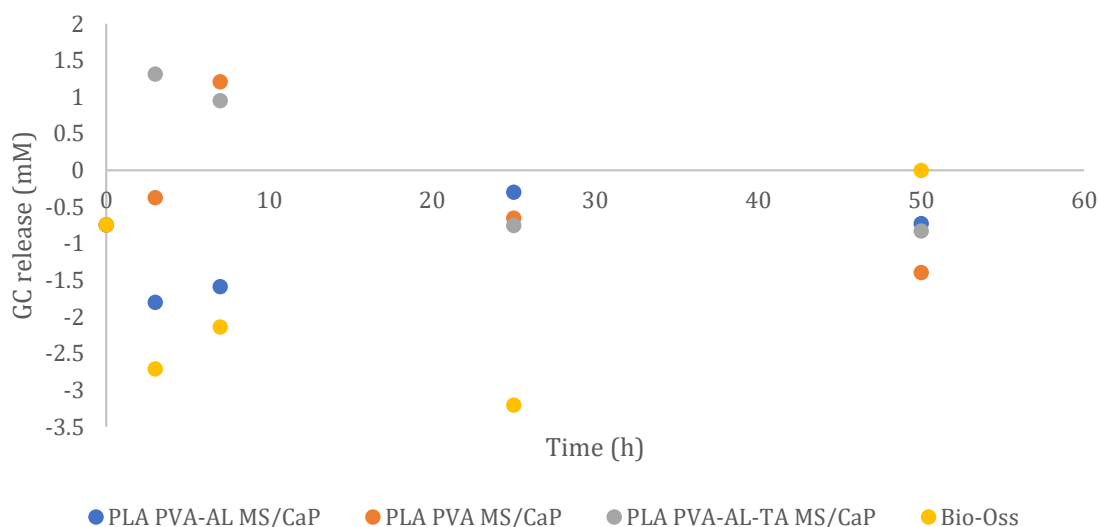


Figure XII-4: GC release from CaP coated PLA PVA MS systems. Dose: 1mg of microspheres per ml of Tris-HCl buffer (pH7.4) at 37°C over 50h.

It is possible the presence of the CaP coating covered a significant portion of the adhesion sites of the PLA surface, limiting the amount of drug binding that might have occurred and there's the potential for subsequent GC release. Another probable reason is the fact that gentamicin ionises at pH 7, exposing its positively charged amine groups (Downing *et al.*, 2009). This positive charge coupled with the exposure of the equally positively charged a-axis, normal in the needle like HAp conformations (Aizawa, Matsuura and Zhuang, 2013) -confirmed in the TEM, could have caused a net repulsion of charge. This would then manifest as poor sorption of gentamicin onto to the CaP coated PLA PVA MS system. Bio-Oss itself does not itself seem to have an appreciable ability to adsorb gentamicin.

#### XII.5.1.3.3 Drug release studies in GC-core PLA PVA MS system

The GC-core samples show no release over the 50h observation period (Figure XII-5). It is very likely that encapsulation of the drug during the synthesis process simply failed or that if they cannot now escape. Perhaps further analysis with DSC (XII.5.3) might shed more of a light on what is going on in this samples.

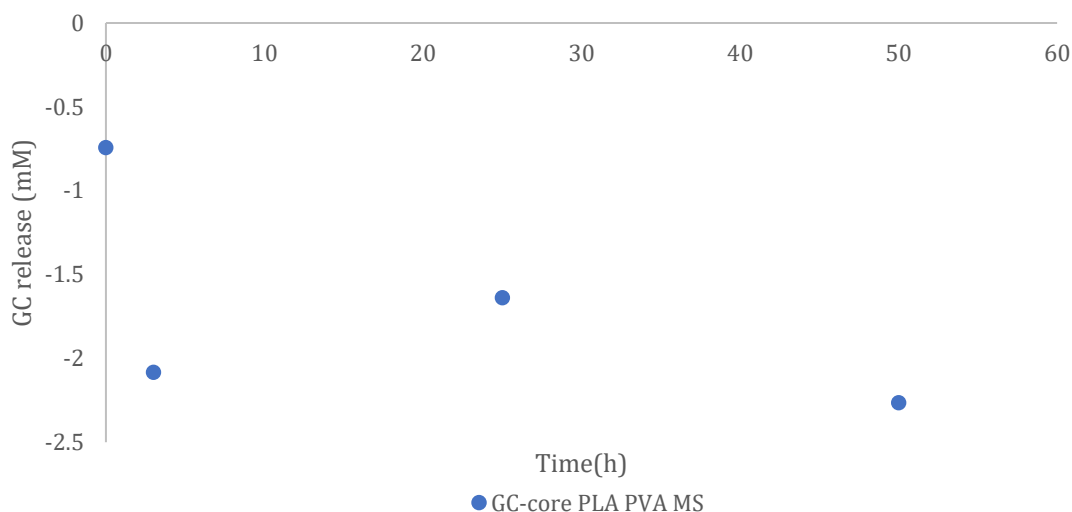


Figure XII-5: GC release from GC-core PLA PVA MS. Dose: 1mg of microspheres per ml of Tris-HCl buffer (pH7.4) at 37°C over 50h.

#### XII.5.2 Electron microscopy characterisation

SEM was used to study the morphology of the microspheres after the GC-release studies were carried out. It is expected that in the course of the samples interacting with a pH7.4 buffered (at 37°C) solution, such an interaction would result in a tangible physical effect on the exterior of the microspheres.



### *XII.5.2.1 PLA PVA MS systems after GC release*

Figure XII-6 shows the shapes of particles'. They are not completely spherical. This is the first visual indication that their GC release from the samples may be accompanied by extensive remodelling of the MS exterior. Although Figure XII-6a contains evidence of particles that are still somewhat spherical, an increasing proportion of other particulates have ambiguous shapes shows that the microspheres did and will undergo degradation in conditions that closely follow those used in this experiment.

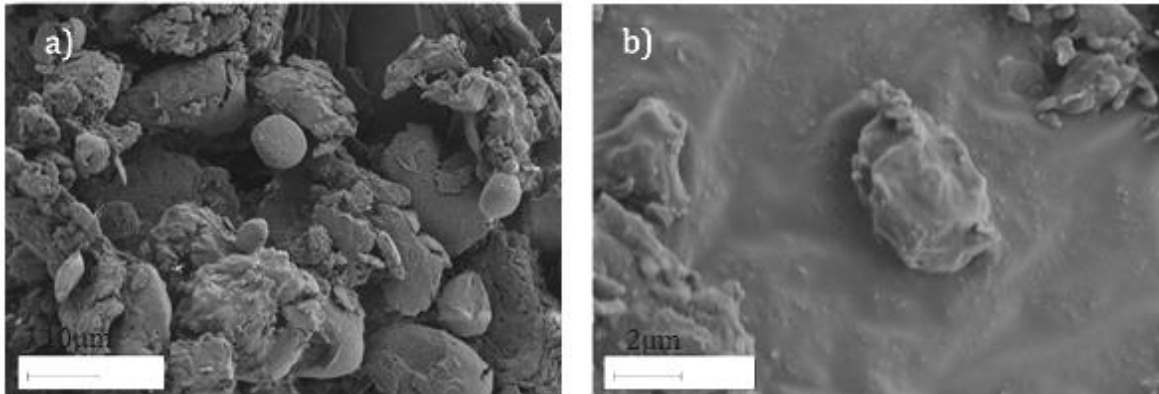


**Figure XII-6: SEM of PLA PVA-AL MS after the completion of their GC release evaluation (a & b).**

The degradation is not only individual to PLA PVA-AL MS samples. Figure XII-7 shows that in the plain PLA PVA MS samples, a similar situation also occurs. Admittedly, if one went only by the images provided, one would be left with the impression that PLA PVA MS were more resilient than PLA PVA-AL MS. The presence of more particles that were still spherical was a telling sign that perhaps the use of different surfactant (composition) could have an effect on not just the shape formed, but on the functional behaviour of drug loading and release. There is always the possibility that the manner of collection of the samples for SEM might simply have discriminated in favour of revealing more rounded particles in this sample than in the previous sample (shown in Figure XII-6). Discounting that, it appears that the mechanism of PLA degradation involves shape warping, facilitated by pore formation and possible connection of channels through the microspheres (Hyon, 2000). In addition to this, more voids/cracks/pores become more obvious as the reaction time increase (see Figure XII-7b). Eventually, it is possible that these particles fracture into small unrecognisable fragments, which can be seen littering the background of the SEM images.

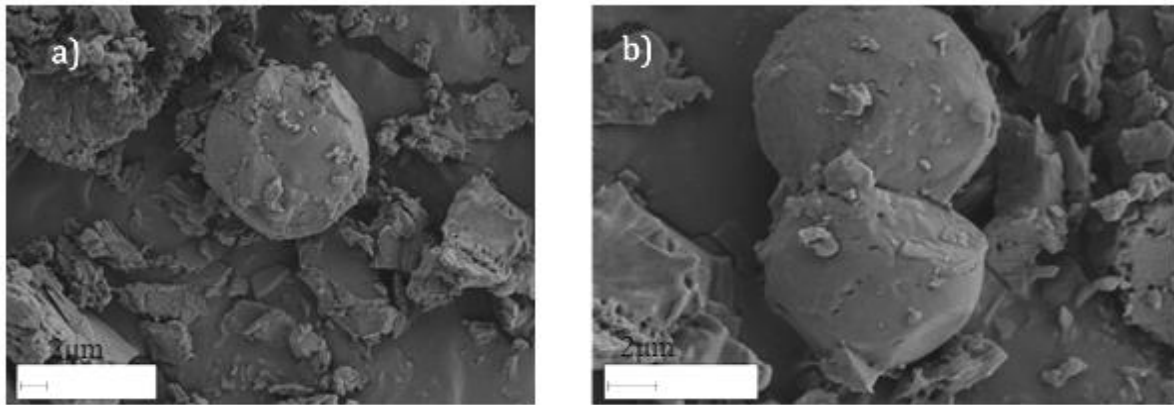


Figure XII-7: SEM of PLA PVA MS after the completion of their GC release evaluation(a & b)

PLA PVA-AL-TA MS (Figure XII-8) shows much of the same loss of shape as the two previous samples together with evidence of pore development (especially in Figure XII-8b where it is possible to make out tiny pin prick marks on the surface of the particulates).

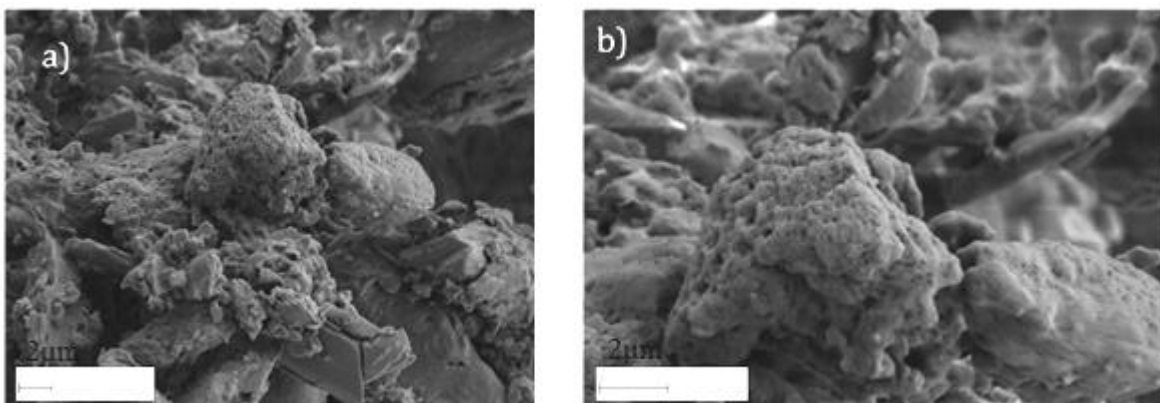


Figure XII-8: SEM of PLA PVA-AL-TA MS after the completion of their GC release evaluation (a & b)

Clearly the microspheres were undergoing changes that were likely brought on by the cleaving of the ester link in PLA, encouraged by the aqueous environment and the presence of GC.

#### ***XII.5.2.2 CaP coated PLA PVA MS systems after GC release***

Starting with PLA PVA-AL MS (Figure XII-9 a & b) it is very easy to make out spherical structures, although some of the samples are quite flat, which is not uncharacteristic of the samples made with PLA PVA-A. It can be inferred that the overall MS surface is relatively untouched by any form of degradation. Perhaps this is due to the CaP coating on the exterior which is still quite noticeable on the micrographs (Figure XII-9). It is possible that the CaP coating is masking the physical evidence of breakdown, or maybe the coating itself has protected the substrate from further damage?

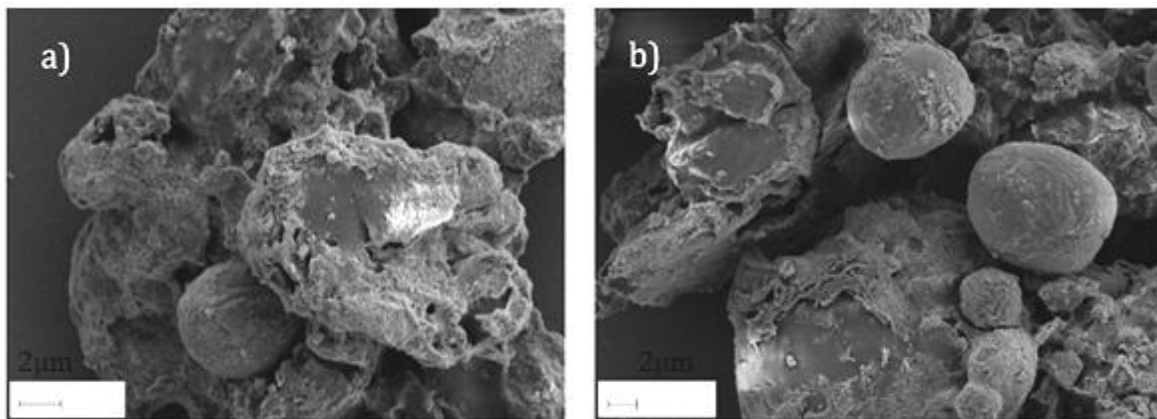


Figure XII-9: SEM of PLA PVA-AL MS/CaP after the completion of their GC release evaluation (a & b)

Again, the samples in Figure XII-10 are almost completely unperturbed after the GC release studies, Figure XII-10a especially. At least here, the exterior coating is much more comprehensive than the other CaP-coated samples. Maybe in this case the CaP coating acted as a barrier to the ingress of the buffered solution. Figure XII-10b gives one a glimpse into what could actually be occurring. At the bottom right corner of that image, one can just about make out an area of the microsphere that has had its CaP coating stripped off. There, one sees small voids that are apparent. It is possible that the CaP acts as a barrier that also blocks the compromised section of the PLA PVA MS CaP interior.

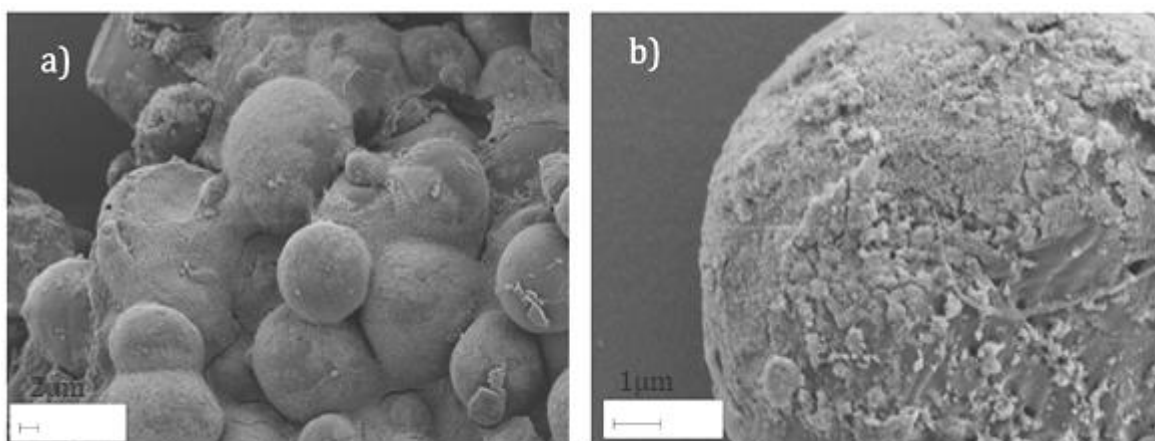


Figure XII-10: SEM of PLA PVA MS/CaP after the completion of their GC release evaluation (a & b)

In Figure XII-11, yet again each MS do not appear to have been affected in the course of the GC release. As well as that, the very limited covering of the CaP layer is another factor that might contradict the explanation given for PLA PVA MS CaP apparent durability. This sample has been shown to have developed a limited covering, so the GC release study cannot necessarily be blamed for its partial/lack of CaP covering. So, consider why would the MS appear almost unaffected after

the release studies if the CaP coating is not as extensive as the other samples? It is possible that the surface properties, may have contributed via residual retained surfactants (e.g. tannic acid).

In any case having such an exterior coating is positive as it can not only increase the resilience of the MS samples against damage (in vivo and in vitro). It can act as an extra site for adsorption of drugs and it can change the hydrophilic character of PLA surface.

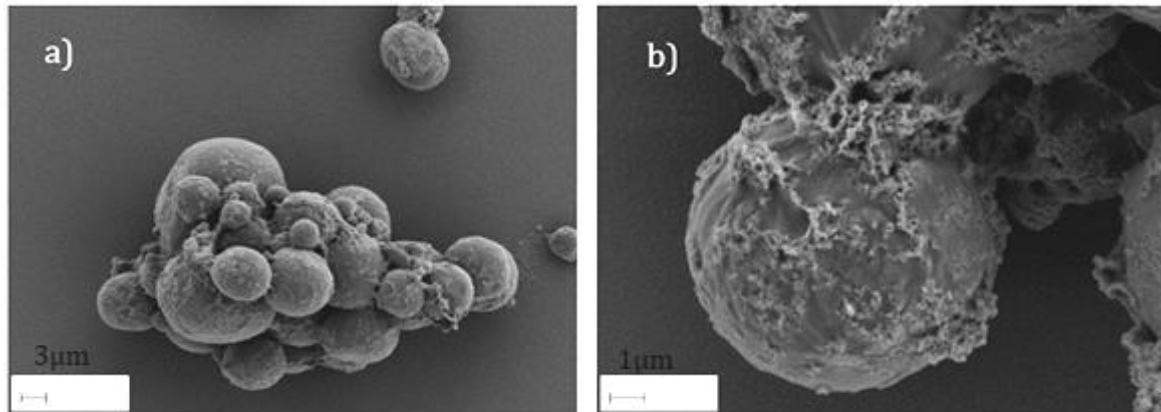


Figure XII-11: SEM of PLA PVA-AL-TA MS/CaP after the completion of their drug release evaluation (a & b)

Micrographs (Figure XII-12) for Bio-Oss® should also be included here. It is much harder to make any comparison between Bio-Oss® and the other samples mainly because it is primarily composed of just hydroxyapatite. As such, the time frame would be inadequate for demineralisation to occur.

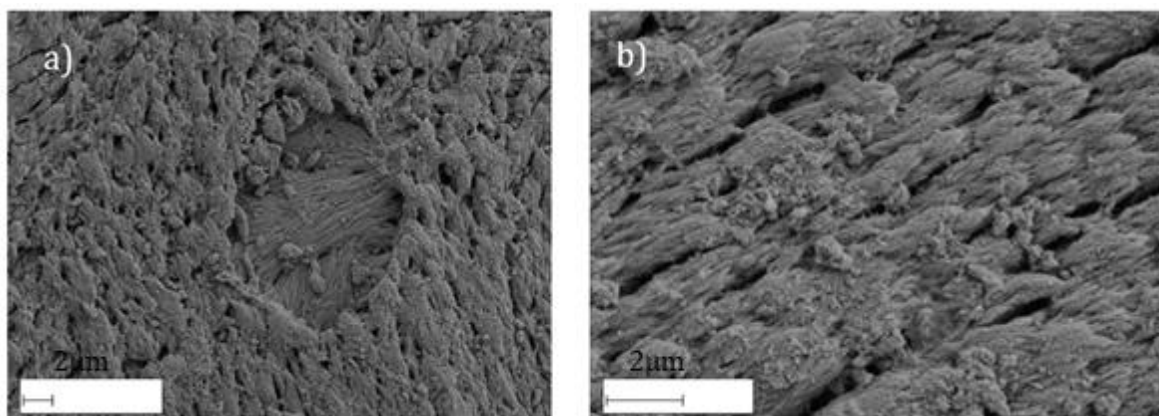


Figure XII-12: SEM of Bio-Oss® after the completion GC release evaluation (a & b)

### *XII.5.2.3 Drug core PLA PVA MS systems after GC release evaluation*

Although this is quite a different system the fact that their outer surface (wall) is composed of PLA means that they should behave in much the same manner as the solid PLA PVA MS systems.

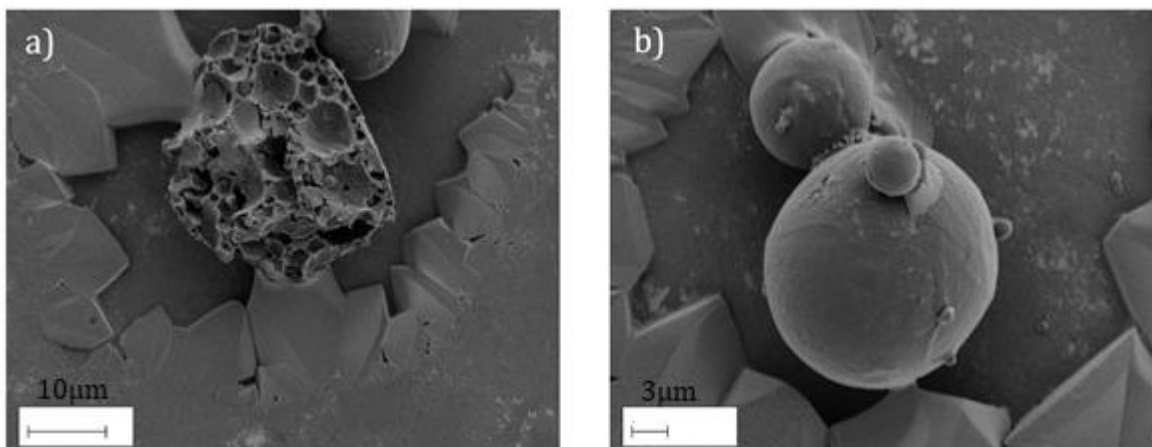


Figure XII-13: SEM of GC-core PLA PVA MS after the completion of their GC release evaluation (a & b)

GC-core PLA PVA MS (Figure XII-13) appears completely undamaged and unblemished after the GC release studies. Each MS rounded and spherical, although some MS are connected.

The same can be said for GC-AA core PLA PVA MS (see Figure XII-14). Other than certain particles which appear flat, these can be linked to the presence of AA during the synthesis process; the overall morphology of the particles observed appear to have remained intact through the GC release.

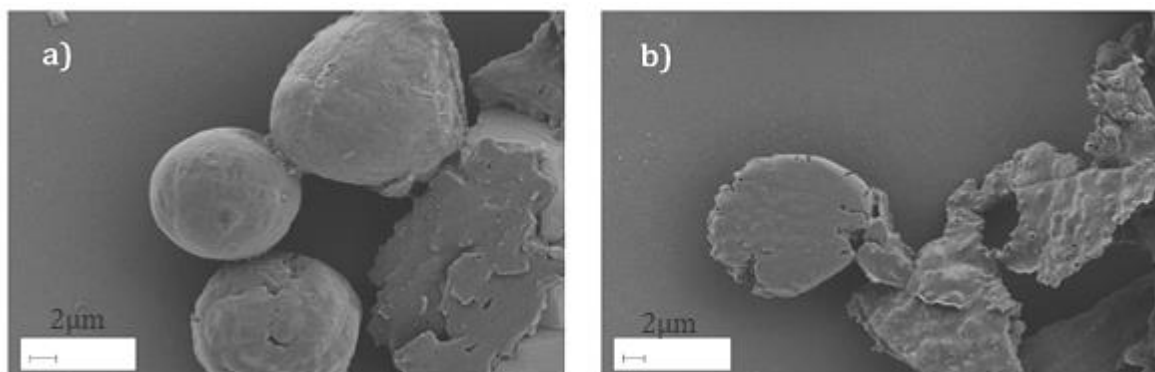


Figure XII-14: SEM of GC AA-core PLA PVA MS after the completion of their drug release evaluation (a & b)

For GC- core PLA PVA MS and GC-AA core PLA PVA MS, there is the possibility of an unsuccessful loading process, which is very likely and would explain the lack of Raman signal for the peak of interest. But in addition, one has to look at the walls of the samples. In the previous sections, TEM micrographs showed walls that seemed to have striation of dark and light contrasted areas. The samples there were treated to enhance the appearance of the semi crystalline domains (Huong *et al.*, 1993). These semi crystalline domains were contrasted dark, against the more amorphous regions which appeared lighter after undergoing special staining. It is increasingly likely that the drug-cored samples have a much higher crystallinity than their other counterparts. This

increased crystallinity would no doubt affect their eventual degradation and thus the release of their GC payload (within a reasonable time frame).

### XII.5.3 DSC analysis

#### XII.5.3.1.1 PLA PVA MS SYSTEMS

Having established an understanding of the important thermal events previously, DSC analysis here was used to examine the difference before and after drug release studies. These drug-core samples would have had to be immersed over a 12h period to enable maximum GC drug loading. Thus, the degradation would have started while loading and then during release. While that may be so, the DSC studies was only carried out on the neat samples (before loading) and then after the release studies had occurred (after 50h).

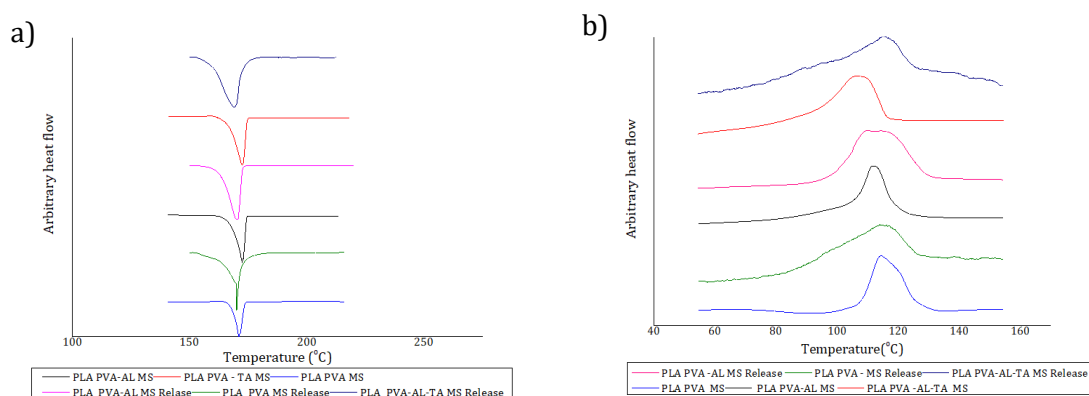


**Figure XII-15 : DSC curves of PLA PVA MS, PLA PVA AL MS and PLA PVA-AL-TA MS before and after release studies. These show their a) heating run from -50 to 250°C; b) cooling run from 250 to 60°C, in N<sub>2</sub>**

The DSC curves (Figure XII-15a) suggest that there is a slight shift in the melting point of the samples. Before the release studies, most of the samples had their melting point closer to 172-173°C, but afterwards the melting point shifts to a lower temperature, 169-170°C. This is expected as exposure to the buffered solution, and at an elevated temperature for 50h period is enough to accelerate the partial degradation of the MS. No doubt the elevated temperature allows some swelling and hydrolysis of the polyester bond, but not to such a significant degree that the melting point falls significantly.

The resilience of the MS is also witnessed in the crystallisation peak on cooling (Figure XII-15b). While the peaks before the release studies are not narrow, they are however well defined. After GC release studies, the crystallisation peak seems to be more asymmetric, not to mention occurring over a much wider temperature range than it did before the GC release studies. So, while the crystallisation peak is still present, the shape change suggests that GC release might

have affected the crystallinity in some form, or perhaps moved the crystallinity products from one major polymorph to a composition of different polymorphs. It is worth mentioning that the crystallisation peak centres at 115-117°C, which is higher than the crystallisation peaks at 107-110°C for the same samples pre-GC-release.

**Table XII-1: Values for the enthalpies of melting ( $\Delta H_m$ ), enthalpies of crystallisation ( $\Delta H_c$ ) and estimated % crystallisation**

Samples	$\Delta H_m$ (J/g)	$\Delta H_c$ (J/g)	% Crystallisation
PLA PVA MS	57.9	31.4	29.1
PLA PVA MS release	5.97	6.3	-0.4
PLA PVA -AL MS	55.3	40.1	16.7
PLA PVA-AL MS release	29.9	21.1	9.1
PLA PVA-AL-TA MS	59.4	9.8	54.6
PLA PVA AL TA MS release	3.9	2.6	1.3

Table XII-1 gives the estimated enthalpies that have been calculated from the calibrated DSC curves in Figure XII-15. There is a general decrease in all the enthalpies of the samples after they have undergone GC release; some more than others. This is reflected in estimated crystallinities of all the samples. This downward trend is expected as the GC release process may be a degradative process, to facilitate the release of the drug payload. A material which is able to actively/passively remodel in response to the body environment is the sort of material required for use as a drug delivery device. It should be pointed out that the presence of tris buffer (as an unintended contaminant) might have had an effect on the enthalpies above, not to mention the crystallinity. So, care should be taken in the detailed interpretation of the values.

#### XII.5.3.1.2 PLA PVA MS CaP systems

Figure XII-16 includes the DSC curves of PLA PVA MS/CaP systems before and after GC release studies. Discounting the nonchanging melting point of the samples, the noticeable absence of the peak that marks the transition from  $\alpha'$  to  $\alpha$  phase around 80°C has been diminished in all the samples that have undergone GC release studies. It is possible that the lack of such an event means that there is less of the metastable phase present to begin with after their release (Chen *et al.*, 2014).

The cooling run is perhaps the most telling of the DSC curve. There is a slight shift in the crystallisation peak all round. Incidentally, the crystallisation onset of all of the samples shift to around 115-116°C which is now closer to just pure PLA PVA MS. It is possible that there is a significant dissolution of the CaP coating after GC release. The presence of the peak still means that the crystallinity or rather the integrity of PLA PVA MS is unaffected after the release, showing

its resilience in the presence of the pH 7.4 buffered solution at 37°C.

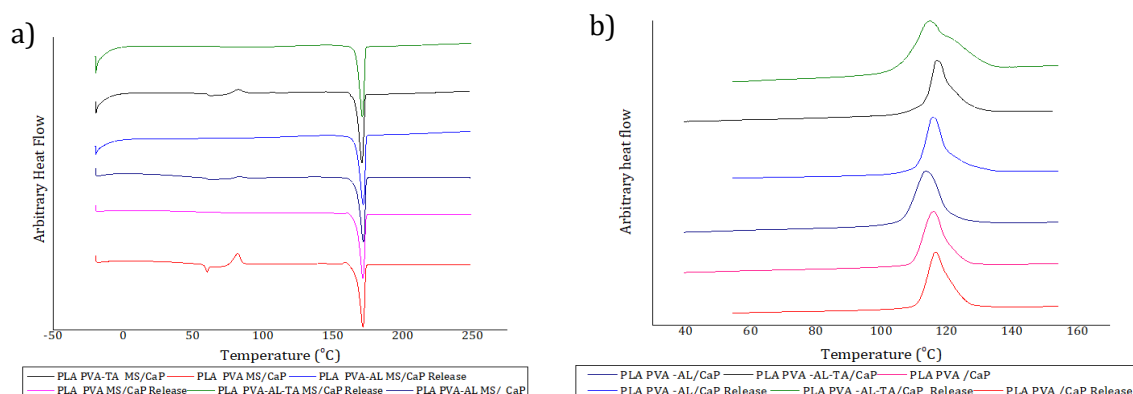


Figure XII-16: DSC curves of PLA PVA MS/CaP, PLA PVA AL MS/CaP and PLA PVA TA MS/CaP before and after GC release showing their a) heating run from -50 to 250°C; b) cooling run from 250 to 60°C, in N<sub>2</sub>

While the other aspects of the DSC were much easier to interpret, the enthalpies calculated in Table XII-2 are more difficult to understand. PLA-PVA MS experienced an increment in both enthalpies ( $\Delta H_m$  &  $\Delta H_c$ ) after the GC release s; this is in contrast to the two-remaining sample (at least for  $\Delta H_m$ ). Taking into account the % crystallinity of the samples, there is a further added complication in their results (i.e. while PLA PVA MS has a drop in crystallinity), PLA PVA-AL-TA MS undergoes a perplexing increase, along with PLA PVA-AL MS (although this is more likely an error).

Table XII-2: Values for the enthalpies of melting ( $\Delta H_m$ ), enthalpies of crystallisation ( $\Delta H_c$ ) and estimated % crystallisation

Samples (CaP)	$\Delta H_m$ (J/g)	$\Delta H_c$ (J/g)	% Crystallisation
PLA PVA MS	39.9	30.4	10.3
PLA PVA MS release	51.5	49.4	2.2
PLA PVA -AL MS	47.7	39.8	8.6
PLA PVA-AL MS release	44.1	36.0	8.9
PLA PVA-AL-TA MS	64.3	56.5	8.5
PLA PVA AL TA MS release	49.6	35.3	15.8

It is difficult to assign the results to GC entrapped affecting the enthalpies, seeing as the shape remains unchanged. But it is also quite possible that the presence of some remaining drug and/or the degradation of the PLA PVA MS structure has affected the aforementioned thermal parameters.



### XII.5.3.1.3 Drug core PLA PVA MS systems

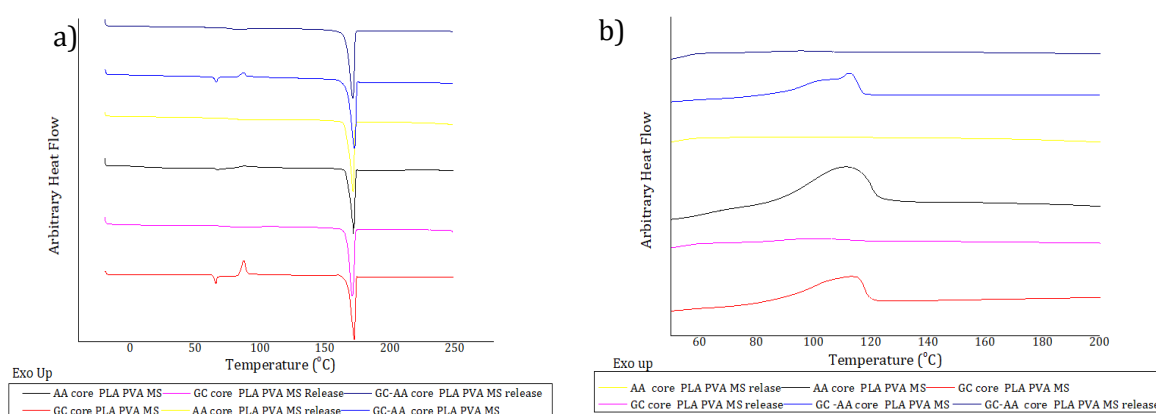


**Figure XII-17 : DSC curves of GC-core PLA PVA MS, AA-core PLA PVA AL MS and GC-AA-core PLA PVA MS before and after GC release studies showing their a) heating run from -50 to 250°C; b) cooling run from 250 to 60°C, in N<sub>2</sub>**

The same behaviour of the samples seen so far after drug release is also replicated here in heating (Figure XII-17a). The melting point is unaffected, but the possible conversion of the polymorphic PLA phases seems to be affected, appearing diminished after GC release.

In cooling, there is almost a complete loss of the crystallisation peak for all of the drug core samples. The peaks are quite imperceptible (when plotted in the manner seen in Figure XII-17b) but further processing and integration revealed the presence of the peaks which were then used for the enthalpies calculation. The main reason for this massive loss of crystallisation peak height, is a major degradation in the molecular configuration of the PLA substrate, to such an extent that crystallisation of the different molecular weight of PLA occurs over a wider temperature range. One can see that even with a drop in the % crystallisation, the value is significantly higher than has been encountered so far.

**Table XII-3: Values for the enthalpies of melting ( $\Delta H_m$ ), enthalpies of crystallisation ( $\Delta H_c$ ) and estimated % crystallisation for drug core samples before and after release studies.**

Samples	$\Delta H_m$ (J/g)	$\Delta H_c$ (J/g)	% Crystallisation
GC core PLA PVA MS	53.2	14.1	43.0
GC core PLA PVA MS release	34.6	3.2	34.6
AA core PLA PVA MS	55.3	17.6	41.5
AA core PLA PVA-AL MS release	41.55	Not present	N/A
GC-AA core PLA PVA MS	59.8	24.3	39.0
GC-AA core PLA PVA MS release	49.1	15.7	36.6

The enthalpies, as well as the % crystallinity, for the drug core samples follow a trend that is

repeated in all of the samples. There is a drop in the  $\Delta H_m$ ,  $\Delta H_c$  and the % crystallinity after GC release. This iterates the earlier point that was made previously about the diminishment of peaks. However, from the values calculated (Table XII-3), one can now say that the changes have indeed affected the crystallinity of the samples. Unlike the non-cored PLA PVA samples that had a complicated behaviour, these samples all experienced a decrease in their crystallinity; some more than others.

It is possible that if the GC release studies had continued for a longer period of time, most of the MS crystallinity would have been lost completely. No doubt for drug release, samples with low crystallinity are usually favoured as it means that their payloads are more accessible to the body. Where the crystallinity is high, it is possible that the payload may never actually get a chance to be released into the physiological system, owing to the fact that they are “locked away” behind an almost impervious wall that has to be “weathered away” (before it is excreted by the body). Referring back to the results obtained from Raman, one can already see that these samples consistently had almost zero drug release (at least imperceptible to the Raman probing). The possibility of an impervious crystalline wall as opposed to a failed encapsulation (during the original synthesis) might be the reason behind the almost futile drug release studies. If truly the encapsulation walls were the reason behind the poor drug release result, the next plausible step would be to introduce a “key” into the resistant wall that could be switched to quicken the degradation process of the PLA wall.

One can look at this as a mixed blessing, because assuming the body has not identified and rid itself of these foreign bodies almost instantly (owing to their size and surface properties) the drug can remain stable inside the body longer until the PLA shells have reached a certain level of crystallinity that would permit the release of their drug payload. Of course, this scenario is only plausible if the microspheres have not been ejected almost instantly. For the moment, the author believes a potential has been established in this first step.

## **XII.6 Summary**

### **XII.6.1 GC release in the microspheres**

The GC release studies on the microspheres made with varying surfactant composition showed that all of the samples revealed a general reduction in the concentration of GC released. However, the degree of reduction from the initial GC burst was much more severe in PLA PVA MS, compared to the other samples; incidentally being the sample that released the highest amount of GC initially. At the end of the drug release studies, PLA PVA MS experienced a 70% drop in the concentration of GC it released, while PLA PVA AL MS showed a 47% drop, and PLA PVA-AL-TA

MS had a drop of 49%. Amongst the samples examined, the ones made with varying composition of multicomponent surfactant composition seem to have provided a much more sensible drug release profile.

Clearly, the shape of the microspheres and possibly the size might have affected the sorption of the drugs GC on the sample, which then produced the altered GC release profile. It is likely that the hydrophobic nature of the PLA might have affected the initial drug uptake.

In the case of the drug-cored system, there was a significant drop in the amount of GC released into the surrounding solution. The coating of the samples appears to have adversely affected the drug release profile, which is incidentally reflected by Bio-Oss® as well. Another possibility is the potential ionisation of gentamicin at the pH chosen. Upon ionisation, gentamicin exposes its amine groups with net positive charges, the presence of apatite in the form of needles around the MS could suggest that the a-plane is exposed. The net positive charge of both the amine moieties of the gentamicin and the exposed a-plane might have resulted in a low uptake, and an even lower release.

- SEM

Microscopy studies on the microspheres after GC release showed interesting results. With regards to the uncoated samples, the exteriors of the microspheres appeared to have significantly deviated from their appearance after initial preparation. The warping of the microspheres, fragmentation, appearances of pores, cracks were just some of the consequence of hydrolytic attack on PLA (Chung and Chung, 2001); and these were all seen (Figure XII-6, Figure XII-7 & Figure XII-8). So, although it is generally considered hydrophobic, the evidence of PLA attack shows that the microspheres were still being attacked by the aqueous environment.

On the coated samples, the degradation behaviour appears quite different. Almost all of the samples appear still roughly spherical, with their exteriors, in the places uncovered by the CaP coating, appearing unblemished (Figure XII-9, Figure XII-10 & Figure XII-11). While it appears that the CaP coating is quite extensive, the presumed advantage of having the coating sorb a large amount of the drug and then release them does not seem to have been fulfilled. One can say that the CaP-coated microspheres certainly appear more resilient against hydrolytic attack and would therefore be more useful as a support material; but as a drug delivery vehicle, more needs to be done to understand why their release was so poor. Even Bio-Oss® appears morphologically unaffected by GC release.

- DSC

The main features that were looked at for DSC was the  $T_m$  and  $T_c$ . The  $T_m$  experienced some reduction after GC release, which is an indication that hydrolytic attack has occurred, reducing the average molecular weight of the PLA chain, and thus the endotherm (Figure XII-15a). Clearly the temperature of the GC release studies (37°C) would have accelerated the hydrolysis of the ester bond. Also, while there was a general increment in the maximum temperature of crystallisation, the actual shape of the peak became much broader (Figure XII-15b) much like those seen after the microspheres were coated. This is likely due to degradation of the polymer chain, increasing the number of oligomers of different length, and thus with different inclination to undergo crystallisation. The enthalpies of melting and crystallisation appears to fall after GC release, the same is true for the % crystallinity (Table XII-1).

Yet again, the coated samples follow a different trend to the uncoated samples. Not only is the  $T_m$  seemingly unaffected,  $T_c$  also appears to be unchanged (Figure XII-16a&b). The enthalpies of melting and crystallisation provide very little help compared to the uncoated samples (Table XII-2).

### XII.6.2 GC release the GC-cored systems

Compared to the samples prepared without encapsulation of the drug, the release profile of GC-core MS was marginal, which could mean either of two things, the initial encapsulation process was a failure, or the possible different crystallinities (seen in the TEM cross section of the samples in the previous chapter) seriously decreased the amount of GC being released.

- SEM

The GC-core encapsulated sample is completely not affected by the release judging by the micrographs in Figure XII-13. Every MS shown was intact, except for the samples in Figure XII-13a which appeared to have been damaged through other means rather than as a result of hydrolysis. From that figure, one can see that singular microspheres are composed of multiple microspheres inside, and then there is the relatively thick wall that encloses all of them. Assuming the encapsulation efficiency was low to start with, the thickness of the walls might be enough to further affect GC release. Then the wall possibly has a higher crystallinity (as explained in section XII.5.2.3), acting as another barrier to GC release.

- DSC

The  $T_m$  for the drug core samples remain unchanged before and after release. However, the presence of an amorphous peak and a cold crystallisation peak decreasing after drug release studies say otherwise (Figure XII-17a). The enthalpies of melting and crystallisation both appear

to drop after GC release (Table XII-3). One important parameter is the % crystallinity, compared to the samples which did not go through encapsulation, their % crystallisation is significantly higher; and this is maintained after the release process.

DSC results are another piece of evidence suggesting that all the encapsulated samples have a different and higher crystallinity compared to the other samples. The consequence of this is the poor GC release profile.

## **XII.7 Conclusion**

The aim of this chapter was to understand the GC release profiles of the different microspheres, coupled with the associated changes in the morphology and their thermal properties. The outcomes of this chapter are as follows:

- Drug release of uncoated microspheres: Samples showed the most appreciable drug release content of all the microspheres tested. PLA PVA MS started with the highest (GC accumulation) concentration of 6.2mM, before dropping closer to 1.7mM, thus displaying a behaviour dangerously close to a burst release. The other samples PLA PVA-AL MS and PLA PVA-AL-TA MS, started with more modest accumulation concentration (3.3mM and 1.4mM respectively), before losing half of their values. Their release behaviour was steadier than PLA PVA MS.

The MS morphology changed, showing that they underwent hydrolytic degradation. This was also mirrored by their decrease in crystallinity after the release.

- GC release of CaP-coated microspheres: Unlike the uncoated samples, these coated samples showed much lower GC release behaviour. PLA PVA MS/CaP and PLA PVA-AL-TA MS/CaP were the only successful sample, showing a GC accumulation concentration of 1.5mM within the first 7h, before dropping considerably.

Their morphology showed very little change, with their CaP coating still intact. This left some doubt as to whether they underwent hydrolytic degradation. This was also mirrored by their crystallinity.

- GC release from encapsulated microspheres: No GC release activity was detected in this sample in the case of gentamicin (and AA/GC mix). Their morphologies after GC release were seemingly unaffected by the release process. Their crystallinity remained relatively high, which can be partly to blame for their non-activity in release.

It has been made apparent that the uncoated sample seems to be the best choice for drug delivery amongst all of the samples investigated. However, their longevity in vivo might be problematic for use for a structural material, thus the other samples: uncoated microspheres and drug

loaded/encapsulated microspheres might be better for function as bone graft materials.

## Chapter XIII Conclusion

### XIII.1 Introduction

The conception of this thesis laid in the need to improve functional materials like titania photocatalysts and calcium phosphate bone graft substitutes, through the incorporation of biomimetic strategies as a means to achieve hierarchical nanomaterials with enhanced functionalities.

As a strategy, the philosophy of biomimetics is not an easy concept to pin down as it transcends the perception that advances can only be obtained through simply copying, it appears more as an abstract approach to problem solving. Because of this ambiguity, it is less obvious when biomimetics has been applied in a manner that suitably satisfies the indistinctiveness of its definition. This researcher hopes that in her struggle to understand biomimicry and utilise a biomimetic approach, she has succeeded in both her aims and in her adherence to the biomimetic mindset.

Thus, this conclusion chapter will serve as a means to form a cohesive path from the introduction, through the experimental, until now.

### XIII.2 Aim

So, for one last time, the aim of this chapter is to highlight how biomimetics has been utilised to achieve the goals (I to V) that were described in section I.2.

### XIII.3 Extent of achieving the initial aims

Considering the extent of achievement of novel TiO<sub>2</sub> overcoats and the photocatalytic goal (i)

1. Leaf biotemplate replicas were made from EC and RR, containing appreciable amounts of the anatase polymorph. RR titania replicas exhibited the more superior photocatalytic performance in breaking down MO ( $k_1 = 3.00 \times 10^{-4}$ ).
2. A floating photocatalytic film was successfully fabricated having two distinct layers: an upper more hydrophobic layer and a base hydrophilic layer, with the photocatalyst (P25 and RR) immobilised on the films. The floating films displayed positive photocatalytic degradation of MO and TX-100 ( $k_1$  for MO =  $2.3 \times 10^{-3}$ ;  $k_1$  for TX-100  $3.3 \times 10^{-3}$ ).
3. The PLA PVA MS were successfully coated with a very thin layer of a titania based coat, using TA.

With regards to the performance of the titania-based foliar replicas, though the performance of the replicas in comparison to P25 would appear to be the most pertinent conclusion from the

photocatalytic tests, this researcher believes that more can be extracted from the outcomes. The formation of calcite appeared to be a pervasive part of utilising leaf/carbon-based materials as a template source. It is interesting that in spite of these replicas having much smaller constituents of titania, with even the wrong proportion of polymorphs present, they still displayed photocatalytic abilities. Clearly, the presence of calcite itself is not an issue, but the size and perhaps its arrangement with titania in the replicas, especially with regards to the overall active sites is key (see section III.5.5.)

This understanding of why certain biotemplates, especially prepared in the manner used in this thesis, behave worse than P25 in a photocatalytic sense. This is something that the literature seems to have been reluctant to address, hence there is the novelty.

The creating of dual/asymmetric floating films as a template for holding photocatalyst and other materials is also another novelty. There seemed to be a lack of floating photocatalyst setup, such as that used by this researcher, with a preference for expanded materials and hollow beads (see section V.4 ).

Clearly the use of multi-component films, paired with the photocatalyst and other substances is an innovative approach to creating a floating support.

Consider the extent of achievement of nanohydroxyapatite composites (goal ii) with bioactivity (goal iii) and drug delivery potential (goal iv)

4. Mineralised hydrogel scaffold were synthesised, with their mineral content comprising primarily of ACP and nano CDHA having platelet shape. They did show positive bioactive properties in the uptake of  $\text{Ca}^{2+}$  and phosphate ions when in SBF. This was coupled with a resilience in PBS over a significant time frame. Finally, they did show selective drug uptake abilities, with a preference for MB, although they did take up AA and MO.
5. PLA PVA MS was synthesised and comprehensively coated with CaP layer with the help of TA. These appeared to be apatitic in nature. They displayed some drug sorption potential towards gentamicin, whether coated or uncoated.

While the use of hydrogels to grow apatitic calcium phosphate is not in itself new (Taguchi, Kishida and Akashi, 1999), the inclusion of carbonate and the introduction of different polymers into the previously PVA dominant matrix is a new take on this method. The subsequent improvement in the bioactive, mechanical, adsorptive and thermal properties of the mineralised hydrogel scaffold has been proven in the different chapters, highlighting the novelty of this approach (and the achievement of goals ii-v).

The use of different surfactant composition showed that the shape of the microspheres can be



altered. The most interesting thing that occurred was the inclusion of tannic acid in the coating process for CaP and titanium surface coating and the possible effect it had in increasing the resilience of the MS despite the extended exposure to PBS. This phenomenon has not been documented before.

Other innovative approach is the utilising of Raman spectroscopy to follow the release of gentamicin.

Overall, the author believes that she had broadly met her objectives and goals with novel outcomes.

### **XIII.4 Future work**

There are aspects that the author given more time and the opportunity would have pursued to improve the current nanomaterial produced here, she can now see how they could be further modified to make them suitable for real world applications

- a better understanding of the role being played by calcite in the bio-templated titania replicas of RR and EC. The presence of some photocatalytic activity despite the many factors that would otherwise destroy any of this activity is something that still needs to be investigated. In principle one could produce  $\text{CaTiO}_3$  perovskite replicas. The fact is, Kaur and Verma (2014) were able to create an improved DSSC device by including calcite along with  $\text{TiO}_2$  rather than using it alone. If one could seemingly control the size and the distribution of the now mixed oxide phases in one another, there is no telling the possible improvement that could be seen. It would be interesting to see if the temperature conditions could be used to affect this, as well as the inclusion of certain molecules that could stunt the growth of calcite at elevated temperatures.
- a better understanding of the effects of algae in the presence of oil, and pollutant would be worthwhile. The increased short-term photosynthetic burst that was suggested may have had a role in improving the degradation of TX-100 is too useful of an outcome to discard.
- the researcher would also be keen to investigate the use of different amino acids, and other biomolecules in actively controlling the growth and shape of the calcium phosphate phases. It has been established that certain amino acids like glutamic acid can suppress the precipitation of apatite in the body (Li *et al.*, 2011). It certainly would be worth trialling out different biomolecules within this confined system, similar to the body, to see the effect on the shape and phases of calcium phosphate formed.
- in the microsphere system, the presence of tannic acid that could potentially have had a more of an effect on the surface properties than in the formation of the microspheres. Another technique to include tracers into the surfactants would be necessary to see if they are truly

eliminated on rinsing. As well as a test of the surface charge of the microspheres as a result of the different surfactants. The researcher is well aware that techniques like XRD and FTIR are fallible in picking up surfaces that are less than 20nm thick, so another technique would be useful.

- also, with respect to tannic acid (and other catechol-based molecule) and the coating of the microsphere surface, more work needs to be done in eliciting the coated layers to form in an orderly manner rather than haphazardly. Whether is through the addition of molecules that cause the spontaneous alignment of the catechol, or through the use of a more linear catechol molecule, this is an important step in the creation of more anisotropic materials (Guardingo *et al.*, 2014).
- perhaps most importantly is the utilisation of better and more sensitive analytical systems to reduce uncertainties (e.g. exafs and MASNMR of P in mineralising hydrogels).

For the moment she believes a first positive step has been made.

P.S for brevity, some work on algal growth and CV interaction with ultrafine particulates were not described.

## Bibliography

- Abdul Hamid, Z. A., Tham, C. Y. and Ahmad, Z. (2018) 'Preparation and optimization of surface-engineered poly(lactic acid) microspheres as a drug delivery device', *J Mater Sci*, 53(7), pp. 4745–4758.
- Abou Neel, E. A., Aljabo, A., Strange, A., Ibrahim, S., Coathup, M., Young, A. M., Bozec, L. and Mudera, V. (2016) 'Demineralization-remineralization dynamics in teeth and bone.', *Int J Nanomedicine*. Dove Press, 11, pp. 4743–4763.
- Abouelmagd, S. A., Meng, F., Kim, B.-K., Hyun, H. and Yeo, Y. (2016) 'Tannic acid-mediated surface functionalization of polymeric nanoparticles', *ACS Biomater Sci Eng*, 2(12), pp. 2294–2303.
- Abrams, B. L. and Wilcoxon, J. P. (2005) 'Nanosize semiconductors for photooxidation', *Crit Rev Solid State Mater Sci*, 30(3), pp. 153–182.
- Adamson, A. W. and Gast, A. P. (Alice P. (1997) *Physical chemistry of surfaces*. Wiley.
- Aizawa, M., Matsuura, T. and Zhuang, Z. (2013) 'Syntheses of single-crystal apatite particles with preferred orientation to the a- and c-axes as models of hard tissue and their applications', *Biol Pharm Bull*. The Pharmaceutical Society of Japan, 36(11), pp. 1654–1661.
- Al-Hosney, H. A. and Grassian, V. H. (2004) 'Carbonic acid: an important intermediate in the surface chemistry of calcium carbonate', *J Am Chem Soc*, 126(26), pp. 8068–8069.
- Al-Musa, S. (1999) 'Evaluation of parameters involved in preparation and release of drug loaded in crosslinked matrices of alginate', *J Control Release*, 57(3), pp. 223–232.
- Alexis, F. (2005) 'Factors affecting the degradation and drug-release mechanism of poly(lactic acid) and poly[(lactic acid)-co-(glycolic acid)]', *Polym Int*. Wiley-Blackwell, 54(1), pp. 36–46.
- Aliofkhazraei, M. (2015) *Handbook of nanoparticles*. Cham: Springer International Publishing. Edited by M. Aliofkhazraei.
- Almarza, A. J. and Athanasiou, K. A. (2004) *Design Characteristics for the Tissue Engineering of Cartilaginous Tissues*, *Ann Biomed Eng*, 32(1) pp. 2-17
- Altavilla, C. and Ciliberto, E. (Enrico) (2011) *Inorganic nanoparticles : synthesis, applications, and perspectives*. CRC Press.
- Alvira, P., Tomás-Pejó, E., Ballesteros, M. and Negro, M. J. (2010) 'Pre-treatment technologies for an efficient bioethanol production process based on enzymatic hydrolysis: A review.', *Bioresour Technol*, 101(13), pp. 4851–61.

- Amini, A. R., Laurencin, C. T. and Nukavarapu, S. P. (2012) 'Bone Tissue Engineering: Recent Advances and Challenges', *Crit Rev Biomed Eng*, 40(5), pp. 363–408.
- Amirian, M., Nabipour Chakoli, A., Cai, W. and Sui, J. (2013) 'Effect of functionalized multiwalled carbon nanotubes on thermal stability of poly (L-LACTIDE) biodegradable polymer', *Sci Iran*. No longer published by Elsevier, 20(3), pp. 1023–1027.
- Amoozegar, M. A., Hajighasemi, M., Hamed, J., Asad, S. and Ventosa, A. (2011) 'Azo dye decolorization by halophilic and halotolerant microorganisms', *Ann Microbiol*, 61(2), pp. 217–230.
- Anderson, A.-L. and Binions, R. (2016) 'A preferential precursor for photocatalytically active titanium dioxide thin films: Titanium bis-ammonium lactato dihydroxide as an alternative to titanium tetra iso-propoxide', *Polyhedron*. Pergamon, 118, pp. 81–90.
- Ansari, R., Alizadeh, N. and Shademan, S. M. (2013) 'Application of silica gel/polyaniline composite for adsorption of ascorbic acid from aqueous solutions', *Iran Polym J*. Springer Berlin Heidelberg, 22(10), pp. 739–748.
- Auroux, A. (ed.) (2013) *Calorimetry and Thermal Methods in Catalysis*. Berlin, Heidelberg: Springer Berlin Heidelberg (Springer Series in Materials Science).
- Balgová, Z., Palou, M., Wasserbauer, J. and Kozánková, J. (2013) 'Synthesis of poly(vinyl alcohol) — hydroxyapatite composites and characterization of their bioactivity', *Open Chem*, 11(9).
- Bar-Cohen, Y. (2006) 'Biomimetics - using nature to inspire human innovation', *Bioinspiration and Biomimetics*, pp. 1–12.
- Barneto, A. G., Hernández, R. B. and Berenguer, J. M. (2011) 'Thermogravimetric characterization of eucalyptus wood', *O Pap*, 72(7), pp. 53–56.
- Bedwell, G. J., Zhou, Z., Uchida, M., Douglas, T., Gupta, A. and Prevelige, P. E. (2015) 'Selective Biotemplated Synthesis of TiO<sub>2</sub> Inside a Protein Cage', *Biomacromolecules*, 16(1), pp. 214–218.
- Bee, S.-L., Hamid, Z. A. A., Mariatti, M., Yahaya, B. H., Lim, K., Bee, S.-T. and Sin, L. T. (2018) 'Approaches to improve therapeutic efficacy of biodegradable PLA/PLGA microspheres: a review', *Polym Rev*. Taylor & Francis, 58(3), pp. 495–536.
- Belala, Z., Jeguirim, M., Belhachemi, M., Addoun, F. and Trouvé, G. (2011) 'Biosorption of basic dye from aqueous solutions by Date Stones and Palm-Trees Waste: Kinetic, equilibrium and thermodynamic studies', *Desalination*, 271(1–3), pp. 80–87.
- Belhachemi, M. and Addoun, F. (2011) 'Comparative adsorption isotherms and modeling of

methylene blue onto activated carbons', *Appl Water Sci*, 1(3–4), pp. 111–117.

Bell, D. C. and Erdman, N. (2012) 'Introduction to the theory and advantages of low voltage electron microscopy: principles and application', in *Low Volt Electron Microsc Princ Appl*. Chichester: John Wiley & Sons, pp. 1–30.

Bellisola, G. and Sorio, C. (2012) 'Infrared spectroscopy and microscopy in cancer research and diagnosis.', *Am J Cancer Res*, 2(1), pp. 1–21.

Bendtsen, S. T., Quinnell, S. P. and Wei, M. (2017) 'Development of a novel alginate-polyvinyl alcohol-hydroxyapatite hydrogel for 3D bioprinting bone tissue engineered scaffolds', *J Biomed Mater Res Part A*. Wiley-Blackwell, 105(5), pp. 1457–1468.

Bezrodna, T., Gavrillo, T., Puchkovska, G., Shimanovska, V., Baran, J. and Marchewka, M. (2002) 'Spectroscopic study of TiO<sub>2</sub> (rutile)–benzophenone heterogeneous systems', *J Mol Struct*, 614(1–3), pp. 315–324.

Bezrodna, T., Puchkovska, G., Shimanovska, V., Chashechnikova, I., Khalyavka, T. and Baran, J. (2003) 'Pyridine-TiO<sub>2</sub> surface interaction as a probe for surface active centers analysis', *Appl Surf Sci*, 214(1–4), pp. 222–231.

Bharat, B. (2010) *Springer Handbook of Nanotechnology*. Edited by B. Bhushan. Berlin, Heidelberg: Springer Berlin Heidelberg.

Bhushan, B. (2009) 'Biomimetics: lessons from nature-an overview', *Philos Trans R Soc A Math Phys Eng Sci*. The Royal Society, 367(1893), pp. 1445–1486.

Birkholz, M. (2005) *Thin Film Analysis by X-Ray Scattering*. Weinheim, FRG: Wiley-VCH Verlag GmbH & Co. KGaA.

Bonapasta, A. A., Buda, F., Colombet, P. and Guerrini, G. (2002) 'Cross-Linking of Poly(Vinyl Alcohol) Chains by Ca Ions in Macro-Defect-Free Cements', *Chem Mater*, 14(3), pp. 1016–1022.

Boskey, A. L. (2007) 'Mineralization of bones and teeth', *Elements*, 3(6), pp. 385–391.

Bottom, C. B., Hanna, S. S. and Siehr, D. J. (1978) 'Mechanism of the ninhydrin reaction', *Biochem Mol Biol Educ*, 2(1), pp. 4–5.

Bowie, B. T., Chase, D. B., Lewis, I. R. and Griffiths, P. R. (2006) 'Anomalies and artifacts in raman spectroscopy', in Griffiths, P. R. (ed.) *Handb Vib Spectrosc*. Chichester, UK: John Wiley & Sons, Ltd.

Burton, A. W., Ong, K., Rea, T. and Chan, I. Y. (2009) 'On the estimation of average crystallite size of zeolites from the Scherrer equation: A critical evaluation of its application to zeolites with

- one-dimensional pore systems', *Microporous Mesoporous Mater.* Elsevier, 117(1–2), pp. 75–90.
- Callister, W. D. and Rethwisch, D. G. (2009) *Fundamentals of Materials Science and Engineering: An Integrated Approach*. 8th edn. Denver: John Wiley & Sons, Inc.
- Callister, W. D. and Rethwisch, D. G. (2012) *Material Sciences and Engineering: An Introduction*. 8th edn. John Wiley & Sons.
- Cao, G. (2004) *Nanostructures and Nanomaterials*. Imperial college press.
- Chakoli, A. N., Sui, J., Amirian, M. and Cai, W. (2011) 'Crystallinity of biodegradable polymers reinforced with functionalized carbon nanotubes', *J Polym Res*. Springer Netherlands, 18(6), pp. 1249–1259.
- Chang, P.-L., Wu, Y.-C., Lai, S.-J. and Yen, F.-S. (2009) 'Size effects on chi to alpha-Al<sub>2</sub>O<sub>3</sub> phase transformation', *J Eur Ceram Soc*, 29, pp. 3341–3348.
- Chappuis, V., Rahman, L., Buser, R., Janner, S. F. M., Belsler, U. C. and Buser, D. (2018) 'Effectiveness of contour augmentation with guided bone regeneration: 10-year results', *J Dent Res*. SAGE Publications, 97(3), pp. 266–274.
- Chauhan, U. P. S. and Ray Sarkar, B. C. (1969) 'Use of calmagite for the determination of traces of magnesium in biological materials', *Anal Biochem*, 32(1), pp. 70–80.
- Chavan, P. N., Bahir, M. M., Mene, R. U., Mahabole, M. P. and Khairnar, R. S. (2010) 'Study of nanobiomaterial hydroxyapatite in simulated body fluid: Formation and growth of apatite', *Mater Sci Eng B*, 168(1–3), pp. 224–230.
- Chen, C.-Y., Yang, C.-F., Jeng, U.-S. and Su, A.-C. (2014) 'Intrinsic metastability of the  $\alpha'$  phase and its partial transformation into  $\alpha$  Crystals during isothermal cold-crystallization of Poly(l-lactide)', *Macromolecules*, 47(15), pp. 5144–5151.
- Chen, T., Wang, Y., Wang, Y. and Xu, Y. (2015) 'Biotemplated synthesis of hierarchically nanostructured TiO<sub>2</sub> using cellulose and its applications in photocatalysis', *RSC Adv*, 5(3), pp. 1673–1679.
- Chen, T., Zheng, Y., Lin, J.-M. and Chen, G. (2008) 'Study on the photocatalytic degradation of methyl orange in water using Ag/ZnO as catalyst by liquid chromatography electrospray ionization ion-trap mass spectrometry.', *J Am Soc Mass Spectrom*, 19(7), pp. 997–1003.
- Chen, Y.-N., Peng, L., Liu, T., Wang, Y., Shi, S. and Wang, H. (2016) 'Poly(vinyl alcohol)–tannic acid hydrogels with excellent mechanical properties and shape memory behaviors', *ACS Appl Mater Interfaces*, 8(40), pp. 27199–27206.

- Chen, Z., Fu, Y., Cai, Y. and Yao, J. (2012) 'Effect of amino acids on the crystal growth of hydroxyapatite', *Mater Lett*. North-Holland, 68, pp. 361–363.
- Choi, H. C., Jung, Y. M. and Kim, S. Bin (2004) 'Characterisation of Raman spectra of size selected TiO<sub>2</sub> nanoparticles by two dimensional correlation spectroscopy', *Bull Korean Chem Soc*, 25(3).
- Chowdhury, S. and Saha, P. Das (2012) 'Biosorption of methylene blue from aqueous solutions by a waste biomaterial: hen feathers', *Appl Water Sci*. Springer Berlin Heidelberg, 2(3), pp. 209–219.
- Chung, K.-T. (1983) 'The significance of azo-reduction in the mutagenesis and carcinogenesis of azo dyes', *Mutat Res Genet Toxicol*, 114(3), pp. 269–281.
- Chung, Y.-Y. H. T.-W. and Chung, T. W. (2001) 'Microencapsulation of gentamicin in biodegradable PLA and/or PLA/PEG copolymer', *J Microencapsul*, 18(4), pp. 457–465.
- Coleyshaw, E. E., Crump, G. and Griffith, W. P. (2003) 'Vibrational spectra of the hydrated carbonate minerals ikaite, monohydrocalcite, lansfordite and nesquehonite', *Spectrochim Acta Part a Mol Biomol Spectrosc*, 59(10), pp. 2231–2239.
- Combes, C. and Rey, C. (2010) 'Amorphous calcium phosphates: Synthesis, properties and uses in biomaterials', *Acta Biomater*, 6(9), pp. 3362–3378.
- Cutler, D. F., Botha, T. and Stevenson, D. W. (2008) *Plant Anatomy: An Applied Approach*. 1st edn. Malden: Blackwell Publishing.
- Daemi, H. and Barikani, M. (2012) 'Synthesis and characterization of calcium alginate nanoparticles, sodium homopolymannuronate salt and its calcium nanoparticles', *Sci Iran*. No longer published by Elsevier, 19(6), pp. 2023–2028.
- De, S., Dutta, S. and Saha, B. (2016) 'Critical design of heterogeneous catalysts for biomass valorization: Current thrust and emerging prospects', *Catal Sci Technol*, pp. 7364–7385.
- DeHayes, D. H., Schaberg, P. G., Hawley, G. J. and Strimbeck, G. R. (1999) 'Acid rain impacts on calcium nutrition and forest health', *Bioscience*. Oxford University Press, 49(10), p. 789.
- Dickerson, M. B., Sandhage, K. H. and Naik, R. R. (2008) 'Protein- and peptide-directed syntheses of inorganic materials.', *Chem Rev*. American Chemical Society, 108(11), pp. 4935–78.
- Diebold, U. (2003) 'The surface science of titanium dioxide', *Surf Sci Rep*, 48(5–8), pp. 53–229.
- Dobrucka, R. (2017) 'Synthesis of titanium dioxide nanoparticles using echinacea purpurea herba.', *Iran J Pharm Res IJPR*. Shahid Beheshti University of Medical Sciences, 16(2), pp. 756–762.

Donald, B. Y. (1955) 'Characterization of physical adsorption system. III. The separate effects of pore size and surface acidity upon the adsorbent capacities of activated carbon', *Adsorpt J Int Adsorpt Soc*, 59, pp. 896–900.

Dorati, R., DeTrizio, A., Modena, T., Conti, B., Benazzo, F., Gastaldi, G. and Genta, I. (2017) 'Biodegradable scaffolds for bone regeneration combined with drug-delivery systems in osteomyelitis therapy'. Multidisciplinary Digital Publishing Institute (MDPI), 10(4), p. 96.

Dorozhkin, S. V (2011) 'Calcium orthophosphates Occurrence, properties, biomineralization, pathological calcification and biomimetic applications', *Biomatter*. Taylor & Francis, 1(2), pp. 121–64.

Dorozhkin, S. V (2012a) 'Amorphous calcium orthophosphates: nature, chemistry and biomedical applications', *Int J Mater Chem*, 2(1), pp. 19–46.

Dorozhkin, S. V (2012b) 'Calcium orthophosphates and human beings: a historical perspective from the 1770s until 1940.', *Biomatter*. Taylor & Francis, 2(2), pp. 53–70.

Drouet, C. (2013) 'Apatite formation: why it may not work as planned, and how to conclusively identify apatite compounds', *Biomed Res Int*, 2013, pp. 1–12.

Downing, B. P. B., Rutenberg, A. D., Touhami, A. and Jericho, M. (2009) 'Subcellular Min Oscillations as a Single-Cell Reporter of the Action of Polycations, Protamine, and Gentamicin on Escherichia coli', *PLoS One*. Edited by J. R. Lu, 4(9), p. e7285.

Du, M., Song, W., Cui, Y., Yang, Y. and Li, J. (2011) 'Fabrication and biological application of nano-hydroxyapatite (nHA)/alginate (ALG) hydrogel as scaffolds', *J Mater Chem*, 21(7), pp. 2228–2236.

El-Hefian, E. A., Nasef, M. M. and Yahaya, A. H. (2010) 'The preparation and characterization of chitosan/poly (vinyl alcohol) blended films', *E-Journal Chem*. Hindawi, 7(4), pp. 1212–1219.

El-Maazawi, M., Finken, A. N., Nair, A. B. and Grassian, V. H. (2000) 'Adsorption and photocatalytic oxidation of acetone on TiO<sub>2</sub>: an in situ transmission FT-IR study', *J Catal*. Academic Press, 191(1), pp. 138–146.

Eliaz, N., Metoki, N., Eliaz, N. and Metoki, N. (2017) 'Calcium phosphate bioceramics: a review of their history, structure, properties, coating technologies and biomedical applications', *Materials (Basel)*. Multidisciplinary Digital Publishing Institute, 10(4), p. 334.

Elliott, J. C., Holcomb, D. W. and Young, R. A. (1985) *Calcified tissue international infrared determination of the Degree of Substitution of Hydroxyl by Carbonate Ions in Human Dental*



*Enamel, Calcif Tissue Int.*

Elliott, J. C., Mackie, P. E. and Young, R. A. (1973) 'Monoclinic hydroxyapatite', *Science* (80- ), 180(4090), pp. 1055–1057.

Elzein, T., Nasser-Eddine, M., Delaite, C., Bistac, S. and Dumas, P. (2004) 'FTIR study of polycaprolactone chain organization at interfaces', *J Colloid Interface Sci*, 273(2), pp. 381–387.

Ertani, A., Francioso, O., Ferrari, E., Schiavon, M. and Nardi, S. (2018) 'Spectroscopic-chemical fingerprint and biostimulant activity of a protein-based product in solid form', *Molecules*, 23(5), p. 1031.

Fathi, M. H., Hanifi, A. and Mortazavi, V. (2008) 'Preparation and bioactivity evaluation of bone-like hydroxyapatite nanopowder', *J Mater Process Technol*, 202(1–3), pp. 536–542.

Faust, B. (1997) *Modern Chemical Techniques: An Essential Reference for Students and Teachers*. Edited by J. Johnston and N. Reed. RSC publishing.

Figueiredo, K. C. S., Alves, T. L. M. and Borges, C. P. (2008) 'Poly(vinyl alcohol) films crosslinked by glutaraldehyde under mild Conditions', *J Appl Polym Sci*. Wiley Periodicals, Inc, 111, pp. 3074–3080.

Fontana, P., Schefer, J. and Pettit, D. (2011) 'Characterization of sodium chloride crystals grown in microgravity', *J Cryst Growth*, 324(1), pp. 207–211.

Fratzl, P. (2008) 'When the cracks begin to show', *Nat Mater*. Nature Publishing Group, 7(8), pp. 610–612.

Friedman, M. (2004) 'Applications of the ninhydrin reaction for analysis of amino acids, peptides, and proteins to agricultural and biomedical sciences', *J Agric Food Chem*, 52(3), pp. 385–406.

Frutos, P., Torrado, S., Perez-Lorenzo, M. E. and Frutos, G. (2000) 'A validated quantitative colorimetric assay for gentamicin', *J Pharm Biomed Anal*, 21(6), pp. 1149–1159.

Fu, J., He, C., Xia, B., Li, Y., Feng, Q., Yin, Q., Shi, X., Feng, X., Wang, H. and Yao, H. (2016) 'c-axis preferential orientation of hydroxyapatite accounts for the high wear resistance of the teeth of black carp (*Mylopharyngodon piceus*)', *Sci Rep*. Nature Publishing Group, 6(1), p. 23509.

Fu, L.-H., Qi, C., Liu, Y.-J., Cao, W.-T. and Ma, M.-G. (2018) 'Sonochemical synthesis of cellulose/hydroxyapatite nanocomposites and their application in protein adsorption', *Sci Rep*. Nature Publishing Group, 8(1), p. 8292.

Gabbott, P. (2008) 'A practical introduction to differential scanning calorimetry', in *Princ Appl*

*Therm Anal.* Oxford: Blackwell Publishing, pp. 1–50.

Gamal, G. A., Al-Mufadi, F. A. and Said, A. H. (2013) *Effect of iron additives on the microstructure of hydroxyapatite*, *Technol Appl Sci Res*.

Ganduglia-Pirovano, M. V., Hofmann, A. and Sauer, J. (2007) 'Oxygen vacancies in transition metal and rare earth oxides: Current state of understanding and remaining challenges', *Surf Sci Rep.* North-Holland, 62(6), pp. 219–270.

Gauthier, M., Luo, J., Calvet, D., Ni, C., Zhu, X. and Garon, M. (2004) 'Degree of crosslinking and mechanical properties of crosslinked poly(vinyl alcohol) beads for use in solid-phase organic synthesis'.

Gaya, U. I. (2014) *Heterogeneous Photocatalysis Using Inorganic Semiconductor Solids*. Dordrecht: Springer Netherlands.

Geng, X. and Henderson, W. A. (2012) 'Pretreatment of corn stover by combining ionic liquid dissolution with alkali extraction.', *Biotechnol Bioeng*, 109(1), pp. 84–91.

Girgsdies, F. (2015) 'Peak profile analysis in X-ray powder diffraction'.

Goldberg, V. M. and Stevenson, S. (1987) 'Natural history of autografts and allografts', *Clin Orthop Relat Res.* London: Springer, (225), pp. 7–16.

Gomez, V., Ferreres, L., Pocurull, E. and Borrull, F. (2011) 'Determination of non-ionic and anionic surfactants in environmental water matrices', *Talanta*, 84(3), pp. 859–866.

Gong, R., Ye, J., Dai, W., Yan, X., Hu, J., Hu, X., Li, S. and Huang, H. (2013) 'Adsorptive removal of methyl orange and methylene blue from aqueous solution with finger-citron-residue-based activated carbon', *Ind Eng Chem Res*, 52(39), pp. 14297–14303.

Gonzalez, J. S. and Alvarez, V. A. (2014) 'Mechanical properties of polyvinyl alcohol/hydroxyapatite cryogel as potential artificial cartilage', *J Mech Behav Biomed Mater*, 34, pp. 47–56.

González, Y. and Rodríguez, S. (2013) 'A comparative study on the ultrafine particle episodes induced by vehicle exhaust: A crude oil refinery and ship emissions', *Atmos Res.* Elsevier, 120–121, pp. 43–54.

Gottlieb, A., Shaw, C., Smith, A., Wheatley, A. and Forsythe, S. (2003a) 'The toxicity of textile reactive azo dyes after hydrolysis and decolourisation', *J Biotechnol*, 101(1), pp. 49–56.

Gottlieb, A., Shaw, C., Smith, A., Wheatley, A. and Forsythe, S. (2003b) 'The toxicity of textile reactive azo dyes after hydrolysis and decolourisation', *J Biotechnol*, 101(1), pp. 49–56.

- Goutam, S. P., Saxena, G., Singh, V., Yadav, A. K., Bharagava, R. N. and Thapa, K. B. (2018) 'Green synthesis of TiO<sub>2</sub> nanoparticles using leaf extract of *Jatropha curcas* L. for photocatalytic degradation of tannery wastewater', *Chem Eng J*, 336, pp. 386–396.
- Gowri, S., Rajiv Gandhi, R., Senthil, S., Suresh, J. and Sundrarajan, M. (2016) 'Enhancing antimicrobial activity of biotemplated TiO<sub>2</sub> nanoparticles using Aloe Vera plant extract', *J Bionanoscience*, 10(3), pp. 181–190.
- Grätzel, M. (2001) 'Photoelectrochemical cells', *Nature*, 414(6861), pp. 338–344.
- Guardingo, M., Bellido, E., Miralles-Llumà, R., Faraudo, J., Sedó, J., Tatay, S., Verdaguer, A., Busqué, F. and Ruiz-Molina, D. (2014) 'Bioinspired catechol-terminated self-assembled monolayers with enhanced adhesion properties', *Small*. John Wiley & Sons, Ltd, 10(8), pp. 1594–1602.
- Guirguis, O. W. and Moselhey, T. H. (2012) 'Thermal and structural studies of poly(vinyl alcohol) and hydroxypropyl cellulose blends', *Nat Sci*, 4(1), pp. 57–67.
- Gunasekaran, S., Anbalagan, G. and Pandi, S. (2006) 'Raman and infrared spectra of carbonates of calcite structure', *J Raman Spectrosc*, 37(9), pp. 892–899.
- Guo, Y.-J., Long, T., Chen, W., Ning, C.-Q., Zhu, Z.-A. and Guo, Y.-P. (2013) 'Bactericidal property and biocompatibility of gentamicin-loaded mesoporous carbonated hydroxyapatite microspheres', *Mater Sci Eng C*. Elsevier, 33(7), pp. 3583–3591.
- Guzmán, P., Fernández, V., Graça, J., Cabral, V., Kayali, N., Khayet, M. and Gil, L. (2014) 'Chemical and structural analysis of *Eucalyptus globulus* and *E. camaldulensis* leaf cuticles: a lipidized cell wall region.', *Front Plant Sci*. Frontiers, 5, p. 481.
- Hall, D. W. and Stern, W. (2012) *Plant Anatomy, Forensic Bot a Pract Guid*.
- Hanaor, D. A. H. and Sorrell, C. C. (2010) 'Review of the anatase to rutile phase transformation', *J Mater Sci*, 46(4), pp. 855–874.
- Hang, P. T., Thompson, T. D. and Brindley, G. W. (1970) 'Cation exchange capacity and surface area determinations of clay minerals by methylene blue adsorption', in *Clay Miner Conf 19th Annu Clay Miner Soc 7th Meet Programs Abstr*. Pergamon Press, p. 21.
- Hanlie, H., Liyun, T. and Tao, J. (2006) *The Crystal Characteristics of Enamel and Dentin by XRD Method*, *J Wuhan Univ Technol Sci Ed*.
- Haque, E., Jun, J. W. and Jhung, S. H. (2011) 'Adsorptive removal of methyl orange and methylene blue from aqueous solution with a metal-organic framework material, iron

terephthalate (MOF-235)', *J Hazard Mater*, 185(1), pp. 507–511.

Harding, J. L., Osmond, M. J. and Krebs, M. D. (2017) 'Engineering osteoinductive biomaterials by bioinspired synthesis of apatite coatings on collagen hydrogels with varied pore microarchitectures', *Tissue Eng Part A*, 23(23–24), pp. 1452–1465.

Harding, V. J. and Warneford, F. H. S. (1916) 'The ninhydrin reaction with amines and amides', *J Biol Chem*, 25(2), pp. 337–350.

Hayakawa, K., Yokobaba, C., Ichiki, N., Muzakkar, M., Shinmura, T. and Nagaoka, S. (2001) 'Utilization of floating materials coated with TiO<sub>2</sub> film for photodegradation of organic compounds', *Res J Chem Environ*, 5(2), pp. 7–15.

He, J., Chen, D., Li, Y., Shao, J., Xie, J., Sun, Y., Yan, Z. and Wang, J. (2013) 'Diatom-templated TiO<sub>2</sub> with enhanced photocatalytic activity: biomimetics of photonic crystals', *Appl Phys A*, 113(2), pp. 327–332.

Hegedűs, P., Szabó-Bárdos, E., Horváth, O., Horváth, K. and Hajós, P. (2015) 'TiO<sub>2</sub>-mediated photocatalytic mineralization of a non-ionic detergent: comparison and combination with other advanced oxidation procedures', *Materials (Basel)*, 8(1), pp. 231–250.

Heredia-Guerrero, J. A., Benítez, J. J., Domínguez, E., Bayer, I. S., Cingolani, R., Athanassiou, A. and Heredia, A. (2014) 'Infrared and Raman spectroscopic features of plant cuticles: a review.', *Front Plant Sci*, 5, p. 305.

Hinton, T. J., Jallerat, Q., Palchesko, R. N., Park, J. H., Grodzicki, M. S., Shue, H.-J., Ramadan, M. H., Hudson, A. R. and Feinberg, A. W. (2015) 'Three-dimensional printing of complex biological structures by freeform reversible embedding of suspended hydrogels', *Sci Adv*, 1(9), p. e1500758.

Hokazono, E., Osawa, S., Nakano, T., Kawamoto, Y., Oguchi, Y., Hotta, T., Kayamori, Y., Kang, D., Cho, Y., Shiba, K. and Sato, K. (2009) 'Development of a new measurement method for serum calcium with chlorophosphonazo-III', *Ann Clin Biochem*, 46(4), pp. 296–301.

Hollinger, J. O. (2005) *Bone tissue engineering*. Florida: CRC Press.

Hong, L., Wang, Y. L., Jia, S. R., Huang, Y., Gao, C. and Wan, Y. Z. (2006) 'Hydroxyapatite/bacterial cellulose composites synthesized via a biomimetic route', *Mater Lett*, 60(13–14), pp. 1710–1713.

Hossain, F. M., Murch, G. E., Belova, I. V. and Turner, B. D. (2009) 'Electronic, optical and bonding properties of CaCO<sub>3</sub> calcite', *Solid State Commun*, 149(29–30), pp. 1201–1203.

- Hossain, K. M. Z., Patel, U. and Ahmed, I. (2015) 'Development of microspheres for biomedical applications: a review.', *Prog Biomater*. Springer, 4(1), pp. 1–19.
- Hou, Y. D., Wang, X. C., Wu, L., Chen, X. F., Ding, Z. X., Wang, X. X. and Fu, X. Z. (2008) 'N-doped SiO<sub>2</sub>/TiO<sub>2</sub> mesoporous nanoparticles with enhanced photocatalytic activity under visible-light irradiation.', *Chemosphere*, 72(3), pp. 414–21.
- Huang, R., Liu, Q., Huo, J. and Yang, B. (2017) 'Adsorption of methyl orange onto protonated cross-linked chitosan', *Arab J Chem*. Elsevier, 10(1), pp. 24–32.
- Huong, D. M., Drechsler, M., Cantow, H. J. and Moeller, M. (1993) 'Novel staining method for transmission electron microscopic investigations of semicrystalline polyesters', *Macromolecules*. American Chemical Society, 26(4), pp. 864–866.
- Hyon, S. H. (2000) 'Biodegradable poly (lactic acid) microspheres for drug delivery systems', *Yonsei Med J*, 41(6), p. 720.
- Ishiguro, M. and Endo, T. (2015) 'Effect of the addition of calcium hydroxide on the hydrothermal-mechanochemical treatment of Eucalyptus.', *Bioresour Technol*, 177, pp. 298–301.
- Ismail, A., Mohamed, F., Rosli, L., Shafri, M., Haris, M. and Adina, A. (2016) 'Spectrophotometric determination of Gentamicin loaded PLGA microparticles and method validation via ninhydrin-gentamicin complex as a rapid quantification approach', *J Appl Pharm Sci*, pp. 007-014.
- Ivanova, O., Williams, C. and Campbell, T. (2013) 'Additive Manufacturing(AM) and nanotechnology: promises and challenges.', *Rapid Prototyp J*, 19(5), pp. 353–364.
- Jaafar, I. H., Li, Q., Pearson, R. A., Esposito, G., Jedlicka, S. S. and Coulter, J. P. (2017) 'Vibration assisted injection molding of poly(lactic acid)-thermal, spectroscopic, and mechanical analysis of hydrolytic degradation', *SPE ANTEC*, pp. 1652–1661.
- Jacobs, J. F., Koper, G. J. M. and Ursem, W. N. J. (2007) 'UV protective coatings: A botanical approach', *Prog Org Coatings*, 58(2–3), pp. 166–171.
- Jaffer Al-Timimi, I. A., Onwukwe, U. K., Worsley, M. P. and Sermon, P. A. (2016) 'Biomimetic TiO<sub>2</sub> formation from interfacial sol-gel chemistry leading to new photocatalysts', in Kobayashi, N., Ouchen, F., and Rau, I. (eds), p. 99280E.
- Jastrzębski, W., Sitarz, M., Rokita, M. and Bułat, K. (2011) 'Infrared spectroscopy of different phosphates structures', *Spectrochim Acta Part a Mol Biomol Spectrosc*. Elsevier, 79(4), pp. 722–727.

- Jeevanandam, J., Barhoum, A., Chan, Y. S., Dufresne, A. and Danquah, M. K. (2018) 'Review on nanoparticles and nanostructured materials: history, sources, toxicity and regulations', *Beilstein J Nanotechnol*, 9, pp. 1050–1074.
- Jeffryes, C., Gutu, T., Jiao, J. and Rorrer, G. L. (2008) 'Peptide-mediated deposition of nanostructured TiO<sub>2</sub> into the periodic structure of diatom biosilica', *J Mater Res*. Cambridge University Press, 23(12), pp. 3255–3262.
- JENSEN, J. E. (1977) 'Binding of dyes to chlorhexidine-treated hydroxyapatite', *Eur J Oral Sci*, 85(5), pp. 334–340.
- Jevtić, M., Mitrić, M., Škapin, S., Jančar, B., Ignjatović, N. and Uskoković, D. (2008) 'Crystal structure of hydroxyapatite nanorods synthesized by sonochemical homogeneous precipitation', *Cryst Growth Des*. American Chemical Society, 8(7), pp. 2217–2222.
- Jung, J. W., Lee, H., Hong, J. M., Park, J. H., Shim, J. H., Choi, T. H. and Cho, D.-W. (2015) 'A new method of fabricating a blend scaffold using an indirect three-dimensional printing technique', *Biofabrication*, 7(4), p. 045003.
- Kalia, P., Vizcay-Barrena, G., Fan, J. P., Warley, A., Di Silvio, L. and Huang, J. (2014) 'Nanohydroxyapatite shape and its potential role in bone formation: an analytical study', *J R Soc Interface*. The Royal Society, 11(93), pp. 1–11.
- Kalyanasundaram, K. and Graetzel, M. (2010) 'Artificial photosynthesis: biomimetic approaches to solar energy conversion and storage.', *Curr Opin Biotechnol*, 21(3), pp. 298–310.
- Kamoun, E. A., Kenawy, E.-R. S., Tamer, T. M., El-Meligy, M. A. and Mohy Eldin, M. S. (2015) 'Poly (vinyl alcohol)-alginate physically crosslinked hydrogel membranes for wound dressing applications: Characterization and bio-evaluation', *Arab J Chem*. Elsevier, 8(1), pp. 38–47.
- Kanagasabapathy, A. . and Kumari, S. (2000) 'Guidelines on standard procedures for clinical chemistry'. New Delhi: World Health Organization, p. 107.
- Karimi, L., Zohoori, S. and Yazdanshenas, M. E. (2011) 'Photocatalytic degradation of azo dyes in aqueous solutions under UV irradiation using nano-strontium titanate as the nanophotocatalyst', *J Saudi Chem Soc*, pp. 581–588.
- Karimi, L., Zohoori, S. and Yazdanshenas, M. E. (2014) 'Photocatalytic degradation of azo dyes in aqueous solutions under UV irradiation using nano-strontium titanate as the nanophotocatalyst', *J Saudi Chem Soc*, 18(5), pp. 581–588.
- Kaur, M. and Verma, N. K. (2014) 'CaCO<sub>3</sub>/TiO<sub>2</sub> nanoparticles based dye sensitized solar cell', *J*

*Mater Sci Technol*, 30(4), pp. 328–334.

Ke, T. and Sun, X. (2003) 'Melting behavior and crystallization kinetics of starch and poly(lactic acid) composites', *J Appl Polym Sci*, 89(5), pp. 1203–1210.

Kerr, J. L., Baldwin, D. S., Tobin, M. J., Puskar, L., Kappen, P., Rees, G. N. and Silvester, E. (2013) 'High spatial resolution infrared micro-spectroscopy reveals the mechanism of leaf lignin decomposition by aquatic fungi.', *PLoS One*, 8(4), p. e60857.

Khan, A. F., Awais, M., Khan, A. S., Tabassum, S., Chaudhry, A. A., Rehman, I. U., Ihtesham, A. and Rehman, U. (2013) 'Applied spectroscopy reviews Raman spectroscopy of natural bone and synthetic apatites Raman spectroscopy of natural bone and synthetic apatites', *Appl Spectrosc Rev*, (48).

Kim, H.-M., Himeno, T., Kawashita, M., Kokubo, T. and Nakamura, T. (2004) 'The mechanism of biomineralization of bone-like apatite on synthetic hydroxyapatite: an in vitro assessment', *J R Soc Interface*, 1, pp. 17–22.

Kirk, J. O. . (1994) *Light and Photosynthesis in aquatic ecosystem*. 2nd edn. Press Syndicate of the University of Cambridge.

Kister, G., Cassanas, G., Vert, M., Pauvert, B. and T  rol, A. (1995) 'Vibrational analysis of poly(L-lactic acid)', *J Raman Spectrosc*, 26(4), pp. 307–311.

Kitano, M., Kobayashi, H., Hayashi, S. and Hara, M. (2017) 'Acid Properties of Protonated Titanate Nanotubes', *J Japan Pet Inst*, 60(3), pp. 113–120.

Klosterman, L., Riley, J. K. and Bettinger, C. J. (2015) 'Control of heterogeneous nucleation and growth kinetics of dopamine-melanin by altering substrate chemistry', *Langmuir*, 31(11), pp. 3451–3458.

Koch, K., Bhushan, B. and Barthlott, W. (2008) 'Diversity of structure, morphology and wetting of plant surfaces', *Soft Matter*, 4(10), p. 1943.

Kokubo, T., Kushitani, H., Sakka, S., Kitsugi, T. and Yamamuro, T. (1990) 'Solutions able to reproduce in vivo surface-structure changes in bioactive glass-ceramic A-W3', *J Biomed Mater Res*, 24(6), pp. 721–734.

Kokubo, T. and Takadama, H. (2006) 'How useful is SBF in predicting in vivo bone bioactivity?', *Biomaterials*. Elsevier, 27(15), pp. 2907–2915.

Krebs, F. C. *et al.* (2008) *Polymer photovoltaics: a practical approach*. Society of Photo-Optical Instrumentation Engineers.

Kung, H. H. (1989) *Transition Metal Oxides: Surface Chemistry and Catalysis*. 1st edn, *Stud surface Sci Catal*. 1st edn. Edited by H.H.Kung.

Kuśnieruk, S., Wojnarowicz, J., Chodara, A., Chudoba, T., Gierlotka, S. and Lojkowski, W. (2016) 'Influence of hydrothermal synthesis parameters on the properties of hydroxyapatite nanoparticles', *Beilstein J Nanotechnol*. Beilstein-Institut, 7(1), pp. 1586–1601.

Langford, J. I. and Cernik, R. J. (1991) *The Breadth and Shape of Instrumental Line Profiles in High-Resolution Powder Diffraction*, *J Appl Cryst*.

Leal, D., Matsuhiro, B., Rossi, M. and Caruso, F. (2008) 'FT-IR spectra of alginic acid block fractions in three species of brown seaweeds', *Carbohydr Res*, 343(2), pp. 308–316.

Lee, J. *et al.* (2015) 'Chemical sporulation and germination: cytoprotective nanocoating of individual mammalian cells with a degradable tannic acid-Fe<sup>III</sup> complex', *Nanoscale*, 7(45), pp. 18918–18922.

Leng, Y. (2013) *Materials Characterisation: Introduction to microscopic and Spectroscopic methods*. 2nd edn. Weinham: Wiley-VCH.

Leshuk, T., Krishnakumar, H., de Oliveira Livera, D. and Gu, F. (2018) 'Floating photocatalysts for passive solar degradation of naphthenic acids in oil sands process-affected water', *Water*, 10(2), p. 202.

Lewis, I. R. and Edwards, H. G. M. (eds) (2001) *Handbook of Raman Spectroscopy: From the Research Laboratory to the Process Line*. 1st edn. New York: Taylor & Francis.

Li, L., Mao, C., Wang, J., Xu, X., Pan, H., Deng, Y., Gu, X. and Tang, R. (2011) 'Bio-inspired enamel repair via glu-directed assembly of apatite nanoparticles: an approach to biomaterials with optimal characteristics', *Adv Mater*. John Wiley & Sons, Ltd, 23(40), pp. 4695–4701.

Li, W., Wang, D., Yang, W. and Song, Y. (2016) 'Compressive mechanical properties and microstructure of PVA-HA hydrogels for cartilage repair', *RSC Adv*, 6(24), pp. 20166–20172.

Lide, D. R. and Haynes, W. M. (2010) *CRC Handbook of Chemistry and Physics*. 90th (Inte. Boca Raton, Florida: CRC Press/Taylor and Francis.

Lin, H.-R. and Yeh, Y.-J. (2004) 'Porous alginate/hydroxyapatite composite scaffolds for bone tissue engineering: Preparation, characterization, and in vitro studies', *J Biomed Mater Res*. Wiley-Blackwell, 71B(1), pp. 52–65.

Linsebigler, A. L., Lu, G. and Yates, J. T. (1995) 'Photocatalysis on TiO<sub>2</sub> Surfaces: Principles, Mechanisms, and Selected Results', *Chem Rev*. American Chemical Society, 95(3), pp. 735–758.



- Liu, J., Yang, Q., Yang, W., Li, M. and Song, Y. (2013) 'Aquatic plant inspired hierarchical artificial leaves for highly efficient photocatalysis', *J Mater Chem A*. Royal Society of Chemistry, 1(26), p. 7760.
- Liyanage, D. D., Thamali, R. J. K. A., Kumbalataru, A. A. K., Weliwita, J. A. and Witharana, S. (2016) 'An analysis of nanoparticle settling times in liquids', *J Nanomater*. Hindawi, 2016, pp. 1–7.
- Lizundia, E., Landa, P. and Sarasua, J. (2011) 'Concurrent  $\alpha'$  and  $\alpha$  crystal formation during isothermal crystallizations of poly (L-lactide)', in *ANTEC Proc*, pp. 230–235.
- Luo, L., Yang, Y., Xiao, M., Bian, L., Yuan, B., Liu, Y., Jiang, F. and Pan, X. (2015) 'A novel biotemplated synthesis of TiO<sub>2</sub>/wood charcoal composites for synergistic removal of bisphenol A by adsorption and photocatalytic degradation', *Chem Eng J*. Elsevier, 262, pp. 1275–1283.
- Luque, A. and Hegedus, S. (eds) (2003) 'Handbook of photovoltaic science and engineering', in Chichester, UK: John Wiley & Sons, Ltd.
- Luttrell, T., Halpegamage, S., Tao, J., Kramer, A., Sutter, E. and Batzill, M. (2014) 'Why is anatase a better photocatalyst than rutile?--Model studies on epitaxial TiO<sub>2</sub> films.', *Sci Rep*. Nature Publishing Group, 4, p. 4043.
- M. I. Zaki, M. A. Hasan, F. A. Al-Sagheer, A. and Pasupulety, L. (1999) 'Surface chemistry of acetone on metal oxides: IR observation of acetone adsorption and consequent surface reactions on silica–alumina versus silica and alumina'. American Chemical Society.
- Ma, G. and Liu, X. Y. (2009) 'Hydroxyapatite: Hexagonal or Monoclinic?', *Cryst Growth Des*. American Chemical Society, 9(7), pp. 2991–2994.
- Ma, H. L., Yang, J. Y., Dai, Y., Zhang, Y. B., Lu, B. and Ma, G. H. (2007) 'Raman study of phase transformation of TiO<sub>2</sub> rutile single crystal irradiated by infrared femtosecond laser', *Appl Surf Sci*. North-Holland, 253(18), pp. 7497–7500.
- Ma, R., Xiong, D., Miao, F., Zhang, J. and Peng, Y. (2009) 'Novel PVP/PVA hydrogels for articular cartilage replacement', *Mater Sci Eng C*. Elsevier, 29(6), pp. 1979–1983.
- Ma, X., Jiugao, Y. and Wang, N. (2006) 'Compatibility characterization of poly(lactic acid)/poly(propylene carbonate) blends', *J Polym Sci Part B Polym Phys*, 44(1), pp. 94–101.
- Mahamid, J., Sharir, A., Gur, D., Zelzer, E., Addadi, L. and Weiner, S. (2011) 'Bone mineralization proceeds through intracellular calcium phosphate loaded vesicles: A cryo-electron microscopy study', *J Struct Biol*. Academic Press, 174(3), pp. 527–535.
- Makadia, H. K. and Siegel, S. J. (2011) 'Poly lactic-co-glycolic acid (PLGA) as biodegradable

controlled drug delivery carrier.', *Polymers (Basel)*. NIH Public Access, 3(3), pp. 1377–1397.

Mal, P., Dutta, S., Bandyopadhyay, D., Dutta, K., Basu, A. and Bishayi, B. (2012) 'Gentamicin in combination with ascorbic acid regulates the severity of staphylococcus aureus infection-induced septic arthritis in mice', *Scand J Immunol*. John Wiley & Sons, Ltd, 76(6), pp. 528–540.

Manhas, M. S., Kumar, P., Mohammed, F. and Khan, Z. (2008) 'Oxidative degradation of non-ionic surfactant (TritonX-100) by chromium(VI)', *Colloids Surfaces a Physicochem Eng Asp*. Elsevier, 320(1–3), pp. 240–246.

Mansur, H. S., Sadahira, C. M., Souza, A. N. and Mansur, A. A. P. P. (2008) 'FTIR spectroscopy characterization of poly (vinyl alcohol) hydrogel with different hydrolysis degree and chemically crosslinked with glutaraldehyde', *Mater Sci Eng C*, 28(4), pp. 539–548.

Marković, D., Milovanović, S., Radovanović, Ž., Zizovic, I., Šaponjić, Z. and Radetić, M. (2018) 'Floating photocatalyst based on poly( $\epsilon$ -caprolactone) foam and TiO<sub>2</sub> nanoparticles for removal of textile dyes', *Fibers Polym*, 19(6), pp. 1219–1227.

Martins, N. C. T., Ângelo, J., Girão, A. V., Trindade, T., Andrade, L. and Mendes, A. (2016) 'N-doped carbon quantum dots/TiO<sub>2</sub> composite with improved photocatalytic activity', *Appl Catal B Environ*, 193, pp. 67–74.

Masaki, D., Fukui, Y., Toyohara, K., Ikegame, M., Nagasaka, B. and Yamane, H. (2008) 'Stereocomplex formation in the poly(L-lactic acid)/poly(D-lactic acid) melt blends and the melt spun fibers', *Fiber*, 64(8), pp. 212–219.

Mathur, S. and Singh, M. (2007) *Nanostructured Materials and Nanotechnology: Ceramic Engineering and Science Proceedings, Volume 28, Issue 6*. John Wiley & Sons.

Meaurio, E., López-Rodríguez, N. and Sarasua, J. R. (2006) 'Infrared spectrum of poly(L-lactide): application to crystallinity studies', *Macromolecules*, 39(26), pp. 9291–9301.

Medeiros, S. K., Albuquerque, E. L., Maia, F. F., Caetano, E. W. S. and Freire, V. N. (2007) 'Electronic and optical properties of CaCO<sub>3</sub> calcite, and excitons in Si@CaCO<sub>3</sub> and CaCO<sub>3</sub>@SiO<sub>2</sub> core-shell quantum dots.', *J Phys D Appl Phys*, 40(18), pp. 5747–5752.

Melchels, F. P. ., Domingos, M. A. ., Klein, T. J., Malda, J., Bartolo, P. J. and Huttmacher, D. W. (2012) 'Additive manufacturing of tissues and organs', *Prog Polym Sci*, 37(8), pp. 1079–1104.

Meldrum, F. C. and Cölfen, H. (2008) 'Controlling mineral morphologies and structures in biological and synthetic systems', *Chem Rev*. American Chemical Society, 108(11), pp. 4332–4432.

- Messerschmidt, A. (2007) *X-ray crystallography of biomacromolecules*. Weinheim, Germany: Wiley-VCH Verlag GmbH & Co. KGaA.
- Meyers, M. A. and Chen, P.-Y. (2014) *Biological Materials Science: Biological Materials, bioinspired materials, biomaterials*. 1st edn. Cambridge: Cambridge University Press.
- Miserocchi, G., Sancini, G., Mantegazza, F. and Chiappino, G. (2008) 'Translocation pathways for inhaled asbestos fibers.', *Environ Health*. BioMed Central, 7, p. 4.
- Mørch, Y. A., Donati, I. and Strand, B. L. (2006) 'Effect of Ca<sup>2+</sup>, Ba<sup>2+</sup>, and Sr<sup>2+</sup> on Alginate Microbeads', *Biomacromolecules*, 7(5), pp. 1471–1480.
- Moreira, M. A., Nascimento, M. A., Bozzo, T. A., Cintra, A., Da Silva, S. M., Dalboni, M. A., Mouro, M. G. and Higa, E. M. S. (2014) 'Ascorbic acid reduces gentamicin-induced nephrotoxicity in rats through the control of reactive oxygen species', *Clin Nutr*. Churchill Livingstone, 33(2), pp. 296–301.
- Morin, L. G. (1974) 'Direct colorimetric determination of serum calcium with o-cresolphthalein complexon', *Am J Clin Pathol*, 61(1), pp. 114–117.
- Mukherjee, D., Barghi, S. and Ray, A. (2013) 'Preparation and characterization of the TiO<sub>2</sub> immobilized polymeric photocatalyst for degradation of aspirin under UV and solar light', *Processes*, 2(1), pp. 12–23.
- Myers, D. (1999) *Surfaces, Interfaces, and Colloids*. New York, USA: John Wiley & Sons, Inc.
- Nakata, K. and Fujishima, A. (2012) 'TiO<sub>2</sub> photocatalysis: Design and applications', *J Photochem Photobiol C Photochem Rev*, 13(3), pp. 169–189.
- Nasuha, N., Hameed, B. H. and Din, A. T. M. (2010) 'Rejected tea as a potential low-cost adsorbent for the removal of methylene blue', *J Hazard Mater*, 175(1–3), pp. 126–132.
- Neagle, W. and Rochester, C. H. (1990) 'Infrared study of the adsorption of water and ammonia on calcium carbonate', *J Chem Soc Faraday Trans*, 86(1), p. 181.
- Ogata, Y. and Kosugi, Y. (1970) 'Ultraviolet spectra of l-ascorbic acid and cupric ascorbate complex', *Tetrahedron*, 26(20), pp. 4711–4716.
- Ogino, M., Ohuchi, F. and Hench, L. L. (1980) 'Compositional dependence of the formation of calcium phosphate films on bioglass', *J Biomed Mater Res*, 14(1), pp. 55–64.
- Ohno, T., Sarukawa, K., Tokieda, K. and Matsumura, M. (2001) 'Morphology of a TiO<sub>2</sub> Photocatalyst (Degussa, P-25) Consisting of Anatase and Rutile Crystalline Phases', *J Catal*, 203(1), pp. 82–86.

- Ohtani, B., Prieto-Mahaney, O. O., Li, D. and Abe, R. (2010) 'What is Degussa (Evonik) P25? Crystalline composition analysis, reconstruction from isolated pure particles and photocatalytic activity test', *J Photochem Photobiol a Chem*, 216(2-3), pp. 179-182.
- Ohtsuki, C., Kushitani, H., Kokubo, T., Kotani, S. and Yamamuro, T. (1991) 'Apatite formation on the surface of ceravital-type glass-ceramic in the body', *J Biomed Mater Res*, 25(11), pp. 1363-1370.
- Pamirsky, I. and Golokhvast, K. (2013) 'Silaffins of Diatoms: From applied biotechnology to biomedicine', *Mar Drugs*, 11(9), pp. 3155-3167.
- Pan, P. and Inoue, Y. (2009) 'Polymorphism and isomorphism in biodegradable polyesters', *Prog Polym Sci*, 34(7), pp. 605-640.
- Pan, Y. and Xiong, D. (2009) 'Study on compressive mechanical properties of nanohydroxyapatite reinforced poly(vinyl alcohol) gel composites as biomaterial', *J Mater Sci Mater Med*. Springer US, 20(6), pp. 1291-1297.
- Pannier, A., Soltmann, U., Soltmann, B., Altenburger, R. and Schmitt-Jansen, M. (2014) 'Alginate/silica hybrid materials for immobilization of green microalgae *Chlorella vulgaris* for cell-based sensor arrays', *J Mater Chem B*, 2(45), pp. 7896-7909.
- Park, J. H., Kim, K., Lee, J., Choi, J. Y., Hong, D., Yang, S. H., Caruso, F., Lee, Y. and Choi, I. S. (2014) 'A cytoprotective and degradable metal-polyphenol nanoshell for single-cell encapsulation', *Angew Chemie Int Ed*. WILEY-VCH Verlag, 53(46), pp. 12420-12425.
- Patidar, V. and Jain, P. (2017) 'Green synthesis of TiO<sub>2</sub> nanoparticle using moringa oleifera leaf extract', *Int Res J Eng Technol*, 04(3), pp. 470-473.
- Pawlak, A., Galeski, A. and Rozanski, A. (2014) 'Cavitation during deformation of semicrystalline polymers', *Prog Polym Sci*. Pergamon, 39(5), pp. 921-958.
- Peng, Y.-K., Hu, Y., Chou, H.-L., Fu, Y., Teixeira, I. F., Zhang, L., He, H. and Tsang, S. C. E. (2017) 'Mapping surface-modified titania nanoparticles with implications for activity and facet control', *Nat Commun*. Nature Publishing Group, 8(1), p. 675.
- Porter, J. R., Ruckh, T. T. and Papat, K. C. (2009) 'Bone tissue engineering: a review in bone biomimetics and drug delivery strategies', *Biotechnol Prog*. American Chemical Society (ACS), 25(6), p. NA-NA.
- Potter, C. s. (1990) 'Nutrient leaching from *Acer rubrum* leaves by experimental acid rainfall', *Can J For Res*, 21(2), pp. 222-229.

- Prior, S., Gamazo, C., Irache, J. ., Merkle, H. . and Gander, B. (2000) 'Gentamicin encapsulation in PLA/PLGA microspheres in view of treating Brucella infections', *Int J Pharm*, 196(1), pp. 115–125.
- Pshezhetskii, V. S., Rakhnyanskaya, A. A., Gaponenko, I. M. and Nalbandyan, Y. E. (1990) 'A differential scanning calorimetry study of polyvinyl alcohol', *Polym Sci USSR*. Pergamon, 32(4), pp. 722–726.
- Puntener, A. and Page, C. (2004) *European Ban on Certain Azo Dyes, Qual Environ.*
- Radhakumary, C. and Sreenivasan, K. (2014) 'Gentamicin induced formation of gold nanoparticles as an assay protocol for its detection', *Colloids Surfaces A Physicochem Eng Asp*. Elsevier, 443, pp. 326–330.
- Ramimoghadam, D., Bagheri, S. and Abd Hamid, S. B. (2014) 'Biotemplated synthesis of anatase titanium dioxide nanoparticles via lignocellulosic waste material.', *Biomed Res Int*. Hindawi, 2014, p. 205636.
- Rechberger, F. and Niederberger, M. (2017) 'Synthesis of aerogels: from molecular routes to 3-dimensional nanoparticle assembly', *Nanoscale Horizons*. Royal Society of Chemistry, 2(1), pp. 6–30.
- Reyes-Gasga, J., Koudriavtseva, O., Herrera-Becerra, R. and Escobosa, A. (2015) 'XRD characterization of crystallinity of human tooth enamel under influence of mechanical grinding', *Mater Sci Appl*, 6(6), pp. 464–472.
- Reyes-Gasga, J., Martínez-Piñeiro, E. L. and Brès, É. F. (2012) 'Crystallographic structure of human tooth enamel by electron microscopy and x-ray diffraction: Hexagonal or monoclinic?', *J Microsc*, pp. 102–109.
- Ronzhina, D. a., Ivanov, L. a. and P'yankov, V. I. (2010) 'Chemical composition of leaves and structure of photosynthetic apparatus in aquatic higher plants', *Russ J Plant Physiol*, 57(3), pp. 368–375.
- Ronzhina, D. a. and P'yankov, V. I. (2001) 'Structure of the photosynthetic apparatus in leaves of freshwater hydrophytes:1. General characteristic of the Leaf mesophyll and a comparison with terrestrial plants', *Russ J Plant Physiol*, 48(5), pp. 567–575.
- Ronzhina, D. A. and P'yankov, V. I. (2001) 'Structure of the photosynthetic apparatus in leaves of freshwater hydrophytes: 2. Quantitative characterization of leaf mesophyll and the functional activity of leaves with different degrees of submersion', *Russ J Plant Physiol*, 48(6), pp. 723–732.
- Roobottom, H. K., Jenkins, H. D. B., Passmore, J. and Glasser, L. (1999) 'Thermochemical radii of

complex ions', *J Chem Educ*, 76(11), p. 1570.

Rudra, R., Kumar, V. and Kundu, P. P. (2015) 'Acid catalysed cross-linking of poly vinyl alcohol (PVA) by glutaraldehyde: effect of crosslink density on the characteristics of PVA membranes used in single chambered microbial fuel cells', *RSC Adv*, 5(101), pp. 83436–83447.

Sancilio, S., Gallorini, M., Di Nisio, C., Marsich, E., Di Pietro, R., Schweikl, H. and Cataldi, A. (2018) 'Alginate/hydroxyapatite-based nanocomposite scaffolds for bone tissue engineering improve dental pulp biomineralization and differentiation', *Stem Cells Int*. Hindawi, 2018, pp. 1–13.

Sarti, B. and Scandola, M. (1995) 'Viscoelastic and thermal properties of collagen/poly(vinyl alcohol) blends', *Biomaterials*. Elsevier, 16(10), pp. 785–792.

Scanlon, D. O., Dunnill, C. W., Buckeridge, J., Shevlin, S. A., Logsdail, A. J., Woodley, S. M., Catlow, C. R. A., Powell, M. J., Palgrave, R. G., Parkin, I. P., Watson, G. W., Keal, T. W., Sherwood, P., Walsh, A. and Sokol, A. A. (2013) 'Band alignment of rutile and anatase TiO<sub>2</sub>', *Nat Mater*. Nature Publishing Group, 12(9), pp. 798–801.

Schaffler, M. B., Cheung, W.-Y., Majeska, R. and Kennedy, O. (2014) 'Osteocytes: master orchestrators of bone.', *Calcif Tissue Int*. NIH Public Access, 94(1), pp. 5–24.

Schneider, J., Matsuoka, M., Takeuchi, M., Zhang, J., Horiuchi, Y., Anpo, M. and Bahnemann, D. W. (2014) 'Understanding TiO<sub>2</sub> photocatalysis: mechanisms and materials', *Chem Rev*. American Chemical Society, 114(19), p. 140919080959008.

Schwarcz, H. P., Abueidda, D. and Jasiuk, I. (2017) 'The Ultrastructure of Bone and Its Relevance to Mechanical Properties', *Front Phys*. Frontiers, 5, p. 39.

Schwarzenbach, R. P., Egli, T., Hofstetter, T. B., von Gunten, U. and Wehrli, B. (2010) 'Global water pollution and human health', *Annu Rev Environ Resour*. Annual Reviews, 35(1), pp. 109–136.

Serpone, N., Terzian, R., Lawless, D., Kennepohl, P. and Sauvé, G. (1993) 'On the usage of turnover numbers and quantum yields in heterogeneous photocatalysis', *J Photochem Photobiol A Chem*. Elsevier, 73(1), pp. 11–16.

Sharma, V. K., Anquandah, G. A. K., Yngard, R. A., Kim, H., Fekete, J., Bouzek, K., Ray, A. K. and Golovko, D. (2009) 'Nonylphenol, octylphenol, and bisphenol-A in the aquatic environment: A review on occurrence, fate, and treatment', *J Environ Sci Heal Part A*, 44(5), pp. 423–442.

Sharpe, L. A., Daily, A. M., Horava, S. D. and Peppas, N. A. (2014) 'Therapeutic applications of hydrogels in oral drug delivery.', *Expert Opin Drug Deliv*. NIH Public Access, 11(6), pp. 901–15.

- Sheikh, F. A., M Barakat, N. A., Kanjwal, M. A., Jin Park, S., Kwang Park, D. and Yong Kim, H. (2010) 'Synthesis of poly(vinyl alcohol) (PVA) nanofibers incorporating hydroxyapatite nanoparticles as future implant materials', *Macromol Res*, 18(1), pp. 59–66.
- Shi-Fu, C. and Xue-Li, C. (2010) 'Photocatalytic decomposition of oil films floating on water using TiO<sub>2</sub> supported on hollow glass microbeads by sunlight', *Chinese J Chem*, 16(5), pp. 421–424.
- Shi, X., Jiang, J., Sun, L. and Gan, Z. (2011) 'Hydrolysis and biomineralization of porous PLA microspheres and their influence on cell growth', *Colloids Surfaces B Biointerfaces*. Elsevier, 85(1), pp. 73–80.
- Shkarina, S., Shkarin, R., Weinhardt, V., Melnik, E., Vacun, G., Kluger, P., Loza, K., Epple, M., Ivlev, S. I., Baumbach, T., Surmeneva, M. A. and Surmenev, R. A. (2018) '3D biodegradable scaffolds of polycaprolactone with silicate-containing hydroxyapatite microparticles for bone tissue engineering: high-resolution tomography and in vitro study', *Sci Rep*. Nature Publishing Group, 8(1), p. 8907.
- Singh, S., Singh, P. K. and Mahalingam, H. (2015) 'A novel and effective strewn polymer-supported titanium dioxide photocatalyst for environmental remediation', *J Mater Environ Sci*, 6(2), pp. 349–358.
- Singh, S., Singh, P. K. and Mahalingam, H. (2015) 'An effective and low-cost TiO<sub>2</sub>/polystyrene floating photocatalyst for environmental remediation', *Int J Environ Res*, 9(2), pp. 535–544.
- Sisson, A. L., Ekinici, D. and Lendlein, A. (2013) 'The contemporary role of ε-caprolactone chemistry to create advanced polymer architectures', *Polymer (Guildf)*. Elsevier, 54(17), pp. 4333–4350.
- Skinner, L. and Sambles, J. (1972) 'The Kelvin equation: A review', *Aerosol Sci*, 3, pp. 199–210.
- Soares, J. P., Santos, J. E., Chierice, G. O. and G Cavalheiro, E. T. (2004) 'Thermal behavior of alginic acid and its sodium salt', *Eclat Quimca*, 29(2), pp. 53–56.
- Somorjai, G. A. (1995) *Introduction to surface chemistry and catalysis*, *Chem Vap Depos*. New York: Wiley-Interscience.
- Son, H. Y., Kim, K. R., Hong, C. A. and Nam, Y. S. (2018) 'Morphological evolution of gold nanoparticles into nanodendrites using catechol-grafted polymer templates', *ACS Omega*, 3(6), pp. 6683–6691.
- Song, J., Xu, J., Filion, T., Saiz, E., Tomsia, A. P., Lian, J. B., Stein, G. S., Ayers, D. C. and Bertozzi, C. R. (2009) 'Elastomeric high-mineral content hydrogel-hydroxyapatite composites for orthopedic

applications.', *J Biomed Mater Res A*. Howard Hughes Medical Institute, 89(4), pp. 1098–107.

Sotiropoulou, S., Sierra-Sastre, Y., Mark, S. S. and Batt, C. A. (2008) 'Biotemplated nanostructured materials', *Chem Mater*. American Chemical Society, 20(3), pp. 821–834.

Stetefeld, J., Mckenna, S. A. and Patel, T. R. (2016) 'Dynamic light scattering: a practical guide and applications in biomedical sciences', *Biophys Rev*.

Stroyuk, A. L., Kryukov, A. I., Kuchmii, S. Y. and Pokhodenko, V. D. (2005) 'Quantum size effects in semiconductor photocatalysis', *Theor Exp Chem*, 41(4), pp. 207–228.

Su, B.-L., Sanchez, C. and Yang, X.-Y. (2012) *Hierarchically structured porous materials : from nanoscience to catalysis, separation, optics, energy, and life science*. Wiley-VCH.

Sun, J. and Tan, H. (2013) 'Alginate-based biomaterials for regenerative medicine applications', *Materials (Basel)*. Multidisciplinary Digital Publishing Institute, pp. 1285–1309.

Suzuki, K., Yumura, T., Mizuguchi, M., Sato, K., Tanaka, J. and Akashi, M. (2001) *Apatite-silica gel composite materials prepared by a new alternate soaking process*, *J Sol-Gel Sci Technol*.

Syazwan, M. and Sasaki, T. (2018) 'Rapid crystallization and mesophase formation of poly(L-lactic acid) during precipitation from a solution', *e-Polymers*, 18(4), pp. 331–337.

Tabe, Y., Hibino, M. and Yao, T. (2007) 'Fabrication of hydroxyapatite microcapsules by biomimetic method', *Key Eng Mater*, 330–332, pp. 1029–1032.

Tábi, T., Hajba, S. and Kovács, J. G. (2016) 'Effect of crystalline forms ( $\alpha'$  and  $\alpha$ ) of poly(lactic acid) on its mechanical, thermo-mechanical, heat deflection temperature and creep properties', *Eur Polym J*. Pergamon, 82, pp. 232–243.

Taguchi, T., Kishida, A. and Akashi, M. (1998) 'Hydroxyapatite formation on/in poly(vinyl alcohol) hydrogel matrices using a novel alternate soaking process', *Chem Lett*, 27(8), pp. 711–712.

Taguchi, T., Kishida, A. and Akashi, M. (1999) 'Apatite formation on/in hydrogel matrices using an alternate soaking process (III) : Effect of physico-chemical factors on apatite formation on/in poly(vinyl alcohol) hydrogel matrices', *J Biomater Sci Polym Ed*, 10(8), pp. 795–804.

Takagahara, T. and Takeda, K. (1992) 'Theory of the quantum confinement effect on excitons in quantum dots of indirect-gap materials', *Phys Rev B*, 46(23), pp. 15578–15581.

Tang, H., Prasad, K., Sanjinès, R., Schmid, P. E. and Lévy, F. (1994) 'Electrical and optical properties of TiO<sub>2</sub> anatase thin films', *J Appl Phys*, 75(4), pp. 2042–2047.

Tavafoghi, M. and Cerruti, M. (2016) 'The role of amino acids in hydroxyapatite mineralization.'



*J R Soc Interface*. The Royal Society, 13(123), p. 20160462.

Teng, L., Xu, X., Nie, W., Zhou, Y., Song, L. and Chen, P. (2015) 'Synthesis and degradability of a star-shaped polylactide based on l-lactide and xylitol', *J Polym Res*. Springer Netherlands, 22(5), p. 83.

Thamaphat, K., Limsuwan, P. and Ngotawornchai, B. (2008) 'Phase Characterization of TiO<sub>2</sub> Powder by XRD and TEM', *Nat Sci*, 42, pp. 357–361.

The Royal Society, Engineering, T. R. A. of, Dowling, A., Clift, R., Grobert, N., Hutton, D., Oliver, R., O'Neill, O., Pethica, J., Pidgeon, N., Porritt, J., Ryan, J. and Et Al. (2004) 'Nanoscience and nanotechnologies: opportunities and uncertainties', *London R Soc R Acad Eng Rep*, 46(July), pp. 618–618.

Tian, F., Zhang, Y., Zhang, J. and Pan, C. (2012) 'Raman spectroscopy: A new approach to measure the percentage of anatase TiO<sub>2</sub> exposed (001) facets', *J Phys Chem C*, 116(13), pp. 7515–7519.

Tsuji, H. and Ikada, Y. (1998) 'Properties and morphology of poly(L-lactide). II. hydrolysis in alkaline solution', *J Polym Sci Part A Polym Chem*. Wiley-Blackwell, 36(1), pp. 59–66.

Tsuji, H., Mizuno, A. and Ikada, Y. (2000) 'Properties and morphology of poly(L-lactide). III. Effects of initial crystallinity on long-term in vitro hydrolysis of high molecular weight poly(L-lactide) film in phosphate-buffered solution', *J Appl Polym Sci*. Wiley-Blackwell, 77(7), pp. 1452–1464.

Turco, G., Marsich, E., Bellomo, F., Semeraro, S., Donati, I., Brun, F., Grandolfo, M., Accardo, A. and Paoletti, S. (2009) 'Alginate/hydroxyapatite biocomposite for bone ingrowth: A trabecular structure with high and isotropic connectivity', *Biomacromolecules*, 10(6), pp. 1575–1583.

Vallet-Regí, M., Balas, F. and Arcos, D. (2007) 'Mesoporous materials for drug delivery', *Angew Chemie Int Ed*. John Wiley & Sons, Ltd, 46(40), pp. 7548–7558.

Vasilescu, E., Maria, J., Moreno, C., Vasilescu, C., Grigore, F. and Drob, S. I. (2011) 'Interactions of some new scaffolds with simulated body fluids', *REV CHIM*, 62(2).

Vázquez, G., Fontenla, E., Santos, J., Freire, M. S., González-Álvarez, J. and Antorrena, G. (2008) 'Antioxidant activity and phenolic content of chestnut (*Castanea sativa*) shell and eucalyptus (*Eucalyptus globulus*) bark extracts', *Ind Crops Prod*, 28(3), pp. 279–285.

Venkateswarlu, K., Chandra Bose, A. and Rameshbabu, N. (2010) 'X-ray peak broadening studies of nanocrystalline hydroxyapatite by Williamson–Hall analysis', *Phys B Condens Matter*,

405(20), pp. 4256–4261.

Vincent, J. F. V., Bogatyreva, O. A., Bogatyrev, N. R., Bowyer, A. and Pahl, A.-K. (2006) 'Biomimetics: its practice and theory', *J R Soc Interface*, 3(9), pp. 471–482.

Vorholt, J. A. (2012) 'Microbial life in the phyllosphere.', *Nat Rev Microbiol*. Nature Publishing Group, a division of Macmillan Publishers Limited. All Rights Reserved., 10(12), pp. 828–40.

Wang, C.-G., Liao, J.-W., Gou, B.-D., Huang, J., Tang, R.-K., Tao, J.-H., Zhang, T.-L. and Wang, K. (2009) 'Crystallization at multiple sites inside particles of amorphous calcium phosphate', *Cryst Growth Des*, 9(6), pp. 2620–2626.

Wang, C.-Y., Huang, K.-S., Yang, C.-H., Chang, W.-R., Grumezescu, A. M. and Chemistry, A. (2014) 'A facile synthesis of gold nanoparticles-alginate composite spheres', *Int J Latest Res Sci Technol*, 3(2), pp. 139–143.

Wang, K., Leng, Y., Lu, X., Ren, F., Geb, X. and Ding, Y. (2005) 'Theoretical analysis of calcium phosphate precipitation in simulated body fluid', *Biomaterials*, 26(10), pp. 1097–1108.

Wang, L. and Nancollas, G. H. (2008) 'Calcium orthophosphates: crystallization and dissolution.', *Chem Rev*. NIH Public Access, 108(11), pp. 4628–69.

Wang, P., Wu, C., Guo, Y. and Wang, C. (2016) 'Experimental and theoretical studies on methylene blue and methyl orange sorption by wheat straw-derived biochar with a large surface area', *Phys Chem Chem Phys*. The Royal Society of Chemistry, 18(43), pp. 30196–30203.

Wang, W., Oaki, Y., Ohtsuki, C., Nakano, T. and Imai, H. (2013) 'Formation of c-axis-oriented columnar structures through controlled epitaxial growth of hydroxyapatite', *J Asian Ceram Soc*, 1(2), pp. 143–148.

Wang, X. X., Yu, J. C., Liu, P., Wang, X. X., Su, W. and Fu, X. (2006) 'Probing of photocatalytic surface sites on  $\text{SO}_4^{2-}/\text{TiO}_2$  solid acids by in situ FT-IR spectroscopy and pyridine adsorption', *J Photochem Photobiol A Chem*, 179(3), pp. 339–347.

Wang, Z., Yang, C., Lin, T., Yin, H., Chen, P., Wan, D., Xu, F., Huang, F., Lin, J., Xie, X. and Jiang, M. (2013) 'Visible-light photocatalytic, solar thermal and photoelectrochemical properties of aluminium-reduced black titania', *Energy Environ Sci*, 6(10), p. 3007.

Watanabe, J. and Akashi, M. (2008) 'Anisotropic hydroxyapatite formation inside agarose gels by integration of electrophoretic and alternate soaking approaches', *J Biomater Sci Polym Edn*, 19(12), pp. 1625–1635.

Wessing, B., Dent, M., Lettner, S. and Zechner, W. (2017) 'Guided bone regeneration with

collagen membranes and particulate graft materials: A systematic review and meta-analysis', *Int J Oral Maxillofac Implant.*

Williamson, G. . and Hall, W. . (1953) 'X-ray line broadening from filed aluminium and wolfram', *Acta Metall*, 1(1), pp. 22–31.

Wise, F. W. (2000) 'Lead salt quantum dots: the limit of strong quantum confinement', *Acc Chem Res*, 33(11), pp. 773–780.

Xu, F., Li, Y., Deng, Y. and Xiong, J. (2008) 'Porous nano-hydroxyapatite/poly(vinyl alcohol) composite hydrogel as artificial cornea fringe: characterization and evaluation in vitro', *J Biomater Sci Polym Ed*, 19(4), pp. 431–439.

Xue, H., Jiang, Y., Yuan, K., Yang, T., Hou, J., Cao, C., Feng, K. and Wang, X. (2016) 'Floating photocatalyst of B–N–TiO<sub>2</sub>/expanded perlite: a sol–gel synthesis with optimized mesoporous and high photocatalytic activity', *Sci Rep.* Nature Publishing Group, 6(1), p. 29902.

Yang, W., Xi, X. F., Li, J. . and Cai, K. . (2013) 'Comparison of crystal structure between carbonated hydroxyapatite and natural bone apatite with theoretical calculation', *Asian J Chem*, 25(8).

Yang, X.-Y., Chen, L.-H., Li, Y., Rooke, J. C., Sanchez, C. and Su, B.-L. (2017) 'Hierarchically porous materials: synthesis strategies and structure design', *Chem Soc Rev.* The Royal Society of Chemistry, 46(2), pp. 481–558.

Yao, B., Wang, L., Wang, C., Wang, Y. and Zhao, G. (2007) 'Preparation and performances of RuO<sub>2</sub>/TiO<sub>2</sub>films photocatalyst supported on float pearls', *Chinese J Chem Phys*, 20(6), pp. 789–795.

Yu, J. C., Zhang, L. and Yu, J. (2002) 'Direct sonochemical preparation and characterization of highly active mesoporous TiO<sub>2</sub> with a bicrystalline framework', *Chem Mater*, 14(11), pp. 4647–4653.

Yu, L., Xi, J., Li, M.-D., Chan, H. T., Su, T., Phillips, D. L. and Chan, W. K. (2012) 'The degradation mechanism of methyl orange under photo-catalysis of TiO<sub>2</sub>', *Phys Chem Chem Phys*, 14(10), p. 3589.

Yuniarto, K., Purwanto, Y. A., Purwanto, S., Welt, B. A., Purwadaria, H. K. and Sunarti, T. C. (2016) 'Infrared and Raman studies on polylactide acid and polyethylene glycol-400 blend', in *J Chem Phys*, p. 020101.

Zaki, M., Hasan, M., Al-Sagheer, F. and Pasupulety, L. (2001) 'In situ FTIR spectra of pyridine adsorbed on SiO<sub>2</sub>-Al<sub>2</sub>O<sub>3</sub>, TiO<sub>2</sub>, ZrO<sub>2</sub> and CeO<sub>2</sub>: general considerations for the identification of acid sites on surfaces of finely divided metal oxides', *Collids Surfaces A-Physiochemical Eng Asp*,

190(3), pp. 261–274.

Zaki, M. I., Hasan, M. A. and Pasupulety, L. (2001) 'Surface reactions of acetone on Al<sub>2</sub>O<sub>3</sub>, TiO<sub>2</sub>, ZrO<sub>2</sub>, and CeO<sub>2</sub>: IR spectroscopic assessment of impacts of the surface acid–base properties', *Langmuir*, 17(3), pp. 768–774.

Zaleski, S., Clark, K. A., Smith, M. M., Eilert, J. Y., Doty, M. and Van Duyne, R. P. (2017) 'Identification and quantification of intravenous therapy drugs using normal Raman spectroscopy and electrochemical surface-enhanced Raman spectroscopy', *Anal Chem*. American Chemical Society, 89(4), pp. 2497–2504.

Zayat, M., Garcia-Parejo, P. and Levy, D. (2007) 'Preventing UV-light damage of light sensitive materials using a highly protective UV-absorbing coating', *Chem Soc Rev*, 36(8), p. 1270.

Zhang, J., Wang, Q. and Wang, A. (2010) 'In situ generation of sodium alginate/hydroxyapatite nanocomposite beads as drug-controlled release matrices', *Acta Biomater*. Elsevier, 6(2), pp. 445–454.

Zhang, J., Zhou, P., Liu, J. and Yu, J. (2014) 'New understanding of the difference of photocatalytic activity among anatase, rutile and brookite TiO<sub>2</sub>', *Phys. Chem. Chem. Phys.*, 16(38), pp. 20382–20386.

Zhang, S., Li, H. and Yang, Z. (2018) 'Synthesis, structural characterization and evaluation of a novel floating metal-free photocatalyst based on g-C<sub>3</sub>N<sub>4</sub> grafted expanded perlite for the degradation of dyes', *Mater Technol*, 33(1), pp. 1–9.

Zhang, W. F., He, Y. L., Zhang, M. S., Yin, Z. and Chen, Q. (2000) 'Raman scattering study on anatase TiO<sub>2</sub> nanocrystals', *J Phys D Appl Phys*, 33(8), pp. 912–916.

Zhang, Z. B., Wang, C. C., Zakaria, R. and Ying, J. Y. (1998) 'Role of particle size in nanocrystalline TiO<sub>2</sub>-based photocatalysts', *J Phys Chem Biol*. American Chemical Society, 102(52), pp. 10871–10878.

Zhao, J., Liu, Y., Sun, W.-B. and Zhang, H. (2011) 'Amorphous calcium phosphate and its application in dentistry.', *Chem Cent J*. Springer, 5, p. 40.

Zhao, Y., Wang, Z. and Yang, F. (2005) 'Characterization of poly(D,L-lactic acid) synthesized by direct melt polymerization and its application in Chinese traditional medicine compound prescription microspheres', *J Appl Polym Sci*, 97(1), pp. 195–200.

Zhao, Z., Buscaglia, V., Viviani, M., Buscaglia, M. T., Mitoseriu, L., Testino, A., Nygren, M., Johansson, M. and Nanni, P. (2004) 'Grain-size effects on the ferroelectric behavior of dense

nanocrystalline BaTiO<sub>3</sub> ceramics', *Phys Rev B -Condensed Matter Mater Phys*, 70(2), p. 024107.

Zhe, Z., Zhang, S., Venkatraman, S. S. and Lei, S. (2011) 'Growth of hydroxyapatite coating on polymer microspheres', *Nanosci Nanotechnol Lett*, 3, pp. 472–476.

Zhou, H., Guo, J., Li, P., Fan, T., Zhang, D. and Ye, J. (2013) 'Leaf-architected 3D hierarchical artificial photosynthetic system of perovskite titanates towards CO<sub>2</sub> photoreduction into hydrocarbon fuels.', *Sci Rep*. Nature Publishing Group, 3, p. 1667.

Zhou, H., Li, X., Fan, T., Osterloh, F. E., Ding, J., Sabio, E. M., Zhang, D. and Guo, Q. (2010) 'Artificial inorganic leaves for efficient photochemical hydrogen production inspired by natural photosynthesis.', *Adv Mater*, 22(9), pp. 951–6.

Zhu, B., Wang, S., Wang, L., Yang, Y., Liang, J., Cao, B., Zhu, B., Wang, S., Wang, L., Yang, Y., Liang, J. and Cao, B. (2017) 'Preparation of hydroxyapatite/tannic acid coating to enhance the corrosion resistance and cytocompatibility of AZ31 magnesium alloys', *Coatings*. Multidisciplinary Digital Publishing Institute, 7(7), p. 105.